Politecnico di Bari

Repository Istituzionale dei Prodotti della Ricerca del Politecnico di Bari

Numerical investigation of chemiluminescence and acoustic radiation in hydrogen flames

This is a PhD Thesis

Original Citation:
Numerical investigation of chemiluminescence and acoustic radiation in hydrogen flames / Schiavone, Francesco Gabriele. - ELETTRONICO. - (2026).

Availability:
This version is available at http://hdl.handle.net/11589/301020 since: 2026-05-14

Published version
DOI:

Publisher: Politecnico di Bari

Terms of use:

(Article begins on next page)

03 June 2026

Politecnico di Bari

Department of Mechanics, Mathematics and Management

Mechanical and Management Engineering

Ph.D. Program

SSD: IIND-06/A – Fluid Machinery

Final Dissertation

Numerical investigation of chemiluminescence and acoustic radiation in hydrogen flames

by

Francesco Gabriele Schiavone

Supervisors:

Prof. Marco Torresi

Prof. Davide Laera

Coordinator of the Ph.D. Program:
Prof. Giuseppe Casalino

Course No. 38, 01/11/2022 – 28/02/2026

Politecnico di Bari

Department of Mechanics, Mathematics and Management

Mechanical and Management Engineering

Ph.D. Program

SSD: IIND-06/A – Fluid Machinery

Final Dissertation

Numerical investigation of chemiluminescence and acoustic radiation in hydrogen flames

by

Francesco Gabriele Schiavone

Referees:

Prof. Tommaso Capurso

Dr. Carmen Jiménez

Supervisors:

Prof. Marco Torresi

Prof. Davide Laera

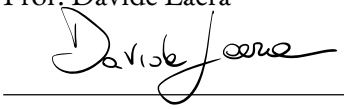

Coordinator of the Ph.D. Program:
Prof. Giuseppe Casalino

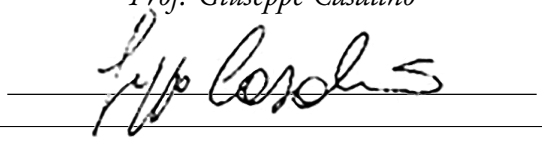

Course No. 38, 01/11/2022 – 28/02/2026

Politecnico di Bari

LIBERATORIA PER L'ARCHIVIAZIONE DELLA TESI DI DOTTORATO

Al Magnifico Rettore
del Politecnico di Bari

Il sottoscritto Schiavone Francesco Gabriele nato a Bari (BA) il 23/12/1998

residente a Bitetto (BA) in via Gatti Francesco 13 e-mail f.schiavone11@phd.poliba.it

iscritto al 3° anno di Corso di Dottorato di Ricerca in Ingegneria Meccanica e Gestionale ciclo XXXVIII

ed essendo stato ammesso a sostenere l'esame finale con la prevista discussione della tesi dal titolo:

Numerical investigation of chemiluminescence and acoustic radiation in hydrogen flames

DICHIARA

1) di essere consapevole che, ai sensi del D.P.R. n. 445 del 28.12.2000, le dichiarazioni mendaci, la falsità negli atti e l'uso di atti falsi sono puniti ai sensi del codice penale e delle Leggi speciali in materia, e che nel caso ricorressero dette ipotesi, decade fin dall'inizio e senza necessità di nessuna formalità dai benefici conseguenti al provvedimento emanato sulla base di tali dichiarazioni;
2) di essere iscritto al Corso di Dottorato di ricerca in Ingegneria Meccanica e Gestionale ciclo XXXVIII, corso attivato ai sensi del "*Regolamento dei Corsi di Dottorato di ricerca del Politecnico di Bari*", emanato con D.R. n.286 del 01.07.2013;
3) di essere pienamente a conoscenza delle disposizioni contenute nel predetto Regolamento in merito alla procedura di deposito, pubblicazione e autoarchiviazione della tesi di dottorato nell'Archivio Istituzionale ad accesso aperto alla letteratura scientifica;
4) di essere consapevole che attraverso l'autoarchiviazione delle tesi nell'Archivio Istituzionale ad accesso aperto alla letteratura scientifica del Politecnico di Bari (IRIS-POLIBA), l'Ateneo archivierà e renderà consultabile in rete (nel rispetto della Policy di Ateneo di cui al D.R. 642 del 13.11.2015) il testo completo della tesi di dottorato, fatta salva la possibilità di sottoscrizione di apposite licenze per le relative condizioni di utilizzo (di cui al sito http://www.creativecommons.it/Licenze), e fatte salve, altresì, le eventuali esigenze di "embargo", legate a strette considerazioni sulla tutelabilità e sfruttamento industriale/commerciale dei contenuti della tesi, da rappresentarsi mediante compilazione e sottoscrizione del modulo in calce (Richiesta di embargo);
5) che la tesi da depositare in IRIS-POLIBA, in formato digitale (PDF/A) sarà del tutto identica a quelle **consegnate**/inviate/da inviarsi ai componenti della commissione per l'esame finale e a qualsiasi altra copia depositata presso gli Uffici del Politecnico di Bari in forma cartacea o digitale, ovvero a quella da discutere in sede di esame finale, a quella da depositare, a cura dell'Ateneo, presso le Biblioteche Nazionali Centrali di Roma e Firenze e presso tutti gli Uffici competenti per legge al momento del deposito stesso, e che di conseguenza va esclusa qualsiasi responsabilità del Politecnico di Bari per quanto riguarda eventuali errori, imprecisioni o omissioni nei contenuti della tesi;
6) che il contenuto e l'organizzazione della tesi è opera originale realizzata dal sottoscritto e non compromette in alcun modo i diritti di terzi, ivi compresi quelli relativi alla sicurezza dei dati personali; che pertanto il Politecnico di Bari ed i suoi funzionari sono in ogni caso esenti da responsabilità di qualsivoglia natura: civile, amministrativa e penale e saranno dal sottoscritto tenuti indenni da qualsiasi richiesta o rivendicazione da parte di terzi;
7) che il contenuto della tesi non infrange in alcun modo il diritto d'Autore né gli obblighi connessi alla salvaguardia di diritti morali od economici di altri autori o di altri aventi diritto, sia per testi, immagini, foto, tabelle, o altre parti di cui la tesi è composta.

Luogo e data Bari, 14/05/2026 Firma Francesco Gabriele Schiavone

Il sottoscritto, con l'autoarchiviazione della propria tesi di dottorato nell'Archivio Istituzionale ad accesso aperto del Politecnico di Bari (POLIBA-IRIS), pur mantenendo su di essa tutti i diritti d'autore, morali ed economici, ai sensi della normativa vigente (Legge 633/1941 e ss.mm.ii.),

CONCEDE

- al Politecnico di Bari il permesso di trasferire l'opera su qualsiasi supporto e di convertirla in qualsiasi formato al fine di una corretta conservazione nel tempo. Il Politecnico di Bari garantisce che non verrà effettuata alcuna modifica al contenuto e alla struttura dell'opera.
- al Politecnico di Bari la possibilità di riprodurre l'opera in più di una copia per fini di sicurezza, back-up e conservazione.

Luogo e data Bari, 14/05/2026 Firma Francesco Gabriele Schiavone

Numerical investigation of chemiluminescence and acoustic radiation in hydrogen flames

DOCTORAL DISSERTATION BY

Francesco Gabriele Schiavone

Supervisors

Prof. Marco Torresi

Department of Mechanics, Mathematics and Management, Polytechnic University of Bari – Bari, Italy

Prof. Davide Laera

Department of Mechanics, Mathematics and Management, Polytechnic University of Bari – Bari, Italy

Referees

Prof. Tommaso Capurso

LIFSE, Arts et Métiers Institute of Technology, CNAM – Paris, France

Dr. Carmen Jiménez

Department of Energy, CIEMAT – Madrid, Spain

Board of Examiners

Prof. Maria Grazia De Giorgi

Department of Engineering for Innovation, University of Salento – Lecce, Italy

Prof. Francesco Fornarelli

Department of Agricultural Sciences, Food, Natural Resources and Engineering, University of Foggia – Foggia, Italy

Dr. Thierry Poinsot

Institut de Mécanique des Fluides de Toulouse, Université de Toulouse, CNRS – Toulouse, France

Dr. Giancarlo Sorrentino

Istituto di Scienze e Tecnologie per l'Energia e la Mobilità Sostenibili (STEMS-CNR) – Naples, Italy

Defended on May 22, 2026 in Bari, Italy

To my parents.

Hâtez-vous lentement, et sans perdre courage,
Vingt fois sur le métier remettez votre ouvrage,
Polissez-le sans cesse, et le repolissez,
Ajoutez quelquefois, et souvent effacez.

Slowly make haste, and without losing courage;
Twenty times redo your work;
Polish and re-polish endlessly,
And sometimes add, but often take away.

— Nicolas Boileau-Despréaux
The Art of Poetry, 1674

Numerical investigation of chemiluminescence and acoustic radiation in hydrogen flames

Abstract

Hydrogen combustion is a promising solution to reduce carbon emissions in gas turbines for aircraft propulsion and power generation. However, the markedly different physical and chemical properties of hydrogen compared to conventional hydrocarbon fuels pose significant modeling and technological challenges. To improve the efficiency and reduce nitrogen oxide emissions, gas turbines are commonly operated under lean premixed conditions, which, however, promote thermoacoustic instabilities. Moreover, for hydrogen flames, this regime is characterized by a subunity Lewis number, promoting strong thermodiffusive effects and intrinsic flame instabilities. To characterize thermoacoustic instabilities, it is fundamental to capture the unsteady heat release rate (HRR). Its direct experimental measurement, however, is impractical, hence chemiluminescence of excited radicals is often used as a surrogate. Moreover, thermoacoustic instabilities can be triggered by combustion noise, which has become an increasingly critical concern also due to stricter noise regulations. This dissertation addresses these challenges, focusing on chemical modeling, applicability of chemiluminescence as a HRR surrogate, and combustion noise generation, through high-fidelity numerical simulations. Indeed, Computational Fluid Dynamics is a fundamental tool for investigating hydrogen flames, yet most of the existing numerical approaches require adaptation.

First, a global one-step reaction mechanism is developed for premixed hydrogen–air flames. The reduced scheme is designed to reproduce the main laminar flame properties over a wide range of pressures, unburned gas temperatures, equivalence ratios, and stretch conditions. An explicit analytical dependence of the reaction rate parameters on pressure and equivalence ratio is introduced, together with a correction for the thermal flame thickness. The model is validated in canonical laminar flame configurations, providing sufficiently accurate results, while yielding a significant improvement in computational efficiency.

Second, the adequacy of the excited hydroxyl radical OH* as a HRR marker is investigated for laminar and turbulent hydrogen–air flames. In laminar premixed hydrogen flames, a systematic spatial shift between the OH* and HRR peaks is observed, attributed to the specific chemistry of hydrogen oxidation, and to the role of the H-radical in the OH* formation, which enhances post-flame OH* production. The effects of pressure, unburned gas temperature, and flame stretch are analyzed, showing that stretch and intrinsic flame instabilities can significantly degrade the OH*–HRR correlation in premixed flames, while OH* remains a reliable HRR marker for stretched hydrogen–air diffusion flames. These conclusions are supported by three-dimensional simulations of turbulent diffusion and partially premixed flames stabilized in the HYLON burner, highlighting the importance of explicitly accounting for OH* kinetics in numerical simulations when interpreting experimental chemiluminescence measurements.

Finally, combustion noise generation is studied in laminar and turbulent premixed hydrogen–air flames using Direct Numerical Simulations. In laminar acoustically forced M-shaped jet flames, numerical simulations, validated by experimental measurements, show that thermodiffusive ef-

fects modify the HRR distribution and flame dynamics, reducing the contribution of flame annihilation events to the overall acoustic radiation. At higher frequencies, resonance with intrinsic flame dynamics triggers thermodiffusive instabilities, leading to enhanced local HRR unsteadiness. Comparisons between simulations performed with detailed and reduced chemical schemes reveal that the latter captures the main trends, but overestimates noise at high forcing frequencies due to an exaggerated stretch response. The reduced scheme is further exploited to isolate Lewis number effects by artificially modifying the transport properties of species, while preserving the main laminar flame properties. Removing thermodiffusive effects promotes flame annihilation, similarly to hydrocarbon flames, but a separate analysis of differential and preferential diffusion reveals an antagonistic interaction of the two, with preferential diffusion mitigating the impact of differential diffusion in thermodiffusively unstable lean premixed hydrogen flames.

In turbulent premixed slot jet flames, thermodiffusive effects strongly influence HRR fluctuations and flame surface dynamics, leading to increased low-frequency acoustic radiation and to a steeper high-frequency spectral decay compared to thermodiffusively stable methane flames. A theoretical framework extending the classical flamelet theory to thermodiffusively unstable flames is proposed, linking combustion noise to flame surface fluctuations. In addition, instabilities at the shear layer between hydrogen combustion products and ambient air are enhanced, thereby promoting localized density gradients and finer scale structures that affect the acoustic emission at low frequencies. These results suggest that hydrogen differential diffusion impacts both direct and indirect combustion noise generation mechanisms. By varying the Karlovitz number, it is shown that increasing turbulence intensity suppresses thermodiffusive instabilities and shifts the acoustic emission toward higher frequencies, reducing the contribution of thermodiffusive effects on direct combustion noise. Additional simulations of the low Karlovitz case using reduced chemistry confirm that, as in the laminar M-shaped flame, the global mechanism captures the main features of the flame, albeit overestimating its response to stretch in the highly corrugated regions and the high-frequency acoustic radiation. Imposing unity Lewis numbers significantly attenuates the acoustic radiation, confirming the noise-amplifying role of thermodiffusive effects in lean premixed hydrogen flames.

Studio numerico della chemiluminescenza e della radiazione acustica nelle fiamme alimentate con idrogeno

Sommario

La combustione dell'idrogeno rappresenta una soluzione promettente per la riduzione delle emissioni di anidride carbonica nelle turbine a gas per la propulsione aeronautica e la produzione di energia. Ciononostante, le proprietà fisiche e chimiche dell'idrogeno, significativamente diverse da quelle dei combustibili idrocarburici convenzionali, pongono rilevanti sfide tecnologiche e di modellazione. Per migliorare il rendimento e ridurre le emissioni di ossidi di azoto, le turbine a gas sono comunemente operate in condizioni di combustione premiscelata magra. Queste, tuttavia, favoriscono l'insorgenza di instabilità termoacustiche. Inoltre, nel caso delle fiamme alimentate con idrogeno, tale regime è caratterizzato da un numero di Lewis inferiore a uno. In tali condizioni, gli effetti termodiffusivi e le instabilità intrinseche della fiamma sono promossi. La caratterizzazione delle instabilità termoacustiche richiede una descrizione corretta del rilascio di calore (HRR) non stazionario. La sua misura sperimentale diretta risulta tuttavia impraticabile, e la chemiluminescenza di radicali eccitati viene pertanto utilizzata come surrogato. Inoltre, le instabilità termoacustiche possono essere innescate dal rumore di combustione, che rappresenta una problematica sempre più rilevante anche a causa delle recenti stringenti normative sull'inquinamento acustico. Questa tesi affronta tali tematiche, concentrandosi sulla modellazione chimica, sull'applicabilità della chemiluminescenza come surrogato dell'HRR e sulla generazione del rumore di combustione, mediante simulazioni numeriche ad alta fedeltà. In questo contesto, la Fluidodinamica Computazionale rappresenta uno strumento fondamentale per lo studio delle fiamme alimentate con idrogeno, sebbene la maggior parte dei modelli numerici esistenti richieda opportuni adattamenti.

In primo luogo, viene sviluppato un meccanismo cinetico globale a una solo reazione per fiamme premiscelate a idrogeno, al fine di ridurre il costo computazionale senza l'introduzione di modelli di combustione. Lo schema ridotto è progettato per riprodurre le principali proprietà delle fiamme laminari su un ampio intervallo di pressioni, temperature della miscela fredda, rapporti di equivalenza, e livelli di *stretch*. Viene introdotta una dipendenza analitica esplicita dei parametri cinetici dalla pressione e dal rapporto di equivalenza, insieme a una correzione per lo spessore termico della fiamma. Il modello viene validato su configurazioni canoniche di fiamme laminari, fornendo risultati sufficientemente accurati e un significativo miglioramento dell'efficienza computazionale.

In secondo luogo, viene analizzata l'idoneità del radicale idrossile eccitato OH* come marcatore del rilascio di calore per fiamme idrogeno–aria laminari e turbolente. Nelle fiamme premiscelate laminari a idrogeno si osserva uno scostamento spaziale sistematico tra i picchi di OH* e dell'HRR, attribuito alla cinetica chimica specifica dell'idrogeno, e al ruolo del radicale H nei meccanismi di formazione dell'OH*, che favorisce la produzione di OH* nella regione di post-fiamma. Gli effetti della pressione, della temperatura del gas incombusto e dello stretch vengono analizzati, mostrando che lo stretch e le instabilità intrinseche della fiamma possono degradare significativamente la correlazione tra OH* e HRR nelle fiamme premiscelate, mentre l'OH* rimane un marcatore affidabile dell'HRR per fiamme di diffusione idrogeno–aria. Tali conclusioni

sono supportate da simulazioni tridimensionali di fiamme turbolente diffusive e parzialmente premiscelate, stabilizzate nel bruciatore HYLON. Queste evidenziano l'importanza di includere esplicitamente la cinetica chimica dell'OH* nelle simulazioni numeriche per l'interpretazione delle misure sperimentali di chemiluminescenza.

Infine, la generazione del rumore di combustione viene studiata in fiamme premiscelate a idrogeno laminari e turbolente mediante simulazioni DNS. In fiamme laminari a forma di M, sottoposte a forzaggio acustico, le simulazioni numeriche, validate da misure sperimentali, mostrano che gli effetti termodiffusivi modificano la distribuzione dell'HRR e la dinamica della fiamma, riducendo l'impatto degli eventi di distruzione della fiamma sulla radiazione acustica. A frequenze più elevate, la risonanza con la dinamica intrinseca della fiamma innesca instabilità termodiffusive, che conducono a un aumento delle fluttuazioni locali dell'HRR. Il confronto tra chimica dettagliata e chimica ridotta mostra che quest'ultima è in grado di catturare le caratteristiche principali della dinamica di fiamma, ma tende a sovrastimare il rumore alle alte frequenze di forzaggio, a causa di una risposta eccessiva allo stretch. Il meccanismo ridotto viene ulteriormente utilizzato per isolare gli effetti del numero di Lewis, modificando artificialmente le proprietà di trasporto delle specie pur mantenendo inalterate le proprietà di fiamma. L'eliminazione degli effetti termodiffusivi favorisce la distruzione della fiamma, in modo analogo a quanto osservato nelle fiamme di idrocarburi. Tuttavia, un'analisi separata della diffusione differenziale e preferenziale evidenzia un'interazione antagonista tra i due meccanismi, con la diffusione preferenziale che mitiga l'impatto della diffusione differenziale nelle fiamme premiscelate magre di idrogeno termodiffusivamente instabili.

Nelle fiamme turbolente premiscelate di tipo *slot jet*, gli effetti termodiffusivi influenzano fortemente le fluttuazioni dell'HRR e la dinamica della superficie di fiamma, portando a un aumento della radiazione acustica alle basse frequenze e a un decadimento spettrale più ripido alle alte frequenze rispetto alle fiamme di metano termodiffusivamente stabili. Viene proposto un quadro teorico che estende la teoria *flamelet* classica alle fiamme termodiffusivamente instabili, collegando il rumore di combustione alle fluttuazioni della superficie di fiamma. Inoltre, le instabilità nello *shear layer* tra i prodotti della combustione dell'idrogeno e l'aria ambiente sono rafforzate, promuovendo gradienti di densità localizzati e strutture più fini che influenzano l'emissione acustica alle basse frequenze. Questi risultati suggeriscono che la diffusione differenziale dell'idrogeno influisce sia sui meccanismi diretti che indiretti di generazione del rumore di combustione. Variando il numero di Karlovitz, si mostra che l'aumento dell'intensità turbolenta sopprime le instabilità termodiffusive e sposta l'emissione acustica verso frequenze più elevate, riducendo l'impatto degli effetti termodiffusivi sul rumore di combustione diretto. Ulteriori simulazioni nel caso a basso numero di Karlovitz, effettuate con chimica ridotta, confermano che, analogamente al caso laminare, lo schema globale riproduce le caratteristiche principali della fiamma, pur sovrastimando la risposta allo stretch nelle regioni altamente corrugate e la radiazione acustica alle alte frequenze. L'imposizione di numeri di Lewis unitari attenua significativamente la radiazione acustica, confermando l'amplificazione del rumore di combustione indotta dagli effetti termodiffusivi nelle fiamme premiscelate magre a idrogeno.

Preface

This dissertation is the result of the research activity carried out as PhD Student in the Department of Mechanics, Mathematics and Management of the Polytechnic University of Bari in Bari, Italy, from November 2022 to February 2026, under the supervision of Prof. Marco Torresi, Full Professor, and Prof. Davide Laera, Associate Professor. The work was financed with a doctoral grant by the Polytechnic University of Bari, and partly under the National Recovery and Resilience Plan funded by the European Union - NextGenerationEU with the Project REACTANT (Grant No. CUP - D53D23018150001) and with the Project "Network 4 Energy Sustainable Transition - NEST" (Grant No. CUP - D93C22000900001).

Part of the doctoral research work was carried out as Visiting PhD Student at the *Centre Européen de Recherche et de Formation Avancée en Calcul Scientifique* (CERFACS) in Toulouse, France, from October 2024 to April 2025, under the supervision of Dr. Guillaume Daviller, Senior Researcher. The visiting period at CERFACS was partly funded by the French Ministry of Foreign Affairs and Europe and Campus France through a French Government Scolarship (*Bourse du Gouvernement Français*).

High-Performance Computing (HPC) resources from CINECA under the ISCRA (Italian SuperComputing Resource Allocation) initiative, EuroHPC JU on the Luxembourg national supercomputer MeluXina at LuxProvide, CRESCO/ENEAGRID [171], and CERFACS are highly acknowledged.

Scientific Production

The research activity conducted during the PhD has led to the following scientific production, published in, accepted in, or submitted to peer-reviewed international journals and conference proceedings:

Published works

[i] F. G. Schiavone, N. Detomaso, M. Torresi, and D. Laera. "An Arrhenius-based one-step reaction mechanism for hydrogen-air flames simulations in an extended range of operating conditions". In: *International Journal of Hydrogen Energy* 57 (2024), pp. 1229–1243.

[ii] F. G. Schiavone, A. Aniello, E. Riber, T. Schuller, and D. Laera. "On the adequacy of OH* as heat release marker for hydrogen-air flames". In: *Proceedings of the Combustion Institute* 40 (2024), p. 105248.

[iii] F. G. Schiavone, M. Torresi, S. M. Camporeale, and D. Laera. "Impact of the operating conditions on the OH* distribution and its correlation with the heat release rate in hydrogen-air flames". In: *Combustion and Flame* 282 (2025), p. 114452.

[iv] C. Vankelekom, F. G. Schiavone, S. M. Camporeale, W. De Paepe, and D. Laera. "Numerical investigations of high-frequency thermoacoustic combustion instabilities in a micro gas turbine". In: *Applied Thermal Engineering* 280 (2025), p. 128119.

Manuscripts accepted for publication

[v] F. G. Schiavone, M. Torresi, S. M. Camporeale, and D. Laera. "Chemical Modeling and Lewis Number Effects on Noise Generation in Lean Premixed Hydrogen–Air Flames". *Accepted for publication in Proceedings of the ASME Turbo Expo 2026* (2026).

[vi] E. B. Porcelli, F. Y. Farrokhi, F. G. Schiavone, C. Vankelekom, S. M. Camporeale, W. De Paepe, and D. Laera. "A Numerical Study on the Effect of Hydrogen Addition and Exhaust Gas Recirculation on the Combustion Dynamics in a Micro Gas Turbine". *Accepted for publication in Proceedings of the ASME Turbo Expo 2026* (2026).

Manuscripts submitted for publication

[vii] F. G. Schiavone, G. Daviller, and D. Laera. "Acoustic radiation from thermodiffusively unstable turbulent lean premixed hydrogen–air flames". *Submitted to Journal of Fluid Mechanics* (2026).

[viii] F. G. Schiavone, G. Daviller, and D. Laera. "Influence of Karlovitz number on turbulent lean premixed hydrogen-air slot jet flames acoustics". *Submitted to Proceedings of the Combustion Institute* (2026).

[ix] F. G. Schiavone, M. Durand, T. Schuller, and D. Laera. "Influence of thermodiffusive effects on sound generation in perturbed laminar premixed annular jet flames". *Submitted to Combustion and Flame* (2026).

[x] R. Intranuovo, S. Zitouni, F. G. Schiavone, P. Brequigny, C. Mounaïm-Rousselle, and D. Laera. "On the saturation of thermodiffusive effects in turbulent partially cracked ammonia premixed flames". *Submitted to Proceedings of the Combustion Institute* (2026).

[xi] N. Misceo, F. G. Schiavone, S. M. Camporeale, and D. Laera. "Quenching mechanisms and their generated sound in thermodiffusively unstable laminar lean premixed hydrogen-air flames". *Submitted to Proceedings of the Combustion Institute* (2026).

Scientific Dissemination

The author of this dissertation has contributed to the following talks in national and international conferences and workshops:

[i] F. G. Schiavone, and D. Laera. "Derivation and validation of an Arrhenius-based reduced global mechanism for hydrogen-air flames". In: *KAUST – Combustion Institute Summer School: Carbon Free Combustion*. Thuwal, Saudi Arabia, May 2023.

[ii] F. G. Schiavone, M. Torresi, S. M. Camporeale, and D. Laera. "Derivation and validation of an Arrhenius-based reduced global mechanism for hydrogen-air flames". In: *45th Meeting of the Italian Section of the Combustion Institute*. Florence, Italy, May 2023.

[iii] F. G. Schiavone, M. Torresi, S. M. Camporeale, and D. Laera. "Impact of the operating conditions on the correlation between OH* and heat release rate in hydrogen-air flames". In: *46th Meeting of the Italian Section of the Combustion Institute*. Bari, Italy, June 2024.

[iv] C. Vankelekom, F. G. Schiavone, W. De Paepe, and D. Laera. "Analysis of thermoacoustic instabilities in a micro gas turbine". In: *46th Meeting of the Italian Section of the Combustion Institute*. Bari, Italy, June 2024.

[v] F. G. Schiavone, and D. Laera. "A DNS study of flame interactions as a source of noise in hydrogen-air flames". In: *3rd International Combustion Institute Summer School on Near-Wall Reactive Flows*. Darmstadt, Germany, June 2024.

[vi] F. G. Schiavone, A. Aniello, E. Riber, T. Schuller, and D. Laera. "On the adequacy of OH* as heat release marker for hydrogen-air flames". In: *40th International Symposium on Combustion*. Milan, Italy, July 2024.

[vii] F. G. Schiavone, M. Durand, T. Schuller, and D. Laera. "Comparative study of the noise generated by laminar hydrogen and methane-hydrogen flames". In: *26th International Congress of Theoretical and Applied Mechanics*. Daegu, Republic of Korea, Aug. 2024.

[viii] M. Durand, F. G. Schiavone, D. Laera, and T. Schuller. "Assessment of current prediction models for hydroxyl radical distributions in lean premixed hydrogen-air flames". In: *26th International Congress of Theoretical and Applied Mechanics*. Daegu, Republic of Korea, Aug. 2024.

[ix] F. G. Schiavone, M. Durand, M. Torresi, S. M. Camporeale, T. Schuller, and D. Laera. "Experimental and numerical investigation of noise generation in hydrogen and methane-hydrogen laminar flames". In: *34th Congress of the International Council of Aeronautical Sciences*. Florence, Italy, Sept. 2024.

[x] F. G. Schiavone and D. Laera. "Impact of the chemical modeling on the noise generated by hydrogen-air flames". In: *12th European Combustion Meeting*. Edinburgh, United Kingdom, Apr. 2025.

[xi] F. G. Schiavone, M. Torresi, S. M. Camporeale, G. Daviller, and D. Laera. "Numerical study of noise emission from turbulent H_2 and CH_4 flames". In: *47th Meeting of the Italian Section of the Combustion Institute*. Pisa, Italy, May 2025.

[xii] R. Intranuovo, F. G. Schiavone, and D. Laera. "DNS study of the impact of thermodiffusive effects on the turbulent flame speed in partially cracked ammonia flames". In: *47th Meeting of the Italian Section of the Combustion Institute*. Pisa, Italy, May 2025.

[xiii] N. Misceo, F. G. Schiavone, S. M. Camporeale, M. Torresi, and D. Laera. "Flame quenching mechanisms and noise generation in premixed methane and hydrogen flames". In: *47th Meeting of the Italian Section of the Combustion Institute*. Pisa, Italy, May 2025.

[xiv] F. G. Schiavone, G. Daviller, and D. Laera. "Investigation of acoustic emission of turbulent hydrogen and methane slot jet flames via Direct Numerical Simulations". In: *2nd Combustion-DNS Strategy & Data Analysis Workshop*. Corfu, Greece, June 2025.

[xv] F. G. Schiavone, M. Torresi, S. M. Camporeale, G. Daviller, and D. Laera. "Numerical investigation of noise generation mechanisms in turbulent hydrogen and methane flames". In: *4th Symposium on Thermoacoustics in Combustion*. Trondheim, Norway, Sept. 2025.

[xvi] N. Misceo, F. G. Schiavone, M. Torresi, S. M. Camporeale, and D. Laera. "Flame Quenching Mechanisms and Noise Generation in Premixed Methane and Hydrogen Flames". In: *4th Symposium on Thermoacoustics in Combustion*. Trondheim, Norway, Sept. 2025.

[xvii] F. G. Schiavone, G. Daviller, and D. Laera. "DNS study of sound generation in turbulent lean premixed hydrogen-air flames". In: *20th International Conference on Numerical Combustion*. Rome, Italy, Oct. 2025.

[xviii] R. Intranuovo, F. G. Schiavone, S. Zitouni, P. Brequigny, C. Mounaïm-Rousselle, and D. Laera. "DNS study of the impact of thermodiffusive effects on the turbulent flame speed in partially cracked ammonia flames". In: *20th International Conference on Numerical Combustion*. Rome, Italy, Oct. 2025.

[xix] F. G. Schiavone, M. Torresi, S. M. Camporeale, and D. Laera. "Chemical Modeling and Lewis Number Effects on Noise Generation in Lean Premixed Hydrogen–Air Flames". In: *ASME Turbo Expo 2026*. Milan, Italy, June 2026 (accepted).

[xx] E. B. Porcelli, F. Y. Farrokhi, F. G. Schiavone, C. Vankelekom, S. M. Camporeale, W. De Paepe, and D. Laera. "A Numerical Study on the Effect of Hydrogen Addition and Exhaust Gas Recirculation on the Combustion Dynamics in a Micro Gas Turbine". In: *ASME Turbo Expo 2026*. Milan, Italy, June 2026 (accepted).

[xxi] F. G. Schiavone, G. Daviller, and D. Laera. "Influence of Karlovitz number on turbulent lean premixed hydrogen-air slot jet flames acoustics". In: *41st International Symposium on Combustion*. Kyoto, Japan, July 2026 (accepted).

[xxii] R. Intranuovo, S. Zitouni, F. G. Schiavone, P. Brequigny, C. Mounaïm-Rousselle, and D. Laera. "On the saturation of thermodiffusive effects in turbulent partially cracked ammonia premixed flames". In: *41st International Symposium on Combustion*. Kyoto, Japan, July 2026 (accepted).

[xxiii] N. Misceo, F. G. Schiavone, S. M. Camporeale, and D. Laera. "Quenching mechanisms and their generated sound in thermodiffusively unstable laminar lean premixed hydrogen-air flames". In: *41st International Symposium on Combustion*. Kyoto, Japan, July 2026 (accepted).

Honors and Awards

The author of this dissertation has received the following honors and awards:

[i] Best Speaker Author Award from the Italian Section of the Combustion Institute for the presentation of the research work titled "Impact of the operating conditions on the correlation between OH* and heat release rate in hydrogen-air flames" at the 46th Meeting of the Italian Section of the Combustion Institute in Bari, Italy (June 2024).

[ii] French Government Scholarship (*Bourse du Gouvernement Français*) from the French Ministry for Europe and Foreign Affairs for the research project "Investigation of direct combustion noise generation in turbulent hydrogen flames by means of Direct Numerical Simulations" carried out as Visiting PhD Student at CERFACS (Toulouse, France).

Scientific Responsibility

The author of this dissertation has been Co-Principal Investigator (Principal Investigator: Davide Laera) of the following research projects:

[i] CINECA ISCRA Class C Project "Comparative study on the impact of intrinsic instabilities on combustion noise generation in laminar hydrogen flames" (INTONATE), with HPC resources allocated on Leonardo Booster (40 thousand standard-hours, corresponding to 5 thousand GPU-hours) and Galileo100 (16 thousand standard-hours, corresponding to 48 thousand CPU-hours) from March 2023 to March 2024.

[ii] EuroHPC JU Regular Access Mode Project "Production of noise by flame-turbulence interaction and instabilities in H_2 lean combustion" (Project No. EHPC-REG-2023R03-184 - PROMETH$_2$EUS), with HPC resources allocated on MeluXina CPU at LuxProvide (125 thousand node-hours, corresponding to 16 million CPU-hours) from March 2024 to March 2025.

[iii] CINECA ISCRA Class B Project "Study of combustion noise generation by intrinsic instabilities in laminar hydrogen combustion" (SONIC-H_2), with HPC resources allocated on Leonardo Booster (1.92 million standard-hours, corresponding to 240 thousand GPU-hours) from April 2024 to July 2025.

[iv] CINECA ISCRA Class B Project "Study of pollutant emissions and flame-turbulence interaction at variable Karlovitz numbers in NH_3 flames" (SPARKNH$_3$), with HPC resources allocated on Leonardo Booster (1.632 million standard-hours, corresponding to 204 thousand GPU-hours) from June 2025 to June 2026.

[v] EuroHPC JU Regular Access Mode Project "Systematic Investigation and Modelling of Turbulent Ammonia Combustion" (Project No. EHPC-REG-2025R01-023 - SIMTAC), with HPC resources allocated on MeluXina CPU at LuxProvide (156 thousand node-hours, corresponding to 20 million CPU-hours) from August 2025 to August 2026.

Acknowledgments

These three years have left their mark on my work, and on myself. Yet this journey would have looked very different without the people who shaped it along the way.

First and foremost, I would like to express my gratitude to Prof. Tommaso Capurso and Dr. Carmen Jiménez for agreeing to review my (quite long) thesis manuscript, and to Prof. Maria Grazia De Giorgi, Prof. Francesco Fornarelli, Dr. Thierry Poinsot and Dr. Giancarlo Sorrentino for accepting to be part of my final exam jury.

I am deeply grateful to my two thesis supervisors for their guidance, which greatly contributed to the successful outcome of this doctorate. I would like to thank Prof. Marco Torresi for his support with both scientific and administrative matters, the latter often proving more stressful than the former. My most heartfelt thanks go to Prof. Davide Laera, for believing in me from the very beginning and providing me with all the tools and support to succeed in the challenging field of combustion. Working with you meant combining critical thinking, scientific rigor, and common sense, with a healthy dose of academic vacation (otherwise known as scientific dissemination at conferences). Our discussions have always been engaging, even when we did not agree, and I truly believe our collaboration had good (hydrogen) chemistry: my infinite patience meeting your enthusiasm and drive. This allowed us to achieve a great deal together, which is, in the end, the most valuable thing I take from these years.

A sincere thanks also to Dr. Guillaume Daviller, who welcomed me at CERFACS during my seven months in Toulouse. Your guidance in the field of acoustics broadened my perspective well beyond the combustion domain. Our discussions on the physical aspects of noise, and your insightful comments on my papers, sharpened my ability to think outside my comfort zone, and to make my results not only sound, but also understandable to others.

As a firm believer in collaborative research, I would also like to thank all those with whom I had the pleasure of working over these years. I am particularly grateful to Nicola D. and Andrea A., with whom I co-authored my first two papers and shared several meaningful experiences and discussions. A sincere thanks to Matthieu for all the wonderful moments we spent together, from Toulouse to Korea. A special mention goes to Prof. Thierry Schuller: on the several occasions we met and discussed, I found your passion and dedication truly inspiring.

I would also like to thank the other senior members of my research group. To Prof. Sergio Camporeale, who was the first to reach out to me about a thesis, managing to find the one week during my first Parisian period when I was homesick, and convincing me to pursue a doctorate in Bari. A choice I have never regretted, even when I had to prepare a last minute exercise for Master students. To Prof. Michele Stefanizzi, the *master of elegance*: thank you for your aggregating spirit. The *FantaSanteramo* remains the highlight of the year, and I hope to keep joining it as a proud member of the expat community.

A sincere thanks to all the colleagues and friends who filled the *open space* at the Polytechnic University of Bari. The work environment shapes the people inside it, and in this sense the

office in Bari became a second home, not only because I spent more time there than in my actual home, but also because my colleagues became a sort of odd, lively, and genuinely warm family. I am grateful to my older seniors Vito C., Giuseppe A., and Gianmarco, who first welcomed me and helped me find my footing. Our shared table was without doubt the finest outcome of that chaotic desk assignment, and I think we can all agree that splitting it was the destruction of a dream. I am equally grateful to the younger members of the group: Raffaele, Emanuele, Leonardo, Domenico, Davide M., Nicola. As your senior, I apologize for having raised the bar, but I have no doubt you will achieve incredible results during your academic journey. To Mariantonietta, Fabio A., Alessia, Mastro, Simona, Claudio, Costa, Davide N., Michele S., Vito D., Luana, Alessandro, with whom I shared many entertaining, fun episodes, which colored my doctorate. To Felice, the Stakhanovist doctoral student, with whom I had the pleasure (if we can call it that) of sharing the trials of our respective doctoral journeys. To Davide G., whose academic *remuntada* taught me something about believing in change. To Paola and Denny, who are now almost my neighbors in my new Parisian life.

To the city of Toulouse: what a wonderful discovery. I loved every day I spent there, and I am grateful for the company I found at CERFACS. I am particularly thankful to Raul and Lakshmanan, who hosted me in their office, and to Etienne, Felicia, Hector, Florent, and Maëlys for the shared lunches and many good conversations. My time in Toulouse was also the occasion to meet, or meet again, some dear friends: Laura, Francesco O. and Francesco M., my companions from my first Parisian era, and Leslie, whom I met in a rather peculiar way, and who became a good friend of mine. A special mention to Tarik, who played a quite significant role in shaping the final chapter of my doctorate: my transition to industry. It was a good choice, and I am confident we will share many good moments, both professionally and personally.

Finally, I would like to thank my long-standing friends: Domenico, Francesco A., and Cristiano. I have lost count of how many years our friendship has lasted, and I often wonder how it has managed to endure this long. Perhaps another doctorate would be needed to answer that question, though certainly not by me. I value what we have, and I hope it will carry us still further, despite the distance and the different paths each of us is walking.

My most heartfelt thanks, in the end, go to my family. If I was able to give so much of myself to this work over these years, it is because you gave me the space and the support to do so. Knowing you were there made everything easier. This achievement is as yours as mine.

Contents

List of Figures

List of Tables

Nomenclature

Acronyms

0D	Zero-Dimensional
1D	One-Dimensional
2D	Two-Dimensional
3D	Three-Dimensional
CFD	Computational Fluid Dynamics
DNS	Direct Numerical Simulation
HPC	High-Performance Computing
HRR	Heat Release Rate
K-H	Kelvin–Helmholtz (instability)
KDE	Kernel Density Estimate
LES	Large Eddy Simulation
LW	Lax–Wendroff (scheme)
NSCBC	Navier–Stokes Characteristic Boundary Conditions
OASPL	Overall Sound Pressure Level
PDF	Probability Density Function
PEA	Pre-Exponential Adjustment
PEF	Pre-Exponential Factor
PIV	Particle Image Velocimetry
PLIF	Planar Laser-Induced Fluorescence
PSD	Power Spectral Density
QSS	Quasi-Steady State (approximation)
r.m.s.	Root-mean-square
RANS	Reynolds-Averaged Navier Stokes

SPL	Sound Pressure Level
SPOD	Spectral Proper Orthogonal Decomposition
TD	Thermodiffusive (effect/instability)
TF	Thickened Flame (model)
TTGC	Two-step Taylor–Galerkin 'C' (scheme)

Chemical species

CH_4	Methane
CO_2	Carbon dioxide
H_2	Hydrogen
NO_x	Nitrogen oxide
OH^*	Excited hydroxyl radical
OH	Hydroxyl radical

Greek alphabet

δ	Diffusive laminar flame thickness
δ_L^0	Thermal laminar flame thickness
$\dot{\omega}_k$	Reaction rate of the species k
$\dot{\omega}_T$	Volumetric heat release rate
η	Kolmogorov lengthscale
λ	Thermal conductivity
μ	Dynamic viscosity
ν	Kinematic viscosity
ϕ	Equivalence ratio
ρ	Density
σ	Expansion ratio
ξ	Mixture fraction

Latin alphabet

$\mathcal{A}_f$	Flame surface area
$\mathcal{A}_i$	Pre-exponential factor of the reaction i
$\mathcal{A}_T$	Turbulent flame surface area

C	Progress variable
c	Speed of sound
c_p	Specific heat capacity at constant pressure
D_k	Diffusivity coefficient of the species k
D_{th}	Heat diffusivity coefficient
E	Energy
E_a	Activation energy
K_i	Rate constant of the reaction i
l_t	Integral turbulent lengthscale
m^0	Laminar burning flux
p	Pressure
R	Universal gas constant
S_c	Laminar flame consumption speed
S_d	Flame displacement speed (density-weighted)
S_L^0	Laminar flame speed
S_T	Turbulent flame speed
T	Temperature
T_{ad}	Adiabatic flame temperature
u'	Turbulent velocity fluctuation (r.m.s. of velocity)
u_j	Velocity component in the direction j
W_k	Molecular weight of the species k
X_k	Mole fraction of the species k
Y_k	Mass fraction of the species k

Non-dimensional numbers

Da	Damköhler number
Ka	Karlovitz number
Le	Lewis number
M	Mach number
Ma	Markstein number

Nu	Nusselt number
Pr	Prandtl number
Re	Reynolds number
Re_t	Turbulence Reynolds number
Sc	Schmidt number
St	Strouhal number
Ze	Zel'dovich number

Subscripts and superscripts

∞	Far field
b	Burned mixture
u	Unburned mixture

1 Introduction

Contents

1.1 Energy transition and sustainable combustion

The last ten years have represented a period of critical change for the global energy sector. Extreme perturbation was caused by the Covid-19 pandemic first, and by geopolitical events after (e.g, the wars in Ukraine and in the Middle East), intensifying the global energy crisis and making energy security a priority [178]. Moreover, in 2024 the total global energy demand increased by over 2%, well above the long term average in the period from 2010 to 2023, equal to 1.4% [178]. Even though renewable energy sources were able to meet much of this growing demand, the request for natural gas also rose faster than in previous years [178]. Furthermore, the demand of oil and, more importantly, coal still remained relevant, especially in emerging markets and developing economies in Asia [178].

A rapid transformation of the global energy systems toward carbon-free or carbon-neutral technologies is needed to fight climate change and the associated dangers for mankind [307]. Indeed, energy-related carbon dioxide (CO_2) emissions rose by nearly 1% in 2024, reaching a record high of 38.2 Gt [178]. In this way, they contributed to an unprecedented peak in the increase of global average temperature over 1.5 °C with respect to pre-industrial levels, as shown in Figure 1.1. According to the International Energy Agency (IEA) [178], considering either the Current Policies Scenario (CPS), which relies on policies that are already in place, or the exploratory Stated Policies Scenario (STEPS), reflecting official strategies that have not been adopted yet, global CO_2

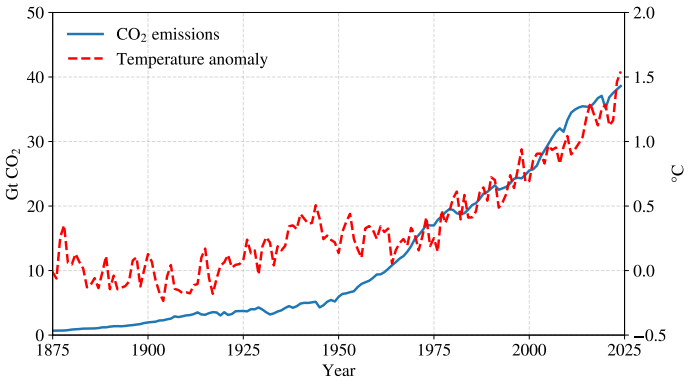

Figure 1.1: Global CO_2 emissions and average temperature anomaly relative to the pre-industrial period between the years 1875 and 2025 (adapted from [328]).

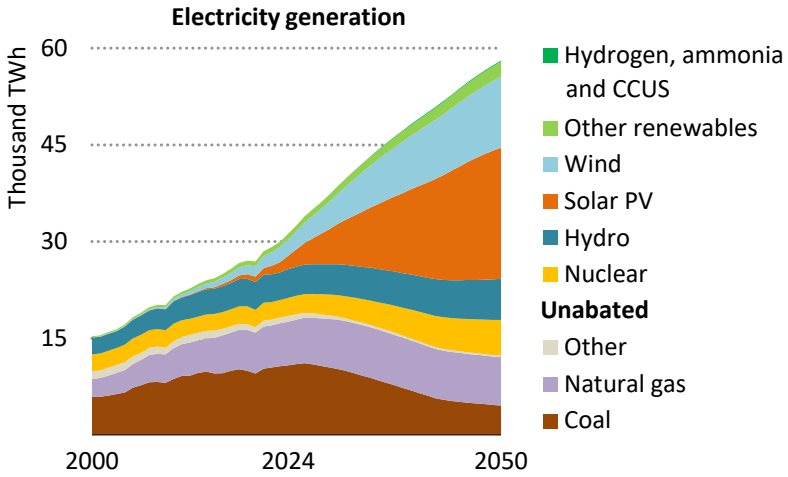

Figure 1.2: Global electricity generation by source in the Stated Policies Scenario by 2050 (from [178]). The abbreviation CCUS in the legend stands for Carbon Capture, Utilization and Storage. Other renewables: bioenergy and renewable waste, concentrating solar power, geothermal and marine. Other: oil, non-renewable waste and other sources.

emissions are still expected to grow in the next years and then, in the more optimistic STEPS case, decline with respect to the level of 2024, by around 8% in 2035 and by 20% in 2050 [178]. Based on these trajectories, the temperature increase in the year 2100 would be of 2.5 °C, in the STEPS case, or 3.0 °C, in the CPS one. For reference, the goal of the 2015 Paris Agreement [404] is to keep the rise in the global average surface temperature well below 2 °C above pre-industrial levels, and preferably below 1.5 °C.

To abate the share of fossil fuels in the final consumption and, consequently, CO_2 emissions, the global energy production will need to rely on a combination of different sources. Figure 1.2 shows the share of electricity generation by source predicted for the next years until 2050 by the IEA in the STEPS, while Figure 1.3 proposes the same analysis in the Net Zero Emissions by 2050 (NZE) Scenario, i.e., the scenario limiting the global temperature rise to 1.5 °C, as required by the Paris Agreement. In the more realistic STEPS case, the role of combustion technologies, based both on fossil and sustainable fuels, will remain crucial, while the optimistic NZE Scenario is designed with a strong shift toward renewable sources and with a limited contribution of combustion technologies, based exclusively on low emission fuels. Nevertheless, the NZE Scenario

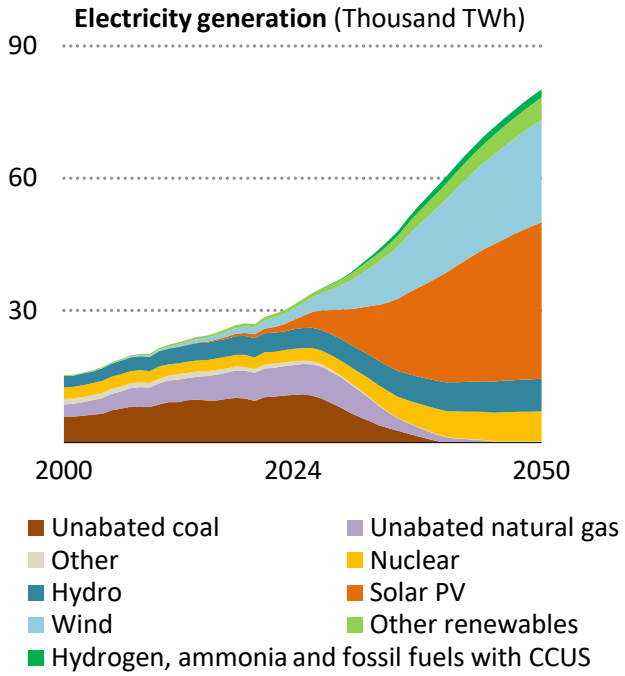

Figure 1.3: Global electricity generation by source in the Net Zero Emissions Scenario by 2050 (from [178]). The abbreviation CCUS in the legend stands for Carbon Capture, Utilization and Storage. Other renewables: bioenergy and renewable waste, concentrating solar power, geothermal and marine. Other: oil, non-renewable waste and other sources.

illustrates only a possible global path to reach the target of net-zero emissions by 2050 [178]. In practice, the enormous scale of the energy market makes it unfeasible to replace fossil fuels solely with renewable energy sources. Furthermore, renewable energy sources, such as wind and solar energies, are located in geographically limited areas, which are not necessarily close to the major consumers, adding the additional challenge of suitable energy transport over long distances [307]. Finally, the volatility of the electricity generated from renewable sources requires long-term storage of large amount of energy to smooth fluctuations [283]. The combustion of low-emissions synthetic chemical energy carriers is well suited to tackle this issue and, therefore, will continue to gain importance in the future global energy scenario [29, 307, 407].

1.2 The role of hydrogen

In this context, low-emissions hydrogen (H_2) has gained an increased interest, and is widely recognized as a key solution to decarbonize hard-to-abate sectors, e.g., heavy industry, power generation, shipping and aviation [52, 177, 433]. Indeed, since H_2 is the building block for other synthetic fuels and, consequently, requires fewer transformations, its production leads to lower exergy losses [307]. Furthermore, its high versatility makes it a viable solution in several contexts, thereby explaining the strong support by national governments and international organizations for the transformation toward an H_2-based society [307].

On the other hand, a main drawback of H_2 is represented by its low energy density. Figure 1.4 compares the energy density (per volume) and the specific energy (per mass) of H_2 with those of metal fuels, hydrocarbons, and batteries. While the specific energy of H_2 is significantly higher

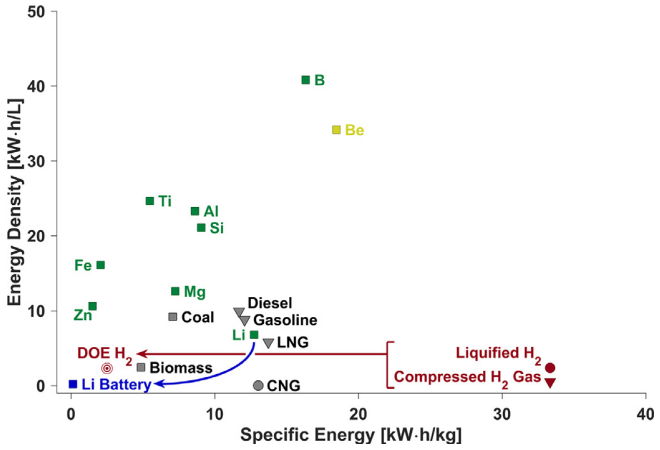

Figure 1.4: Energy density and specific energy of various metal fuels (green), hydrocarbons (gray), hydrogen (red), and batteries (blue) (from [29]). CNG: compressed natural gas. LNG: liquefied natural gas. CH_2G: compressed hydrogen gas. LH_2: liquid hydrogen. DOE H_2: energy density goal for hydrogen storage materials set by the United States Department of Energy.

than other fuels, the contrary occurs for the specific energy. This is due to the fact that H_2 has sensibly low boiling (20.37 K, 1.013 bar) and critical (33.18 K, 13 bar) points, above which the fluid cannot be liquefied [55]. Consequently, this poses significant challenges in terms of transport and storage, which, added to the possible difficulties in the production process, can drop the overall efficiency [307].

In addition to the aforementioned issue, which is intrinsic to the utilization of H_2 as energy vector, additional critical aspects are to be considered when adopting it as a fuel in combustion systems [307]. In particular, H_2 laminar burning velocity is almost an order of magnitude higher than the one of conventional hydrocarbon fuels, thereby impacting the flame dynamics and stability, and, consequently, the fuel flexibility [412]. Furthermore, the molecular mass diffusivity of H_2 is high compared with both the diffusivity of other species (i.e., preferential diffusion) and of thermal energy (i.e., differential diffusion). This impacts the flame response to stretch and can possibly lead to thermodiffusive intrinsic flame instabilities, which promote the increase in the consumption speed of H_2 flames [307]. Finally, the rather high adiabatic flame temperature of H_2 combustion can strongly promote the formation of nitrogen oxides (NO_x) [307]. While these issues make it impossible to use H_2 as a drop-in solution, i.e., to use it as a mere substitute of hydrocarbons in current combustion technologies, they also pose novel research questions, as well as potential for optimization. For example, the high burning velocity of H_2-air flames and the wide flammability range of this fuel allow for the development of ultra-lean combustion systems.

In this context, Computational Fluid Dynamics (CFD) is an indisputably valuable tool to gain a further understanding of H_2 combustion characteristics. Indeed, numerical simulations are easier to implement with respect to experimental campaigns, and allow access to a wider information dataset, including quantities like reaction rates, species and temperature distributions [307]. Furthermore, the increased availability, in recent years, of High-Performance Computing resources, has made it possible to use massively parallel codes to perform high-fidelity numerical simulations of unsteady flows in increasingly complex conditions. Nevertheless, the design of novel H_2-based combustion systems still requires the implementation of accurate combustion models for the lightweight simulation of industrial-scale configurations [307]. Since

most of the current models were conceived for hydrocarbon combustion, their direct application to H_2 reacting flows is often not possible, posing an additional challenge in the transition to sustainable H_2-fueled combustion.

1.3 Hydrogen combustion for gas turbines

The importance of gas turbines in the global energy scenario is undoubted, as they provide an efficient and versatile solution for power generation and industrial applications [437]. Furthermore, they are widely implemented in the aviation sector, being them a constitutive element of jet engines [338]. In the context of the current energy transition process, gas turbines represent a key solution to maximize the fuel efficiency and minimize fuel consumption. For this reason, they are currently widely used with natural gas, which is considered as a transition fuel, to minimize CO_2 emissions for power generation, while developing alternatives leading to net-zero emissions. Moreover, given the reduced time needed for them to change the power output, gas turbines can be used to stabilize the electric grid and compensate for the intermittency of renewable energy sources. On the other hand, aviation, which accounts for over 2.5% of the global energy-related CO_2 emissions [178], is a sector that heavily relies on oil as primary fuel. The aircraft fuel efficiency has risen by about 25% in the last decade [178], due to design modifications that improved the aerodynamics and the choice of more lightweight materials. Nevertheless, these efforts are not enough to achieve the ambitious objective of net-zero carbon emissions by 2050 set up by the International Civil Aviation Organization (ICAO) [176]. Therefore, it is necessary to introduce alternative fuels also in the aviation industry.

In this sense, H_2-fueled gas turbines are considered as a possible solution in both sectors. While the drop-in utilization of blends of H_2 and natural gas is a currently feasible and already implemented solution for power generation stationary gas turbines, the utilization of pure H_2 as a fuel presents several challenges and requires additional technological developments [233]. Still, gas turbines are already being adapted for the use of alternative fuels like H_2 or ammonia (NH_3), and gas turbine manufacturers aim to provide modern gas turbines fully operating on H_2 by 2030. For example, Hanwha proposed a full H_2-fueled combustor for an 80 MW gas turbine [177], while Ansaldo Energia successfully demonstrated the ability of an optimized combustor for its well-known GT36 gas turbine [294] to operate on 100% H_2 [8]. Projects for H_2-fueled gas turbines are also underway at GE Vernova [128] and Siemens Energy [366]. Even though in 2024 the global installed power capacity using H_2 or NH_3, equal to 360 MW, represented less than 0.01% of the total global capacity of the power sector, this could reach 7.5 GW by 2030 based on announced projects (4.9 GW if projects at a very early stage of development are excluded) [177]. Figure 1.5 shows the historical and estimated share of power generation capacity using H_2 and NH_3 by region and technology over the years up to 2030. Almost half of the announced capacity by 2030 is located in the Asia-Pacific region (mostly Japan and Korea), followed by Europe with 38% and North America with 14% [177]. Moreover, while current H_2-based power generation technologies mostly rely on fuel cells, gas turbines are expected to become dominant, reaching a share of 55% in 2030 [177].

As for aviation, H_2-related activities in the short-to-medium term are expected to be concentrated in the synthesis of sustainable aviation fuels (SAF) and e-SAF, being these easier to drop-in with minimal changes to fuel storage infrastructure and aircraft [177]. The direct use of H_2 in aircraft engines is still under development. In this sense, the most relevant technical issues are represented by the necessity for an aircraft redesign to allow for larger tanks, and to the establishment

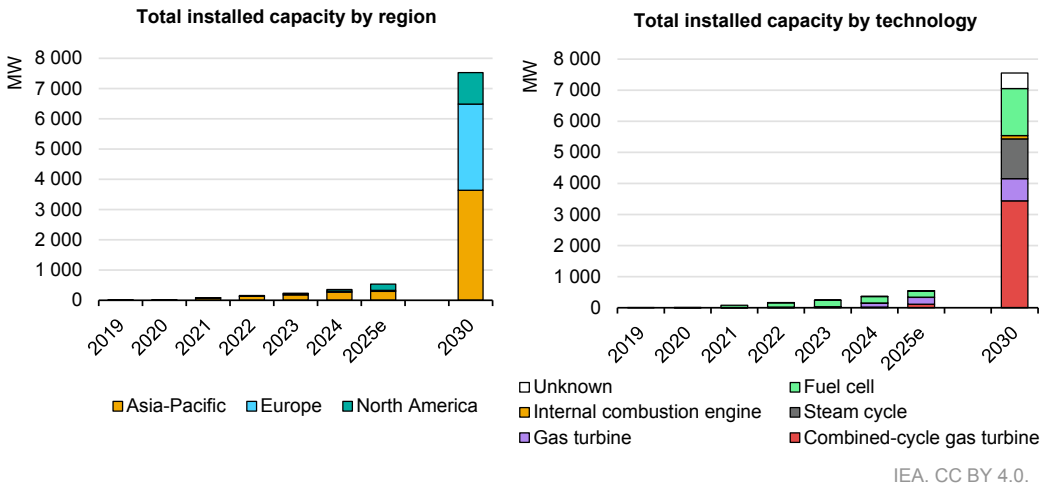

Figure 1.5: Power generation capacity using hydrogen and ammonia by region (left) and technology (right) between the years 2019 and 2030, based on historical and announced projects (from [177]). Values for 2025 are estimates, assuming that plants with an announced start date in 2024 that are under construction or have reached final investment decision actually start operation in 2025.

of airport infrastructure for safely handling cryogenic fuels [177]. Still, several announcements were made both by start-ups [177] and major companies, such as Safran and Rolls–Royce. The former successfully tested in 2024 an H_2-fueled gas turbine engine for the light aviation market, in the framework of the French BeautHyFuel project to explore H_2 propulsion solutions for light airplanes [333], while the latter performed in 2022 the first run of a modern aero engine on H_2, and is committed to develop the technology to allow for H_2 combustion in gas turbine engines, so that a range of aircraft can be powered with this fuel starting from 2035 [73]. However, given the strict regulations in this industry, any novel H_2-fueled aircraft is expected to spend a long time at the demonstration phase before being commercialized [177].

1.4 Flame–acoustics interaction and combustion noise

To improve the overall fuel efficiency and reduce pollutant emissions, with particular reference to NO_x, modern gas turbines are operated under lean premixed conditions [379]. In this regime, however, combustion systems are more prone to combustion (or thermoacoustic) instabilities, which arise from the resonant coupling between acoustic waves and unsteady combustion. These can induce self-sustained pressure oscillations and, in the worst case scenario, cause irreversible damage to combustion systems [310]. The mechanism at the origin of combustion instabilities has been known for a long time [322], and can be summarized by the scheme in Figure 1.6: velocity fluctuations u', which can be imposed externally, as in the case of acoustically excited laminar flames, or be induced by turbulence, lead to fluctuations in the heat release rate q'. These generate acoustic pressure fluctuations p', which propagate upstream under subsonic conditions and, as a consequence, alter u' upstream of the flame, closing the coupling loop. It should be noted that, in many practical applications, flames are acoustically compact in a wide part of the acoustic spectrum, i.e., their characteristic dimension is much smaller than the acoustic wavelength. In this case, p' affects the flame structure only indirectly by its action on u'. In this framework, flow perturbations represent the active element of the loop, directly modulating the

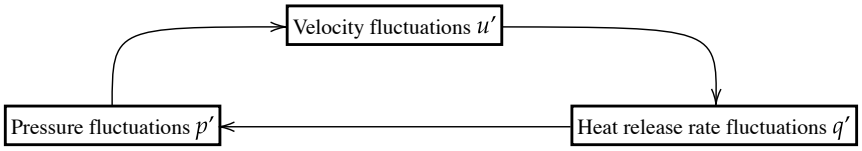

Figure 1.6: Schematic representation of the coupling mechanism leading to combustion instability.

flame, while the acoustic perturbations provides the retroactive pathway that couples combustion back to turbulence.

The analysis of combustion instabilities is often based on the establishment of a Flame Transfer Function, in the linear regime, and of a Flame Describing Function, in the non-linear regime, both relating the fluctuations of heat release rate and velocity [99, 280, 354]. The experimental measurement of these functions has been performed extensively in the literature (e.g., [223, 285]), and is based on the assessment of the flame response under forced flow conditions, i.e., on the measure of the heat release rate fluctuations corresponding to a fixed level of forcing of the inlet velocity. Nevertheless, the direct measurement of the heat release rate is impractical from an experimental point of view, as it would require the simultaneous measurement of several species and temperature [273]. For this reason, other measurable quantities are used as a tracer of heat release rate, such as chemiluminescence, i.e., the spontaneous light emission from excited chemical species [275].

In enclosed systems like gas turbines or aircraft engines, the combustion instability can be triggered by the noise emitted by flames, i.e., combustion noise [96, 172, 310]. Furthermore, combustion noise is emerging as an important issue also due to increasingly stringent noise regulations [209], notably in aviation. A better understanding of combustion noise is, therefore, crucial to improve the knowledge and the prediction of combustion instabilities, and to favor the design of safer and quieter H_2-fueled combustion systems.

1.5 Objectives and structure of the dissertation

This dissertation addresses some challenges of H_2 combustion by means of high-fidelity numerical simulations, with a focus on three main aspects:

- Chemical modeling, aiming to develop a global reaction mechanism for H_2–air combustion valid under varying operating conditions.
- Applicability of chemiluminescence as a heat release rate surrogate, with the aim of determining under which conditions the excited hydroxyl radical OH* can be considered a reliable heat release rate marker for H_2–air flames.
- Combustion noise generation, to investigate the impact of thermodiffusive effects on the acoustic radiation of lean premixed H_2–air flames both in laminar and turbulent conditions.

The dissertation is organized as follows.

- Part I presents general features of reacting flows. The fundamental concepts on laminar and turbulent premixed flames are reported in Chapter 2. Chapter 3 deals with the numerical methods related to the code AVBP adopted in the numerical simulations in this work, while the peculiar features of H_2 combustion are discussed in Chapter 4.

- Part II investigates chemical characteristics of H_2 flames, focusing on the chemical modeling and on the impact of chemical pathways on chemiluminescence and its relation with the heat release rate. Chapter 5 is dedicated to the derivation of a simplified global reaction mechanism for H_2 combustion valid under varying operating conditions, while Chapter 6 discusses chemiluminescence as a diagnostics technique for combustion and analyzes the suitability of OH* as heat release rate marker for H_2–air flames.

- Part III focuses on the generation of combustion noise in lean premixed H_2-air jet flames. The combustion noise fundamentals, including a literature review, are presented in Chapter 7. Chapter 8 introduces the laminar premixed M-shaped jet flame configuration, either stationary or subjected to harmonic acoustic forcing, whose numerical set-up has been validated by experiments performed at the *Institut de Mécanique des Fluides de Toulouse* (Toulouse, France). The acoustic radiation of these flames is investigated in Chapter 9. Simulations are performed both with detailed kinetics and with the reduced scheme developed in Chapter 5, providing a first assessment of the impact of chemical modeling on noise prediction. Subsequently, the numerical configuration and set-up of the high-fidelity dataset of turbulent premixed slot jet flames developed in this work is described in Chapter 10. Chapter 11 deals with noise generation mechanisms in this turbulent configuration, comparing results obtained under different Reynolds and Karlovitz numbers to elucidate the impact of flame–turbulence interaction and of thermodiffusive instabilities on the radiated noise. The analysis of the impact of chemical modeling commenced in Chapter 9 is here extended to the turbulent case, highlighting also the influence of the Lewis number on the acoustic emission and sustaining the noise-amplifying role of stretch effects associated with the thermodiffusive response of lean premixed H_2–air flames.

- The Conclusion summarizes the main findings and contributions of this dissertation, discussing also the potential future work.

PART I

General concepts of theoretical and numerical hydrogen combustion

... and they watched the fire which does contain within it something of men themselves inasmuch as they are less without it and are divided from their origins and are exiles. For each fire is all fires, the first fire and the last ever to be.

— Cormac McCarthy
Blood Meridian, 1985

2

Fundamentals of combustion and flames

Combustion is a chemical process, involving several species and based on a sequence of multiple reactions. Flames are the gaseous, visible product of the combustion process. This Chapter provides a fundamental knowledge of chemical kinetics and fluid dynamics, as well as of the interaction between these two domains, to allow for an understanding of flame dynamics.

Contents

2.1 Chemical kinetics

All chemical reactions, including combustion processes, occur at a definite rate and depend on the conditions of the system, e.g., the concentrations of the reactants and the temperature [136]. Let us consider an arbitrary chemical system of N species reacting through M reversible reactions:

$$\sum_{k=1}^{N} \nu'_{k,j} \mathcal{S}_k \rightleftharpoons \sum_{k=1}^{N} \nu''_{k,j} \mathcal{S}_k \quad \text{for } j = 1, ..., M, \tag{2.1}$$

where $\nu'_{k,j}$ and $\nu''_{k,j}$ are the stoichiometric coefficients of the species k as reactant and product in the reaction j, respectively, and $\mathcal{S}_k$ is a symbol for the species k. If W_k is the molecular weight of the species k, then mass conservation enforces:

$$\sum_{k=1}^{N} \nu_{k,j} \mathcal{S}_k = 0 \quad \text{for } j = 1, ..., M, \tag{2.2}$$

where $\nu_{k,j} = \nu''_{k,j} - \nu'_{k,j}$. For each species k, a (mass) reaction rate $\dot{\omega}_k$ can be defined as the sum of all its rates $\dot{\omega}_{k,j}$ corresponding to each reaction j:

$$\dot{\omega}_k = \sum_{j=1}^{M} \dot{\omega}_{k,j} = W_k \sum_{j=1}^{M} \nu_{k,j} \mathcal{Q}_j, \tag{2.3}$$

where $\mathcal{Q}_j$ is the rate of progress of the reaction j:

$$\mathcal{Q}_j = \frac{\dot{\omega}_{k,j}}{W_k \nu_{k,j}}. \tag{2.4}$$

By summing all reaction rates $\dot{\omega}_k$ and applying Equation (2.2), one obtains:

$$\sum_{k=1}^{N} \dot{\omega}_k = 0. \tag{2.5}$$

According to the law of mass actions, the rate of progress is expressed as:

$$\mathcal{Q}_j = K_{f,j} \prod_{k=1}^{N} [\mathcal{S}_k]^{\nu'_{k,j}} - K_{b,j} \prod_{k=1}^{N} [\mathcal{S}_k]^{\nu''_{k,j}} = K_{f,j} \prod_{k=1}^{N} \left(\frac{\rho Y_k}{W_k}\right)^{\nu'_{k,j}} - K_{b,j} \prod_{k=1}^{N} \left(\frac{\rho Y_k}{W_k}\right)^{\nu''_{k,j}}, \tag{2.6}$$

where $K_{f,j}$ and $K_{b,j}$ are the rate constants of the forward and backward steps of the reaction j, respectively, ρ is the density of the mixture, Y_k is the mass fraction of the species k, i.e., the ratio of the mass of the species k over the mass of the mixture, and $[\mathcal{S}_k] = (\rho Y_k)/W_k$ is the molar concentration of the species k, i.e., the ratio of the moles of the species k over the volume of the mixture. The exponents represent the so-called *partial orders of reaction*, while their sum is referred to as the (overall) *order of the reaction*, quantifying to which extent the rate of progress depends on the concentration of the species. In elementary reactions, the partial orders of reactions are equal to the stoichiometric coefficients for each reactant, and, consequently, the overall order of the reaction is equal to the molecularity, i.e., the number of reacting molecules. This assumption has been made when writing Equation (2.6). When considering more complex systems, such as

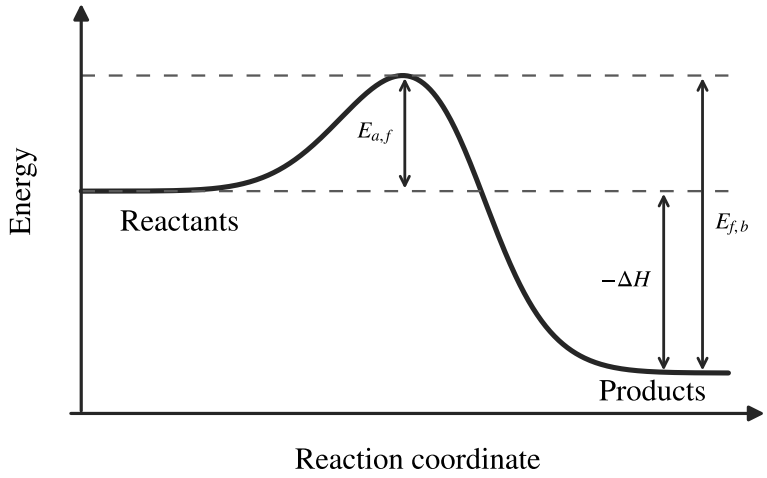

Figure 2.1: Schematic representation of the energy as a function of the reaction coordinate (adapted from [136]).

multi-step reactions, which are typical of combustion, explicit partial reaction orders, different from the stoichiometric coefficients, can be defined. Consequently, in actual combustion processes, the overall reaction order may be different from the molecularity, and needs to be assessed, either experimentally or based on analytical approaches (see Section 5.2.2).

The backward rate constant is related to the forward one through the relation:

$$K_{b,j} = \frac{K_{f,j}}{K_{eq,j}}, \tag{2.7}$$

where $K_{eq,j}$ is the equilibrium constant, defined as [212]:

$$K_{eq,j} = \left(\frac{p_0}{RT}\right)^{\sum_{k=1}^{N} \nu_{kj}} \exp\left(\frac{\Delta S_j^0}{R} - \frac{\Delta H_j^0}{RT}\right), \tag{2.8}$$

where $p_0 = 1$ bar, ΔS_j^0 and ΔH_j^0 are, respectively, the entropy and enthalpy changes for the reaction j, R is the universal gas constant, and T is the temperature.

Therefore, to characterize the rate of progress of a reaction j, it is sufficient to evaluate $K_{f,j}$. Arrhenius [10] provided a convenient theory to express it, based on its dependence on T:

$$K_{f,j} = A_{f,j} T^{\beta_j} \exp\left(-\frac{E_{a,j}}{RT}\right), \tag{2.9}$$

where $A_{f,j}$ is the pre-exponential factor, β_j is the temperature exponent, and $E_{a,j}$ is the activation energy. The forward and backward steps of a reaction j have different activation energy, with the backward step having a much larger energy, as schematized in Figure 2.1.

Elementary reaction rates expressed in the form of Equation (2.1) constitute the basis for the chemical modeling of combustion. However, they are not able to describe more complex, but relevant phenomena. To this scope, more elaborated formulations have been proposed, e.g., the three-body reaction [229], the falloff formulation [240], and the pressure-dependent Arrhenius expression [138], the characteristics of which are briefly recalled hereafter.

Given two reactants $\mathcal{A}$ and $\mathcal{B}$, and the product of their reaction $\mathcal{AB}$, the three-body reaction can be described in the form:

$$\mathcal{A} + \mathcal{B} + \mathcal{M} \rightleftharpoons \mathcal{AB} + \mathcal{M}, \tag{2.10}$$

where $\mathcal{M}$ is a collision partner that, in the forward direction, stabilizes $\mathcal{AB}$ by removing excess energy, and, in the backwards direction, breaks the bond of the $\mathcal{AB}$ molecule by supplying energy. Different species can act at the same time as collision partner, with different efficacy. To this scope, a collision efficiency ϵ is defined for each species k, and the effective concentration of the third body, to be introduced in Equation (2.6) to compute the rate of progress of the three-body reaction, is given by:

$$[\mathcal{M}] = \sum_{k=1}^{N} \epsilon_k [\mathcal{S}_k]. \tag{2.11}$$

The falloff reaction is characterized by the fact that, at low pressures, the third-body collider $\mathcal{M}$ is of order one, similarly to the previously described three-body reaction, while at high pressures the order of $\mathcal{M}$ becomes zero. In the formulation by Lindemann [240], the rate coefficient is evaluated as:

$$K_f(T, p_r) = K_\infty \left(\frac{p_r}{1 + p_r} \right), \tag{2.12}$$

where $p_r = K_0[\mathcal{M}]/K_\infty$ is a reduced pressure, and K_0 and K_∞ are two constants. With this definition, K_f approaches $K_0[\mathcal{M}]$ in the low-pressure limit, and K_∞ in the high-pressure one. To account for unimolecular processes, the expression in Equation (2.12) can be multiplied by a falloff function $F(T, p_r)$, as it is, for example, the Troe Falloff Function [135]:

$$\log_{10} F(T, p_r) = \frac{\log_{10} F_{cent}(T)}{1 + f_1^2}, \tag{2.13}$$

where $F_{cent}(T)$ is a function of temperature, and f_1 depends on both p_r and F_{cent}.

Another possible way to account for pressure effects on the rate of progress is by introducing a pressure-dependency in the Arrhenius rate expression of Equation (2.9):

$$p_i : K_{f,p_i}(T) = \mathcal{A}_{p_i} T^{\beta_{p_i}} \exp\left(-\frac{E_{a,p_i}}{RT} \right) \quad \text{for } i = 1, \ldots, N_p. \tag{2.14}$$

A logarithmic interpolation is performed at intermediate pressures $p_i < p < p_{i+1}$:

$$\log K_f(T, p) = \log K_{f,p_i}(T) + \left[\log K_{f,p_{i+1}}(T) - \log K_{f,p_i}(T) \right] \frac{\log p - \log p_i}{\log p_{i+1} - \log p_i}. \tag{2.15}$$

It is also possible to give different rate expressions for the same pressure p_i, in which case the rate constant $K_{f,p_i}(T)$ is given by the sum of all the rates at the pressure p_i.

2.2 Chemiluminescence

The chemical processes associated with combustion not only govern species conversion and the release of energy, but also lead to the formation of electronically excited atoms, molecules, or radicals. When these return from the unstable electronically excited state to the stable ground

state, light is emitted under the form of a photon [225]. This phenomenon, which is intrinsically linked to reaction pathways and radical production, is known as *chemiluminescence*, where the prefix *chemi-* underlines the fact that this light emission originates directly from chemical reactions, and not from thermal radiation [225].

Chemiluminescence constitutes a valuable experimental diagnostic technique to access the structure of flames and shed light on the chemical kinetics of combustion processes [189]. In particular, it has been widely adopted as an experimental marker of the heat release rate distribution [90, 275]. Among the different electronically excited species that can arise in combustion, the excited hydroxyl radical OH^* is particularly relevant, as it is present in any process containing oxygen (O_2) and hydrogen (H_2) atoms [246], i.e., in all flames burning a gaseous fuel. Moreover, in H_2–air flames, OH^* is the only chemiluminescence emitter [225].

For these reasons, an overview of the spectral characteristics of OH^* is given in the following. Its chemical kinetics will be detailed in Section 6.2, together with a presentation of the reaction mechanisms adopted in this dissertation for the numerical prediction of the OH^* distribution.

2.2.1 Spectral characteristics of OH^*

In quantum mechanics, a single electron in the potential field of an atom or molecule is characterized by four quantum numbers [225, 303]:

- The *principal quantum number* $n = 1, 2, 3, \ldots$.
- The *azimuthal quantum number* $\ell = 0, 1, 2, \ldots, n-1$.
- The *magnetic quantum number* $m_\ell = \ell, -\ell+1, \ldots, 1, 0, 1, \ldots, \ell-1, \ell$.
- The *spin magnetic quantum number* $m_s = \pm 1/2$.

Each electron is described by a unique set of quantum numbers, as stated by the Pauli exclusion principle [303]. A further description of these quantum designations is outside the scope of this work, and interested readers are referred, among others, to [225, 303].

In the ground state, the electron configuration of the hydroxyl radical OH is:

$$(1s\sigma)^2(2s\sigma)^2(2p\sigma)^2(2p\pi)^3,$$

where the superscript identifies the number of electrons in each state. This is often shortened in $X^2\Pi_i$. The excited OH^* state, on the other hand, is obtained when one of the $2p\sigma$ electrons is promoted to the $2p\pi$ orbital:

$$(1s\sigma)^2(2s\sigma)^2(2p\sigma)^1(2p\pi)^4.$$

This state is commonly denoted as $A^2\Sigma^+$, and the electronic transition responsible for OH^* chemiluminescence is consequently identified as the $A^2\Sigma^+ - X^2\Pi_i$ electronic system [246]. In the transition from the unstable excited state $A^2\Sigma^+$ to the stable ground state $X^2\Pi_i$, the energy difference is released in the form of a photon $h\nu$ [225], where h is the Planck constant and ν is the frequency of the associated electromagnetic wave.

The wavelength of the emitted photon is related to the energy difference between the two states. For the OH^* chemiluminescence, this leads to a wavelength $\lambda \approx 308$ nm [436], meaning that the resulting light emission is ultraviolet. It should be noted that other, less frequent transitions are possible. In particular, a radiation at around 280 nm can also be observed, while other

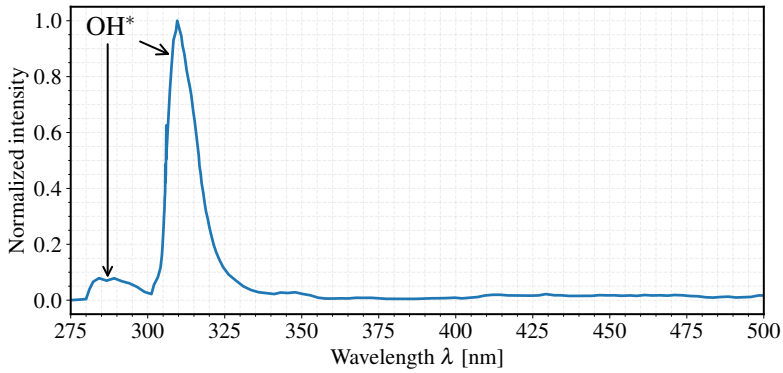

Figure 2.2: Typical chemiluminescence spectrum of an atmospheric H_2–air flame (adapted from [225]). OH^* is the sole chemiluminescence emitter.

transitions are generally too weak to be relevant [225]. Figure 2.2 shows a typical chemiluminescence spectrum for an atmospheric H_2–air flame, where the signature of the OH* emission is clearly identifiable.

2.3 Conservation equations for reacting flows

The flow of Newtonian fluids is well-described by the Navier–Stokes equations [313]. For a constant-property compressible flow, the solution of these equations leads to five primitive variables: the density ρ, the three-dimensional velocity field $\mathrm{u} = [u, v, w]^T$, and the energy E, which can be represented by the pressure p, the enthalpy h or the temperature T.

When passing to reacting flows, additional primitive variables must be introduced to characterize each of the N species involved in the chemical process. This is done through the mass fraction Y_k of the species k. Therefore, the number of primitive variables and, consequently, of equations to solve, passes from 5 to $N + 5$, marking the fundamental obstacle arising when numerically solving reacting flows. The equations to solve for a reacting compressible flow are recalled in the following.

The equation of momentum is unchanged with respect to the non-reacting case:

$$\frac{\partial}{\partial t}(\rho u_j) + \frac{\partial}{\partial x_i}(\rho u_i u_j) = -\frac{\partial p}{\partial x_j} + \frac{\partial \tau_{ij}}{\partial x_i} + \rho \sum_{k=1}^{N} Y_k f_{k,j}, \tag{2.16}$$

where u_j is the component j of velocity, $f_{k,j}$ is the volume force acting on the species k in the direction j, and τ_{ij} is the tensor of viscous forces, expressed, for a Newtonian fluid, as:

$$\tau_{ij} = \mu \left(\frac{\partial u_i}{\partial x_j} + \frac{\partial u_j}{\partial x_i} \right) - \frac{2}{3} \mu \delta_{ij} \left(\frac{\partial u_k}{\partial x_k} \right), \tag{2.17}$$

with μ being the dynamic viscosity of the mixture and δ_{ij} the Kronecker delta. It should be noted that, even though no term accounts explicitly for chemical reactions, the properties of the flow, such as μ or ρ, are modified by the combustion process. Therefore, even though Equation (2.16) is written in the same form as in the non-reacting case, the behavior described by it is different [311].

The equation of total mass conservation is identical to the one for non-reacting flows, since, as per the Lavoisier's Law, no mass is created or destroyed during a chemical process:

$$\frac{\partial \rho}{\partial t} + \frac{\partial \rho u_i}{\partial x_i} = 0. \tag{2.18}$$

On the other hand, an equation of mass conservation must be written for each species k:

$$\frac{\partial}{\partial t}(\rho Y_k) + \frac{\partial}{\partial x_i}(\rho u_i Y_k) = -\frac{\partial}{\partial x_i}(\rho V_{k,i} Y_k) + \dot{\omega}_k \quad \text{for } k = 1, \ldots, N, \tag{2.19}$$

where $V_{k,i}$ is the component i of the diffusion velocity of the species k. Recalling Equations (2.5) and (2.18), a necessary condition arises for $V_{k,i}$:

$$\sum_{k=1}^{N} Y_k V_{k,i} = 0. \tag{2.20}$$

The exact solution of $V_{k,i}$ is based on a system of size N^2, making its computation expensive and difficult [107]. Consequently, simplifications are required to retrieve its value in numerical simulations. Applying the Hirschfelder and Curtiss approximation [159], the diffusion velocity reads as:

$$V_{k,i} = -\frac{D_k}{X_k}\frac{\partial X_k}{\partial x_i} \quad \text{with} \quad D_k = \frac{1 - Y_k}{\sum_{j \neq k} X_j / \mathcal{D}_{jk}}, \tag{2.21}$$

where $X_k = WY_k/W_k$ is the mole fraction of the species k, with W being the molecular weight of the mixture, and $\mathcal{D}_{jk} = \mathcal{D}_{kj}$ is the binary mass diffusion coefficient of the species j into the species k. The coefficient D_k represents an equivalent diffusion coefficient of the species k into the rest of the mixture. While computationally convenient, this approximation does not ensure mass conservation, since Equation (2.20) is not fully respected. To overcome this issue, a correction velocity $V_{c,i}$ is introduced in Equation (2.21):

$$V_{k,i} = -\frac{D_k}{X_k}\frac{\partial X_k}{\partial x_i} + V_{c,i}, \tag{2.22}$$

whose value is retrieved by substitution in Equation (2.20):

$$V_{c,i} = \sum_{k=1}^{N} D_k \frac{W_k}{W}\frac{\partial X_k}{\partial x_i} \tag{2.23}$$

This formulation does not take into account the so-called Soret effect, namely the molecular species diffusion due to temperature gradients, as well as the molecular transport due to pressure gradients.

Finally, if h_s is the sensible enthalpy of the mixture, defined as:

$$h_s = \sum_{k=1}^{N} Y_k h_{s,k} = \sum_{k=1}^{N} Y_k \int_{T_0}^{T} c_{p,k} dT, \tag{2.24}$$

where $c_{p,k}$ is the specific heat capacity at constant pressure of the species k and T_0 is a reference temperature, then the conservation of energy can be expressed in the following form:

$$\frac{\partial}{\partial t}(\rho h_s) + \frac{\partial}{\partial x_i}(\rho u_i h_s) = \frac{\partial}{\partial t}(\rho p) + \frac{\partial}{\partial x_i}(\rho u_i p) + \frac{\partial}{\partial x_i}\left(\lambda \frac{\partial T}{\partial x_i}\right) - \frac{\partial}{\partial x_i}\left(\rho \sum_{k=1}^{N} h_{s,k} Y_k V_{k,i}\right) + \tau_{ij}\frac{\partial u_i}{\partial x_j} + \dot{Q} + \rho \sum_{k=1}^{N} Y_k f_{k,i} V_{k,i} + \dot{\omega}_T. \tag{2.25}$$

The term $\lambda \partial T/\partial x_i$ derives from Fourier's law and is related to heat diffusion, while the term $\rho \sum_{k=1}^{N} h_{s,k} Y_k V_{k,i}$ is associated with the diffusion of species with different enthalpies, as it occurs in multi-species gas. The heat flux due to species mass fraction gradients (Dufour effect) is neglected. The expression $\tau_{ij}\partial u_i/\partial x_j$ defines the viscous heating source term, $\dot{Q}$ is the heat source term, and $\rho \sum_{k=1}^{N} Y_k f_{k,i} V_{k,i}$ denotes the power produced by volume forces f_k on the species k. Finally, $\dot{\omega}_T$ is the heat release rate due to combustion:

$$\dot{\omega}_T = -\sum_{k=1}^{N} \Delta h^0_{f,k} \dot{\omega}_k, \tag{2.26}$$

where $\Delta h^0_{f,k}$ is the formation enthalpy of the species k.

The diffusion terms in Equations (2.17), (2.21) and (2.25) are often characterized in terms of dimensionless parameters. The Schmidt number relates the momentum and molecular diffusion of the species k:

$$Sc_k = \frac{\mu}{\rho D_k} = \frac{\nu}{D_k}, \tag{2.27}$$

where $\nu = \mu/\rho$ is the kinematic viscosity. Heat transport and momentum are compared by the Prandtl number, defined as:

$$Pr = \frac{\mu c_p}{\lambda} = \frac{\rho \nu c_p}{\lambda} = \frac{\nu}{D_{th}}, \tag{2.28}$$

where $c_p = \sum_{k=1}^{N} c_{p,k} Y_K$ is the specific heat capacity at constant pressure of the mixture, while $D_{th} = \lambda/(\rho c_p)$ is the heat diffusion coefficient. This can be linked to the species diffusion coefficient D_k through the Lewis number of the species k:

$$Le_k = \frac{D_{th}}{D_k} = \frac{Sc_k}{Pr}. \tag{2.29}$$

2.4 Flame regimes

To improve the understanding of reacting flows, canonical situations have been identified by the combustion research community, for which the equations described in Section 2.3 can be directly solved. Furthermore, flame regimes have been defined to classify the level of complexity of a given flame.

A first classification is based on whether the reactants are premixed or not before the combustion process. Indeed, for the combustion to occur, three elements are required, namely a fuel, an oxidizer, and high temperature. In other words, a certain degree of mixing must be achieved

between fuel and oxidizer in a high temperature region. Based on this, it is possible to distinguish *premixed* flames, for which fuel and oxidizer are mixed prior to combustion, and *non-premixed* flames, where this preliminary mixing does not occur. The latter are also called *diffusion* flames when fuel and oxidizer are injected separately into the combustion chamber. Premixed flames are more intense and less polluting, but more dangerous since any high temperature point can lead to ignition and undesired combustion [311]. Non-premixed flames, instead, are less rapid and reach higher local maximum temperatures, leading to enhanced production of pollutants, but are safer since the reactants are stored separately [311]. Moreover, non-premixed flames can burn for any combination of fuel and oxidizer flow rates, while premixed flames are limited by a lower and an upper flammability limit for the mixing of the reactants [311].

A second classification is based on turbulence, leading to the distinction between *laminar* and *turbulent* flames, depending on the flow Reynolds number Re. Evidently, most practical combustors in industrial applications experience turbulent combustion, while laminar flames are limited to academic configurations, both experimentally and numerically. Nevertheless, the more simple laminar flames allow for a more detailed understanding of flame properties in turbulent cases, and are fundamental from a theoretical and modeling point of view, thus explaining their relevance for the combustion research community.

Most of the results presented in this work concern premixed flames, both laminar and turbulent. For this reason, the remaining of this Chapter is dedicated to the description of their main features.

2.5 Laminar premixed flames

In the most general form, the premixed combustion process can be described by the global reaction:

$$\nu'_F F + \nu'_O O \longrightarrow P, \tag{2.30}$$

where F and O are the fuel and oxidizer, ν'_F and ν'_O their respective stoichiometric coefficients, and P the product of the combustion process. Under stoichiometric conditions, the fuel and oxidizer mass fractions are in the ratio:

$$s = \left(\frac{Y_O}{Y_F}\right)_{st} = \frac{\nu'_O W_O}{\nu'_F W_F}, \tag{2.31}$$

called the mass stoichiometric ratio. The *equivalence ratio* ϕ is then defined as:

$$\phi = s\frac{Y_F}{Y_O}, \tag{2.32}$$

and controls premixed combustion. Depending on the operating conditions, in terms of temperature and pressure, and on the fuel, flammability limits are defined, indicating the lowest and highest possible concentrations of fuel with respect to the oxidizer, for which the combustion process can occur [136]. Therefore, the value of ϕ is limited by a lower and an upper bound.

Most practical combustors are operated under lean conditions, i.e., $\phi < 1$, while rich conditions ($\phi > 1$) are less relevant for many practical applications, since fuel consumption is not optimal. In lean conditions, the premixed reactant mixture contains mostly air, while the fuel addition does not impact significantly the gas properties, such as the mixture molecular weight, the transport properties, and the heat capacities. This allows for simplifications in combustion models [311]. Laminar premixed flames are characterized by two main properties, described in the following: the speed and the thickness.

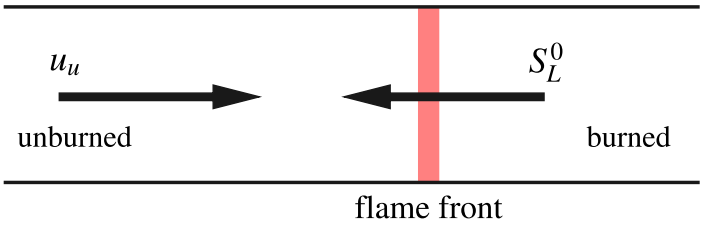

Figure 2.3: Freely propagating one-dimensional laminar premixed flame.

2.5.1 Flame speed

The *laminar flame speed* (or *laminar burning velocity*) S_L^0 is defined as the propagation speed of a perfectly planar one-dimensional (1D) flame into fresh gases at rest [68]. Therefore, in a steady state, i.e., when the flame position is constant in time, S_L^0 must be equal and opposite to the velocity of the unburned mixture u_u, as schematized in Figure 2.3 [311]. Based on the mass conservation of the fuel (see Equation (2.19)) in the flame reference frame, the value of S_L^0 can be related to the integral of the fuel reaction rate $\dot{\omega}_F$ (see Equation (2.3)):

$$S_L^0 = -\frac{1}{\rho_u (Y_F^u - Y_F^b)} \int_{-\infty}^{+\infty} \dot{\omega}_F dx, \tag{2.33}$$

where x is the direction of propagation of the flow, from the unburned to the burned mixture.

This velocity is influenced by the operating conditions under which the fresh gases are. More specifically, the laminar flame speed increases for a higher temperature of the unburned mixture T_u, and decreases for higher pressures, as shown in Figure 2.4 for H_2–air premixed flames at variable equivalence ratio. It can also be observed that S_L^0 does not peak at stoichiometry, but rather at a richer equivalence ratio ($\phi \approx 1.5 - 2.0$), due to the high diffusivity of H_2 [229], as it will be further discussed in Section 4.2. Based on experimental results, a polynomial expression can be defined:

$$S_L^0(p, T) = S_L^0(p^0, T_u^0) \left(\frac{p}{p^0}\right)^{\alpha_p} \left(\frac{T_u}{T_u^0}\right)^{\alpha_T}, \tag{2.34}$$

where α_p and α_T are defined for a range of operating conditions, under which combustion is operated.

The definition of S_L^0 is based on the implicit assumption that the flame front is an infinitely thin interface separating fresh and burnt gases. Actual flames, however, are multi-dimensional, and have a finite thickness (see Section 2.5.2). The interface between fresh and burnt gases can be therefore seen as a continuous set of isosurfaces, and a progress variable C can be defined to measure the evolution of the combustion process from the reactants ($C = 0$) to the products ($C = 1$). The progress variable can be based on any variable, provided that its value is monotonic across the flame, as it occurs, for example, for the temperature or the fuel mass fraction. Then, the flame surface can be defined as the locus where $C = C^*$, even though this introduces some uncertainties, since this definition is strongly dependent on the quantity chosen to compute C, and on the value considered for C^* [229]. Given a flame surface $C = C^*$, the normal to the flame front can be defined on any point on this surface (see Figure 2.5):

$$\mathrm{n} = -\frac{\nabla C}{|\nabla C|}, \tag{2.35}$$

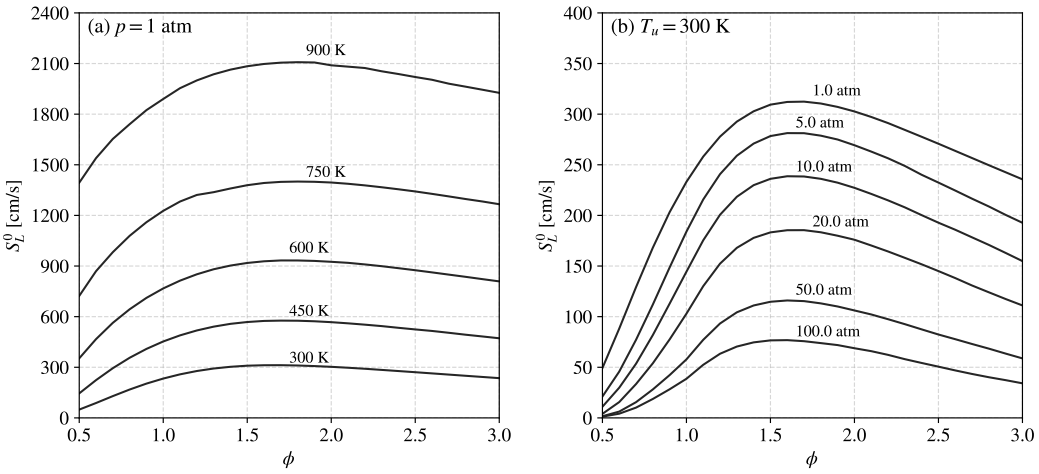

Figure 2.4: Laminar flame speed S_L^0 of hydrogen–air premixed flames as a function of the equivalence ratio ϕ at p = 1 atm and variable unburned gas temperature T_u (a), and T_u = 300 K and variable pressure p (b). Calculations are performed with the San Diego mechanism [339] using Cantera [137].

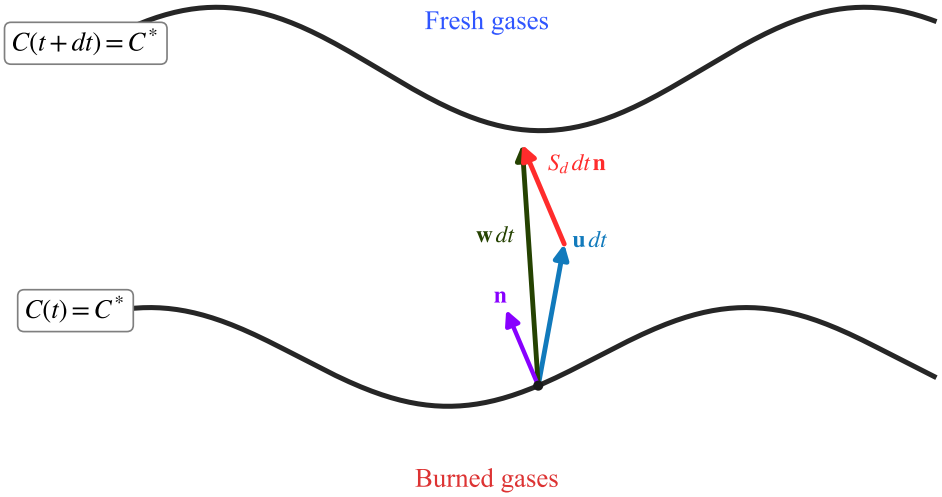

Figure 2.5: Notations for the definitions of flame speed and flame surface normal (adapted from [311]).

with n pointing toward the fresh gases.

The *absolute flame speed* S_a is defined as the velocity component normal to the flame front:

$$S_a = \mathrm{w} \cdot \mathrm{n} = \frac{1}{|\nabla C|} \frac{\partial C}{\partial t}, \tag{2.36}$$

where w is the flame front speed, i.e., the velocity at which a point must move to remain attached to the isosurface $C = C^*$. Evidently, the value of S_a strongly depends on the chosen value for C^*, except when the flame front is not thickened or thinned by the flow, in which case all isosurfaces must move at the same speed to keep the same thickness [311].

The *flame displacement speed* $S_d|_{C=C^*}$ measures the speed of the flame front relative to the flow:

$$S_d|_{C=C^*} = (\mathrm{w} - \mathrm{u}) \cdot \mathrm{n} = S_a - \mathrm{u} \cdot \mathrm{n}, \tag{2.37}$$

where u is the flow velocity. This quantity has also a strong local variability, since it depends both on the value of C^* and on the point chosen on the isosurface $C = C^*$. Moreover, it is affected by flow acceleration, straining, curvature and transport phenomena [409]. To reduce the ambiguity in the definition of this quantity, a density-weighted version has been introduced [133, 134]:

$$S_d = \frac{\rho S_d|_{C=C^*}}{\rho_u}, \tag{2.38}$$

allowing for a meaningful comparison between values defined on different isosurfaces.

Finally, a chemical definition of the flame speed can be introduced, based on reaction rates only. This is the *flame consumption speed*:

$$S_c = -\frac{1}{\rho_u(Y_F^u - Y_F^b)} \int_\Gamma \dot{\omega}_F ds, \tag{2.39}$$

where Γ is a streamline normal to the flame front, i.e., parallel to n for any isosurface $C = C^*$ [133]. Evidently, S_c has the great advantage of being independent of the chosen value of C^* to identify the flame surface. On the other hand, this definition can be adopted only in numerical simulations, for which the value of $\dot{\omega}_F$ is available. Experimentalists, instead, measure the flame speed by considering S_d [311]. Finally, recalling Equation (2.33), it can be observed that S_L^0 and S_c are equivalent for a laminar 1D unstretched premixed flame. As it will be further discussed in Section 2.5.3, this correspondence is not necessarily verified in the case of stretched flames.

2.5.2 Flame thickness

Thickness is another fundamental quantity to characterize flames. From a numerical combustion point of view, it holds even more importance, as it defines the computational grid resolution necessary to capture the physics of a flame front. Moreover, from a theory and modeling point of view, it is compared to the length scales of turbulence to assess flame–turbulence interaction [301] (see Section 2.7.4).

As for the flame speed, different definitions exist also for the flame thickness. A definition based on scaling laws is the *diffusive flame thickness*:

$$\delta = \frac{\lambda_u}{\rho_u c_p S_L^0} = \frac{D_{th,u}}{S_L^0}. \tag{2.40}$$

This definition, albeit easier to compute, is too approximate and usually too small [311]. For this reason, one of the most widely implemented in the literature is the *thermal flame thickness*, determined from the temperature profile along a streamline Γ normal to the flame front [179, 378] (see Figure 2.6):

$$\delta_L^0 = \frac{T_b - T_u}{\max_\Gamma \left(\left|\frac{\partial T}{\partial x}\right|\right)} \tag{2.41}$$

The thickness represents one of the major constraints for numerical simulations of flames. Indeed, as shown in Figure 2.7 for H_2–air flames at variable equivalence ratio and pressure, its value is in the order of few hundreds micrometers, and is sensibly reduced at high pressures, compatible with engineering-relevant applications. This imposes a severe constraint on the mesh resolution, even in the case of laminar flows, and often makes mandatory to introduce combustion models for the simulation of turbulent industrial-scale cases. It should be noted that the flame thickness reaches its minimum value for rich conditions ($\phi \approx 1.5 - 2.0$), where S_L^0 is the highest (see Figure 2.4), while lean flames have the advantage of being thicker.

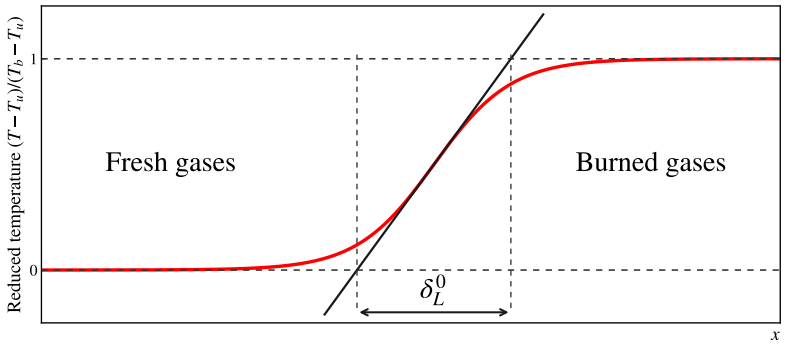

Figure 2.6: Definition of thermal flame thickness for a premixed flame (adapted from [311]).

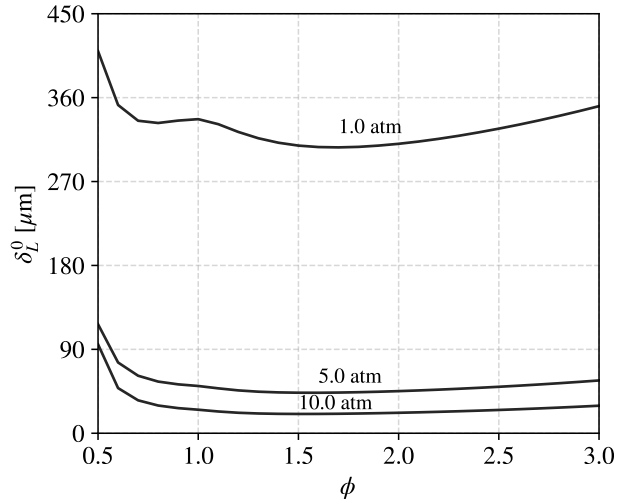

Figure 2.7: Laminar flame thickness δ_L^0 of hydrogen–air premixed flames as a function of the equivalence ratio ϕ at T_u = 300 K and variable pressure p. Calculations are performed with the San Diego mechanism [339] using Cantera [137].

2.5.3 Flame stretch

The values of laminar flame speed and thickness are usually retrieved in the case of fully planar, unstretched flames. Actual flames, however, are subject to stretch due to their interaction with the flow field. The *flame stretch* is defined as the fractional rate of change of a flame surface element $\mathcal{A}$ [50, 186, 258]:

$$\kappa = \frac{1}{\mathcal{A}} \frac{d\mathcal{A}}{dt}. \tag{2.42}$$

From this definition, it derives that stretch is positive when the flame surface increases, and negative otherwise. Another definition of stretch, derived from a purely kinematic approach for a thin flame sheet, is [50]:

$$\kappa = -\mathrm{nn} : \nabla \mathrm{w} + \nabla \cdot \mathrm{w}, \tag{2.43}$$

which, recalling Equation (2.37), becomes:

$$\kappa = \underbrace{-\mathrm{nn} : \nabla \mathrm{u} + \nabla \cdot \mathrm{u}}_{\kappa_s} + \underbrace{S_d|_{C=C^*} (\nabla \cdot \mathrm{n})}_{\kappa_c}, \tag{2.44}$$

The term κ_s represents the strain in the plane locally parallel to the flame, and can be written as $\nabla_t \cdot \mathrm{u}$ to underline the fact that it is tangential to the flame [66]. On the other hand, κ_c is related to the geometrical curvature of the flame front $K = (\nabla \cdot \mathrm{n})/2$. Given this definition and the one adopted for n (see Equation (2.35)), κ_c is positive when the flame element is curved convexly toward the fresh gases, while the opposite holds when $\kappa_c < 0$.

2.5.4 Lewis number in premixed combustion

Let us consider, for simplicity, a lean combustion process occurring according to the global reaction in Equation (2.30), and denote by D_F and D_O the diffusion coefficients of fuel and oxidizer, respectively. If $D_F/D_O > 1$, the concentration of fuel increases in proximity of the reaction zone, enhancing the local equivalence ratio and making the mixture burn more rapidly (see Figure 2.4). On the other hand, if $D_F/D_O < 1$, the opposite occurs, and the mixture burns less rapidly. This mechanism, based on the unbalance of the species diffusivities, is denominated *preferential diffusion*.

If $D_F = D_O$, but both are different from the heat diffusion coefficient D_{th}, i.e, $Le \neq 1$ (see Equation (2.29)), then the diffusion of species toward the flame front tends to promote the combustion process, while the diffusion of heat out of the flame does the opposite. Therefore, for $Le < 1$ ($D_{th} < D_F = D_O$), the combustion process is enhanced, and a higher flame temperature can be achieved, while the reverse occurs for $Le > 1$. This mechanism is called *differential diffusion* or *non-unity Lewis number effect*.

In real flames, D_F, D_O and D_{th} are generally different, meaning that preferential and differential diffusion mechanisms can coexist, a situation sometimes denominated *non-equidiffusional effect*. In first approximation, for equivalence ratios sufficiently different from one, the overall molecular diffusion of the mixture is governed by the deficient reactant, i.e., the species present in the lowest amount, which is the fuel for lean mixtures [72, 230, 293]. A more rigorous approach, however, is based on the definition of an effective mixture Lewis number [20, 185]:

$$Le_{eff} = 1 + \frac{(Le_E - 1) + (Le_D - 1)B}{1 + B}, \tag{2.45}$$

where the subscripts E and D denote the excess and deficient reactants, respectively, and B is a weight:

$$B = \begin{cases} 1 + Ze(\phi - 1) & \text{if } \phi > 1 \\ 1 + Ze(1/\phi - 1) & \text{if } \phi < 1 \end{cases}. \tag{2.46}$$

The reduced activation energy Ze, also denominated Zel'dovich number [434], is defined as:

$$Ze = \frac{E_a(T_b - T_u)}{RT_b^2}, \tag{2.47}$$

where E_a is the global activation energy of the combustion process (see Section 5.2.3). For $\phi \gg 1$ and $\phi \ll 1$, $B \to \infty$ and $Le_{eff} \approx Le_D$, coherently with the aforementioned approximation.

For conventional hydrocarbons (e.g., methane), $Le_{eff} \approx 1$. On the other hand, this hypothesis does not hold true for light molecules such as H_2. As discussed in the next Section, the Lewis number impacts the behavior of the flame, most notably its response to stretch. Therefore, the non-unity Lewis number deeply affects the properties of H_2 flames, as it will be further detailed in Chapter 4.

2.5.5 Flame response to stretch

Stretch can have a strong impact on the structure and dynamics of premixed flames. Based on the seminal work by Markstein [252] and on subsequent more rigorous asymptotic theories [70, 118, 258, 293], in the limit of small strain and curvature, the displacement and consumption speeds are a linear function of the sole stretch κ:

$$\frac{S_d}{S_L^0} = 1 - \frac{\mathcal{L}_d}{S_L^0}\kappa, \tag{2.48}$$

and

$$\frac{S_c}{S_L^0} = 1 - \frac{\mathcal{L}_c}{S_L^0}\kappa, \tag{2.49}$$

where $\mathcal{L}_d$ and $\mathcal{L}_c$ are denominated Markstein lengths, and S_d is measured on the fresh gases side (i.e., $C^* = 0$). The two Markstein lengths are generally different, highlighting the different response to stretch of the two flame speeds [311]. In non-dimensional form, the Markstein numbers Ma_d and Ma_c can be introduced, given by the ratio of the corresponding Markstein lengths and of the diffusive flame thickness δ (see Equation (2.40)). Several theoretical expressions are available in the literature to compute the Markstein lengths or numbers. In particular, for constant viscosity, single-step flames with variable density, Clavin and Joulin [67] derived the following expressions:

$$Ma_d = \frac{\mathcal{L}_d}{\delta} = \frac{T_b}{T_b - T_u}\ln\left(\frac{T_b}{T_u}\right) + \frac{1}{2}Ze(Le_D - 1)\frac{T_u}{T_b - T_u}\int_0^{(T_b-T_u)/T_u}\frac{\ln(1+x)}{x}dx, \tag{2.50}$$

and

$$Ma_c = \frac{\mathcal{L}_c}{\delta} = \frac{1}{2}Ze(Le_D - 1)\frac{T_u}{T_b - T_u}\int_0^{(T_b-T_u)/T_u}\frac{\ln(1+x)}{x}dx. \tag{2.51}$$

These relations highlight the impact of Le_D on the value and the sign of the Markstein numbers. Based on Equations (2.49) and (2.51), S_c is almost insensitive to stretch when $Le_D = 1$, since $Ma_c = 0$, meaning that the only effect of increasing stretch is the thinning of the flame front. For $Le_D < 1$, instead, $Ma_c < 0$, and S_c increases with the stretch, with gains that can be quite significant [406]. For $Le_D > 1$, on the other hand, the heat release decreases with increasing stretch, slowing down the flame ($Ma_c > 0$).

Stretch has an impact also on the temperature of the burned gases. Indeed, when a flame characterized by $Le_{eff} > 1$ is subject to positive stretch, heat losses are increased due to the thickening of the flame front, overcoming the positive contribution due to the diffusion of reactants. As a result, the local flame temperature becomes lower than the adiabatic one. Evidently, the opposite occurs for $Le_{eff} < 1$, and these flames can reach super-adiabatic temperatures. Analytical relations for the dependency of the flame temperature on stretch have been provided by Clavin and Williams [70] and by Giannakopoulos et al. [133].

2.6 Intrinsic flame front instabilities

Flame fronts can be affected by intrinsic instabilities, i.e., instabilities directly associated to the combustion process, and not to the interaction of the flame with the surrounding environment. The insurgence of cellular structures on otherwise planar flame fronts, in different forms

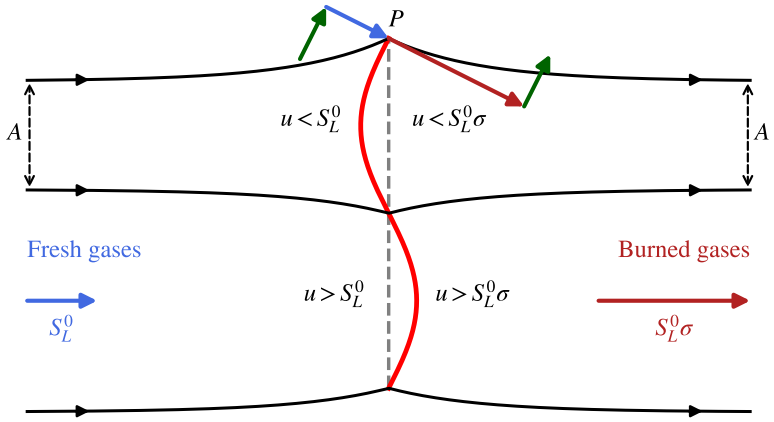

Figure 2.8: Schematic representation of the hydrodynamic instability mechanism (adapted from [229]).

and scales, has been observed in the literature for several flame configurations and fuels, including both hydrocarbons and hydrogen [144, 182, 239, 253, 317, 430].

In the following, two main mechanisms leading to the insurgence of instabilities are described: the hydrodynamic (or Darrieus–Landau) instability, and the thermodiffusive one.

2.6.1 Hydrodynamic instability

Under the assumption of infinitely thin flame, i.e., a flame whose thickness is sensibly small compared to the flow lengthscales, the flame front represents a discontinuity between the fresh gases, with density ρ_u, and the burned ones, with density ρ_b. In this framework, known as *Landau propagation* [229], stretch effects (see Section 2.5.5) are not considered, and the flame consumption speed is assumed to be equal to S_L^0 on the whole flame surface. In the burned gases, for continuity reasons, the velocity is equal to $S_L^0\sigma$, where $\sigma = \rho_u/\rho_b$ is the expansion ratio across the flame. Furthermore, the fluid is taken as incompressible, inviscid and non-conducting.

The hydrodynamic instability can be triggered by the density discontinuity across the flame, when the initially planar flame front is subjected to a weak perturbation, as illustrated in Figure 2.8. Since the disturbance is located in proximity of the flame front, the area $\mathcal{A}$ of the streamtubes in the undisturbed far upstream and far downstream regions must be equal. On a point P on the flame interface, however, the normal component of velocity abruptly changes due to the density variation, while the tangential component is conserved. Consequently, the streamlines must diverge (converge) when approaching a convex (concave) flame segment relative to the unburned gases. The variation in the streamtube section leads to a reduction of velocity in the convex regions, and to an increase of velocity in the concave ones, thus amplifying the initial perturbation. Since the flame speed is always equal to S_L^0, an unbalance arises between the flow and flame velocities, resulting in a further distortion of the flame front. Therefore, the hydrodynamic instability mechanism is absolutely unstable, and, since it is independent of the lengthscale, can affect any flame subjected to perturbations of any wavelength [229].

The first theoretical studies on this instability were conducted, independently, by Darrieus [82] and Landau [219]. Based on linear stability analysis, it is possible to solve the linearized Euler equations together with the Rankine–Hugoniot jump relations [320], leading to the definition of a dispersion relation, relating the wavenumber k and the growth rate ω of a harmonic flame

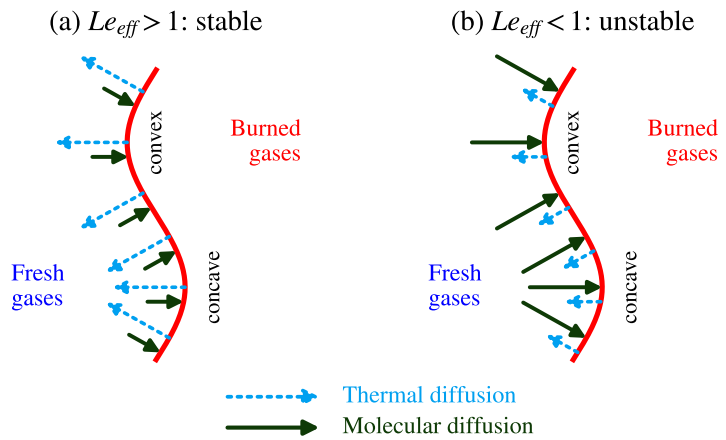

Figure 2.9: Schematic representation of the thermodiffusive instability mechanism: stable case for $Le_{eff} > 1$ (a) and unstable case for $Le_{eff} < 1$ (b) (adapted from [229]).

perturbation:

$$\omega = \underbrace{\frac{-\sigma + \sqrt{\sigma^3 + \sigma^2 - \sigma}}{\sigma + 1}}_{\omega_{DL}} S_L^0 k, \tag{2.52}$$

with $\omega_{DL} > 0$, meaning that the perturbation growth rate is always positive and confirming the unconditional instability of this mechanism. Furthermore, Equation (2.52) indicates that the growth rate is proportional to the wavenumber, hence perturbations associated with short spatial lengths are amplified more rapidly than those characterized by larger wavelengths. Nevertheless, this model is not able to capture the impact of disturbances on spatial scales comparable to the flame thickness, since the infinitely thin flame assumption is not valid anymore.

2.6.2 Thermodiffusive instability

Differential diffusion has a relevant role on the dynamics of flames [234], impacting their stability [229, 311]. Let us consider a planar flame front, perturbed into a series of alternating convex and concave segments toward the fresh gases, as shown in Figure 2.9. For $Le_{eff} > 1$, when the flame front is concave, the diffusion of heat toward the fresh gases is faster than the diffusion of reactants toward the burned gases. The reactants are then heated and burn faster (see Figure 2.4), augmenting the local flame speed with respect to S_L^0. In the convex regions, instead, heat diffuses in a broader region, and the flame speed decreases compared to S_L^0. As a result, the flame front wrinkling is smoothed out and the flame is cellularly stable. On the contrary, when $Le_{eff} < 1$, for similar, but opposite reasons, the flame is cellularly unstable. Since this mechanism is associated with the thermal diffusion, the instability is usually referred to as thermodiffusive (TD). Nevertheless, it should be noted that, recalling the concept of preferential diffusion (see Section 2.5.4), the same instability phenomenon can be interpreted on the basis of the different diffusivities of the deficient and excess reactants, indicating that the flame is unstable when the deficient reactant is more mobile, i.e., when $D_D/D_E > 1$.

Since the instability is caused by the modification of the diffusional structure of the flame, the size of the wrinkles is of the order of the flame thickness [229], meaning that Equation (2.52) is not valid. This also explains why, experimentally, stable flames have been observed even in the

presence of hydrodynamic effects, which should lead unconditionally to the Darrieus–Landau instability described in Section 2.6.1. Indeed, when $Le_{eff} > 1$, TD phenomena stabilize the flame at the small scales against the hydrodynamic mechanism, leading to globally stable flames. For $Le_{eff} < 1$, instead, the TD instability is combined with the hydrodynamic instability, as described in the following.

The TD instability mechanism has been widely investigated in the literature, following different approaches [19, 118, 184, 256–258, 293, 368]. In particular, based on a perturbative approach, Matalon and Matkowsky [258] developed a fully non linear hydrodynamic model for the flame, and Matalon et al. [256] subsequently derived a comprehensive dispersion relation, including the effects of stoichiometry, temperature-dependent transport coefficients, and reaction orders [221]. For a planar flame, this corresponds to:

$$\omega = \omega_{DL} S_L^0 k \underbrace{- \left[B_1 + Ze(Le_{eff} - 1)B_2 + PrB_3 \right]}_{\omega_2} S_L^0 \delta k^2, \tag{2.53}$$

where ω_{DL} is the first-order growth rate associated with the hydrodynamic instability defined in Equation (2.52), while B_1, B_2, and B_3 are positive coefficients depending on the expansion ratio σ [4, 165, 256, 259]. From a physical point of view, B_1 takes into account the thermal diffusion contribution, which tends to stabilize the flame due to heat loss. The term associated with B_2 includes the Zel'dovich number, which appears in the expression of the Markstein length (see Equation (2.51)), indicating that the stability to TD phenomena is related to the flame response to stretch. Evidently, for $Le_{eff} < 1$, this term is destabilizing, while the opposite occurs for $Le_{eff} > 1$. Finally, the term associated with B_3 is related to the impact of viscosity via the Prandtl number Pr, and is stabilizing. Therefore, the overall stability of the flame depends on the sign of the sum of these terms, leading to the definition of a critical value of the effective Lewis number Le_{eff}^c where $\omega_2 = 0$. This value marks the passage from unconditional instability ($\omega_2 > 0$) to partial stability ($\omega_2 < 0$):

$$Le_{eff}^c = 1 - \frac{B_1 + PrB_3}{ZeB_2}. \tag{2.54}$$

For $Le_{eff} > Le_{eff}^c$, a cut-off wavenumber k_c can be defined, beyond which the hydrodynamic instability is damped by the TD mechanism. Figure 2.10 describes these different possible scenarios based on the dispersion relation of Equation (2.53).

Based on this description, one may conclude that flames characterized by low values of Le_{eff} are unstable, whatever perturbation is applied. Nevertheless, as it will be detailed in Chapter 4, for lean premixed H_2–air flames, characterized by $Le_{eff} < 1$, the TD mechanism, while being destabilizing on a wide range of wavenumbers, can indeed be stabilizing for very low perturbation wavelengths [25]. From a physical standpoint, this can be related to the transverse thermal and molecular diffusive fluxes acting in a curved flame [68, 221]. These diffusive fluxes, acting normally to the curved front, can be decomposed in a longitudinal and in a transverse component. The longitudinal fluxes determine the structure of the preheat zone, in terms of temperature and reactant profiles. On the other hand, the transverse fluxes, which are absent in a planar flame, grow with the flame curvature, as the ratio of the flame thickness δ and of the perturbation wavelength λ increases. This determines the insurgence of hotter and cooler reaction zones, leading to local flame acceleration and deceleration and, consequently, to the previously described TD mechanism (see Figure 2.9). This mechanism, however, cannot grow indefinitely. Indeed, for $\lambda < \delta$, the TD mechanism is hindered by the increasing local transverse gradients of heat and reactants, which promote transverse heat conduction and reactant diffusion [221]. As a con-

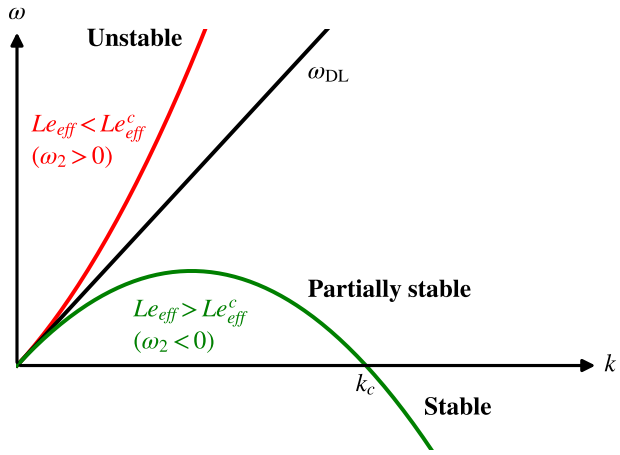

Figure 2.10: Dispersion relation of Equation (2.53) for a planar flame considering hydrodynamic and thermodiffusive effects, highlighting the different flame stability regimes.

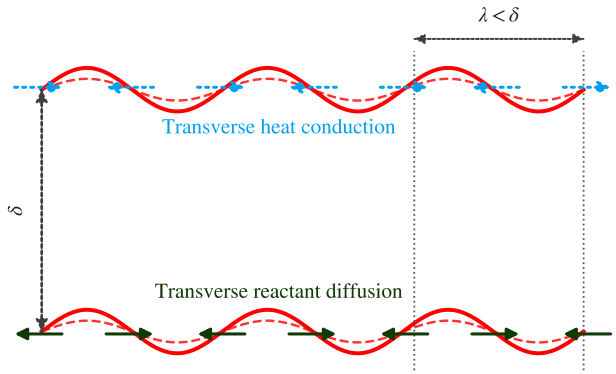

Figure 2.11: Stabilization of the thermodiffusive mechanism induced by transverse conduction/diffusion for very low perturbation wavelength $\lambda < \delta$ (adapted from [221]).

sequence, the flame perturbation is damped, irrespective of the Lewis number, as schematically illustrated in Figure 2.11.

This stabilizing mechanism can be taken into account by including higher order terms in the dispersion relation. For example, based on a weakly nonlinear phenomenological model, the following dispersion relation is reported in [221]:

$$\omega = k - \frac{\mathcal{M}a}{\sigma - 1}k^2 - \frac{\gamma^2}{\sigma - 1}k^4, \tag{2.55}$$

where σ is the expansion ratio across the flame, $\mathcal{M}a$ is the Markstein number, highlighting the impact of stretch effect on the flame dynamics in analogy with the B_2-related term in Equation (2.53), while γ modulates higher-order effects. The interplay of the destabilizing TD second-order term and of the stabilizing small wavelength fourth-order term can be considered as responsible for the unsteady nature of TD instabilities in the nonlinear regime [221]. Indeed, the destabilizing term leads to the increase in the local flame curvature, which eventually triggers the stabilizing mechanism, with opposite effect, thus decreasing the local curvature and leading to an unsteady behavior caused by the competition of the two processes.

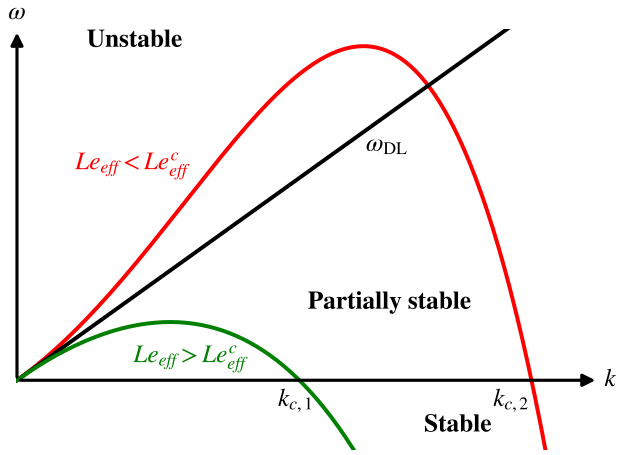

Figure 2.12: Dispersion relation of Equation (2.55) for a planar flame considering the thermodiffusive stabilizing effect at high wavenumbers, highlighting the different flame stability regimes.

A qualitative representation of the dispersion relation of Equation (2.55) is shown in Figure 2.12. In analogy with Equation (2.53), a critical Lewis number Le^c_{eff} can be defined, for which the second order term is null. For $Le_{eff} > Le^c_{eff}$, aside from the different shape of the curve, similar consideration can be made as for the dispersion relation shown in Figure 2.10. For $Le_{eff} < Le^c_{eff}$, however, a stark difference arises. Indeed, while destabilizing TD effects act synergistically with the hydrodynamic instability at low perturbation wavenumbers, at very large wavenumbers the higher-order stabilizing mechanism associated with transverse heat and mass diffusion can become dominant over destabilizing TD effects. In this framework, a cut-off wavelength $k_{c,2}$ can be achieved, at which the flame stabilizes.

2.7 Turbulent premixed flames

In a turbulent premixed flame, the laminar flame front, whose main features have been described in Section 2.5, interacts with turbulent eddies, of variable speed and size. This interaction can lead to significant variations in the flame properties. Indeed, it has been observed experimentally that the action of turbulence on combustion leads to an increase of the flame brush thickness and of the combustion rate [311].

In the following, the general features of turbulent premixed flames are recalled. This knowledge will be applied in Section 4.3 to describe the peculiar characteristics of turbulent lean premixed H_2–air flames.

2.7.1 Turbulent flame speed

Let us consider the turbulent equivalent of the freely-propagating 1D laminar flame represented in Figure 2.3, a configuration often referred to in the literature as *flame-in-a-box* [15, 166]. A planar turbulent flame is placed in a box of transversal section $\mathcal{A}_0$ and volume V, and can freely propagate in the longitudinal direction. Figure 2.13 reports a schematic representation of the longitudinal section.

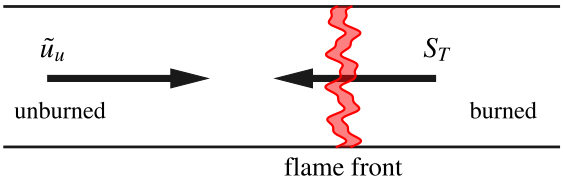

Figure 2.13: Freely propagating one-dimensional turbulent premixed flame.

In analogy with the definition of S_L^0, the *turbulent flame speed* S_T can be defined as the velocity necessary at the inlet of the box to keep the flame statistically steady, i.e., stationary *in the mean*. Due to continuity, the following condition holds:

$$\overline{\rho}\widetilde{u}_u = \rho_u S_T, \tag{2.56}$$

where $\bar{\cdot}$ denotes the Reynolds average, while $\widetilde{\cdot}$ indicates the Favre average (see Section 3.2). Furthermore, by considering the Favre-averaged version of the species mass conservation equation (see Equation (2.19)):

$$\frac{\partial}{\partial t}(\overline{\rho}\widetilde{Y}_k) + \frac{\partial}{\partial x_i} = -\frac{\partial}{\partial x_i}(\overline{\rho}\widetilde{u}_i\widetilde{Y}_k)\left(\overline{V_{k,i}Y_k} + \overline{\rho}\widetilde{u_i''Y_k''}\right) + \overline{\dot{\omega}}_k \quad \text{for } k = 1, \ldots, N, \tag{2.57}$$

and writing it for the fuel in the reference frame of the flame for the considered configuration, the following expression is derived:

$$\rho_u S_T \frac{\partial \widetilde{Y}_F}{\partial x_i} = -\frac{\partial}{\partial x_i}\left(\overline{V_{F,i}Y_F} + \overline{\rho}\widetilde{u_i''Y_F''}\right) + \overline{\dot{\omega}}_F. \tag{2.58}$$

By integrating Equation (2.58) in the whole longitudinal direction x and recalling that diffusive terms at the boundaries of the domain are zero, it is possible to obtain:

$$S_T = -\frac{1}{\rho_u(Y_F^u - Y_F^b)\mathcal{A}_0}\int_V \dot{\omega}_F dV, \tag{2.59}$$

where $dV = \mathcal{A}_0 dx$. Equation (2.59) represents the generalization of Equation (2.39), highlighting the fact that S_T is the turbulent version of the laminar flame consumption speed S_c.

It has been known for a long time that the turbulent flame speed is always larger than the laminar one [217, 311], and approximate expressions have been formulated [1, 146]:

$$\frac{S_T}{S_L^0} \approx 1 + \frac{u'}{S_L^0}, \tag{2.60}$$

where u' is the turbulence intensity, highlighting the enhancement of the flame speed by turbulence. This roughly linear increase of S_T is true for moderate levels of turbulence, while, for large values of u', S_T levels off, leading to the so-called *bending effect*, before total quenching of the flame occurs for too intense turbulence levels [311].

Based on Damköhler's first hypothesis [81], flame surface wrinkling is the dominant mechanism controlling the increase of S_T in turbulent flames, leading to the following relation:

$$\frac{S_T}{S_L^0} = \frac{\mathcal{A}_T}{\mathcal{A}_0} = \Xi, \tag{2.61}$$

where $\mathcal{A}_T$ is the turbulent flame surface area and Ξ is the flame surface wrinkling factor. It should be noted that $\mathcal{A}_0$ denotes a reference flame surface. While its definition is straightforward for the *flame-in-a-box* configuration, the choice of $\mathcal{A}_0$ is less trivial for more complex flame configurations, and can lead to some ambiguity. Evidently, Ξ increases with the Reynolds number Re [98, 212, 301].

2.7.2 The flame surface density

To determine the turbulent flame surface area $\mathcal{A}_T$, it is useful to introduce the concept of flame surface density Σ, i.e. the available flame surface area per unit volume, which is used in several turbulent combustion models [32]. This can be evaluated as [62, 312, 399]:

$$\Sigma(C^*) = |\nabla C|\,\delta(C - C^*), \tag{2.62}$$

where δ is the Dirac delta function. Then, the turbulent flame surface $\mathcal{A}_T$ is defined as [414, 415]:

$$\mathcal{A}_T = \int_0^1 \Sigma(C^*)dC^* = \int_V |\nabla C|\,dV. \tag{2.63}$$

The generation and destruction of the flame surface density are described by a transport equation [399, 414]:

$$\frac{\partial \Sigma}{\partial t} + \nabla \cdot (\langle \mathrm{u} + S_d \mathrm{n} \rangle_S \Sigma) = \langle \kappa \rangle_S \Sigma, \tag{2.64}$$

where S_d denotes the flame displacement speed relative to the fresh gases, and $\langle \cdot \rangle_S$ is the surface average operator, i.e., the average on the surface S identified by the condition $C = C^*$. This is defined, for a generic quantity ς, as:

$$\langle \varsigma \rangle_S = \frac{\int_S \varsigma dA}{\int_S dA} = \left. \frac{\int_V \varsigma\,|\nabla C|\,dV}{\int_V |\nabla C|\,dV} \right|_{C=C^*}. \tag{2.65}$$

The terms on the left-hand-side of Equation (2.64) correspond to the unsteady effects and to the convection of the flame surface by the flow field velocity u and by the normal component of the displacement speed S_dn, while the term on the right-hand-side is the source term, proportional to the flame stretch κ.

From a modeling point of view, a Favre decomposition (see Section 3.2) can be applied to Equation (2.64) for convective and strain terms, leading to a closed balance equation for Σ, which takes the general form [50]:

$$\frac{d\Sigma}{dt} = \epsilon\Sigma - \beta\Sigma^2, \tag{2.66}$$

indicating that Σ increases when the flame is positively stretched ($\varepsilon > 0$), but with a limiting term ($\beta > 0$). This latter is necessary, otherwise Equation (2.66) would lead to an infinite growth of the flame surface.

Various closures can be found in the literature to express Equation (2.66) [311]. Depending on the fuel properties and on the considered configuration, additional features and physical phenomena can be incorporated in Equation (2.66), thereby modifying the proportion between flame surface generation and destruction. For example, flame front instabilities, described in Section 2.6, enhance flame surface generation, and an additional term to account for this effect in Equation (2.66) was proposed, among others, by Paul and Bray [290]. This is especially relevant when $Le_{eff} < 1$, in which case the strong generation of flame surface area makes flame surface destruction less relevant to the overall variation of the flame surface [61, 152, 399].

2.7.3 Stretch effects

According to Equation (2.64), stretch drives the flame surface variations, which then affect the flame speed due to the action of flame wrinkling on S_T described in Equation (2.61). Nevertheless, as discussed in Section 2.5.5, the flame consumption speed can be differently impacted by stretch, especially when $Le_{eff} \neq 1$.

Based on this and recalling the work of Bray [39], a *stretch factor* I_0 can be defined at any arbitrary position on the turbulent flame surface as:

$$I_0 = \frac{S_c}{S_L^0}, \tag{2.67}$$

where S_c is the local consumption speed, defined in Equation (2.39). The global effect of stretch on S_T can then be assessed by considering $\langle I_0 \rangle_S$, i.e., the surface-averaged value of I_0 (see Equation (2.65)).

Coherently with the laminar case (see Section 2.5.5), $\langle I_0 \rangle_S \approx 1$ when $Le_{eff} = 1$, meaning that stretch effects can be neglected and Damköhler's first hypothesis (see Equation (2.61)) holds true [60]. For $Le_{eff} \neq 1$, however, $\langle I_0 \rangle_S$ must be included in Equation (2.61):

$$\frac{S_T}{S_L^0} = \langle I_0 \rangle_S \Xi. \tag{2.68}$$

Equation (2.68) can be seen as the turbulent extension of the Markstein relation for the laminar flame consumption speed expressed in Equation (2.49). For $Le_{eff} < 1$, coherently with the stretch-induced enhancement of S_c observed in the laminar case, $\langle I_0 \rangle_S > 1$.

In addition to the direct application of Equation (2.67), other methods can be found in the literature to estimate the stretch factor. For example, given the relation between S_T and the integral over the flame surface of the density-weighted displacement speed S_d [83]:

$$S_T = \frac{1}{A_0} \int_S S_d dA, \tag{2.69}$$

the stretch factor can be estimated, on an isosurface representative of the reaction zone, as [79, 102, 108, 243, 382, 405]:

$$\langle I_0 \rangle_S = \frac{\langle S_d \rangle_S}{S_L^0}. \tag{2.70}$$

This approach, as well as the one in Equation (2.67), albeit conceptually simple, can be tedious and expensive from a numerical point of view.

An alternative method is based on the application of Equation (2.68) to indirectly retrieve $\langle I_0 \rangle_S$ from S_T, computed with Equation (2.59), and A_T, obtained from Equation (2.63) [27, 79, 325]. Equations (2.59) and (2.68) can be combined to avoid the computation of A_0, leading to the following expression [17]:

$$\langle I_0 \rangle_S = -\frac{1}{S_L^0 A_T} \frac{1}{\rho_u (Y_F^u - Y_F^b)} \int_V \dot{\omega}_F dV = \frac{\Omega_F^*}{S_L^0 A_T}, \tag{2.71}$$

where Ω_F^* is a normalized total fuel consumption rate. This expression has the advantage of being easily applicable in numerical simulations, since all the terms in Equation (2.71) can be retrieved during the calculation, whatever flame configuration is considered.

2.7.4 Premixed turbulent combustion regimes

In first approximation, turbulent premixed combustion can be described as the interaction between a flame front, characterized by a thickness* δ and a velocity S_L^0, and an ensemble of eddies, with size r ranging from the Kolmogorov lengthscale η to the integral turbulent lengthscale l_t, and with characteristic speed $u'(r)$ between the Kolmogorov velocity u'_η and the integral velocity fluctuation u' [311]. The value of u' is usually identified with the r.m.s. of the velocity. Under the assumption of homogeneous and isotropic turbulence, the length and velocity scales are related by:

$$\varepsilon = \frac{u'^3(r)}{r}, \tag{2.72}$$

where ε is the local dissipation rate of the turbulent kinetic energy.

In a simplified framework, where the combustion process is described by a single irreversible reaction [311] and no distinction is made between the diffusion coefficients of the species [15], the flame–turbulence interaction can be characterized by the comparison of the chemical timescale $\tau_c = \delta/S_L^0$ with the turbulent one, defined as:

$$\tau_m(r) = \frac{r}{u'(r)} = \frac{r^{2/3}}{\varepsilon^{1/3}}. \tag{2.73}$$

If $\tau_c < \tau_m(r)$, turbulence is not able to affect the flame inner structure significantly, while, if $\tau_c > \tau_m(r)$, the flame is strongly modified by the turbulent eddies [311]. Two non-dimensional parameters can then be defined, the Damköhler number Da and the Karlovitz number Ka. The former compares τ_c with the turbulent timescale defined at the largest eddies, i.e., at the integral lengthscale:

$$Da = \frac{\tau_m(l_t)}{\tau_c} = \frac{S_L^0 l_t}{u'\delta}. \tag{2.74}$$

The latter, on the other end, performs the same comparison at the smallest eddies, i.e., at the Kolmogorov scale:

$$Ka = \frac{\tau_c}{\tau_m(\eta)} = \frac{u'_\eta \delta}{S_L^0 \eta}. \tag{2.75}$$

Recalling that $\eta \sim (\nu^3/\varepsilon)^{1/4}$ [201] and that $\delta \sim \nu/S_L^0$, where ν is the dynamic viscosity, Ka can also be expressed as:

$$Ka = \left(\frac{l_t}{\delta}\right)^{-1/2} \left(\frac{u'}{S_L^0}\right)^{3/2}. \tag{2.76}$$

The turbulence Reynolds number Re_t, based on l_t and u', is then:

$$Re_t = \frac{u' l_t}{\nu} = \left(\frac{u'}{S_L^0}\right)\left(\frac{l_t}{\delta}\right), \tag{2.77}$$

and the following relation holds:

$$Re_t = Da^2 Ka^2. \tag{2.78}$$

*Here, the diffusive flame thickness δ defined in Equation (2.40) is considered, coherently with the work of Peters [301]. However, it should be noted that δ is commonly replaced by the thermal flame thickness δ_L^0 in the literature (e.g., [15, 79]). This latter approach will be adopted in Chapters 10 and 11.

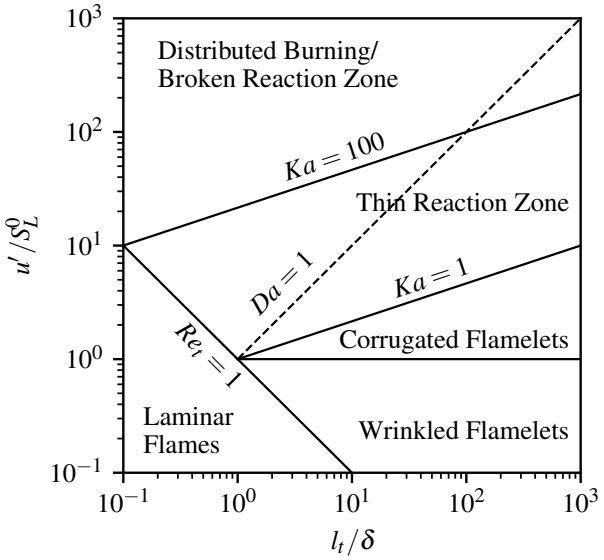

Figure 2.14: Borghi-Peters turbulent combustion diagram, in the version proposed by Peters [301]. The combustion regimes are identified in terms of length l_t/δ and velocity u'/S_L^0 ratios in logarithmic scale.

To simplify the understanding of premixed turbulent flames and ease their modeling, different turbulent combustion regimes have been defined, based on the physical analysis and comparison of the temporal and spatial scales [311]. Moreover, multiple *turbulent combustion diagrams* have been proposed in the literature [14, 17, 34, 35, 38, 63, 97, 198, 301, 302, 308, 369], where the different regimes can be identified and delineated based on non-dimensional parameters. One of the most commonly accepted diagrams is the one originally proposed by Borghi [34] and Peters [302], subsequently modified by Peters [301] in the form reported in Figure 2.14. Based on it, the flame remains laminar for $Re_t < 1$, while four turbulent combustion regimes can be identified for $Re_t > 1$, depending on the values of the velocity ratio u'/S_L^0 and of Ka.

The *Wrinkled Flamelets* regime is achieved for $u'/S_L^0 < 1$ and $Ka < 1$. In this case, the chemical timescale is shorter than any turbulent timescale and the flame thickness is smaller than the smallest turbulent lengthscale, i.e., η. Therefore, the flame structure and properties are similar to the laminar case, with a negligible flame wrinkling induced by turbulence that mildly increases the flame surface area. The turbulent flame can then be seen as an ensemble of laminar flame elements, called *flamelets* [301]. These are thin reactive-diffusive layers embedded in an otherwise non-reacting turbulent flow field, whose internal chemical and diffusive structure is essentially identical to the one of a laminar flame. Turbulence acts on the flame only by wrinkling, stretching, and convecting it [299].

The *Corrugated Flamelets* regime corresponds to $u'/S_L^0 > 1$ and $Ka < 1$. Given the higher velocity fluctuation, the flame is more strongly affected by turbulence and is wrinkled by the turbulent eddies, leading to sharp cusps and highly curved regions in the flame surface. Nevertheless, since $Ka < 1$, the reaction zone is not affected by the smallest turbulent structures, and the flamelet concept remains valid.

The *Thin Reaction Zone* regime holds for $1 < Ka < 100$, where $Ka = 1$ corresponds to the condition $\delta = \eta$, known as Klimov-Williams criterion, while $Ka = 100$ is a critical Karlovitz value for which Kolmogorov scales are able to enter the reaction zone[†]. In this regime, the flame

[†]It should be noted that $Ka = 100$ as critical value is an approximation, based on the assumption, valid for most

keeps a coherent structure, but the smallest turbulent eddies are able to enter and thicken the flame preheat zone. The inner reaction layer, however, is not affected by turbulent eddies and remains thin and close to a wrinkled laminar flame.

Finally, the *Broken Reaction Zone* regime is obtained for $Ka > 100$. Under these intense turbulence conditions, both the diffusion and the reaction zones are affected by the Kolmogorov eddies. No laminar structure can be identified anymore, and the reaction occurs in a highly disrupted layer with frequent local extinction/re-ignition and strong mixing. For $Da < 1$, the mixing is fast, and the overall reaction rate is limited by chemistry, tending toward the *well-stirred reactor* condition.

It should be noted that regime diagrams are based on intuitive arguments and strong assumptions, providing only an order-of-magnitude analysis rather than precise demonstrations [311]. Therefore, care should be taken in their interpretation [369, 415]. In this sense, based on several numerical studies, a controversial debate has arisen in recent years on the validity of the regime classification in the Borghi–Peters diagram, especially on the location and validity of the flamelet regimes, and on the possibility to define a premixed turbulent combustion regime based solely on its two axes [97, 198, 369]. This is especially true in the presence of TD instabilities (see Section 2.6.2), due to their impact on the local values of the flame speed and thickness, which affect the flame timescale [11].

premixed flames, that $\delta_r \approx 0.1\delta$, where δ_r is the reaction thickness [311]. Its actual value can be higher [14].

3

Numerical methods for the simulation and analysis of reacting flows

The Navier–Stokes equations are highly non-linear in their general form, and their numerical solution by means of CFD is the only available way to obtain an approximate solution for most flow configurations. To this scope, the problem is discretized in time and space on a computational grid, with the accuracy of the solution dependent on the resolution of the spatial and temporal scales.

In this Chapter, after a presentation of the steady-state one-dimensional (1D) solver Cantera, the possible approaches to numerically solve the conservation equations for reacting flows are described. The focus is on the numerical methods adopted in the AVBP solver used in this work. Moreover, modal decomposition methods, which can be used for the analysis of the results of numerical simulations, are introduced.

Contents

3.1 Numerical solution of steady-state laminar flames

The set-up of high-fidelity numerical simulations requires a prior knowledge of the flame properties, e.g., the laminar flame thickness (see Equation (2.41)) to define the resolution of the grid. To this scope, laminar flames are computed, often using simplified steady-state solvers. This work uses the Python-based version of Cantera* [137], an open-source toolkit that is suited to solve steady-state problems involving chemical kinetics, thermodynamics, and transport processes. Despite its apparent simplicity, Cantera provides a powerful solution to investigate the chemical features of the combustion process, as well as to assess, with a reduced computational cost, the sensitivity of the results to different parameters, e.g., the transport model or the reaction mechanism. Therefore, although limited to 1D laminar cases, it is useful also in the context of high-fidelity numerical simulations of turbulent flames.

In addition to this, Cantera constitutes a fundamental tool used in this dissertation to derive and validate the global reaction mechanism in Chapter 5, and to investigate the relation between OH* and heat release rate in Chapter 6. For this reason, a brief description of its main features, with a focus on the solution of laminar 1D flames, is given in the following.

3.1.1 Discretization of the one-dimensional problem

Cantera is well-suited to solve a variety of zero- and one-dimensional systems. In particular, it is able to solve 1D laminar premixed and diffusion flames, taking into account also stretch effects. To this scope, flames are assumed to be stabilized in an axisymmetric stagnation flow, and the solution is computed along the stagnation streamline [137]. The three-dimensional (3D) governing equations are reduced to a single dimension using a similarity solution [195].

The equations are solved based on a hybrid time stepping/steady-state algorithm, relying on a damped Newton's method solver [195]. The computational domain is discretized using a progressive mesh refinement, i.e., the system is initially solved on a coarse mesh, and then on a more refined mesh, where additional grid points are introduced in regions of steep gradients. This procedure is iterated until the solution is deemed well-resolved. Four refinement criteria can be set to control this process.

The *ratio* R_j controls the maximum ratio of two adjacent segments in the 1D grid. The condition is evaluated at each grid point j as:

$$R_j = \max\left(\frac{x_j - x_{j-1}}{x_{j+1} - x_j}, \frac{x_{j+1} - x_j}{x_j - x_{j-i}}\right) \quad \text{for } j = 1, \ldots, N_n, \tag{3.1}$$

with x_j and N_n being, respectively, the coordinate of the point j and the total number of grid points. If R_j is greater than the maximum acceptable user-defined threshold, an additional point is inserted between the two adjacent grid points.

The *slope* S_j takes into account the maximum change in the solution of a quantity ς between two adjacent grid points, compared to the maximum change across the entire domain:

$$S_j = \frac{\left|\varsigma_{j+1} - \varsigma_j\right|}{\max_{j=1,\ldots,N_n}\varsigma - \min_{j=1,\ldots,N_n}\varsigma} \quad \text{for } j = 1, \ldots, N_n. \tag{3.2}$$

If this value is greater than a given threshold S_{max}, with $0 \leq S_{max} \leq 1$, then an additional grid point is inserted.

*https://www.cantera.org

The *curve* follows the same logic, but comparing the spatial derivatives of the solution ς':

$$C_j = \frac{\left|\varsigma'_{j+1} - \varsigma'_j\right|}{\max_{j=1,\dots,N_n} \varsigma' - \min_{j=1,\dots,N_n} \varsigma'} \quad \text{for } j = 1, \dots, N_n. \tag{3.3}$$

Also in this case, the maximum threshold C_{max} must be comprised between 0 and 1.

Finally, the *prune* control is introduced to avoid an unnecessarily excessive refinement. In particular, given a value P for this parameter, the grid point j is removed if both the following conditions are satisfied:

$$\frac{S_j}{S_{max}} < P \quad \text{and} \quad \frac{C_j}{C_{max}} < P. \tag{3.4}$$

3.1.2 Canonical laminar flame configurations

Cantera allows to solve both unstrained and strained flames. In the following, the main features of the different canonical laminar configurations considered in this work are reported.

The unstrained flame corresponds to the canonical laminar premixed flame schematized in Figure 2.3, and is modeled in Cantera by the class `FreeFlame`, assuming adiabatic combustion at constant pressure. The solution of these flames is obtained from the given values for the temperature, pressure and composition of the unburned gases. The mass flow rate is not an input, but is determined indirectly by fixing the temperature at an intermediate location of the domain.

Two typologies of strained premixed flames, schematized in Figure 3.1, are solved in Cantera: the *counterflow premixed flame* and the *twin counterflow premixed flame*. These are also known in the literature as *stagnation point flames*, since the flame stabilizes in proximity of a stagnation plane, i.e., a location in which the velocity is zero due to the two opposing streams. Under these conditions, the flames are subject to pure strain, generated by the rapid velocity gradients in the flame tangent plane [311]. Furthermore, a global strain rate can be defined, equal to the velocity gradient across the domain a [311]:

$$a = \frac{u_1 - u_2}{d} = \frac{|u_1| + |u_2|}{d}. \tag{3.5}$$

In the counterflow premixed flame, schematized in Figure 3.1a and represented in Cantera by the class `CounterflowPremixedFlame`, a steady jet of premixed gases is injected, with velocity u_1, in opposition to another stream of combustion products at the equilibrium, with velocity u_2. The distance d between the two jets corresponds to the dimension of the domain. The main issue associated with this configuration is the fact that it is sensitive to the composition and velocity of the equilibrium products. This influence is removed in the twin flame, represented in Figure 3.1b and identified in Cantera with the `CounterflowTwinPremixedFlame` class. In this case, two opposed jets of fresh gases with the same composition and velocity are considered. Given the symmetry, only half the domain is actually solved in this case.

Finally, the *diffusion counterflow flame*, shown in Figure 3.2 and associated with the class `CounterflowDiffusionFlame` in Cantera, is considered. As in its premixed counterpart, two opposing jets are present, with the distance d between each other defining the domain length, and the flame is subject to pure strain. However, in this case, one jet, at velocity u_1, injects pure fuel, while the other one, at velocity u_2, is composed of pure oxidizer. These flames are characterized by a stiffer nature, making it more difficult to reach numerical convergence, especially when high values of strain are considered [419]. In this sense, scaling rules were proposed by Fiala and Sattelmayer [114] to improve the convergence behavior for this flame configuration.

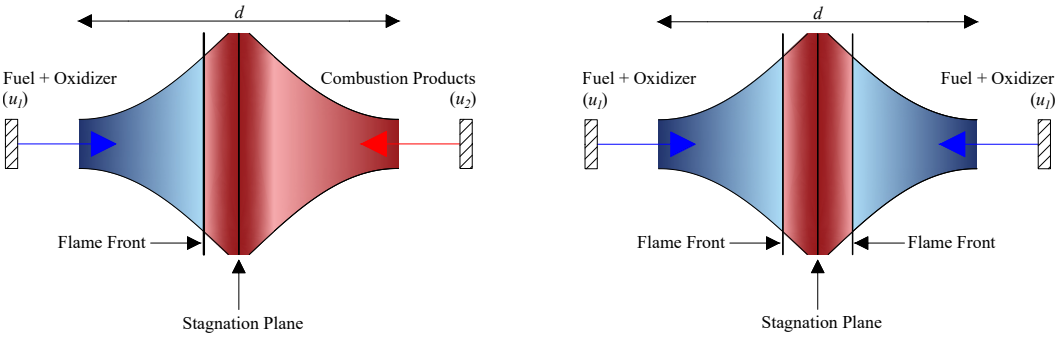

(a) Premixed Counterflow Flame

(b) Premixed Twin Counterflow Flame

Figure 3.1: One-dimensional laminar premixed counterflow flame (a) and twin counterflow flame (b).

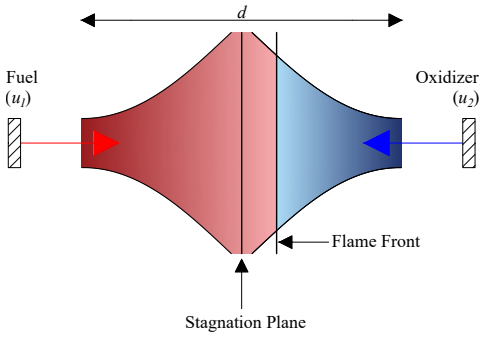

Figure 3.2: One-dimensional laminar diffusion counterflow flame.

3.2 Computational approaches for turbulent combustion

In a homogeneous and isotropic turbulent flow, the integral (l_t) and Kolmogorov (η) length scales are related by $l_t/\eta \sim Re_t^{3/4}$ [313], with the turbulence Reynolds number Re_t defined in Equation (2.77). Therefore, to solve numerically the conservation equations defined in Section 2.3 in a 3D domain of size ${l_t}^3$, capturing all the turbulence scales, a grid size $N \sim Re_t^{9/4}$ is required. This can become extremely large, since the value of Re_t can be high, reaching 100 to 2000 in most combustion devices [311]. Moreover, the extension of practical configurations is well above l_t, further increasing the computational cost. In addition to the spatial constraint, time is also an issue, since the duration of the simulation should be long enough to capture the statistical behavior of the flow, and the discretization should be sufficient to capture the temporal variations of the flow structures. Indeed, to complete a turnover time of the most energetic eddies, with a time step given by η/u' to capture the dynamics of the smallest eddies, the number of temporal iterations scales as $Re_t^{3/4}$. Therefore, the total computational cost, considering spatial and temporal constraints, scales as Re_t^3. Moreover, when dealing with turbulent combustion, additional constraints arise from the non-linear interaction between the flow field, the chemical reaction and the molecular transport, with resolution constraints that arise, in space, from the necessity to solve the flame inner structure, and in time, due to the discretization of the chemical time scales [311].

Therefore, the solution of all turbulence scales can become computationally unsustainable

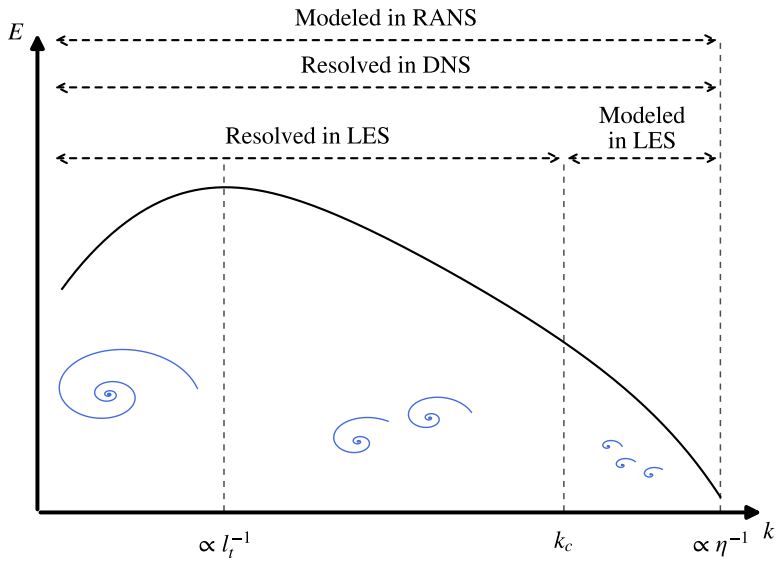

Figure 3.3: Representative turbulence energy spectrum as a function of the wavenumber in logarithmic scale, highlighting the modeled and resolved scales for the different numerical approaches. k_c is the cut-off wavenumber used in LES.

for many turbulent reacting flows, and some modeling often needs to be introduced. Three families of approaches for the numerical solution of the Navier–Stokes equations are generally identified, with the distinction based on the proportion between resolved and modeled turbulent scales, schematically represented in Figure 3.3.

Direct Numerical Simulations (DNS), first introduced by Orszag [284] in the 1970s, rely on the full resolution of the flow conservation equations (see Section 2.3), without the application of any turbulent combustion model. Therefore, all turbulence scales and their effects on combustion are explicitly captured. With the increased availability of High-Performance Computing (HPC) resources, DNS has become a quite diffused approach in the combustion research community [93]. Indeed, they allow to gain a deep physical understanding of turbulent flames, providing detailed information on quantities not accessible with experiments, and to calibrate turbulent combustion models to be used in more engineering-relevant configurations [330]. Given the demanding computational cost, DNS are mostly limited to academic configurations [13, 23, 27, 79, 161, 332]. They have also been adopted to investigate the generation of combustion noise in canonical jet flame configurations [44, 149, 160]. Nevertheless, the current developments in the HPC field have allowed for the DNS of increasingly demanding configurations. For example, they have been applied to high-pressure flames (e.g., [325, 327]), for which a sensible reduction of the flame thickness (see Figure 2.7), hence of the necessary spatial resolution, is present, as well as to flame–wall interaction (e.g., [438]) and laboratory-scale burners (e.g., [377]).

On the opposite side, the *Reynolds-Averaged Navier Stokes* (RANS) modeling, introduced in the early 1970s by Launder and Spalding [226], is the most simple and less computationally expensive approach, based on the solution of Navier–Stokes equations to retrieve the mean values. To this scope, following Reynolds decomposition [324], each quantity ς is decomposed in

its statistical mean[†] $\overline{\varsigma}$ and fluctuating ς' parts:

$$\varsigma = \overline{\varsigma} + \varsigma', \tag{3.6}$$

with $\overline{\varsigma'} = 0$. Since the Reynolds average introduces several unclosed terms for compressible flows, the density-weighted Favre decomposition [109] is usually preferred [212]:

$$\widetilde{\varsigma} = \frac{\overline{\rho\varsigma}}{\overline{\rho}}, \tag{3.7}$$

with the flow decomposed in the sum of the mean $\widetilde{\varsigma}$ and of the fluctuating ς'' components, and $\widetilde{\varsigma''} = 0$ by definition. To deal with the unclosed terms introduced by the averaging operation, robust turbulent combustion models are required. Since all turbulence scales are modeled, a relatively coarse resolution in terms of spatial and temporal scales can be adopted, leading to a low computational cost. For this reason, despite its limits [311, 415], RANS remains a popular approach, especially in commercial codes adopted in industrial contexts. Although RANS has been applied to investigate flame–acoustics interaction, especially in combination with solvers for the linearized Navier–Stokes or the Helmholtz equations (e.g., [59, 216]), the reliability of this method is strongly dependent on the quality of the adopted combustion model. Moreover, as RANS yields only time-averaged quantities, it does not provide access to the actual dynamic behavior of the system. Therefore, issues can arise when dealing with strongly unsteady phenomena.

The *Large Eddy Simulation* (LES) approach, first proposed by Smagorinsky [370] in the early 1960s, is intermediate between RANS and LES. Indeed, it is based on the explicit solution of the large scales of turbulence, whereas the effects of the smaller ones are modeled using subgrid models. To this scope, any quantity in the flow conservation equations (see Section 2.3) is filtered in spectral space with a low-pass filter function [313]. The filtering operation imposes a cut-off wavenumber $k_c = 2\pi/\Delta$ (see Figure 3.3), where Δ is the filter spatial size, similar to the grid size in numerical simulations [334]. The LES-filtered Navier–Stokes equations are able to capture the low-frequency dynamics of reacting flows, but not the effects of small turbulent scales on combustion, making it necessary to introduce an appropriate subgrid modeling. The LES approach has gained increased attention, since it provides an improved accuracy with respect to RANS, without the demanding computational cost of DNS. For this reason, LES are considered a standard tool in turbulent combustion research, and are adopted also in industrial practice, especially for configurations where RANS models cannot provide an adequate solution [311]. They have been widely implemented in the literature, especially in recent years thanks to HPC developments, for demanding configurations ranging from supersonic combustion (e.g., [122]) to rocket propulsion (e.g., [85]) or full-scale engines (e.g. [295, 296]). Moreover, eventually coupled with tools such as Computational Aeroacoustics, Helmholtz solvers or Reduced Order Modeling, they represent the foundation for the investigation of flame–acoustics interaction, thermoacoustic instabilities and combustion noise in engineering-relevant case studies (e.g., [45, 131, 210, 305]). Therefore, it is not surprising that a fair share of the current research effort in the numerical combustion community is oriented toward the development of reliable and robust LES models for turbulent reacting flows, especially with the increased interest for alternative fuels, for which the adequacy of previously established frameworks may be hindered [24].

[†]This averaging process is usually defined as *ensemble average*. For steady mean flow fields, this is replaced by the temporal average over a sufficiently long time period. This implicit assumption is adopted also in this work.

3.2.1 Thickened Flame model

All the numerical simulations of turbulent flows performed in the framework of this dissertation are DNS, hence no turbulence combustion model is applied. Therefore, a thorough presentation of the different LES models developed in the literature is outside the scope of this work. Nevertheless, it is deemed useful to recall the fundamental features of the Thickened Flame (TF or TFLES) model, based on a threefold rationale:

- Adapting the TF framework to H_2 combustion is a relevant ongoing research challenge, as discussed in Section 4.4.
- The TF model constitutes the foundation for the flame thickness correction introduced in the global reaction mechanism developed in Chapter 5.
- The results of the LES reported in Chapter 6, corroborating the analysis of OH* chemiluminescence and of its adequacy as HRR marker in H_2 flames, have been obtained using the TF model.

The concept of artificially thickened flame was originally proposed in the 1970s by Butler and O'Rourke [47] for laminar flame simulations. Relying on asymptotic theory [212], scaling laws can be defined for the laminar flame speed:

$$S_L^0 \propto \sqrt{DA}, \tag{3.8}$$

and the laminar flame thickness:

$$\delta_L^0 \propto \sqrt{\frac{D}{A}}, \tag{3.9}$$

where A is the pre-exponential factor in the reaction rate expression[‡] (see Equation (2.9)), and D denotes the thermal and species diffusivities. Based on Equations (3.8) and (3.9), if D is multiplied by a factor $\mathcal{F}$ and, at the same time, A is divided by $\mathcal{F}$, then S_L^0 remains unchanged, while δ_L^0 is increased:

$$\delta_L^0 \Rightarrow \mathcal{F}\delta_L^0. \tag{3.10}$$

Since this transformation results in a thickening of the flame front, $\mathcal{F}$ is denominated *thickening factor*. Evidently, in the context of numerical simulation, $\mathcal{F}$ is chosen so that:

$$\mathcal{F}\delta_L^0 = N_c\Delta_x, \tag{3.11}$$

where Δ_x is the grid resolution and N_c is the desired number of grid points to discretize the flame.

From a modeling point of view, the advantage of this approach is that the reaction rate keeps an Arrhenius-based expression (see Equation (2.9)), limiting the need for additional modeling [311]. For this reason, its application in LES of turbulent premixed combustion is attractive [76], and has been adopted for a wide range of applications, such as swirled (e.g. [3, 6]) and stratified (e.g., [316]) flames, deflagration (e.g., [88]), and multi-fuel multi-injection combustion (e.g., [411]). Nevertheless, while straightforward for the laminar case, the thickening operation, given its impact on the flame structure, affects the flame–turbulence interaction, and so the reactivity of the turbulent flame. Indeed, recalling Equations (2.74) and (2.75), the Damköhler and Karlovitz

[‡]While derived for a single-step reaction with a unique pre-exponential factor, the same reasoning applies to multi-step chemistry [311].

numbers are, respectively, decreased and increased by a factor $\mathcal{F}$, meaning that the flame becomes less sensitive to turbulence. This modifies the flame surface wrinkling and its effect on the turbulent flame speed (see Equation (2.61)). To account for this, the pre-exponential factor and the diffusivities are generally multiplied by an efficiency function $\mathcal{E}$, corresponding to a subgrid wrinkling factor [311]. Several expressions for the efficiency function have been derived in the literature (e.g., [62, 76]). Readers interested in a more detailed discussion of the implementation of the TF model in LES are referred to [311].

While the TF framework is well established for hydrocarbons, lean premixed H_2 combustion poses additional challenges, since the flame dynamics is impacted also by stretch effects (see Section 2.7.3) and thermodiffusive instabilities (see Section 2.6.2), thus explaining the current research effort to robustly introduce TD effects in the TF model (see Section 4.4).

3.3 Numerical methods for the simulation of unsteady reacting flows

The high-fidelity numerical simulations presented in this work have been performed using the multi-species solver AVBP[§] [350] developed at CERFACS, well suited to perform LES and DNS on massively-parallel CPU and GPU architectures. The code, written in Fortran, is widely adopted both for academic research and industrial purposes, and it has been successfully implemented in the literature for the investigation of flame–acoustics interaction and combustion noise (e.g., [129, 130, 264, 272]), and for DNS of turbulent flames (e.g., [79, 125, 248, 382]).

The solver relies on the solution of the fully compressible Navier–Stokes, energy and species conservation equations (see Section 2.3) on unstructured grids. The equations are considered in their conservative form, meaning that the solution U_j at the node j, where $j = 1, \ldots, N_n$ and N_n is the total number of nodes in the domain, takes the following form:

$$\mathrm{U}_j = [\rho, \rho u, \rho v, \rho w, \rho E, \rho Y_k]^T \quad \text{with } k = 1, \ldots, N. \tag{3.12}$$

Hereafter, the main features of the numerical methods implemented in the code and adopted in this work are described.

3.3.1 Time-marching method

In AVBP, the advancement in time of the solution is based on an explicit multi-stage Runge–Kutta scheme [350], meaning that the solution U_j at the time t^{n+1} is achieved using information only from the current time t^n, with N_s intermediate stages within a single time step Δ_t to achieve higher-order accuracy:

$$\begin{aligned} \mathrm{U}_j^{(0)} &= \mathrm{U}^n \\ \mathrm{U}_j^{(i)} &= \mathrm{U}^n + a_i \Delta_t \mathcal{R}\left(\mathrm{U}_j^{(i)}\right) \quad \text{for } i = 1, \ldots, N_s, \\ \mathrm{U}_j^{n+1} &= \mathrm{U}_j^{(s)} \end{aligned} \tag{3.13}$$

where a_i are real coefficients, and $\mathcal{R}(\mathrm{U})$ is the spatially discretized residual, resulting from the semi-discrete approximation of the integral form of the conservation equations (see Section 2.3):

$$\frac{d\mathrm{U}_j}{dt} = \mathcal{R}\left(\mathrm{U}_j\right). \tag{3.14}$$

[§] https://avbp-wiki.cerfacs.fr

A single, global value of Δ_t is adopted for the whole domain, and the stability of the time-marching algorithm is ensured by limiting Δ_t with constraints for the convective, diffusive and chemical processes.

For the convective part, a constraint on the acoustic Courant–Friedrichs–Lewy (*CFL*) number is applied:

$$CFL = \frac{\Delta_t^c(|\mathrm{u}| + c)}{\Delta_x}, \tag{3.15}$$

where $|\mathrm{u}|$, c and Δ_x are the local values of the magnitude of the flow velocity vector, the speed of sound, and the spatial resolution of the grid, respectively, and Δ_t^c is the global convective time step. The value of *CFL* is limited by an upper bound CFL_{max}, representing the critical value to ensure the stability of the numerical scheme adopted for the discretization of convective terms (see Section 3.3.2). For the simulations reported in this work, $CFL_{max} = 0.7$. As a consequence, the convective time step is given by:

$$\Delta_t^c = CFL_{max} \min_{j=1,\dots,N_n} \left(\frac{\Delta_x}{|u| + c} \right)_j. \tag{3.16}$$

For diffusive terms, the limiting condition is represented by the Fourier number:

$$Fo = \frac{D_{eq}\Delta_t^d}{\Delta_x^2}, \tag{3.17}$$

where Δ_t^d is the diffusive time step and D_{eq} is an equivalent diffusion coefficient, i.e., the maximum of momentum, heat and species diffusivities. For stability reasons, $Fo \leq Fo_{max}$, with $Fo_{max} = 0.1$ in the present work. Therefore, by assuming, as it usually occurs, that the momentum diffusivity dominates, the global diffusive time step is given by:

$$\Delta_t^d = Fo_{max} \min_{j=1,\dots,N_n} \left(\frac{\Delta_x^2}{\nu} \right)_j, \tag{3.18}$$

where ν is the kinematic viscosity.

Finally, when dealing with reacting flows, it may be necessary to take into account the constraints related to chemical source terms, which are highly non-linear both in space and time. This occurs in the presence of very stiff reactions, which, in the absence of a chemical constraint on the time step, would lead to non-physical negative values of pressure or mass fractions. For the simulations in the present work, this third constraint was found to be unnecessary.

Evidently, the global value of the time step is taken as the smallest of the three. In practice, the condition on Δ_t^c was found to be the most restrictive for the simulations here reported. Recalling that, for an ideal gas, $c \sim \sqrt{T}$, and that, for low subsonic conditions, as most of those considered in the present work, $|u| \ll c$, the global time step Δ_t scales, for a fixed value of CFL_{max}, as:

$$\Delta_t \sim \min_{j=1,\dots,N_n} \left(\frac{\Delta_x}{\sqrt{T}} \right)_j. \tag{3.19}$$

This poses a severe limitation when performing DNS of reacting flows, for which the value of Δ_x must be sufficiently small to capture, at the same time, the smallest turbulent eddies and the flame front, while T is increased by an order of magnitude when passing from the fresh to the burned gases due to the combustion process. For this reason, an optimization of the computational grid, avoiding unnecessary small grid elements, especially in the burned mixture region, is mandatory to efficiently exploit computational resources.

3.3.2 Spatial and temporal discretization

The AVBP code relies on a cell-vertex finite-volume formalism [350], where conservation equations are applied to the grid cells, following the finite volume approach, while the solution is stored at the grid nodes. This allows to optimize memory usage, since, in an unstructured grid, the number of nodes is sensibly smaller than the number of cells.

The diffusive and convective fluxes in the conservation equations (see Section 2.3) are solved based on different numerical schemes. For the diffusive fluxes, a second-order finite-element Galerkin scheme developed by Colin [78], denominated FE2Δ, is adopted for all the simulations in this dissertation. For the convective terms, instead, two schemes are considered in this work, based either on finite-volume or finite-element discretization methods. The finite-volume Lax–Wendroff (LW) scheme [231], adapted to the cell-vertex formalism [151, 277], is second-order accurate in space and time, while the finite-element Two-step Taylor–Galerkin 'C' scheme (TTGC) [77] is third-order accurate in space and time. Both convection schemes are total schemes, in the sense that they treat the spatial discretization together with the temporal advancement described in Section 3.3.1, with one step for the LW scheme and two steps for the TTGC one. In both cases, a Taylor expansion in time is performed first, so that the temporal derivatives can be replaced by spatial derivatives.

Compressible flow simulations commonly show high-frequency numerical errors, and a filtering operation is needed to damp the spurious waves [40]. This is the case also for AVBP. Indeed, the considered numerical schemes are spatially centered, and therefore require stabilization operators to avoid node-to-node oscillations, or *wiggles*, especially close to regions of strong gradients. To damp these fluctuations, the concept of artificial viscosity is introduced. In this sense, Equation (3.14) is modified as follows:

$$\frac{d\mathrm{U}_j}{dt} = \mathcal{R}(\mathrm{U}_j) + \mathcal{D}_j^{2*}(\mathrm{U}_j) + \mathcal{D}_j^{4*}(\mathrm{U}_j), \tag{3.20}$$

where $\mathcal{D}_j^{2*}$ and $\mathcal{D}_j^{4*}$ are, respectively, the second-order and fourth-order artificial viscosity operators. The local value of artificial viscosity is determined based on a sensor, detecting strong oscillations and non-linear variations that may occur in poorly resolved regions. For the high-fidelity numerical simulation of reacting flows, as in the present work, the most suitable sensor is the one developed by Colin [78]. In this case, $\mathcal{D}_j^{2*}$, which allows for damping non-linearities and stiff gradients, is applied to all the transported conservative variables, only for large values of the sensor, i.e., in the case of steep gradients. On the other hand, $\mathcal{D}_j^{4*}$ diffuses the very low amplitude wiggles and is applied everywhere in the domain, except for the regions where $\mathcal{D}_j^{2*}$ is used, to ρ, ρE ρY_k. To avoid additional dissipation of the smallest flow scales, $\mathcal{D}_j^{4*}$ is either not applied or applied in the measure of 10% for the velocity field.

The choice of the convection scheme is crucial in determining the quality of the solution. This becomes even more relevant when dealing with flame–acoustics interaction, since the prediction of acoustic waves is sensibly affected by numerical errors. In particular, two errors can arise: the *dissipation* error and the *dispersion* one. The former leads to an attenuation of the amplitude and gradients of the acoustic waves, hence affecting the intensity of the acoustic radiation. The latter, instead, impacts the wave propagation speed, inducing wiggles, which affect the high-frequency characteristics of the acoustic waves. Given the Fourier coefficients in space $\hat{\mathrm{U}}^n$ of the solution U^n at the time t^n, the errors introduced by the combined spatial and temporal discretiza-

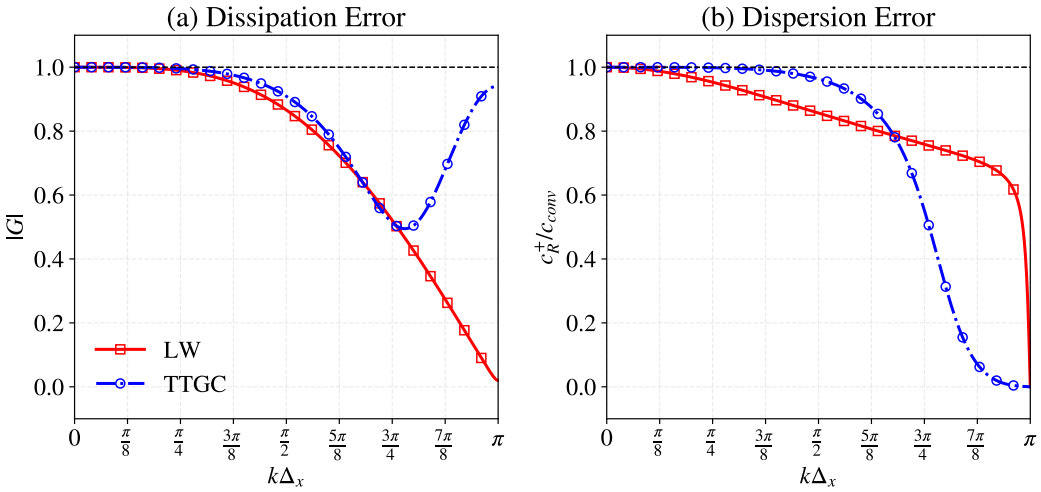

Figure 3.4: Dissipation (a) and dispersion (b) errors for the LW and TTGC schemes with CFL=0.7 (adapted from [77]).

tion can be estimated from the amplification coefficient G, defined as:

$$G(k) = \frac{\hat{U}^{n+1}}{\hat{U}^n} = |G(k)|\, e^{i\phi_G}, \tag{3.21}$$

where $k = (2\pi)/\lambda$ is the wavenumber, and λ is the wavelength. The dissipation error corresponds to the modulus of the amplification coefficient $|G(k)|$, while the dispersion error is given by the normalized phase velocity:

$$\frac{c_R^+}{c_{conv}} = -\frac{\phi_G}{CFLk\Delta_x}, \tag{3.22}$$

where c_R^+ is the phase velocity, i.e., the *numerical* velocity at which the Fourier mode of wavenumber k propagates, while c_{conv} is the *physical* convection velocity.

Considering the 1D linear convection equation of a quantity ς, without any diffusion term:

$$\frac{\partial \varsigma}{\partial t} + c_{conv}\frac{\partial \varsigma}{\partial x}, \tag{3.23}$$

a Von Neumann analysis allows to retrieve the dissipation and dispersion errors for the two schemes considered in this dissertation. These are reported in Figure 3.4 for $CFL = 0.7$, i.e., the value adopted for the simulations in the present work.

In analogy with [40], a criterion to find the maximum acceptable grid spacing can be established, depending on the considered scheme. The LW scheme, while computationally cheap, introduces significant dissipation and dispersion errors for high wavenumbers. Based on the results in Figure 3.4 and considering a maximum tolerable error of 2% both for dissipation and dispersion, the LW scheme is well-suited only for wavenumbers $k\Delta_x \lessapprox \pi/6$, corresponding to a minimum of 13 grid points per acoustic wavelength λ. With the same reasoning, the TTGC scheme introduces a negligible error for $k\Delta_x \lessapprox \pi/2$, which corresponds to at least 5 grid points per λ, sensibly extending the range of validity of the numerical scheme. The TTGC scheme, however, introduces a computational cost approximately 2.5 times higher with respect to the LW one. Moreover, in multi-dimensional domains, the TTGC scheme is more sensitive to mesh quality.

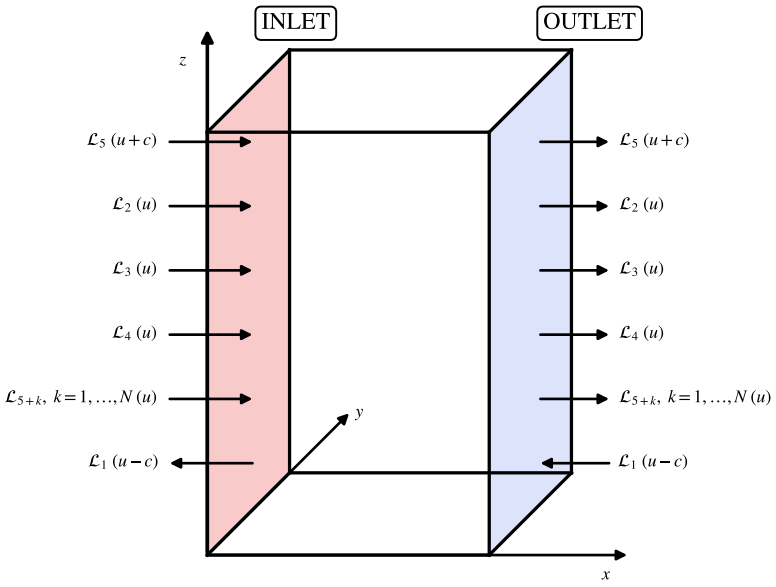

Figure 3.5: Incoming and outgoing characteristic waves $\mathcal{L}$ for inlet and outlet subsonic boundary conditions (adapted from [311]). The flow velocity and speed of sound are denoted, respectively, with u and c.

While this issue is not relevant in this work, where well-refined grids with smooth variations of the element lengths are adopted, attention should be paid for LES of engineering-relevant cases, where the local mesh quality can be sensibly poorer due to geometrical constraints.

In this dissertation, the LW scheme is adopted for the simulations reported in Chapter 9, since, for acoustically excited laminar flames, the frequency of the acoustic waves of interest is related to the forcing of the flame, which remains relatively low[¶]. For the turbulent cases in Chapter 11, on the other hand, the high-frequency dynamics is far more relevant, and the more expensive TTGC scheme is therefore adopted.

3.3.3 Boundary conditions

Boundary conditions play a crucial role in compressible numerical simulations of reacting flows, as they drive the introduction of external disturbances, while ensuring a physically consistent behavior. This becomes even more important when investigating the acoustic radiation of flames, since the boundary conditions may induce non-physical interactions with the pressure field, thus affecting the predicted noise. In the following, we first introduce the characteristic boundary conditions formulation adopted in AVBP, and then describe the implementation, within this framework, of the injection of acoustic and vortical waves in the numerical simulations performed in this dissertation.

The AVBP solver relies on the *Navier–Stokes Characteristic Boundary Conditions* (NSCBC) formulation [309]. In this framework, the equations are decomposed in characteristic waves, in a number equal to the total of conservative variables in the solution (see Equation (3.12)), either entering or leaving the domain, as schematized in Figure 3.5 for a subsonic case.

For the inlet, the $\mathcal{L}_1$ wave is known, since it is *upwind*, i.e., it leaves the domain, and can then be determined from the interior solution. The other waves, instead are *downwind*, i.e., entering

[¶] The frequency f and wavelength λ of an acoustic wave are related by $\lambda = c/f$, where c is the speed of sound.

the domain, and therefore require the prescription of a boundary condition for their evaluation. With an analogous reasoning, the same applies to the incoming $\mathcal{L}_1$ wave at the outlet. In the NSCBC formalism, the prediction of the incoming characteristic waves is based on the Local One-Dimensional Inviscid (LODI) assumption, which allows to evaluate the ingoing waves from the outgoing ones, neglecting transverse, viscous and reaction terms [311]. A detailed description of the NSCBC/LODI formalism can be found in [311].

The main goal of this methodology is to remove spurious wave reflections arising from the boundaries, making it well suited for the investigation of acoustic radiation. However, in multi-dimensional domains, the computed solution may drift from the target one, due to the presence of transverse and viscous terms [84]. For this reason, a relaxation coefficient K is introduced. This, for example, allows to write the mean velocity normal to the inlet $u(t)$ as:

$$\frac{\partial u}{\partial t} = K[u_{target} - u(t)], \tag{3.24}$$

where u_{target} is the target value of velocity on the inlet boundary. Increasing the value of K allows to reach the target value more rapidly, but at the cost of an increased acoustic reflection at the boundary [358]. In particular, a cut-off frequency f_c can be defined [358]:

$$f_c = \frac{K}{4\pi}, \tag{3.25}$$

and the boundary is non-reflective only for frequencies above this value. For this reason, the boundary is said to be partially reflecting.

A partial reflection is acceptable in many cases of interest, but can be troublesome when investigating flame–acoustics interaction, since the reflecting component for $f < f_c$ can affect the acoustic wave dynamics. This is especially true at the inlet boundary in the presence of unsteady target values, e.g., when acoustic pulsations or turbulence are injected, as it occurs in the present work. In this sense, to conciliate non-reflecting properties with the need to avoid an excessive drift at the inlet, Daviller et al. [84] proposed the Non-Reflecting Inlet NSCBC formulation (NRI-NSCBC), which allows for respecting target unsteady values of the inlet velocity, without a drift of the mean values. Moreover, the NRI-NSCBC formulation allows to sensibly increase the relaxation coefficient without inducing acoustic reflection, hence it leads to a faster convergence. This formulation is adopted for the inlet boundaries in the simulations reported in Chapters 9 and 11, whose numerical configurations are described, respectively, in Chapters 8 and 10. The main features regarding the implementation of the unsteady inlet boundary conditions in AVBP are described hereafter.

Acoustically forced laminar premixed flames are investigated in Chapter 9. To this scope, a sinusoidal perturbation is superimposed to the velocity entering the domain, leading to the following expression for the velocity component normal to the inlet:

$$U_n(t) = \mathcal{A} \sin\left[2\pi f_a (t - \tau)\right], \tag{3.26}$$

where $\mathcal{A}$ is the amplitude of the velocity fluctuation, f_a is the frequency of the perturbation, and τ is its starting time, i.e., no pulsation is applied for $t < \tau$.

In the NSCBC formulation, the forcing is applied to the ingoing characteristic waves. Therefore, considering the relation for an isentropic propagating acoustic wave, this leads also to a perturbation of the temperature at the inlet with respect to the target value [194]:

$$T(t) = \frac{c\mathcal{A}}{c_p} \sin\left[2\pi f_a (t - \tau)\right], \tag{3.27}$$

where c is the speed of sound and c_p is the specific heat capacity at constant pressure. It should be noted that $\mathcal{A}$ corresponds to the desired amplitude of the perturbation only if no acoustic wave leaves the domain through the inlet boundary [194].

For the turbulent flames discussed in Chapter 11, a homogeneous and isotropic turbulent perturbation is injected at the jet inlet and superimposed to the velocity entering the domain, coherently with previous studies in the literature [79, 248]. The turbulent velocity fluctuation u' is obtained with the synthetic generation method by Kraichnan [205] and Celik [371], based on a Fourier series decomposition:

$$\mathrm{u}'(\mathrm{x},t) = \sum_{n=1}^{N} \left[\hat{\mathrm{v}}^n \mathrm{k}^n \cos\left(\mathrm{k}^n \mathrm{x} + \omega^n t\right) + \hat{\mathrm{w}}^n \mathrm{k}^n \sin\left(\mathrm{k}^n \mathrm{x} + \omega^n t\right)\right], \tag{3.28}$$

with $N = 200$ modes in the present work. The Fourier modes $\{\mathrm{v}^n, \mathrm{w}^n\}$, wave vectors k^n and pulsations ω^n are random variables sampled to obtain a Passot–Pouquet turbulence spectrum [289]:

$$E(k) = 16\frac{u'^2}{k_e}\sqrt{\frac{2}{\pi}}\left(\frac{k}{k_e}\right)^4 \exp\left[-2\left(\frac{k}{k_e}\right)^2\right], \tag{3.29}$$

where u' is the target turbulent fluctuation intensity, i.e., the temporal r.m.s. of velocity, while k_e is the wave number associated with the most energetic eddies, related to the integral length scale of turbulence through $l_t = \sqrt{2\pi}/k_e$. The spatio-temporal signal, superimposed to the mean velocity field at the inlet, is obtained by applying Taylor's hypothesis.

3.3.4 Chemical and transport modeling

The number of equations to be solved is strongly dependent on the number of species, hence on the chemical mechanism adopted for the description of the combustion process. For hydrocarbons, detailed kinetics cannot be implemented in high-fidelity numerical simulations of reacting flows, since it involves hundreds of species and thousands of reactions. For example, the detailed mechanism for C_1–C_{16} hydrocarbons developed by the CRECK Modeling Group[‖] at the Polytechnic University of Milan [321] involves, in its most simple version, 114 species and 1999 reactions and, in its most complete form accounting also for NO_x and soot kinetics, 497 species and 24501 reactions. On the other hand, the kinetics of H_2–air combustion represents a subset of the full kinetics of hydrocarbons and accounts only for 9 species, when considering air as a mixture of solely oxygen (O_2) and nitrogen (N_2) and neglecting NO_x. This makes it feasible to perform high-fidelity numerical simulations of H_2 flames using a detailed kinetics description, especially in academic configurations. In this work, the reference scheme adopted for hydrogen combustion is the San Diego mechanism[**] [339] (UCSD), involving 9 species and 21 reactions, the main features of which will be discussed in Section 4.1.

Besides this reference mechanism, other chemical kinetic schemes have been employed at different stages of the research work presented in this dissertation, depending on the specific objectives. In Chapter 5, the global reaction mechanism derived in the framework of this work is compared with the UCSD scheme. Moreover, laminar flame calcuations are performed in Cantera using also two other schemes, i.e., those developed by Konnov [202] and by Capurso et al. [51] (H2_NOX_15_94_TC). The former involves 15 species and 75 reactions, since it considers also

[‖] https://www.creckmodeling.polimi.it

[**] https://web.eng.ucsd.edu/mae/groups/combustion/mechanism.html

helium (He) and argon (Ar), together with ozone (O_3) and the excited species $O(^1D)$, OH*, and $O_2(a^1\Delta g)$. The latter, instead, involves 15 species and 47 reactions, and was reduced from the detailed CRECK mechanism using the library ARCANE [58], co-developed by CERFACS and Cornell University.

In Chapter 6, the OH* kinetics is investigated by considering two different sub-mechanisms developed for this excited species, which are to be added to the main reaction scheme describing the combustion process. First, the scheme developed by Kathrotia et al. [190, 191] is adopted, which comprises, in its most complete version adapted both for H_2 and methane (CH_4) combustion, 11 species and 12 reactions. When focusing on H_2 combustion, especially at varying operating conditions, the scheme by Sharipov et al. [362, 363] is considered. This latter, which involves 20 species and 21 reactions, was specifically designed for H_2 combustion, including the interaction between OH* and NO_x, and was validated on a wide range of temperatures and pressures. While their adoption for steady-state calculations in Cantera is straightforward, their implementation in numerical simulations in AVBP is more cumbersome. Indeed, the extremely low concentration of OH*, compared to other species, increases the numerical stiffness. As it will be discussed in Section 6.2, a convenient solution is offered by applying the Quasi-Steady State (QSS) approximation to compute the OH* concentration.

In Chapters 9 and 11, simulations of H_2 flames are performed using either the UCSD scheme or the global reaction mechanism developed in the framework of this dissertation. For the CH_4–H_2 flames in Chapter 9, the scheme derived by Pestre [255, 298] (CH4_15_138_9_AP) is adopted. This was reduced from the CRECK detailed mechanism using ARCANE, and involves 15 transported species, 9 QSS species, and 138 reactions. Finally, the turbulent CH_4 flames in Chapter 11 are simulated with a semi-global scheme [357], here labeled CH4-2S, which involves 6 species and the following 2 reactions:

$$CH_4 + 1.5\,O_2 \longrightarrow CO + 2\,H_2O, \tag{R3.1}$$

$$CO + 0.5\,O_2 \rightleftharpoons CO_2. \tag{R3.2}$$

In addition to chemical kinetics, it is necessary to model also transport phenomena. The multicomponent transport model [91, 195] takes into account the diffusion of each species relative to each of the other species, by adopting binary diffusion coefficients. It is the most accurate from a physical standpoint, and it naturally incorporates thermal diffusion, i.e., the Soret effect. However, given its structure, it is also the most expensive, making it not suitable for high-fidelity numerical simulations. For this reason, this model is here adopted solely for laminar flame calculations using Cantera. A more approximate model is the mixture-averaged one [195], for which an equivalent diffusion coefficient is defined for each species, accounting for its diffusion in the rest of the mixture. This approach corresponds to the one described in Section 2.3, and has been recently implemented in AVBP [331], based on the mixing law by Wilke [422] for viscosity, the Hirschfelder and Curtiss approximation [159] (see Equation (2.21)) for diffusivities, and the Mathur's law [260] for thermal conductivity.

The numerical simulations in this work have been performed using a simplified transport model, historically employed in the AVBP code. In this framework, the molecular viscosity is computed with a power law function of the temperature:

$$\mu = \mu_{ref} \left(\frac{T}{T_{ref}} \right)^{\alpha}, \tag{3.30}$$

while the diffusion coefficients of each species and the thermal conductivity are calculated, respectively, by considering a constant Schmidt number Sc_k specific for each species k (see Equation (2.27)), and a constant Prandtl number Pr for the mixture (see Equation (2.28)). The values of μ_{ref}, T_{ref}, α, Sc_k and Pr are tuned to fit the flame properties obtained with the multicomponent model in the targeted operating conditions. The values adopted for the three schemes (i.e., UCSD, CH4_15_138_9_AP, and CH4-2S) used for the simulations shown in Chapters 9 and 11 are reported in Appendix A.

Soret and Dufour transport processes are not included in this model. While these effects may be relevant, especially for wrinkled H_2–air flames [12, 143, 344, 408], neglecting them still allows for adequately well capturing TD effects and instabilities [12, 16, 79, 248]. In this work, no significant impact on the prediction of the structure of H_2 laminar flames in Chapter 9 has been observed by considering the more detailed mixture-averaged model (see Section 8.2.2). A similar analysis was performed by Malé et al. [248] for H_2–air turbulent premixed flames under operating conditions analogous to those presented in Chapter 10, showing negligible differences between the two and sustaining the validity of the choice adopted in this work.

3.4 Modal decomposition methods

Modal decomposition methods are mathematical tools to extract the dominant features of the flow, exploiting the spatial and temporal information [386]. In particular, they are useful to identify *coherent structures*. These can be defined as regions over which at least one flow variable shows relevant correlation with itself or with another variable over a range of spatial and temporal scales significantly larger than the smallest flow scales [329]. Coherent structures are formed in unconfined non-reacting turbulent jets [304], and are responsible for acoustic radiation [183]. Brouzet et al. [42] noted that these have a relevant role also for combustion noise in turbulent premixed CH_4–air flames, given their impact on the flame front deformation. Three main modal decomposition methods have been applied in the literature to investigate coherent structures.

The *Proper Orthogonal Decompostion* (POD), introduced in the context of turbulence by Lumley [245], is used to decompose the flow field into *modes* $\Phi(x)$, which represent a set of deterministic spatial functions. These are orthogonal, meaning that:

$$\langle \Phi(x), \Phi(x) \rangle = I, \tag{3.31}$$

where $\langle \cdot, \cdot \rangle$ denotes the inner product chosen to analyze the problem, and I is the identity matrix. The modes are ranked by their energy content, but are purely spatial, with the temporal information taken into account only indirectly by random time coefficients. Therefore, modes are coherent in space, but not necessarily in time, and each spatial mode represents a physical structure associated with multiple frequencies.

The *Dynamic Mode Decomposition* (DMD), defined by Schmid [345], allows for the decomposition of a time-evolving flow dataset into modes, each of which is associated with a single frequency. In this case, the modes are coherent both in space and time, overcoming the main issue of POD. However, they are spatially non-orthogonal, and are not ranked by their energy content, but by their growth/decay rate. This makes it difficult to assess the physical relevance of each mode. Finally, DMD may be unreliable when non-linearities are important [386], as it occurs for turbulent reacting flows.

To combine the advantages of the two methods, i.e., the orthogonality and energy-based ranking of the POD modes, and the coherence in space and time of the DMD modes, the *Spectral Proper Orthogonal Decomposition* (SPOD) was proposed by Sieber et al. [365]. It is an effective methodology to extract coherent structures in a turbulent flow, as it allows for finding orthogonal space-time correlated modes that optimally describe the turbulent flow statistics at a given frequency [397]. In the remainder of this Section, the main features of this method are reported, with a focus on its implementation in the present work.

3.4.1 Spectral Proper Orthogonal Decomposition

The SPOD is here performed using the Python library antares[††] developed at CERFACS [9], with the implementation based on the work of Schmidt and Colonius [346]. Each instantaneous spatial field $\mathrm{q}(\mathrm{x}, t)$ is broken down in the sum of a temporal mean $\overline{\mathrm{q}}(\mathrm{x})$ and a fluctuating part $\mathrm{q}'(\mathrm{x}, t)$. The time series is then divided into N_b blocks of N_{freq} instantaneous snapshots:

$$\mathrm{Q}^{(i)} = \left[\mathrm{q}'\left(\mathrm{x}, t_1^{(i)}\right), \ldots, \mathrm{q}'\left(\mathrm{x}, t_{N_{freq}}^{(i)}\right)\right], \tag{3.32}$$

where $i = 1, \ldots, N_b$, and a Hanning window with 75% overlap is employed over each block to prevent spectral leakage. The periodogram method by Welch [420] is applied to compute the direct Fourier transform in the time domain for each block:

$$\hat{\mathrm{Q}}_{\omega_k}^{(i)} = \left[\hat{\mathrm{q}}_{\omega_1}^{(i)}, \ldots, \hat{\mathrm{q}}_{\omega_{N_{freq}}}^{(i)}\right]. \tag{3.33}$$

The cross-spectral density tensor at a given angular frequency ω_k is then given by:

$$\hat{\mathrm{C}}_{\omega_k} = \hat{\mathrm{Q}}_{\omega_k}\hat{\mathrm{Q}}_{\omega_k}^{*} = \frac{1}{N_b}\sum_{i=1}^{N_b}\hat{\mathrm{q}}_{\omega_k}^{(i)}\hat{\mathrm{q}}_{\omega_k}^{(i)*}, \tag{3.34}$$

where the superscript $*$ denotes the complex conjugate. The N_b SPOD modes $\hat{\Phi}_{\omega_k}$ and eigenvalues $\hat{\Lambda}_{\omega_k}$ at a given frequency are then obtained by solving:

$$\hat{\mathrm{C}}_{\omega_k}\mathrm{W}\hat{\Phi}_{\omega_k} = \hat{\Phi}_{\omega_k}\hat{\Lambda}_{\omega_k}, \tag{3.35}$$

where W is a weighting matrix, here taken as the weighted 2-norm [346]:

$$\mathrm{W} = \int_V dV. \tag{3.36}$$

The choice of the number of blocks N_b and of the number of snapshots per block N_{freq} is based on a trade-off between convergence of the SPOD modes, which increases with N_b, and frequency resolution, which is improved for higher N_{freq} [42, 304].

In the framework of this dissertation, SPOD is applied in Chapter 11 to the HRR and pressure fields of turbulent reacting flows. For the former, 1500 2D snapshots are extracted on the xy plane, and the SPOD is applied with $N_b = 9$ and $N_{freq} = 512$. For the latter, instead, 2700 3D snapshots, extracted during the simulation and interpolated on a coarser cylindrical domain with grid size equal to 2.4 million tetrahedral cells, are fed to the SPOD algorithm, with $N_b = 11$ and

[††] https://cerfacs.fr/antares/

$N_{freq} = 768$. With the chosen values, the frequency resolution is equal to $\Delta St \approx 0.05$ for all cases, where St is the Strouhal number:

$$St = \frac{f L_{ref}}{U_{ref}}, \tag{3.37}$$

with f being the frequency, while L_{ref} and U_{ref} are, respectively, a reference length and a reference velocity. Even though this is not sufficient to capture stationary structures such as streaks [304, 335] (see Section 7.3), which appear for $St \to 0$, it is enough to highlight the different features observed in the acoustic radiation of the studied flames (see Section 11.4). The use of different values of overlap, N_b and N_{freq} was not found to affect significantly the eigenvalues and the spatial patterns of the dominant SPOD modes.

4

Flammability characteristics of hydrogen

The specific properties of hydrogen as a fuel, which differ significantly from those of conventional hydrocarbons, introduce a number of relevant challenges. Its low critical temperature and density, combined with the high diffusivity, flame speed and temperature, give rise to combustion-related issues concerning flame stability, flame dynamics, nitrogen oxides formation, and safety [307]. These aspects hinder the direct replacement of hydrocarbons with hydrogen in industrial and domestic applications [233]. Moreover, the peculiar flammability characteristics of hydrogen restrict the applicability of many turbulent combustion models for numerical simulations, which have been developed and validated for hydrocarbons [24]. This results in a dual challenge: not only existing combustion systems must be adapted to work with hydrogen, but the numerical tools employed for their design need also to be revised to accurately capture the dynamics of hydrogen flames under engineering-relevant conditions.

This Chapter recalls some key aspects of hydrogen combustion, focusing on the link between chemical properties and the dynamics of lean premixed hydrogen–air flames. The extent to which numerical combustion can accurately describe these flames is also discussed, highlighting the need for high-fidelity numerical simulations to advance our physical understanding.

Contents

4.1 Chemical description of hydrogen combustion

The chemistry of hydrogen oxidation is significantly simpler than that of other fuels [261]. Moreover, it is part of the oxidation mechanisms of all hydrocarbons. For this reason, it has been extensively investigated in the literature, and several reaction mechanisms for its description are available [337]. In the numerical simulations performed in this work, the reference scheme for H_2–air combustion is based on the San Diego mechanism [339], as reported in Table 4.1. The 21 elementary reactions are grouped in four different categories to reflect their main role in the H_2 combustion process [337]. A detailed explanation of the contribution of each reaction at different operating conditions is available in [337, 402]. In the following, the main features of the four different groups are recalled.

Table 4.1: Scheme for hydrogen–air combustion, based on the San Diego reaction mechanism [339]. Reaction rate constant $k = AT^{\beta}\exp[-E_a/(RT)]$, units are cm^3 mol s cal K.

No.	Reaction		A	β	E_a
Shuffle reactions					
(H1)	$H + O_2 \rightleftharpoons OH + O$		3.52×10^{16}	-0.70	17070
(H2)	$H_2 + O \rightleftharpoons OH + H$		5.06×10^{4}	2.67	6291
(H3)	$H_2 + OH \rightleftharpoons H_2O + H$		1.17×10^{9}	1.30	3635
(H4)	$H_2O + O \rightleftharpoons 2\,OH$		7.60×10^{0}	3.84	12780
Hydroperoxyl reactions					
(H5)	$H + O_2 + M \rightleftharpoons HO_2 + M^*$	k_0	5.75×10^{19}	-1.40	0
		k_∞	4.65×10^{12}	0.44	0
(H6)	$HO_2 + H \rightleftharpoons OH + OH$		7.08×10^{13}	0.00	295
(H7)	$HO_2 + H \rightleftharpoons H_2 + O_2$		1.66×10^{13}	0.00	823
(H8)	$HO_2 + H \rightleftharpoons H_2O + O$		3.10×10^{13}	0.00	1721
(H9)	$HO_2 + O \rightleftharpoons OH + O_2$		2.00×10^{13}	0.00	0
(H10)	$HO_2 + OH \rightleftharpoons H_2O + O_2$		2.89×10^{13}	0.00	-497
Radical–radical recombination reactions[†]					
(H11)	$H + OH + M \rightleftharpoons H_2O + M$		4.00×10^{22}	-2.00	0
(H12)	$H + H + M \rightleftharpoons H_2 + M$		1.30×10^{18}	-1.00	0
(H13)	$O + O + M \rightleftharpoons O_2 + M$		6.17×10^{15}	-0.50	0
(H14)	$H + O + M \rightleftharpoons OH + M$		4.71×10^{18}	-1.00	0
(H15)	$O + OH + M \rightleftharpoons HO_2 + M$		8.00×10^{15}	0.00	0
Hydrogen peroxide recombination reactions					
(H16)	$OH + OH + M \rightleftharpoons H_2O_2 + M^{\ddagger}$	k_0	2.30×10^{18}	-0.90	-1702
		k_∞	7.40×10^{13}	-0.37	0
(H17)	$HO_2 + HO_2 \rightleftharpoons H_2O_2 + O_2$		3.02×10^{12}	0.00	1386
(H18)	$H_2O_2 + H \rightleftharpoons HO_2 + H_2$		2.30×10^{13}	0.00	7950
(H19)	$H_2O_2 + H \rightleftharpoons H_2O + OH$		1.00×10^{13}	0.00	3585
(H20)	$H_2O_2 + OH \rightleftharpoons H_2O + HO_2$		7.08×10^{12}	0.00	1434
(H21)	$H_2O_2 + O \rightleftharpoons HO_2 + OH$		9.63×10^{6}	2.00	3991

[*] Third-body efficiencies: 2.5 (H_2), 16.0 (H_2O), and 1.0 for all other species. Troe falloff with $F_{cent} = 0.5$.

[†] Third-body efficiencies for all the radical–radical recombination reactions: 2.5 (H_2), 12.0 (H_2O), and 1.0 for all other species.

[‡] Third-body efficiencies: 2.0 (H_2), 6.0 (H_2O), and 1.0 for all other species.
Troe falloff with $F_{cent} = 0.265\exp(-T/94) + 0.735\exp(-T/1756) + \exp(-5182/T)$.

The *shuffle reactions* describe the rapid interconversion among the radical pool of H, O, and OH, controlling the local flame composition. Due to their temperature dependence, these reactions are faster in the hot regions, where they are usually found in equilibrium conditions [337]. As a consequence, Reactions (H1) to (H3) are sufficient to describe the radical pool, while Reaction (H4), whose equilibrium is a direct consequence of the equilibrium of the others, can be neglected [111, 360]. This, however, is not true in low-temperature regions, including the reaction layers of ultra-lean flames, i.e., flames with equivalence ratio close to the lean flammability limit [337]. As discussed in Section 4.2, these reactions, which dominate the fast chemical time scales, strongly influence the structure and speed of premixed H_2 flames.

The *hydroperoxyl reactions* play a central role in defining H_2 flammability limits, especially at low temperatures and elevated pressures. In the presence of a third body M, the collision of H with O_2, instead of producing OH and O through Reaction (H1), can lead to the formation of the hydroperoxyl radical HO_2 through Reaction (H5), described as a Troe falloff reaction (see Equations (2.12) and (2.13)). The HO_2 radical is subsequently consumed through Reactions (H6) to (H10), which are fast in high-temperature regions, leading to small concentrations of HO_2 in flames [337]. These reactions are relevant in ignition processes, determining the ignition delay time and the extinction behavior [337].

The recombination of the radicals H, O, and OH, although mainly controlled by Reaction (H5), can occur also through the *radical–radical recombination reactions*. These represent termination pathways, in which highly reacting radicals recombine in the presence of a third body. In particular, Reactions (H11) and (H12) are relevant in the downstream region of stoichiometric and rich premixed flames, in the fuel side of non-premixed flames, and in the chemical equilibrium at high temperature, which is relevant for detonation processes [337]. Moreover, while autoignition processes are typically triggered by the backward path of Reaction (H7) [265], the backward step of Reaction (H12) is a relevant additional source of radicals in hydrogen-rich high-temperature environments [337].

Finally, the *hydrogen peroxide recombination reactions* introduce a delayed radical production mechanism through the accumulation and subsequent decomposition of H_2O_2. Under high pressures and low temperatures, the associated high concentrations of HO_2 promote the formation of H_2O_2 through the forward step of Reaction (H17). This promotes radical regeneration by the backward step of Reaction (H16), described as a Troe falloff reaction (see Equations (2.12) and (2.13)), which is relevant for high-pressure flames near the flammability limits, for detonations near the detonability limits, and for autoignition at low temperatures. On the other hand, the consumption of H_2O_2 through Reactions (H18) to (H21) is typically small [337].

4.2 Laminar premixed hydrogen flames

The main features of laminar premixed flames have been described in Section 2.5, with particular reference to the flame speed and to the impact of stretch effects on it. Here, we discuss how these are influenced by the chemical characteristics of H_2 combustion.

4.2.1 Enhancement of the laminar flame speed

Compared to methane, natural gas or ammonia, the laminar flame speed S_L^0 of H_2 premixed flames is about one order of magnitude higher for a wide range of equivalence ratios [221, 307]. Law and Sung [228] derived, based on asymptotic analyses, an expression for the laminar burning

flux m^0:

$$m^0 = \rho_u S_L^0 = \frac{Le_{eff}}{Ze^2}\frac{\lambda}{c_p}\exp\left(-\frac{E_a}{RT_b}\right), \tag{4.1}$$

where Ze is the Zel'dovich number, related to the global activation energy E_a and the temperature in the burned gases T_b (see Equation (2.47)).

Equation (4.1) indicates that the enhancement of the laminar flame speed in premixed H_2 flames can be associated to three main parameters: the adiabatic flame temperature T_b, the effective Lewis number Le_{eff} (see Equation (2.45)), and the activation energy E_a. Hydrogen presents a higher value of T_b compared to other fuels at the same equivalence ratio. However, this has a small effect on the enhancement of laminar flame speed [307]. Moreover, the high diffusivity of the H_2 molecule leads to a non-unity value of Le_{eff}. For stoichiometric and rich mixtures, this leads to an increase in S_L^0, although this enhancement is not sufficient to account for the substantial differences observed when compared to hydrocarbon fuels [307]. In contrast, for lean flames, where H_2 is the deficient reactant and therefore governs the value of $Le_{eff} < 1$ (see Section 2.5.4), the laminar flame speed is actually reduced when compared to the $Le_{eff} = 1$ case [307], in agreement with Equation (4.1). Therefore, the main explanation for the enhancement of S_L^0 in premixed H_2 flames lies in the activation energy term, and, consequently, in the peculiar chemical kinetics of H_2 combustion.

The H_2 oxidation process is governed by the balance of radicals, and, in particular, by the competition between radical production and radical consumption. The former is dominated by Reaction (H1), which is relevant at high temperatures, while the latter is associated mostly with Reaction (H5), which dominates at low temperatures [337]. At atmospheric conditions, the crossover temperature, i.e., the temperature at which the overall H_2 oxidation process shifts from a chain-branching behavior (i.e., promoting radical generation) to a chain-terminating one (i.e., favoring radical removal), is $T_0 \approx 1050$ K [221, 300]. Therefore, recalling the 1D premixed flame schematized in Figure 2.3 and recognizing the pivotal role of the H radical on the propagation mechanism of H_2 flames [261], it is possible to divide the reacting zone in a downstream high-temperature region, where H is produced, and in an upstream low-temperature region, where it is consumed.

Overall, the shuffle reactions in Table 4.1 exhibit a chain branching behavior, summarized by the global fuel consumption process [261, 337]:

$$3\,H_2 + O_2 \rightleftharpoons 2\,H_2O + 2\,H, \tag{R4.1}$$

which has a reaction rate that, in first approximation, is equal to the one of Reaction (H1) [229, 337]. Therefore, H_2 consumption leads to the formation of a large H radical pool, which can back-diffuse and recombine exothermically in the upstream radical consumption region, enhancing the burning velocity of H_2 premixed flames [221].

In hydrocarbon flames, on the other hand, other relevant reactions occur, in addition to those governing the H_2 oxidation. Considering methane (CH_4), the overall fuel consumption process can be described as [221, 229]:

$$CH_4 + 2\,H + H_2O \rightleftharpoons CO + 4\,H_2, \tag{R4.2}$$

which is chain-terminating and leads to the depletion of H radicals when consuming the fuel. Consequently, the generation of the H radical pool is hindered, slowing down the fuel consumption and the flame propagation. This leads to the strong discrepancy in the laminar flame speed between H_2 and hydrocarbon premixed flames.

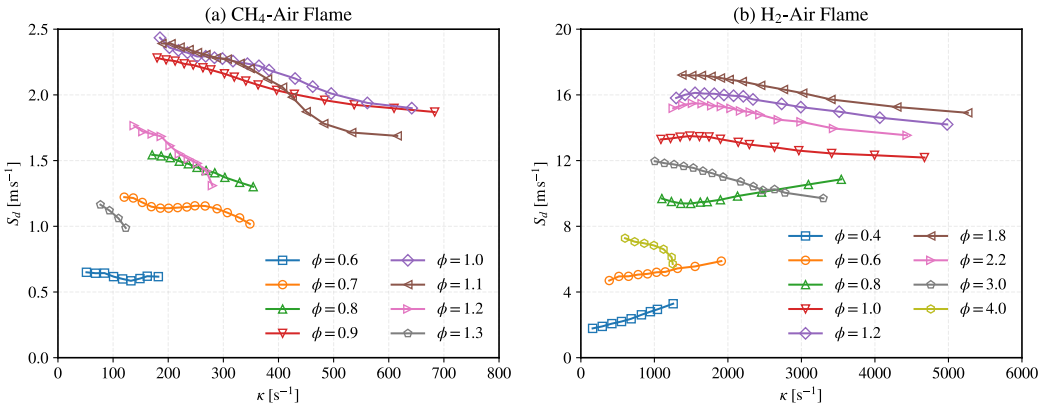

Figure 4.1: Stretched flame propagation speed S_d versus stretch rate κ for premixed methane–air (a) and hydrogen–air (b) flames in a constant volume combustion chamber at $p = 1$ bar and $T_u = 303$ K (adapted from [168]).

4.2.2 Stretch effects

As discussed in Section 2.7.3, stretch can impact the propagation speed of laminar flames, depending on the value of Le_{eff}. This is the case of lean premixed H_2–air flames, which, due to the high diffusivity of hydrogen, are characterized by a value of $Le_{eff} \approx 0.3 - 0.4$ [11, 416]. Consequently, these flames show a negative value of the Markstein length (see Equation (2.51)) and an enhancement of the flame consumption (and displacement) speed for increasing stretch (see Equation (2.49)). Figure 4.1 compares experimental measurements by Hu et al. [168] of the flame displacement speed S_d as a function of the stretch rate κ for expanding CH_4–air and H_2–air spherical premixed flames[§]. For the CH_4 flame (see Figure 4.1a), the flame speed is almost independent of the stretch for lean mixtures, while a negative dependence, associated with a positive Markstein length (see Equation (2.48)), is present for stoichiometric and rich mixtures. On the other hand, the H_2 flame (see Figure 4.1b) shows an increasing trend of the flame speed with stretch for lean mixtures.

In addition to the different slopes associated with the Markstein length value, the comparison of the two fuels in Figure 4.1 highlights also the strong enhancement of the flame propagation speed when burning H_2. This provides a quantitative evidence of the discussion in Section 4.2. Furthermore, it is possible to observe the strong differences in the stretch values between the two fuels, highlighting another relevant feature of premixed H_2–air flames, i.e., the enhanced resistance to stretch and, consequently, the higher stretch extinction limit [221]. This is another consequence of the high molecular diffusivity of the H_2 molecule, which enhances the reactivity of the stretched flames [221].

Another effect of stretch, and more specifically of curvature, is the tip opening in lean premixed H_2–air jet flames [268]. This feature is typically characterized for Bunsen flames, but the same reasoning holds for other kind of jet flames, as shown in Section 9.1. At the tip of a Bunsen flame, the concave curvature toward the fresh gases focuses the heat ahead of the flame, inducing an increase of temperature above the adiabatic value [229]. On the other hand, the same curvature leads to a defocusing of the concentration of the deficient reactant, which tends to reduce the flame temperature [229]. For hydrocarbon flames, since $Le_{eff} \geq 1$, the heat focusing dominates the reactant defocusing, promoting the burning rate at the tip. For H_2 flames, however, given

[§]For this configuration, $S_d = dr/dt$ and $\kappa = (2/r)/(dr/dt)$, where r is the flame radius.

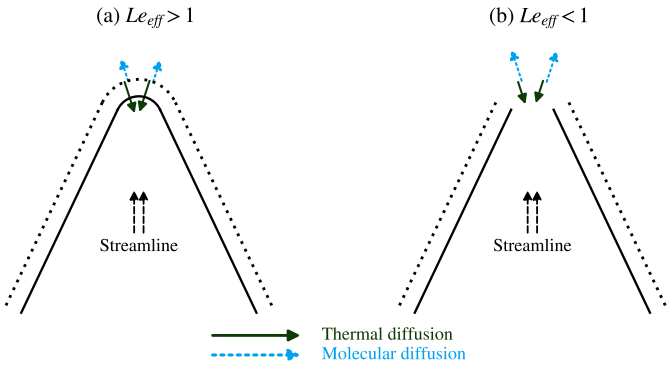

Figure 4.2: Effect of stretch and non-unity Lewis number on the tip of a Bunsen flame (adapted from [229]). Comparison of tip closing for $Le_{eff} > 1$ (a) and tip opening for $Le_{eff} < 1$ (b).

that $Le_{eff} < 1$, the opposite occurs, thus leading to a less intense burning and to local extinction, i.e., tip opening [229]. This mechanism is schematized in Figure 4.2. Numerical simulations by Mizobuchi et al. [267] showed that this effect, related to the reduced fuel consumption rate due to the radial outward H_2 diffusion, is enhanced for lower equivalence ratios.

4.2.3 Thermodiffusive instabilities

In Section 2.6.2, the theory of thermodiffusive instabilities has been discussed, highlighting the crucial role of Le_{eff} in determining the flame stability. Here, we provide an overview of how these instabilities impact the structure and dynamics of laminar lean premixed H_2–air flames.

The onset of cellular structures associated with the TD mechanism has been extensively observed in experiments. Figure 4.3 provides an example, taken from [110], in a Hele–Shaw cell, wherein the flame propagates between two parallel plates separated by a narrow gap. The TD instability leads to a small scale wrinkling, superimposed to the large-scale finger-like structures protruding toward the fresh gases. This experimental image allows for highlighting two characteristic features associated with the TD instability. In positively curved regions, where the flame is convex toward the fresh gases, differential diffusion leads to a focusing of the H_2 diffusive flux, increasing the local H_2 consumption and the heat release rate [307]. Indeed, given the sub-unity Lewis number, the heat diffusion is slower than the H_2 diffusion, leading to a local increase of temperature, eventually above the adiabatic flame temperature, and of the reaction rates. In the experimental image, this results in local brighter regions [221]. The opposite occurs in the negatively curved cusp regions, where the flame is concave toward the fresh gases. In this case, the temperature is significantly lowered, leading to local extinction phenomena, based on a mechanism similar to the one leading to tip opening in Bunsen flames (see Figure 4.2). It should be noted that this TD mechanism, although associated with differential diffusion, is impacted in lean H_2–air flames also by the preferential diffusion of H_2 with respect to the other species (see Section 2.5.4), which leads to local enrichment in the positively curved regions [307].

To improve the understanding of this phenomenon, several numerical studies, based on DNS of laminar flames, have been performed in the literature (e.g., [4, 25, 26, 28, 121, 143, 165, 166]). In particular, two regimes have been investigated: the *linear* regime and the *non-linear* one. The former refers to weakly perturbed flame fronts and allows for a comparison with theoretical models (see Section 2.6.2), while the latter involves strongly wrinkled flame fronts with large stretch rates, corresponding to the long term behavior of the flame. Here, we recall the main features

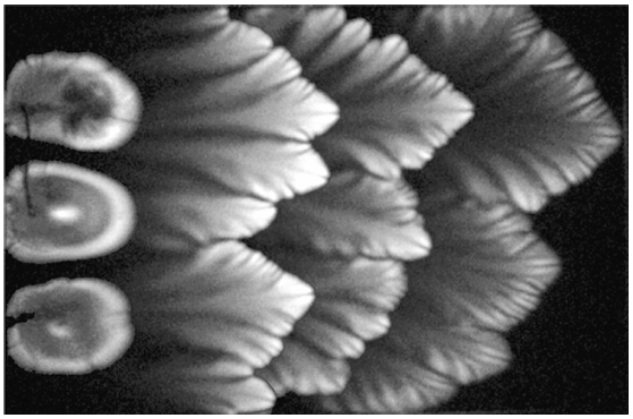

Figure 4.3: Onset of thermodiffusive instabilities in a lean premixed hydrogen–air flame ($Le_{eff} \approx 0.34$) in a Hele–Shaw cell (from [110]). The figures reports snapshots at different time instants, with the flame propagating from left to right.

of the two. Interested readers can refer, among others, to [25, 26, 221, 307] for a more detailed description.

Berger et al. [25] investigated the onset of intrinsic instabilities for premixed H_2–air flames under varying operating conditions, allowing for the derivation of dispersion relations based on their numerical dataset. To this scope, the flame front was perturbed by a weak harmonic perturbation. In all cases, even for $Le_{eff} < 1$, they observed the presence of a cut-off wavenumber, confirming the necessity to include a high-order stabilizing term in the expression of the dispersion relation (see Equation (2.55) and Figure 2.12). In particular, they observed that the TD mechanism becomes stabilizing for perturbation wavelengths in the order of the thermal flame thickness δ_L^0. Furthermore, they showed that TD instabilities are enhanced for leaner mixtures, lower temperatures, and higher pressures [25].

In the non-linear regime, the instability is characterized by two length scales, one for the large-scale structures and the other for the small-scale structures. The former has been found to be independent of the domain size, provided that this is sufficiently large [28, 348]. The latter, instead, is strongly related to the wavelength of the maximum growth rate observed in the linear regime, and has been found to be approximately equal to $6\delta_L^0$ [307].

The influence of the perturbation wavelength on the TD mechanism was investigated also by Young and Ahmed [432] using a different approach, i.e., by considering 2D lean H_2–air planar flames subjected to acoustic oscillations originating from a monopole source, rather than to a harmonic perturbation of the flame. They showed that forcing frequency and amplitude strongly influence the TD mechanism. At low frequencies, the dispersion relation terminates at small wavenumbers, indicating an early transition of small-scale perturbations to the nonlinear regime, whereas at higher frequencies linear growth persists up to larger wavenumbers. For very lean mixtures ($\phi = 0.4$), acoustic forcing was shown to enhance the growth of TD instabilities at low wavenumbers. This behavior was attributed to pressure gradients penetrating the preheat zone and modifying mass transport and H_2 differential diffusion. Depending on the forcing frequency, this resulted in either an attenuation or amplification of the TD instability.

The impact of the forcing frequency on TD instabilities was investigated numerically also in [429, 435] for lean premixed H_2–air conical jet flames subjected to inflow harmonic velocity oscillations. By defining a Damkhöhler number *Da* for the laminar case (not to be confused with

its turbulent counterpart expressed in Equation (2.74)):

$$Da = \frac{\tau_m}{\tau_c} = \frac{1/f}{\delta_L^0/S_L^0} = \frac{S_L^0}{f\delta_L^0}, \tag{4.2}$$

it was shown that the flame response is the strongest for $Da \sim \mathcal{O}(1)$. Under these conditions, the flame wrinkling due to the unsteady inflow is amplified, and the flame naturally resonates with the flow disturbance [262, 263]. This leads to stronger deviations of the local flame dynamics with respect to the steady-state solution, and to larger increases in the fluctuations of flame surface area and heat release rate. For $Da \ll 1$, the flame is almost unaffected by the forcing, since it cannot respond to rapid flow perturbations. For $Da \gg 1$, on the other hand, the flame oscillates synchronously with the inflow, since the spatial amplitude of the wrinkles approaches or exceeds the length of the flame brush. Under these conditions, however, despite the weaker local response to the unsteady inflow, the global stretch response is stronger, meaning that the conversion of flame surface wrinkling in global consumption speed fluctuations is amplified for $Da > 10$ [435].

The strong fluctuations in the heat release rate and wrinkling of the flame front have an effect on the flame consumption speed S_c that is, conceptually, analogous to the one described in Equation (2.68) for turbulent flames. Indeed, an enhancement of the flame speed is observed for thermodiffusively unstable laminar H_2 flames, due to the combined action of two mechanisms. First, the flame surface is increased by the wrinkling of the flame front, resulting from the combined action of hydrodynamic (see Section 2.6.1) and TD instabilities, coherently with Damkhöhler's first hypothesis (see Equation (2.61)). In addition to this, H_2 differential and preferential diffusions on the flame structure further enhance the flame speed by impacting the response to stretch (see Section 4.2.2). Coherently with the observations made in the linear regime [25], the enhancement of S_c is promoted for leaner mixtures, lower temperatures, and higher pressures. An empirical power law scaling was derived by Berger et al. [26], relating the flame speed enhancement S_c/S_L^0 to the thermodynamic operating point through Ze, Le, and the expansion ratio σ. Notably, the sole chemical kinetic parameter is Ze, which is associated with the global activation energy of the combustion process (see Equation (2.47)). This implies that the radical balance is not relevant in this context, and that the TD instability can be captured by a global reaction mechanism, at least at low pressures [165, 307].

Numerical simulations allow also to investigate the influence of single parameters on the TD instability. In particular, the influence of the transport modeling was investigated for 2D planar laminar flames in [307, 349]. By using a methodology analogous to the one adopted by Aspden [12] for turbulent H_2 flames in a flame-in-a-box configuration, they investigated the influence of preferential and differential diffusion on the TD mechanism. To this scope, they imposed:

- $Le_k = 1$ for each species k, suppressing both differential and preferential diffusion.
- $Le_k = Le_{H_2}$, removing the H_2 preferential diffusion with respect to other species, but preserving the differential diffusion.
- $Le_k = Le_k/Le_{H_2}$, hence suppressing the H_2 differential diffusion by imposing a unity Lewis number to this species, while keeping the preferential diffusion.

Evidently, when removing both effects, TD instabilities are suppressed in the planar flame, and only weak large-scale structures associated with the hydrodynamic mechanism are present [307]. When considering the sole differential diffusion, no local variation of equivalence ratio was observed in [307]. Nevertheless, the resulting flame structure and consumption speed were found

to be very close to the one obtained with realistic transport parameters [307], in agreement with the findings of Aspden [12] for the turbulent case. On the other hand, for the case including the sole preferential diffusion, similar results to the one considering $Le_k = 1$ for all species were obtained. Analogous conclusions were drawn in the context of flame-wall interaction by Schneider et al. [349], who showed that the quenching characteristics depend mostly on the ability to capture TD effects when considering the sole differential diffusion, rather than on the variability of the local thermochemical state associated with preferential diffusion. These results suggest that differential diffusion is the main driver of TD instabilities, while preferential diffusion, despite its action on the local equivalence ratio, has a limited effect on the flame dynamics [307, 349], at least for the planar flame configuration. This holds significance from a modeling point of view [307].

4.3 Turbulent lean premixed hydrogen flames

The dynamics of unstable hydrogen flames is associated with its molecular transport properties. In turbulent combustion, these are often neglected when compared to the turbulent mixing [307]. While this would suggest that TD instabilities are less relevant for turbulent premixed flames, the opposite is actually true. Indeed, the persistence of TD instabilities in lean premixed turbulent H_2–air flames was consistently observed in experiments [87, 139], and associated to the H_2 differential diffusion [12, 27]. The main qualitative features of thermodiffusively unstable turbulent flames are the insurgence of finger-like structures penetrating into the unburned gases, and the presence of super-adiabatic temperatures in the positively curved regions of the flame [307]. Moreover, Rieth et al. [326] showed that the TD instabilities in turbulent flames are enhanced at high pressures, a result which is consistent with the observations made in the laminar case (see Section 4.2.3).

In the following, the main features of turbulent premixed H_2–air flames are discussed, with particular reference to the relevance of TD effects and instabilities on the flame structure and dynamics, and on the influence of the turbulent combustion regime.

4.3.1 Synergy between thermodiffusive instabilities and turbulence

For moderate values of *Ka*, TD effects and instabilities not only persist in turbulent premixed flames, but interact synergistically with the turbulence and are amplified. This synergy can be quantified globally by the increase in the stretch factor I_0 (see Section 2.7.3) with increasing turbulence intensity. In this sense, Berger et al. [27] have observed an increase of this quantity from $I_0 = 2.6$ in a laminar flame to $I_0 = 4 - 5$ in a turbulent one, while keeping the same thermodynamic conditions.

This enhancement was associated to a strong increase in the local equivalence ratio, which promotes a local enhancement of the heat release rate and of the consumption speed. The origin of this effect lies in the turbulent straining, which locally affects the transport processes within the flame and leads to a local enrichment [27, 86, 166]. Notably, this strain-driven mechanism, enhancing the flame speed with respect to the laminar case, is present even in the absence of curvature [307]. In turbulent flames, however, the local curvature is significantly increased with respect to the laminar case, due to the action of turbulence on the flame surface. This leads to a further enhancement of the local reaction rate, and consequently, of the flame speed.

The flame surface wrinkling is also affected by TD instabilities in turbulent flames. More specifically, the deformation of the flame front is enhanced in thermodiffusively unstable turbulent flames, compared to stable ones [307]. Indeed, the TD instability remains dominant at smaller scales [166], leading to a different flame surface dynamics. Recalling Section 2.5.3, the variation of the flame surface is governed by the combined action of strain and curvature, with positive curvatures promoting flame surface generation, while negative curvatures lead to flame surface destruction [307]. While strain is the dominant source of flame surface area for thermodiffusively stable flames, the positive curvature contribution is equally important for unstable cases, thus promoting the flame surface generation [27, 65]. Consequently, when considering the balance for the flame surface density in Equation (2.66), the flame surface generation term is enhanced, making flame surface destruction less relevant to the net variation of flame surface [61, 152, 399]. This does not necessarily imply a net increase of the flame surface area, since the destructive term is also intensified [27, 65]. Nevertheless, it indicates an impact of TD instabilities in the balance of the two terms, as well as on the flame surface dynamics and evolution.

Experimental evidence was provided by Lapenna et al. [220], who analyzed the interaction between TD instabilities and turbulence in turbulent premixed CH_4–H_2–air Bunsen flames, with varying H_2 content. They observed that the synergistic interplay between TD instabilities and turbulence enhances primarily the flame reactivity, rather than the flame area. Moreover, a spectral analysis of the flame curvature revealed that thermodiffusively unstable flames present more energetic curvature spectra at low wavenumbers, and a broader range of unstable scales interacting with the turbulent integral scale, highlighting the multiscale nature of this coupling.

4.3.2 Influence of the Karlovitz number

Although different definitions of Ka are adopted in the literature, thus introducing some ambiguity when comparing results, it is generally accepted that, for sufficiently high values of Ka, the flame is located in the broken reaction zones regime (see Section 2.7.4), in which the inner flame structure is affected by turbulent eddies. Under these conditions, TD effects are expected to be progressively suppressed. Indeed, as Ka increases, the coherent cellular structures associated with TD instabilities are increasingly disrupted by the smallest turbulent eddies, which penetrate into the flame reaction zone. Nevertheless, characteristic features of TD instabilities have been reported to persist up to $Ka \approx 100$ in lean premixed H_2 flames [15].

Berger et al. [23] investigated numerically the influence of the Karlovitz number on TD instabilities in a turbulent slot burner configuration. When increasing Ka up to values well above 100, they observed a substantial reduction of the super-adiabaticity associated with TD effects, despite an increase of the stretch factor with increasing turbulence. From a flame surface perspective, however, the finger-like structures characteristic of TD instabilities and responsible for the enhancement of the flame surface area progressively disappeared. Consequently, it was observed that the flame surface destruction term becomes dominant in defining the flame surface dynamics, coherently with the behavior of thermodiffusively stable flames.

A more comprehensive analysis was performed by Russell et al. [332] by considering DNS of turbulent lean premixed H_2–air flames, both in piloted jet flame and flame-in-a-box configurations, over a wide range of Ka values. At low Ka, they observed that the turbulence exaggerates the TD response [15, 27, 166], enhancing the local and global flame speeds with increasing turbulence levels, together with the local temperature, which reaches super-adiabatic values. For sufficiently intense turbulence, a transition was observed, with a drop in the mean local flame speed, in the local super-adiabatic temperature, and in the heat release rate. This transition marked a

regime in which turbulent mixing dominates over the TD mechanism. The underlying physical mechanism was summarized as follows. At low *Ka*, the TD response leads to a diffusive focusing of the H_2 fuel into regions of positive curvature, which results in locally richer, thinner, faster and hotter flames. Consequently, the equivalence ratio increases, eventually exceeding the global value of the unburned mixture and leading to super-adiabaticity. Turbulence enhances the flame surface wrinkling and curvature, thus amplifying the TD response and further enriching the positively curved regions. Eventually, for increasing *Ka*, turbulence becomes sufficiently intense that the flame curvature cannot be further increased. At this point, the turbulent mixing at the flame scale is sufficient to overcome the TD response driven by differential diffusion. The fuel and temperature distributions are consequently governed by turbulence, limiting the further increase in the local equivalence ratio, suppressing the super-adiabaticity, and attenuating the impact of TD effects on the flame dynamics.

4.4 The impact on numerical combustion

All the numerical studies reported in the previous literature review are based on DNS. To enable the transition of combustion systems toward H_2, however, it is necessary to capture TD effects and instabilities in engineering-relevant configurations using RANS and LES. Therefore, predictive models accounting for these mechanisms are necessary [307]. Any turbulent combustion model should be able to capture the interaction between the sub-grid unresolved scales and the larger resolved ones. When considering TD instabilities, however, this already difficult challenge becomes even more complex.

Indeed, the modeling of TD instabilities is an open question even in the context of laminar flames, where differential diffusion and cellular wrinkling are already present [221]. When interacting with turbulence, this issue is amplified, since TD instabilities are highly non-linear and lead to a synergistic interplay, as discussed in Section 4.3.1. Moreover, the TD instabilities originate at small scales and grow to larger scales, with a reverse cascade that impacts multiple scales in space and time [307]. Several approaches are present in the literature to tackle this issue, relying either on a physics-based methodology or on machine learning. A comprehensive overview of the different models in the literature is available, for example, in [307].

Among the different turbulent combustion models, the Thickened Flame model is one of the most widely implemented (see Section 3.2.1). Therefore, it is not surprising that the extension of the TF model to include stretch and TD effects is a relevant research question. The artificial thickening operation is known to amplify the impact of stretch on the flame consumption speed [314]. While this issue is relevant also in hydrocarbon flames, which can be characterized by a positive Markstein length (see Figure 4.1a), it becomes even more relevant for H_2 flames with negative Markstein lenghts. For this reason, the so-called Stretched-TF model was proposed by Detomaso et al. [89] for hydrocarbon flames, and extended to H_2 flames by Hok et al. [163, 164]. This approach is based on the application of different thickening factors to the pre-exponential factor, the thermal diffusivity and the species diffusivities, to ensure that the flame response to stretch is preserved. Albeit effective, the main limit of this model lies in the fact that, in the present state, it is applicable only to global reaction mechanisms.

To perform simulations with detailed kinetics, several alternative sub-grid-scale models accounting for TD effects in the TF framework have been proposed in the literature (e.g., [5, 126, 351, 352]). These are mainly based on the correction of the efficiency function (see Section 3.2.1) to account for the additional contribution of TD effects to the local flame speed, and are validated by comparison with DNS data.

When investigating a complex, multi-physics phenomenon such as flame–acoustics interaction, however, modeling can introduce relevant approximations, which can sensibly affect the results and hinder the physical understanding of phenomena. This motivates, in the present work, the adoption of DNS, without applying any combustion model, for the investigation of combustion noise in lean premixed H_2–air flames.

PART II

Chemical reduction and chemiluminescence in hydrogen combustion

Химия, брат, химия! Нечего делать, ваше преподобие, подвиньтесь немножко, химия идет!

It's chemistry, brother, chemistry! There's no help for it, your reverence, you must make way for chemistry.

— Fyodor Dostoevsky
The Brothers Karamazov, 1880

5

Derivation of a global reaction mechanism for hydrogen combustion

A REDUCED ONE-STEP GLOBAL REACTION MECHANISM, denominated 1S_H2AIR_FGS, is here derived for hydrogen–air combustion. The Pre-Exponential Adjustment approach [120], based on an explicit analytical dependence of reaction rate parameters on the equivalence ratio, is extended to include a pressure-based scaling. Moreover, a correction is proposed to improve the prediction of the thermal flame thickness, and transport properties are adjusted to reproduce the flame response to stretch.

The reduced scheme is validated by computations of 1D unstrained and strained laminar premixed flames for a wide range of operating conditions, with a good agreement in the predicted main flame properties between the reduced scheme and reference kinetic mechanisms. Moreover, a first assessment of the performance of the reduced scheme in AVBP is given, by considering the simulation of 2D premixed cylindrical expanding flames under several mixture conditions, with a significant improvement of the computational efficiency. This reduced scheme will be further exploited for the numerical simulation of 3D laminar flames in Section 9.4, and of 3D turbulent ones in Section 11.6.

Results from this Chapter are included in:

- F. G. Schiavone, N. Detomaso, M. Torresi, and D. Laera. "An Arrhenius-based one-step reaction mechanism for hydrogen–air flames simulations in an extended range of operating conditions". In: *International Journal of Hydrogen Energy* 57 (2024), pp. 1229–1243.

Contents

5.1 Context and motivations

Computational Fluid Dynamics is a reliable tool to analyze complex phenomena characterizing H_2 flames. When considering engineering-relevant operating conditions, however, modeling is required to make the simulations computationally sustainable [307]. As discussed in Section 4.4, existing combustion models may not be appropriate for these flames, and, therefore, require to be adapted.

An alternative approach consists in shifting the modeling from the flame to the combustion process, by adopting a reduced reaction mechanism to describe the fuel oxidation with a lower computational cost. Indeed, even though the full kinetics of H_2 oxidation is well-known and significantly simpler than the one of hydrocarbons [339], a further simplification is desirable, since, in 3D simulations of reacting flows based on a finite-rate formulation, a balance equation must be solved for each species in the three directions, rapidly increasing the overall cost. Moreover, the reduced time scales of intermediate species require a finer temporal discretization, making the numerical problem stiffer. On the other hand, given the low number of species and reactions involved in H_2 combustion, the accuracy of simplified approximations for radical pools is reduced, making in this sense more difficult to obtain asymptotic descriptions, and introducing a clearly identifiable degradation in accuracy in at least some part of the flame for each step of kinetics reduction [261].

In light of this, a significant effort has been put into the derivation of effective and sufficiently accurate simplified chemical mechanisms for H_2 combustion, with different approaches. For example, Wang et al. [418] proposed a reduced mechanism based on a tabulated activation energy factor to predict ignition for a wide range of operating conditions (i.e., excess air coefficients between 0.56 and 8.4, unburned mixture temperatures between 850 and 1800 K, and pressures between 0.1 and 100 atm). Nevertheless, tabulated chemistry methods often require the use of expensive algorithms for efficiently storing and searching out data in tables [337].

An alternative approach is based on an analytical description of the reaction rate, based on first-principles-derived approaches. A two-step reduced mechanism for premixed H_2 flames was proposed by Mauss et al. [261], based on the Quasi-Steady-State (QSS) approximation* for the O, OH and HO_2 radicals. A three-step overall scheme was systematically derived by Boivin et

*In the QSS approximation, the concentration of a species k is assumed as constant in time, meaning that its production and consumption rates are equal: $\dot{\omega}_k^{prod} \approx \dot{\omega}_k^{cons}$.

al. [33], by applying the QSS approximation to O, OH and H_2O_2, and introducing a correction factor to better predict autoignition in lean and stoichiometric H_2 flames. The QSS approach was subsequently extended to the H radical, leading to a systematically derived one-step reduced mechanism for H_2–air combustion [53, 111, 112]. More recently, a variable stoichiometric coefficient formalism was adopted in [266, 403] to derive a one-step scheme for H_2 flames, able to adequately retrieve the laminar burning velocity and the adiabatic flame temperature. Even though the rigorous formalism of this approach is attractive, its implementation in existing numerical simulation codes may be challenging.

Finally, reduced mechanisms can be derived based on a *best-fit* targeting of reaction rate parameters to match detailed kinetics or experimental results. Several examples in this sense are available in the literature. Coffee et al. [74, 75] proposed stoichiometry-dependent Arrhenius-based reaction rate parameters for a single overall irreversible reaction, relying on the least squares fit of the heat release rate profiles obtained from detailed kinetics. Marinov et al. [251] determined a global rate expression for H_2–air combustion, which, however, correctly reproduced the detailed chemistry only at atmospheric pressure and for $0.55 < \phi < 1.1$. One-step global reaction mechanisms were proposed in [200] for different fuels, including H_2. A good agreement was found with respect to detailed kinetics in the prediction of the laminar flame speed for various equivalence ratios, ranging from lean ($\phi = 0.5$) to rich ($\phi = 5.0$) conditions, at 300 K and 1 bar, as well as for moderate temperature variations up to 600 K. Subsequently, this was further extended up to 5 atm in [428]. More recently, an irreversible single-step mechanism was developed by Hok et al. [163, 164] in the framework of the Stretched-TF model (see Section 4.4). This is based on the tuning of the model parameters to reproduce detailed chemistry predictions in terms of laminar flame speed, flame thickness, and response to stretch in the targeted operating point.

Despite these recent advances, the development of Arrhenius-based global reaction mechanisms capable of capturing the main properties of H_2–air flames over a broad range of operating conditions remains limited. In particular, existing approaches are often tailored to specific thermochemical states or modeling frameworks. Based on these considerations, the numerical simplicity of the best-fitting approach is here exploited to construct a one-step reduced mechanism able to describe the main properties of H_2–air flames (i.e., laminar flame speed, laminar flame thickness, adiabatic flame temperature, and flame response to stretch) for a various set of initial conditions of the reactants, in terms of equivalence ratio, unburned gas temperature, and pressure. Simple analytical expressions are adopted for the reaction rate adjustment functions, and the terms depending on pressure and equivalence ratio are explicitly decoupled, hence preserving the computational efficiency of the reduced scheme.

5.2 Methodology

A flame is characterized by four main properties: the laminar flame speed S_L^0, the laminar flame thickness δ_L^0, the adiabatic flame temperature T_{ad}, and the response to stretch. A reduced mechanism should be able to capture with sufficient accuracy these properties in the widest possible range of initial temperatures, pressures and compositions. Here, the one-step reaction mechanism is developed to accurately predict S_L^0. Moreover, adjustments in the transport properties of the mixture are introduced so that also the other main flame properties can be predicted with sufficient accuracy.

The San Diego mechanism [339] (UCSD) is taken as a reference to design and validate the reduced one-step scheme, based on calculations of 1D unstretched laminar premixed flames with

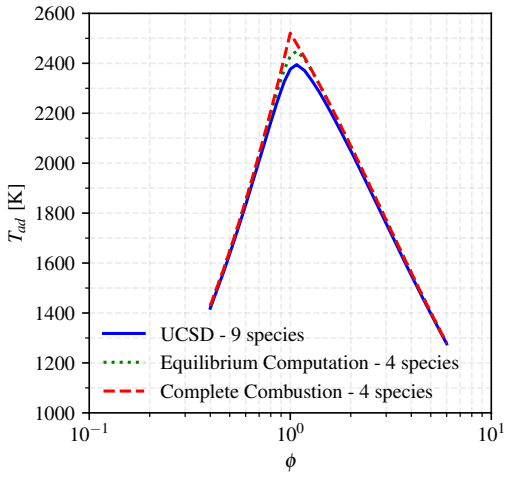

Figure 5.1: Adiabatic flame temperature of H_2–air flames as a function of equivalence ratio at atmospheric conditions ($T_u = 300$ K, $p = 1$ atm). Comparison between 0D equilibrium and complete combustion calculations involving 4 species (H_2, O_2, H_2O, and N_2), and reference 1D flame calculations based on the UCSD mechanism with 9 species.

Cantera [137]. The results from 1D flame calculations obtained with the reduced scheme are compared also with two other mechanisms, the one by Konnov [202], and the H2_NOX_15_94_TC scheme by Capurso et al. [51] (see Section 3.3.4).

The calculations are performed for varying values of pressure (1 atm $\leq p \leq$ 30 atm), unburned gas temperature (300 K $\leq T_u \leq$ 800 K), and equivalence ratio ($0.4 \leq \phi \leq 6.0$). These operating ranges are typical of air-breathing combustion systems, such as gas turbines, boilers, furnaces, and internal combustion engines. Nevertheless, the procedure described hereafter can be further extended to other applications of interest.

5.2.1 Fundamental considerations

The overall reaction for H_2 oxidation can be expressed as:

$$2\,H_2 + O_2 \longrightarrow 2\,H_2O. \tag{R5.1}$$

This is implicitly based on the assumption of complete combustion, since minor species are not considered. For hydrocarbons, this hypothesis is well in agreement with chemical equilibrium, which strongly favors the conversion of the fuel molecule. However, when considering H_2–air combustion, the equilibrium solution involving the four main species (i.e., H_2, O_2, H_2O, and N_2) does not lead to complete fuel oxidation. In this sense, Figure 5.1 shows the adiabatic flame temperature as a function of ϕ at atmospheric conditions ($T_u = 300$ K and $p = 1$ atm), resulting from premixed flame simulations considering either chemical equilibrium or complete combustion of the four main species, as well as 1D flame calculations with the UCSD mechanism involving nine species. The complete combustion process, which intrinsically behaves like a single irreversible step and is based on mixture enthalpy conservation for constant pressure processes, overestimates the adiabatic flame temperature, especially in the near-stoichiometry region, and misplaces the peak value. Conversely, the equilibrium computation, consistent with a single reversible step, provides a solution closer to the one obtained with the detailed scheme.

Therefore, here two reduced schemes are compared, one based on the irreversible step defined in Reaction (R5.1), denominated 1S_IRR_H2AIR_FGS, and the other, hereafter labeled

as 1S_REV_H2AIR_FGS, which relies on the following global reversible reaction:

$$2\,H_2 + O_2 \rightleftharpoons 2\,H_2O. \tag{R5.2}$$

In both cases, S_L^0 is related to the rate of progress of the forward reaction, which depends on the product of the rate constant K_f and of the species concentration at the power of their reaction order (see Equation (2.6)). Recalling Equation (2.9), the free parameters to determine this quantity are, in addition to the overall reaction order n, the pre-exponential factor $\mathcal{A}_f$, the temperature exponent β, and the activation energy $E_{a,f}$. Consequently, given the values of S_L^0 obtained with detailed kinetics (in this case, the UCSD mechanism) in the operating conditions of interest, a set of these reaction rate parameters can be found, for which the one-step scheme most closely follows the detailed one.

In principle, the fresh gas mixture conditions have an impact on the flame structure, and, consequently, the reaction rate parameters should be defined as a function of ϕ, p, and T_u. At first, we consider a combustion process at atmospheric temperature and pressure, and introduce a dependency on ϕ in Equation (2.9):

$$K_f(\phi) = \mathcal{A}_{f(\phi)}\, T^{\beta(\phi)} \exp\left[-\frac{E_{a,f}(\phi)}{RT}\right]. \tag{5.1}$$

To simplify the numerical implementation, the impact of ϕ on β and $E_{a,f}$, is made implicit, by discharging the whole dependency on ϕ over the Pre-Exponential Factor $\mathcal{A}_f$, as proposed by the Pre-Exponential Adjustment (PEA) method [120]. This leads to the following expression for the forward reaction rate constant:

$$K_f(\phi) = B_f(\phi)\, T^{\beta^*} \exp\left(-\frac{E^*_{a,f}}{RT}\right), \tag{5.2}$$

where

$$B_f(\phi) = \mathcal{A}_f(\phi)\, T^{\beta(\phi)-\beta^*} \exp\left[-\frac{E_{a,f}(\phi) - E^*_{a,f}}{RT}\right], \tag{5.3}$$

with the superscript $*$ denoting the value computed at $\phi = 1$. With the same reasoning, the reaction rate constant for the backward reaction in the reversible mechanism is defined as

$$K_b(\phi) = B_b(\phi) \exp\left(-\frac{E^*_{a,b}}{RT}\right), \tag{5.4}$$

with

$$B_b(\phi) = \mathcal{A}_b(\phi) \exp\left[-\frac{E_{a,b}(\phi) - E^*_{a,b}}{RT}\right]. \tag{5.5}$$

For this backward reaction, $\beta = 0$, while B_b and $E_{a,b}$ are estimated from the values of the forward reaction, exploiting equilibrium considerations.

As observed in [383], ϕ affects also the overall reaction order n, as well as the ratio between the orders of fuel and oxidizer, driving the species concentrations in the overall reaction rates of progress:

$$\mathcal{Q}_f = B_f(\phi)\, T^{\beta^*} \exp\left(-\frac{E^*_{a,f}}{RT}\right) [H_2]^{n_{H_2}} [O_2]^{n_{O_2}}, \tag{5.6a}$$

and

$$\mathcal{Q}_b = B_b(\phi) \exp\left(-\frac{E^*_{a,b}}{RT}\right) [\mathrm{H_2O}]^{n_{\mathrm{H_2O}}}. \tag{5.6b}$$

Based on the previous considerations, also the reaction orders are evaluated at stoichiometry ($n^*_{\mathrm{H_2}}$ and $n^*_{\mathrm{O_2}}$ for the forward step, and $n^*_{\mathrm{H_2O}}$ for the backward step in the reversible mechanism) and estimated from n^*.

5.2.2 Estimation of the reaction order and of the temperature exponent

Based on heat and mass balance considerations, Egolfopoulos and Law [103] proposed the concept of overall reaction order, defined as

$$n = 2 \left.\frac{\partial[\ln(m^0)]}{\partial[\ln(p)]}\right|_{T_{ad}}, \tag{5.7}$$

where $m^0 = \rho_u S^0_L$ is the laminar burning flux, and ρ_u is the density of the unburned mixture. Differently from the reaction order introduced in Section 2.1, which is referred to the single reaction and is equal to the molecularity in the case of elementary transformations, the present definition includes in a single parameter the complex physics of the multi-step combustion process, and is evaluated *a posteriori* from the numerical data. The derivative in Equation (5.7) can be approximated numerically as:

$$n \approx 2 \left.\frac{\ln[m^0(p_1)] - \ln[m^0(p_2)]}{\ln(p_1) - \ln(p_2)}\right|_{T_{ad}}, \tag{5.8}$$

where $p_1 = p - \Delta p$, $p_2 = p + \Delta p$, and Δp is a small perturbation of the initial pressure p, which keeps the variation of T_{ad} negligible. Figure 5.2 compares, for varying ϕ, values of n derived from Equation (5.8) at atmospheric conditions with those extracted from [383]. The dashed black vertical line denotes the value at $\phi = 1$, i.e., n^*. A good agreement is found between the two, with a slight overestimation observed for the values obtained in the present work from Equation (5.8). This can be imputed to the differences in the method applied for the assessment of the derivative in Equation (5.8), and in the reaction mechanism adopted for the calculation.

As observed in Section 2.5.1, variations in T_u and p affect S^0_L (and, consequently, m^0) in opposite ways, and polynomial expressions can be introduced to account for this. Even though numerics and experiments converge on such correlations for hydrocarbons, the same relations are not as accurate for H_2–air flames, and the temperature and pressure exponents cannot be treated as constant for these flames, even in first approximation [203]. Moreover, from an engineering point of view, a separation of temperature and pressure effects is not so meaningful, since, in actual combustors, no compression occurs without a concurrent increase in temperature. Consequently, the influence of the initial thermodynamic state is assessed hereafter by considering only p as independent variable, while T_u is obtained, in first approximation, from the isentropic relation $T_u = T^0_u (p/p^0)^{(k-1)/k}$, where $T^0_u = 300$ K, $p^0 = 1$ atm, and $k = 1.4$. Figure 5.3 shows the pressure dependence of the overall reaction order n^*, evaluated using Equation (5.8), and the values obtained from the following logarithmic fit law, with a coefficient of determination $R^2 = 0.983$, indicating an excellent agreement:

$$n^* = 1.909 - 0.2583 \ln\left(\frac{p}{p^0}\right). \tag{5.9}$$

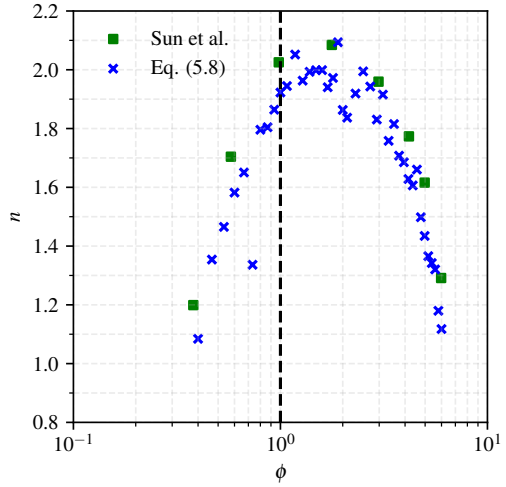

Figure 5.2: Dependence on the equivalence ratio of the overall reaction order n for H_2–air flames at atmospheric conditions ($T_u = 300$ K, $p = 1$ atm). Comparison between values computed with Equation (5.8) and results by Sun et al. [383]. The dashed black vertical lines denotes the value at $\phi = 1$.

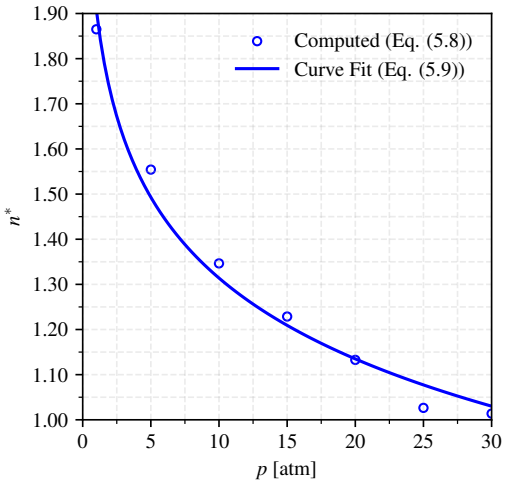

Figure 5.3: Pressure dependence of the overall reaction order n^* for H_2–air flames at $\phi = 1$. Comparison between values computed with Equation (5.8) and the fitting curve of Equation (5.9).

As previously anticipated, n^* is used to estimate the temperature exponent β^*. In the proposed global mechanism, no radical formation (or consumption) is considered, and the preheat and reaction zones of the flame are expected to be sensibly reduced. Moreover, Figure 5.1 highlights that the predicted value of T_{ad} is higher than in the case of detailed kinetics. Consequently, a negative value of β^*, equal to $n^*/2 - 1$, is introduced, to compensate for the overestimation of temperature. As for the reaction orders of the single species, $n^*_{H_2}$ and $n^*_{O_2}$ are determined from n^* by considering that $n^*_{H_2} + n^*_{O_2} = n^*$, and $n^*_{H_2}/n^*_{O_2} = \nu_{H_2}/\nu_{O_2} = 2$. By keeping the parallelism between stoichiometric coefficients and reaction orders, the value of $n^*_{H_2O}$ for the backward reaction is taken as equal to the value of $n^*_{H_2}$ in the forward step.

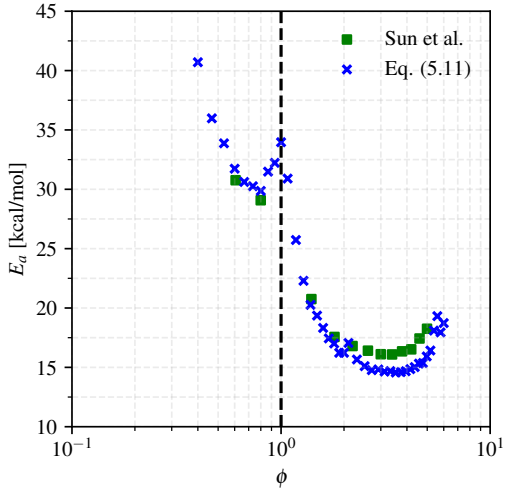

Figure 5.4: Dependence on the equivalence ratio of the overall activation energy E_a for H_2–air flames at atmospheric conditions ($T_u = 300$ K, $p = 1$ atm). Comparison between values computed with Equation (5.11) and results by Sun et al. [383]. The dashed black vertical line denotes the value at $\phi = 1$.

5.2.3 Estimation of the overall activation energy

The overall activation energy of the reaction process was defined in [103] as:

$$E_a = -2R \left. \frac{\partial[\ln(m^0)]}{\partial(1/T_{ad})} \right|_p . \tag{5.10}$$

Based on [383], to change the adiabatic flame temperature, and thereby the laminar burning flux, at constant pressure, unburned gas temperature and composition, the molar fraction of the inert species (i.e., N_2) is varied by a small perturbation ΔX_{N_2}. Consequently, Equation (5.10) can be rewritten as:

$$E_a \approx -2R \left. \frac{\ln[m^0(X_{N_2,1})] - \ln[m^0(X_{N_2,2})]}{1/T_{ad}(X_{N_2,1}) - 1/T_{ad}(X_{N_2,2})} \right|_p , \tag{5.11}$$

where $X_{N_2,1} = X_{N_2} - \Delta X_{N_2}$ and $X_{N_2,2} = X_{N_2} + \Delta X_{N_2}$. Figure 5.4 compares the overall activation energy computed using Equation (5.11) at atmospheric conditions with the results found in [383]. The stoichiometric value E_a^* is denoted by the dashed black vertical line. A good agreement is found for lean and rich flames, with a slight underestimation obtained in the present work, for reasons analogous to those observed for Figure 5.2. In the near-stoichiometric region, a local maximum is present. Even though this region was not considered by Sun et al. [383], a similar result was found in [162].

The activation energy of the forward reaction $E_{a,f}^*$ is obtained by applying this methodology for $\phi = 1$. A logarithmic dependence with respect to p is found:

$$E_{a,f}^* \, [\text{kcal/mol}] = 4.893 \ln\left(\frac{p}{p^0}\right) + 32.97. \tag{5.12}$$

For the backward reaction, the enthalpy of reaction ΔH_R at $\phi = 1$ is used to determine the corresponding activation energy $E_{a,b}^*$ (see Figure 2.1):

$$E_{a,b}^* = E_{a,f}^* - \Delta H_R|_{\phi=1} . \tag{5.13}$$

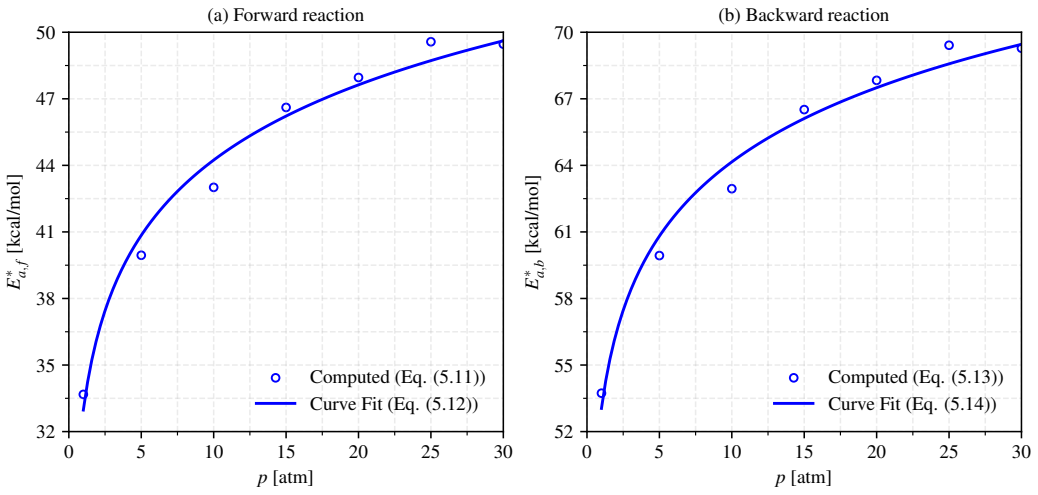

Figure 5.5: Pressure dependence of the overall activation energies $E^*_{a,f}$ (a) and $E^*_{a,b}$ (b) for H_2–air flames at $\phi = 1$. Comparison between values computed with Equations (5.11) and (5.13), and fitting curves of Equations (5.12) and (5.14).

Since combustion is an exothermic process, $\Delta H_R < 0$, leading to $E_{a,b} > E_{a,f}$ (see Figure 2.1). A second logarithmic law, analogous to Equation (5.12), can be derived:

$$E^*_{a,b}\,[\text{kcal/mol}] = 4.825 \ln\left(\frac{p}{p^0}\right) + 53.05. \tag{5.14}$$

Figure 5.5 compares the values of $E^*_{a,F}$ and $E^*_{a,b}$ computed using, respectively, Equations (5.11) and (5.13) and the corresponding fitting functions of Equations (5.12) and (5.14). In both cases, $R^2 = 0.981$, confirming the strong agreement between the computed and fitted values.

5.2.4 Definition of the Pre-Exponential Adjustment laws

Two PEA laws are defined, respectively, for the irreversible and reversible schemes. Both laws are based on the product of three terms:

$$B_f(\phi, p) = B^*_f(p)\, f(\phi)|_{p=p^0}\, g(\phi, p). \tag{5.15}$$

These are derived by computing 1D steady laminar unstretched premixed flames, and by defining the best-fitting function matching the values of m^0 (and, consequently, of S^0_L) computed with the detailed UCSD mechanism. The target values of $B(\phi, p)$ are found by numerically solving the equation:

$$\varepsilon(B(\phi,p),\phi,p) = \frac{|m^0(B(\phi,p),\phi,p) - m^0_{ref}(\phi,p)|}{m^0_{ref}(\phi,p)} = 0, \tag{5.16}$$

where m^0_{ref} is the value of m^0 evaluated with the reference UCSD mechanism.

Subsequently, the expressions for the three functions in Equation (5.15) are defined by determining, for each of them, the curve most similar to the target distribution and estimating its coefficients. As it will be shown later (see Figure 5.7), the reaction constant of the backward reaction is much lower than the forward one, meaning that the backward step of Reaction (R5.2)

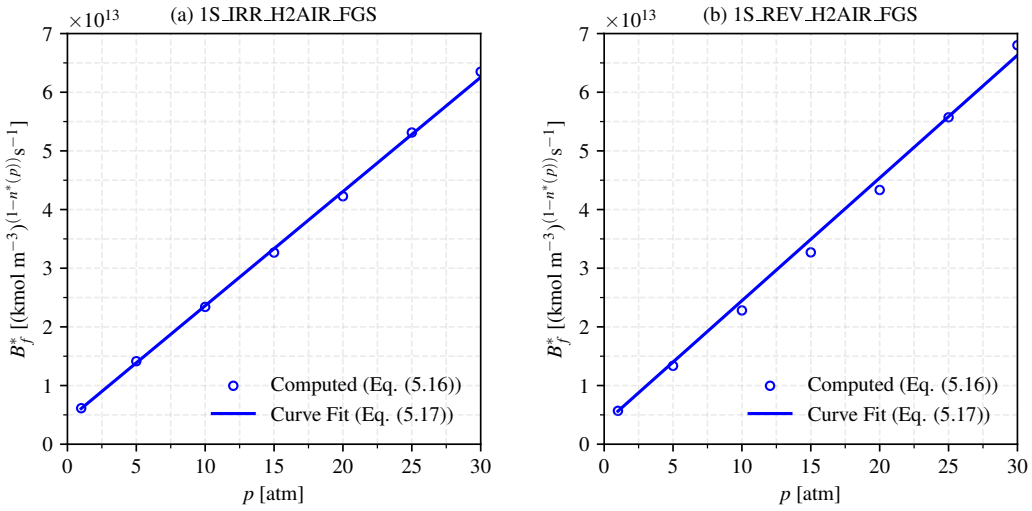

Figure 5.6: Dependence on pressure of the Pre-Exponential Factors of the irreversible (a) and reversible (b) schemes for H_2–air flames at $\phi = 1$. Comparison between values computed with Equation (5.16) and fitting curves of Equation (5.17).

Table 5.1: Coefficients for the corrective function $f(\phi)|_{p=p^0}$.

Mechanism	ψ_0	ψ_1	ψ_2	ψ_3	ψ_4	φ_0	φ_1
1S_IRR_H2AIR_FGS	0.6917	1.856	2.693	0.8530	0.1710	0.3635	3.910
1S_REV_H2AIR_FGS	0.7514	1.987	36.50	3.014	0.1818	0.3635	3.953

affects only in a limited way m^0 (and, consequently, S_L^0). As a result, the PEA law and the Pre-Exponential Factor (PEF) are modeled in the same way for the irreversible and reversible global mechanisms, and the latter can be seen as an extension, or improvement, of the first, rather than a different reaction scheme. In the following, the derivation of the three terms in Equation (5.15) is presented for the reduced schemes.

The term $B_f^*(p)$ corresponds to the PEF allowing to match the value m_{ref}^0 at $\phi = 1$. As shown in Figure 5.6, a linear dependence between this coefficient and pressure is observed:

$$B_f^*(p)\ \left[(\mathrm{kmol\,m^{-3}})^{(1-n^*(p))}\mathrm{s}^{-1}\right] = \left(m\frac{p}{p^0} + q\right) \times 10^{12}, \tag{5.17}$$

where m and q are equal, respectively, to 1.947 and 4.125 for the irreversible mechanism, and to 2.092 and 3.535 for the reversible one. It is worth noticing the low difference between the values obtained with the two expressions for the irreversible and reversible mechanisms.

The corrective function $f(\phi)|_{p=p^0}$ accounts for the impact of ϕ at $p = p^0 = 1$ atm. This is obtained by solving Equation (5.16) at atmospheric conditions for 40 different values of ϕ between 0.4 and 6.0. It takes the following form:

$$f(\phi)|_{p=p^0} = \psi_0 + \psi_1 \exp\left[-\psi_2\left(\frac{\phi - \varphi_0}{\psi_3}\right)^2\right] + \psi_4 \tanh(\phi - \varphi_1), \tag{5.18}$$

with the values of the coefficients given in Table 5.1.

The function $g(\phi, p)$ considers the effect of increasing pressure (and, in the present framework, of unburned gas temperature) at different values of ϕ. This is necessary, since lean and

Table 5.2: Coefficients for the corrective function $g(\phi, p)$.

Mechanism	ξ_0	ξ_1	ξ_2	φ_2
1S_IRR_H2AIR_FGS	6.416	6.744	0.1583	2.057
1S_REV_H2AIR_FGS	7.670	8.077	0.1377	2.138

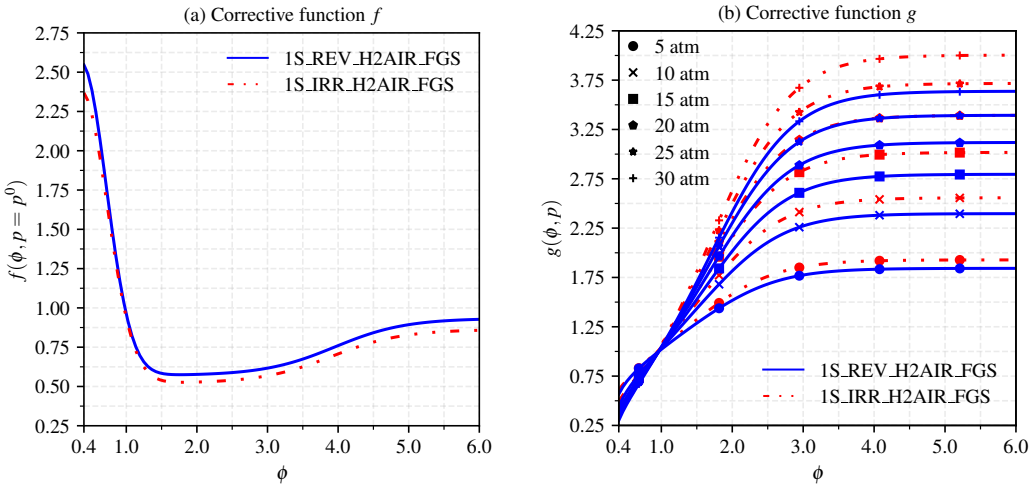

Figure 5.7: Dependence on the equivalence ratio ϕ of the corrective functions $f(\phi)|_{p=p^0}$ (a) and $g(\phi, p)$ (b).

rich H_2–air flames show contrasting behaviors. Indeed, coherently with the analysis of pressure effects performed in [227], when the value of m^0 is imposed to match m^0_{ref}, lean flames show a decreasing trend in the value of the PEF, while the opposite holds for rich flames. This results in the following expression†:

$$g(\phi, p) = \left[\xi_0 + \xi_1 \tanh(\phi - \varphi_2)\right]^{\left[\xi_2 \ln(p/p^0)\right]}. \tag{5.19}$$

The corresponding values of the coefficients are reported in Table 5.2 both for the irreversible and reversible schemes. This formalism has been developed to separate the effects of ϕ and p, so that the integration of the corrective functions in numerical codes is simpler. The functions f and g, with the impact of pressure on the latter, are shown in Figure 5.7 for varying equivalence ratio.

The PEF for the backward reaction of the reversible scheme is evaluated through an explicit expression, which models equilibrium by imposing the equality between the forward and backward reaction rates:

$$B^*_b(\phi) = \frac{k_f(\phi)[H_2]^{n^*_{H_2}}_{eq}[O_2]^{n^*_{O_2}}_{eq}}{\exp\left(-\frac{E^*_{a,b}}{RT_{eq}}\right)[H_2O]^{n^*_{H_2O}}_{eq}} = B^*_f(\phi)\frac{T^{\beta^*}_{eq}\exp\left(-\frac{E^*_{a,f}}{RT_{eq}}\right)[H_2]^{n^*_{H_2}}_{eq}[O_2]^{n^*_{O_2}}_{eq}}{\exp\left(-\frac{E^*_{a,b}}{RT_{eq}}\right)[H_2O]^{n^*_{H_2O}}_{eq}}. \tag{5.20}$$

The scaling factor between $B_f(\phi)$ and $B_b(\phi)$, which can be easily evaluated by 0D equilibrium

†With this mathematical expression, $g(\phi, p)$ is defined for $[\xi_0 + \xi_1 \tanh(\phi - \varphi_2)] \geq 0$, namely for $\phi \gtrapprox 0.3108$. To avoid any error if applying the reduced scheme at $p > 1$ atm in the ultra-lean regime, outside the range of validation and optimization of the mechanism (i.e., $0.4 \leq \phi \leq 6.0$), the condition $\phi = \max(\phi, \phi_{lim})$, with $\phi_{lim} \gtrapprox 0.3108$, should be adopted. Here, $\phi_{lim} = 0.3125$.

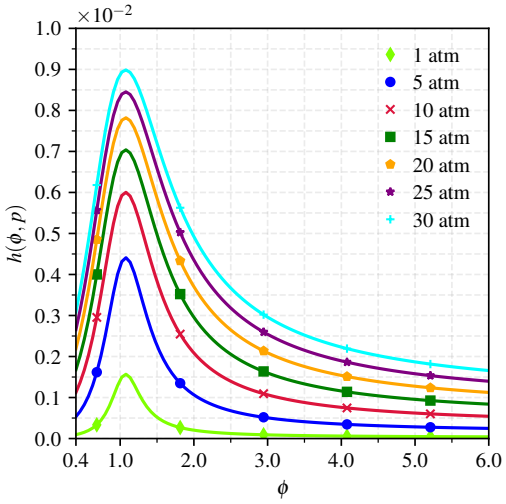

Figure 5.8: Dependence on the equivalence ratio ϕ of the corrective function $h(\phi, p)$.

calculations, is here analytically defined as:

$$h(\phi,p)\ \left[(\text{kmol m}^{-3})^{n^*_{O_2}(p)}\right] = \frac{B^*_b(\phi)}{B^*_f(\phi)} = \frac{\varsigma_0(p)\varsigma_1^2(p)}{(\frac{40\phi}{40\phi+43} - \frac{1}{2})^2 + \varsigma_1^2(p)}, \tag{5.21}$$

where ς_0 and ς_1, which depend on p, are modeled, respectively, as:

$$\varsigma_0(p) = \left[0.2320\ln^2\left(\frac{p}{p^0}\right) + 1.392\ln\left(\frac{p}{p^0}\right) + 1.568\right] \times 10^{-2}, \tag{5.22a}$$

and

$$\varsigma_1(p) = \left[0.8336\ln^2\left(\frac{p}{p^0}\right) + 0.3220\ln\left(\frac{p}{p^0}\right) + 5.815\right] \times 10^{-2}. \tag{5.22b}$$

The function $h(\phi, p)$ is shown in Figure 5.8, highlighting the impact of varying p. The maximum value of $h(\phi, p)$ is in the order of 10^{-2}, meaning that the influence of the backward step is negligible for many flame conditions, and mostly limited to the near-stoichiometric region, where the peak value is reached. This is in agreement with the observations made in Figure 5.1.

5.2.5 Correction for the flame thickness

The impact of simplified kinetics on the flame thickness is often neglected in the definition and validation of reduced chemistry mechanisms for combustion. Nevertheless, since the best-fit approach involves global flame properties such as m^0 and S_L^0, the chemical source terms are well-described by the reduced kinetics only in an integral form. The local flame structure is not controlled, and, in particular, the adequate prediction of mass fractions and thermal gradients, defining the thermal flame thickness δ_L^0 (see Equation (2.41)), is not ensured. Numerical calculations show that, compared to the detailed mechanism, the reduced schemes predict higher values of the adiabatic flame temperature, and of the heat release rate, leading to a steeper gradient in the profiles of species mass fractions and temperature (see Figure 5.15). This generates a nonphysical thinner flame, which may represent an issue from a numerical point of view in CFD simulations.

Table 5.3: Coefficients for the FTA function.

i	1	2	3	4	5	6
σ_i	1043	20.00	41.26	0.3670	8.060	1.148

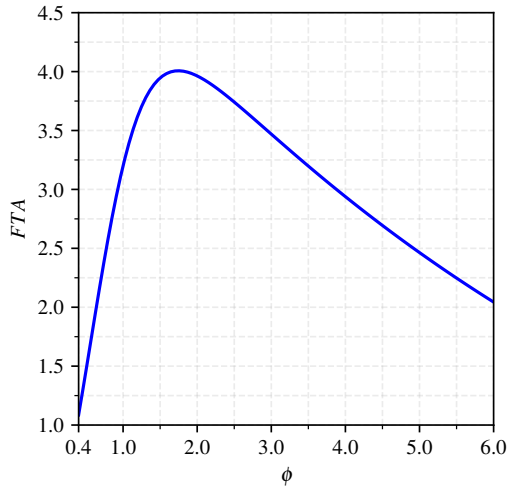

Figure 5.9: Dependence on the equivalence ratio ϕ of the corrective function FTA.

A correction is here proposed to match the flame thickness when using a global reaction mechanism. Since the reaction rate parameters are already defined to match m^0 and S_L^0, the here proposed adjustment intervenes on the thermal and species diffusivities, adapting the methodology implemented in the Thickened Flame model (see Section 3.2.1). An approach based on the same framework was also adopted more recently in [163, 164] in the framework of the Stretched-TF model, with the model parameters tuned to reproduce the prediction of the detailed mechanism in the targeted operating point.

In this work, a single analytical expression for the thickening factor is introduced, based on a function hereafter denominated Flame Thickness Adjustment (FTA). The FTA is defined from the ratio between the actual flame thickness, computed with detailed chemistry, and the one deriving from the one-step scheme. It is modeled as:

$$FTA(\phi) = \frac{\sigma_1}{1+\exp\left(-\frac{\phi+\sigma_2-\sigma_3/2}{\sigma_4}\right)}\left[1-\frac{1}{1+\exp\left(-\frac{\phi+\sigma_2+\sigma_3/2}{\sigma_5}\right)}\right]-\sigma_6, \tag{5.23}$$

with the coefficients σ_i reported in Table 5.3. Figure 5.9 shows its dependence on ϕ. In principle, this function should depend also on pressure. However, this would increase the stiffness of the model, limiting the advantages of a reduced scheme in terms of computational cost. For this reason, a single function is here adapted to capture, with a unique set of coefficients, the behavior of the reduced kinetics in the whole range of pressures of interest. Such a compromise does not introduce a significant error, since the dependence on pressure of the thickness when passing from detailed to global kinetics is negligible (see Figure 5.13).

As in the TF model, all diffusivities are multiplied by the FTA function, while the PEFs of the forward and backward reaction are divided by it. The simplified transport model described

Table 5.4: Parameters adopted in the simplified transport model for the reduced scheme.

μ_{ref} [kg/(m s)]	T_{ref} [K]	α	Pr_0	Sc_{0,H_2}	Sc_{0,O_2}	Sc_{0,H_2O}	Sc_{0,N_2}
8.063×10^{-5}	2645	0.6481	0.6292	0.2507	0.7732	1.168	0.9056

in Section 3.3.4 is adopted for the reduced scheme, with the parameters reported in Table 5.4, where μ_{ref}, T_{ref} and α are the parameters to use in Equation (3.30) to compute the viscosity, while Pr_0 and Sc_0 denote the values of the Prandtl and Schmidt numbers before the application of the *FTA* correction.

5.3 Application to one-dimensional unstretched laminar flames

The validity of the one-step mechanism, with particular reference to the reversible one (1S_REV_H2AIR_FGS), is first assessed by applying it in the computation of multiple 1D freely-propagating, unstretched laminar premixed flames using Cantera [137], with various combinations of ϕ, p and T_u. The domain is of length $L_x = 5$ cm, which is 2-3 orders of magnitude larger than the flame thickness, thus avoiding any impact of boundaries on the flame solution. The mesh refinement criteria described in Section 3.1 are adopted, so that the number of grid points for each case is in the order of 10^3.

To better match experimental measurements, computations with detailed schemes are performed using the multicomponent transport model, including Soret effect (see Section 3.3.4). The parameters of the global reaction scheme are therefore optimized to fit the reference values computed using the UCSD mechanism with this model.

5.3.1 Laminar flame speed

The values of laminar flame speed S_L^0 predicted by the reduced mechanism and the reference detailed schemes at atmospheric conditions are compared in Figure 5.10, where results from experimental measurements in the literature are reported as additional reference. Given that the methodology in Section 5.2.4 includes the function f to adjust the PEF at $p = p^0$, an excellent agreement is present between the reduced and detailed mechanisms in the prediction of S_L^0 in the whole range of validation of the reduced scheme (i.e., $0.4 \leq \phi \leq 6.0$). Since detailed transport properties are considered for the reference calculations, the results are also well in agreement with the reported values deriving from experimental measurements taken from the literature. A reasonable agreement is found with experimental data in the shape of the curve also for very lean mixtures (i.e., $\phi < 0.4$), as shown by the dashed red line in Figure 5.10. Overall, this indicates a robustness of the adopted methodology, which allows for obtaining coherent results even outside the range of values considered for the definition and validation of the global reaction mechanism.

The impact of pressure on S_L^0 is investigated in Figure 5.11, which compares the results at $p = 15$ atm and $p = 30$ atm, with the corresponding unburned gas temperatures T_u computed according to the isentropic law. The logarithmic exponent in Equation (5.19), introduced to take into account the effect of increasing pressure, allows for a reasonably good agreement in the whole range of pressures, especially for lean flames. Compared to the UCSD and Konnov mechanisms, a moderate overprediction of velocity is present for rich flames, in particular for what concerns the peak value of S_L^0, due to the simplifications adopted in the definition of the PEA laws. As

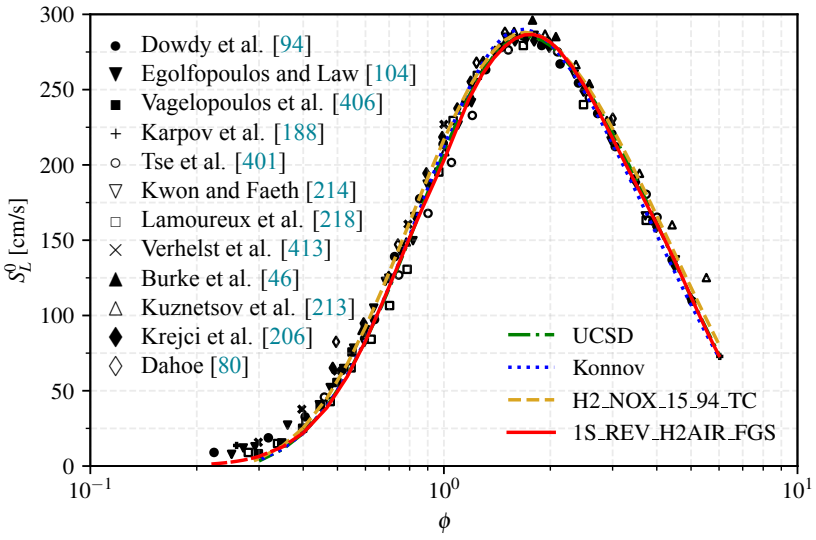

Figure 5.10: Laminar flame speed S_L^0 of unstretched premixed H_2–air flames as a function of the equivalence ratio ϕ at atmospheric conditions. Comparison between numerical calculations with reduced 1S_REV_H2AIR_FGS scheme and reference UCSD [339], Konnov [202] and H2_NOX_15_94_TC [51] mechanisms. Results, denoted by a dashed red line, are added for the reduced scheme in very lean mixture conditions ($\phi < 0.4$), outside its range of validation. Experimental measurements (symbols) taken from [336] and references therein are included too.

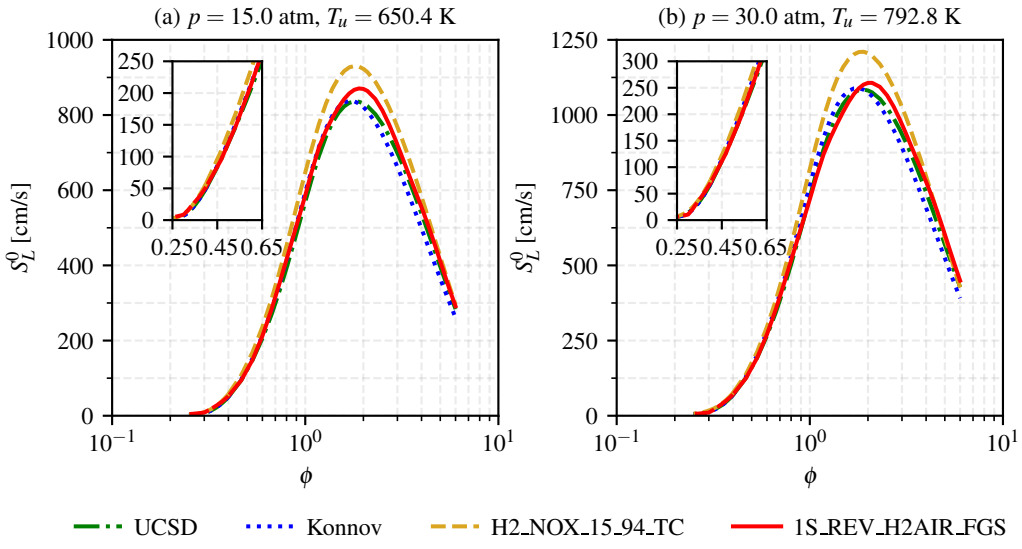

Figure 5.11: Laminar flame speed S_L^0 of unstretched premixed H_2–air flames as a function of the equivalence ratio ϕ at $p = 15$ atm (a) and $p = 30$ atm (b). Comparison between numerical calculations with reduced 1S_REV_H2AIR_FGS scheme and reference UCSD [339], Konnov [202] and H2_NOX_15_94_TC [51] mechanisms. The insets enhance the values obtained in the lean regime for $0.25 \leq \phi \leq 0.65$. Results, denoted by a dashed red line, are added for the reduced scheme in very lean mixture conditions ($\phi < 0.4$), outside its range of validation.

very lean H_2–air flames at these pressure levels are of interest for practical applications (e.g., H_2-fueled gas turbines), values of S_L^0 are computed with the reduced scheme also for very lean flames, up to $\phi = 0.25$, and marked with dashed red lines in Figure 5.11. A consistency can be observed

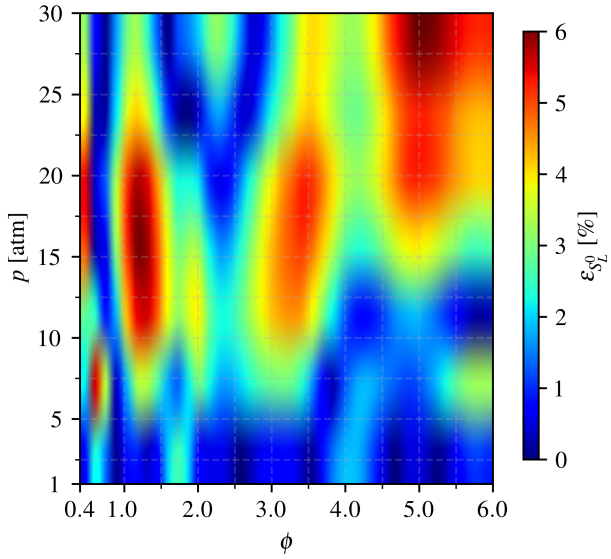

Figure 5.12: Relative percentage error $\varepsilon_{S_L^0}$ between the reduced reversible 1S_REV_H2AIR_FGS scheme and the reference UCSD [339] mechanism on the prediction of the laminar flame speed S_L^0 for unstretched premixed H_2–air flames as a function of the equivalence ratio ϕ and of the pressure p.

between the reduced scheme and the detailed mechanisms even in this regime, despite the limits on the validity domain of the pressure-scaling function $g(\phi, p)$ discussed in Section 5.2.4.

Figure 5.12 shows, for the whole range of ϕ and p considered in the definition of the reduced mechanism (i.e., $0.4 \leq \phi \leq 6.0$ and $1 \text{ atm} \leq p \leq 30$ atm), the relative percentage error $\varepsilon_{S_L^0}$ on the prediction of S_L^0 between the reduced 1S_REV_H2AIR_FGS scheme and the reference UCSD mechanism. The error $\varepsilon_{S_L^0}$ is defined as:

$$\varepsilon_{S_L^0}(\phi, p)\ [\%] = 100 \frac{|S_L^0(\phi, p) - S_{L,ref}^0(\phi, p)|}{S_{L,ref}^0(\phi, p)}. \tag{5.24}$$

For all operating points, the error remains well below the threshold of 10%.

5.3.2 Laminar flame thickness

Here, the impact of the *FTA* function on the prediction of the laminar flame thickness δ_L^0 is assessed. Figure 5.13 shows the values of δ_L^0 resulting from the 1S_REV_H2AIR_FGS scheme and the detailed mechanisms for varying equivalence ratios and three pressure levels (i.e., $p = 1$ atm, $p = 15$ atm, and $p = 30$ atm).

The importance of introducing the *FTA* correction is evident, as it allows to adjust the temperature gradient, and, consequently, the value of δ_L^0 of the reduced scheme. Since no pressure dependence has been introduced in the expression of FTA, the thickness adjustment works better at $p = 15$ atm, which is at the center of the interval of pressures considered for the definition of the reduced scheme, while a larger, yet tolerable, error is found at 1 and 30 atm. Nevertheless, even though the value of δ_L^0 varies significantly throughout the considered pressure range, the scaling factor between the detailed chemistry and the reduced scheme proposed in this work remains almost unaffected and independent of the system pressure.

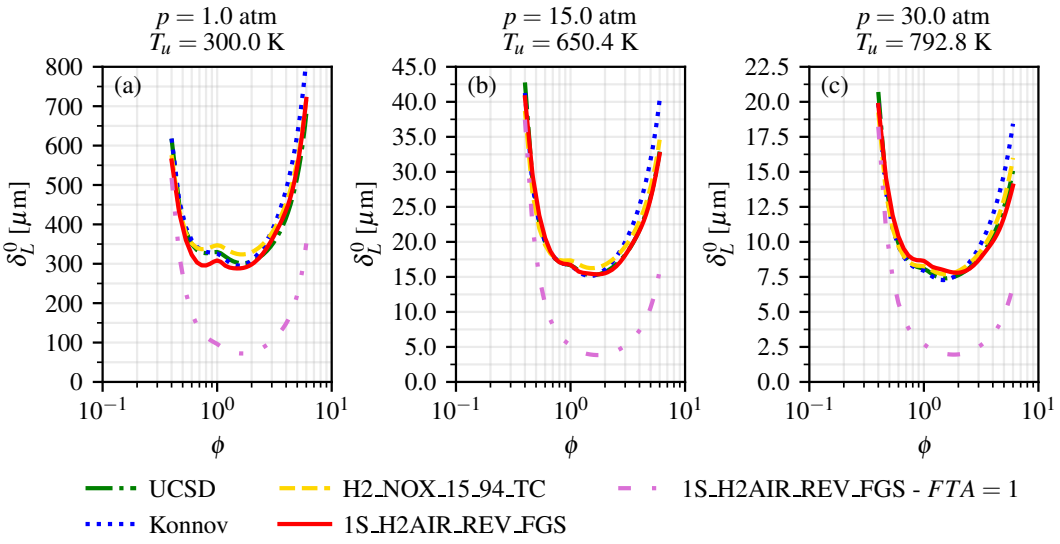

Figure 5.13: Laminar flame thickness δ_L^0 of unstretched premixed H_2–air flames as a function of the equivalence ratio ϕ at $p = 1$ atm (a), $p = 15$ atm (b) and $p = 30$ atm (c). Comparison between numerical integrations with reduced 1S_REV_H2AIR_FGS scheme and reference UCSD [339], Konnov [202] and H2_NOX_15_94_TC [51] mechanisms. Results for the reduced 1S_REV_H2AIR_FGS scheme without applying the Flame Thickness Adjustment (FTA) are also reported.

5.3.3 Flame temperature and structure

As observed in Section 5.2.1, the backward step of Reaction (R5.2) becomes significant when considering the adiabatic flame temperature T_{ad}, especially for $\phi \approx 1$. This is highlighted in Figure 5.14, which shows the values of T_{ad} obtained with the reduced 1S_REV_H2AIR_FGS and 1S_IRR_H2AIR_FGS schemes, and with the detailed mechanisms at $p = 1$ atm, $p = 15$ atm, and $p = 30$ atm. It can be observed how the irreversible scheme, based on the assumption of complete combustion, strongly overestimates the maximum value of T_{ad}, and incorrectly predicts the location of the peak at $\phi = 1.0$, while it should be obtained for a slightly rich mixture. The 1S_REV_H2AIR_FGS scheme, on the other hand, which considers chemical equilibrium, allows for predicting T_{ad} in a more consistent way. In this sense, the relative percentage error computed with respect to the UCSD scheme is halved, and now approximately equal to 2 % for all pressures considered.

The impact of the backward reaction is even more evident when considering the flame structure. Figure 5.15 compares the profiles of species mole fractions X_k and temperature T across the flame for lean ($\phi = 0.4$), stoichiometric ($\phi = 1.0$), and rich ($\phi = 4.0$) mixtures, computed at $p = 1$ atm, $p = 15$ atm, and $p = 30$ atm with the two reduced schemes and the detailed mechanisms. For the lean and rich flames, the results obtained with the irreversible and reversible reduced schemes are similar, and well in agreement with the detailed mechanisms at all pressures. Indeed, recalling the evolution of $h(\phi, p)$ shown in Figure 5.8, the contribution of the backward reaction for these values of ϕ is limited. Moreover, it is possible to notice that, at ambient conditions and $\phi = 0.4$ (see Figure 5.15a-i), the reduced schemes match almost perfectly the detailed ones. This is well in agreement with the analysis performed in [111], where it was shown that, near the lean flammability limit, the concentrations of radicals H, O, OH, and HO_2 become so small that their resulting transport rates are negligible compared with their chemical rates everywhere across the reaction zone. Therefore, the error introduced by the reduced schemes when neglecting these radicals is small for these conditions. Furthermore, Carpio et al. [53] showed that

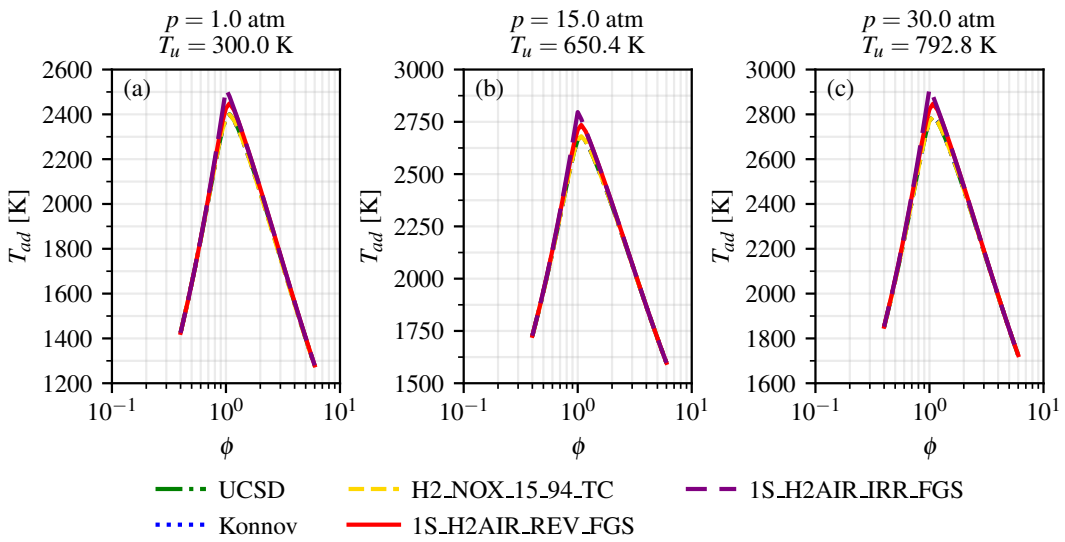

Figure 5.14: Adiabatic flame temperature T_{ad} of unstretched premixed H_2–air flames as a function of the equivalence ratio ϕ at $p = 1$ atm (a), $p = 15$ atm (b) and $p = 30$ atm (c). Comparison between numerical integrations with reduced 1S_REV_H2AIR_FGS scheme and reference UCSD [339], Konnov [202] and H2_NOX_15_94_TC [51] mechanisms. Results for the reduced 1S_IRR_H2AIR_FGS scheme are also reported.

the radical transport rates diminish for higher pressures. In this sense, it can be observed that, at $\phi = 4.0$ (see Figure 5.15c), the reduced scheme follows the detailed kinetics with higher precision at $p = 15$ atm and $p = 30$ atm, rather than at $p = 1$ atm. On the other hand, coherently with the considerations made for the adiabatic flame temperature in Figure 5.14, strong differences between the reversible and irreversible schemes can be found at $\phi = 1$ (see Figure 5.15b). Indeed, besides the already discussed difference in the prediction of flame temperature, the irreversible scheme wrongly predicts the final composition of the mixture, assuming that all H_2 and oxygen are consumed, which is not physical in the actual H_2 oxidation process. On the other hand, albeit showing steeper gradients in the flame reaction region with respect to the detailed schemes, the 1S_REV_H2AIR_FGS matches the final composition of the mixture obtained with detailed kinetics at all pressures.

5.4 Application to stretched laminar flames

The previous results have shown the capabilities of the reduced scheme to properly predict the properties and structure of laminar unstretched flames. Nevertheless, premixed flames are commonly subject to stretch, which, as discussed in Section 2.5.5, modifies the internal flame structure and the resulting burning rate, especially in the case of H_2 combustion (see Section 4.2.2).

The impact of stretch is here investigated at atmospheric conditions in two configurations: a 1D premixed counterflow flame (see Section 3.1), computed with Cantera, and a 2D expanding flame, computed in AVBP. The former is subjected to the sole strain (see Section 2.5.3), while for the latter curvature effects are relevant. This allows for a comprehensive characterization of the stretch response.

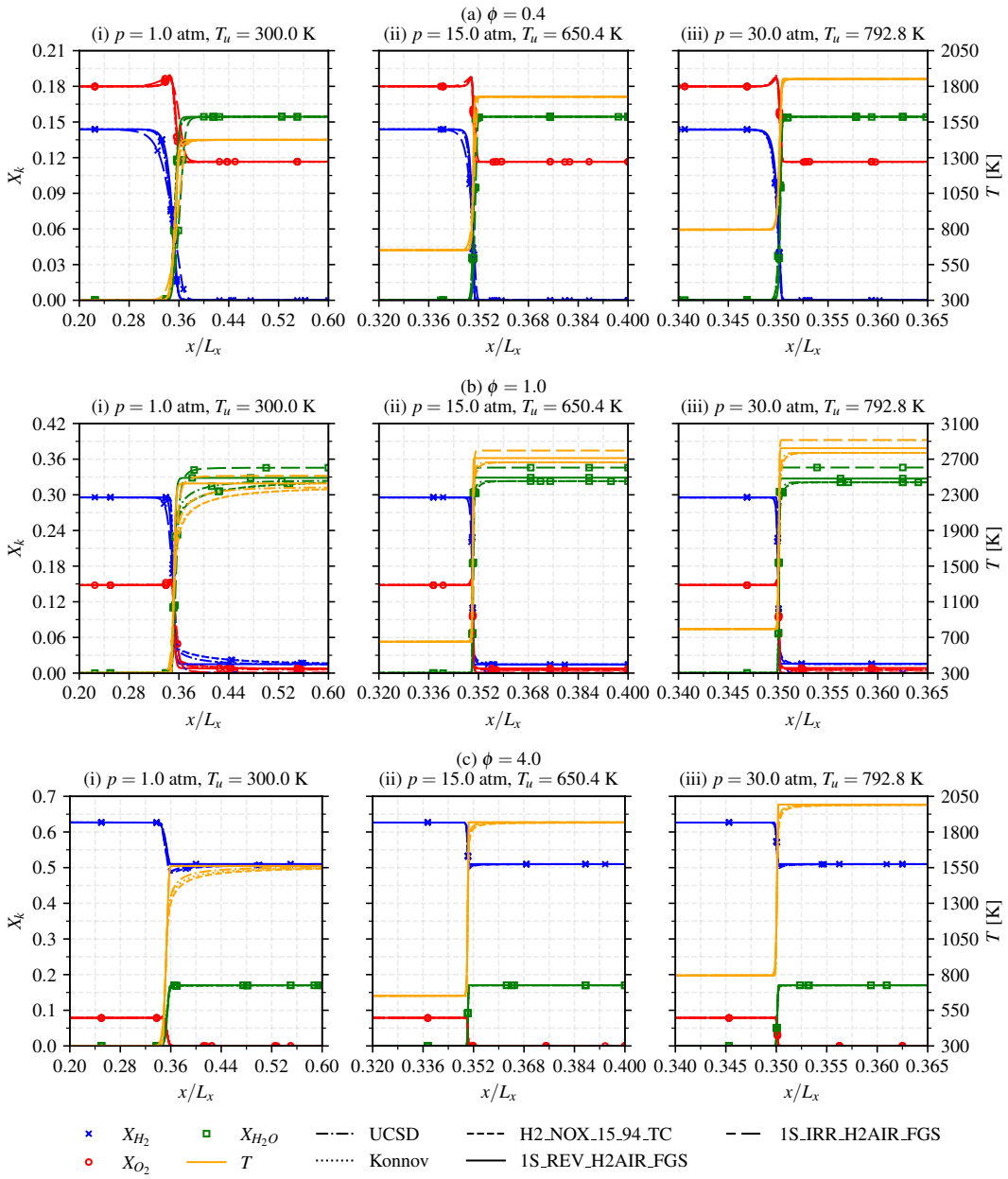

Figure 5.15: Profiles along the normalized coordinate x/L_x of mole fractions X_k (left axis) and temperature T (right axis) for unstretched premixed H_2–air flames at $\phi = 0.4$ (a), $\phi = 1.0$ (b), and $\phi = 4.0$ (c) for $p = 1$ atm (i), $p = 15$ atm (ii), and $p = 30$ atm (iii). Comparison between reduced 1S_REV_H2AIR_FGS and 1S_IRR_H2AIR_FGS schemes and reference UCSD [339], Konnov [202] and H2_NOX_15_94_TC [51] mechanisms.

5.4.1 One-dimensional counterflow premixed flames

In the counterflow premixed flame configuration, a steady jet of premixed fresh gases is injected in opposition to another stream composed of combustion products at the equilibrium (see Section 3.1). The value of the distance d between the jets is equal to 5 cm.

Figure 5.16 compares the normalized flame consumption speed S_c/S_L^0 as a function of the mean strain rate a (see Equation (3.5)) for lean ($\phi = 0.4$), stoichiometric ($\phi = 1.0$), and rich

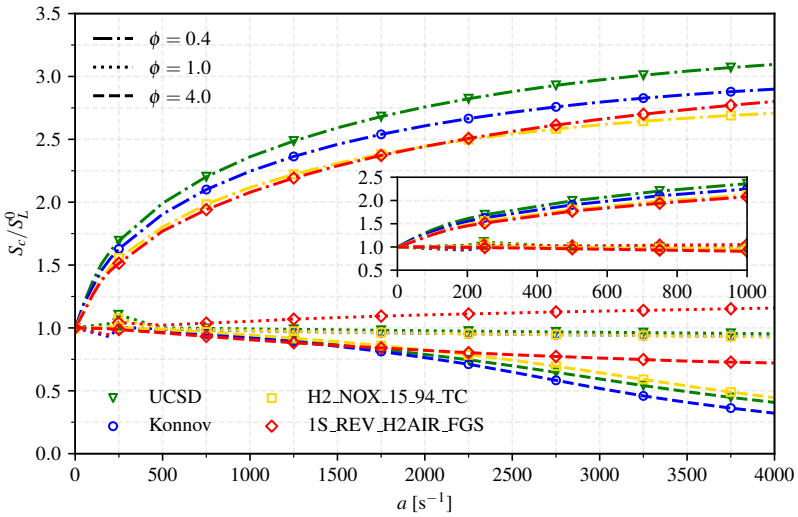

Figure 5.16: Normalized consumption speed S_c/S_L^0 versus mean strain rate a for lean ($\phi = 0.4$), stoichiometric ($\phi = 1.0$) and rich ($\phi = 4.0$) counterflow premixed flames at atmospheric conditions. The inset enhances the values calculated in the low-strain regime ($a \leq 1000\ \mathrm{s}^{-1}$). Comparison between numerical calculations performed with the reduced 1S_REV_H2AIR_FGS scheme and reference UCSD [339], Konnov [202] and H2_NOX_15_94_TC [51] mechanisms.

Table 5.5: Effective Lewis numbers Le_{eff} at atmospheric conditions for different kinetic schemes and equivalence ratios.

ϕ	Le_{eff}			
	UCSD	Konnov	H2_NOX_15_94_TC	1S_H2AIR_REV_FGS
0.4	0.417	0.437	0.417	0.451
1.0	1.058	1.195	1.057	0.814
4.0	2.168	2.621	2.167	1.199

($\phi = 4.0$) flames. The reduced scheme well reproduces the behavior of the detailed schemes for the lean ($\phi = 0.4$) and rich ($\phi = 4.0$) flames. For $\phi = 1$, however, the reduced scheme predicts an increasing value of speed (i.e., a negative Markstein length), while reference calculations indicate a slightly decreasing trend (i.e., a slightly positive Markstein length). Recalling Section 2.5.5, the sign of the Markstein length is related to the value of the effective Lewis number Le_{eff}, with $Le_{eff} > 1$ corresponding to a positive Markstein length. To investigate these differences, Table 5.5 reports the values of Le_{eff} for the different equivalence ratios and schemes considered in Figure 5.16, with Le_{eff} computed through Equation (2.45). With the Lewis numbers of species considered by the simplified transport model for the reduced scheme (see Table 5.4), the resulting value of Le_{eff} at $\phi = 1.0$ is lower than 1, inducing an increasing consumption speed, while Le_{eff} is actually slightly higher than 1 when considering detailed kinetics. A modification of the transport parameters, and in particular of the Lewis numbers of species, could allow for better predicting the strain-dependent behavior at stoichiometry, as done by Franzelli et al. [119] for a reduced scheme describing CH_4–air combustion. This modification, still based on constant Lewis numbers, is not introduced here, since it would induce major differences in the prediction of stretch response in the lean regime, which is of the greatest interest for H_2–air flames from an application perspective. Nevertheless, a modification of the FTA function, taking into account a dynamic variation of the Lewis numbers, could be introduced in future work to further extend the validity of the reduced mechanism, in analogy to the formalism adopted in the Stretched-TF

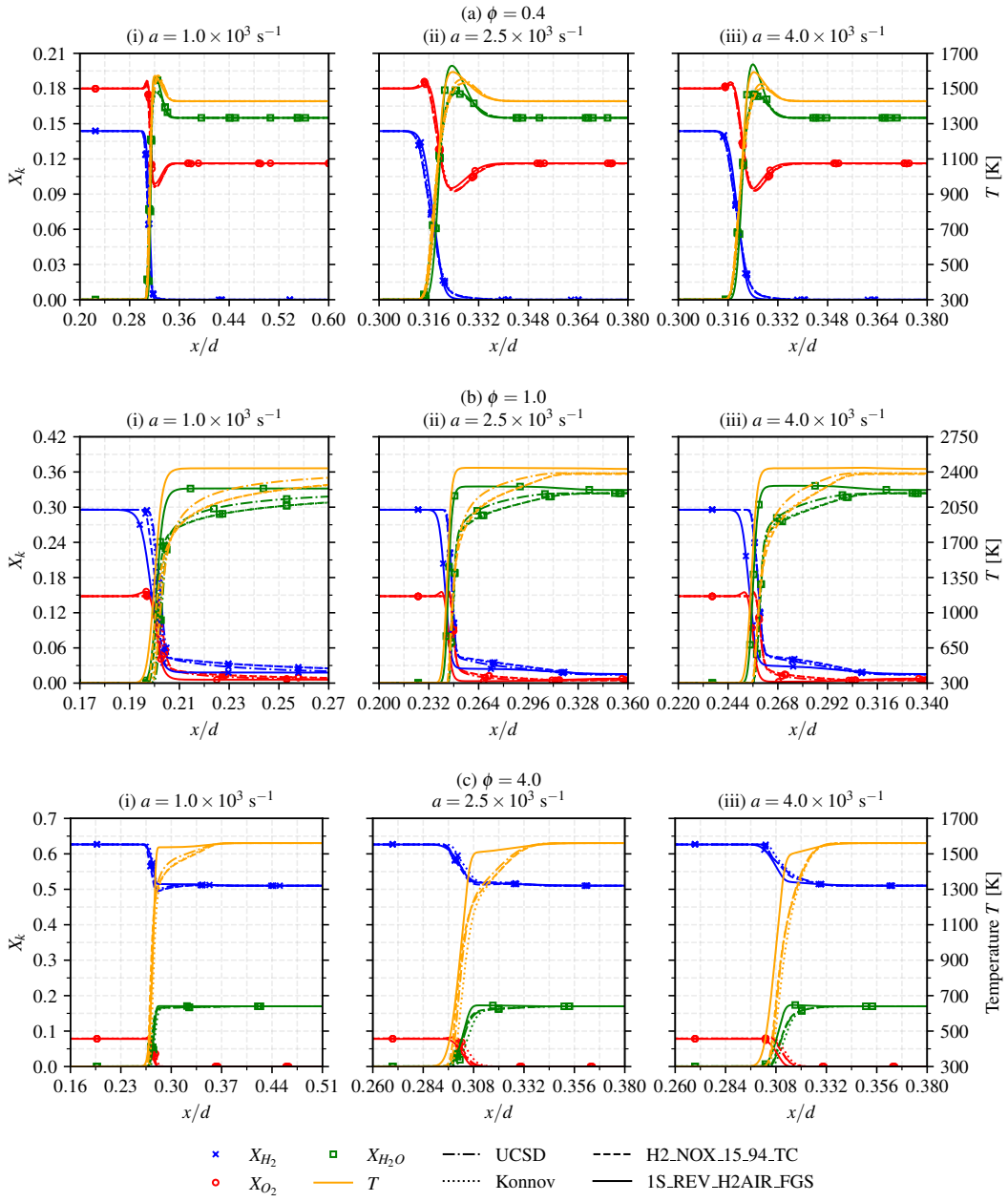

Figure 5.17: Profiles along the normalized coordinate x/d of mole fractions X_k (left axis) and temperature T (right axis) for strained counterflow premixed H_2–air flames at atmospheric conditions and $\phi = 0.4$ (a), $\phi = 1.0$ (b), and $\phi = 4.0$ (c) for $a = 1 \times 10^3$ s^{-1} (i), $a = 2.5 \times 10^3$ s^{-1} (ii), and $a = 4.0 \times 10^3$ s^{-1} (iii). Comparison between reduced 1S_REV_H2AIR_FGS and reference UCSD [339], Konnov [202] and H2_NOX_15_94_TC [51] mechanisms.

model [89] (see Section 4.4).

To further analyze the differences between the schemes at the three equivalence ratios considered in Figure 5.16, Figure 5.17 compares the corresponding flame structures (i.e., species mole fractions and temperature) for $a = 1 \times 10^3$ s^{-1}, $a = 2.5 \times 10^3$ s^{-1}, and $a = 4.0 \times 10^3$ s^{-1}. For the lean flame (see Figure 5.17a), a very good agreement is found in the predicted flame structure between reduced and detailed kinetics. Being this value of ϕ close to the lean flammability

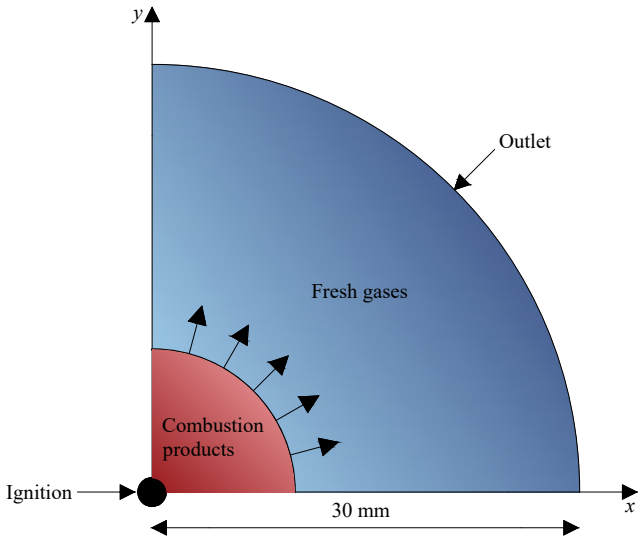

Figure 5.18: Schematic representation of the computational domain adopted for the 2D cylindrical expanding flame. The flame is initialized in $x = 0, y = 0$ and propagates in a quarter-circle-shaped domain.

limit, this result is well in agreement with the QSS-based analysis in [111]. The most significant difference is represented by the overestimation of the peak value of X_{H_2O} in the reaction zone of the flame front, due to the absence of radicals. This is enhanced as the strain rate increases, leading also to a mild overprediction of the peak temperature. For the stoichiometric flame (see Figure 5.17b), strong differences are observed in the flame front structure, which are consistent with the differences in the prediction of S_c/S_L^0 observed in Figure 5.16. In particular, discrepancies are found in the prediction of the position of the flame front, which is placed further upstream with the reduced scheme. Moreover, the reduced scheme predicts a steeper variation of mole fractions and temperature across the reacting region. In this context, the impact of detailed kinetics, and in particular of radical production and consumption, is non-negligible. Finally, the rich case (see Figure 5.17c) shows no significant differences in the mole fraction profiles, while a stronger inconsistency is found for the temperature in the reaction zone. More specifically, the temperature gradient predicted by the reduced scheme is lower than the one of the detailed mechanisms, especially at higher strain values. This explains the lower slope of the S_c/S_L^0 curve observed in Figure 5.16 for the reduced scheme at larger strain values.

5.4.2 Two-dimensional cylindrical expanding flames

The reversible global reaction mechanism is here applied to a 2D cylindrical expanding laminar flame configuration at atmospheric conditions. Three different equivalence ratios are considered: $\phi = 0.4$, $\phi = 1.0$, and $\phi = 4.0$. This allows to complement the analysis performed for the sole strain in Section 5.4.1, since for this 2D configuration the curvature component of stretch is relevant. Moreover, this multidimensional configuration allows for observing, if present, the impact of flame front instabilities described in Section 2.6.

The computational domain is schematized in Figure 5.18. It is defined by a circle of radius 30 mm, at the center of which the flame is initialized. By exploiting symmetry arguments, only a quarter-circle is considered in the simulations, so that the overall computational cost is reduced.

The numerical simulations are performed in AVBP using the Lax–Wendroff finite-volume

scheme [231] (see Section 3.3.2). The domain is discretized on an unstructured grid of triangular elements, with a grid resolution $\Delta_x = 0.025$ mm, corresponding to approximately 10 points in the laminar flame thickness δ_L^0 of the stoichiometric flame, for which the lower value is reached (see Figure 5.13). The mesh is spatially uniform throughout the considered domain, ensuring a homogeneous resolution in both the radial and tangential directions, without the need for further refinement strategies. The NSCBC formalism (see Section 3.3.3) is adopted at the outlet, and the mixture is ignited using the Energy Deposition model [215]. The simplified non-unity Lewis number transport model described in Section 3.3.4 is adopted for both schemes.

Figures 5.19 to 5.21 compare the flame fronts derived from the numerical simulations with reduced and detailed mechanisms at the same flame radius r for the lean, stoichiometric, and rich cases, respectively. Coherently with the methodology in [424], the flame front is here identified by considering an isocontour of the progress variable $C = 0.5$, where:

$$C = \frac{Y_{H_2O}}{Y_{H_2O}^{eq}}, \tag{5.25}$$

with $Y_{H_2O}^{eq}$ being the mass fraction of water in the equilibrium products. The mean flame radius r is determined from the area A_b of the burned gas region, identified by the condition $C \geq 0.5$ [424]:

$$r = \sqrt{\frac{A_b}{\pi}}. \tag{5.26}$$

For the lean case (see Figure 5.19), both mechanisms predict visible hydrodynamic instabilities in the flame front, while thermodiffusive instabilities do not have sufficient time to develop (since no initial perturbation is applied to the flame). For $\phi = 1.0$ (see Figure 5.20) and $\phi = 4.0$ (see Figure 5.21) cases, both mechanisms agree in predicting no instabilities on the flame front within the simulated physical time. Overall, the reduced scheme well retrieves the flame structure predicted by the reference UCSD mechanism at all equivalence ratios. The main difference is the absence, for the reduced scheme, of a visible post-flame region with relevant heat release rate, which is consistent with the absence of radicals in this simplified kinetics description.

The validity of the reduced scheme is further assessed by considering the global stretch response. In particular, the values of S_c/S_L^0 predicted at different radii by the global reaction mechanism are compared with the values given by the UCSD scheme. For this configuration, Equation (2.39) is rewritten as follows [133]:

$$S_c = -\frac{1}{A_f \rho_u (Y_F^u - Y_F^b)} \int_S \dot{\omega}_F dA, \tag{5.27}$$

where A_f is the area of the flame surface S. Since the flame is two-dimensional, A_f has the dimension of a length, and is equal to the circumference of radius r. Figure 5.22 shows the values of S_c/S_L^0 as a function of r for the three different mixtures. For this configuration, the (mean) flame stretch $\bar{\kappa}$ is related to r by [311]:

$$\bar{\kappa} = \frac{1}{r}\frac{dr}{dt}, \tag{5.28}$$

indicating that the stretch decreases for increasing r at constant flame propagation speed dr/dt. The ignition affects the early-stage flame propagation [196]. This is evident from the spike in the value of S_c/S_L^0 observed in Figure 5.22 for all cases at low values of r. After this initial phase, a good agreement is observed between the two reaction schemes in the prediction of S_c/S_L^0 for the

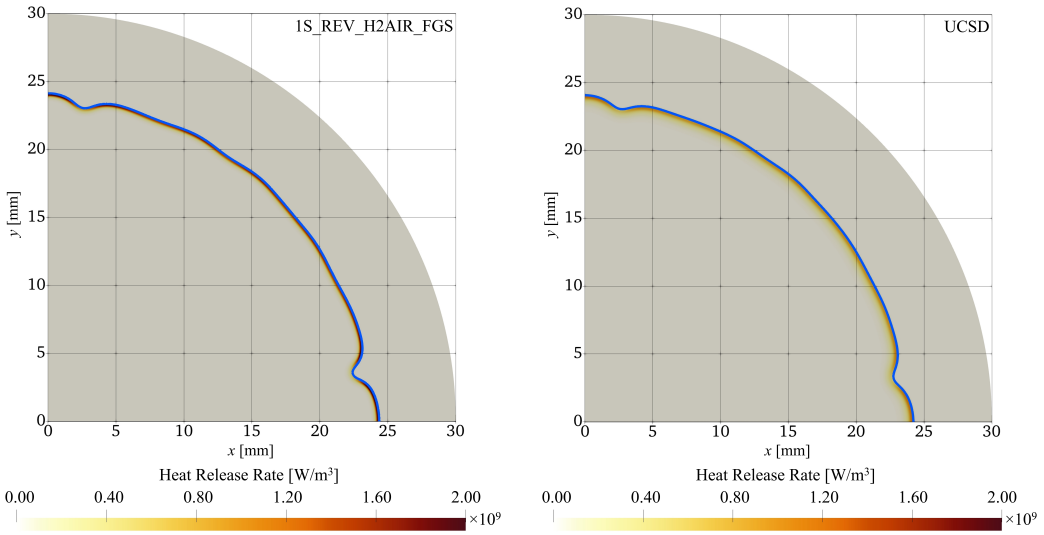

Figure 5.19: Flame front of the lean ($\phi = 0.4$) 2D cylindrical expanding flame for $r = 24$ mm, identified by the isocontour of the progress variable $C = 0.5$ (blue line), and superimposed to the heat release rate field. Comparison between CFD simulations performed with the reduced 1S_REV_H2AIR_FGS scheme (left) and the reference UCSD mechanism [339] (right).

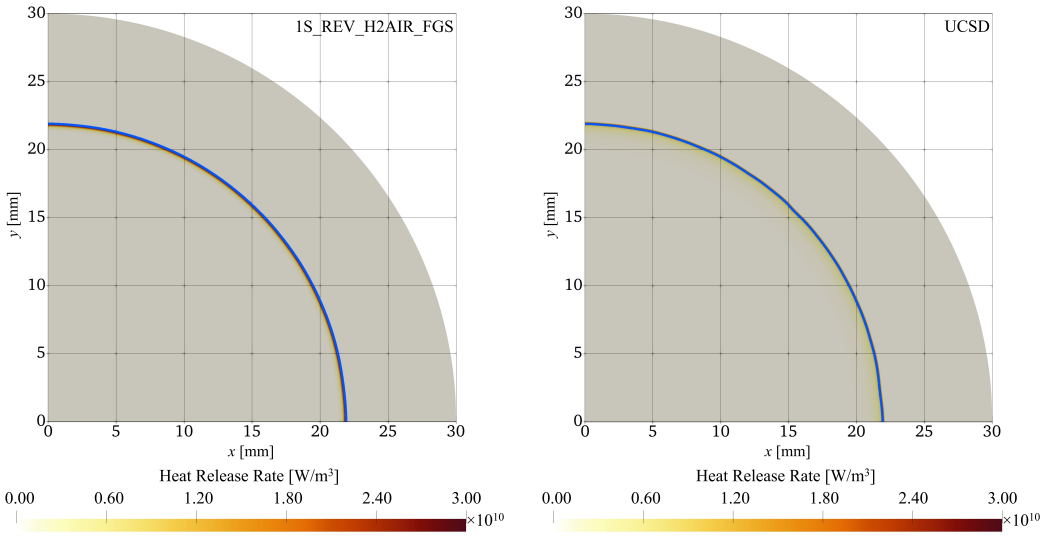

Figure 5.20: Flame front of the stoichiometric ($\phi = 1.0$) 2D cylindrical expanding flame for $r = 22$ mm, identified by the isocontour of the progress variable $C = 0.5$ (blue line), and superimposed to the heat release rate field. Comparison between CFD simulations performed with the reduced 1S_REV_H2AIR_FGS scheme (left) and the reference UCSD mechanism [339] (right).

lean and rich mixtures, with a maximum error lower than 5%, as highlighted in the inset. Coherently with the results in Figure 5.16, larger discrepancies are found for the stoichiometric case. Interestingly, for larger radii (i.e., lower values of stretch), both mechanisms predict $S_c/S_L^0 > 1$ for the lean case. This highlights the impact of TD effects for this mixture, which, despite the absence of visible TD instabilities (see Figure 5.19), still lead to an enhancement of the flame speed due to stretch (see Section 4.2.2).

Finally, the reduction in computational costs, due to the simplifications in the kinetics de-

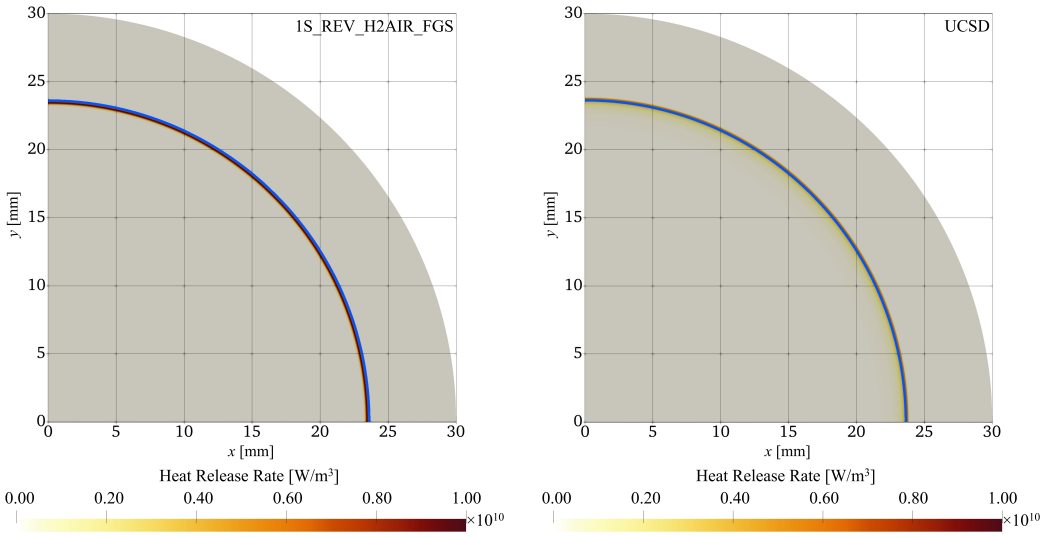

Figure 5.21: Flame front of the rich ($\phi = 4.0$) 2D cylindrical expanding flame for $r = 23.5$ mm, identified by the isocontour of the progress variable $C = 0.5$ (blue line), and superimposed to the heat release rate field. Comparison between CFD simulations performed with the reduced 1S_REV_H2AIR_FGS scheme (left) and the reference UCSD mechanism [339] (right).

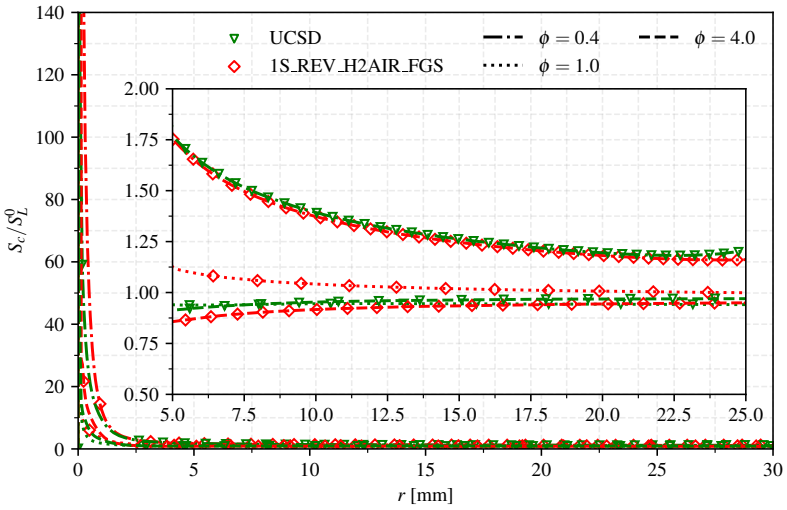

Figure 5.22: Normalized consumption speed S_c/S_L^0 versus mean flame radius r for lean ($\phi = 0.4$), stoichiometric ($\phi = 1.0$) and rich ($\phi = 4.0$) 2D cylindrical expanding flames at atmospheric conditions. The inset enhances the values calculated in the domain region not affected by energy deposition ignition and outlet boundary conditions. Comparison between numerical integrations with the reduced 1S_REV_H2AIR_FGS scheme and the reference UCSD mechanism [339].

scription, is considered. Table 5.6 compares the maximum computed time step Δ_t, derived from the imposed values for the *CFL* and Fourier numbers (see Section 3.3.1), and the iterations per second I_s, resulting from the calculations performed with the reduced 1S_REV_H2AIR_FGS scheme and the reference UCSD mechanism. The computational advantage of the one-step scheme is evident, with an increase in I_s of approximately 55% when passing from the detailed to the reduced chemistry. Moreover, Δ_t is higher for the reduced scheme than for the UCSD mechanism for all cases considered, leading to a lower number of iterations required to simulate the same physical time.

Table 5.6: Comparison of computational costs for the reduced 1S_REV_H2AIR_FGS scheme and the reference UCSD mechanism [339] in terms of maximum computed time step Δ_t and iterations per second I_s. All calculations are performed with the same set-up (7.64×10^5 grid nodes, 192 CPU cores, $CFL = 0.7$, $Fo = 0.1$).

ϕ	1S_REV_H2AIR_FGS		UCSD	
	Δ_t [ns]	I_s [s^{-1}]	Δ_t [ns]	I_s [s^{-1}]
0.4	9.02	36.6	7.80	23.8
1.0	5.93	36.2	3.36	23.6
4.0	4.48	36.5	3.64	23.6

5.5 Summary and concluding remarks

In this Chapter, a global one-step reduced scheme, based on an Arrhenius formulation, was derived for hydrogen–air premixed combustion in an extended range of equivalence ratios, temperatures and pressures. The derivation was based on an analytical modeling of hydrogen oxidation to reduce the number of species, hence improving the computational efficiency.

A best-fitting methodology, based on the laminar flame speed value computed with detailed kinetics, was applied to derive explicit, analytical relations for the reaction rate parameters. In particular, the Pre-Exponential Adjustment method proposed in [120] was extended, by combining the dependence on equivalence ratio with a pressure-dependent scaling law, so that the structure of the reduced scheme is preserved at different pressure values, and the validity of the mechanism is extended to engineering-relevant operating conditions. Particular attention was posed to separate the dependence on pressure and equivalence ratio in the definition of the Pre-Exponential Adjustment laws, so that the obtained global reaction scheme may be easily implemented in CFD numerical codes. Moreover, a correction was introduced to improve the prediction of the temperature profile in the flame reaction zone, hence of the thermal flame thickness.

To define and validate the parameters of the reduced scheme, computations of unstrained and strained one-dimensional laminar premixed flames were performed for a wide range of values of pressure (1 atm$\leq p \leq$30 atm), unburned gas temperature (300 K$\leq T_u \leq$800 K), and equivalence ratio ($0.4 \leq \phi \leq 6.0$). A good agreement was found for the main flame parameters (i.e., the laminar flame speed, the adiabatic flame temperature, and the thermal flame thickness) between the proposed reduced scheme and three reference detailed mechanisms: the San Diego mechanism [339], the scheme by Konnov [202], and the mechanism by Capurso et al. [51]. The importance of a global reversible reaction for the prediction of the flame structure was highlighted, and the adequacy of the proposed correction for the flame thickness was assessed. Nevertheless, some limits were found in the prediction of the response to stretch, especially for stoichiometric flames. This indicates potential for further optimization of the reduced scheme parameters, with particular reference to the molecular transport properties.

The applicability of the scheme in CFD simulations was assessed in AVBP for the computation of two-dimensional cylindrical expanding flames at atmospheric conditions and variable equivalence ratio. The reduced mechanism showed a good agreement with the reference San Diego mechanism in the prediction of the flame structure and properties, especially under lean conditions, and a sensible reduction of computational costs, both in terms of iterations per second and total number of iterations required. The performance of the reduced scheme will be further assessed in Sections 9.4 and 11.6 for the simulation, respectively, of three-dimensional laminar and turbulent flames, highlighting the impact of chemical modeling on the prediction of

the unsteady flame dynamics and of the acoustic radiation.

The proposed global reaction mechanism represents a practical solution to avoid computationally expensive numerical simulations of hydrogen–air combustion, especially in a preliminary design phase. This allows to optimize computational resources by delaying the adoption of expensive detailed reaction schemes to more advanced phases of the design process. Moreover, the methodology introduced to develop the reduced mechanism is applicable to other fuels or to different operating conditions.

6

OH* chemiluminescence as heat release marker for hydrogen flames

The adequacy of OH* as a heat release rate marker is investigated in this Chapter for laminar and turbulent hydrogen–air flames. The peculiar features for hydrogen combustion, arising from the chemical pathways governing OH* formation and consumption, are first highlighted by comparing the spatial correlation between OH* and heat release rate in laminar one-dimensional unstretched premixed methane–air, methane–hydrogen–air, and hydrogen–air flames at atmospheric conditions.

The differences between premixed and non-premixed regimes in hydrogen–air flames are then analyzed in laminar counterflow flames and further illustrated in a laminar two-dimensional triple flame. These findings are complemented by the analysis of experimental measurements of OH* in diffusion and partially premixed hydrogen–air flames stabilized on the coaxial dual-swirl HYLON injector at the *Institut de Mécanique des Fluides de Toulouse* (IMFT), and by corresponding Large Eddy Simulations performed by Andrea Aniello at IMFT [6].

Finally, the impact of the operating conditions is assessed through a systematic numerical investigation over a wide range of equivalence ratios, pressures, unburned gas temperatures, and stretch levels. Overall, this Chapter provides a broad-spectrum assessment of the applicability and limitations of OH* as a heat release rate surrogate in hydrogen–air flames.

Results from this Chapter are included in:

- F. G. Schiavone, A. Aniello, E. Riber, T. Schuller, and D. Laera. "On the adequacy of OH* as heat release marker for hydrogen-air flames". In: *Proceedings of the Combustion Institute* 40 (2024), p. 105248.
- F. G. Schiavone, M. Torresi, S. M. Camporeale, and D. Laera. "Impact of the operating conditions on the OH* distribution and its correlation with the heat release rate in hydrogen-air flames". In: *Combustion and Flame* 282 (2025), p. 114452.

Contents

6.1 Context and motivations

The heat release rate is a fundamental quantity to characterize the energy outcome of the overall combustion process [127]. Its distribution is crucial for understanding and predicting thermoacoustic instabilities, pulsed combustion, flame propagation, and combustion noise [224]. The direct experimental measurement of HRR remains impractical, as it requires simultaneous measurements of temperature and concentrations of several species [273]. For this reason, the correlation of HRR with other quantities, more easily measurable through optical techniques such as laser-induced fluorescence (LIF) or natural chemiluminescence (see Section 2.2), has been widely investigated to define HRR surrogates [18, 154, 224, 254, 275, 278, 282, 385, 425]. In particular, the chemiluminescence measurement is relatively simple and feasible also in practical combustion devices, where LIF is not applicable [273]. For this reason, chemiluminescence is often used as a tracer of the HRR [90, 275].

For hydrocarbon flames, it has been shown that the chemiluminescent emissions of CH*, OH* and CO_2* well correlate with the HRR [92, 153, 224]. For pure methane flames, the peak-to-peak distance between the profiles of OH* intensity and HRR is smaller than the spatial resolution of most optical chemiluminescence measurement devices [287]. Hu et al. [169], adopting the methodology described in [278], investigated the quantitative relation between HRR and chemiluminescence, and found a strong linear correlation of HRR with OH* at fixed equivalence ratio. Therefore, OH* chemiluminescence is well appropriate to detect the flame front for these flames [90]. A correspondence between OH* intensity and HRR distributions has been found also for methane–hydrogen fuel blends of various compositions [323].

When burning carbon-free fuels such as hydrogen, excited OH* radicals are still formed and emit ultraviolet radiation [190]. However, compared to hydrocarbons, the OH* chemiluminescent intensity is significantly weaker [340, 373]. Moreover, the distance between the peaks of OH* and HRR is rather wide [254, 356, 431], raising doubts on the adequacy of OH* chemiluminescence as HRR marker when pure H_2 is burned, and leading to the investigation of alternative HRR markers [254]. The presence of OH* in the burned gases for premixed H_2–air flames close to stoichiometry was also observed in [208].

Despite these previous works, a systematic investigation of the underlying mechanisms leading to the differences between H_2 and hydrocarbon flames in OH* production and in its correlation with the HRR is lacking. Moreover, although several studies have examined the effect of varying flame properties on OH* chemiluminescence for different fuels (e.g., [21, 115, 140, 148, 158, 192, 281, 417]), investigations of premixed and diffusion H_2–air flames have largely been limited to atmospheric pressure and relatively low unburned gas temperatures. Since a varying range of operating conditions is involved in practical combustion systems, understanding the OH*–HRR correlation beyond atmospheric conditions is of significant interest. Therefore, a broad-spectrum investigation is performed in this Chapter under varying operating conditions and flame configurations, hence providing a detailed assessment of the applicability of OH* as HRR marker in H_2 flames.

6.2 Chemical kinetics of OH*

The spectral characteristics of OH* chemiluminescent emission were described in Section 2.2.1. In this Section, a description of its chemical kinetics is provided, including the reaction mechanisms adopted in this Chapter for the numerical prediction of the OH* distribution.

Most of the literature essentially represents OH* kinetics in H_2–air flames as the ensemble of three main reactions [150, 190, 372]:

$$\mathrm{H + O\,(+M) \rightleftharpoons OH^*\,(+M)}, \tag{R6.1}$$

$$\mathrm{OH^* \longrightarrow OH} + h\nu, \tag{R6.2}$$

and

$$\mathrm{OH^* + M \rightleftharpoons OH + M}. \tag{R6.3}$$

The non-adiabatic association process described by Reaction (R6.1) is considered to be the main OH* formation path at low temperatures (below 2800 K), while the other two represent the pathways for the unstable OH* to return to the ground state, either by emitting light through Reaction (R6.2) or by the non-reacting collisional quenching of Reaction (R6.3) [190, 363, 436]. At temperatures above 2800 K, instead, OH* is mainly produced through thermal excitation of the OH molecule via the reverse path of Reaction (R6.3) and consumed via the reverse path of Reaction (R6.1) [157, 190]. When considering carbonated fuels, the OH* kinetics still relies on Reactions (R6.1) to (R6.3), with CO_2, CO and CH_4 as additional collision partners. The main OH* formation path, however, is given by [431]:

$$\mathrm{CH + O_2 \rightleftharpoons OH^* + CO}. \tag{R6.4}$$

It should be noted that the presence of Reaction (R6.4) in the OH* kinetics highlights the necessity to include the CH radical in the reaction mechanism adopted for the hydrocarbon oxidation process.

Different reaction mechanisms have been developed in the literature to describe OH* kinetics. As anticipated in Section 3.3.4, in this Chapter two mechanisms are considered to describe the OH* kinetics: the one developed by Kathrotia et al. [190, 191], and the more recent scheme by Sharipov et al. [362, 363].

Table 6.1: OH^* sub-scheme derived from Kathrotia et al. [190, 191].
Reaction rate constant $k = AT^{\beta} \exp[-E_a/(RT)]$, units are cm^3 mol s cal K.

No.	Reaction	A	β	E_a
(K1)*	$H + O + M \rightleftharpoons OH^* + M$	1.50×10^{13}	0.0	5975
(K2)	$OH^* \longrightarrow OH + h\nu$	1.45×10^{6}	0.0	0
(K3)	$OH^* + O_2 \rightleftharpoons OH + O_2$	2.10×10^{12}	0.5	-483
(K4)	$OH^* + H_2O \rightleftharpoons OH + H_2O$	5.93×10^{12}	0.5	-863
(K5)	$OH^* + H_2 \rightleftharpoons OH + H_2$	2.95×10^{12}	0.5	-445
(K6)	$OH^* + OH \rightleftharpoons OH + OH$	6.01×10^{12}	0.5	-762
(K7)	$OH^* + H \rightleftharpoons OH + H$	1.31×10^{12}	0.5	-167
(K8)	$OH^* + N_2 \rightleftharpoons OH + N_2$	1.08×10^{11}	0.5	-1240
(K9)	$CH + O_2 \rightleftharpoons OH^* + CO$	1.80×10^{11}	0.0	0.0
(K10)	$OH^* + CO_2 \rightleftharpoons OH + CO_2$	2.76×10^{12}	0.5	-970
(K11)	$OH^* + CO \rightleftharpoons OH + CO$	3.23×10^{12}	0.5	-789
(K12)	$OH^* + CH_4 \rightleftharpoons OH + CH_4$	3.36×10^{12}	0.5	-636

The mechanism by Kathrotia et al. [190, 191], and in particular the rate constant for Reaction (R6.1) proposed therein, have been considered as the reference OH* sub-mechanism for several studies in the literature (e.g., [140, 197, 208, 410, 436]). Moreover, in its extended version [191], it is applicable both to H_2 and hydrocarbon flames, making it suitable to investigate the differences between the two fuels in the OH* emission and its correlation with the HRR. Table 6.1 reports the corresponding OH* sub-mechanism adopted in this work. Reactions (K1) to (K8) are present for both hydrocarbon and H_2 flames, while Reactions (K9) to (K12) are specific of carbonated fuels. The third body efficiencies for the carbon-based species in Reaction (K1) are taken from [156]. While reliable, this mechanism was validated against experimental measurements at atmospheric pressure only, assuming the rate constant for Reaction (R6.1) to be dependent only on the temperature.

The more recent work by Sharipov et al. [362, 363] provides a novel OH* sub-mechanism for H_2–air combustion, extensively validated against experimental measurements of OH* concentration at different temperatures and pressures. This shows significantly better performance compared to other mechanisms in the literature [363], making it more suitable to investigate the impact of operating conditions on the OH* distribution and its relation with HRR in H_2–air flames. The major differences with respect to the scheme by Kathrotia et al. [190] lie in the bivariate dependence on both temperature and pressure of the rate constant of Reaction (R6.1) and in the presence of several reactive (i.e., chemical) quenching reactions. In addition, Sharipov et al. [362, 363] introduced the exoergic termolecular reaction:

$$H + OH + OH \rightleftharpoons OH^* + H_2O \qquad \text{(R6.5)}$$

as supplemental OH* formation path, deeming it significant, especially at very high temperatures.

In their work, Sharipov et al. [362, 363] proposed also additional reactions related to minor N-containing species (i.e., NH_3, N_2O, NO and NO_2), which may be significant for H_2–air flames at elevated temperatures and pressures, where the thermal dissociation of N_2 becomes noticeable. For the operating conditions considered in this Chapter, however, these species have no significant impact on the OH* distribution, as shown in Appendix B. Therefore, the mechanism by Sharipov et al. [362, 363] is adopted, in this Chapter, in the form reported in Table 6.2.

*With $M = [H_2] + 6.5[H_2O] + 0.4[O_2] + 0.4[N_2] + 1.5[CO_2] + 0.75[CO] + 3.0[CH_4]$.

Table 6.2: OH^* sub-mechanism derived from Sharipov et al. [362, 363].
Reaction rate constant $k = AT^{\beta}\exp[-E_a/(RT)]$, units are cm^3 mol s cal K.

No.	Reaction	A	β	E_a
(S1)†	$H + O \rightleftharpoons OH^*$			
	$p = 10^{-3}$ bar	1.09×10^{9}	-1.30	13745
		5.38×10^{38}	-13.30	5572
	$p = 10^{-2}$ bar	5.75×10^{12}	-1.97	16011
		1.14×10^{21}	-6.55	3541
	$p = 10^{-1}$ bar	5.43×10^{18}	-3.25	20607
		1.85×10^{-3}	2.10	34
	$p = 1$ bar	3.67×10^{18}	-2.90	18545
		2.94×10^{-5}	2.90	131
	$p = 10$ bar	1.81×10^{25}	-4.35	25255
		7.24×10^{-9}	4.19	-459
	$p = 10^{2}$ bar	3.25×10^{23}	-3.52	27712
		1.15×10^{-12}	5.56	1023
(S2)	$OH^* \longrightarrow OH + h\nu$	1.46×10^{6}	0.00	0
(S3)	$OH^* + O_2 \rightleftharpoons OH + O_2$	8.95×10^{11}	0.50	-483
(S4)	$OH^* + H_2O \rightleftharpoons OH + H_2O$	6.09×10^{12}	0.50	-767
(S5)	$OH^* + H_2 \rightleftharpoons OH + H_2$	1.00×10^{12}	0.50	-445
(S6)	$OH^* + OH \rightleftharpoons OH + OH$	1.95×10^{12}	0.50	-1717
(S7)	$OH^* + H \rightleftharpoons OH + H$	2.75×10^{13}	0.50	2458
(S8)	$OH^* + N_2 \rightleftharpoons OH + N_2$	1.08×10^{11}	0.50	-1240
(S9)	$OH^* + O \rightleftharpoons OH + O$	1.50×10^{12}	0.50	0
(S10)	$OH^* + H_2O_2 \rightleftharpoons OH + H_2O_2$	4.57×10^{12}	0.50	-270
(S11)	$OH^* + O_2 \rightleftharpoons O + HO_2$	6.54×10^{11}	0.50	-483
(S12)	$OH^* + H_2 \rightleftharpoons H_2O + H$	4.70×10^{11}	0.50	-445
(S13)	$OH^* + H_2O \rightleftharpoons H_2O_2 + H$	2.40×10^{14}	0.00	42526
(S14)	$H_2O + O \rightleftharpoons OH + OH^*$	1.30×10^{8}	1.30	110461
(S15)	$OH^* + OH \rightleftharpoons H_2O_2$	7.45×10^{13}	-0.37	0
(S16)	$OH^* + O \rightleftharpoons H + O_2$	0.00	0.00	0
(S17)	$OH^* + O + M \rightleftharpoons HO_2 + M$	0.00	0.00	0
(S18)	$OH^* + H \rightleftharpoons O + H_2$	5.64×10^{12}	0.50	0
(S19)	$OH^* + H \rightleftharpoons H_2O$	0.00	0.00	0
(S20)	$OH^* + H_2O_2 \rightleftharpoons H_2O + HO_2$	4.73×10^{12}	0.50	-270
(S21)	$OH^* + HO_2 \rightleftharpoons H_2O + O_2$	4.90×10^{8}	0.50	0
(S22)	$H + OH + OH \rightleftharpoons OH^* + H_2O$	3.88×10^{3}	3.32	0

Based on the former discussion, in this Chapter the sub-scheme by Kathrotia et al. [190, 191] in Table 6.1 is adopted in Section 6.3, where both CH_4–air and H_2–air flames are considered, making it meaningful to use a OH* sub-scheme applicable to both fuels. On the other hand, the sub-scheme by Sharipov et al. [362, 363], reported in Table 6.2, is adopted, if not specified otherwise, in Section 6.4, where the impact of the operating conditions on the spatial correlation between OH* and HRR in H_2 flames is investigated. In all cases, the OH* sub-mechanism is simply added to the main reaction scheme describing fuel oxidation, since the relative change in the concentration of ground species due to its addition is negligible [140].

The low concentration of OH*, compared to other species, makes its direct computation as a transported species in CFD simulations computationally expensive. For this reason, in the results of CFD simulations shown hereafter, the OH* distribution is evaluated using a post-processing algorithm based on the Quasi-Steady State (QSS) approximation. This approximation has been

† $k_{R1}(T, p)$ is obtained via a logarithmic interpolation, as shown in Equation (2.15).

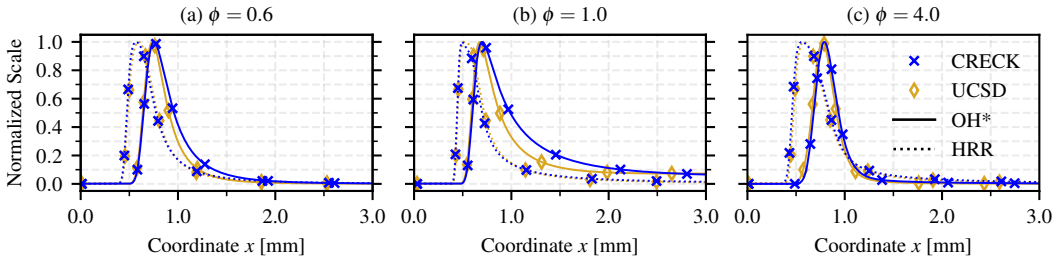

Figure 6.1: Normalized distributions of HRR and OH* molar concentration for lean (a), stoichiometric (b) and rich (c) hydrogen–air flames at atmospheric conditions ($T_u = 300$ K, $p = 1$ atm). Comparison between the UCSD [339] and CRECK [321] mechanisms. All calculations are performed with the OH* sub-scheme by Kathrotia et al.

already validated in the literature for premixed H_2-air flames at atmospheric conditions [140]. More details on this post-processing procedure, together with a validation for the operating conditions of interest in this work, are provided in Appendix B.

6.3 Influence of fuel chemistry and flame regime

The spatial correlation between the distributions of OH* and HRR is first examined at atmospheric conditions (i.e., $T_u = 300$ K and $p = 1$ atm) for laminar and turbulent H_2–air flames, considering both premixed and non-premixed regimes. First, 1D CH_4–air, CH_4–H_2–air and H_2–air laminar unstretched premixed flames are compared, highlighting the impact of fuel chemistry and of the associated OH* formation pathways on the observed correlation. The focus is then shifted to 1D laminar diffusion H_2–air flames, for which a markedly different behavior is observed compared to the premixed case.

The differences between the premixed and non-premixed regimes observed in 1D laminar H_2–air flames are then confirmed by the study of a 2D laminar triple flame and of turbulent 3D partially premixed and diffusion flames. Overall, this Section provides a systematic investigation of the mechanisms leading to the peculiar features of the OH* distribution in H_2–air premixed flames.

6.3.1 Laminar one-dimensional flames

Steady, one-dimensional, laminar H_2–air flames are computed with Cantera [137] to investigate the relation between the spatial distributions of OH* and HRR[‡]. In the unstretched case, these are compared to CH_4–H_2–air flames with variable H_2 content ranging from 10% to 90% by volume, and with pure CH_4–air flames taken as reference. One-dimensional flame simulations are performed with the multicomponent transport model [91], including Soret effect. Two detailed mechanisms, namely the San Diego (UCSD) [339] and the CRECK [321], are used to describe ground species oxidation. The former is adopted for pure H_2–air flames, while the latter, involving hydrocarbons, is used when comparing H_2–air, CH_4–H_2–air and CH_4–air flames. The two schemes are compared for H_2–air flames in Figure 6.1, which reports the normalized HRR and OH* molar concentration distributions for unstretched 1D laminar flames at three different equivalence ratios (i.e., $\phi = 0.6$, $\phi = 1.0$, and $\phi = 4.0$). Despite some slight differences in

[‡]If not otherwise specified, OH* refers to the molar concentration of OH* (c_{OH^*}), and HRR refers to the volumetric heat release rate $\dot{\omega}_T$. The notation has been simplified for clarity.

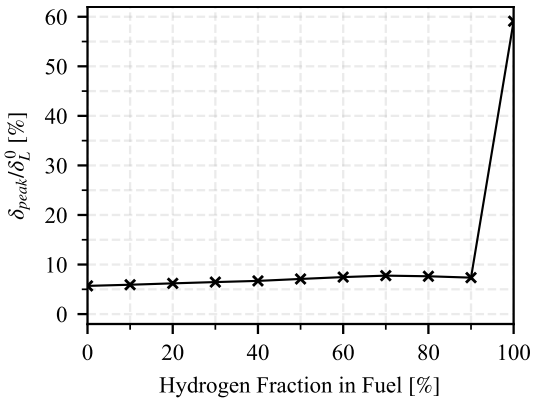

Figure 6.2: Peak distances δ_{peak}, normalized by δ_L^0, between OH* and total HRR versus hydrogen volume fraction in the methane–hydrogen fuel mixture. Results obtained for $\phi = 1$, $T_u = 300$ K, and $p = 1$ atm.

the OH* distributions, especially for $\phi \geq 1$, the two mechanisms are well in agreement in the prediction of the OH* peak location, which is the main focus of the discussion in this Section.

First, the reaction pathways leading to the differences in the OH* and HRR distributions are investigated. Subsequently, laminar H_2–air diffusion flames are considered, to assess the impact of the different flame regime on the correlation between OH* and HRR. The analysis is further expanded by comparing the OH*-HRR relation in the different cases from a quantitative perspective.

Unstretched premixed flames

Pure H_2–air and CH_4–air stoichiometric flames are compared in Figure 6.2, together with CH_4–H_2 blends with various H_2 contents, to investigate the different behaviors when modifying the fuel blend composition. The adequacy of OH* as HRR marker for the different cases is first characterized by considering the peak shift δ_{peak} between the two distributions, here normalized by the thermal flame thickness δ_L^0 (see Equation (2.41)). When CH_4 is present, the peak shift δ_{peak} remains almost constant and lower than 10% of δ_L^0, sustaining the adequacy of OH* as HRR marker for carbon-based fuels. For pure H_2, however, δ_{peak} suddenly rises to approximately 60% of δ_L^0.

To explain this behavior, the most important reactions responsible for the position of the OH* and HRR peaks are investigated in Figure 6.3. For OH*, the rates of progress of the two main formation paths, namely Reactions (R6.1) and (R6.4), are considered. For HRR, the heat production rate[§] (HPR) of the following reactions is instead taken into account:

$$H + O_2 + M \rightleftharpoons HO_2 + M, \tag{R6.6}$$

and

$$OH + CH_2O \rightleftharpoons HCO + H_2O. \tag{R6.7}$$

Reaction (R6.6) corresponds to Reaction (H5) in Section 4.1, and is here rewritten for convenience. As discussed in Sections 4.1 and 4.2, this Reaction is related to the recombination and production of the hydroperoxyl radical HO_2, and dominates the radical consumption process in H_2 combustion. On the other hand, for CH_4–air flames, the exothermic Reaction (R6.7) has

[§]The heat production rate represents the contribution of the single reaction to the total HRR [229].

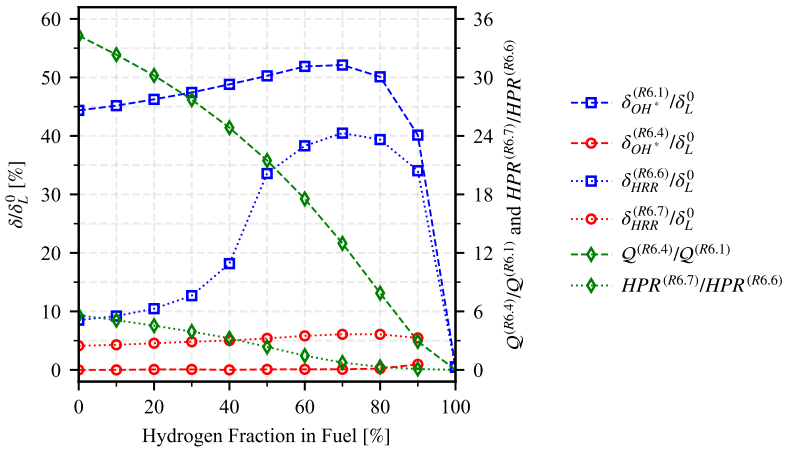

Figure 6.3: Peak distances, normalized by δ_L^0, between the rate of progress of Reaction (R6.1) and OH* ($\delta_{OH^*}^{(R6.1)}$), rate of progress of Reaction (R6.4) and OH* ($\delta_{OH^*}^{(R6.4)}$), HRR of Reaction (R6.6) and total HRR ($\delta_{HRR}^{(R6.6)}$), HRR of Reaction (R6.7) and total HRR ($\delta_{HRR}^{(R6.7)}$) (left axis), and ratio of peak values of rates of progress of Reactions (R6.4) and (R6.1) ($\mathcal{Q}^{(R6.4)}/\mathcal{Q}^{(R6.1)}$), and of HRR of Reactions (R6.7) and (R6.6) ($HRR^{(R6.7)}/HRR^{(R6.6)}$) (right axis), versus hydrogen volume fraction in the methane–hydrogen fuel mixture. Results obtained for $\phi = 1$, $T_u = 300$ K, and $p = 1$ atm.

a strong linear correlation with HRR and, therefore, the formyl radical HCO can be used as a HRR marker [169, 287]. Figure 6.3 reports the ratios $\mathcal{Q}^{(R6.4)}/\mathcal{Q}^{(R6.1)}$ between the peak values of the rates of progress $\mathcal{Q}$ (see Equation (2.6)) of Reactions (R6.4) and (R6.1) (diamond-marked green dashed line), and $HPR^{(R6.7)}/HPR^{(R6.6)}$ between the HPR of Reactions (R6.7) and (R6.6) (diamond-marked green dotted line) as a function of the H_2 content in the fuel mixture. Both ratios decrease almost linearly with increasing H_2 content, highlighting the growing importance of the H_2-related OH* and HRR pathways (i.e., Reactions (R6.1) and (R6.6), respectively) compared to the CH_4 flame.

To outline the relation of these reactions with the peak location of either OH* or HRR, four characteristic distances are also introduced in Figure 6.3: $\delta_{OH^*}^{(R6.1)}$ and $\delta_{OH^*}^{(R6.4)}$ are evaluated as the distances between the peak of OH* and the peaks of the rates of progress of Reactions (R6.1) and (R6.4), while $\delta_{HRR}^{(R6.6)}$ and $\delta_{HRR}^{(R6.7)}$ measure the distances between the peak of the total *HRR* and the peaks of *HPR* of Reactions (R6.6) and (R6.7), respectively. The evolution versus the H_2 content of these distances, normalized by δ_L^0, is also shown in Figure 6.3. Differently from the ratios $\mathcal{Q}^{(R6.4)}/\mathcal{Q}^{(R6.1)}$ and $HPR^{(R6.7)}/HPR^{(R6.6)}$, when CH_4 is present in the fuel mixture, $\delta_{OH^*}^{(R6.4)}$ and $\delta_{HRR}^{(R6.7)}$ (circle-marked red dashed and dotted lines, respectively) are relatively low (approximately equal to $0.05\delta_L^0$) and remain almost constant, regardless of the relative concentration of H_2 and CH_4. Analogous curves for the H_2-related Reaction (R6.1), $\delta_{OH^*}^{(R6.1)}$ (square-marked dashed blue line), and Reaction (R6.6), $\delta_{HRR}^{(R6.6)}$ (square-marked dotted blue line), show that these peak distances increase at first, reaching a maximum for the 30% CH_4 + 70% H_2 (by volume) fuel blend, then decrease becoming almost zero for pure H_2. Therefore, these trends suggest that the H_2 content in the fuel mixture has a limited impact on the CH-driven OH* formation pathway of Reaction (R6.4) and on the correlation between HCO and HRR through Reaction (R6.7), while Reactions (R6.1) and (R6.6), driven by the H radical, are representative of the OH* and HRR peaks, respectively, only for pure H_2–air flames. This is coherent with the trend of δ_{peak} versus H_2 content shown in Figure 6.2.

To investigate the underlying reasons for these different behaviors, the flame structures for

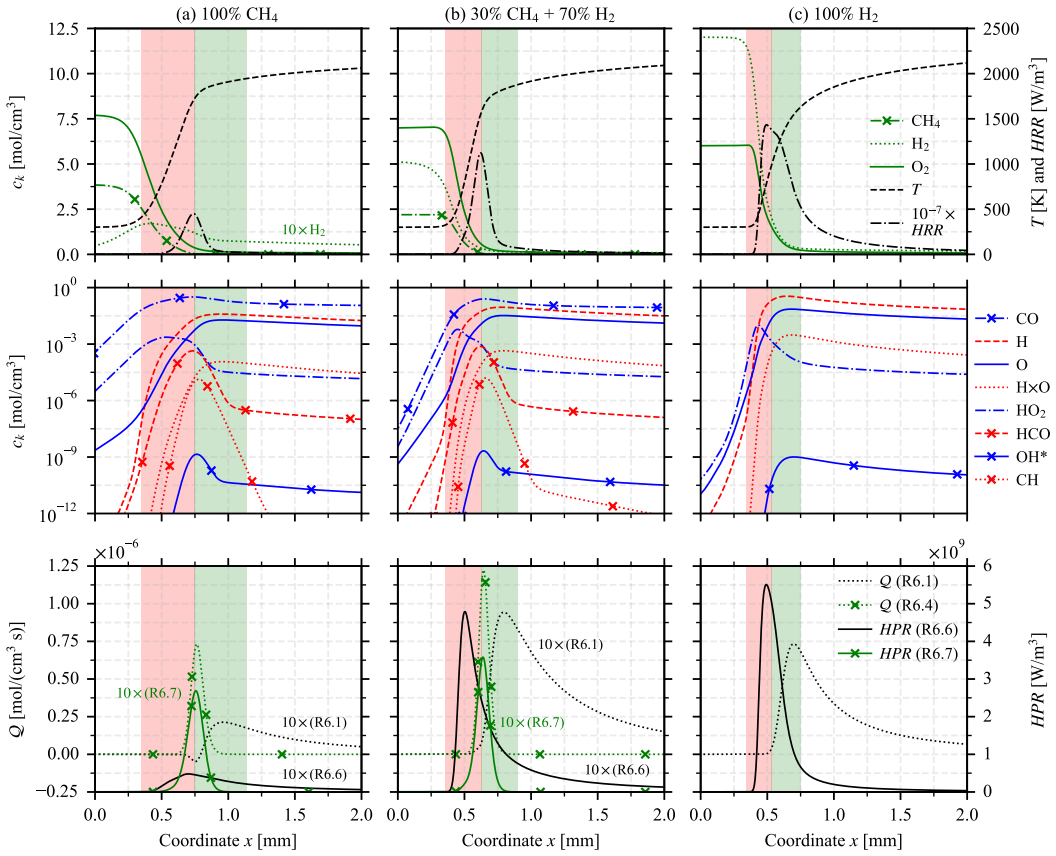

Figure 6.4: Structures of stoichiometric CH_4–air (a), 30%CH_4+70%H_2–air (b) and H_2–air (c) flames at T_u = 300 K and p = 1 atm. Molar concentrations of fuel and oxidizer, temperature and heat release rate profiles (top), molar concentrations of selected minor species (middle), chemical rates and heat production rates of selected reactions (bottom). The red and green zones represent, respectively, the main H-consumption and production regions.

CH_4–air, CH_4–H_2–air (30% CH_4 + 70% H_2 fuel by volume) and H_2–air flames are compared in Figure 6.4. From the asymptotic analysis standpoint, the structure of a premixed flame, apart from the upstream transport region, can be considered as two-layered, with a thin fuel consumption layer and a thicker downstream region, where chemical equilibrium is approached [423]. In CH_4 flames (see Figure 6.4a), the threshold between the two layers is marked by the H radical profile: in the downstream layer, H is produced (green-shaded zone) and supplied through back-diffusion to the fuel consumption layer (red-shaded zone). Observing the H radical profile (dashed red line), this is also a H-consumption region, where CH_4 is depleted with H radicals according to the chain-terminating reaction previously described in Reaction (R4.2) and reported hereafter for convenience:

$$CH_4 + 2\,H + H_2O \rightleftharpoons CO + 4\,H_2. \qquad \text{(R6.8)}$$

This limits the H radical upstream diffusion and pool generation. The so-produced secondary fuels H_2 and CO are then consumed in the downstream oxidation layer to obtain the final products H_2O and CO_2 [229].

For H_2 flames (see Figure 6.4c), instead, the asymptotic analysis is more difficult, given the chain-branching nature of the global fuel consumption process [359], already described in Reac-

tion (R4.1) and rewritten hereafter:

$$3\,H_2 + O_2 \rightleftharpoons 2\,H_2O + 2\,H. \tag{R6.9}$$

Nevertheless, H maintains a pivotal role, and downstream H-production (green-shaded zone) as well as upstream H-consumption (red-shaded zone) layers can still be identified [221]. As discussed in Section 4.2, this H-consumption layer corresponds to an upstream radical recombination region [337], coinciding with the maximum of the HO_2 profile (dash-dotted blue line), coherently with Reaction (R6.6). Heat is mostly released in this zone, despite the moderate temperatures [221, 229]. Downstream, equilibrium is reached in a second, thicker radical recombination region, with the transition between the two occurring in a thin radical branching layer, near the H profile peak [337].

Figure 6.4 shows that, as observed in [140], the two-layered structure of the host flame is kept by the OH*, which is produced in the fuel consumption layer, where it reaches the peak value, and then slowly decays to the equilibrium value in the downstream region. In the pure CH_4 flame (see Figure 6.4a), given the low availability of H, rapidly consumed through Reaction (R6.8), the main production pathway of OH*, namely Reaction (R6.4) (cross-marked dotted green line), peaks at the front of the inner layer, following its precursor CH (cross-marked dotted red line) together with HCO (cross-marked dashed red line), which is a HRR surrogate through Reaction (R6.7). This explains why no significant peak shift is observed in this case. For the pure H_2 flame (see Figure 6.4c), instead, the OH* concentration profile (cross-marked solid blue line) follows those of the rate of progress $\mathcal{Q}$ of Reaction (R6.1) (dotted black line) and of the product of the concentrations of its reactants H and O (dotted red line), peaking at the back of the active reaction zone. On the other hand, HRR (dash-dotted black line) peaks at the front, given the strong exothermic nature of Reaction (R6.6) (solid black line) and the fast back-diffusion of H (dashed red line), leading to the observed peak shift. For the CH_4–H_2 fuel mixture (see Figure 6.4b), although the reduced CH_4 content facilitates the H radical pool generation, the path provided by Reaction (R6.4) remains by far the most important for OH* production. The highest HRR still occurs in the back high-temperature region of the active reaction zone, keeping the peak shift between OH* and HRR negligible.

As a final remark, it can be observed that, for the CH_4 and CH_4–H_2 flames (see Figure 6.4a-b), a peak in the OH* distribution can be clearly identified, with the OH* concentration dropping by more than one order of magnitude in the burned gases region. On the other hand, the decay in the H_2 flame is slower, and a non-negligible OH* concentration, comparable to the peak value, persists in the high temperature post-flame zone. Since the HRR is almost null in this region, this means that, in addition to be shifted in space, the HRR and OH* distributions differ also in the shape for stoichiometric premixed H_2–air flames. This result finds confirmation in experiments and numerical simulations of near-stoichiometry premixed H_2–air flames reported in the literature [140, 208, 356], and will be further analyzed in Section 6.4.

Strained counterflow diffusion flames

Strained counterflow diffusion H_2-air flames are considered for varying global strain rate a, defined as in Equation (3.5). The objective is to investigate the impact of the different flame regime on the OH* and HRR distributions, combined to the effect of increasing strain rate.

Figure 6.5 shows that the HRR exhibits a bimodal distribution for all strain rates. The two peaks are here referred to as HRR^F_{max}, on the fuel side, and HRR^O_{max}, on the oxidizer side. A similar behavior was found for CH_4 inverse diffusion flames in [427]. Differently from the premixed

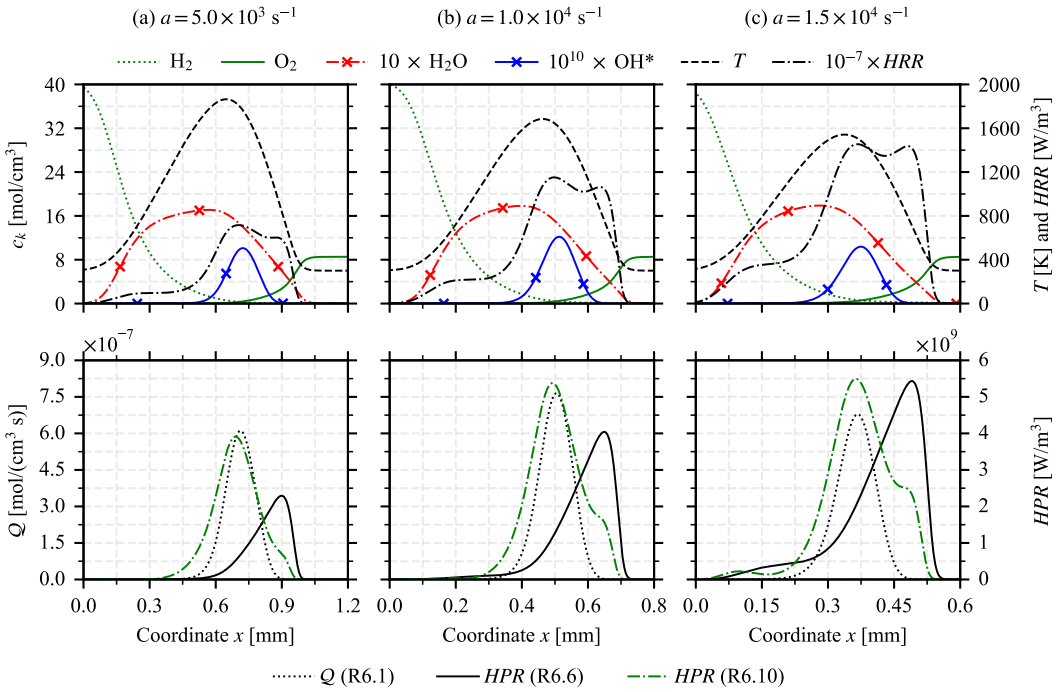

Figure 6.5: Structure of hydrogen-air diffusion flames at T_u = 300 K and p = 1 atm for a global strain rate a equal to 5.0×10^3 s^{-1} (a), 1.0×10^4 s^{-1} (b) and 1.5×10^4 s^{-1} (c). Molar concentrations c_k of fuel and oxidizer, temperature T and heat release rate HRR profiles (top), chemical rates of progress $\mathcal{Q}$ and heat release rates HRR of selected reactions (bottom).

configuration, in H_2-air diffusion flames HRR is dominated, on the fuel side, by the radical-radical recombination Reaction (H11), presented in Section 4.1 and reported hereafter for convenience:

$$\mathrm{H + OH + M \rightleftharpoons H_2O + M,} \qquad \text{(R6.10)}$$

which needs the production of H radicals on the fuel side. This marks a difference with respect to Reaction (R6.6), previously investigated for premixed flames, which instead requires O_2 and, therefore, peaks on the oxidizer side [229].

At low and moderate strain rates (Figure 6.5a-b), Reaction (R6.10) (dash-dotted green line) prevails on Reaction (R6.6) (solid black line). Since Reaction (R6.1) (dotted black line) requires the H radical, its rate of progress $\mathcal{Q}$ and so the OH* concentration (cross-marked solid blue line) well correlate with Reaction (R6.10). Therefore, OH* well behaves as a HRR global peak tracer, differently than in premixed flames.

Increasing the strain rate appears to weaken the OH*-HRR correlation. Indeed, for higher strain rates (see Figure 6.5c) the HPR of Reaction (R6.6) increases, and so does the magnitude of HRR^O_{max}, which eventually overtakes HRR^F_{max}. Since OH* does not follow the bimodal nature of HRR and, as in premixed flames, does not correlate well with Reaction (R6.6), a shift between the OH* peak and the HRR global maximum appears. Still, as these regimes are close to extinction (the extinction strain rate being approximately equal to 1.8×10^4 s^{-1}), they are not of the utmost interest for practical applications.

Table 6.3: Error measure $\bar{\zeta}$ for different quantities in premixed and diffusion flames.

Quantity	Premixed flames ($\phi = 1$)			Diffusion flames		
	CH_4 (Figure 6.4a)	$CH_4 + H_2$ (Figure 6.4b)	H_2 (Figure 6.4c)	$a = 5.0 \times 10^3$ (Figure 6.5a)	$a = 1.0 \times 10^4$ (Figure 6.5b)	$a = 1.5 \times 10^4$ (Figure 6.5c)
Molar concentrations c_k						
OH^*	1.45×10^{-2}	1.22×10^{-2}	5.89×10^{-2}	1.11×10^{-1}	1.45×10^{-1}	1.73×10^{-1}
$O_2 \times H$	1.06×10^{-1}	4.49×10^{-2}	1.07×10^{-2}	8.71×10^{-2}	8.77×10^{-2}	8.10×10^{-2}
$OH \times H_2$	4.46×10^{-1}	3.62×10^{-1}	2.78×10^{-2}	1.36×10^{-1}	1.35×10^{-1}	1.20×10^{-1}
HCO	1.43×10^{-3}	3.11×10^{-3}	–	–	–	–
Chemical rates of progress $\mathcal{Q}$						
Reaction (R6.1)	2.62×10^{-1}	2.16×10^{-1}	5.50×10^{-2}	1.12×10^{-1}	1.46×10^{-1}	1.74×10^{-1}
Reaction (R6.4)	1.50×10^{-2}	1.32×10^{-2}	–	–	–	–
Heat production rate *HPR*						
Reaction (R6.6)	9.81×10^{-2}	3.79×10^{-2}	1.85×10^{-2}	1.20×10^{-1}	1.13×10^{-1}	9.65×10^{-2}
Reaction (R6.7)	4.69×10^{-3}	5.32×10^{-3}	–	–	–	–
Reaction (R6.10)	2.84×10^{-1}	2.17×10^{-1}	3.53×10^{-2}	5.99×10^{-2}	6.68×10^{-2}	6.43×10^{-2}

Quantitative analysis

The differences between premixed and diffusion flames when switching from CH_4 to CH_4–H_2 blends and, finally, to pure H_2 have been so far characterized qualitatively. To allow for a direct comparison between different cases, it is of interest to define a numerical parameter to quantify the OH*-HRR correlation.

Nikolau and Swaminathan [278] proposed an error estimator method to determine the reliability of HRR markers for premixed combustion of carbon-based fuels. This method is based on the evaluation of an error measure $\zeta(v)$ for a variable v, where a lower value of $\zeta(v)$ indicates a better correlation of v with HRR. The definition of $\zeta(v)$ proposed in [278], however, is well posed for unstrained premixed flames only, and strongly depends on the overall dimension of the computational domain, hindering the comparison of different flame configurations. Therefore, a modified definition is here adopted:

$$\bar{\zeta}(v) = \int_{reac} \frac{\left(|HRR(x)|_{norm} - |v(x)|_{norm}\right)^2}{L_r} dx \tag{6.1}$$

The error measure $\bar{\zeta}(v)$ is the mean of $\zeta(v)$ over the reactive region of size L_r, here defined by the condition $|HRR(x)| \geq 0.01 \max(|HRR(x)|)$. As in [278], $|HRR(x)|$ and $|v(x)|$ are normalized by their respective maxima.

Table 6.3 reports the values of $\bar{\zeta}$ computed for OH* in the premixed and diffusion flames shown in Figures 6.4 and 6.5, respectively. The products of the concentrations of O_2 and H, which react in Reaction (R6.6), and of OH and H_2, identified as the most adequate HRR marker for H_2-air premixed flames in [254], are also considered, together with HCO for CH_4 and CH_4–H_2 flames. The chemical rates of progress of Reactions (R6.1) and (R6.4), and the HPR of Reactions (R6.6) to (R6.10) are included too. The premixed cases show that for CH_4 and CH_4–H_2 flames, as expected, the lowest values of the error measure are obtained for HCO and for Reaction (R6.7), by which it is produced. For these flames, the value of $\bar{\zeta}(OH^*)$ is close to the one of $\bar{\zeta}$(R4) and lower than $\bar{\zeta}$(R1) by one order of magnitude. This confirms that, when CH_4 is

present, H_2 has a limited impact on the OH* chemical pathway through Reaction (R6.4), coherently with the observations made for Figure 6.3. For pure H_2 flames, the value of $\bar{\zeta}(OH^*)$ is the largest, confirming a worse correlation between OH* and HRR for these flames. Here, the lowest values are obtained for the $O_2 \times H$ product and for Reaction (R6.6), coherently with the analysis of the flame structures in Figure 6.4c. The product of OH and H_2 concentrations shows also a low value, in agreement with [254]. Overall, no variable reaches a value of $\bar{\zeta}$ as low as $\bar{\zeta}(HCO)$ in CH_4 and CH_4-H_2 flames, indicating that a reliable HRR marker is harder to define for pure H_2-air premixed flames. As for H_2-air diffusion flames, the values of $\bar{\zeta}$ are higher than in the premixed case and the variability among different quantities is less pronounced. Indeed, the bimodal nature of the HRR distribution introduces a bias in the evaluation of $\bar{\zeta}$, because none of the variables can reproduce it. The OH* and the Reaction (R6.1) by which it is produced, as well as Reaction (R6.10) and the product of OHand H_2, peak on the fuel side, while Reaction (R6.6) and the product of its reactants O_2 and H peak on the oxidizer side. Coherently with the results in Figure 6.5, the value of $\bar{\zeta}(OH^*)$ increases with the strain rate, suggesting a worse correlation of OH* with HRR. Nevertheless, the dependency of $\bar{\zeta}$ on strain rate is quite limited for all variables, since the normalization of the integral in Equation (6.1) cancels out the variation of the relative magnitude of variables shown in Figure 6.5. The sole error measure $\bar{\zeta}$ is thus insufficient to assess the adequacy of a HRR marker for these flames.

6.3.2 Laminar two-dimensional triple flame

A 2D triple flame at $T_u = 300$ K and $p = 1$ atm is now considered. In this configuration, three zones, i.e., a lean premixed branch, a rich premixed branch, and a diffusion branch, coexist. This allows to investigate the impact of the flame regime in the same canonical configuration.

Figure 6.6 schematizes the computational domain adopted for this case. Once stabilized, the triple flame propagates downwards, in opposition to the incoming flow. At the inlet, the composition varies from pure oxidizer (on the left) to pure fuel (on the right), by imposing a profile of mixture fraction Z [311]. The size of the mixing layer, where Z varies from 0 to 1, is equal to 1 mm. The flame is computed at $T_u = 300$ K and $p = 1$ atm, thus requiring a grid resolution of 25 μm in the reacting region to discretize the flame front with at least 10 points. This results in a grid size of approximately 1.3×10^6 nodes. The mesh is unstructured and made of quadrilateral elements.

Simulations are performed in AVBP using the TTGC scheme [77] (see Section 3.3.2) for convective terms, and the NSCBC formulation [141, 309] for inlet and outlet boundaries (see Section 3.3.3). The simplified transport model described in Section 3.3.4 is adopted, but the mixture viscosity μ_m is here computed based on the Wilke mixing rule [422], with the hypothesis of a binary mixture of H_2 and air [124]:

$$\mu_m = \frac{X_{H_2}\mu_{H_2}}{X_{H_2} + (1 - X_{H_2})\phi_{H_2,air}} + \frac{(1 - X_{H_2})\mu_{air}}{1 - X_{H_2} + X_{H_2}\phi_{air,H_2}}, \tag{6.2}$$

where X_k is the mole fraction of the species k and

$$\phi_{k,j} = \frac{\left[1 + (\mu_i/\mu_j)^{1/2}(\mathcal{M}_j/\mathcal{M}_i)^{1/4}\right]^2}{\left[8(1 + \mathcal{M}_i/\mathcal{M}_j)\right]^{1/2}}, \tag{6.3}$$

with $\mathcal{M}_k$ being the molecular weight of the species k. The values of viscosity μ_{H_2} and μ_{air} are computed according to two distinct power laws, analogous to the one described in Equation (3.30).

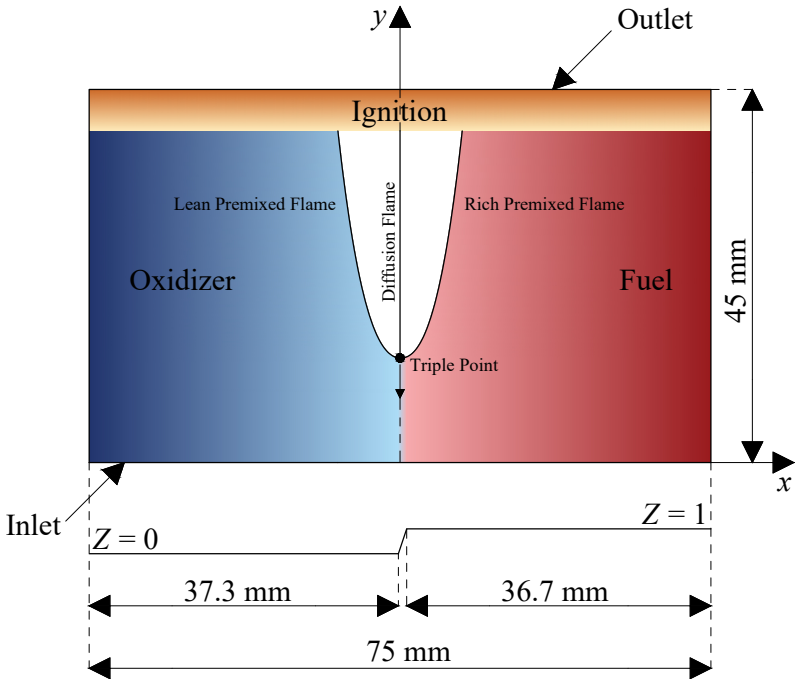

Figure 6.6: Schematic representation of the computational domains adopted for the two-dimensional triple flame.

This approach is more suited than the global power law approximation presented in Section 3.3.4 for H_2–air non-premixed combustion. Indeed, the low viscosity of H_2 with respect to air induces significant local variations when pure H_2 is involved, which cannot be taken into account when a single power law is used for the whole mixture [124].

Figure 6.7 reports the HRR fields for the premixed (Figure 6.7a) and diffusion (Figure 6.7b) regions, normalized by the maximum value in the corresponding zones, together with isolines of the normalized OH* concentration at 5%, 10%, 20%, 50% and 90%. To distinguish the three flame zones, the modified flame index by Lock et al. [242] is adopted, defined as:

$$FI_M = \left(\frac{\xi - \xi_s}{|\xi - \xi_s|} \right) \cdot \frac{1}{2} \left(1 + \frac{FI}{|FI|} \right), \tag{6.4}$$

where FI is the Takeno flame index [426], ξ is the mixture fraction defined by Bilger [30], and ξ_S its stoichiometric value. In the premixed region, $FI_M = \pm 1$ (positive for the rich branch and negative for the lean branch), while $FI_M = 0$ in the non-premixed (i.e., diffusion) region. To separate the lean and rich premixed zones, the stoichiometric line is added (in black), defined by the condition $\xi = \xi_s$, with $\xi_s \approx 0.0285$ for H_2-air flames.

Focusing on the premixed region first (see Figure 6.7a), a sensible axial shift between the OH* and HRR peaks can be observed. The OH* concentration peaks close to the stoichiometric line and in proximity to the triple point (i.e., the intersection of the three branches), while the HRR peaks further down, in the rich premixed zone. This is in agreement with 1D calculations of counterflow premixed flames performed by Kruljevic et al. [208], who observed a maximum of OH* mass fraction at $\phi \approx 1.2$ and a maximum of HRR at $\phi \approx 1.6 - 1.7$. A much better agreement between the two distributions can be found instead in the diffusion branch (see Figure 6.7b), with the two peaks located in the same spatial region. Moreover, the OH* field shows a more similar

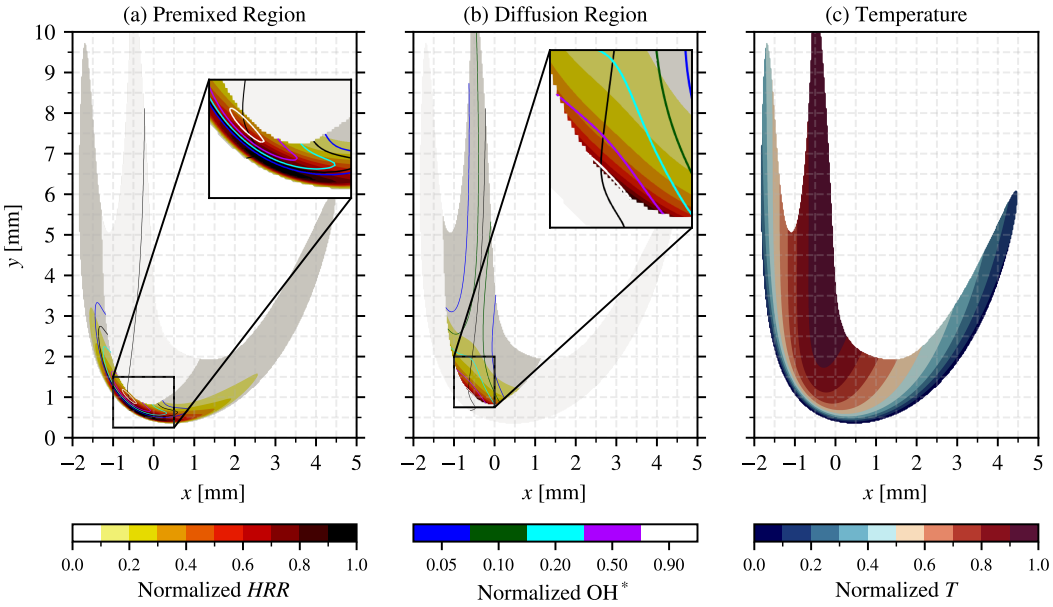

Figure 6.7: Normalized distributions of HRR in the premixed (a) and diffusion (b) regions of a 2D triple flame at $T_u = 300$ K and $p = 1$ atm, together with isolines at 5%, 10%, 20%, 50% and 90% of normalized OH* concentration, and normalized distribution of temperature T (c). The distributions are normalized by the maximum value in the corresponding region. The black line denotes the stoichiometric line. The insets highlight the regions of maximum HRR and OH*.

shape to the HRR one and is therefore sufficiently adequate to capture the HRR variation in this zone.

Overall, a good agreement can be found with the analysis performed for 1D premixed and diffusion flames. Differently from the 1D configuration in Figure 6.5, however, the reactants of the diffusion branch are at higher temperature than the unburned gases, as it can be clearly observed from the temperature field in Figure 6.6c. Consequently, a sensibly higher temperature is achieved in this region if compared to the premixed zones, especially close to the stoichiometric line, where a residual OH* concentration, in the order of 10% of the maximum value, is present (see Figure 6.7b). These results are coherent with those obtained for premixed flames in [140, 208], as well as with the premixed flame structures shown in Figure 6.4. This highlights the impact, for all flame regimes, of the temperature on the OH* concentration in the combustion products, which will be discussed further in detail in Section 6.4.

6.3.3 Turbulent three-dimensional flames

To sustain the previous analysis on the influence of the flame regime on the OH*-HRR correlation, LES predictions of the OH* field in turbulent H_2-air flames are here analyzed and compared to experimental data. The reference configuration is the HYLON injector from IMFT, shown in Figure 6.8a, which consists of two swirling coaxial ducts to separately inject H_2 and oxidizer [6]. At the outlet section of the injector, turbulent mixing competes with the chemical time scales of H_2-air flames, leading to the stabilization of either an anchored diffusion flame (denoted as Flame A in Figure 6.8b) or of a lifted partially premixed flame (Flame L in Figure 6.8c). The global equivalence ratio is kept constant and equal to $\phi_g = 0.45$ for both flames.

The same numerical methodology and computational mesh described in [6] are employed, and only key features are recalled hereafter. Flame-turbulence interaction for premixed flames

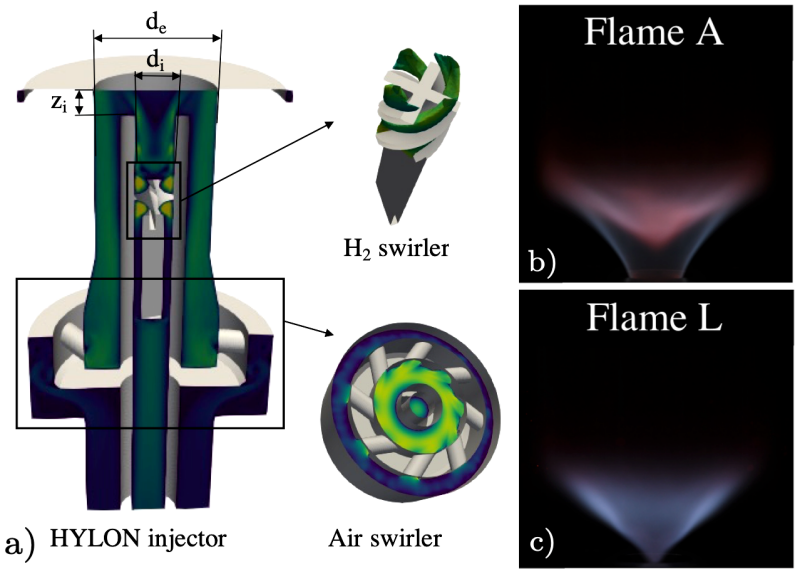

Figure 6.8: Main components of the HYLON injector (a), and line-of-sight integrated images of attached (b, Flame A) and lifted (c, Flame L) flames (from [6]).

is addressed with the Dynamic TF model [232], while a sufficient mesh refinement is imposed to avoid flame thickening in zones of stabilized diffusion flames. Inlet and outlet boundary conditions are treated with the NSCBC formalism [309] (see Section 3.3.3) and a thermal resistance is imposed to account for wall heat losses. Solutions are time-averaged over a whole flow through time, corresponding to approximately 55 ms for Flame A and 25 ms for Flame L. In addition to the results in [6], the Kathrotia OH* sub-mechanism [190] is added to the San Diego scheme [339] to retrieve the OH* distribution.

Figure 6.9 compares the experimental images of the mean normalized OH^*_{norm} chemiluminescence signal with LES normalized time-averaged OH^*_{norm} fields. Isolines at 20%, 50% and 90% of OH^*_{norm} (white lines) and HRR_{norm} (red lines) are superimposed to the latter. Being controlled by diffusion reaction, the attached flame (see Figure 6.9a) shows a good match between numerical OH^*_{norm} and HRR_{norm} fields. This is in agreement with the laminar 1D counterflow flame simulations for moderate strain rates in Figure 6.5a-b. For the lifted flame (see Figure 6.9b), instead, albeit the flame shape is globally well predicted, differences on the axial extension of the experimental OH^*_{norm} and numerical HRR_{norm} fields are observed, as noted also in [6]. A better match is achieved when the experimental and LES time-averaged OH^*_{norm} fields are directly compared, as highlighted by horizontal dashed lines. The Flame L, burning in the partially premixed regime, features an axial shift between the HRR_{norm} and OH^*_{norm} peaks, as observed in Section 6.3.1 for canonical 1D premixed flames and in Section 6.3.2 for the 2D triple flame.

6.4 Impact of the operating conditions

The previous Section has shown the peculiar characteristics of the OH*-HRR correlation in premixed H_2–air flames at atmospheric conditions. Here, the analysis is extended by including the effect of varying operating conditions.

To this scope, laminar premixed unstrained 1D H_2-air flames are considered in Section 6.4.1

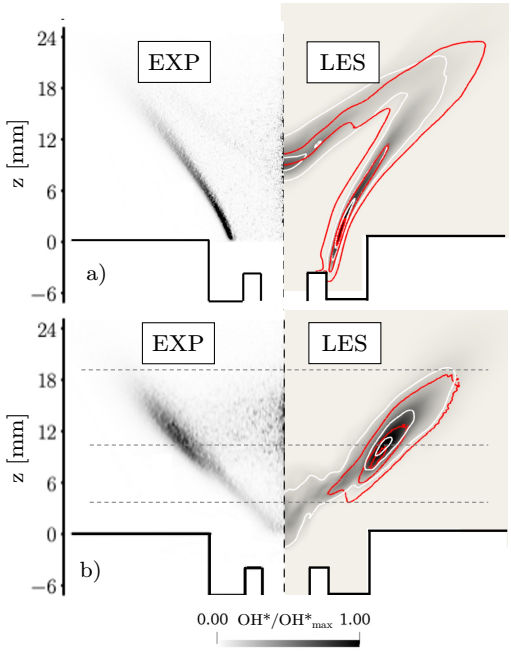

Figure 6.9: Experimental normalized mean OH^*_{norm} Abel-deconvoluted chemiluminescence signal (left) and LES normalized time-averaged OH^*_{norm} mass fraction (right) for Flame A (a) and Flame L (b), with isolines at 20%, 50% and 90% of OH^*_{norm} (white lines) and HRR_{norm} (red lines).

under different values of equivalence ratio, unburned gas temperature and pressure, allowing to study the impact of the state of the reactants on the OH* distribution and its correlation with the HRR one. The effect of flame stretch in laminar premixed flames is subsequently investigated in Section 6.4.2 by considering lean ($\phi = 0.35$) and stoichiometric ($\phi = 1.00$) flames in two different canonical configurations: 1D counterflow flames to isolate strain effects, and two-dimensional (2D) expanding flames, which are subjected also to curvature. Finally, in Section 6.4.3, the OH*-HRR correlation in 1D laminar counterflow diffusion flames at variable strain rate levels, unburned gas temperature and pressure is discussed.

6.4.1 Unstretched laminar premixed flames

Unstretched laminar premixed flames are solved with Cantera [137] on a domain of length equal to 5 cm, using the multi-component transport model [91] and considering the Soret effect. Severe refinement criteria are applied, with a ratio of 2.0, a slope of 0.001, a curve of 0.001 and a prune of 0.0005 (see Section 3.1), leading to a grid of at least 6000 points. Parametric studies are performed in a wide range of operating conditions, in terms of pressure p (1 to 20 atm), unburned gas temperature T_u (300 to 900 K) and equivalence ratio ϕ (0.3 to 3.0).

Figure 6.10 reports the normalized distributions of OH* and HRR for lean ($\phi = 0.35$) and stoichiometric ($\phi = 1.00$) freely-propagating, unstretched 1D premixed H_2-air flames at three representative operating conditions: $T_u = 300$ K and $p = 1$ atm (a), $T_u = 600$ K and $p = 1$ atm (b), and $T_u = 600$ K and $p = 10$ atm (c). The OH* concentration is computed both with the scheme reported in Table 6.2, derived from Sharipov et al. [362, 363], and with the OH* sub-mechanism by Kathrotia et al. [190] in Table 6.1, to investigate the impact of the different OH* kinetics description, and allow for a better comparison with the analysis in Section 6.3.

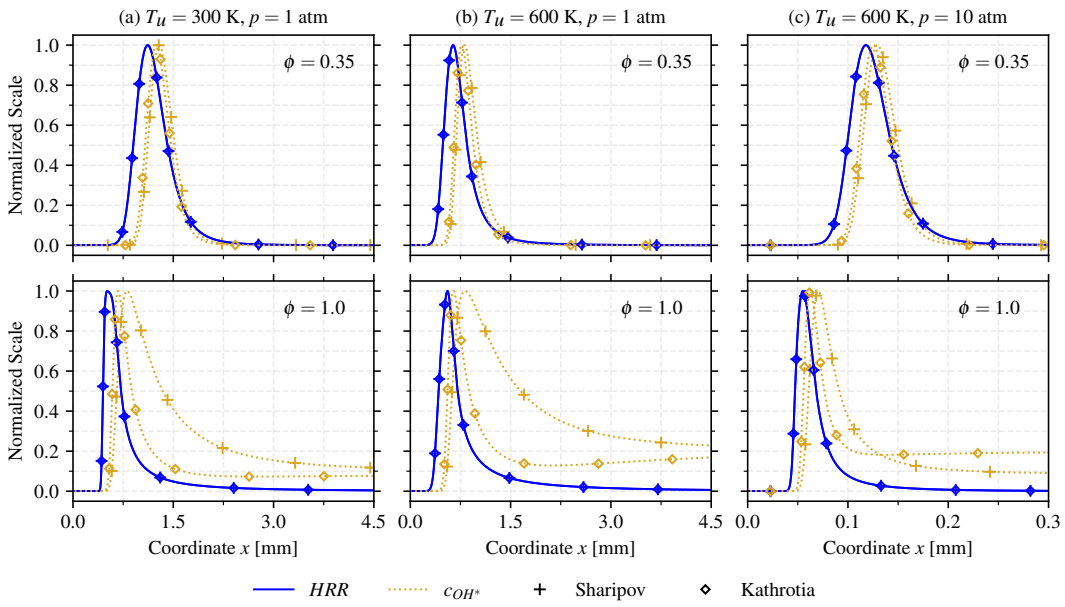

Figure 6.10: Normalized distributions of HRR and OH* concentration for unstrained lean ($\phi = 0.35$, top) and stoichiometric ($\phi = 1.00$, bottom) premixed flames at $T_u = 300$ K and $p = 1$ atm (a), $T_u = 600$ K and $p = 1$ atm (b), and $T_u = 600$ K and $p = 10$ atm (c). The OH* concentration is computed both with the OH* sub-schemes by Sharipov et al. [362, 363] and Kathrotia et al. [190]

In Section 6.3, two characteristic features were observed in the OH* distribution for premixed H_2–air flames: the peak shift with respect to the HRR distribution, and the presence of a non-negligible concentration of OH* in the post-flame zone for stoichiometric flames. Both features are predicted by the two OH* sub-schemes, supporting the non-dependence on numerical artifices of the analysis carried out in Section 6.3. In particular, an agreement exists between the two normalized OH* distributions for the lean flames, with only slight variations in terms of peak position. This is in line with the results in [105], where experimental OH* chemiluminescent intensity images are compared with numerical OH* concentration fields obtained with both OH* sub-mechanisms in lean premixed H_2 flames. At stoichiometry, the scheme by Sharipov et al. [362, 363] accentuates the peak shift, placing the maximum of OH* further downstream. Moreover, while both schemes predict the presence of OH* in the post-flame region, this decays more rapidly towards the equilibrium value with the sub-mechanism by Kathrotia et al. [190]. Finally, a major difference is observed for the stoichiometric flame at $p = 10$ atm, which can be related to the pressure scaling introduced by Sharipov et al. [362, 363] for Reaction (R6.1). Indeed, while for the other operating conditions both mechanisms tend to similar values for the normalized equilibrium OH* concentration, the two strongly disagree at higher pressure, with the sub-scheme by Kathrotia et al. [190] overestimating the final OH* concentration compared to the scheme by Sharipov et al. [362, 363]. Recalling that the scheme by Sharipov et al. [362, 363] was validated against experimental data in a wide range of pressures and temperatures, the results reported above suggest that this mechanism provides a more reliable prediction of OH* for the different operating conditions of interest in this Section.

A quantitative assessment of the OH*-HRR correlation for varying operating conditions is now cosidered, based on three parameters at the same time. In addition to the normalized peak-to-peak distance between the OH* and HRR distributions δ_{peak}/δ_L^0, hereafter denominated δ for

Table 6.4: Values of parameters characterizing the correlation between OH* and HRR, the flame and the OH* distribution for unstrained lean ($\phi = 0.35$) and stoichiometric ($\phi = 1.0$) premixed flames at different operating points. The OH* concentration is computed using the sub-scheme by Sharipov et al. [362, 363].

Quantity	Operating point					
	$p = 1$ atm $T_u = 300$ K $\phi = 0.35$	$p = 1$ atm $T_u = 300$ K $\phi = 1.0$	$p = 1$ atm $T_u = 600$ K $\phi = 0.35$	$p = 1$ atm $T_u = 600$ K $\phi = 1.0$	$p = 10$ atm $T_u = 600$ K $\phi = 0.35$	$p = 10$ atm $T_u = 600$ K $\phi = 1.0$
Correlation coefficients						
δ	0.1642	0.9063	0.3869	0.6019	0.1207	0.5909
$\bar{\zeta}$	0.07468	0.1848	0.09982	0.2004	0.04616	0.1353
r_{OH^*}	0.7231	-0.08402	0.4640	0.01037	0.8053	0.2035
Flame parameters						
δ_L^0 [μm]	960.6	329.6	450.8	437.6	97.18	25.87
T_{ad} [K]	1310.5	2385.4	1570.6	2528.7	1570.6	2623.1
OH distribution parameters*						
$c_{\mathrm{OH}^*}^{\mathrm{peak}}$ [mol/cm^3]	1.34×10^{-16}	6.14×10^{-13}	1.43×10^{-14}	1.44×10^{-12}	6.28×10^{-15}	4.38×10^{-11}
$c_{\mathrm{OH}^*}^{\mathrm{eq}}$ [mol/cm^3]	2.67×10^{-23}	5.93×10^{-14}	8.24×10^{-20}	2.97×10^{-13}	3.59×10^{-19}	3.79×10^{-12}

simplicity, and to the error estimator $\bar{\zeta}$ (see Equation (6.1)), the Pearson coefficient r_{OH^*} is considered to assess the spatial correlation between the HRR and OH* concentration distributions:

$$r_{\mathrm{OH}^*} = \frac{N\sum_i c_{\mathrm{OH}^*,i}\mathrm{HRR}_i - \sum_i c_{\mathrm{OH}^*,i}\sum_i \mathrm{HRR}_i}{\sqrt{\left[N\sum_i c_{\mathrm{OH}^*,i}^2 - \left(\sum_i c_{\mathrm{OH}^*,i}\right)^2\right]\left[N\sum_i \mathrm{HRR}_i^2 - \left(\sum_i \mathrm{HRR}_i\right)^2\right]}}, \tag{6.5}$$

where N is the number of grid points. Its value can vary between -1 and 1, where $|r_{\mathrm{OH}^*}| = 1$ indicates a perfect correlation, whereas $r_{\mathrm{OH}^*} = 0$ denotes no correlation. Since this coefficient is a normalized measurement of the covariance between the two distributions, it allows for a comparison of flames in varying operating conditions and regimes, and has been successfully adopted by Hardaya et al. [154] to investigate HRR surrogates in NH_3–H_2–N_2–air premixed flames. Moreover, by taking into account the whole domain and not only the reactive region as for $\bar{\zeta}$, it allows for verifying whether a correlation between OH* and HRR exists in the post-flame zone.

Table 6.4 reports the values of the three correlation coefficients δ, $\bar{\zeta}$ and r_{OH^*} for the operating points in Figure 6.10, together with some characteristic parameters of the flames (laminar flame thickness δ_L^0 and adiabatic flame temperature T_{ad}) and of the OH* distributions (peak $c_{\mathrm{OH}^*}^{peak}$ and final downstream equilibrium $c_{\mathrm{OH}^*}^{eq}$ values of OH* concentration). The values of the two correlation coefficients $\bar{\zeta}$ and r_{OH^*} reflect the qualitative features observed in Figure 6.10, i.e., the peak shift and the presence of OH* in the burned gases of stoichiometric flames. Indeed, for the lean case, the two coefficients are mostly affected by the sole peak shift: as δ gets smaller, the value of $\bar{\zeta}$ tends to zero whereas the value of $|r_{\mathrm{OH}^*}|$ tends to one, indicating a better correlation. For the stoichiometric case, the values of $\bar{\zeta}$ and r_{OH^*} are also affected by the equilibrium value of OH*, reducing the impact of the sole peak shift δ. Nevertheless, the correlation is much poorer in this case, with $\bar{\zeta}$ reaching a higher value and r_{OH^*} becoming closer to zero, if compared to the corresponding lean cases.

To further investigate the differences between the HRR and OH* distributions, a Rate of Production (*ROP*) analysis is provided in Figure 6.11, showing the different contributions of the

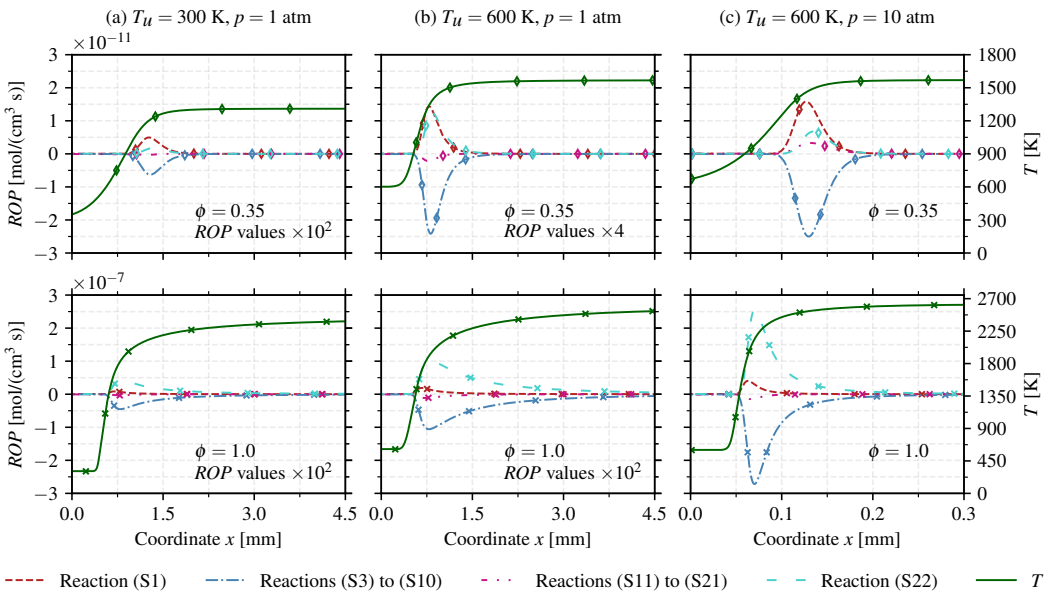

Figure 6.11: Contributions of different reactions to the Rate of Production of OH* and temperature profiles for unstrained lean ($\phi = 0.35$, top) and stoichiometric ($\phi = 1.00$, bottom) premixed flames at $T_u = 300$ K and $p = 1$ atm (a), $T_u = 600$ K and $p = 1$ atm (b), and $T_u = 600$ K and $p = 10$ atm (c).

OH* formation and consumption pathways reported in Table 6.2: the non-adiabatic association Reaction (S1), the non-reacting collisional quenching of Reactions (S3) to (S10), the reactive quenching of Reactions (S11) to (S21), and the exothermic Reaction (S22). For each reaction j, the *ROP* corresponds to the term $\nu_{k,j}\mathcal{Q}_j$ in Equation (2.3), where k is the species (in this case, OH*). The profile of temperature T is added to Figure 6.11 for reference.

The different contributions of the two formation pathways of Reactions (S1) and (S22) can be clearly observed, with the former prevailing for the low-temperature lean flame, while the latter is more significant for the high-temperature stoichiometric flame. Although both reactions peak downstream compared to the HRR, as they rely on the H radical, which is pivotal in this sense, as discussed in Section 6.3, Reaction (S22) peaks further downstream compared to Reaction (S1), since it requires the OH radical produced in the back of the reacting region [229]. As for the consumption pathways, the non-reacting quenching of Reactions (S3) to (S10) is dominant over the collisional one, at least in the operating conditions considered in this work. Consequently, the final OH* concentration is mostly determined by the chemical equilibrium between OH and OH* radicals.

In their study, based on 1D laminar unstretched premixed H_2–air flames, Graña-Otero and Mahmoudi [140] observed that the equilibrium OH* concentration is sensitive to the final flame temperature, due to the temperature dependence of both the OH concentration and the equilibrium constant of Reaction (R6.3). Kruljevic et al. [208] reached an analogous conclusion in their experimental and numerical study. Therefore, the impact of the equivalence ratio on the OH* concentration in the post-flame equilibrium region is only indirect, as the pivotal role is played by the temperature reached in this zone. This is evident from the plot in Figure 6.12, which shows the OH and OH* concentrations deriving from equilibrium calculations at constant temperature and pressure for lean ($\phi = 0.35$) and stoichiometric ($\phi = 1.0$) mixtures. Calculations are performed adopting the Villars-Cruise-Smith algorithm [375] for $p = 1$ atm and T varying between 1300 K and 2400 K, i.e., the adiabatic flame temperatures obtained from the 1D calcu-

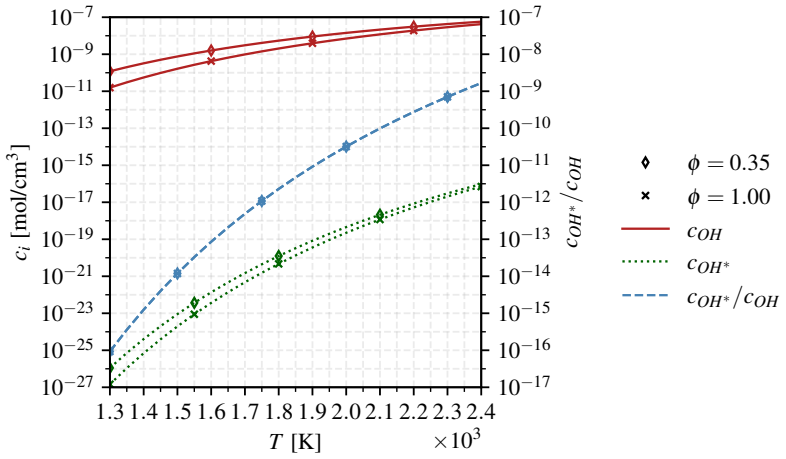

Figure 6.12: OH and OH* concentration obtained from equilibrium calculations at constant temperature and pressure, and ratio of the two concentrations.

lations at $p = 1$ atm and $T_u = 300$ K for $\phi = 0.35$ and $\phi = 1.0$, respectively. Under chemical equilibrium conditions, the concentration of OH* can be estimated from the kinetic equilibrium of Reaction (R6.3), described by:

$$\frac{c_{\mathrm{OH}^*}}{c_{\mathrm{OH}}} = \frac{1}{K_{\mathrm{OH}^*}(T)}, \tag{6.6}$$

where $K_{\mathrm{OH}^*}(T)$ is the equilibrium constant [140]. Figure 6.12 shows that this ratio is coincident for the two equivalence ratios, and depends only on the temperature.

Therefore, the formation pathways of Reactions (S1) and (S22) impact mostly on the shape of the OH* distribution, especially in the post-flame region, while the final value of OH* intensity depends mainly on Reaction (R6.3) (i.e., Reactions (S3) to (S10) for the mechanism in Table 6.2), as well as on the correct prediction of the OH concentration by the adopted main reaction mechanism describing H_2 oxidation. This also explains the results previously observed in Figure 6.10 when comparing the two OH* sub-schemes by Kathrotia et al. [190] and by Sharipov et al. [362, 363]. Indeed, for lean flames, differences are less accentuated as both rely on Reaction (R6.1) as the main OH* formation pathway. However, for the stoichiometric flames, the OH* peak position and the shape of the distribution in the post-flame region are significantly affected by the presence, in the OH* sub-scheme by Sharipov et al. [362, 363], of Reaction (S22) as OH* formation pathway. This further accentuates the peak shift between the OH* and HRR distributions previously observed in Section 6.3 using the OH* sub-scheme by Kathrotia et al. [190].

The analysis on the OH*-HRR correlation is now extended to the whole set of operating conditions of interest in Figure 6.13, which reports the values of the normalized peak shift δ under varying operating conditions, in terms of equivalence ratio ϕ, pressure p and unburned gas temperature T_u. Two maps are reported, one fixing the unburned gas temperature at $T_u = 600$ K, and the other fixing the operating pressure at $p = 1$ atm, to which isolines of the error estimator $\bar{\zeta}$ and of the Pearson coefficient r_{OH^*} are superimposed. The widest peak shift is obtained for equivalence ratios close to stoichiometry at all pressures and temperatures. When keeping the unburned gas temperature constant (see Figure 6.13a), the normalized peak shift is not significantly affected by the variation of pressure. On the other hand, when keeping the pressure constant, the peak shift is positively affected by an increase in temperature, while for atmospheric conditions

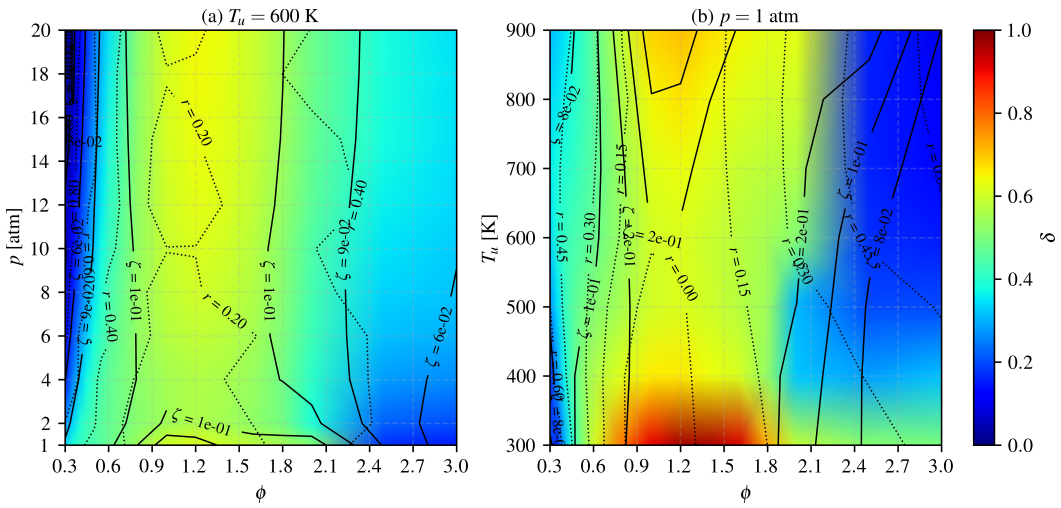

Figure 6.13: Normalized peak shift δ in unstrained premixed flames as a function of ϕ, p and T_u, for $T_u = 600$ K (a) and $p = 1$ atm (b). The isolines indicate the corresponding values of $\bar{\zeta}$ (solid lines) and r_{OH^*} (dotted lines).

(i.e., $p = 1$ atm and $T_u = 300$ K) it reaches the highest value. As for the other two coefficients, $\bar{\zeta}$ and r_{OH^*}, both have a good agreement, in terms of trends, with δ. This result is expected for $\bar{\zeta}$, since its value is computed in the reactive region, where the peak shift occurs. However, this agreement is less trivial for r_{OH^*}, as this is computed in the whole domain. For this latter, as previously observed in Figure 6.10, the results are affected by the concurrent presence of OH* in the post-flame region for near-stoichiometry mixtures. Overall, the observations made for the three representative operating conditions in Figure 6.10 and Table 6.4 can be extended to the whole range of interest.

6.4.2 Stretched laminar premixed flames

To investigate the effect of the two components of stretch, namely strain and curvature (see Section 2.5.3), two different laminar premixed configurations, i.e., the 1D twin counterflow flame (see Figure 3.1b) and the 2D cylindrical expanding flame (see Figure 5.18), are here considered. The first one is subject to pure strain, while the second one to both strain and curvature [36].

Response to strain

Twin counterflow premixed flames are computed at the same three operating points previously investigated for unstrained 1D flames in Figure 6.10, to isolate the effect of varying pressure, unburned gas temperature and equivalence ratio. The distance d between the jets in the numerical domain is of 5 cm, and only half the domain is solved, exploiting symmetry arguments (see Section 3.1). The grid refinement is imposed with a ratio of 2.0, a slope of 0.0025, a curve of 0.0025 and a prune of 0.001 (see Section 3.1), resulting in a grid size of at least 2500 points.

Figure 6.14 shows the normalized distributions of OH* concentration and HRR for lean ($\phi = 0.35$) and stoichiometric ($\phi = 1.0$) premixed flames, considering two strain rate values: $a = 2.5 \times 10^3$ s^{-1} (top and mid) and $a = 1.0 \times 10^4$ s^{-1} (bottom). The values of the normalized peak distance δ for the strained flames (δ_{st}) are reported, together with those of the corresponding unstrained cases of Figure 6.10 (δ_{un}) to ease the comparison.

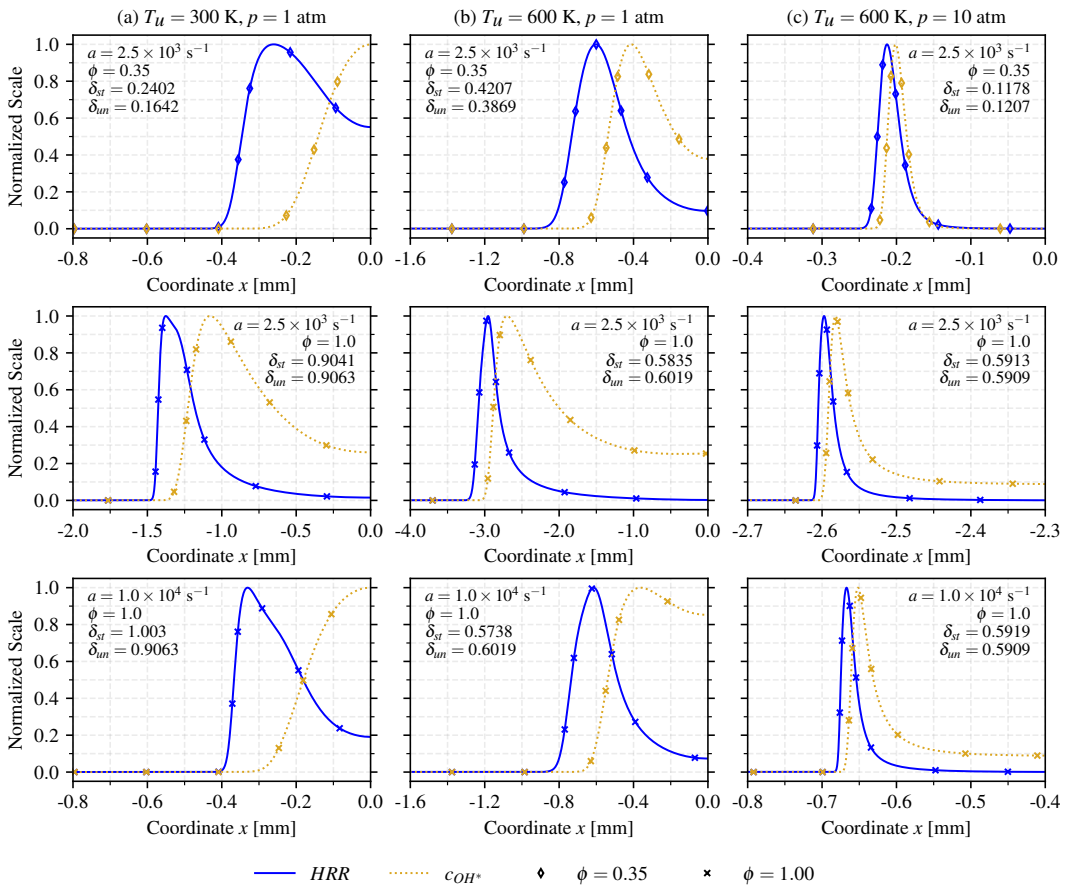

Figure 6.14: Normalized distributions of HRR and OH* concentration for strained counterflow lean ($\phi = 0.35$, top) and stoichiometric ($\phi = 1.00$, mid and bottom) premixed flames at $T_u = 300$ K and $p = 1$ atm (a), $T_u = 600$ K and $p = 1$ atm (b), and $T_u = 600$ K and $p = 10$ atm (c) for a strain rate a equal to 2.5×10^3 s^{-1} (top and mid) and 1.0×10^4 s^{-1} (bottom). The coordinate $x = 0$ corresponds to the symmetry plane of the twin counterflow flame configuration. The values of the normalized peak distance δ for the strained flames (δ_{st}) and the corresponding unstrained flames (δ_{un}) are reported too.

It is noted that flame strain has a limited impact on the peak shift between the OH* and HRR distributions, with the value of δ for each case remaining close to the one obtained for the corresponding unstrained flame. The sole exceptions are represented by the lean premixed flame with strain $a = 2.5 \times 10^3$ s^{-1} (see Figure 6.14a-top) and the stoichiometric premixed flame with strain $a = 1.0 \times 10^4$ s^{-1} (see Figure 6.14a-bottom) at atmospheric conditions. For these cases, however, the strain value is close to the extinction one and the OH* concentration does not reach the equilibrium at the symmetry plane, thus justifying the discrepancies with the other cases.

The most significant impact of flame strain is represented by an increased production of OH* in the burnt gas region, with the final concentration being much closer to the peak value than in the unstrained case. This is evident, for example, for the lean flame with strain $a = 2.5 \times 10^3$ s^{-1} at $T_u = 600$ K and $p = 1$ atm (see Figure 6.14b-top), and is the result of stretch-chemistry interaction. Indeed, as discussed in Section 4.2.3, H_2 preferential diffusion induces local variations of the equivalence ratio for lean premixed H_2-air flames. In stretched flames, these promote the flame temperature, thus favoring faster reaction rates and the production of radicals such as H and OH [64], which were shown in Sections 6.3.1 and 6.4.1 to determine the OH* concentration. Overall, the correlation between OH* and HRR, in terms of similarity of the two distributions,

Table 6.5: Main parameters for the 2D cylindrical expanding flame simulations.

Description [unit]	Value		
	EF-1	EF-2	EF-3
Equivalence ratio ϕ [-]	0.35	1.0	0.35
Pressure p [atm]	1.00	1.00	10.0
Unburned gas temperature T_u [K]	300	300	600
Laminar flame speed S_L^0 [m/s]	0.11	0.21	0.25
Adiabatic flame temperature T_{ad} [K]	1310	2385	1570
Laminar flame thickness δ_L^0 [μm]	960	330	100
Grid resolution Δ_x [μm]	90	30	9
Number of grid nodes N_{nodes} [-]	1.1×10^5	6.2×10^5	2.8×10^6

is worsened by strain.

Response to strain and curvature

For the 2D expanding flame, the computational domain is defined, as in Section 5.4.2, by a quarter-circle of radius 30 mm. Three cases are considered: a lean ($\phi = 0.35$) flame and a stoichiometric ($\phi = 1.00$) flame at $T_u = 300$ K and $p = 1$ atm, denoted as EF-1 and EF-2, respectively, and a lean ($\phi = 0.35$) flame at $T_u = 600$ K and $p = 10$ atm, referred to as EF-3. Table 6.5 reports the main flame properties and computational grid parameters for the three cases. The mesh is unstructured and made of tetrahedral elements. The numerical methodology is analogous to the one adopted for the simulation of the triple flame in Section 6.3.2. An initial sinusoidal perturbation is imposed to the flame front to promote intrinsic instabilities. The same definition of the mean flame radius r in Section 5.4.2 (see Equation (5.26)) is adopted, based on the progress variable C defined on the water mass fraction [424]. The mean flame stretch $\bar{\kappa}(t)$ at each time instant (t) is derived from r based on Equation (5.28), while the instantaneous mean geometrical curvature is given by $\bar{\kappa}^*(t) = 1/r(t)$.

The results obtained for the three operating points are reported in Figures 6.15 to 6.17. For each flame, the 2D normalized HRR distributions and normalized OH* isolines (at 20%, 50% and 90%) are shown, together with 1D profiles of both HRR and OH* retrieved along radii at two angular coordinates: $\theta = \pi/12$ and $\theta = \pi/4$, with $\theta = 0$ corresponding to the x axis. Two values of $\bar{\kappa}^*$ are considered: a low geometrical curvature case at $\bar{\kappa}^* = 40$ m^{-1}, and a high geometrical curvature case at $\bar{\kappa}^* = 400$ m^{-1}.

Overall, the 1D profiles obtained for this flame configuration are similar in shape to those retrieved for the 1D unstrained and strained premixed flames in Figures 6.10 and 6.14, showing the characteristic peak shift between the two distributions and the presence of a non-negligible concentration of OH* in the post-flame zone for the stoichiometric case (see Figure 6.16). Nevertheless, the 2D configuration allows to gain further insights due to the presence of intrinsic cellular instabilities, both hydrodynamic and thermodiffusive. The latter, in particular, are evident in the lean cases of Figures 6.15 and 6.17, due to the sub-unity Lewis number of the mixture.

Considering first the two flames at atmospheric conditions (see Figures 6.15 and 6.16), due to the presence of intrinsic cellular instabilities at lower stretch values, local differences are promoted for both OH* and HRR distributions in the lean EF-1 case (see Figure 6.15). The two distributions peak in the zones with positive local curvature. Furthermore, the OH* concentration isolines show that, for the regions of lower HRR (i.e., the zones with negative local curvature), the OH* concentration becomes negligible, hence making this quantity unable to capture the entire

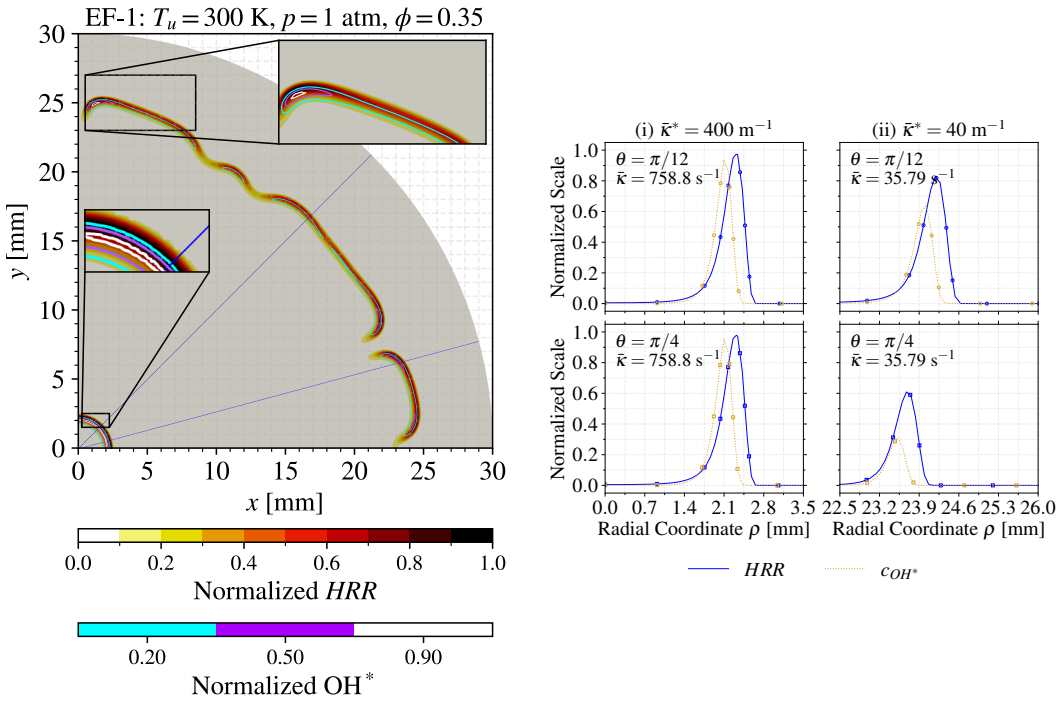

Figure 6.15: Normalized distributions of HRR and OH* concentration for premixed cylindrical expanding flames with mean geometrical curvatures equal to $\bar{\kappa}^* = 40$ m^{-1} and $\bar{\kappa}^* = 400$ m^{-1}. The 2D normalized distribution of HRR and isolines at 20%, 50% and 90% of normalized OH* concentration are reported on the left, with insets zooming in selected regions. The blue lines denote the radii at $\theta = \pi/12$ and $\theta = \pi/4$, along which the 1D profiles of the distributions are reported on the right, with the corresponding mean flame stretch $\bar{\kappa}$. The distributions are normalized by the global maximum value. Case EF-1: $T_u = 300$ K, $p = 1$ atm and $\phi = 0.35$.

flame front. The worse OH*-HRR correlation is obtained at low stretch values, where the instabilities are enhanced, coherently with the analysis performed in [254] for lean premixed H_2–air cellular tubular flames. Therefore, while, for the stable stoichiometric EF-2 case (see Figure 6.16), the 1D profiles at $\theta = \pi/12$ and $\theta = \pi/4$ are similar, this is not true anymore for the lean one, for which the peak values both of HRR and OH* concentration are different for the two radii. Finally, the peak values of the two distributions do not scale in the same way, indicating that the OH* is not a reliable HRR marker both qualitatively (i.e., in terms of distribution shape and peak position) and quantitatively. This confirms the pivotal role of the H radical for the OH*-HRR correlation discussed in Section 6.3, as this species drives the differential diffusion mechanism at the basis of TD instabilities.

The case EF-3 (see Figure 6.17) shows more pronounced cellular structures and flame front wrinkling compared to the case EF-1 (see Figure 6.15). This is caused by the increased pressure, which enhances TD instabilities (see Section 4.2.3), overcoming the opposite effect of the increased unburned gas temperature. Similar features as for the corresponding lean case at atmospheric conditions can still be observed, with the intrinsic cellular instabilities significantly impacting the OH* and HRR distributions. Interestingly, for the case at $\bar{\kappa}^* = 40$ m^{-1} and $\theta = \pi/12$, in which the flame is locally extinguished, the normalized OH* concentration is sensibly lower than the normalized HRR, confirming that the two distributions do not respond similarly to TD effects.

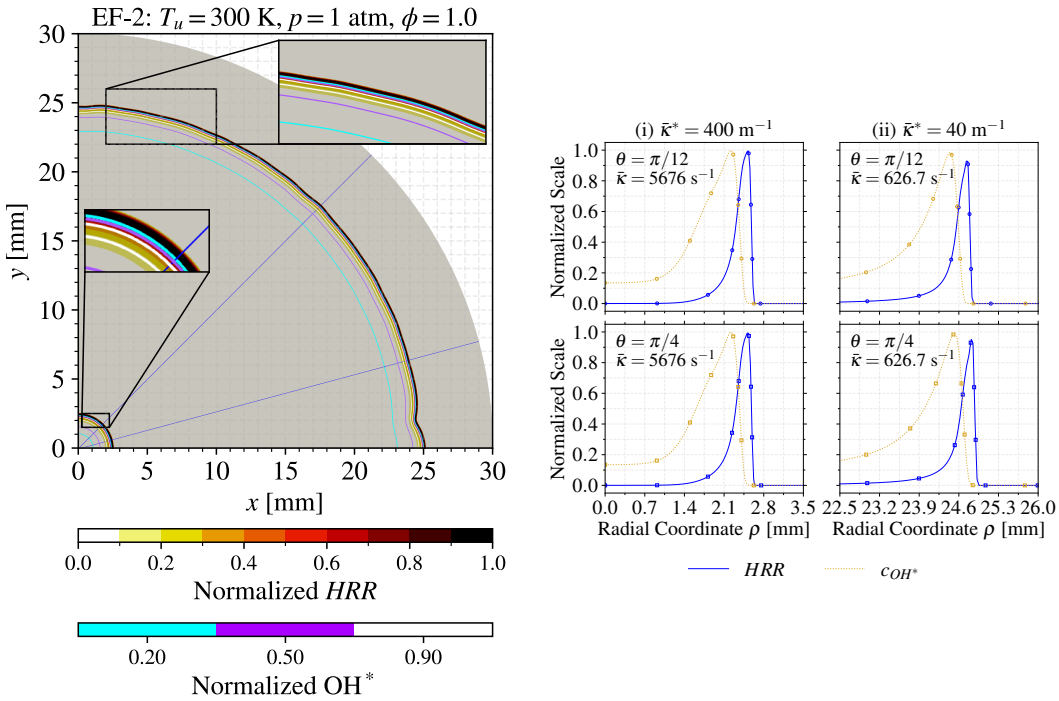

Figure 6.16: Case EF-2: $T_u = 300$ K, $p = 1$ atm and $\phi = 1.0$. Normalized distributions of HRR and OH* concentration, as labeled in Figure 6.15.

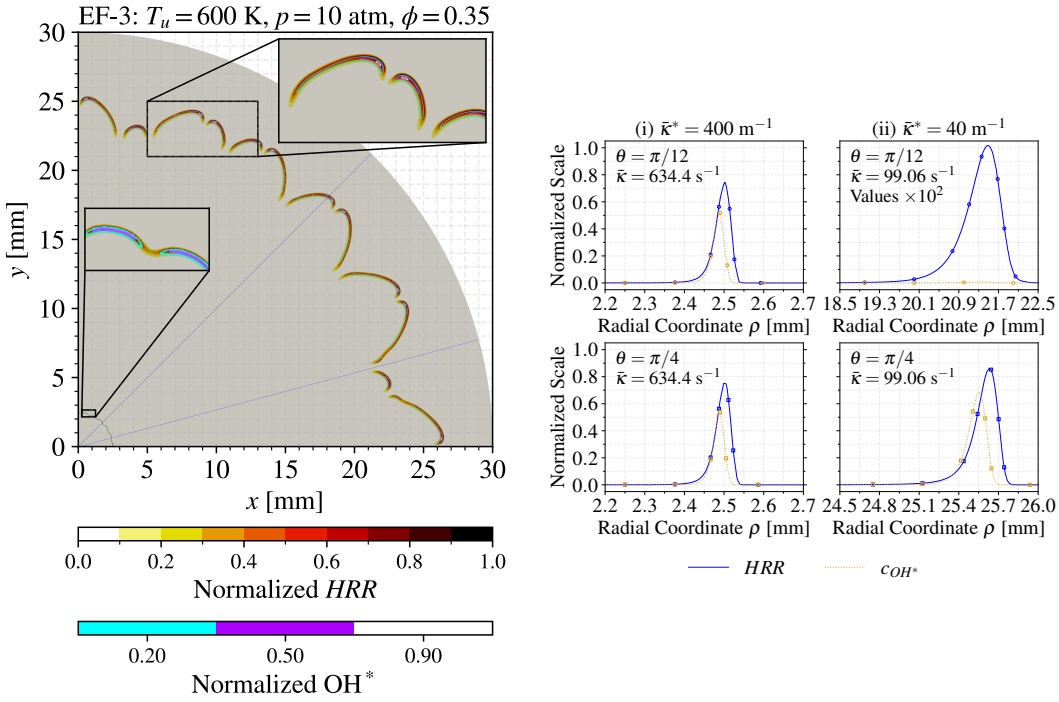

Figure 6.17: Case EF-3: $T_u = 600$ K, $p = 10$ atm and $\phi = 0.35$. Normalized distributions of HRR and OH* concentration, as labeled in Figure 6.15.

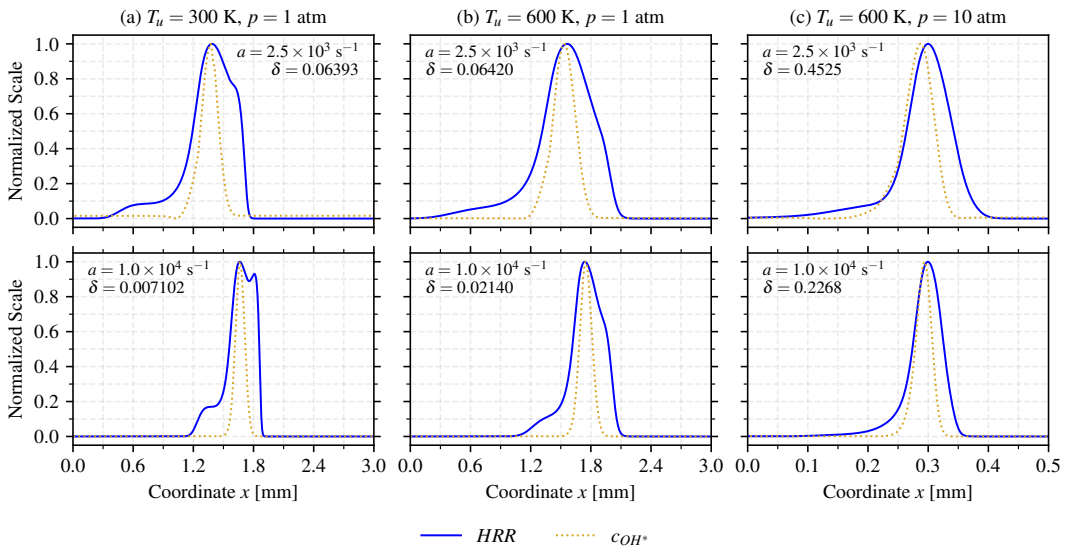

Figure 6.18: Normalized distributions of HRR and OH* concentration for strained counterflow diffusion flames at $T_u = 300$ K and $p = 1$ atm (a), $T_u = 600$ K and $p = 1$ atm (b), and $T_u = 600$ K and $p = 10$ atm (c) for a strain rate a equal to 2.5×10^3 s^{-1} (top) and 1.0×10^4 s^{-1} (bottom). The peak distance δ, normalized by the corresponding stoichiometric premixed flame thickness, is reported too.

6.4.3 Laminar diffusion flames

Finally, the impact of varying operating conditions is here considered for counterflow laminar diffusion flames, thereby complementing the analysis performed at atmospheric conditions in Section 6.3. Due to the stiffer nature of the counterflow diffusion flame configuration compared to the premixed ones, the scaling rules presented in Section 3.1 are implemented, and less severe refinement criteria are adopted (a ratio of 2.0, a slope of 0.05, a curve of 0.05 and a prune of 0.04), resulting in a grid size in the order of 250 points.

Figure 6.18 reports the normalized distributions of OH* concentration and HRR for H_2-air counterflow diffusion flames, together with the peak-to-peak distance δ, here normalized by the laminar flame thickness of the corresponding unstrained stoichiometric premixed flame. To ease the comparison with the premixed flames in Figures 6.10 and 6.14, the same operating points (i.e., $T_u = 300$ K and $p = 1$ atm, $T_u = 600$ K and $p = 1$ atm, and $T_u = 600$ K and $p = 10$ atm) and global strain rate values (i.e., $a = 2.5 \times 10^3$ s^{-1} and $a = 1.0 \times 10^4$ s^{-1}) are considered.

At least for the cases at atmospheric pressure (see Figure 6.18a-b), the peak shift between the two distributions is sensibly reduced, with the value of δ being one order of magnitude smaller than in the corresponding premixed cases. Due to the significantly smaller size of the flame front, the reduction of δ for the case at $p = 10$ atm (see Figure 6.18c) is less accentuated. The peak shift is also reduced for an increased strain rate value, sustaining the adequacy of OH* concentration as a marker of the HRR peak in diffusion H_2-air flames.

A special remark has to be done, however, for the case at atmospheric conditions. As previously observed in Section 6.3, in this case the peak shift actually increases for strain rate values closer to the extinction condition due to the bimodal nature of the HRR distribution shown in Figure 6.5 and, here, in Figure 6.18a (bottom). The impact of this on the OH*-HRR correlation can be quantified through the coefficients $\bar{\zeta}$ and r_{OH^*}. Indeed, at atmospheric conditions, when passing from $a = 2.5 \times 10^3$ s^{-1} to $a = 1.0 \times 10^4$ s^{-1}, the value of $\bar{\zeta}$ increases from 0.1038

to 0.1622, and the value of r_{OH^*} decreases from 0.6874 to 0.5769, both denoting a worse correlation. Nevertheless, these values of $\bar{\zeta}$ and r_{OH^*} are significantly higher if compared to the premixed cases (e.g., see Table 6.4), thus confirming the adequacy of OH* concentration as a HRR marker in diffusion H_2-air flames for all the operating conditions of interest.

6.5 Summary and concluding remarks

The OH* distribution and its relation with the heat release rate were investigated numerically in this Chapter for laminar and turbulent hydrogen–air flames.

First, the differences in the OH* production between hydrogen and hydrocarbons were investigated in laminar premixed one-dimensional flames, by comparing stoichiometric methane–hydrogen–air mixtures with variable hydrogen content. For pure hydrogen, OH* was found not to adequately mark the position of maximum heat release rate, since a shift between the two peaks was observed. For fuel mixtures containing methane, instead, a good correlation between OH* and heat release rate was retrieved. To understand the mechanisms at the origin of these differences, flame structures were analyzed, emphasizing the pivotal role of the H radical, in particular in the main reaction pathways leading to OH* formation and heat release rate. The chain-branching nature of hydrogen–air flames was found to enhance the H radical pool in the post-flame region leading to OH* formation. Heat release rate was shown to peak further upstream than OH*, being linked to the HO_2 radical generated by the recombination reactions of the back-diffused H radical. A chain-terminating behavior was observed, instead, for methane and methane-hydrogen flames, where CH_4 consumes the H radical, generating heat release rate and preventing the radical pool formation in the post-flame zone, thereby leading to different OH* formation pathways linked to CH.

Subsequently, the role of the flame regime was highlighted in hydrogen–air flames. Indeed, OH* was shown to be a more adequate heat release rate marker for laminar strained counterflow diffusion flames, at least at strain rates far from extinction. Indeed, differently from premixed flames, in this case heat release rate is dominated by the direct consumption of the H radical on the fuel side. At higher strains, reactions based on the HO_2 radical were observed to become more important, leading to a shift in the heat release rate global maximum not followed by OH*. Still, being close to the extinction strain rate, this has limited practical interest. The difference between the premixed and diffusion regimes was further confirmed in a laminar two-dimensional triple flame, where the two cohexist in the same configuration. Moreover, in this configuration, OH* was observed in the burned gases of the diffusion branch, due to the significantly high temperature of the reactants, highlighting the role of temperature in the OH* formation process independently of the flame regime. Furthermore, the capabilities of OH* numerical predictions to well represent experimental findings were investigated by analyzing LES data of attached and lifted turbulent hydrogen–air flames stabilized over the HYLON injector at IMFT. In agreement with the observations made for laminar one-dimensional flames, a good match was observed for the diffusion flame branch between the LES-computed time-averaged normalized heat release rate and the experimental mean normalized Abel-deconvoluted OH* chemiluminescence distributions. For the lifted partially premixed flame branch, instead, LES-predicted heat release rate showed an axial shift with respect to the experimental OH*, while a better agreement was found between experimental and numerical normalized OH* fields, highlighting the importance of adding a OH* sub-scheme to directly compare numerical simulations of premixed and partially premixed hydrogen-air flames with experiments.

The impact of operating conditions, in terms of equivalence ratio, unburned gas temperature, pressure, and stretch, on the correlation between OH* and heat release rate was further investigated numerically. To this scope, first, one-dimensional unstrained premixed flames were studied. The impact of the equivalence ratio was highlighted by the fact that near-stoichiometry flames showed a significant amount of OH* in the equilibrium post-flame region, where the heat release rate is instead zero, thus introducing a clear discrepancy in the shapes of the two distributions that worsens the correlation between OH* and heat release rate. A Rate of Production analysis highlighted that the shape of the OH* distribution is mostly impacted by the formation pathways $H + O(+M) \rightleftharpoons OH^*(+M)$ and $H + OH + OH \rightleftharpoons OH^* + H_2O$, while the final OH* concentration depends on the quenching process $OH + M \rightleftharpoons OH^* + M$ and the chemical equilibrium between OH and OH* radicals. Increasing the unburned gas temperature positively affected the peak shift, but increased the OH* content in the burnt gases for near-stoichiometry flames, while an increase of pressure, albeit favoring the correlation, seemed to have a less significant impact. Subsequently, the impact of flame stretch in premixed flames was studied, by considering one-dimensional twin counterflow premixed flames, subjected to flame strain, and two-dimensional cylindrical expanding flames, subjected to both flame strain and curvature. Increasing strain was shown to worsen the correlation in one-dimensional counterflow flames, due to an increased production of OH* in the post-flame region. The two-dimensional simulations showed, instead, the impact of intrinsic flame instabilities on the correlation between OH* and heat release rate in lean hydrogen-air flames. These led to local inhomogeneities both in the OH* and heat release rate distributions, thus worsening the overall correlation. In the diffusive flame regime, instead, increasing stretch was shown to have a positive effect on the correlation between OH* and heat release rate in laminar one-dimensional counterflow flames. Overall, this confirmed that OH* is an adequate marker of the spatial heat release rate distribution only for hydrogen-air diffusion flames, while an error has to be considered both in the peak location and in the distribution shape when dealing with premixed cases.

In addition to the spatial correlation between OH* and heat release rate, the temporal one is also important when studying the dynamics of unsteady flames. Indeed, the OH* chemiluminescent emission has been related to the volume-integrated heat release rate [48, 193], and, since the time derivative of the global heat relese rate drives the acoustic radiation (see Section 7.1.4), it has been used to investigate combustion noise in hydrocarbons (e.g., [49]). Therefore, despite the limits in the spatial correlation with the heat release rate, OH* chemiluminescence may remain an useful technique for the experimental study of flame–acoustics interactions. This will be further investigated in Sections 9.3 and 11.2.2 for acoustically forced laminar M-shaped and turbulent slot jet lean premixed hydrogen–air flames, respectively.

Overall, the results in this Chapter highlight that further investigation is needed to establish a robust spatio-temporal correlation between experimentally measurable markers and the heat release rate for premixed hydrogen–air flames. Some research effort has recently been devoted to this problem (e.g., [105, 208]), by combining experimental OH* chemiluminescence measurements with high-fidelity numerical simulations. Extending such an approach to a wider range of operating conditions and observable quantities could lead to the identification of more adequate markers, thereby enabling a more meaningful validation of numerical simulations. This is especially relevant for engineering-relevant configurations involving turbulent combustion at demanding operating conditions, where turbulence is expected to further degrade the correlation between heat release rate and chemical markers, and high-fidelity numerical simulations are not always computationally sustainable. In this context, the definition of reliable experimental observables becomes a key requirement for the validation of turbulent combustion models.

PART III

Combustion noise in lean premixed hydrogen-air jet flames

Ne pourrait-on conjecturer que le Bruit [...] n'est lui-même que la somme d'une multitude de Sons divers qui se font entendre à la fois ?

Could we not imagine that noise ... is itself nothing more than the sum of a multitude of different sounds, which are being heard simultaneously?

— Jean-Jacques Rousseau
Dictionary of Music, 1767

7

Overview of combustion noise

Noise is a major concern in the design of gas turbines. Prolonged exposure to high noise levels has been shown to produce both short- and long-term physiological effects on humans [96]. As a consequence, increasingly stringent regulations have been introduced to limit noise emissions, particularly in the aviation sector.

A significant contribution to overall noise emissions is provided by the acoustic radiation of flames, commonly referred to as *combustion noise* [96]. This phenomenon originates from the direct coupling between unsteady combustion processes and acoustics. In addition to the environmental impact, combustion noise is also closely related to the broader problem of combustion instabilities. In this context, the flame not only radiates acoustic waves, but is also influenced by them, leading to a potentially destructive resonant amplification [310].

This Chapter focuses on combustion noise, presenting the theoretical foundations required to understand its underlying physical mechanisms and reviewing relevant research developments in the field, in order to place the work of this dissertation within the existing literature.

Contents

7.1 Fundamental concepts

Combustion noise is generally distinguished into two components: direct and indirect [249, 381]. The direct noise is associated to the volumetric expansion and contraction in the reacting region, generated by the fluctuations of heat release rate [37, 95, 381, 393]. It is broadband [392] and monopolar [173]. Moreover, since it is related to the inherent unsteadiness of the combustion process, it occurs even in unbounded spaces [96]. The indirect noise, first identified by Marble and Candel [249] and by Morfey [271] in the 1970s, is an additional noise generated by the interaction of the flame with the surrounding environment. More specifically, it stems from dipole sources associated to the unsteady motion of non-uniform entropy, vorticity or composition distributions [129, 130, 167, 247], which are generated by the unsteady combustion process. Indirect noise typically arises at the outlet of the combustion chamber of a gas turbine [96], where the flow is accelerated through the chocked nozzle [113, 167], or when interacting with the turbine blades [31]. A schematic summary of the different noise sources in a gas turbine combustion chamber is reported in Figure 7.1. This dissertation focuses on direct noise, which is the most relevant for low Mach number flows [235]. In the following, the classical combustion noise theory developed for premixed flames is summarized.

7.1.1 Classical theory of combustion noise

One of the earliest investigations on combustion noise was carried out in the 1960s by Thomas and Williams [393], who measured the acoustic radiation of soap bubbles filled with a reacting mixture. They found that the pressure fluctuation p' generated by this monopolar source and recorded at a position x with respect to the flame was directly related to the rate of volume generation of the flame $\dot{V}$:

$$p'(\mathrm{x},t) = \frac{\rho_\infty}{4\pi|\mathrm{x}|}\left.\frac{d\dot{V}}{dt}\right|_{t-|\mathrm{x}|/c_\infty}, \tag{7.1}$$

where ρ_∞ is the density of the far-field medium at the measurement location. The temporal derivative is to be evaluated at a retarded time $t - |\mathrm{x}|/c_\infty$, where c_∞ is the speed of sound in the

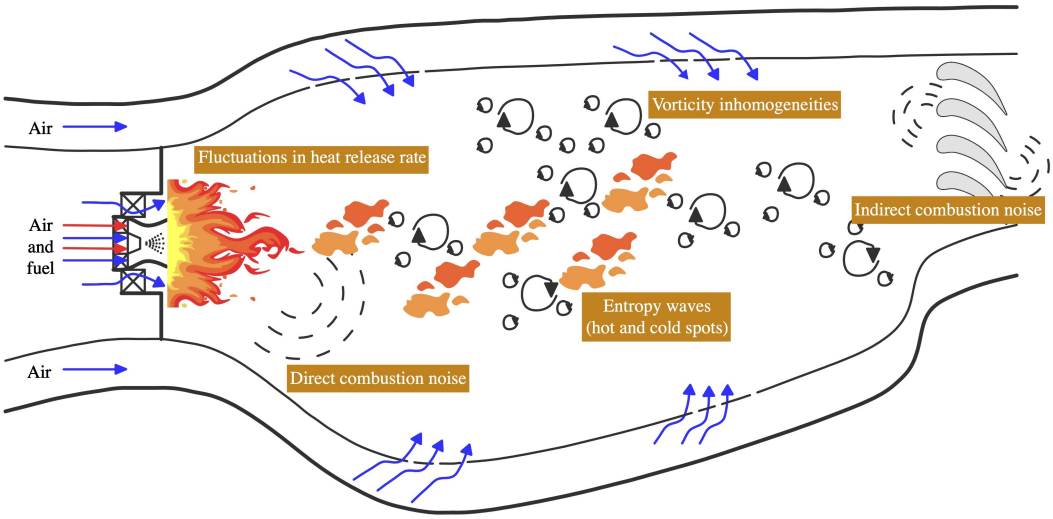

Figure 7.1: Schematic representation of the different combustion noise sources in a gas turbine (adapted from [96]).

far-field medium, to account for the delay necessary for the acoustic wave to propagate. Based on Equation (7.1), a fundamental consideration can be made: noise is associated with unsteadiness in the combustion process. In other terms, steady combustion does not emit noise.

This result, developed for a laminar case [393], has been extended to turbulent premixed flames. Indeed, Bragg [37] postulated that a turbulent flame can be seen as a distribution of multiple combustion elements, each acting as a monopolar noise source. This theory was subsequently verified experimentally by Hurle et al. [170] and Price et al. [315], by associating $\dot{V}$ to the volumetric rate of consumption of the reacting mixture v_c:

$$\dot{V} = (\sigma - 1) v_c, \tag{7.2}$$

where σ is the expansion ratio across the flame, equal to the ratio of the densities of the unburned (ρ_u) and burned (ρ_b) mixtures for a combustion process at constant pressure. Then, Equation (7.1) can be reformulated to express the sound radiation of a single flame element i [170]:

$$p_i(\mathrm{x}, t) = \frac{\rho_\infty}{4\pi|\mathrm{x}|} \left(\frac{\rho_u}{\rho_b} - 1 \right) \left. \frac{dv_c}{dt} \right|_{t-|\mathrm{x}|/c_\infty}. \tag{7.3}$$

For an acoustically compact flame, i.e., when the wavelength of the emitted sound is large compared to the flame dimension, the global radiated noise is given simply by the sum of the terms obtained by applying Equation (7.3) for all flame elements [170, 315].

Based on the flamelet theory (see Section 2.7.4), each infinitesimal element of a turbulent flame can be seen as a laminar flame. This propagates at a constant flame speed S_L^0, when the effect of stretch (see Section 2.5.5) is neglected, which is acceptable in the case of unity effective Lewis number Le_{eff} of the reacting mixture. In this framework, Abugov and Obrezkov [2] and, independently, Clavin and Siggia [69], related the fluctuations of v_c to those of the flame surface $\mathcal{A}_f$:

$$\frac{dv_c}{dt} = S_L^0 \frac{d\mathcal{A}_f}{dt}, \tag{7.4}$$

allowing for the following expression of the acoustic radiation at the location x [48]:

$$p'(\mathrm{x}, t) = \frac{\rho_\infty}{4\pi|\mathrm{x}|} \left(\frac{\rho_u}{\rho_b} - 1 \right) S_L^0 \left. \frac{d\mathcal{A}_f}{dt} \right|_{t-|\mathrm{x}|/c_\infty}. \tag{7.5}$$

This relation has been adopted in experimental studies to evaluate the sound radiated both by acoustically forced laminar flames [353, 355] and turbulent flames [22, 400]. When stretch effects are relevant, as it occurs for $Le_{eff} < 1$ (see Section 2.5.5), the following expression may be considered [48]:

$$p'(\mathrm{x}, t) = \frac{\rho_\infty}{4\pi|\mathrm{x}|} \left(\frac{\rho_u}{\rho_b} - 1 \right) \left. \frac{d}{dt} \int_{\mathcal{A}_f} S_d d\mathcal{A} \right|_{t-|\mathrm{x}|/c_\infty}, \tag{7.6}$$

which takes into account the local flame displacement speed S_d (see Section 2.5.1), depending both on stretch and time.

All the above expressions are based on the assumption that the acoustic source is monopolar, as verified in experimental works both for laminar [199, 393] and turbulent flames [2, 170, 315, 374]. While this indicates that combustion noise is radiated isotropically, directivity effects are still present in actual flames, which are spatially extended sources that interact with the mean flow. For example, Smith and Kilham [374] observed, for open turbulent jet flames, a preferred

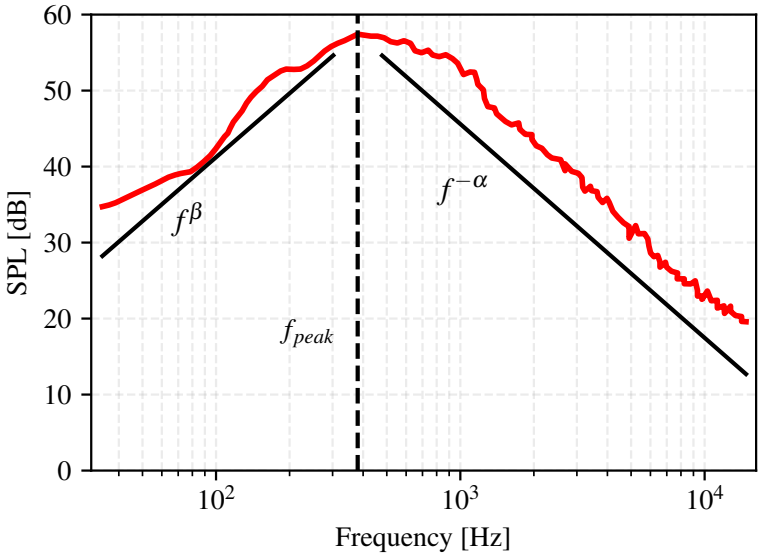

Figure 7.2: Typical direct combustion noise spectrum (adapted from [318]).

direction of acoustic radiation between 40° and 80° from the burner axis. A similar result was obtained by Truffaut [400] for the directivity of torch flames in the azimuthal plane, while an absence of directivity was observed in the plane perpendicular to the burner axis, in agreement with the monopolar nature of combustion noise.

7.1.2 Spectral characteristics

Direct combustion noise is broadband, as verified in several studies (e.g., [155, 204]). Rajaram and Lieuwen [318, 319] investigated a wide range of turbulent premixed hydrocarbon unconfined jet flames, focusing on the spectral features. Based on their work, a direct combustion noise spectrum is characterized by a low-frequency side ($f < f_{peak}$) and a high-frequency one ($f > f_{peak}$), both described by a power law dependency, as shown in Figure 7.2. For the low-frequency side, they found that the exponent β is equal to 2, while for the high-frequency one $2.1 \leq \alpha \leq 3.2$ [319]. Similar values have been found in other works in the literature [2, 22, 69, 204, 241].

In between the two, the peak of the acoustic spectrum is found at the frequency f_{peak}. It was shown in [318, 319] that this frequency scales as the ratio of the mean inlet flow speed U and the mean length of the flame brush L_f:

$$f_{peak} \approx \frac{U}{L_f}. \tag{7.7}$$

This result is in agreement with the previous observations by Abugov and Obrezkov [2], who observed that, for a turbulent Bunsen flame, the peak frequency of the acoustic spectrum should be related to the inverse of the residence time of a gas particle in the unburned region. Overall, these results indicate that the spectral characteristics of direct combustion noise for an unconfined flame are not directly dependent on the geometry of the burner or on the particular operating condition.

Tam [391] compared the acoustic spectra of hydrocarbon open flames, low Mach number jets, can-type combustor, auxiliary power units and turbofan engines, showing that the same

spectral shape was retained across the different configurations. This can be explained by the argument contained in the earlier work by Strahle [380], who observed that the frequency content of combustion noise is dominated by the distortion of the flame surface, which is governed by the large scale motions of turbulence. In their recent work, however, based on a large experimental and numerical dataset comprising flames of different fuels and configurations, Kumar et al. [209, 211] observed, in confined flames, a high-frequency decay of f^{-5} for the heat release rate and, consequently, for direct combustion noise (see Section 7.1.4). This was associated to local mixture inhomogeneities in enclosed partially premixed flames, and to the local variation of the chemical time scales within the combustion zone [209].

7.1.3 Scaling laws

The studies by Thomas and Williams [393] on outwardly propagating flames and by Kidin et al. [199] on inwardly propagating flames showed that the sound amplitude is proportional to the square of the flame burning velocity. An empirical scaling law was introduced by Smith and Kilham [374], based on experimental measurements, for the acoustic power $\mathcal{P}$, defined as:

$$\mathcal{P} = \frac{\overline{p'^2}}{\rho_\infty c_\infty} 4\pi |\mathrm{x}|^2. \tag{7.8}$$

In particular, they found, for turbulent jet flames, that:

$$\mathcal{P} \propto \left(\frac{\rho_\infty}{c_\infty}\right) (UDS_L^0)^2, \tag{7.9}$$

where U is the mean inlet flow velocity and D is the burner diameter. Equation (7.9) highlights that the acoustic radiation is related to the flow (U), geometrical (D) and flame (S_L^0) characteristic parameters, as well as to the far-field medium properties (ρ_∞/c_∞).

The impact of the far-field medium is particularly relevant. Indeed, several numerical studies (e.g. [44, 149, 160]) investigated the noise radiation in an environment of burned gases. On the other hand, experimental studies (e.g., [49, 353, 400]) are generally conducted in ambient air. This impacts the term ρ_∞/c_∞ in Equation (7.9), which, for an ideal gas, scales as $T_\infty^{-3/2}$. Consequently, when passing, for example, from an environment of ambient air at the same temperature of the unburned gases T_u to an environment of burned gases at the temperature T_b, the corresponding values of acoustic power are in the ratio:

$$\frac{\mathcal{P}_u}{\mathcal{P}_b} \approx \left(\frac{T_b}{T_u}\right)^{3/2}. \tag{7.10}$$

Typically, $T_b/T_u \approx 6$, which corresponds to a reduction in the acoustic power of 11 dB when passing from an ambient air environment to a burned gas one [400]. In practical flames, where an interface between the burned gases of the reacting region and the ambient medium is present, this affects also the directivity of the radiated sound, as discussed by Truffaut [400].

The more recent work by Rajaram et al. [318] provided the following scaling law for the acoustic power:

$$\mathcal{P} \propto \frac{(\gamma-1)^2}{4\pi\rho_\infty c_\infty^5} f_{char}^2 P_{th}^2, \tag{7.11}$$

where f_{char} is a characteristic frequency, and the thermal power P_{th}, given by the product of the fuel mass flow rate and of the fuel heating value, corresponds to the volume-integrated steady heat

release rate. The value of f_{char} scales with the peak frequency of the acoustic spectrum, which, as discussed in Section 7.1.2, is related, for a jet flame, to the ratio of the mean length of the flame brush L_f and of the mean inlet velocity U. Therefore, Equation (7.11) indicates that:

$$p' \propto \frac{U}{L_f} P_{th}, \tag{7.12}$$

providing a useful practical law to compare the acoustic radiation of different flames.

7.1.4 Acoustic analogy for reacting flows

Acoustic analogies are based on the solution on an inhomogeneous wave equation, derived from the flow conservation equations (see Section 2.3). Different acoustic analogies have been derived in the literature for non-reacting flows. The one proposed by Lighthill [237] is among the most well-known ones. It reads as follows:

$$\frac{\partial^2 \rho}{\partial t^2} - c_\infty^2 \nabla^2 \rho = \frac{\partial^2}{\partial x_i \partial x_j} \left(\rho u_i u_j - \tau_{ij} \right) - \frac{\partial^2 \rho_e}{\partial t^2}. \tag{7.13}$$

The term $\rho u_i u_j$ represents the *fluctuating Reynolds stress*, while τ_{ij} is the viscous stress tensor. Finally, ρ_e is the *excess density*:

$$\rho_e = \rho - \rho_\infty - \frac{p - p_\infty}{c_\infty^2}. \tag{7.14}$$

This term is null in the far-field, but is non-zero in regions where the entropy is significantly different from the ambient [95].

In non-reacting flows, noise is radiated mainly due to the quadrupole source term $\rho u_i u_j$. The other two terms, instead, are of thermoacoustic origin and are often neglected for non-reacting flows, especially at high values of the Reynolds number [237]

On the other hand, they become much more relevant in regions of appreciable irreversible processes, such as combustion [95]. Dowling [95] reformulated Equation (7.13) for reacting flows:

$$\begin{aligned} \frac{1}{c_\infty^2} \frac{\partial^2 p}{\partial t^2} - \nabla^2 p = & \underbrace{- \frac{\partial}{\partial t} \left[\frac{\alpha_v \rho_\infty}{c_p \rho} \left(\sum_{k=1}^{N} \left. \frac{\partial h}{\partial Y_k} \right|_{\rho, p, Y_n \neq Y_k} \rho \frac{D Y_k}{D t} + \nabla \cdot \mathrm{q} - \frac{\partial u_i}{\partial x_j} \tau_{ij} \right) \right]}_{S_1} \\ & + \underbrace{\frac{\partial^2}{\partial x_i x_j} (\rho u_i u_j - \tau_{ij})}_{S_2} \\ & + \underbrace{\frac{1}{c_\infty^2} \frac{\partial}{\partial t} \left[\left(1 - \frac{\rho_\infty c_\infty^2}{\rho c^2} \right) \frac{D p}{D t} - \frac{p - p_\infty}{\rho} \frac{D \rho}{D t} \right]}_{S_3} \\ & + \underbrace{\frac{\partial^2}{\partial x_i \partial t} (u_i \rho_e)}_{S_4}. \end{aligned} \tag{7.15}$$

The operator D/Dt denotes the material derivative, i.e., for a generic quantity ς:

$$\frac{D \varsigma}{D t} = \frac{\partial \varsigma}{\partial t} + \mathrm{u} \cdot \nabla \varsigma. \tag{7.16}$$

The term S_1 is monopolar and describes the sound generated by irreversible flow processes. Its first component, for which α_v is the volumetric expansion coefficient (equal to $1/T$ for an ideal gas) and h is the enthalpy, accounts for the unsteady heat release rate, for the non-isomolar combustion, which is negligible when fuels are burned in air due to the strong dilution in inert nitrogen [400], and for the diffusion of species. Its second part ($\nabla \cdot \mathrm{q}$) is the divergence of the heat flux q, and accounts for the heat conduction noise source [367]. The third part, instead, is associated to viscous dissipation [96].

The term S_2 is the quadrupole source term previously discussed in Equation (7.13) and associated to jet noise in Lighthill's theory [95]. It leads to an acoustic intensity that scales with $\mathcal{M}^8$, where $\mathcal{M}$ is the Mach number [95]. This source generates sound when vorticity is accelerated and when combustion occurs in a confined geometry with a downstream section reduction, contributing to indirect noise [96].

The term S_3 also scales as $\mathcal{M}^8$, with a different coefficient with respect to S_2, and is appreciable in regions of unsteady flow with different mean density and sound speed from the ambient [95]. Nevertheless, its contribution to the overall noise is negligible for low Mach numbers [48, 367].

Finally, the term S_4 is dipole in nature and describes the effect of momentum changes due to density inhomogeneities [95]. It is the source term associated with the entropy and compositional components of indirect combustion noise [96].

When unsteady combustion occurs in a low Mach number flow, S_1 is commonly considered as dominant, taking a value about two orders of magnitude larger than the other source terms [116, 174]. This means that the other terms on the right-hand-side of Equation (7.15) can be neglected. For an ideal gas [95]:

$$\frac{\alpha_v}{c_p} = \frac{\gamma - 1}{c^2}. \tag{7.17}$$

If the heat capacity ratio γ is assumed to be independent of temperature and the combustion process occurs at ambient pressure, as it occurs for an unconfined turbulent flame, then the following relation holds:

$$\rho c^2 = \gamma p_\infty = \rho_\infty c_\infty^2. \tag{7.18}$$

Moreover, by assuming a constant average molecular weight and by neglecting the diffusion of species, the sole HRR source term remains, and then:

$$S_1 = \frac{\gamma - 1}{c_\infty^2} \dot{\omega}_T, \tag{7.19}$$

where $\dot{\omega}_T$ is the volumetric HRR. Consequently, Equation (7.15) reduces to:

$$\frac{1}{c_\infty^2} \frac{\partial^2 p}{\partial t^2} - \nabla^2 p = \frac{\gamma - 1}{c_\infty^2} \frac{d\dot{\omega}_T}{dt}. \tag{7.20}$$

By using the free-space Green function [95], it is then possible to find the solution of Equation (7.20), giving the far-field pressure perturbation p' due to an open flame [95]:

$$p'(\mathrm{x}, t) = \frac{\gamma - 1}{4\pi |\mathrm{x}| c_\infty^2} \int \frac{d\dot{\omega}_T}{dt} d^3\mathrm{y} \Bigg|_{t - |\mathrm{x}|/c_\infty}. \tag{7.21}$$

For an acoustically compact flame, Equation (7.21) leads to the following expression [147]:

$$p'(\mathrm{x}, t) = \frac{\gamma - 1}{4\pi |\mathrm{x}| c_\infty^2} \left. \frac{dq}{dt} \right|_{t - |\mathrm{x}|/c_\infty}, \tag{7.22}$$

where $q = \int \dot{\omega}_T d^3\mathrm{y}$ denotes the volume-integrated HRR. The solution in Equation (7.22) highlights the direct proportionality between the acoustic pressure perturbation and the time derivative of the HRR evaluated at a retarded time [96]. It should be noted that, while valid in the acoustic far-field, Equation (7.22) does not hold true in the near field, which is of particular interest for the investigation of thermoacoustic instabilities in confined systems, such as gas turbine combustion chambers [291].

The fundamental assumption at the basis of Equation (7.22), i.e., the dominance of the HRR term as noise source, is generally accepted. Nevertheless, indirect noise sources, related to local variations of entropy gradients, flow velocity and composition, may become dominant over HRR fluctuations, even in an unconfined space [291, 387]. In this sense, Ho and Talei [160] observed, for hydrogen–methane turbulent premixed jet flames, that, in addition to flame-generated noise associated with the unsteady HRR, additional contributions to the acoustic radiation arise from the boundary noise, due to the interaction of turbulent structures with the domain boundaries, and from turbulence-generated noise, resulting from turbulent eddies in the burned region. This indicates that, depending on the considered configuration, multiple noise sources may actually be present and need to be taken into account.

7.2 Sources of direct combustion noise

Recalling Equation (7.5), the far-field pressure fluctuation can be related to the rate of change of the flame surface area. Based on the discussion in Section 2.7.2, this rate of change increases linearly with the flame surface when this is generated due to the effect of stretch, while it varies with the square of the flame surface when this is destroyed. As a consequence, mechanisms promoting flame surface destruction, or *flame annihilation*, induce more rapid variations of flame surface area, and, consequently, should be stronger noise sources [49].

In the following, two main mechanisms are discussed, based on the literature for hydrocarbons. The first is the *flame–flame interaction*, which leads to mutual annihilation of neighboring flame elements, while the second one is the *flame–vortex interaction*, which involves the extinction of the flame due to large scale vortex structures obtained in the shear layer between a premixed reacting jet and the ambient.

7.2.1 Flame–flame interactions and annihilation events

In their work on inwardly propagating spherical laminar flames, Kidin et al. [199] obtained the detachment of a flame bubble from an acoustically forced conical jet of fuel–air mixture. In this configuration, they observed two peaks in the far-field pressure trace, as shown in Figure 7.3. The first peak is associated with the collapse of the flame neck, leading to the detachment of the bubble from the jet, while the second one is related to the collapse of the bubble itself [199].

These mechanisms were further investigated experimentally by Schuller et al. [353] and Candel et al. [49] in acoustically forced axisymmetric laminar M-shaped premixed jet flames. In this configuration, acoustic waves are generated at the flame neck due to the interaction of the different flame branches and the consequent flame annihilation. The initial deformation occurs at the flame base and is then convected towards the tip, stretching the two flame branches and making them closer. Depending on the operating condition, this leads to the detachment of a flame torus, no torus or multiple tori, highlighting the impact of the spatial position of the first interaction between the flame branches. This mechanism is rapid, hence it produces a faster rate of

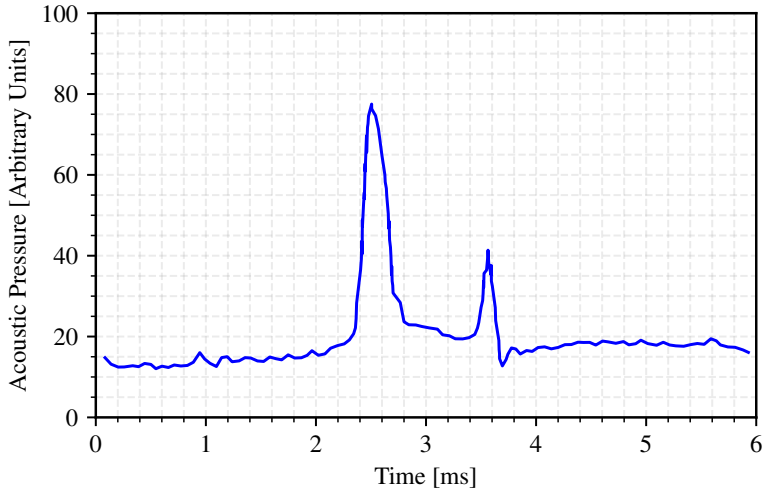

Figure 7.3: Temporal pressure trace, highlighting annihilation events (adapted from [199]).

change of the flame surface with respect to the longer phase of flame surface production due to stretch. Moreover, when in phase quadrature with the inflow forcing, the so-generated pressure fluctuations can lead to self-sustained instabilities [353].

More recently, several numerical studies have been performed to further investigate this mechanism in hydrocarbon flames, considering different configurations. Talei et al. [389] studied the effect of various flame parameters on the sound generated by laminar 1D planar, axisymmetric and spherically symmetric flame annihilation events, providing also a theoretical model to describe it. In particular, they found a dependence of the radiated sound on the laminar flame speed and thickness. Ghani and Poinsot [132] analyzed the impact of chemical modeling on direct combustion noise in a 1D head-on quenching configuration, observing a strong overestimation of the pressure amplitude when adopting a simplified kinetics description. They related this difference to the too rapid extinction of the post-flame region after quenching, due to the absence, in a reduced chemical scheme, of minor species.

The response of acoustically forced 2D slit flames was investigated by Talei et al. [387]. In this configuration, coherently with previous experimental works [49, 199, 353], two typologies of annihilation events were identified. The first one, denominated *flame pinch-off*, corresponds to the detachment of a pocket of reactants from the elongated flame, close to the flame tip. The second one, called *flame island burn-out* in [387], is represented by the progressive consumption of the detached pocket. The pinch-off was found to be the strongest noise source between the two, a result that is consistent with the previously discussed work of Kidin et al. [199] (see Figure 7.3).

A DNS investigation of direct combustion noise in turbulent premixed open jet flames was performed by Haghiri et al. [149], showing that flame annihilation events are strong monopolar sources, which contribute to the far-field acoustics. They also observed that most of these sources are located at the flame tip, in agreement with the previous experimental work of Rajaram and Lieuwen [319]. The same dataset was exploited by Brouzet et al. [41] to investigate the impact of different annihilation event topologies on the generated sound. Most notably, they found that these annihilation events are the dominant noise source in turbulent premixed flames at high frequencies, i.e., for $St > 1$, where St is the Strouhal number. The impact of chemical modeling on the acoustic radiation of 3D turbulent premixed methane–air flames was investigated using

DNS by Brouzet et al. [44], who observed that the flame modeled with detailed kinetics had a lower acoustic power, due to the smaller HRR fluctuations. Nevertheless, they found a stronger content, with the detailed scheme, at high frequencies, due to the formation of more wrinkled flame surfaces with this chemical description.

7.2.2 Flame–vortex interactions

Candel et al. [49] investigated flame–vortex interaction in acoustically excited inverted conical laminar premixed flames. In this configuration, vortical structures are created in the outer mixing layer of the jet, and atmospheric air is entrained by the inner jet of premixed reactants. These vortices stretch the flame, changing the flame surface area and, consequently, generate sound. In this configuration, a lower coherence was observed between the radiated pressure and the chemiluminescent emission, used as a marker of the flame surface and HRR variations. This was attributed to the mixing layer between the jet and the surrounding air, which altered the local composition and, consequently, the local equivalence ratio, thereby affecting the flame speed. Similar results were found also by Durox et al. [101].

The impact of shear layer and hydrodynamic instabilities was investigated by Schlimpert et al. [341, 343] for acoustically forced laminar premixed flames and for turbulent premixed flames. They found that the shear layer triggers the initial wrinkling of the flame at the base, while the hydrodynamic instabilities contribute to the downstream amplification of the disturbance, thereby enhancing the generation of pockets at the flame tip. Moreover, they observed that the flame–vortex interaction is a stronger noise source when the expansion ratio σ is low. Indeed, in this case, the vortices more strongly perturb the flame, enhancing the generated noise [341]. On the other hand, when σ is high, the baroclinic vorticity, associated with the gradient of density, tends to damp the incoming vortices [341].

7.3 Coherent structures and acoustic radiation

Modal decomposition methods, described in Section 3.4, have been widely used to identify coherent structures in reacting and non-reacting flows. In particular, since the leading mode at a given frequency corresponds to the dominant coherent structure at that frequency, SPOD (see Section 3.4.1) is ideal to identify amplitude-modulated instability waves in turbulent flows.

For non-reacting jets, the flow dynamics is governed by three main mechanisms. At very low Strouhal numbers ($St \leq 0.05$), the lift-up mechanism [106] is dominant, based on which streamwise vortices lead to the exchange of fluid perpendicular to the shear layer [335]. The resulting coherent structures are characterized by streamwise elongated regions of high velocity, known as *streaks* [279], which are non-symmetric ($m \neq 0$), and can persist for various azimuthal orders* [304]. An example of streaks, obtained by Pickering et al. [304] using SPOD on a LES dataset of a turbulent non-reacting jet, is reported in Figure 7.4

For the low-intermediate frequency range ($St \lessapprox 0.6$), axisymmetric ($m = 0$) fluctuations appear, associated with coherent structures denominated *wavepackets*, which are responsible for the transport of mass, momentum and energy, and for acoustic radiation [183, 304]. First identified in turbulent jets by Mollo-Christensen [269, 270] in the 1960s, wavepackets are spatial-temporal

*For axisymmetric systems, e.g., round jets, it is possible to work in cylindrical coordinates (r, θ, z). Then, it is possible to decompose the fluctuation in time $\mathrm{q}'(\mathrm{x}, t)$ of a spatial field $\mathrm{q}(\mathrm{x}, t)$ in Fourier modes $\hat{\mathrm{q}}_m$ in the azimuthal direction as $\mathrm{q}'(r, \theta, z, t) = \Sigma_m \hat{\mathrm{q}}_m(x, r, t) e^{im\theta}$, where m is the azimuthal order.

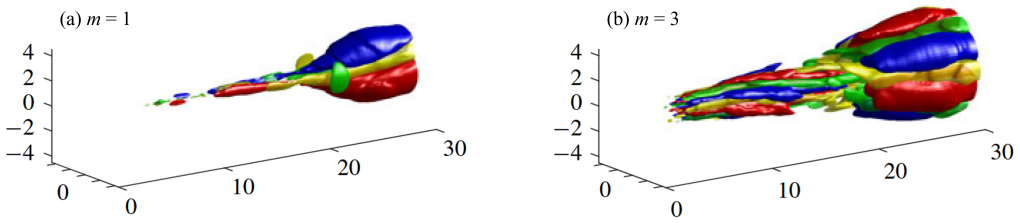

Figure 7.4: Most energetic SPOD mode at $St \to 0$ for azimuthal orders $m = 1$ (a) and $m = 3$ (b) obtained from the LES of a turbulent non-reacting round jet (from [304]). Isosurfaces of streamwise velocity (red and blue) and streamwise vorticity (yellow and green) at $\pm 25\%$ of their maximum value.

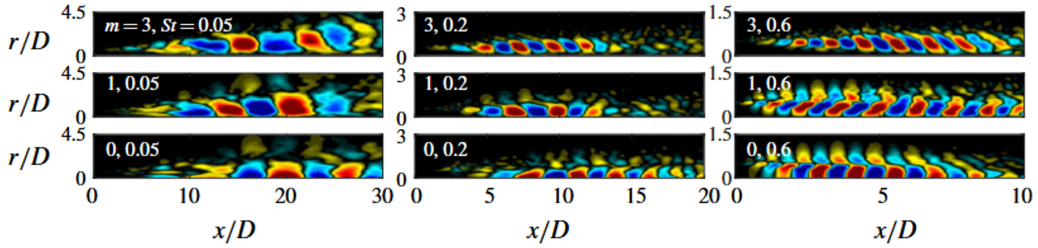

Figure 7.5: Most energetic SPOD modes for $St = [0.05, 0.2, 0.6]$ and azimuthal orders $m = [0, 1, 3]$ obtained from the LES of a turbulent non-reacting round jet (from [304]). Streamwise velocity perturbation, with contours corresponding to $\pm 50\%$ of the streamwise velocity in the ambient far from the jet. The K-H wavepackets dominate at $St = 0.6$ for $m = 0$ and $m = 1$, while the Orr-type wavepackets are more relevant at $St = 0.05$ and $St = 0.2$ for $m = 0$.

structures of size exceeding the integral length scale of turbulence. They can be described as regions of alternating positive and negative fluctuations, coupled with an envelope that modulates their local amplitude [40]. The wavepackets radiate sound due to their subsonic advection, which leads to a leakage of a small amount of their energy to the acoustic far field [183]. In non-reacting turbulent jets, the wavepackets, given their high space-time coherence and intermittency, are considered to dominate the low-frequency acoustic radiation [183]. The wavepackets have been historically related to the Kelvin–Helmholtz (K-H) shear layer instability [56, 57, 304, 347, 384]. In particular, they represent a modal spatial instability wave [347], originating from the amplification of the shear layer instability near the jet nozzle exit, and they decay, becoming stable, as they are convected downstream. The K-H mechanism dominates the dynamics of non-reacting turbulent jets at intermediate frequencies ($St \approx 0.3 - 1$) [304].

In addition to this, however, the presence of a second kind of wavepackets has been observed [347], prominent in the zone downstream of the jet potential core. These have been denominated Orr-type wavepackets [347]. Indeed, Tissot et al. [395, 396] argued that the presence of large-scale structures in this region is related to the non-modal growth of wavepackets through the Orr mechanism. This non-modal mechanism is associated with structures that are initiated with an orientation at 45° against the direction of the mean shear, while the response appears downstream with orientation of 45° along the direction of the mean shear [304]. Therefore, due to the Orr mechanism, structures are tilted, inducing an amplification of the fluctuations [181]. This mechanism dominates in the region where the K-H wavepackets become stable, and is relevant at lower frequencies ($St \approx 0.05 - 0.2$) [304, 347], as well as at high frequencies ($St > 2$), where they dominate at all m [304]. An example of K-H and Orr-type wavepackets, identified by Pickering et al. [347], is reported in Figure 7.5.

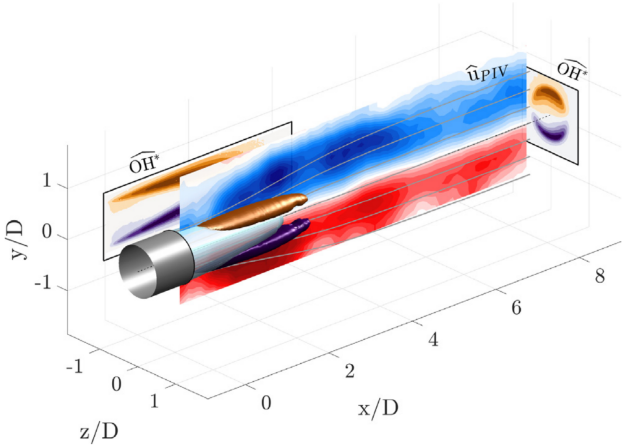

Figure 7.6: Most energetic SPOD mode at $St = 0.006$ obtained from experimental measurements of a turbulent hydrogen jet flame (from [335]). Two-dimensional SPOD modes of PIV (red and blue) and OH^* (orange and purple), and reconstructed three-dimensional OH^* mode. The turquoise isosurface represents the mean flame shape.

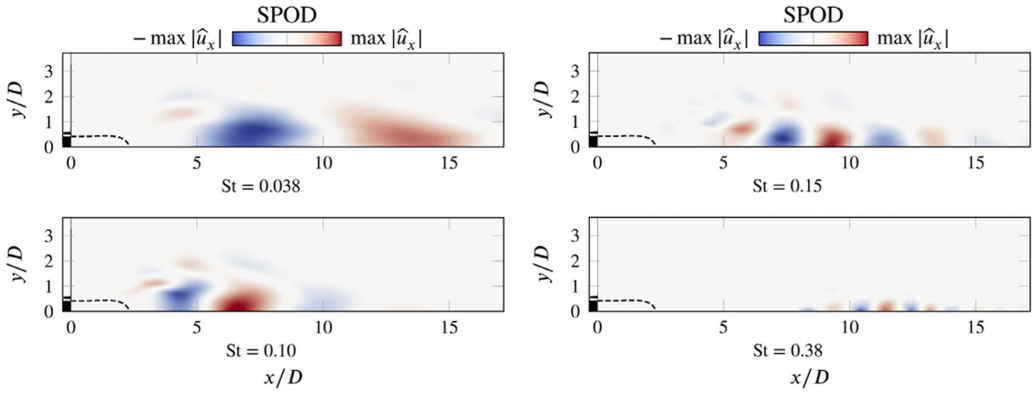

Figure 7.7: SPOD mode at $St = [0.038, 0.10, 0.15, 0.38]$ obtained from the LES of a turbulent methane jet flame (from [54]). Two-dimensional SPOD modes of streamwise velocity u_x. K-H wavepackets are observable for $St < 0.2$. The dashed black line denotes the mean flame position.

These coherent structures have been investigated also in turbulent reacting flows. For example, von Saldern et al. [335] used SPOD to investigate the low frequency dynamics of turbulent lean premixed H_2–air jet flames. By analyzing experimental datasets of OH* chemiluminescence and Particle Induced Velocimetry, they highlighted the presence of almost stationary streaky structures at $St \leq 0.05$, an example of which is reported in Figure 7.6.

As for the wavepacket structures, the K-H mechanism has been observed also when forcing a jet flame with a planar acoustic forcing, leading to a roll-up phenomenon [207, 394]. Moreover, this mechanism shifts to lower frequencies with respect to the non-reacting case. In this sense, Casel et al. [54] applied SPOD to investigate a LES dataset of a swirl-stabilized turbulent CH_4–air jet flame in open air, showing that, when passing from non-reacting to reacting conditions, the K-H wavepackets, present at the shear layer between the combustion products and the ambient air, shifted from $St \approx 0.5$ to $St \approx 0.1$. An example of the K-H wavepackets identified by Casel et al. [54] is reported in Figure 7.7. The presence of the K-H mechanism at $St = 0.1$ was observed also for H_2–air jet flames by von Saldern et al. [335].

The SPOD has been adopted also to investigate thermoacoustic instabilities [123, 187] and combustion noise [42, 364]. In particular, Brouzet et al. [42] applied SPOD to DNS of CH_4–air turbulent premixed round jet flames to investigate the role of wavepackets developed at the flame front in the generation of direct combustion noise. They observed that K-H instabilities are dominant at low-frequency, while the Orr-type mechanism prevails at high frequencies.

7.4 Impact of the Lewis number on combustion noise

Most of the results presented so far have been achieved for hydrocarbon flames. As discussed in Chapter 4, the sub-unity Lewis number strongly affects the dynamics of lean premixed H_2–air flames. This is expected to impact also the features of the acoustic radiation.

Wichman and Vance [421] investigated numerically the annihilation dynamics of 1D laminar premixed flames and found that the flame annihilation characteristic time t_{ann} scales as:

$$t_{ann} \propto 0.98 Le_{eff} \exp\left[-0.416 Ze(Le_{eff}-1)\right], \tag{7.23}$$

where Ze is the Zel'dovich number, defined in Equation (2.47), and Le_{eff} is the effective Lewis number of the mixture. This indicates that, for $Le_{eff} < 1$, the value of t_{ann} is larger and, consequently, the flame annihilation features a less rapid dynamics, weakening its impact as noise source. This was further investigated by Talei et al. [388], who showed, by means of 1D numerical simulations of laminar premixed flames, that, for $Le_{eff} < 1$, the flame consumption speed decreases upon annihilation, slowing down the annihilation event. In a subsequent work, Talei et al. [390] performed numerical simulations of acoustically forced 2D laminar slit flames, and observed that, when $Le_{eff} < 1$, the pressure fluctuation is reduced, even in the presence of larger flame surface fluctuations. They associated this to the reduction in consumption speed previously observed in the 1D case [388]. Moreover, they assessed the validity of the flamelet theory by Clavin and Siggia [69] relating the flame surface to the reaction rate (see Equation (7.4)) for $Le_{eff} \neq 1$. To take into account the effect of stretch on the flame speed (see Section 2.5.5), they replaced S_L^0 with the time-averaged consumption speed $\overline{S_c}$, and they found an overprediction of the radiated sound for $Le_{eff} < 1$. Consequently, they stated that the flamelet theory is not valid in this case, due to the local variation of consumption speed.

These studies, however, were based on a simplified chemical description, in which the Lewis number was artificially modified to retrieve the desired flame properties. Jiménez et al. [180] investigated numerically the noise generated by the flame annihilation of 1D laminar premixed H_2–air flames, considering both detailed and simplified kinetics. In this context, they confirmed the observations made in [388, 390] on the reduction of consumption speed upon annihilation, and, consequently, on the role of Le_{eff} in the sound generation process. Moreover, they observed that a simplified kinetics is able to well predict the radiated sound due to the annihilation phenomenon for $Le_{eff} \leq 1$, while an overestimation was observed for higher values.

All these works did not address the role of thermodiffusive instabilities, which are characteristic of lean premixed H_2–air flames and influence the flame wrinkling and annihilation dynamics (see Section 4.2.3). Pedro-Beltran et al. [292] investigated numerically the impact of non-equidiffusion on both the dynamics and acoustic radiation of 2D unforced lean premixed H_2–air slit flames over a range of equivalence ratios ($0.4 \leq \phi \leq 0.7$). In this configuration, flame pinch-off, pocket shedding, and flame tip oscillations were observed as part of a sustained, quasi-periodic instability cycle, and influenced the acoustic response, leading, particularly, for $\phi > 0.5$, to pronounced spectral peaks at intermediate frequencies, between 1000 and 1200 Hz. While this is

apparently in contradiction with the previously discussed work of Talei et al. [390], the two sets of results are not fundamentally inconsistent. Rather, they point to different flame–acoustics interaction: in [390], isolated annihilation events were observed in externally forced flames with no TD instabilities, while in [292] TD instabilities leaded to sustained phase-coherent HRR oscillations that actively shaped the acoustic radiation. Overall, all the studies consistently demonstrate the importance of diffusion properties in combustion noise generation.

Studies specifically devoted to the acoustic radiation of turbulent lean premixed H_2–air flames are relatively scarce in the literature. Shoji et al. [364] performed an experimental analysis of a low swirl turbulent jet flame, and observed, for $\phi \geq 0.45$, the insurgence of double peaks at intermediate frequencies (between 500 and 1500 Hz) in the acoustic spectrum, as well as in the spectrum of OH* chemiluminescence, used as a marker of HRR. Based on a SPOD analysis (see Section 3.4.1), they related the first peak to the large scale flame fluctuations, and the second one to the local insurgence of vortical structures periodically generated around the flame surface. These were shown to be the result of the engulfment of the lean fuel zone by a large scale vortex, generated by the interaction of the flame with the shear layers. Further insights on the acoustic radiation of this experimental configuration were provided by Pillai et al. [305], who investigated it by means of LES, coupled with a Computational Aeroacoustics solver. In this work, they verified that the second peak in the acoustic spectrum was associated to local HRR fluctuations, due to flame–vortex interaction.

Numerical investigations of combustion noise of turbulent H_2–air flames using DNS are even rarer in the literature. A notable contribution in this sense is represented by the work of Swaminathan et al. [385], who exploited an existing DNS dataset, including lean ($\phi = 0.6$) premixed H_2–air turbulent planar flames from [274], to investigate the two-point HRR spatial correlation, responsible for acoustic radiation. They also evaluated the overall acoustic radiation, but did not consider the frequency content of the emitted sound. Pillai [306] used DNS to investigate the direct combustion noise generated by two open turbulent non-premixed H_2 jet flames at different Reynolds number, and found that the increase in the Reynolds number promoted turbulent velocity fluctuations, leading to stronger HRR fluctuations and, consequently, to enhanced radiated noise. Based on the available literature, the acoustic radiation of turbulent open lean premixed H_2–air flames, and its interplay with TD instabilities characteristic of these flames, has not been addressed using DNS.

7.5 Summary and positioning of the present work

The provided literature review showed that, while the knowledge of the physical mechanisms associated with direct combustion noise generation are well consolidated for hydrocarbon flames, this is not true anymore for lean premixed hydrogen–air flames, due to the impact of diffusion properties.

Acoustically forced laminar flames have been widely used in the literature to investigate the dynamics and noise generation of premixed hydrocarbon flames, especially from an experimental point of view [49, 353]. The different annihilation dynamics in the case of sub-unity Lewis numbers [180, 388, 390], however, mandates a thorough study of the interaction between laminar premixed hydrogen–air flames and acoustic perturbations, and of the role of thermodiffusive instabilities in this interplay. In Chapter 9, acoustically forced laminar M-shaped premixed flames will be investigated to elucidate this mechanism and highlight the differences with respect to conventional hydrocarbons in the noise generation process.

Numerical investigations of direct combustion noise in turbulent flames using DNS are rare in the literature (e.g., [44, 149]), and even rarer for lean premixed hydrogen–air flames, with no study, based on available literature, focusing on the interplay between thermodiffusive instabilities, turbulent mixing, unsteady heat release rate, and acoustic radiation. In Chapter 11, a robust DNS dataset of turbulent lean premixed hydrogen–air flames will be exploited to this scope, highlighting the peculiar features in the acoustic radiation of these flames.

Moreover, the impact of the far-field medium and of shear layers on the acoustic field will be investigated in Chapter 11. Indeed, when switching from methane to hydrogen, the density and the speed of sound of combustion products become, respectively, significantly lower and higher compared to pure air conditions [276]. This is expected to induce differences in the mixing and shear layers when an unconfined jet in ambient air is considered, affecting the coherent structures observed using modal decomposition methods for hydrocarbon flames [54].

Another relevant aspect to consider is the influence of the Karlovitz number. Indeed, as detailed in Section 4.3.2, the synergistic interplay between thermodiffusive instabilities and turbulence is modified depending on this parameter. This inevitably affects the flame dynamics and, consequently, the direct combustion noise, as will be discussed in Section 11.5.

Finally, while the impact of chemical modeling has been investigated in 3D configurations for turbulent premixed hydrocarbon flames [44], investigations for premixed hydrogen–air flames, based on available literature, are limited to simplified 1D configurations [180]. In addition to this, transport modeling is relevant for the dynamics of hydrogen flames (see Section 4.2.3) and impacts their acoustic radiation [292]. In this sense, DNS will be performed using the simplified global reaction mechanism developed in Chapter 5 with different transport properties, and will be compared to detailed kinetics. This analysis will be performed first for acoustically excited laminar flames in Section 9.4, and subsequently extended to turbulent ones in Section 11.6, thereby providing a broad-spectrum investigation of the impact of chemical and transport modeling on combustion noise of lean premixed hydrogen–air flames.

8

Laminar premixed M-shaped jet flame configuration

The dataset used in Chapter 9 to investigate the acoustically forced response and sound generation of laminar flames is presented hereafter. The configuration of reference is an axisymmetric M-shaped laminar flame at atmospheric temperature (i.e., $T_u = 300$ K) and pressure (i.e., $p = 1$ atm), obtained via a passive stabilization method using a thin cylindrical bluff-body.

This configuration is characterized by smaller vertical and horizontal oscillations of the flame tip with respect to a conical flame [207]. Its response to harmonic inflow perturbations has been widely investigated in the literature for hydrocarbons (e.g., [48, 49, 353]) to analyze flame annihilation phenomena induced by flame-flame interactions and their impact on the generated noise.

Experimental measurements for this configuration have been performed by Matthieu Durand at the *Institut de Mécanique des Fluides de Toulouse* (IMFT). Further details on his experimental work are available in [100].

Contents

Table 8.1: Operating conditions and main parameters for the laminar M-shaped flames.

Description [unit]	Value	
	$CH_4 - H_2$ Flame	H_2 Flame
Equivalence ratio ϕ [-]	1.0	0.5
Thermal power P_{th} [kW]	1.77	1.21
Mass flow rate $\dot{m}$ [g/s]	0.61	0.69
Bulk velocity U_B [m/s]	6.86	8.27
Laminar flame speed S_L^0 [m/s]	0.60	0.55
Laminar flame thickness δ_L^0 [μm]	330	380
Adiabatic flame temperature T_{ad} [K]	2250	1640
Maximum HRR in the 1D flame $\dot{\omega}_{T,max}^{1D}$ [W/m^3]	7.88×10^9	2.42×10^9

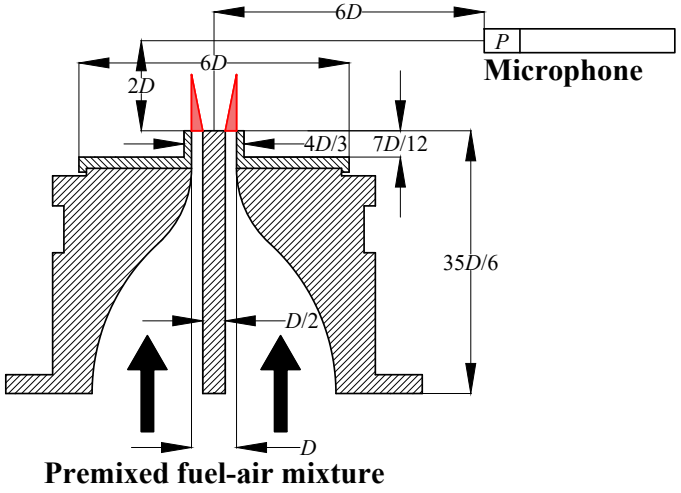

Figure 8.1: Cross-section of the burner nozzle and of the central bluff-body with placement of the microphone. The position of the flame is reported in red.

8.1 Experimental configuration

Two operating points are considered in this work, with different values of Le_{eff}, to highlight the impact of thermodiffusive effects on the flame structure and acoustic response. More specifically, a stoichiometric ($\phi = 1.0$) CH_4–H_2 flame ($Le_{eff} \approx 1$) is compared with a lean ($\phi = 0.50$) H_2 flame ($Le_{eff} \approx 0.3$). In the CH_4–H_2 flame, the H_2 content is fixed at 24% of the total flame thermal power $P_{th} = Y_{F,u}\dot{m}H_F$*, where $Y_{F,u}$ is the fuel mass fraction, $\dot{m}$ is the mass flow rate, and H_F is the fuel lower heating value, equal to 5.0×10^7 J/kg for CH_4 and to 1.20×10^8 J/kg for H_2. Both flames are at atmospheric conditions, i.e., $T_u = 300$ K and $p = 1$ atm. With the chosen operating points, the two flames have comparable values of laminar flame speed S_L^0 and thermal flame thickness δ_L^0 (see Equation (2.41)). The mass flow rate of the two flames is adjusted to obtain the same flame height $h = 14.5$ mm, determined through experimental imaging. Table 8.1 summarizes the main operating parameters for the two flames. The bulk velocity

*For the CH_4–H_2 mixture, the thermal power is equal to $P_{th} = (Y_{CH_4,u}H_{CH_4} + Y_{H_2,u}H_{H_2})\dot{m}$.

is evaluated at the burner outlet as $U_B = \dot{m}/(\rho_u \mathcal{A}_{out})$, where ρ_u is the density of the unburned gases and $\mathcal{A}_{out}$ is the outlet section of the annular burner nozzle, while the flame properties are estimated through 1D unstretched flame calculations using Cantera [137].

Figure 8.1 schematizes the experimental set-up at IMFT. The burner, denominated AMELI, includes a plenum, where the fuel–air mixture is injected through a set of honeycomb meshes to produce a premixed laminar flow, and a nozzle to accelerate the fresh gases towards the outlet section of outer diameter $D = 12$ mm and inner diameter $0.5D$.

The flames are forced with a loudspeaker (MONACOR SP-6/108PRO) installed at the base of the burner. A sinusoidal modulation signal of frequency f_a is created by a Tektronix function generator (AFG1062). The peak-to-peak voltage is chosen to obtain the desired modulation amplitude $u_{rms}/\bar{u}$, where u_{rms} and $\bar{u}$ are, respectively, the temporal root-mean-square and mean of the axial velocity $u(t) = \bar{u} + u_{rms}\sqrt{2}\sin(2\pi f_a t)$. This is measured with a hot-wire placed flush at the center of the annular burner outlet section under equivalent air flow conditions, i.e., the airflow with the same bulk velocity as in the reactive case. The acoustic pressure fluctuations are recorded using a Brüel & Kjær 1/4" free-field microphone (type 4954B) in the position P placed at a radius of $6D$ and a distance $2D$ above the burner outlet (see Figure 8.1).

The annular upper wall of the burner exchanges heat with the flame in correspondence of the bluff body, i.e., for radius r lower than $r_i = D/4$, and of the outer lip, i.e., for $r_o \leq r \leq r_{lip}$, where $r_o = D/2$ and $r_{lip} = 2D/3$ (see Figure 8.1). The mean temperature on these surfaces is determined following the procedure described in [90, 297] with a Type K contact thermocouple. The velocity field is measured via Particle Image Velocimetry (PIV), using solid TiO_2 particles with a mean diameter of 200 nm, illuminated with two 10 Hz CRF-400 lasers, whose beams are shaped into sheets of approximately 50 mm in height and 0.5 mm in width. Images of the illuminated particles are recorded using a LaVision Imager sCMOS camera and the acquisition is controlled using the LaVision Davis software suite, leading to a vector separation of approximately 0.113 mm.

Planar laser-induced fluorescence imaging (OH-PLIF) is adopted to retrieve the spatial distribution of OH, employing a 10 Hz laser system, which includes a Q-smart lamp pumped Nd:YAG laser with a second-harmonic generator and a Sirah Lasertechnik CobraStretch tunable narrow-bandwidth dye laser. For the forced case, phase-averaging is performed in increments of 18 degrees (i.e., 20 realizations per forcing cycle).

8.2 Numerical methodology

The numerical set-up adopted for the simulation of the M-shaped flames presented in Section 8.1 is detailed hereafter.

8.2.1 Description of the computational domain

The 3D computational domain, discretized with an unstructured mesh of tetrahedral elements, is schematized in Figure 8.2. It includes the entire burner nozzle and the top wall of the burner support, surrounded by a laminar coflow of inlet velocity $U_{coflow} = 0.1$ m/s.

The ambient is defined by a cylinder of radius $24D$ and length $8D$ surmounted by a hemisphere, with the outlet boundaries placed sufficiently far to avoid any nonphysical interaction with the flame and the acoustic field. The region of interest for the investigation of the acoustic radiation is represented by a cylinder of radius $L_i = 8D$ with respect to the burner axis and

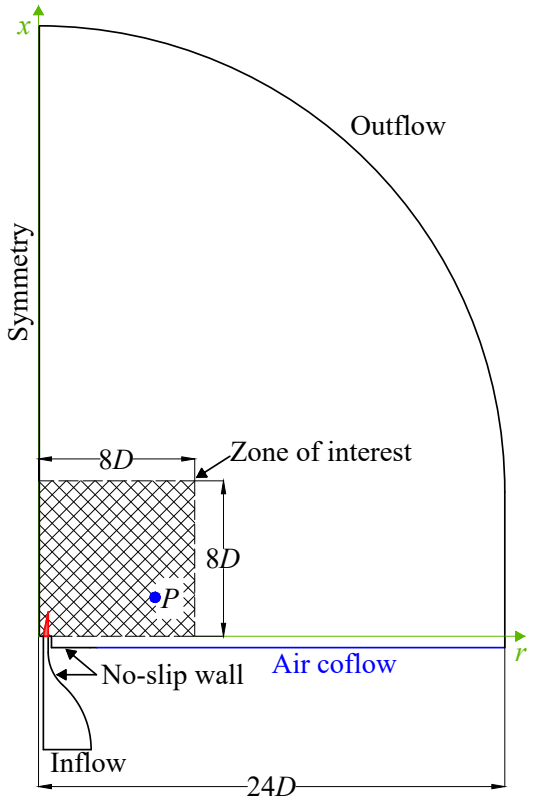

Figure 8.2: Cross-section of the 3D computational domain reporting the boundary conditions and geometrical dimensions. The position of the flame is reported in red. The blue dot denotes the position of the pressure probe.

length L_i from the burner outlet (see Figure 8.2). Inside this domain, the grid is sensibly refined to resolve the flame front and capture the acoustic waves. Outside it, the grid is further stretched to avoid acoustic reflections from the outlet. Being the flow laminar and axisymmetric, a sector of 18° is actually solved in the numerical simulations.

In the baseline configuration, replicating the experimental set-up, the flame develops in an ambient air environment. For the analysis of chemical and transport modeling effects on the H_2 acoustic response presented in Section 9.4, however, both the ambient medium and the coflow are instead composed of equilibrium burned gases at the adiabatic flame temperature, in order to remove the influence of the external medium on the flame dynamics under these artificially modified conditions.

The numerical methodology described in the following refers to the baseline configuration in ambient air, but similar considerations hold for all case studies. The specificities of the remaining cases will be recalled in Section 9.4, together with the corresponding results.

8.2.2 Chemical and transport modeling

The Analytically Reduced Chemistry scheme CH4_15_256_9_AP [255] and the San Diego mechanism [339], presented in Section 3.3.4, are here used, respectively, for the CH_4-H_2 and H_2 flames. Transport is modeled based on the simplified approach described in Section 3.3.4, relying on constant non-unity Lewis numbers for the species.

No significant impact on the H_2 flame structure has been found by considering the more

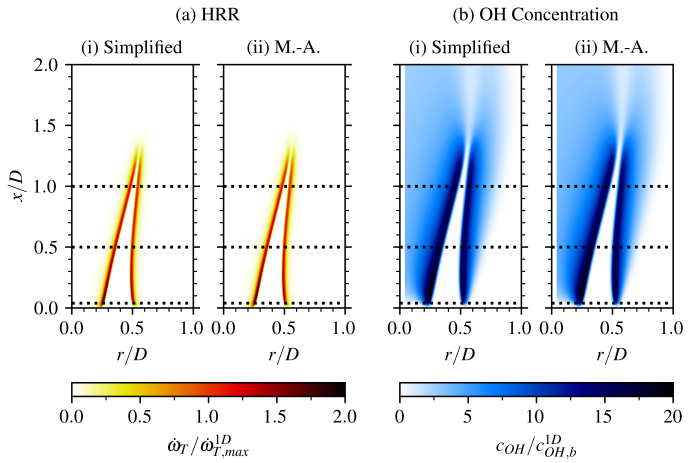

Figure 8.3: Distributions of normalized heat release rate $\dot{\omega}_T/\dot{\omega}^{1D}_{T,max}$ (a) and normalized OH molar concentration $c_{OH}/c^{1D}_{OH,b}$ (b) for the H_2 flame computed with the simplified (i) and the mixture-averaged (ii) transport models. The dotted horizontal lines correspond to the plots in Figure 8.4.

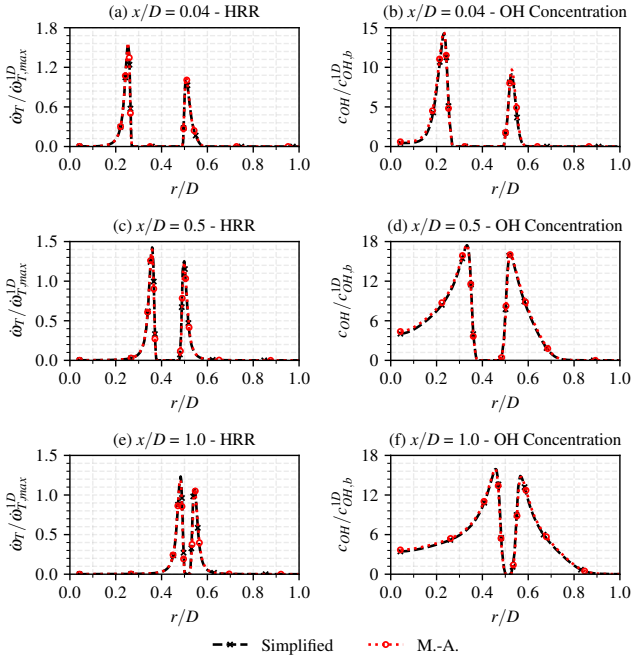

Figure 8.4: Radial profiles of normalized heat release rate $\dot{\omega}_T/\dot{\omega}^{1D}_{T,max}$ (a) and normalized OH molar concentration $c_{OH}/c^{1D}_{OH,b}$ (b) for the H_2 flame computed with the simplified (i) and the mixture-averaged (ii) transport models.

complex mixture-averaged transport model [331]. This is shown in Figure 8.3, which compares, for the H_2 flame using the two transport models, the distributions of heat release rate $\dot{\omega}_T$, normalized by the maximum value in the 1D unstretched flame $\dot{\omega}^{1D}_{T,max}$, and of OH molar concentration c_{OH}, normalized by the value in the burned gases of the 1D unstretched flame $c^{1D}_{OH,b}$. The dotted horizontal lines correspond to the plots in Figure 8.4, where the same quantities are reported along the radial coordinate at different heights from the burner outlet.

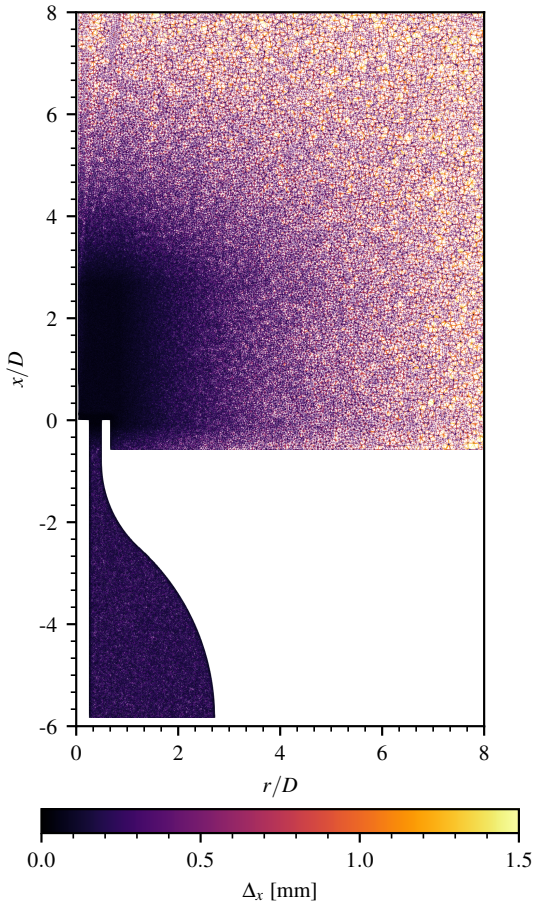

Figure 8.5: Local edge length Δ_x in the burner nozzle and in the region of interest, taken on a cross-section.

8.2.3 Grid resolution

The grid resolution in the zone of interest (see Figure 8.2) should be sufficient to capture the flame structure and the acoustic waves. Here, the flame is fully resolved without any combustion model, and the flame front is discretized with a *maximum* grid size $\Delta_x = 80$ μm, ensuring at least 7 – 10 points in the flame front. A grid independence study (see Appendix C) has been performed for both flames by reducing Δ_x to 60 μm, and for the H_2 flame, sensible to TD effects, by further reducing Δ_x to 40 μm. In all cases, no relevant impact on the prediction of the flame structure has been found by further refining the mesh.

To reduce the computational cost, a smooth grid stretching is applied outside the flame region, with a growth factor of the cell sizes not greater than 2% to avoid spurious waves [44]. This can be visualized in Figure 8.5, which reports the local edge length Δ_x, on a cross-section of the domain. The maximum grid size in the region of interest for the study is of approximately 1.5 mm, leading to a mesh of 20.7 million tetrahedral cells.

Numerical simulations are performed in AVBP using the second-order Lax–Wendroff finite-volume scheme [231]. As discussed in Section 3.3.2, to capture acoustic waves with this scheme without introducing a significant error, the wavelength should be discretized with at least 13 points. Among the different forcing levels and compositions of the ambient medium considered in this work, the shortest acoustic wavelength λ is achieved for the ambient air environment, for

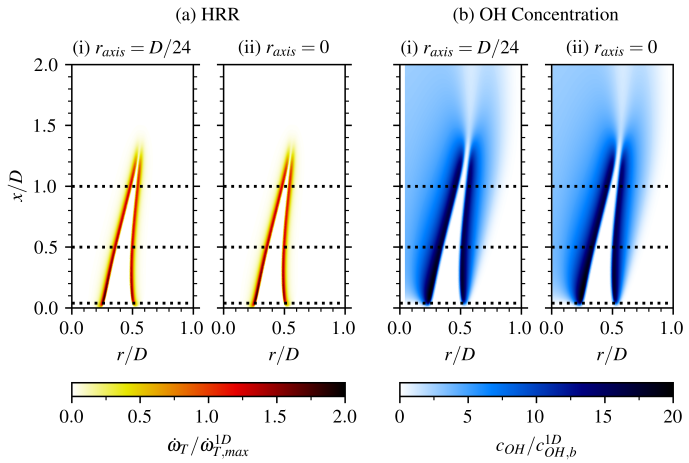

Figure 8.6: Distributions of normalized heat release rate $\dot{\omega}_T/\dot{\omega}^{1D}_{T,max}$ (a) and normalized OH molar concentration $c_{OH}/c^{1D}_{OH,b}$ (b) for the H_2 flame computed with the symmetry boundary placed at $r_{axis} = D/24$ (i) and $r_{axis} = 0$ (ii). The dotted horizontal lines correspond to the plots in Figure 8.7.

which the far field speed of sound is $c_\infty = 348$ m/s, and for the forcing frequency $f_a = 1368$ Hz. Under these conditions, $\lambda = c_\infty/f_a \approx 254$ mm, meaning that the maximum acceptable grid size is $\Delta_x^{max} = \lambda/12 \approx 21$ mm. Therefore, the adopted maximum grid resolution in the zone of interest (i.e., 1.5 mm) allows for well capturing not only the acoustic wave radiated from the flame at the fundamental frequency f_a, but also the first 12 harmonics.

8.2.4 Boundary conditions

As highlighted in Figure 8.2, four kinds of boundary conditions are here considered: symmetry, wall, inflow, and outflow. The symmetry boundary does not correspond to the actual burner axis, to avoid an excessive cell distortion near the x-axis in correspondence of the outlet, but it is rather placed at the radius $r_{axis} = D/24$. This has a negligible impact on the prediction of the flame structure, as shown in Figure 8.6, which reports the spatial distributions of normalized HRR $\dot{\omega}_T/\dot{\omega}^{1D}_{T,max}$ and OH concentration $c_{OH}/c^{1D}_{OH,b}$ for the H_2 flame, and in Figure 8.7, which shows corresponding radial profiles at different heights from the burner outlet.

A no-slip boundary condition is applied for the walls. To account for the heat exchange between the flame and the burner, a heat flux Φ_q is imposed at each point of the nozzle walls:

$$\Phi_q = \frac{T_f - T_{ref}}{R_w}, \tag{8.1}$$

where T_{ref} is a reference temperature, T_f is the fluid temperature at the wall, and R_w is a thermal resistance. For the upper walls of the burner, $T_{ref} = T_u$ and R_w is estimated based on experimental measurements of the mean surface temperatures, following the Heat Resistance Tuning method [3]. The values of the surface-averaged temperatures from numerical simulations and experiments on the bluff body T_{bb} and on the outer lip T_{lip} for the two flames are reported in Table 8.2. Simulations overpredict the mean surface temperatures, but within acceptable limits, and in line with other simulations performed for the same H_2 flame using Conjugate Heat Transfer [105]. While a reduction of the numerical mean surface temperature is possible by increasing the value of R_w, this would result in an overestimation of the lift-off distance compared to the one obtained from experimental imaging (see Section 8.3).

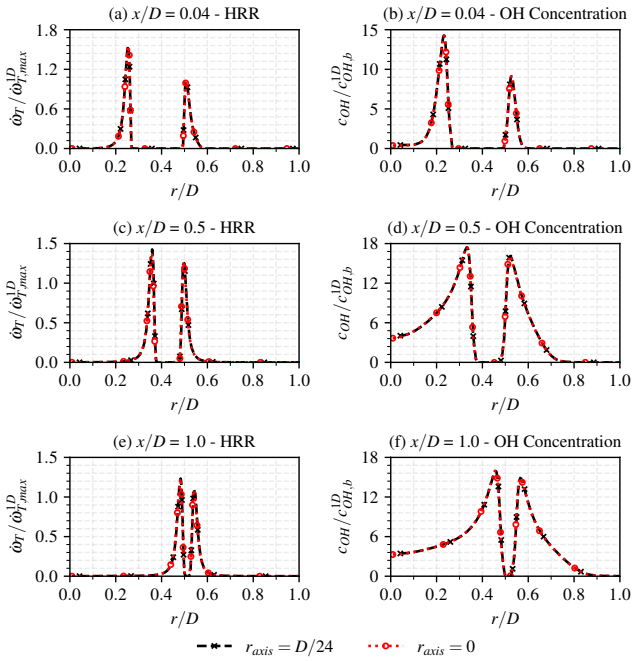

Figure 8.7: Radial profiles of normalized heat release rate $\dot{\omega}_T/\dot{\omega}^{1D}_{T,max}$ (a) and normalized OH molar concentration $c_{OH}/c^{1D}_{OH,b}$ (b) for the H_2 flame computed with the symmetry boundary placed at $r_{axis} = D/24$ (i) and $r_{axis} = 0$ (ii).

Table 8.2: Surface-averaged wall temperature on the bluff body (*bb*) and the outer lip (*lip*).

Description [unit]	Value	
	$CH_4 - H_2$ Flame	H_2 Flame
T_{bb} (numerical simulation) [K]	410	447
T_{bb} (experimental measurement) [K]	352 ± 6	386 ± 4
T_{lip} (numerical simulation) [K]	325	332
T_{lip} (experimental measurement) [K]	311 ± 6	318 ± 2

The velocity profiles downstream the burner nozzle outlet are impacted by the preheating of the fresh gases (at temperature $T_u = 300$ K) by the burner walls and, consequently, by the thermal expansion in the convergent duct [105]. This effect is here taken into account by assigning a variable profile along the axial direction for T_{ref} (see Equation (8.1)) on the walls of the convergent, based on an approximated balance of heat fluxes [250]. The thermal resistance R_w is computed, in first approximation, by considering the heat resistance of a cylinder of radius r_i for the bluff body, and of a hollow cylinder of inner and outer radii equal, respectively, to r_o and r_{lip} (see Section 8.1) [175]. It should be noted that, even though the outer lip is shaped as a hollow cylinder only in the upper part of the nozzle (see Figure 8.1), the modest difference between T_u and T_{lip} (see Table 8.2) makes this simplification reasonable.

Figure 8.8 schematizes the main heat fluxes influencing the temperature of an elementary volume of the bluff body and of the outer lip of the burner, highlighting the conductive heat flux Φ_c inside the material and the convective heat flux Φ_u between the burner walls and the unburned mixture.

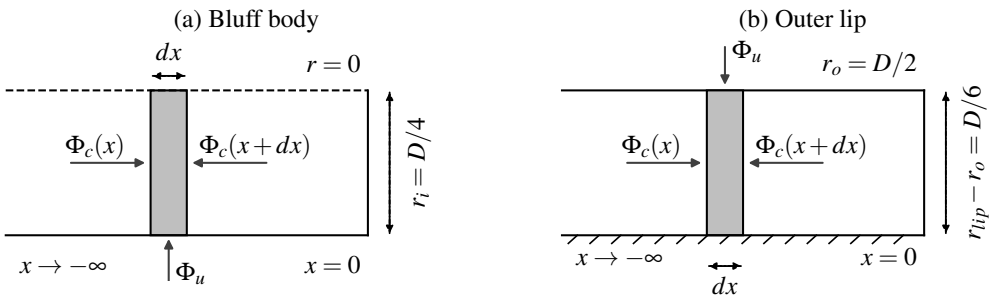

Figure 8.8: Schematic representation of the heat fluxes in an elementary volume of the bluff body (a) and outer lip (b) walls. The conductive flux is denoted by Φ_c, while the convective flux with the unburned mixture is denoted by Φ_u.

Under steady state conditions, the sum of the heat fluxes is equal to zero:

$$\sum_k \Phi_k = 0. \tag{8.2}$$

For the bluff body (Figure 8.8a), the heat fluxes can be expressed as:

$$\Phi_c(x) = -\mathcal{A}_{bb}\lambda \left.\frac{\partial T}{\partial x}\right|_x = -\pi r_i^2 \lambda \left.\frac{\partial T}{\partial x}\right|_x, \tag{8.3a}$$

$$\Phi_c(x+dx) = \mathcal{A}_{bb}\lambda \left.\frac{\partial T}{\partial x}\right|_x = \pi r_i^2 \lambda \left.\frac{\partial T}{\partial x}\right|_{x+dx}, \tag{8.3b}$$

and:

$$\Phi_u = h_{u,i}[T_u - T(x)]\mathcal{A}_{bb,side} = h_u[T_u - T(x)](2\pi r_i dx), \tag{8.3c}$$

where $h_{u,i}$ is the convective heat coefficient for the unburned mixture at the radius r_i, and λ is the thermal conductivity of the burner material. By applying Equation (8.2), the following expression holds:

$$\cancel{\pi r_i^2}\lambda\left(-\left.\frac{\partial T}{\partial x}\right|_x + \left.\frac{\partial T}{\partial x}\right|_{x+dx}\right) - 2dx h_{u,i}[T(x) - T_u]\cancel{\pi r_i} = 0, \tag{8.4}$$

leading to:

$$\frac{\left.\frac{\partial T}{\partial x}\right|_{x+dx} - \left.\frac{\partial T}{\partial x}\right|_x}{dx} - \frac{2h_{u,i}}{r_i\lambda}[T(x) - T_u] = 0, \tag{8.5}$$

which becomes, for $dx \to 0$:

$$\left.\frac{\partial^2 T}{\partial x^2}\right|_x - \frac{2h_{u,i}}{r_i\lambda}[T(x) - T_u] = 0. \tag{8.6}$$

By setting $\theta(x) = T(x) - T_u$ and $m_{bb} = \sqrt{2h_{u,i}/(r_i\lambda)}$, Equation (8.6) can be rewritten as:

$$\left.\frac{\partial^2 \theta}{\partial x^2}\right|_x - m_{bb}^2\theta(x) = 0, \tag{8.7}$$

whose homogeneous solution is given by:

$$\theta(x) = Ae^{m_{bb}x} + Be^{-m_{bb}x}. \tag{8.8}$$

The integration constants A and B are given by the Dirichlet boundary conditions $T = T_u$ (i.e., $\theta = 0$) for $x \to -\infty$ and $T = T_{bb}$ (see Table 8.2) for $x = 0$. Therefore, the temperature on the bluff-body outer wall in the axial direction is given by:

$$T_{ref,bb}(x) = T_u + (T_{bb} - T_u)e^{m_{bb}x}. \tag{8.9}$$

For the outer lip (see Figure 8.8b), considering the external wall as adiabatic[†] and recalling that the cross-section is equal to $\mathcal{A}_{lip} = \pi(r_{lip}^2 - r_o^2)$, an analogous reasoning leads to the following expression for the temperature on the inner wall:

$$T_{ref,lip}(x) = T_u + (T_{lip} - T_u)e^{m_{lip}x}, \tag{8.10}$$

where:

$$m_{lip} = \sqrt{\frac{2h_{u,o}r_o}{(r_{lip}^2 - r_o^2)\lambda}}. \tag{8.11}$$

Based on Equations (8.9) and (8.10), the axial variation of temperature on the two surfaces of the nozzle is determined, provided that $h_{u,i}$, $h_{u,o}$, and λ are known. The latter can be evaluated as a function of the temperature for the material of the burner, i.e., AISI 304L stainless steel [142]:

$$\lambda\,[\mathrm{W/(m\,K)}] = 7.9318 + 0.023051T - 6.4166 \times 10^{-6}T^2. \tag{8.12}$$

On the other hand, the evaluation of the convection coefficients $h_{u,i}$ and $h_{u,o}$ is less straightforward. Considering a laminar flow in a circular tube annulus, the Nusselt numbers for the two walls are given by:

$$Nu_i = \frac{h_{u,i}D_h}{\lambda}, \tag{8.13a}$$

at the inner radius, and:

$$Nu_o = \frac{h_{u,o}D_h}{\lambda}, \tag{8.13b}$$

at the outer one, where $D_h = 2(r_o - r_i)$ is the hydraulic diameter. Assuming uniform heat fluxes on the inner and outer surfaces, the Nusselt numbers can be computed as [175]:

$$Nu_i = \frac{Nu_{ii}}{1 - (\Phi_o/\Phi_i)\theta_i^*}, \tag{8.14a}$$

for the inner surface, and:

$$Nu_o = \frac{Nu_{oo}}{1 - (\Phi_i/\Phi_o)\theta_o^*}, \tag{8.14b}$$

for the outer one, where $\Phi_i = h_{u,i}(T_i - T_u)$ and $\Phi_o = h_{u,o}(T_o - T_u)$ are the heat fluxes from the inner and outer surfaces, respectively, and T_i and T_o are the temperatures on the two surfaces. The coefficients Nu_{ii}, θ_i^*, Nu_{oo}, and θ_o^* depend on the ratio r_i/r_o. For the present case, this is equal to 0.5, leading to $Nu_{ii} = 6.248$, $\theta_i^* = 0.538$, $Nu_{oo} = 5.039$, and $\theta_o^* = 0.214$ [175].

At $x = 0$, $T_i = T_{bb}$ and $T_o = T_{lip}$. Since the heat fluxes are assumed uniform along each surface, this condition leads, neglecting the variation of λ, to:

$$\frac{\Phi_o}{\Phi_i} = \frac{h_{u,o}(T_{lip} - T_u)}{h_{u,i}(T_{bb} - T_u)} = \underbrace{\frac{Nu_o}{Nu_i}}_{n}\underbrace{\frac{T_{lip} - T_u}{T_{bb} - T_u}}_{t}. \tag{8.15}$$

[†]This assumption is reasonable given the geometry of the burner (see Figure 8.1) and the fact that this wall is in contact with the ambient.

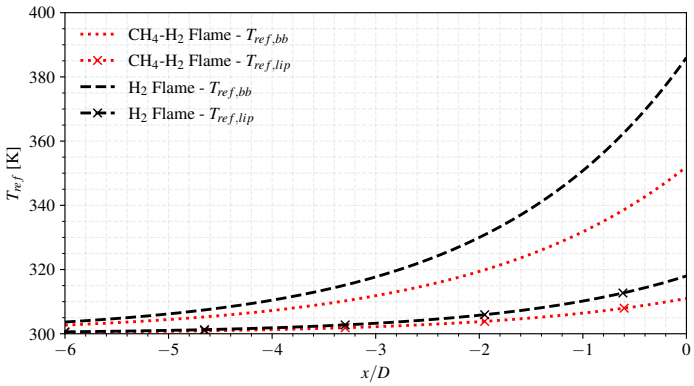

Figure 8.9: Axial profiles of T_{ref} along the nozzle convergent walls for the methane–hydrogen and hydrogen flames.

By substituting Equations (8.14a) and (8.14b) in this expression, it is possible to obtain:

$$n = \frac{Nu_{oo}t + Nu_{ii}\theta_o^*}{Nu_{ii}t + Nu_{oo}\theta_i^* t^2}. \tag{8.16}$$

Then, Equations (8.14a) and (8.14b) become, respectively:

$$Nu_i = \frac{Nu_{ii}}{1 - nt\theta_i^*}, \tag{8.17a}$$

and:

$$Nu_o = \frac{Nu_{oo}}{1 - \frac{\theta_o^*}{nt}}. \tag{8.17b}$$

This allows for the computation of $h_{u,i}$ and $h_{u,o}$, and, consequently, of m_{bb} and m_{lip}. The resulting profiles of T_{ref}, considering the experimental values in Table 8.2 as target values for T_{bb} and T_{lip} at $x = 0$, are shown in Figure 8.9.

Inlet and outlet boundaries are treated with the NSCBC formulation [309]. The relaxation coefficients for the coflow inlet and for the outlet are set to 100, leading to a cutoff frequency $f_c \approx 8$ Hz [358] (see Equation (3.25)). For the nozzle unsteady velocity inlet, the non-reflecting NSCBC formulation [84] is adopted to avoid acoustic reflection, and the velocity forcing is imposed as detailed in Section 3.3.3. The amplitude of the fluctuation is adjusted to achieve the desired value of $u_{rms}/\bar{u}$ at the same location of the experimental hot-wire at the nozzle outlet. After reaching a statistically steady state, simulations are run for 15 cycles, to retrieve well-resolved temporal statistics. To isolate the noise due to the inflow forcing, simulations in equivalent air flow conditions have been performed. For each case, the resulting overall sound pressure level, defined as:

$$OASPL = 20 \log_{10}\left(\frac{p_{rms}}{p_{ref}}\right), \tag{8.18}$$

where $p_{ref} = 2 \times 10^{-5}$ Pa is a reference acoustic pressure [48], is reported in Table 8.3. As expected, the noise due to the unsteady inflow increases with the amplitude and frequency of the forcing.

Table 8.3: OASPL in equivalent air flow conditions at different forcing levels.

Forcing level [unit]		OASPL [dB]	
$u_{rms}/\bar{u}$ [-]	f_a [Hz]	$CH_4 - H_2$ Flow	H_2 Flow
0.17	228	83.29	84.99
0.24	228	86.44	88.03
0.17	456	89.04	90.66
0.17	1368	-	100.3

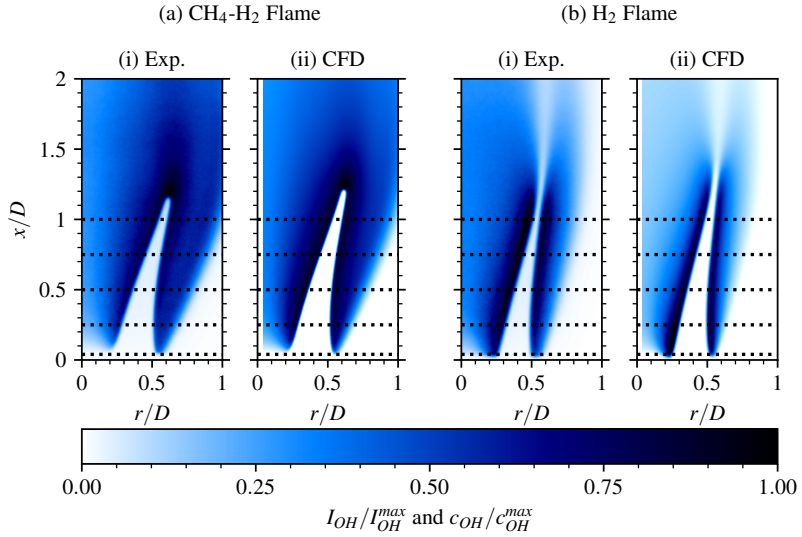

Figure 8.10: Distributions of normalized light intensity I_{OH}/I_{OH}^{max} from experimental OH-PLIF (i) and of normalized OH molar concentration c_{OH}/c_{OH}^{max} from time-averaged numerical solutions (ii) for the CH_4-H_2 (a) and the H_2 (b) flames. The dotted horizontal lines correspond to the plots in Figures 8.11 and 8.12.

8.3 Experimental validation of the numerical set-up

To validate the computational set-up, simulations are here compared to experiments in the unforced case. Numerical results are time-averaged over 5 flow through times $\tau = L_i/U_B$ to improve the quality of the analysis.

Figure 8.10 compares the experimental OH-PLIF measurement with the numerical OH concentration field for the two flames. All distributions are normalized by their respective maximum value. The main features of the two flames are well retrieved in terms of flame shape and distribution of the OH radical, with only a slight overestimation of approximately $0.04D$ (i.e., 0.48 mm) of the flame length in the numerical simulations. In this sense, it should be noted that the uncertainty associated with the OH-PLIF measurement is of ± 0.30 mm.

A comparison of the mean axial and radial velocity profiles is offered in Figures 8.11 and 8.12, respectively, at different heights from the burner outlet, denoted by black dotted lines in Figure 8.10 The velocity r.m.s. is not reported, being it not significant for this quasi-steady laminar configuration. An excellent agreement is found for both velocity components at all positions, confirming the adequacy of the approximation made for the estimation of the temperature and the heat exchange at the burner walls (see Section 8.2.4). Overall, the results in Figures 8.10 to 8.12 sustain the adequacy of the adopted computational set-up.

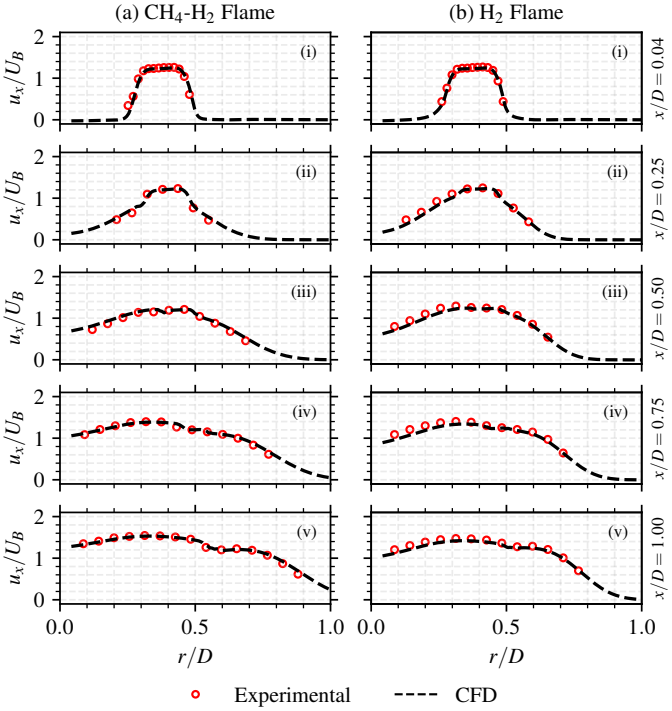

Figure 8.11: Profiles of normalized axial velocity u_x/U_B from experimental PIV and time-averaged numerical solutions for the CH_4-H_2 (a) and H_2 (b) flames at $x/D = 0.04$ (i), $x/D = 0.25$ (ii), $x/D = 0.50$ (iii), $x/D = 0.75$ (iv), and $x/D = 1.0$ (v).

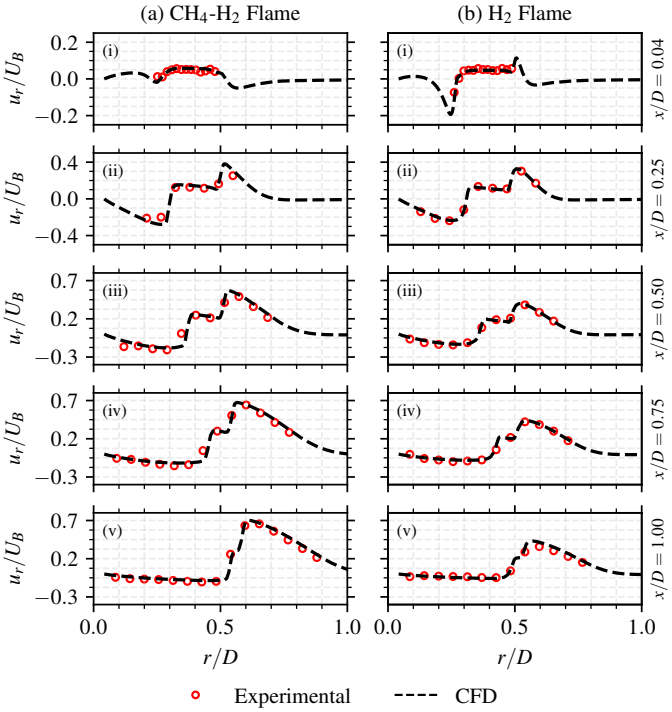

Figure 8.12: Profiles of normalized radial velocity u_r/U_B from experimental PIV and time-averaged numerical solutions for the CH_4-H_2 (a) and H_2 (b) flames at $x/D = 0.04$ (i), $x/D = 0.25$ (ii), $x/D = 0.50$ (iii), $x/D = 0.75$ (iv), and $x/D = 1.0$ (v).

9

Sound generation by acoustically forced laminar premixed flames

Flame–acoustics interaction and sound generation are investigated in laminar lean ($\phi = 0.50$) hydrogen and stoichiometric ($\phi = 1.0$) methane-hydrogen premixed M-shaped flames subjected to harmonic inlet flow modulations, based on numerical simulations of the configuration presented in Chapter 8, supported by experiments performed at the *Institut de Mécanique des Fluides de Toulouse* (IMFT). The impact of the forcing amplitude and frequency is investigated, highlighting how thermodiffusive effects and instabilities affect the structure and acoustic response of the hydrogen flame. The combustion noise theory relating fluctuations of flame surface area and heat release rate is verified also for the hydrogen flame, provided that stretch effects on the flame speed are accounted for. The spatial and temporal correlation between OH* and heat release rate is also examined in this unsteady configuration, extending the analysis in Chapter 6.

Finally, the impact of chemical modeling is investigated by performing additional simulations using the reduced scheme developed in Chapter 5. The impact of the transport modeling is assessed too, by removing either the differential or preferential diffusion of hydrogen, or both of them. When imposing unity Lewis numbers for all species, flame annihilation events are promoted, while the separate analysis of differential and preferential diffusion effects on the flame annihilation dynamics indicates that the two have an antagonist behavior, with the latter mitigating the impact of the former.

Results from this Chapter are included in:

- F. G. Schiavone, M. Durand, T. Schuller, and D. Laera. "Influence of thermodiffusive effects on sound generation in perturbed laminar premixed annular jet flames". *Submitted to Combustion and Flame* (2026).
- F. G. Schiavone, M. Torresi, S. M. Camporeale, and D. Laera. "Chemical Modeling and Lewis Number Effects on Noise Generation in Lean Premixed Hydrogen–Air Flames". *Accepted for publication in Proceedings of the ASME Turbo Expo 2026* (2026).

Contents

9.1 Steady flames

The impact of the Lewis number on the flame structure is first assessed in the stable, unforced case. It is recalled that, with the chosen operating conditions, the stoichiometric ($\phi = 1.0$) CH_4–H_2 and the lean ($\phi = 0.50$) H_2 flames at atmospheric temperature and pressure share the same flame lengths, and have comparable laminar burning velocity and thickness (see Section 8.1). The similarity in the flame height between the two cases is observable in Figure 9.1, which compares the heat release rate fields, normalized by the maximum value in the corresponding 1D unstretched laminar flame $\dot{\omega}_T$ (see Table 8.1). The results are time-averaged over 5 convective times $\tau = L_i/U_B$, where $L_i = 8D$ (see Section 8.2.1), with $D = 12$ mm being the diameter of the burner, while U_B is the bulk velocity, given in Table 8.1.

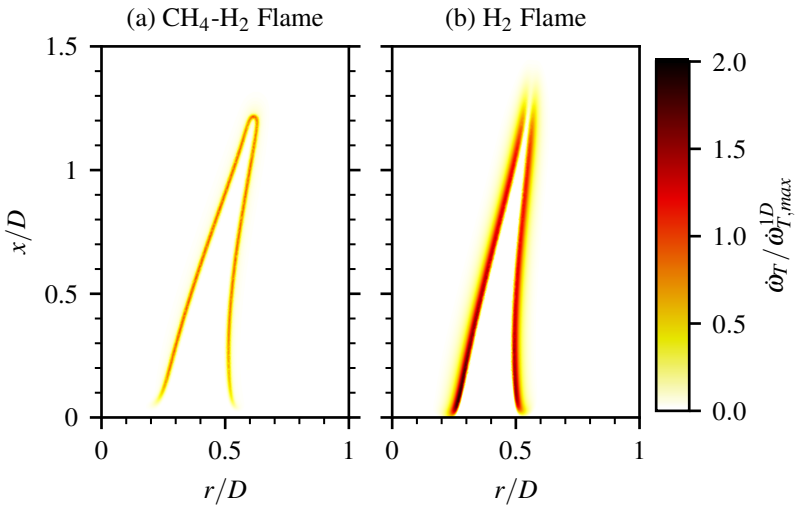

Figure 9.1: Distributions of normalized HRR $\dot{\omega}_T/\dot{\omega}^{1D}_{T,max}$ from time-averaged numerical solutions for the unforced CH_4–H_2 (a) and H_2 (b) flames.

The differences in the value of Le strongly affect the HRR distribution of the two flames. Indeed, while the CH_4–H_2 flame presents a well-defined, continuous flame front with uniform HRR, indicating the absence of any TD effect ($Le \approx 1$), the H_2 flame features a tip opening, resulting from the H_2 sub-unity Le [229]. This leads to the radial outward diffusion of H_2 molecules and, consequently, to reduced fuel consumption rate and local extinction at the tip [267] (see Section 4.2.3).

Furthermore, a redistribution of HRR towards the flame root can be observed in the H_2 flame, corroborating DNS results in [117]. Indeed, in correspondence of the inner branch (the one closer to the x-axis), a value of HRR twice as much as the one of the unstretched premixed flame (see Table 8.1) is obtained at the root, while close to the tip the value is sensibly lower. This results in a reduced lift-off distance compared to the CH_4–H_2 flame.

9.2 Forced flames

Four different forcing levels are here considered. First, a reference configuration with modulation of amplitude $u_{rms}/\bar{u} = 0.17$ and forcing frequency $f_a = 228$ Hz is considered, for which experimental measurements are available, hence allowing to further validate the numerical set-up in the unsteady condition.

Subsequently, the impact of the modulation amplitude and frequency is studied numerically for the H_2 flame by increasing the forcing amplitude to $u_{rms}/\bar{u} = 0.24$ or the frequency to $f_a = 456$ Hz. Finally, to promote TD instabilities, an additional forcing level, i.e., $u_{rms}/\bar{u} = 0.17$ and $f_a = 1368$ Hz, is considered. This frequency has been chosen as it is close to the flame characteristic frequency $f_c = S_L^0/\delta_L^0 \approx 1425$ Hz, to enhance the flame response to the unsteady inflow [429] (see Section 4.2.3).

9.2.1 Comparison of methane–hydrogen and hydrogen flames

Figure 9.2 compares, for the forced flames at $u_{rms}/\bar{u} = 0.17$ and $f_a = 228$ Hz, the phase-averaged distributions of the experimental OH-PLIF and of the numerical OH concentration and HRR at four phase angles $\theta = 2\pi f_a t$, where t is time, chosen to follow the most relevant flame dynamics: $\theta = 162°$, $\theta = 198°$, $\theta = 216°$, and $\theta = 252°$.

First, the comparison of experimental and numerical results indicates that the simulations well retrieve the dynamics of both flames, and the OH distribution in the burnt gases region, thus confirming the reliability of the numerical set-up to predict the acoustic response in both cases. Moving to the differences between the two flames, Figure 9.2a shows that the continuous flame front of the CH_4–H_2 flame, which features a nearly constant HRR distribution, is distorted by the unsteady inflow, leading to modifications in the flame surface and to the collision of the two flame branches, i.e., flame–flame interaction [353] (see Section 7.2.1). This leads to flame pinch-off near the annular tip, with the detachment of a flame toroidal pocket that is rapidly consumed. The H_2 flame in Figure 9.2b, instead, is lowly distorted by the unsteady flow, with no significant wrinkling of the flame surface. In particular, no small-scale curvature of the flame front is observed, which would lead to the insurgence of cellular structures associated with TD effects and to the enhancement of the local fuel consumption rate [221]. Consequently, the whole flame oscillates with the inflow, and the HRR distribution is similar to the stable case (see Figure 9.1).

Figure 9.3 reports, for both flames, the temporal traces of the flame tip axial position x_{tip}, normalized by the burner diameter D, retrieved from 20 experimental OH-PLIF images and from

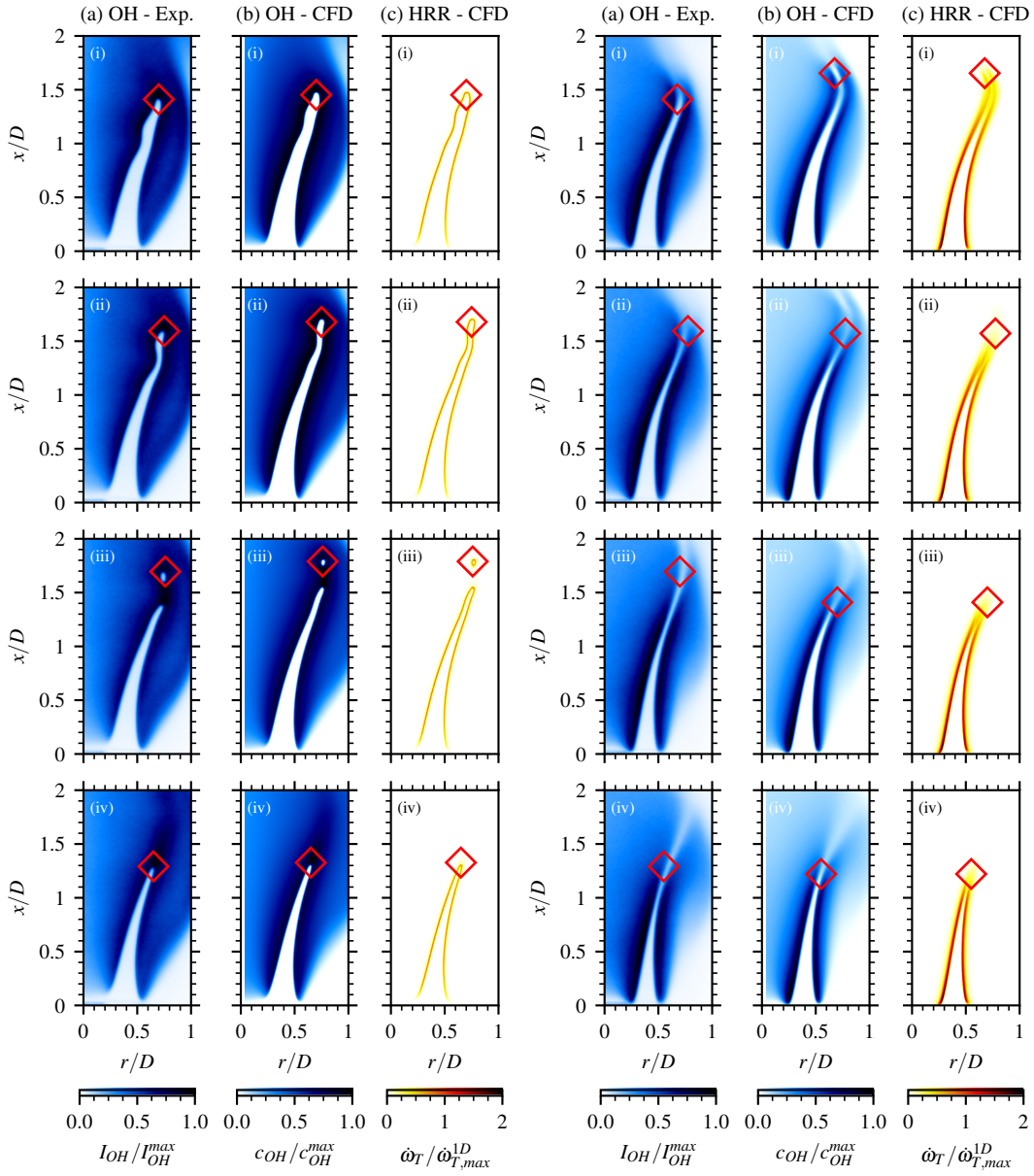

(a) CH_4–H_2 flame. **(b)** H_2 flame.

Figure 9.2: Phase-averaged distributions of normalized light intensity I_{OH}/I_{OH}^{max} from experimental OH-PLIF (1), and of normalized OH molar concentration c_{OH}/c_{OH}^{max} (2) and HRR $\dot{\omega}_T/\dot{\omega}_{T,max}^{1D}$ from numerical solutions (3) for the CH_4–H_2 (a) and the H_2 flames (b) forced at $u_{rms}/\bar{u} = 0.17$ and $f_a = 228$ Hz at θ = 162° (i), θ = 198° (ii), θ = 216° (iii), and θ_4 = 252° (iv). The red diamonds denote the flame tip position x_{tip}.

numerical simulations. In these latter, x_{tip} is defined as the maximum coordinate of the isosurface $C = C^*$, where $C = 1 - Y_F/Y_{F,u}$ is the progress variable (for the CH_4–H_2 flame, CH_4 is considered), while C^* corresponds to the maximum HRR for a 1D unstretched flame ($C^* = 0.88$ for the CH_4–H_2 flame and $C^* = 0.80$ for the H_2 one). All signals are synchronized with respect to

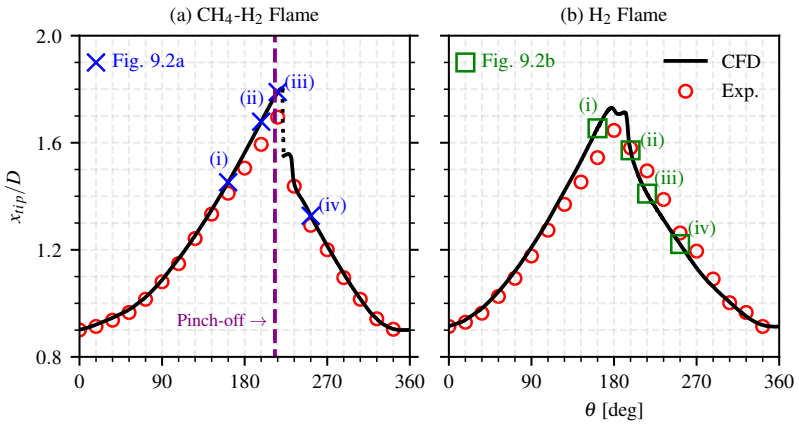

Figure 9.3: Phase-averaged temporal history for the CH_4–H_2 (a) and H_2 (b) flames at $f_a = 228$ Hz and $u_{rms}/\bar{u} = 0.17$ of the normalized flame tip position x_{tip}/D from experiments and numerical simulations. The purple dashed line identifies the flame pinch-off. The blue crosses and green squares denote, respectively, flame patterns in Figures 9.2a and 9.2b.

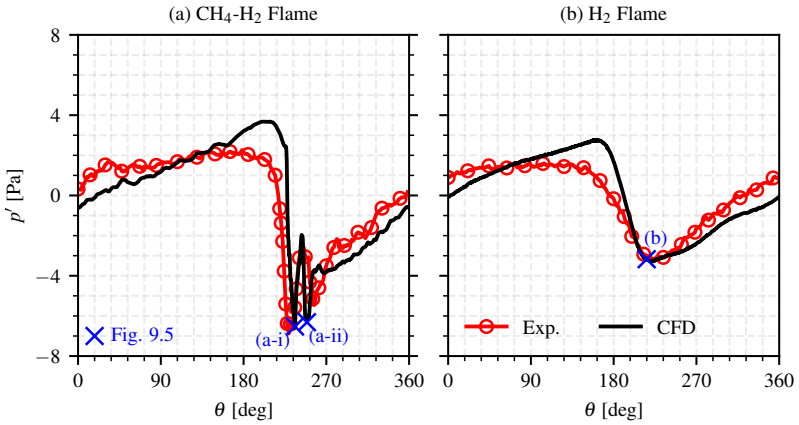

Figure 9.4: Phase-averaged temporal history for the CH_4–H_2 (a) and H_2 flames (b) at $f_a = 228$ Hz and $u_{rms}/\bar{u} = 0.17$ of the pressure fluctuation p' from experiments and numerical simulations. The blue crosses correspond to flame patterns in Figure 9.5.

the sinusoidal axial velocity fluctuation at the burner outlet (see Section 8.1):

$$\frac{u - \bar{u}}{u_{rms}\sqrt{2}} = \sin\theta, \tag{9.1}$$

and phase-averaged over the oscillation cycles. The blue crosses and green squares in Figure 9.3 denote, respectively, flame patterns in Figures 9.2a and 9.2b, where the values of x_{tip} are marked by red diamonds. Overall, a good agreement is found between experiments and simulations, further sustaining the validity of the numerical set-up. The CH_4–H_2 flame (see Figure 9.3a) exhibits a sharp discontinuity (denoted by the dotted black line), due to the consumption of the fresh gases pocket, detached from the flame shortly before, in correspondence of the purple dashed line marking the phase angle at which pinch-off occurs. The short extension of this discontinuity in x_{tip} confirms the rapid nature of the annihilation phenomenon. For the H_2 flame (see Figure 9.3b), instead, the (open) tip follows the flame motion, with some oscillations around the peak value, but no pinch-off is observed.

The impact of these differences on the acoustic radiation is shown in Figure 9.4, which re-

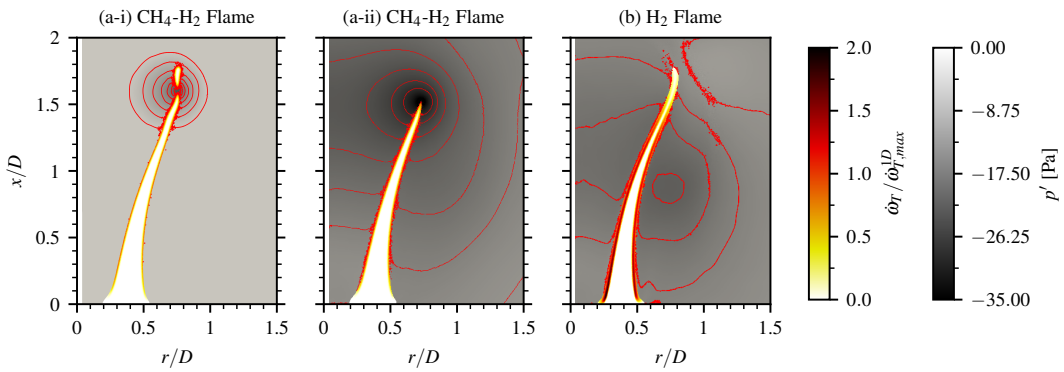

Figure 9.5: Snapshots of normalized HRR $\dot{\omega}_T/\dot{\omega}^{1D}_{T,max}$ and pressure fluctuation p' for the CH_4–H_2 flame (a) at $\theta = 213°$ (i) and $\theta = 231°$ (ii), and for the H_2 flame (b) at $\theta = 193°$ at $f_a = 228$ Hz and $u_{rms}/\bar{u} = 0.17$ from numerical simulations. Isocontours of pressure (in red) are superimposed to highlight the acoustic radiation.

ports the experimental and numerical traces of pressure fluctuation p' for the two flames. The numerical simulations are able to adequately predict the temporal dynamics of the experimental pressure trace. In particular, the numerical signal well captures the main feature of the CH_4–H_2 flame (see Figure 9.4a), i.e., the double negative peak associated with the rapid annihilation dynamics at the flame tip [49, 199, 353, 387] (see Section 7.2.1). This is absent in the H_2 flame (see Figure 9.4b), highlighting that the tip opening induced by TD effects impacts also the acoustic response of the flame, removing this relevant noise source.

The relation of these acoustic features with the flame dynamics is highlighted in Figure 9.5, which compares, for the two flames, the instantaneous numerical distributions of HRR in the unburned and flame front region (identified by $C \leq 0.95$) and of p' corresponding to the strongest negative p' values in Figure 9.4 (marked by blue crosses)*: the two negative peaks for the CH_4–H_2 flame, and the global minimum of p' for the H_2 one. For the CH_4–H_2 flame, Figure 9.5a confirms, in agreement with the literature [49, 319, 353], that, for both the negative pressure fluctuations, the noise source is located at the flame tip, where the mutual interaction of the flame branches occurs. In particular, Figure 9.5a-i clearly shows the role of the flame pinch-off as a noise generation mechanism for this flame. For the H_2 flame (see Figure 9.5b), on the other hand, the tip has no relevant role in the noise generation process, which is associated to the sole unsteady motion of the whole flame. The strongest noise source is located where the curvature of the flame brush and the local HRR are enhanced.

To further confirm that the differences in the acoustic radiation plotted in Figure 9.4 are associated to the different flame dynamics, Figure 9.6i compares the numerical p' signal with the one reconstructed from the numerical volume-integrated HRR q using the following relation, which corresponds to Equation (7.22) and is here recalled for convenience:

$$p'(\mathrm{x}, t) = \frac{\gamma - 1}{4\pi|\mathrm{x}|c_\infty^2} \left.\frac{dq}{dt}\right|_{t-|\mathrm{x}|/c_\infty}, \tag{9.2}$$

A strong match is found for both flames. This can be assessed quantitatively by the concordance correlation coefficient r_c [238], which measures the agreement between the two distributions, in

*Recalling Equation (7.22), the pressure fluctuation measured by the probe is delayed with respect to the flame dynamics by a time $t - |\mathrm{x}|/C_\infty$. Therefore, the phase angles of the snapshots in Figure 9.5 do not coincide with the pgase angles marked by blue crosses in Figure 9.4.

terms of both precision and accuracy. The coefficient is defined, for two generic quantities ς and $\varkappa$ as:

$$r_c = \frac{2\sigma_\varsigma \sigma_\varkappa}{\sigma_\varsigma^2 + \sigma_\varkappa^2 + (\mu_\varsigma - \mu_\varkappa)^2} r_P, \tag{9.3}$$

where σ_i and μ_i denote, respectively, the standard deviation and mean of the quantity i, while r_P is the Pearson correlation coefficient previously defined in Equation (6.5). Its value is above 0.95 for both flames, indicating a very good agreement (a perfect match corresponds to $r_c = 1$), and confirming the role of the unsteady HRR as dominant noise source.

The relation between q and the flame surface area $\mathcal{A}_f$ is considered in Figure 9.6ii. To this scope, the numerical signal of dq/dt, normalized by the steady thermal power P_{th} (see Table 8.1), is compared with the one reconstructed from the flame surface area $\mathcal{A}_f$. First, the classical combustion noise theory [2, 49, 69] (see Equation (7.4)) flamelet is considered. This stems from the linear relation between q and $\mathcal{A}_f$, which reads as [49]:

$$q = \rho_F S_L^0 (-\Delta h_F^0) \mathcal{A}_f, \tag{9.4}$$

where ρ_F is the fuel density, equal to the product of the density ρ_u and of the fuel mass fraction $Y_{F,u}$ of the unburned mixture, and $(-\Delta h_F^0)$ is the enthalpy released by the conversion of a unit mass of fuel, i.e., the fuel lower heating value H_F for a gas-state combustion. By taking the time derivative of Equation (9.4) and substituting ρ_F and $-\Delta h_F^0$, the following relation between dq/dt and $d\mathcal{A}_f/dt$ can then be obtained:

$$\frac{dq}{dt} = \rho_u Y_{F,u} H_F S_L^0 \frac{d\mathcal{A}_f}{dt}. \tag{9.5}$$

When $Le < 1$, however, the flame consumption speed S_c is not coincident with S_L^0, since it depends on stretch, which varies over time [311] (see Section 2.5.5). In first approximation and based on [390], the dependence of S_c on stretch is considered in the mean, by taking the global flame consumption speed time-averaged over the forcing cycle $\overline{S_c}$. Then, Equation (9.5) becomes:

$$\frac{dq}{dt} = \rho_u Y_{F,u} H_F \overline{S_c} \frac{d\mathcal{A}_f}{dt}. \tag{9.6}$$

Here, $\mathcal{A}_f$ is evaluated from $|\nabla C|$ as in Equation (2.63), while S_c is obtained from:

$$S_c = -\frac{1}{\rho_u Y_{F,u} \mathcal{A}_0} \int_V \dot{\omega}_F dV, \tag{9.7}$$

where $\mathcal{A}_0$ is a reference flame surface, taken as the value of $\mathcal{A}_f$ in the unforced flame.

For the CH_4–H_2 flame (see Figure 9.6a-ii), the temporal signals obtained from Equations (9.5) and (9.6) are almost superimposed, since, for this flame, stretch does not significantly affect the flame speed and $\overline{S_c} \approx S_L^0$ (see Section 2.5.5). Both are also well in agreement with the recorded HRR signal ($r_c > 0.9$), confirming, as expected, the validity of the flamelet theory in [2, 69] for this CH_4–H_2 blend. For the H_2 flame (see Figure 9.6b-ii), instead, a difference can be observed between the two signals reconstructed through Equations (9.5) and (9.6) in terms of agreement with the HRR. While the result for Equation (9.5) underestimates the actual HRR fluctuation, a good agreement is found when using Equation (9.6), differently from the previous work by Talei et al. [390]. This improvement can be locally quantified through the instantaneous peak value of $|dq/dt|/P_{th}$, i.e., $|dq/dt|_{max}/P_{th}$, which corresponds to the most rapid rate of change of HRR

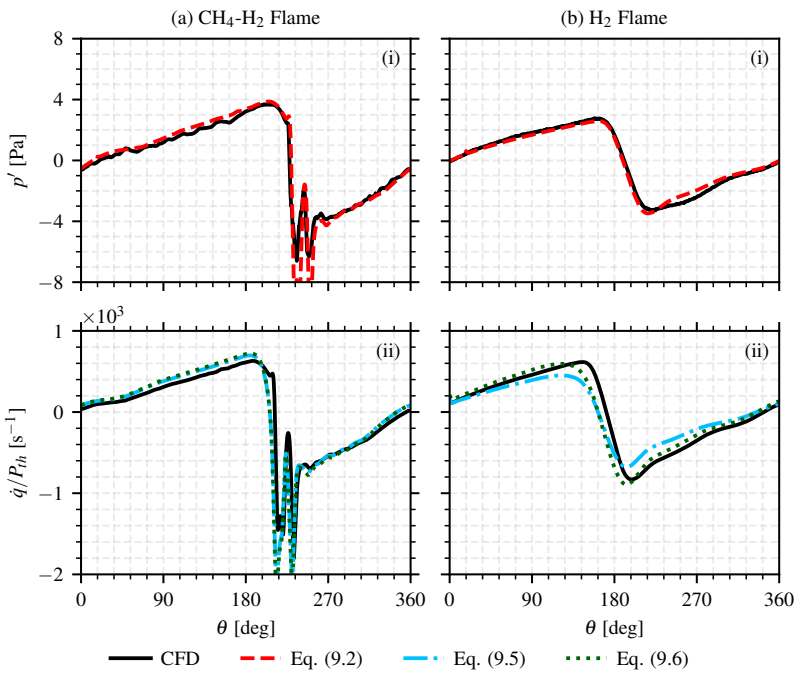

Figure 9.6: Phase-averaged temporal history for the CH_4–H_2 (a) and H_2 flames (b) at $f_a = 228$ Hz and $u_{rms}/\bar{u} = 0.17$. Top: pressure fluctuation p' from simulations and reconstructed from Equation (9.2). Bottom: normalized time derivative of the volume-integrated HRR $\dot{q}/P_{th}$ from simulations and reconstructed from the flame surface through Equations (9.5) and (9.6).

and is associated to the strongest p' radiated by the flame (see Equation (9.2)). This peak value is equal to 680 s^{-1} for the signal reconstructed with Equation (9.5) (blue dashed line), while it increases to 896 s^{-1} when Equation (9.6) (green dotted line) is employed, much closer to the actual value (black solid line), i.e., 831 s^{-1}. From a global perspective, a consistent trend is observed when considering the normalized temporal r.m.s. of dq/dt, i.e., $\dot{q}_{rms}/P_{th}$. Evaluated over the entire forcing cycle, this metric provides an estimate of the impact of the selected model on the predicted OASPL, since, based on Equation (9.2), the OASPL is proportional to $\dot{q}_{rms}$. In particular, $\dot{q}_{rms}/P_{th}$ is equal to 334 s^{-1} when computed with Equation (9.5), and increases to 440 s^{-1} if Equation (9.6) is adopted. This latter value is almost coincident with the actual one (black line in Figure 9.6b-ii), which is equal to 436 s^{-1}. Further confirmation on the improvement of the correlation is given by the value of r_c, which increases from 0.93 when considering S_L^0 to 0.96 when using $\overline{S_c}$.

It should be noted that, whether a local (i.e., $|dq/dt|_{max}/P_{th}$) or a global (i.e., $\dot{q}_{rms}/P_{th}$) quantity is considered, the ratio between the value reconstructed with Equation (9.6) and the one obtained with Equation (9.5) is about 1.3, which corresponds to $\overline{S_c}/S_L^0$. Therefore, even though this value is relatively small with respect to other laminar configurations (e.g., Berger et al. [26] obtained $\overline{S_c}/S_L^0 \approx 2.7$ in 2D planar H_2 flames under analogous operating conditions), these results highlight the importance of considering stretch effects when applying the flamelet model to $Le < 1$ flames.

9.2.2 Impact of the forcing amplitude

The impact of the flow perturbation amplitude is assessed numerically by considering the H_2 flame with a forcing level $u_{rms}/\bar{u} = 0.24$. The analysis is repeated for the CH_4–H_2 flame, and

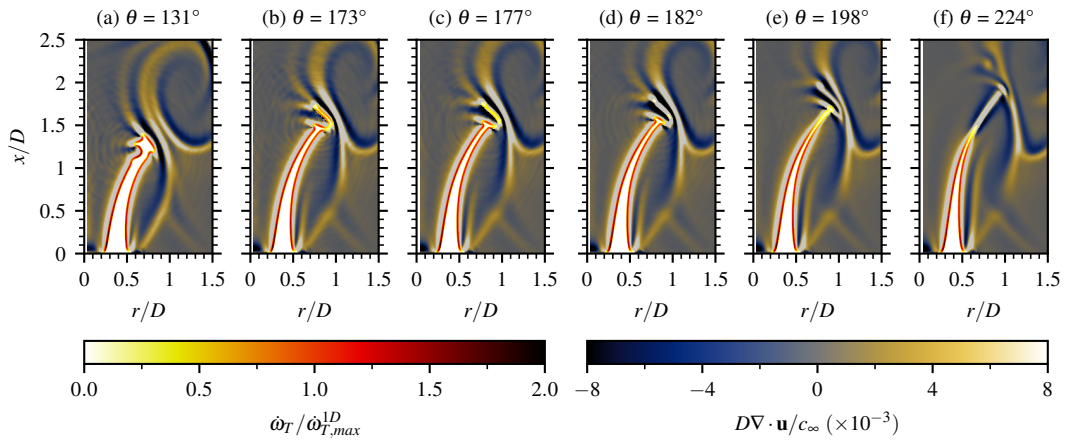

Figure 9.7: H_2 flame at $f_a = 228$ Hz and $u_{rms}/\bar{u} = 0.24$. Snapshots of normalized HRR $\dot{\omega}_T/\dot{\omega}^{1D}_{T,max}$ in the unburned and flame front region, identified by $c \leq 0.95$, and normalized dilatation $D\nabla \cdot \mathbf{u}/c_\infty$ at six different phase angles.

the corresponding results are given in Appendix E.

Figure 9.7 reports the normalized HRR, together with the dilatation $\nabla \cdot \mathbf{u}$, i.e., the divergence of the velocity field, normalized by the burner diameter D and the speed of sound in the far-field medium c_∞. This quantity is commonly used as a marker of sound in aeroacoustic studies [387, 390]. Six different snapshots are considered to describe the flame dynamics associated with the strongest flame surface and HRR variations.

Figure 9.7a shows small-scale wrinkling of the flame front in the tip region, leading to the enhancement of HRR in the positively curved zones (convex toward the fresh gases) and to local annihilation in the cusp regions, features associated with TD instabilities [221]. These structures lead to an enhanced flame perturbation at the flame tip (see Figure 9.7b-e) with respect to the previous case, forced at a lower modulation level. Nevertheless, the strength of this phenomenon is sensibly low if compared to flame annihilation in the CH_4–H_2 flame of Figure 9.5a, and, therefore, does not lead to a strong acoustic radiation. Moreover, acoustic waves radiate from the flame well before the annihilation event (see the dilatation field in Figure 9.7a), and are induced by the local HRR fluctuation associated with TD effects and local flame front wrinkling. Finally, Figure 9.7f highlights that a trace of the open tip wake is present in the dilatation field, due to the variations in the temperature and density fields induced by the H_2 differential diffusion.

Figure 9.8a reports the corresponding time traces of p' recorded and reconstructed from the HRR using Equation (9.2). A very good agreement between the two signals ($r_c = 0.99$) is found also in this case, confirming that the recorded acoustic radiation is associated with direct combustion noise. As expected, the p' magnitude is enhanced by the higher amplitude of the inflow perturbation. Still, despite the enhanced flame motion, no strong p' oscillation, comparable to what observed in the CH_4–H_2 flame of Figure 9.6a-i, is found. This confirms the slower dynamics and reduced impact on the overall noise radiation of the H_2 flame.

The HRR dynamics is related to the flame surface variations in Figure 9.8b. Similar considerations as in the low-amplitude case (see Figure 9.6b-ii) can be made. The signal reconstructed using Equation (9.6) shows a very good match with the recorded curve ($r_c = 0.97$), while stronger discrepancies are found with Equation (9.5) ($r_c = 0.92$). The value of $\dot{q}_{rms}/P_{th}$ obtained when considering Equation (9.6) is equal to 630 s^{-1}, with an underestimation of about 5% with respect to the actual value (black line in Figure 9.8b), equal to 666 s^{-1}. The flame tip position reported in Figure 9.8c confirms that, also in this case, no pinch-off event occurs at the tip. The only dif-

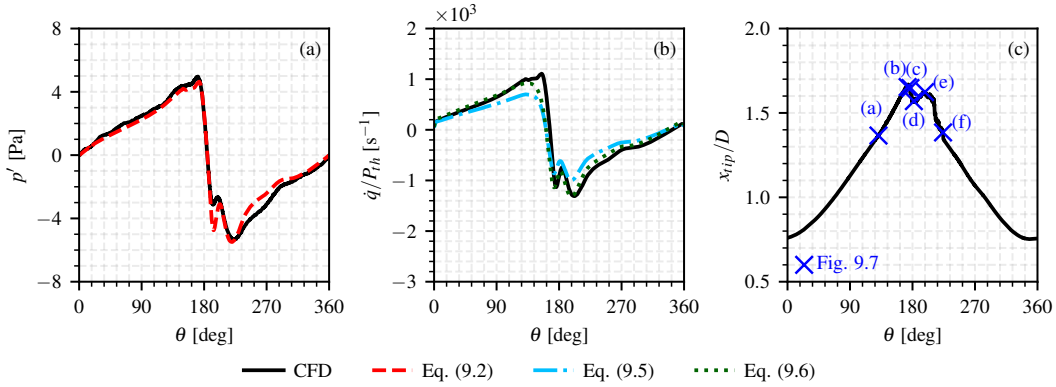

Figure 9.8: Phase-averaged temporal history for the H_2 flame at $f_a = 228$ Hz and $u_{rms}/\bar{u} = 0.24$: pressure fluctuation p' from simulations and reconstructed from Equation (9.2) (a), normalized time derivative of the volume-integrated HRR $\dot{q}/P_{th}$ from simulations and reconstructed from the flame surface via Equations (9.5) and (9.6) (b), and normalized flame tip position x_{tip}/D from numerical simulations (c). The blue crosses correspond to flame patterns in Figure 9.7.

ference with respect to the low-amplitude case in Figure 9.3b is an enhanced oscillation of x_{tip} in correspondence of the peak value, due to the stronger inflow fluctuations. Therefore, the increased forcing amplitude at the flame bottom strengthens the flame dynamics observed for the H_2 flame in Figure 9.6, but without triggering any relevant annihilation phenomenon.

9.2.3 Impact of the forcing frequency

The previous analysis is now reproduced considering the same forcing amplitude of the baseline case of Section 9.2.1 ($u_{rms}/\bar{u} = 0.17$), but at a higher frequency $f_a = 456$ Hz. Results with the same forcing for the CH_4–H_2 flame are reported in Appendix E.

The normalized HRR and dilatation fields are shown in Figure 9.9 for six different phase angles. The small-scale wrinkling features previously observed in Figure 9.7a are retrieved also in this case, but further upstream (see Figure 9.9a) due to the shorter wavelength of the inflow perturbation. As a result, a pinch-off event is now observed, with the detachment of a flame pocket of relevant size (see Figure 9.9b-c). However, differently from the CH_4–H_2 flame of Figure 9.2a, the

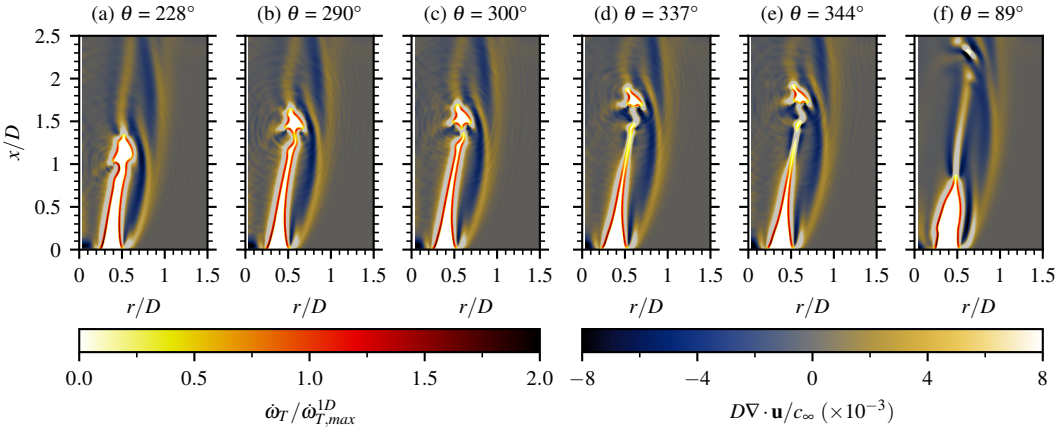

Figure 9.9: H_2 flame at $f_a = 456$ Hz and $u_{rms}/\bar{u} = 0.17$. Snapshots of normalized HRR $\dot{\omega}_T/\dot{\omega}^{1D}_{T,max}$ in the unburned and flame front region, identified by $c \leq 0.95$, and normalized dilatation $D\nabla\cdot\mathbf{u}/c_\infty$ at six different phase angles.

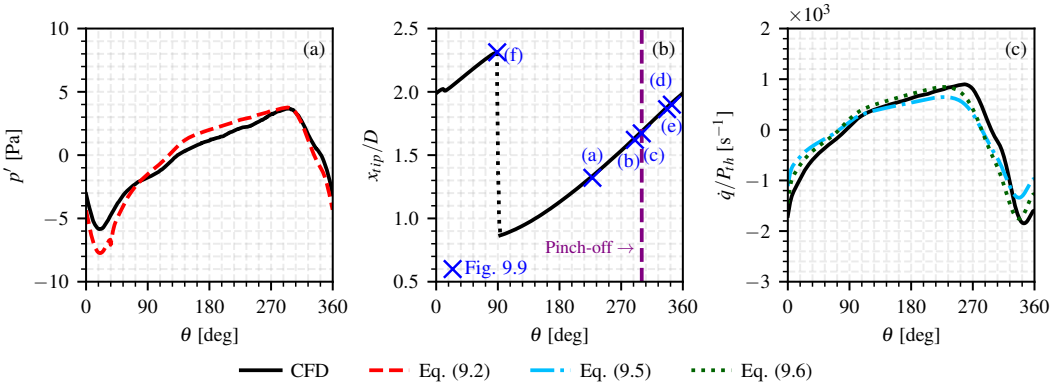

Figure 9.10: Phase-averaged temporal history for the H_2 flame at $f_a = 456$ Hz and $u_{rms}/\bar{u} = 0.17$: pressure fluctuation p' from simulations and reconstructed from Equation (9.2) (a), normalized flame tip position x_{tip}/D from numerical simulations (b), and normalized time derivative of the volume-integrated HRR $\dot{q}/P_{th}$ from simulations and reconstructed from the flame surface via Equations (9.5) and (9.6) (c). The blue crosses correspond to flame patterns in Figure 9.9.

duration of the annihilation event is sensibly longer for this H_2 flame forced at higher frequency (approximately 10° in terms of phase angle).

This suggests that annihilation is not associated with flame-flame interaction as in the CH_4–H_2 flame, but is induced by H_2 differential diffusion, which leads to the local extinction of the flame in the cusp region originated at the flame tip [221]. This is the same mechanism responsible for the tip opening in the stable flame [229], but here obtained in the point where the two flame branches are stretched and brought closer by the perturbation wrinkling the flame front. For flames characterized by $Le < 1$, negative curvatures lead to a progressive reduction of the local reaction rate, and, consequently, of S_c, coherently with observations in [388, 390] (see Section 7.2.1). This leads to a slower annihilation dynamics [421].

Focusing on the detached flame pocket, this does not correspond anymore to a torus as in hydrocarbon flames [49, 353]. Indeed, the pocket presents cellular structures, associated with TD instabilities, which lead to convex and concave regions, and to unsteady local HRR variations. As a result, the detached pocket perturbs the dilatation field in Figure 9.9, indicating acoustic radiation. Nevertheless, this is a weaker noise source with respect to the CH_4–H_2 case, since the enhanced stretch resistance and wide flammability range of the H_2 flame [221] (see Section 4.2.2) allow for the detached pocket to be continuously burned for a long duration (see Figure 9.9d-e). As shown in Figure 9.9f, and coherently with Figure 9.7f, a trace of the consumed pocket is observed in the dilatation field, confirming that H_2 differential diffusion induces a long-term impact in the burned gases region.

Figure 9.10a highlights the increase in the amplitude of p' at this frequency, when compared to the low-frequency case of Figure 9.6b-i. Also in this case, a strong agreement is found between the recorded and reconstructed p' signals ($r_c = 0.96$), confirming the flame-related origin of the acoustic radiation. The presence of the pinch-off event at the flame tip can be clearly observed in Figure 9.10b, which shows a discontinuity of x_{tip}. The discontinuity, however, takes place over a much wider extension when compared to the CH_4–H_2 flame of Figure 9.3a. This is consistent with its slow consumption observed in Figure 9.9, here marked by the distance (in terms of phase angle) between the pinch-off (purple dashed line), corresponding to Figure 9.9c, and the ultimate consumption of the pocket (dotted black line), corresponding to Figure 9.9f. Given this slow consumption, no relevant trace of the flame tip dynamics is present in the p' signal (see Fig-

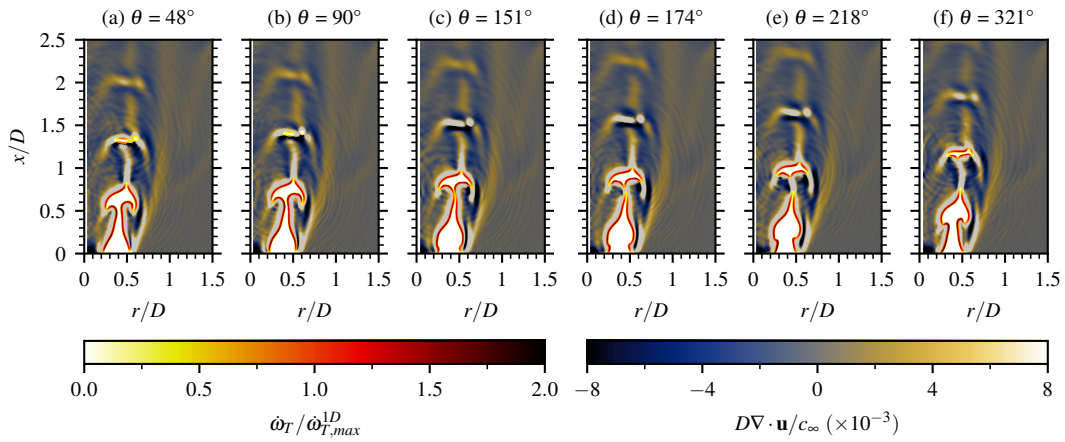

Figure 9.11: H_2 flame at $f_a = 1368$ Hz and $u_{rms}/\bar{u} = 0.17$. Snapshots of normalized HRR $\dot{\omega}_T/\dot{\omega}^{1D}_{T,max}$ in the unburned and flame front region, identified by $c \leq 0.95$, and normalized dilatation $D\nabla \cdot \mathbf{u}/c_\infty$ at six different phase angles.

ure 9.10a), as well as in the HRR time derivatives, either recorded from the CFD or reconstructed from $\mathcal{A}_f$ using Equations (9.5) and (9.6), reported in Figure 9.10c. Indeed, the signals follow the global flame dynamics associated with the flame motion, coherently with the previous cases at lower forcing frequency (see Figures 9.6b and 9.8). This marks a difference with respect to the CH_4–H_2 flame in Figure 9.6a, highlighting the different role of flame annihilation between the two flames. Figure 9.10c also confirms the strong agreement between the recorded dq/dt signal and the one reconstructed using Equation (9.6), with a relative error on $\dot{q}_{rms}/P_{th}$ of about 2%.

To further characterize the peculiar tip annihilation dynamics of the H_2 flame, a final configuration is considered with forcing frequency $f_a = 1368$ Hz, thus enhancing the local flame fluctuations due to the unsteady inflow and, consequently, cellular structures associated with TD instabilities [429, 435] (see Section 4.2.3).

The normalized HRR and dilatation fields are reported in Figure 9.11 for six different phase angles, denoted by the blue crosses in Figure 9.12. Overall, similar considerations as for the previous case of Figure 9.9 can be made. The higher forcing frequency, however, allows to exaggerate the previously described effects. Indeed, the detached pocket features a further extended size, and, due to the stronger local flame curvature and the enhanced unsteady HRR variations, more strongly perturbs the dilatation field. Moreover, the trace of the detached pocket in the burned gases region, previously observed in Figures 9.7f and 9.9f, persists for the whole cycle. This is evident in Figure 9.12f where, at the same time, the dilatation field is perturbed by the current detached pocket and by the two previous ones. This confirms that, for the H_2 flame, the HRR unsteadiness derives not from the rapid consumption of the pocket, but rather by the variability induced by TD effects on its local structure, which strongly differs from the toroidal one observed in the absence of TD effects [49, 353]. Finally, Figure 9.12d highlights also the absence of noise radiation due to the annihilation phenomenon at the flame neck, sustaining the fact that this is not a relevant noise source for the H_2 flame.

From the temporal traces of Figure 9.12, several differences can be observed with respect to the previous cases. Looking at the p' traces in Figure 9.12a, a discrepancy is found between the recorded and HRR-reconstructed p' signals, which originates from the stronger noise due to the inflow forcing, well represented by the pressure fluctuations in cold flow conditions p'_{cf}. Indeed, recalling Table 8.3, the value of the OASPL in cold flow conditions for this forcing level is 100.3 dB, making the noise due to the inflow perturbation dominant over the noise coming from

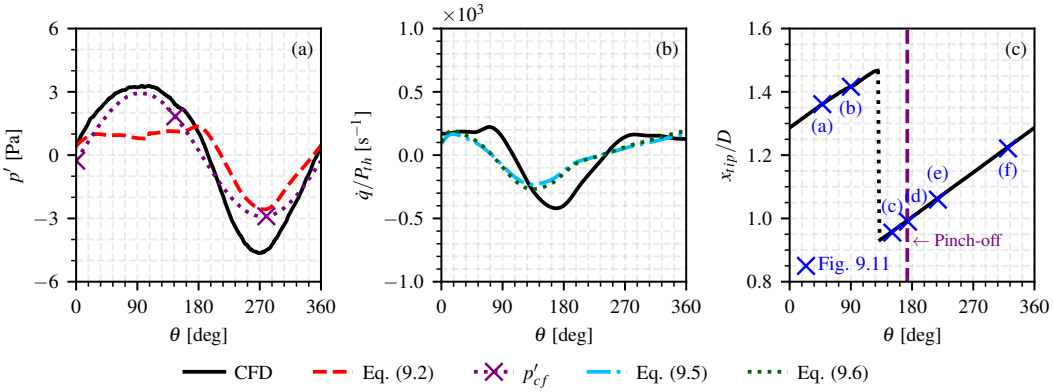

Figure 9.12: Phase-averaged temporal history for the H_2 flame at $f_a = 1368$ Hz and $u_{rms}/\bar{u} = 0.17$: pressure fluctuation p' from simulations and reconstructed from Equation (9.2) (a), normalized time derivative of the volume-integrated HRR $\dot{q}/P_{th}$ from simulations and reconstructed from the flame surface via Equations (9.5) and (9.6) (b), and normalized flame tip position x_{tip}/D from numerical simulations (c). The blue crosses correspond to flame patterns in Figure 9.11. The cold flow pressure fluctuation p'_{cf} is reported too.

the flame, since the OASPL reconstructed from the HRR is 96.3 dB. Moreover, the amplitude of p' is sensibly reduced for this high frequency level, a result which is consistent with those reported in [390]. This can be explained by the fact that, for increasing forcing frequency, the efficiency of the flame response is reduced, meaning that the flow stretch is less able to alter the global flame dynamics [435], and, consequently, to radiate noise. This is further sustained by Figure 9.12b, which highlights the sensibly worsened correlation between the time derivative of HRR and the corresponding signals reconstructed from $\mathcal{A}_f$ using Equations (9.5) and (9.6) ($r_c = 0.75$ when using Equation (9.6)), due to a phase lag of approximately 34° with respect to the recorded signal (black line in Figure 9.12b). The presence of this delay, consistent with the results in [429] for H_2 flames subjected to an analogous forcing, is associated to the non-linearity of the combustion process and of the interaction between the flow disturbance and the flame, which leads to a delay time in the flame response [71]. Moreover, the failure of the flamelet theory [2, 69] for low values of $S_L^0/(\delta_L^0 f_a)$ is consistent with what observed in [390] for $Le = 1$ flames. Therefore, although the flame is more strongly perturbed and the local HRR variability is enhanced, the flame is not able to respond to this perturbation sufficiently fast, resulting in the lower flame-generated acoustic radiation reported in Figure 9.12a. Finally, Figure 9.12c shows, coherently with the previous case of Figure 9.10b, the presence of a clear pinch-off in the x_{tip} signal. This, however, leaves no trace in the p' signal, due to the slow consumption of the detached pocket. Indeed, the phase distance between the pinch-off (purple dashed line) and the full consumption of the pocket (dotted black line) covers almost the whole forcing cycle.

9.2.4 Flame annihilation and acoustic spectrum

The impact of the peculiar annihilation dynamics of the H_2 flame (see Section 9.2) on the acoustic spectrum is here considered. Figure 9.13 compares the Sound Pressure Level (*SPL*) spectra obtained from the experimental and numerical signals for the CH_4–H_2 and H_2 flames at $u_{rms}/\bar{u} = 0.17$ and $f_a = 228$ Hz, i.e., the configurations discussed in Section 9.2.1. The *SPL* is

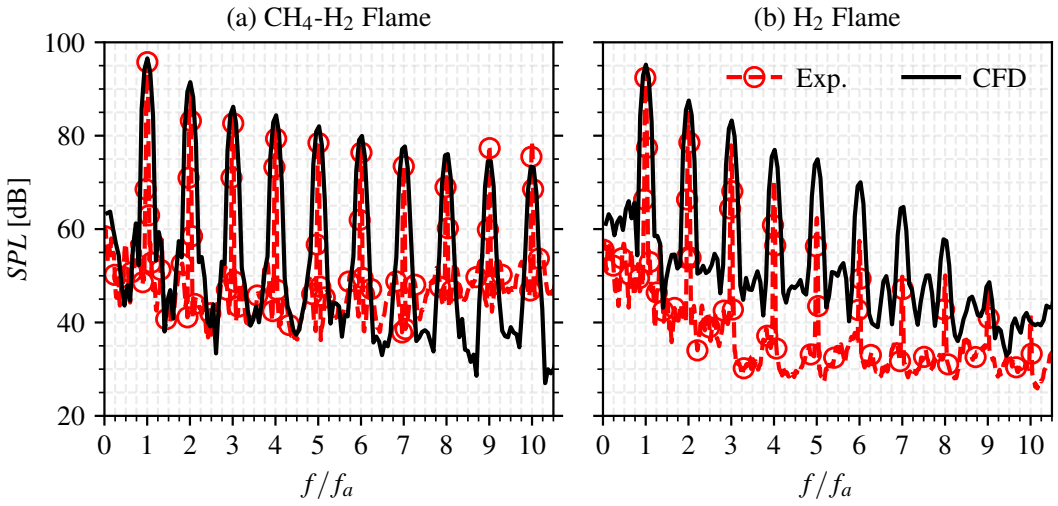

Figure 9.13: Experimental and numerical SPL spectra for the CH_4–H_2 (a) and H_2 (b) flames at $u_{rms}/\bar{u} = 0.17$ and $f_a = 228$ Hz. The frequency f is normalized by the forcing value f_a.

evaluated at the same probe used for the temporal p' signals in Section 9.2 and is computed as:

$$SPL\,[\mathrm{dB}] = 10\log_{10}\left(\frac{S_p \Delta f}{p_{ref}^2}\right), \tag{9.8}$$

where S_p is the Power Spectral Density (PSD) of the pressure signal, Δf is the frequency resolution, and $p_{ref} = 2 \times 10^{-5}$ Pa is a reference acoustic pressure [48]. The PSD is estimated using the periodogram method by Welch [420] and applying a Hanning window with 75% overlap. For the numerical signal, the window length corresponds to 10 forcing cycles, whereas for the longer experimental signal, with a duration of 2280 cycles, a window of length equal to 50 cycles is used.

For this acoustically forced laminar flame configuration, the spectrum is constituted of several well-defined peaks at the fundamental frequency, corresponding to the forcing frequency f_a, and its harmonics [48, 49]. A reasonable correspondence is found between the experimental and numerical spectra, especially in the decay trends of the *SPL* at high frequencies. Indeed, for the CH_4–H_2 flame, both experiments and numerical simulations agree in predicting a strong spectral energy in the high-frequency harmonics, with a saturation for $f/f_a > 7$. This can be related to the presence, for this flame, of the strong noise source related to the flame pinch-off, which is rapid, hence associated with the high-frequency component of the spectrum. This result is coherent with previous experimental studies on an analogous configuration [48, 49], and with the numerical work on turbulent flames by Brouzet et al. [41], who showed that annihilation events have a strong acoustic signature at high frequencies (see Section 7.2.1).

A relevant high-frequency content, however, is absent for the H_2 flame, both in experiments and numerical simulations. In this case, indeed, the absence of the flame pinch-off leads to a steeper roll-off of the *SPL* with increasing frequency, i.e., a larger absolute value of the exponent of the power law governing the decay (linear on a logarithmic scale). As a result, the spectral energy at the third harmonic (i.e., $f/f_a = 4$) is approximately 20 dB lower than at the fundamental frequency, while the same level of noise reduction is achieved, for the CH_4–H_2 flame, at the sixth harmonic (i.e., $f/f_a = 7$). It should be noted that a reduction of 20 dB corresponds to a value of *SPL* four times smaller.

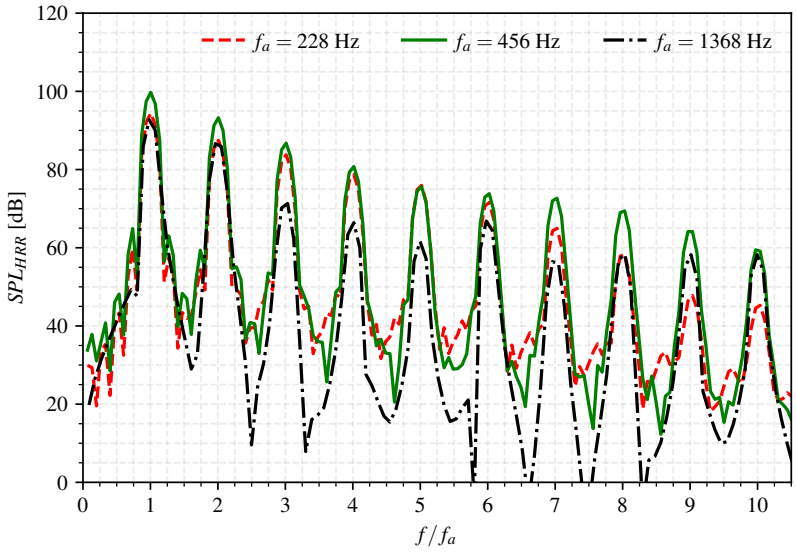

Figure 9.14: Numerical SPL spectra, reconstructed from the HRR using Equation (9.2), for the H_2 flame at $u_{rms}/\bar{u} = 0.17$ and different forcing frequencies. The frequency f is normalized by the forcing value f_a.

The role of the flame pinch-off for the H_2 flame is discussed in Figure 9.14, which compares the acoustic spectra obtained at $u_{rms}/\bar{u} = 0.17$ and at the different forcing frequencies previously explored in Sections 9.2.1 and 9.2.3, i.e., $f_a = 228$ Hz, $f_a = 456$ Hz, and $f_a = 1368$ Hz. Given the impact of the inflow forcing for the latter case (see Figure 9.12), the SPL is here computed for the pressure signal reconstructed from the HRR using Equation (9.2) (SPL_{HRR}). It can be observed that, when passing from $f_a = 228$ Hz to $f_a = 456$ Hz, a slight enhancement of the high-frequency content is achieved, consistently with the stronger fluctuation of HRR associated with the more intense forcing and with the detachment of the flame pocket at the tip. Nevertheless, the decay rate remains similar for both forcing frequencies, and the same sensible reduction of the noise level at the third harmonic (i.e., $f/f_a = 4$) is achieved, confirming the absence of a signature of the pinch-off event in the acoustic spectrum. This is coherent with the analysis previously performed in the time domain (see Figure 9.10). A similar trend is observed when further increasing the forcing frequency to $f_a = 1368$ Hz, with a further reduction of the spectral content due to the reduced efficiency of the flame in the conversion of inflow perturbations to fluctuations of the HRR, as discussed in the analysis of Figure 9.12.

9.3 Relation with the OH* chemiluminescence

The spatial relation between OH* and HRR has been thoroughly discussed in Chapter 6, highlighting its limits for lean premixed H_2–air flames. To further confirm these results, Figure 9.15 shows the HRR distribution, normalized by its maximum value, for the present M-shaped H_2–air flame under unforced conditions, together with isolines of the normalized OH* concentration at 20%, 50% and 90%. The OH* distribution is retrieved with a post-processing algorithm based on the QSS approximation (see Appendix B) and applying the sub-scheme by Kathrotia et al. [190] (see Table 6.1), which is well suited for the considered operating conditions (see Figure 6.10).

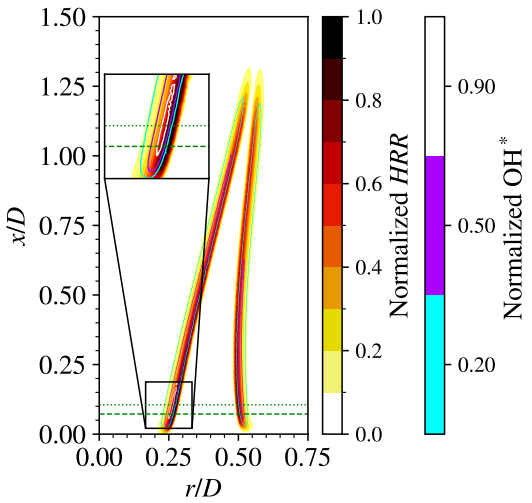

Figure 9.15: Normalized distributions of HRR in the unforced lean M-shaped hydrogen–air premixed flame at atmospheric conditions, together with isolines at 20%, 50% and 90% of normalized OH* concentration. The inset highlights the region of maximum HRR and OH*. The horizontal green lines highlight denote the axial peak positions of the HRR (dashed line) and OH* (dotted line) distributions.

Consistently with the results in Sections 6.3 and 6.4, an axial shift is observed between the peaks of HRR (dashed green line) and OH* (dotted green line). Moreover, the OH* distribution seems not to properly capture the flame shape, particularly near the flame tip, where the HRR is reduced due to the open tip mechanism induced by H_2 differential diffusion (see Section 4.2.2). This behavior is coherent with what observed for the lean expanding flame in Figure 6.15, further supporting the validity of the discussion presented in Section 6.4.2.

In addition to the spatial relation between OH* and HRR, the temporal one is also important to investigate unsteady combustion systems, especially in the context of combustion noise studies. Indeed, for lean premixed flames, a linear relation between the volume-integrated HRR q and the OH* chemiluminescent emission intensity I_{OH^*} has been found [48, 193]:

$$q = kI_{OH^*}, \tag{9.9}$$

where the coefficient k depends on the fuel, the combustion regime, the flame shape and type, and the experimental set-up [48]. This provides a convenient optical method to measure the unsteady fluctuations of HRR, which, as discussed in Section 9.2, govern the acoustic radiation of the M-shaped flame considered in this Chapter.

While extensively validated for hydrocarbons [48], the applicability of the linear relation in Equation (9.9) to H_2–air flames has been scarcely investigated. Experimental results in this sense were provided in [100] for the present M-shaped flame forced at $f_a = 228$ Hz, showing an overall good agreement between the global flame dynamics and the unsteady OH* emission. Here, the analysis is extended to the cases forced at higher frequencies. To this scope, the H_2 flames with modulation amplitude $u_{rms}/\bar{u} = 0.17$ and forcing frequencies $f_a = 228$ Hz, $f_a = 456$ Hz, and $f_a = 1368$ Hz discussed in Section 9.2 are considered hereafter. Figure 9.16 reports the intensities I of the volume-integrated HRR and OH* (top), normalized by their temporal means $\bar{I}$, together with the corresponding normalized time derivatives (bottom) for the three forcing frequencies. The time is reported in terms of phase angle $\theta = t/(2\pi f_a)$. The signals are phase-averaged over 15 forcing cycles, and synchronized with respect to the sinusoidal

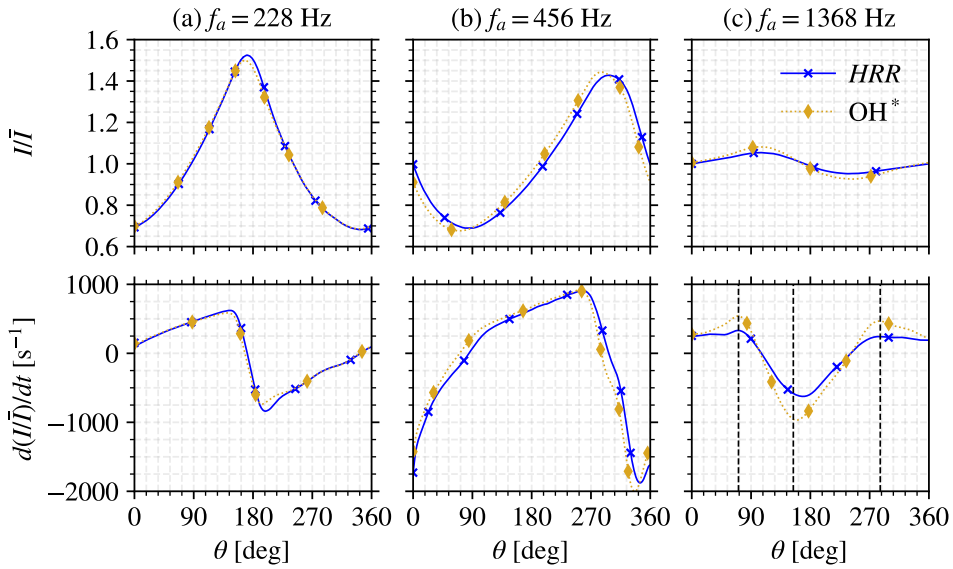

Figure 9.16: Phase-averaged temporal signals of normalized HRR and OH* (top) and corresponding time derivatives (bottom) for $f_a = 228$ Hz (a), $f_a = 456$ Hz (b), and $f_a = 1368$ Hz (c). The inset highlights the region of maximum HRR and OH*. The dashed vertical lines correspond to the snapshots in Figure 9.17.

velocity forcing.

Overall, the OH* and HRR signals are adequately well correlated, even though moderate differences in the position and amplitude of the positive and negative peaks can be observed, suggesting a different response of the two quantities to the acoustic forcing. This effect becomes more evident at the highest forcing frequency (see Figure 9.16c), for which the local flame response is enhanced (see Section 4.2.3), and cellular structures associated with TD instabilities are created, as discussed in Section 9.2. For this latter case, although an overall correlation persists, the OH* signal shows stronger fluctuations with respect to the HRR one. Therefore, this suggests that, while the OH* intensity is able to follow the global behavior of the flame at low frequencies, where local variations of HRR associated with stretch and TD effects are less accentuated, the lack of spatial correlation impacts the temporal one when the local variability of HRR is stronger.

To further investigate this result, Figure 9.17 reports the normalized HRR distributions, together with isolines of the normalized OH* concentration at 20%, 50% and 90%, for the case with $f_a = 1368$ Hz at three phase angles, denoted by the vertical black dashed lines in Figure 9.16c-bottom, which correspond to the widest distances between the time derivatives of HRR and OH*. Overall, coherently with the observations made for the expanding flame in Figure 6.15, the enhancement of TD effects, which in this forced case leads to cellular structures and instabilities, worsens the correlation. Moreover, while at $\theta = 71°$ and $\theta = 154°$ (see Figure 9.17a-b) the peaks of HRR and OH*, albeit not coincident, are close, in the $\theta = 286°$ case (see Figure 9.17c) a stronger disagreement is found, with the maximum HRR located in the detached pocket on top, while the maximum OH* is located in the curved region in the bottom of the flame. Therefore, in this particular configuration, the detachment of a flame pocket from the tip further accentuates the differences between the two quantities, explaining the enhanced discrepancies in the temporal signals of Figure 9.16c.

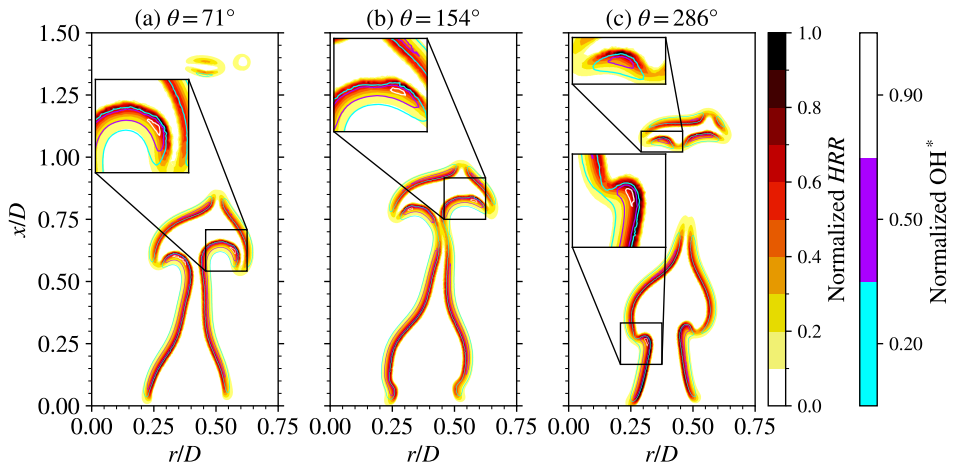

Figure 9.17: Normalized distributions of HRR in the forced lean M-shaped hydrogen–air premixed flame at atmospheric conditions, together with isolines at 20%, 50% and 90% of normalized OH^* concentration, for $f_a = 228$ Hz (a), $f_a = 456$ Hz (b), and $f_a = 1368$ Hz (c). The insets highlight the regions of maximum HRR and OH^*.

9.4 Influence of the chemical and transport modeling

The influence of the chemical modeling on the acoustic response of the laminar H_2 flame is discussed in this Section. To this scope, results obtained with the detailed San Diego (UCSD) scheme [339] are compared with calculations performed with the global reaction mechanism developed in Chapter 5, hereafter denominated 1S_FGS for brevity reasons. For the considered operating conditions, the sole forward reaction is retained, being the impact of the backward step negligible, as discussed in Section 5.2.4.

Moreover, the impact of transport modeling is investigated, by artificially modifying the transport parameters of the 1S_FGS scheme. Three additional schemes are consequently taken into account:

- The 1S_FGS_LE1 scheme, with $Le_k = 1$ for each species k, suppressing both differential and preferential diffusion.
- The 1S_FGS_NOPREF scheme, for which $Le_k = Le_{H_2}$, where Le_{H_2} is the Lewis number of H_2 in the 1S_FGS scheme, thereby suppressing the preferential diffusion of H_2, while retaining the differential one.
- The 1S_FGS_NODIFF scheme, based on the condition $Le_k = Le_k/Le_{H_2}$, which removes the differential diffusion of H_2 while preserving the preferential diffusion of H_2 with respect to the other species.

As discussed in Section 4.2.3, a similar approach was adopted in [12, 307, 349] to analyze the impact of molecular transport in 2D laminar and 3D turbulent thermodiffusively unstable planar premixed flames. However, differently from these works, in the present study the Pre-Exponential Factors and the mixture Prandtl numbers Pr of the three modified schemes are adjusted, in order to match the values of S_L^0 and δ_L^0 of the 1S_FGS mechanism for the operating point of interest. This is necessary since, differently from a planar flame, the laminar flame properties directly influence the geometry of the jet flame, which affects the acoustic radiation (see Section 7.1.2).

Table 9.1: Comparison of flame properties computed with the reference UCSD mechanism [339] and the four reduced reaction schemes for the laminar flame.

Chemical scheme	S_L^0 [m/s]	δ_L^0 [μm]	T_{ad} [K]	$\dot{\omega}_{T,max}^{1D}$ [W/m^3]
UCSD	0.55	380	1640	2.42×10^9
1s_FGS	0.49	385	1640	4.21×10^9
1s_FGS_LE1	0.49	380	1650	4.41×10^9
1S_FGS_NOPREF	0.49	385	1640	4.41×10^9
1S_FGS_NODIFF	0.49	385	1650	4.29×10^9

Table 9.1 compares relevant flame properties obtained from 1D unstrained premixed flame calculations using Cantera [137] with the detailed UCSD scheme and the four reduced mechanisms, while the values of the parameters adopted for the reaction rate and the transport model of the different reduced schemes are given in Appendix A. It is noted that all reduced mechanisms have similar laminar flame properties, which are well in agreement with those obtained using the detailed UCSD scheme. A relevant difference is observed in the value of $\dot{\omega}_{T,max}^{1D}$, which is almost twice for the reduced schemes. This is to be expected, since the value of S_L^0 depends on the integral of $\dot{\omega}_T$, and not on its maximum value. Therefore, given that the flame computed with a reduced scheme has a thinner structure due to the absence of minor species (see Section 5.3.1), the local values of HRR are higher, to achieve a similar integral value and, consequently, a comparable value of S_L^0.

Aside from the chemical and transport modeling, the numerical methodology is the same implemented in the previous Sections, with the sole exception of the ambient medium, which is here composed of equilibrium burned gases at the adiabatic flame temperature, as discussed in Section 8.2.1. In the following, the impact of the chemical and transport modeling on the flame structure is analyzed first in unforced conditions. Subsequently, the acoustic response is investigated, by considering a modulation amplitude $u_{rms}/\bar{u} = 0.17$ and two forcing frequencies: a low-frequency case at $f_a = 228$ Hz, and a high-frequency one at $f_a = 1368$ Hz.

9.4.1 Steady flame

Figure 9.18 compares the HRR distributions, normalized by the maximum value in the 1D unstretched flame $\dot{\omega}_{T,max}^{1D}$ (see Table 9.1), obtained with the detailed UCSD mechanism and the reduced scheme with different transport properties. Overall, the UCSD (see Figure 9.18a) and 1S_FGS (see Figure 9.18b) mechanisms show a significantly good agreement in terms of flame shape and HRR distribution. Still, smaller upstream preheat and downstream equilibrium zones of the flame front are observed in the 1S_FGS case, due to the absence of minor species. Moreover, while both schemes predict an enhancement of HRR at the flame root of the inner branch, this is further accentuated for the reduced scheme. It should be noted that the local HRR for the reduced scheme is much higher than for the UCSD case, since $\dot{\omega}_{T,max}^{1D}$ is almost twice the value (see Table 9.1).

The impact of Lewis effects is evident from the results for the 1S_FGS_LE1 case (see Figure 9.18c), suppressing both preferential and differential diffusion. Most notably, the tip opening, characteristic of H_2 jet flames [267] is absent, and the flame shows a well-defined, continuous front with constant HRR, in analogy to what observed for the CH_4–H_2 flame in Section 9.1. Due to this HRR redistribution, the lift-off distance is sensibly higher, and the length of the flame brush increases from about $1.4D$ to $2D$. When considering the sole differential diffusion (see Fig-

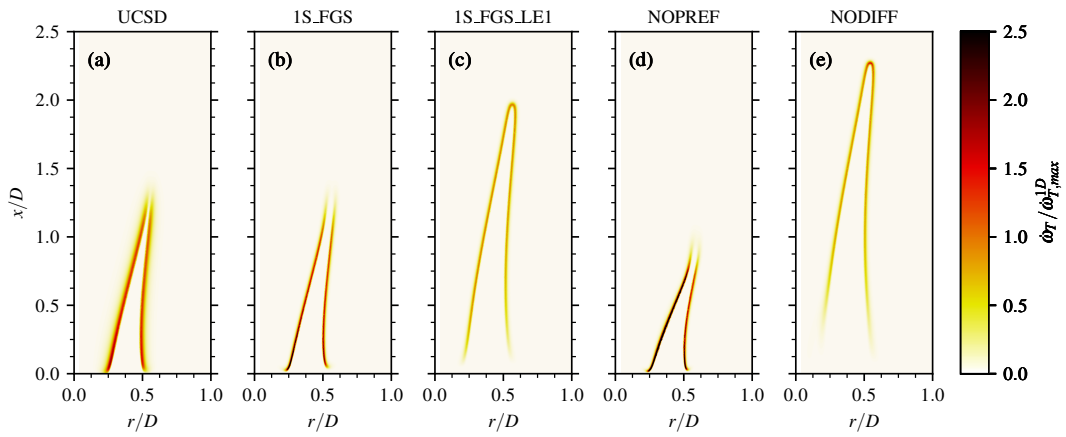

Figure 9.18: Distributions of normalized HRR $\dot{\omega}_T/\dot{\omega}^{1D}_{T,max}$ for the UCSD [339] (a), 1S_FGS (b), 1S_FGS_LE1 (c), 1S_FGS_NOPREF (d) and 1S_FGS_NODIFF (e) mechanisms.

ure 9.18d), the main qualitative features of the sub-unity *Le* flame (see Figure 9.18b) are retrieved, coherently with the observations made in [12, 307, 349] for planar lean H_2 flames. However, in this jet flame configuration, the impact of preferential diffusion on the flame structure is found to be more relevant. In particular, the HRR enhancement in the inner branch, associated with TD effects and already present in the UCSD (see Figure 9.18a) and 1S_FGS (see Figure 9.18b) cases, is further amplified when preferential diffusion is suppressed. This leads to increased HRR levels along the entire flame brush, and to a reduction in the length of the flame of approximately $0.4D$. The suppression of differential diffusion (see Figure 9.18e), on the other hand, further enhances the features observed for the unity *Le* case (see Figure 9.18c). Nevertheless, preferential diffusion still leads to variations in the local equivalence ratio [307], resulting in a local HRR enhancement in correspondence of the flame tip, where the curvature is the most accentuated. This is related to the fact that, in the absence of differential diffusion, the tip closing mechanism is promoted [229], making the flame tip richer and, consequently, increasing the local flame speed. On the other hand, the flame root, which is leaner and burns more slowly, is also cooled down by the heat loss at the burner wall. As a result, the flame length is further increased to approximately $2.3D$, and the lift-off distance is higher than in the unity *Le* case (see Figure 9.18c), especially on the inner branch.

9.4.2 Forced flames

Figure 9.19 reports the temporal history, as a function of the phase angle θ, of the fluctuating pressure fluctuation p', recorded (blue solid lines) and reconstructed from the HRR through Equation (9.2) (red dotted lines) at the two considered forcing frequencies. As in Section 9.2.1, the signals are phase-averaged over 15 forcing cycles and synchronized with respect to the sinusoidal axial velocity measured at the burner outlet.

Focusing on the low-frequency case first (see Figure 9.19a-e), a very good agreement is observed, for all schemes, between the recorded and reconstructed signals, confirming that HRR fluctuations are the major noise source with all chemical mechanisms. Moreover, the two schemes with realistic transport properties, i.e., the UCSD (Fig. 9.19a) and the 1S_FGS (Fig. 9.19b) predict similar profile shapes and fluctuation amplitudes, sustaining the ability of the reduced scheme to reproduce the flame dynamics. Moving to the 1S_FGS_LE1 case (see Figure 9.19c), as expected,

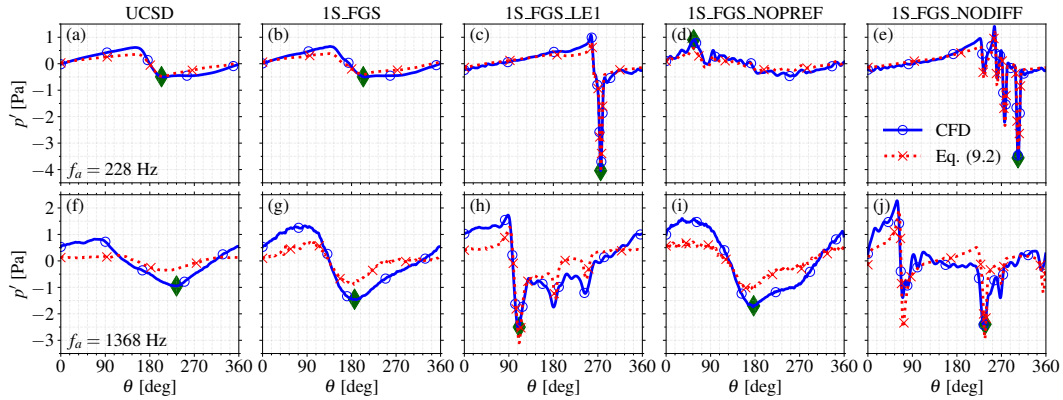

Figure 9.19: Phase-averaged temporal history of pressure fluctuation recorded from CFD and reconstructed from the HRR signal through Equation (9.2) for the UCSD [339] (a-f), 1S_FGS (b-g), 1S_FGS_LE1 (c-h), 1S_FGS_NOPREF (d-i) and 1S_FGS_NODIFF (e-j) mechanisms at f_a = 228 Hz (top) and f_a = 1368 Hz (bottom). The green diamonds correspond to flame patterns in Figure 9.20.

a significantly different behavior is observed, with the presence of sharp peaks, compatible with the flame pinch-off found for the CH_4–H_2 flame in Section 9.2.1. In the 1S_FGS_NOPREF case (see Figure 9.19d), despite the similar unforced flame shape with respect to the UCSD and 1S_FGS cases (see Figure 9.18), discrepancies are found for p', with the presence of abrupt fluctuations for $\theta < 180°$. The 1S_FGS_NODIFF case (see Figure 9.19e), on the other hand, shows a behavior consistent with the 1S_FGS_LE1 case, even though more accentuated, with the presence of multiple annihilation-related negative peaks.

For the high-frequency case (see Figure 9.19f-j), instead, the recorded and reconstructed p' signals are less in agreement, coherently with what observed in Section 9.2.3. Nevertheless, a correspondence is found in the shape of the two signals, indicating that the flame-generated noise still influences the overall acoustic radiation. For this forcing level, the 1S_FGS scheme (see Figure 9.19g) overpredicts p' with respect to the detailed UCSD case (see Figure 9.19f). Moreover, a closer agreement is found between the 1S_FGS (see Figure 9.19g) and 1S_FGS_NOPREF (see Figure 9.19i) cases, both in terms of values and signal shape compared to the low-frequency case. Indeed, the strong fluctuations observed at $\theta < 180$ for the low-frequency 1S_FGS_NOPREF flame (see Figure 9.19c) are now mitigated. For the other two cases (see Figure 9.19h and j), similar considerations can be made as for the low-frequency case, with the presence now of multiple annihilation-related negative peaks.

To better elucidate these differences, Figure 9.20 shows the instantaneous normalized distributions of HRR $\dot{\omega}_T/\dot{\omega}^{1D}_{T,max}$ and dilatation $D\nabla \cdot \mathrm{u}/c_\infty$ for the two flames in correspondence of the maximum (in absolute value) of dq/dt. This maximum is associated to the strongest flame-generated p', denoted by the green diamonds in Figure 9.19, when taking into account the delay for the propagation of the acoustic wave, as discussed in the analysis of Figure 9.5. For the low-frequency case (top row), the UCSD and 1S_FGS cases both show a deformation of the flame with no abrupt flame annihilation, thus explaining the absence of p' peaks, with a good agreement in the flame shape and HRR distribution. In the 1S_FGS_LE1 case, on the other hand, the aforementioned flame pinch-off is observed, with the abrupt detachment of a pocket of unburned gases, which emits noise due to its rapid consumption. These results are well in agreement with the previous discussion in Section 9.2.1. For the 1S_FGS_NOPREF case, pronounced instabilities can be observed in the inner flame branch, resulting in local HRR variations, which explain

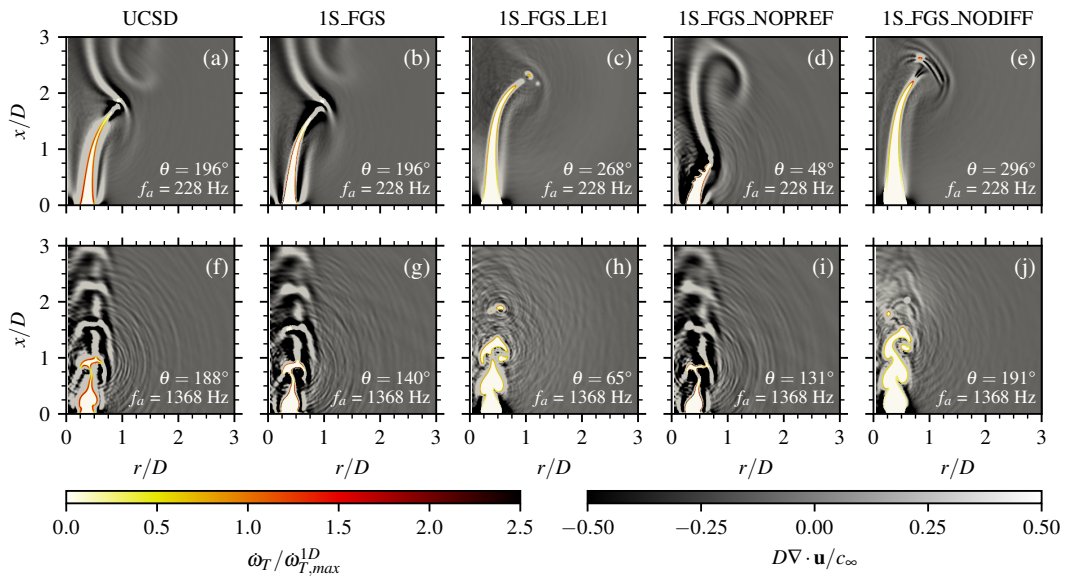

Figure 9.20: Instantaneous fields of normalized HRR $\dot{\omega}_T/\dot{\omega}^{1D}_{T,max}$ and dilatation $D\nabla\cdot\mathbf{u}/c_\infty$ for the UCSD [339] (a-f), 1S_FGS (b-g), 1S_FGS_LE1 (c-h), 1S_FGS_NOPREF (d-i) and 1S_FGS_NODIFF (e-j) mechanisms at $f_a = 228$ Hz (top) and $f_a = 1368$ Hz (bottom) in correspondence of the maximum value of $|dq/dt|$.

the p' fluctuations observed in Figure 9.19c. As expected, the 1S_FGS_NODIFF case shows similar features as for the 1S_FGS_LE1 one, with the main difference being a further enhancement of the local HRR at the flame tip when pinch-off occurs.

Moving to the high-frequency case, the detachment of a pocket of unburned reactants can be observed also for the $Le_{H_2} < 1$ cases. Nevertheless, as discussed in Section 9.2.3, two main differences are found with respect to the unity Le case: the presence of cellular structures on the detached pocket, compatible with TD instabilities, and the local reduction of HRR in correspondence of the detachment point induced by the differential diffusion of H_2 with respect to heat [229]. As in Section 9.2.3, these detached pockets burn more slowly, and the trace of the previously consumed pockets is observed in the dilatation field. The fact that this is an effect of H_2 differential diffusion is here confirmed by its absence for the 1S_FGS_LE1 (see Figure 9.20h) and 1S_FGS_NODIFF (see Figure 9.20j) cases. Consequently, the unsteadiness in the HRR is driven, for these pockets, not by their rapid consumption, as in $Le = 1$ flames [353, 387], but rather by the local spatial and temporal fluctuations induced by the cellular structures associated with TD effects. This is a slower, hence low-frequency, contribution, which adds to the noise generated by the global flame dynamics due to the unsteady inflow. As a result, coherently with the previous analysis in Section 9.2.3, no high-frequency peaks are observed in Figure 9.19f and g due to the annihilation event. The UCSD (see Figure 9.20f) and 1S_FGS (see Figure 9.20g) cases show an overall good agreement. However, the one-step scheme shows a much stronger local HRR enhancement in correspondence of the cellular structures at the tip. While this reduced scheme has been designed to capture the flame response to stretch (see Section 5.4.1), this result suggests some limits in its prediction in the presence of high stretch values. This explains the higher noise level predicted for this case (see Figure 9.19g).

Features similar to those of the 1S_FGS scheme are observed also for the 1S_FGS_NOPREF one (see Figure 9.20i), with particular reference to the formation of cellular structures associated with TD effects. Nevertheless, coherently with what observed in the low-frequency case, these

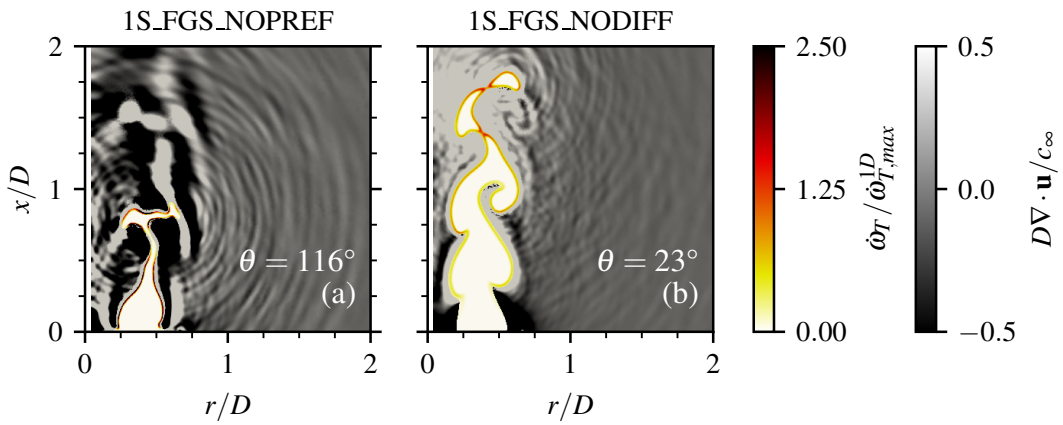

Figure 9.21: Instantaneous fields of normalized HRR $\dot{\omega}_T/\dot{\omega}^{1D}_{T,max}$ and dilatation $D\nabla \cdot \mathbf{u}/c_\infty$ for the 1S_FGS_NOPREF (a) and 1S_FGS_NODIFF (b) mechanisms at f_a = 1368 Hz in correspondence of an annihilation event at the flame tip.

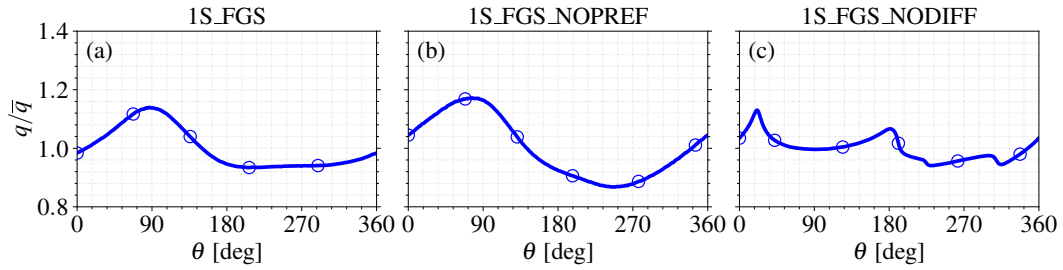

Figure 9.22: Phase-averaged temporal history of normalized volume-integrated HRR $q/\overline{q}$ at f_a = 1368 Hz for the 1S_FGS (a), 1S_FGS_NOPREF (b), and 1S_FGS_NODIFF (c) schemes.

are further enhanced, inducing stronger HRR fluctuations. Therefore, TD effects are accentuated when preferential diffusion is neglected. This is further highlighted in Figure 9.21, which shows snapshots for the high-frequency 1S_FGS_NOPREF and 1S_FGS_NODIFF cases in correspondence of the flame pinch-off. As previously observed in Figures 9.18 and 9.20, the sole differential diffusion induces tip opening, resulting in a local HRR reduction before annihilation. Preferential diffusion, on the other hand, induces a tip closing, with a local HRR increase in the regions of high-curvature. As a result, there is an increase of HRR at the annihilation point, leading to abrupt HRR fluctuations in correspondence of flame annihilation and, consequently, to stronger noise generation associated with mutual flame interactions.

To give a quantitative assessment, the temporal r.m.s. of the normalized volume-integrated HRR $q/\overline{q}$ signals reported in Figure 9.22 is considered, with $\overline{q}$ corresponding to the steady flame thermal power P_{th} (see Table 8.1). For this high frequency forcing case, $q_{rms}/\overline{q} = 0.07$ for the 1S_FGS scheme, which includes both preferential and differential diffusion. When the sole differential diffusion is retained (1S_FGS_NOPREF scheme), $q_{rms}/\overline{q}$ increases to 0.10. On the other hand, when only preferential diffusion is considered (1S_FGS_NODIFF scheme), $q_{rms}/\overline{q}$ decreases to 0.04. The effects of differential and preferential diffusion, therefore, are antagonist. The former promotes local wrinkling and extinction, smoothing the HRR variations associated with mutual flame interactions and reducing the time derivative of q (i.e., the combustion noise source term), despite the larger amplitude of the HRR fluctuation. The latter, instead, leads to a stabilization of the flame surface, which makes the HRR variations associated with pinch-off more abrupt, thereby intensifying dq/dt even in the presence of HRR oscillations of lower am-

plitude. In actual H_2 flames, where both effects are included, preferential diffusion mitigates the effects of differential diffusion, meaning that, if this is neglected, the impact of TD effects on the flame annihilation and HRR variability would be overestimated, a result that may be significant, in a more general framework, when dealing with H_2 combustion modeling.

9.5 Summary and concluding remarks

The impact of thermodiffusive effects on flame-acoustics interactions and noise generation were investigated through numerical simulations, validated by experiments, for lean hydrogen (H_2) and stoichiometric methane-hydrogen (CH_4–H_2) laminar premixed M-shaped flames.

The different transport properties of the two fuels were shown to significantly alter the heat release rate (HRR) distribution, even in unforced conditions. In particular, the H_2 flame showed an enhancement of the HRR near the flame root and tip opening. Under moderate acoustic forcing, strong noise generation in the CH_4–H_2 flame was associated with flame-flame interactions and pinch-off, while no such annihilation was observed in the H_2 flame. In all cases, the HRR fluctuations dominated the acoustic radiation and were well correlated with flame surface fluctuations through the combustion noise flamelet theory, provided that stretch effects on the flame speed were included. It should be noted, however, that the increase in the consumption speed for this flame ($\overline{S_c}/S_L^0 \approx 1.3$) was relatively modest if compared to other configurations (e.g., $\overline{S_c}/S_L^0 \approx 2.7$ in two-dimensional planar H_2 flames under analogous operating conditions [26]), and a reformulation may be necessary when stretch effects are stronger, as it will be further discussed in Section 11.3.1.

At higher forcing amplitudes, the local wrinkling and pressure fluctuations of the H_2 flame increased, with limited annihilation driven by the local extinction in the cusp regions due to stretch and thermodiffusive instabilities, rather than to flame–flame interaction. Increasing the forcing frequency promoted pocket formation and cellular structures, leading to stronger local HRR fluctuations. For frequencies close to the flame characteristic frequency, however, the inflow forcing dominated the noise generation process, while the ability of the flame to convert the flow unsteadiness in combustion unsteadiness was hindered, resulting in a phase lag between the flame surface and HRR responses. The impact on the acoustic spectrum was investigated, showing that, while, in the CH_4–H_2 flame, the annihilation event produced a clear signature in the high-frequency component, this was absent in the H_2 flame, even when the flame pinch-off occurred, leading to a stronger spectral decay. Overall, due to differential diffusion and tip opening, annihilation at the flame tip does not act as a major noise source in acoustically excited lean premixed H_2–air flames, differently from hydrocarbons. At high forcing frequencies, however, lingering detached pockets perturb the acoustic field through continuous deformation.

The temporal correlation between OH* and HRR, main driver of the acoustic radiation, was also investigated. Some differences were observed in the instantaneous signals, especially at high forcing frequencies, due to the limits of OH* in capturing the local variability of HRR induced by thermodiffusive effects and instabilities. Nevertheless, an overall good temporal correlation was found, indicating that the spatially integrated OH* signal remains an adequate tracer of the global HRR dynamics. These results suggest that the OH* chemiluminescence remains a useful quantity for the experimental study of flame–acoustics interactions. However, while similar conclusions were drawn from experiments performed for the laminar M-shaped flame forced at low frequency [100], additional joint experimental and numerical investigations are required to further confirm the validity of the temporal correlation between OH* and HRR in H_2-air flames.

Finally, the impact of chemical and transport modeling on the acoustic radiation of the laminar H_2 flame was also investigated. The reduced global mechanism derived in Chapter 5, designed to reproduce the laminar flame properties and response to stretch (at least up to $\kappa \approx 4000\ s^{-1}$), showed a strong agreement with the detailed San Diego mechanism [339] in terms of flame structure and low-frequency acoustic response. At higher forcing frequencies, however, the reduced scheme overestimated the acoustic emission, due to an enhanced local sensitivity to high stretch levels, leading to increased HRR fluctuations in correspondence of the cellular structures induced by thermodiffusive instabilities. When imposing unity values of the Lewis number for all species, flame annihilation events were promoted, and the flame dynamics was analogous to the one obtained for the CH_4–H_2 flame. Finally, the separate analysis of the impact of differential and preferential diffusion on flame annihilation dynamics showed that the two have antagonist effects, with the former promoting flame instability and local extinction, while the latter leads to an enhancement of HRR in the regions of high curvature, where the detachment of flame pockets occurs. Therefore, preferential diffusion mitigates the effects of the differential one on the annihilation and HRR dynamics of lean premixed H_2 flames, a result which should be taken into consideration, in a more general framework, when dealing with H_2 combustion modeling.

10

Turbulent premixed slot jet flame configuration

The turbulent flame numerical dataset, exploited in Chapter 11 for the analysis of combustion noise, is introduced hereafter. The configuration of reference is a turbulent slot jet flame, widely investigated in the literature for hydrogen combustion (e.g., [27, 79, 248]), as well as for the analysis of combustion noise of methane flames (e.g., [341, 342]).

The flame is at atmospheric conditions (i.e., $T_u = 300$ K and $p = 1$ atm), and is located in an open environment. Hydrogen and methane flames are investigated, with variable values of the jet bulk velocity and different compositions of the ambient medium.

Contents

10.1 Case studies

In the baseline configuration, premixed lean H_2–air slot jet flames are compared with a stoichiometric CH_4–air flame in an open environment of ambient air. This configuration has been chosen to investigate, in addition to combustion noise, also the differences between hydrocarbon and H_2 flames in the shear layer formed at the interface between the hot combustion products and the ambient air, as discussed in Chapter 11.

The H_2–air slot jet flame is employed also in Section 11.6 to analyze the impact of chemical kinetics and transport modeling, thereby complementing the study performed for the laminar

M-shaped jet flame reported in Section 9.4. To isolate the direct noise generated by the flame and remove the influence of the varying composition in the shear layer, the ambient is composed, for these case studies, of equilibrium burned gases at the adiabatic flame temperature. Finally, the influence of the Karlovitz number Ka on the radiated noise is also investigated in Section 11.5, by adopting the configuration with the equilibrium burned gases ambient. In this latter case, consistently with [23], the slot cross-section is reduced while the bulk velocity U_B is increased, thereby incrementing Ka while keeping the same jet Reynolds number Re.

Hereafter, the numerical set-up and methodology adopted for the baseline CH_4 and H_2 flames in ambient air are described, as these constitute the primary case studies in Chapter 11. The numerical framework is analogous for the remaining cases, whose specific features are recalled in Sections 11.5 and 11.6, together with the corresponding results.

10.1.1 Description of the computational domain

A representation of the 3D computational domain, discretized with an unstructured mesh of tetrahedral elements, is given in Figure 10.1, while Figure 10.2 shows a 2D scheme of the xy plane, reporting the geometrical dimensions and boundary conditions. A central rectangular channel of size $H = 8.5$ mm in the cross-stream y direction and $1.5H$ in the spanwise z direction, and length $3H$ in the streamwise x direction, injects a flow of fresh turbulent gases with bulk velocity U_B in an open ambient air domain. This is defined as a cylinder of radius $35H$ with respect to the slot center and spanwise length $L_x = 20H$, surmounted by a hemisphere. The region of interest for the investigation of noise is represented by a cylinder of radius $10H$ with respect to the slot center and length L_x from the channel exit.

Coherently with analogous configurations in the literature (e.g., [79, 222, 248, 341, 342]), two laminar coflows of equilibrium burned gases at the adiabatic flame temperature are introduced to stabilize the flame along the spanwise sides of the rectangular channel outlet. These are of width $H/12$ in the cross-stream direction and have axial velocity $U_C^{bg} = 0.01U_B$. All is surrounded by a laminar coflow of ambient air with axial velocity $U_C^{air} = 0.1$ m/s, with a

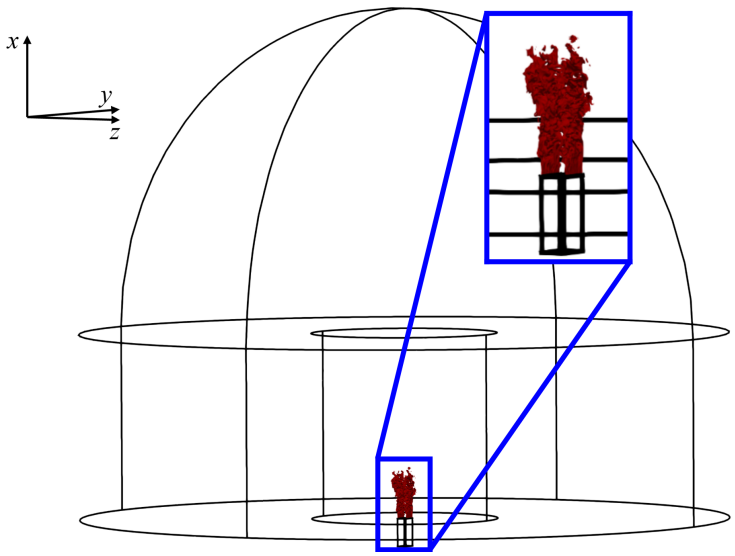

Figure 10.1: Representation of the 3D computational domain, highlighting the position of the flame.

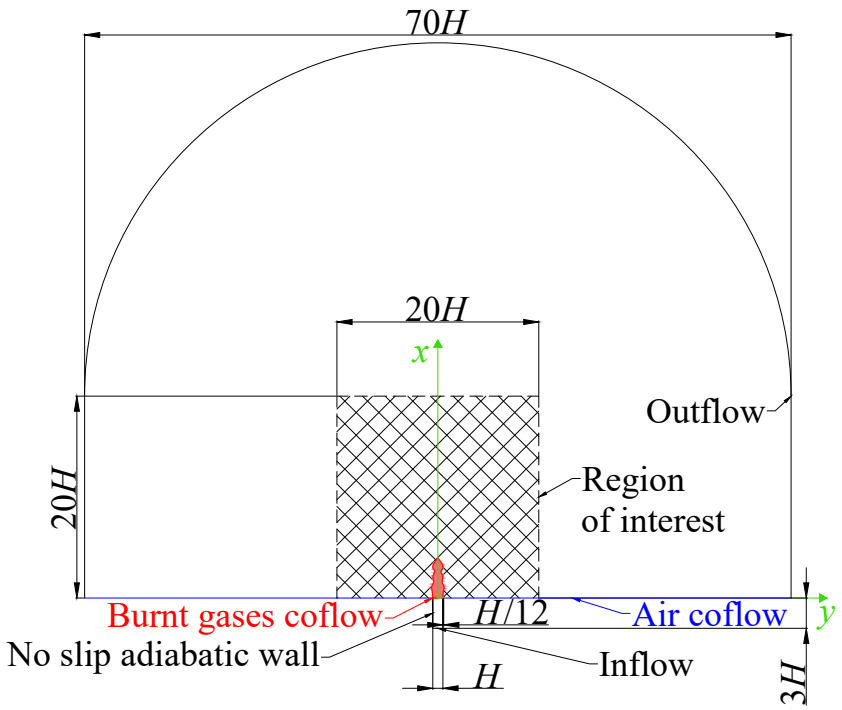

Figure 10.2: Cross-section of the computational domain in the xy plane, reporting the boundary conditions and geometrical dimensions. The position of the flame is reported in red.

Table 10.1: Laminar flame properties of the two reacting mixtures.

Description [unit]	Value	
	CH_4 Flame	H_2 Flame
Equivalence ratio ϕ [-]	1.0	0.45
Laminar flame speed S_L^0 [m/s]	0.38	0.38
Laminar flame thickness δ_L^0 [μm]	400	450
Adiabatic flame temperature T_{ad} [K]	2260	1535
Maximum HRR in the 1D flame $\dot{\omega}_{T,\max}^{1D}$ [W/m^3]	4.60×10^9	1.50×10^9

smooth transition between the different flows achieved through a hyperbolic tangent function. This marks a difference with respect to most of the studies in the literature performed in similar jet flame configurations (e.g., [44, 79, 222, 248]), which consider a burned gases environment.

10.1.2 Flow configuration and operating parameters

A stoichiometric ($\phi = 1.0$) CH_4 flame is compared with a lean ($\phi = 0.45$) H_2 flame. Both flames are at atmospheric conditions (i.e., $T_u = 300$ K and $p = 1$ atm). With the chosen operating points, the two flames have comparable values of the laminar flame speed and thickness. Table 10.1 reports the laminar flame properties for the two considered fuel–air mixtures, obtained through 1D unstretched laminar premixed flame calculations with Cantera [137].

Three flow conditions are considered. For the stoichiometric CH_4–air flame, a bulk velocity $U_B = 10$ m/s is adopted. This case is hereafter denominated M10, and is considered as a reference, since it is designed not to feature TD instabilities. For the lean H_2–air flame, instead, two values

of bulk velocity are taken. One case, here labeled as H25, has bulk velocity $U_B = 25$ m/s, chosen to have a similar average length of the turbulent flame brush with respect to the M10 case, since this dimension impacts the peak frequency of the acoustic spectrum (see Section 7.1.2). The other one, denominated H10, has bulk velocity $U_B = 10$ m/s, i.e., the same value of the M10 flame, allowing for further investigating the impact of the jet Reynolds number.

Table 10.2 provides relevant flow and flame parameters for the three cases. The thermal power is evaluated as $P_{th} = Y_{F,u}\rho_u \mathcal{A}_{ch} U_B H_F$, where $Y_{F,u}$ is the fuel mass fraction in the unburned mixture, ρ_u is the density of the fresh gases, $\mathcal{A}_{ch} = 1.5H^2$ is the section of the rectangular channel, and H_F is the fuel lower heating value, equal to 5.0×10^7 J/kg for CH_4 and to 1.20×10^8 J/kg for H_2. The jet Reynolds number is defined as $Re = (U_B H)/\nu_u$, where ν_u is the kinematic viscosity of the unburned mixture. The inlet Mach number is given by $\mathcal{M} = U_B/c_u$, with c_u being the speed of sound in the unburned mixture, and $\tau = L_x/U_B$ is the flow through time. The average flame length L_f is evaluated by considering the streamwise extension of the mean flame sheet, defined by the average progress variable at $\widetilde{C} = C^*$, i.e., the value of C at the location of the maximum HRR value in the corresponding 1D laminar unstretched premixed flame (see Table 10.1). The progress variable is defined as in [248]:

$$C = \frac{Y_F - Y_{F,u}(\xi)}{Y_{F,b}(\xi) - Y_{F,u}(\xi)}, \tag{10.1}$$

where Y_F is the fuel mass fraction, $Y_{F,u}(\xi) = \xi$ and $Y_{F,b}(\xi) = \max[0, (\xi - \xi_s)/(1 - \xi_s)]$, with ξ being the mixture fraction defined by Bilger [30] and ξ_s its stoichiometric value. With this definition, the values of C^* are, respectively, 0.77 for the CH_4 flame, and 0.80 for the H_2 ones. To isolate the reacting zone from the mixing region with cold ambient air, values of ξ lower than $0.5Y_{F,u}$ are not considered. In analogy with the works by Luca et al. [244] and by Berger et al. [27], the Kolmogorov length scale η is estimated *a posteriori* at $x = L_f/2$ on the previously defined mean flame sheet from the ensemble-averaged kinematic viscosity $\overline{\nu}$ and the Favre-averaged turbulence dissipation rate $\widetilde{\varepsilon}$ as $\eta = (\overline{\nu}^3/\widetilde{\varepsilon})^{1/4}$ [288], with the averages performed in time and in the spanwise direction. The Karlovitz number is evaluated as in Equation (2.76), recalled hereafter for convenience:

$$Ka = \left(\frac{l_t}{\delta_L^0}\right)^{-1/2} \left(\frac{u'}{S_L^0}\right)^{3/2}. \tag{10.2}$$

For all cases, the velocity fluctuation is $u' = 2.5$ m/s and the integral length scale of turbulence is $l_t = H/4 = 2.1$ mm, in analogy with the previous work by Coulon et al. [79].

With the given parameters, the flames are located in the thin reaction zone of the Borghi–Peters turbulent combustion diagram [301] (see Section 2.7.4). This is reported in Figure 10.3, where the present cases are compared with other DNS of CH_4 and H_2 premixed flames in the literature. As discussed in Section 2.7.4, the regime diagram provides only an order-of-magnitude analysis, and care should be taken in its interpretation. Nevertheless, it can be observed that, for the premixed flames considered in this work, viscosity and density are similar, since the mixture properties are dominated by the high nitrogen content [79]. Moreover, with the chosen operating conditions, the flames are subjected to similar turbulence fields, as discussed in the spectral analysis of turbulence reported in Appendix D, and have comparable laminar flame properties (see Table 10.1). This sustains the fact that the three flames belong to the same regime, i.e., the Thin Reaction Zone.

Table 10.2: Flow and flame parameters for the numerical simulations.

Description [unit]	Value		
	M10 Flame	H25 Flame	H10 Flame
Fuel [-]	CH_4	H_2	H_2
Bulk velocity U_B [m/s]	10	25	10
Thermal power P_{th} [kW]	3.4	4.3	1.7
Jet Reynolds number Re [-]	5300	10830	4330
Inlet Mach number M [-]	0.03	0.07	0.03
Flow through time τ [ms]	17.06	6.824	17.06
Average length of the flame brush L_f/H [-]	4.1	4.3	2.4
Kolmogorov length scale η [μm]	90	40	70
Karlovitz number Ka [-]	7	8	8

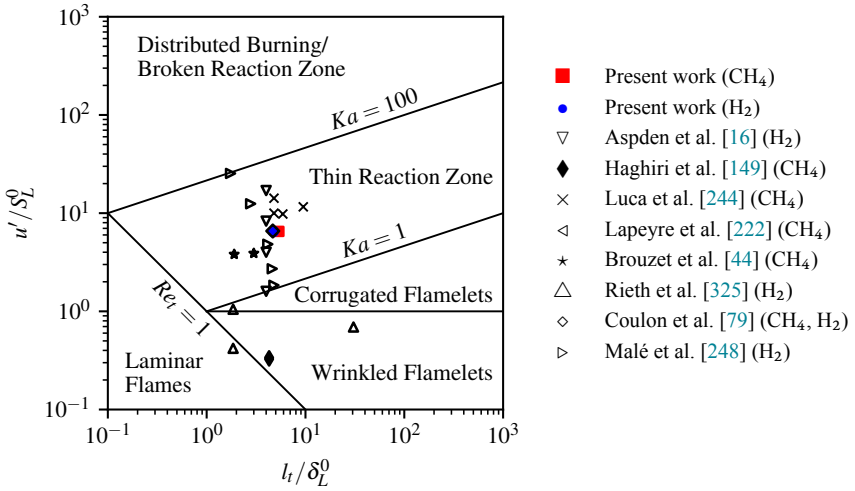

Figure 10.3: Location in the Borghi–Peters turbulent combustion diagram [301] of CH_4 and H_2 flames of the present study and of DNS in the literature.

10.2 Numerical methodology

Direct numerical simulations are performed for the considered turbulent flames using the San Diego mechanism [339] for H_2 and the global reaction mechanism CH4-2S [357] for CH_4. Both schemes have been presented in Section 3.3.4, together with the simplified transport model here implemented. The methodology followed for the definition of the numerical set-up is detailed in the following.

10.2.1 Grid resolution

As in the laminar simulations (see Section 8.2.3), the grid resolution in the region of interest (see Figure 10.2) should be sufficient to capture the flame structure and the acoustic waves. Moreover, the resolution should be enough to capture the small scale turbulent eddies.

The grid resolution in the flame region is not greater than $\Delta_x = 0.1$ mm, in line with previous DNS studies performed for CH_4 [222] and H_2 [248] turbulent premixed flames under analogous operating conditions. This resolution ensures at least 7-10 points in the flame front,

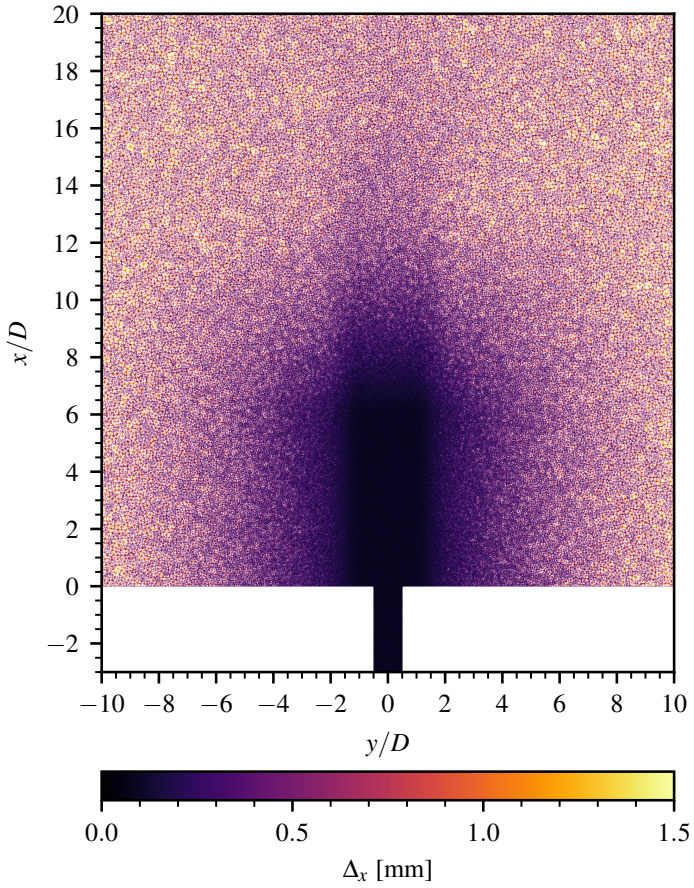

Figure 10.4: Local edge length Δ_x in the rectangular channel and in the region of interest, taken on a cross-section in the xy-plane.

allowing for resolving it without applying any turbulent combustion model. Moreover, it leads to a reasonable value of the global time step Δ_t, based on the acoustic *CFL* number (see Equation (3.15)). The value of Δ_t is equal to 19.7 ns, 23.3 ns and 24.7 ns for the M10, H25 and H10 cases, respectively. A grid independence study has been performed for the H25 case, which features the smallest value of the Kolmogorov length scale (see Table 10.2), to verify that turbulent combustion statistics are not affected by further mesh refinements (see Appendix C).

In analogy with the laminar configuration in Section 8.2.3, a smooth grid stretching is applied outside the reacting region to reduce the computational cost, with a growth factor of the cell sizes not greater than 2% to avoid any spurious waves [44, 149]. The resulting grid size for the DNS is of approximately 210 million cells for the M10 and H25 cases, and of approximately 165 million cells for the H10 case, characterized by a shorter flame length (see Table 10.2). The grid derefinement is observable in Figure 10.4, which reports the local edge length Δ_x on a cross-section taken in the xy plane for the mesh adopted in the H25 and M10 cases. Similar features are present in all the grids adopted for the turbulent slot jet flames throughout this dissertation. The maximum grid size in the region of interest is $\Delta_x^{max} \approx 1.5$ mm.

The simulations are performed using the two-steps finite-element TTGC scheme [77], which provides a third-order accuracy in space and time. For this scheme, at least 5 points are required in the acoustic wavelength to capture the wave without introducing a relevant numerical error

(see Section 3.3.2). Being $\Delta_{max} \approx 1.5$ mm, the smallest acoustic wavelength that can be captured is therefore $\lambda \approx 6.0$ mm. Considering the speed of sound in ambient air ($c_\infty = 348$ m/s), this corresponds to a maximum frequency $f_{max} = c_\infty/\lambda \approx 58$ kHz. This value is well above the audible range for humans, which spans from 20 Hz to 20 kHz. Based on combustion noise scaling laws (see Section 7.1.3), the peak frequency of the acoustic spectrum of a turbulent jet flame is in the order of $f_{peak} = U_B/L_f$. Among the different cases reported in Table 10.2, the highest value is obtained for the H25 flame, with $f_{peak} \approx 680$ Hz. Therefore, the considered grid allows for well capturing the high-frequency acoustic radiation, at least up to $85 f_{peak}$.

10.2.2 Boundary conditions

The boundary conditions, schematically shown in Figure 10.2, are here discussed. The walls are no-slip and adiabatic. Inflows and outflows are treated with the NSCBC formulation [309], presented in Section 3.3.3.

The channel inlet is forced using homogeneous and isotropic turbulence, coherently with previous DNS studies in the literature on analogous configurations [79, 248]. The turbulent velocity fluctuation is obtained with a synthetic generation method [205], based on the Passot–Pouquet turbulence spectrum [289], as detailed in Section 3.3.3. To achieve the turbulence parameters reported in Section 10.1.2, the turbulence spectrum described by Equation (3.29) features $u' = 2.5$ m/s, and $k_e = 1185$ m^{-1}, leading to $l_t = 2.1$ mm.

To avoid non-physical acoustic reflection, the non-reflecting NSCBC formulation [84] is adopted at the inlet, while a relaxation coefficient $K = 100$ s^{-1} is imposed at the outlet, leading to a cut-off frequency $f_c = K/(4\pi) \approx 8$ Hz [358] (see Equation (3.25)). Moreover, the jet turbulent inflow and the outflow are placed far from the reacting region (see Figure 10.2), allowing for further avoiding any non-physical interaction of these boundaries with the flame and its acoustic radiation. Outside the region of interest for the study (see Figure 10.2), the grid is more strongly stretched to hinder acoustic reflections from the outflow boundaries and dissipate high frequency spurious components of pressure. This strategy is alternative to the introduction of sponge layers at the inlet and outlet, adopted in previous DNS-based combustion noise studies in the literature [44, 149, 160].

10.2.3 Initialization and statistical convergence

The simulations were initialized using DNS flame solutions from Lapeyre et al. [222] for the CH_4 case and from Coulon et al. [79] for the H_2 cases. Statistical convergence was assessed by analyzing the cumulative temporal mean and r.m.s. statistics of the volume-integrated heat release rate, of the streamwise velocity at the outlet of the rectangular channel, and of the pressure in the region far from the jet. Results for the H25 case, which required a longer convergence time, are shown in Figure 10.5. Given the use of DNS solutions to initialize the flame, the velocity and HRR rapidly converge, reaching statistically steady mean and r.m.s. values. A longer time is needed for the pressure field. Still, all quantities reach convergence after 7τ, with the value of τ given in Table 10.2. After reaching this state, production runs are performed for 4τ, long enough to capture the peak of the combustion noise acoustic spectrum (see Section 11.2).

From a computational standpoint, the M10 and H25 cases are representative of all the turbulent configurations considered in this work. The total computational cost of the M10 production runs was approximately 1.4 million CPU-hours, obtained using 40 nodes, each equipped with two AMD EPYC Rome 7H12 64-core processors. The H25 case required approximately

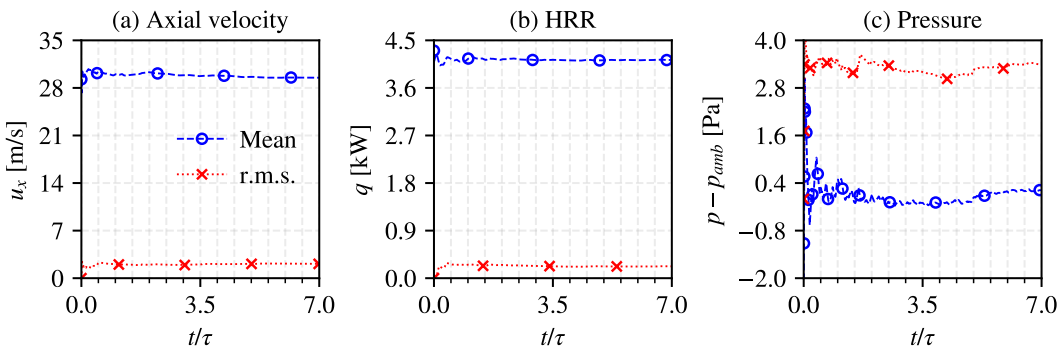

Figure 10.5: Cumulative temporal mean and r.m.s. of the axial velocity u_x at $(x/H, y/H, z/H) = (0, 0, 0)$ (a), of the volume-integrated HRR q (b), and of the relative pressure $p - p_{amb}$ at $(x/H, y/H, z/H) = (8, 8, 0)$ (c) for the H25 flame.

700 thousand CPU-hours, running on 30 nodes. This corresponds to a physical wall-clock time of approximately 270 hours and 180 hours for the M10 and H25 cases, respectively.

11

Noise generation mechanisms in turbulent premixed flames

The acoustic radiation of turbulent lean ($\phi = 0.45$) premixed hydrogen–air flames is investigated in this Chapter, exploiting the dataset of Direct Numerical Simulations obtained for the slot jet configuration presented in Chapter 10. First, the impact of thermodiffusive effects on the acoustic radiation is assessed, by comparing hydrogen–air flames with thermodiffusively stable stoichiometric methane–air flames, and a theoretical framework is developed to highlight the relevance of stretch effects on combustion noise for non-equidiffusive mixtures. Moreover, simulations are performed in an open environment of ambient air, allowing to characterize the impact of differential diffusion also on the shear layer between combustion products and air. Stronger localized density gradients are observed, suggesting that thermodiffusive effects impact both the direct and indirect combustion noise generation mechanisms in hydrogen flames.

Subsequently, the influence of the Karlovitz number on the acoustic radiation is investigated for the hydrogen–air flame, indicating how the reduced importance of thermodiffusive instabilities for increasing Karlovitz number differently shapes the direct combustion noise spectrum. Finally, the analysis on the impact of chemical modeling on combustion noise initiated in Section 9.4 is here extended to turbulent flames.

Results from this Chapter are included in:

- F. G. Schiavone, G. Daviller, and D. Laera. "Acoustic radiation from thermodiffusively unstable turbulent lean premixed hydrogen–air flames". *Submitted to Journal of Fluid Mechanics* (2026).
- F. G. Schiavone, G. Daviller, and D. Laera. "Influence of Karlovitz number on turbulent lean premixed hydrogen-air slot jet flames acoustics". *Submitted to Proceedings of the Combustion Institute* (2026).
- F. G. Schiavone, M. Torresi, S. M. Camporeale, and D. Laera. "Chemical Modeling and Lewis Number Effects on Noise Generation in Lean Premixed Hydrogen–Air Flames". *Accepted for publication in Proceedings of the ASME Turbo Expo 2026* (2026).

Contents

11.1 Flame–turbulence interaction

In this Section, the impact of TD effects and instabilities on the flame dynamics and the flame–turbulence interaction in lean premixed H_2 combustion is discussed, highlighting the differences with respect to conventional hydrocarbons. To this scope, the results of the DNS performed for the stoichiometric CH_4–air flame M10 and the lean ($\phi = 0.45$) H_2–air flames H25 and H10 at atmospheric temperature and pressure presented in Section 10.1.2 are discussed. It is recalled that the operating points are chosen so that they share similar laminar flame properties, in terms of speed and thickness (see Table 10.1). Moreover, the M10 and H10 cases have the same jet bulk velocity $U_B = 10$ m/s, while the H25 features $U_B = 25$ m/s, so that the average length of the turbulent flame brush is comparable to the one of the M10 case (see Table 10.2). The effect of the differences between the CH_4 and H_2 turbulent flames on combustion noise will be addressed in Section 11.3.

11.1.1 Overview of the flames and global stretch effects

Figure 11.1 shows isosurfaces of progress variable C taken at $C = C^*$, i.e., the value corresponding to the maximum HRR in the corresponding 1D laminar flame,($C^* = 0.77$ for the CH_4 flame and $C^* = 0.80$ for the H_2 ones). These are colored by the normalized local HRR $\dot{\omega}_T/\dot{\omega}^{1D}_{T,max}$ (see Table 10.1), for the three cases. As expected, the CH_4 flame has a regular, thermodiffusively stable behavior, with $\dot{\omega}_T$ constant on the whole flame surface and close to the maximum value in the 1D laminar unstretched flame. The sole exception is represented by the external regions, where $\dot{\omega}_T$ lowers due to the mixing with the cold ambient air. The H_2 flames, on the other hand, both show a strongly wrinkled flame front and sensible local variations of $\dot{\omega}_T$, which becomes up to three times higher than the maximum value in the corresponding 1D laminar flame. Furthermore, the H25 case has a length of the turbulent flame brush comparable to the one of the

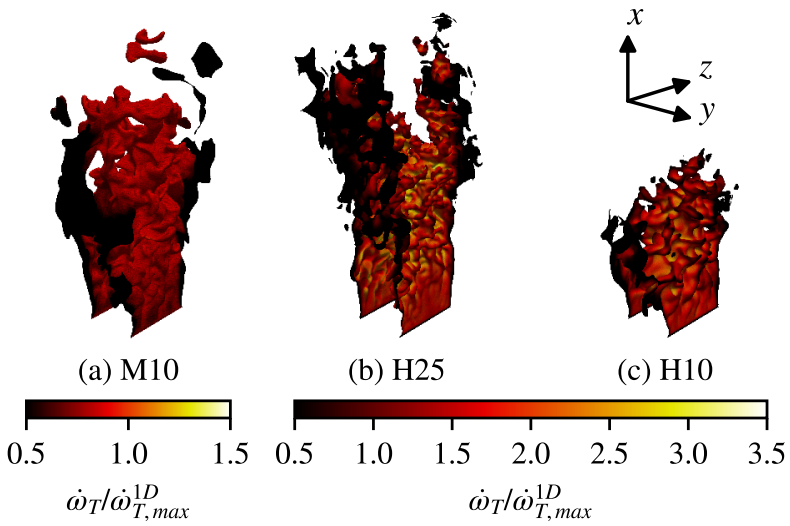

Figure 11.1: Isosurfaces of progress variable $C = C^*$ colored by the normalized HRR $\dot{\omega}_T/\dot{\omega}^{1D}_{T,max}$ taken at $t = 4\tau$ for the three cases.

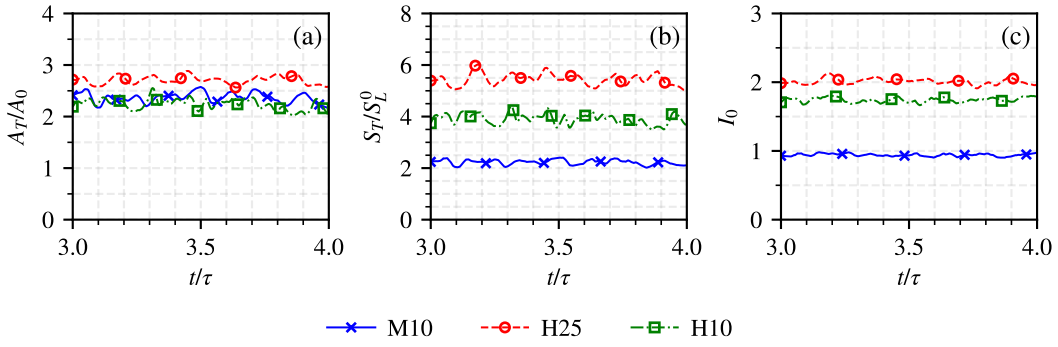

Figure 11.2: Temporal evolution of the normalized turbulent flame surface A_T/A_0, of the normalized turbulent flame consumption speed S_T/S^0_L, and of the stretch factor I_0 for the three cases.

CH_4 flame, coherently with the stated objective for this case (see Section 10.1.2), while the H10 case, featuring the same value of U_B as for the M10 one, has a shorter length, due to the higher burning rate of the H_2 flame [27]. Overall, these results are consistent with previous studies in the literature on analogous configurations [79].

The impact of flame–turbulence interaction on the global flame behavior is highlighted in Figure 11.2, which reports, for the three cases, the temporal evolution over one flow through time τ (see Table 10.2) of the turbulent flame surface A_T, evaluated as in Equation (2.63). This is normalized by the reference flame surface area A_0, defined, in analogy with [27], as the area of the mean flame sheet, taken at $\widetilde{C} = C^*$ (see Section 10.1.2). The turbulent flame consumption speed S_T, defined in Equation (2.59) and normalized by S^0_L, and the stretch factor I_0 (see Equation (2.71)) are also reported. Focusing on A_T first (see Figure 11.2a), a consistency can be observed in the overall trends and values of these quantities for the flames, which is coherent with the fact that these are subjected to analogous turbulence fields (see Section 10.1.2). This is especially true for the M10 and H10 cases, which have the same bulk velocity, while a slight enhancement of the turbulent flame surface is observed for the H25 case. Attili et al. [17] showed for lean premixed

CH_4–air jet flames that, when keeping *Ka* approximately constant and increasing *Re*, the effect of turbulence inside the inner flame layer is enhanced, thus leading to an increase in $\mathcal{A}_T/\mathcal{A}_0$, as well as in S_T/S_L^0. For the present lean H_2–air flame, this effect is further enhanced, since TD instabilities are sustained in turbulent flows and show synergistic interactions with turbulence, enhancing the generation of flame surface area, and promoting local fluctuations of the equivalence ratio, of the HRR, and of S_T (see Section 4.3.1). In this sense, Figure 11.2b shows that, while both H_2 flames have a higher S_T/S_L^0 compared to the thermodiffusively stable M10 case, this enhancement is stronger in the H25 case. As a result, the time-averaged value of the stretch factor $\overline{I_0}$ passes from 1.7 to 2.0 (see Figure 11.2c). It is worth noticing that the value of $\overline{I_0}$ for the H25 case is consistent with the one obtained by Coulon et al. [79], where DNS under analogous operating conditions, in terms of mixture composition and turbulence, were performed. This further sustains the validity of the numerical configuration adopted in the present study. As expected, $\overline{I_0} \approx 1$ for the M10 case, confirming the absence of TD effects for this flame.

Figure 11.3 shows, for the three cases, the average of the normalized HRR $\dot{\omega}_T/\dot{\omega}^{1D}_{T,max}$ conditioned by the progress variable *C*, together with the joint Probability Density Function (PDF) of the two quantities, and the mean for the corresponding 1D unstretched laminar flames. Due to the mixing with cold ambient air, which induces a reduction of the local equivalence ratio in the external regions of the flames, all cases show zones with low values of HRR in the whole range of *C*. For the CH_4 flame (see Figure 11.3a), this leads to a conditional average lower than the 1D unstretched flame and not coincident, as expected in a unity *Le* flame [79]. Nevertheless, a region with very high PDF in correspondence of the 1D unstretched flame curve can be identified. Moreover, the peak value of HRR is located at $C = 0.81$, close to the one of the 1D case (i.e., $C = C^* = 0.77$), and no relevant scatter is observed above the values of the 1D flame. On the other hand, for the H_2 flames (see Figure 11.3b and c), the variability of HRR induced by TD effects is clearly visible. Indeed, a broader region of high PDF is found with respect to the M10 case, together with a significant positive scatter above the mean (white solid line). As a result, despite the effect of the mixing with cold ambient air, the conditional average for the turbulent H_2 flames is still higher than the corresponding unstretched 1D flame (black dashed line), coherently with the behavior of a thermodiffusively unstable flame [27, 79]. The deviation from the 1D flamelet is more accentuated in the preheat zone, as expected in the thin reaction zone regime [79], leading to a shift of the peak location from $C = C^* = 0.80$ in the 1D flame to $C = 0.70$ in the turbulent ones.

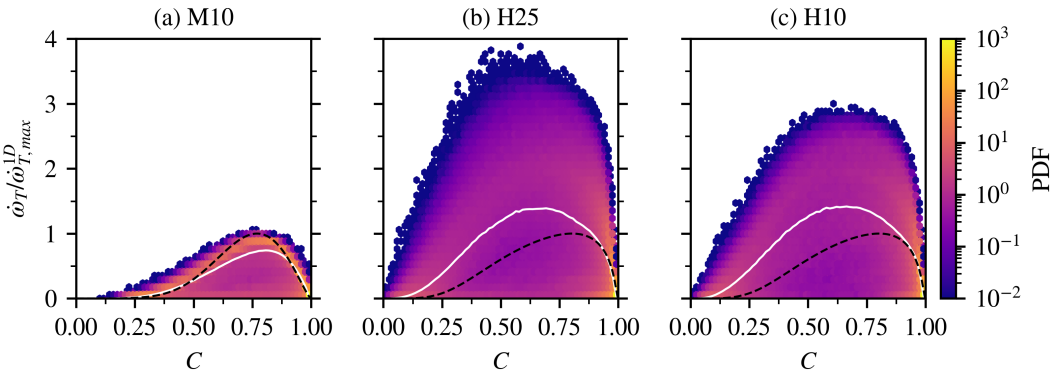

Figure 11.3: Averages of the normalized HRR $\dot{\omega}_T/\dot{\omega}^{1D}_{T,max}$ conditioned by the progress variable *C* (white lines) with the corresponding joint PDF (in logarithmic scale) at $t = 4\tau$ for the three cases. The results for the corresponding 1D unstretched flames (black dashed lines) are added for reference.

11.1.2 Analysis of stretch components

Recalling the balance of the flame surface density in Equation (2.66) and the subsequent remarks made in the literature on the role of flame annihilation in the generation of combustion noise (see Section 7.2.1), the differences in the local generation and destruction of the flame surface among the different cases are assessed in this Section. To this scope, Figure 11.4 reports the stretch components, surface-averaged on the flame sheet defined by $C = C^*$ and normalized by the flame characteristic time $\tau_f = \delta_L^0 / S_L^0$ [27, 79], along the streamwise direction: the total stretch κ and its strain κ_s and curvature κ_c components, as defined in Section 2.5.3. The average of any quantity ς on the surface S identified by the condition $C = C^*$, i.e., $\langle \varsigma \rangle_S$, is defined as in Equation (2.65). It is recalled that the surface-averaged total stretch $\langle \kappa \rangle_S$ is related to the variation of the turbulent flame surface area A_T [23]:

$$\langle \kappa \rangle_S = \frac{1}{A_T} \frac{dA_T}{dt}. \tag{11.1}$$

Moreover, the curvature term κ_c is further decomposed in its positive and negative contributions, defined as [27, 79]:

$$\kappa_c^+ = \int_0^{+\infty} \kappa_c \mathcal{P}(\kappa_c) d\kappa_c, \tag{11.2a}$$

and

$$\kappa_c^- = \int_{-\infty}^{0} \kappa_c \mathcal{P}(\kappa_c) d\kappa_c, \tag{11.2b}$$

where $\mathcal{P}(\kappa_c)$ is the probability to find the curvature value κ_c. Being κ_c related to the product of $S_d|_{C=C^*}$ and the local (geometrical) flame curvature K (see Section 2.5.3), κ_c^- corresponds to regions where the flame propagates in the direction where the center of curvature is located, while the opposite holds for κ_c^+. This is highlighted by Figures 11.5 to 11.7, which report the Kernel Density Estimates (KDE) between $S_d|_{C=C^*}$ and K for the three cases, together with instantaneous isosurfaces colored by κ, κ_s, κ_c and $S_d|_{C=C^*}$ to provide a qualitative understanding.

Focusing on the M10 case first (see Figure 11.4a), the upstream region of the flame, identified by the condition $x/H \leq 3$, shows a strong balance between positive and negative curvature components, resulting in a slightly positive total stretch and indicating a limited enhancement of flame surface controlled by strain. This is further highlighted by the KDE in Figure 11.5e, which

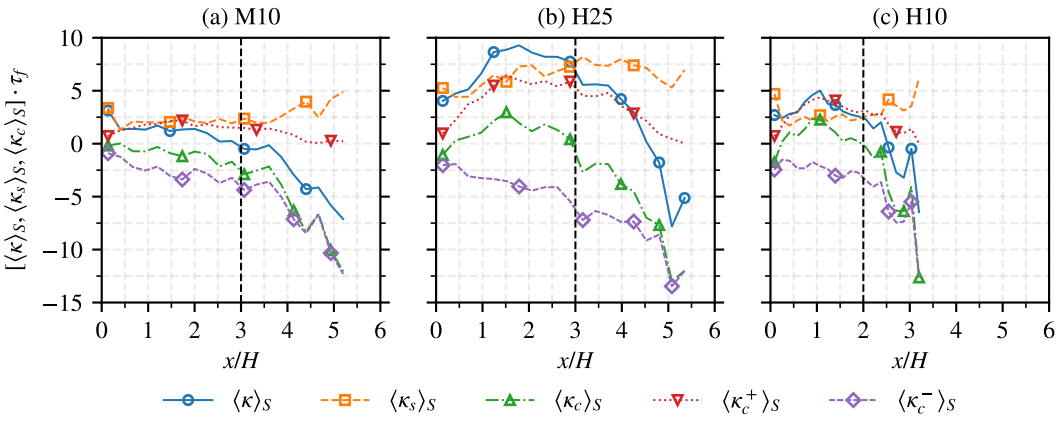

Figure 11.4: Surface-averaged total stretch κ, strain component κ_s, curvature component κ_c and its positive κ_c^+ and negative contributions κ_c^-, normalized by τ_f, retrieved on the isosurface of $C = C^*$ at $t = 4\tau$ for the three cases.

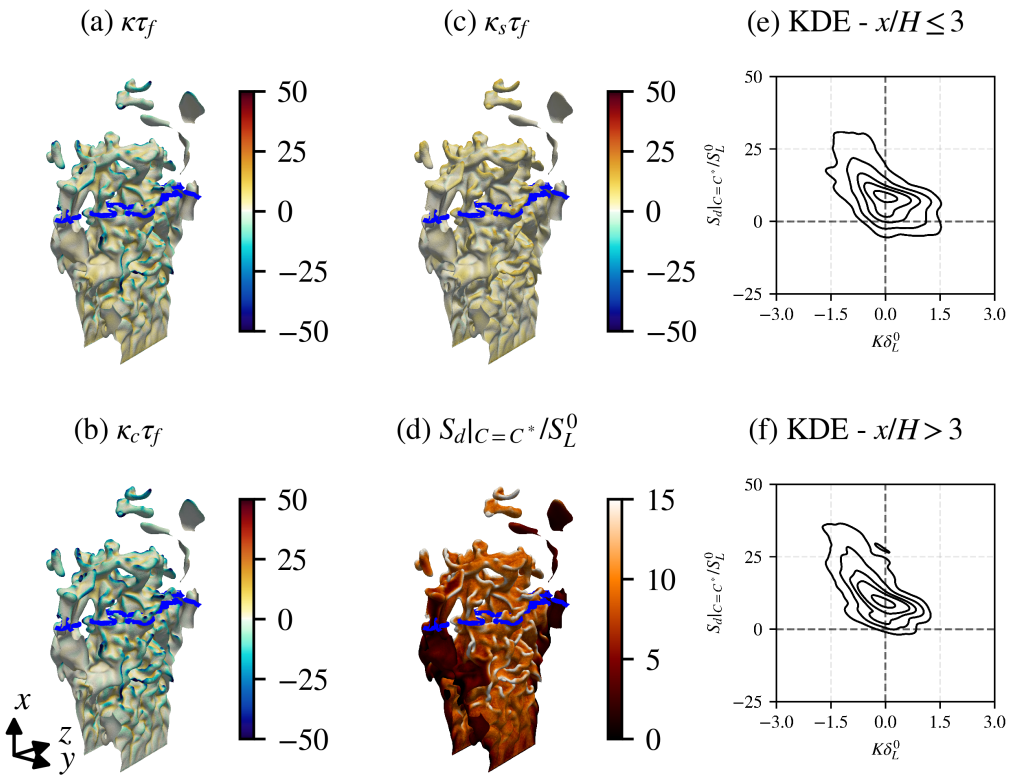

Figure 11.5: M10 case: total stretch κ (a) and its curvature κ_c (b) and strain κ_s (c) components, normalized by τ_f, displacement speed $S_d|_{C=C^*}$ (d) normalized by S_L^0, and Kernel Density Estimates of $S_d|_{C=C^*}$ with respect to the curvature K in the first region $x/H \leq 3$ (e) and second region $x/H > 3$ (f), retrieved on the isosurface of $C = C^*$ at $t = 4\tau$. The blue line in the isosurfaces of $C = C^*$ corresponds to $x/H = 3$.

shows a balance between positive and negative values of K. In the downstream region ($x/H > 3$), however, the contribution of negative curvature becomes dominant, due to the presence of extreme cusp regions [79, 152], leading to the detachment of flame pockets at the tip. The dominance of negative curvature in this region is further highlighted by the KDE in Figure 11.5f, which shows an unbalance toward $K < 0$. An enhancement of $S_d|_{C=C^*}$ with respect to the flame root is present as K becomes further negative, due to the so-called kinematic restoration [301]. This leads to the strong local surface destruction induced by flame–flame interactions [83], which has been associated to high-frequency noise generation in hydrocarbon flames (see Section 7.2.1).

Moving to the H25 case (see Figure 11.4b), a stark difference appears in the first region of the flame ($x/H \leq 3$), with an unbalance of the curvature term $\langle\kappa_c\rangle_S$ toward the positive contribution, which adds up to the turbulence-related strain $\langle\kappa_s\rangle_S$. As a result, a strongly positive total stretch $\langle\kappa\rangle_S$ is found, indicating an enhancement of the flame surface area. This is caused by TD instabilities, which lead to a pronounced wrinkling of the flame surface [325], to the strong enhancement of the local HRR in the highly curved regions (see Figure 11.1b), and to an increase of the local displacement speed (see Figure 11.6d). The differences with respect to the M10 case (see Figure 11.5e) are further highlighted from the KDE in Figure 11.6e, where a wider distribution is observed, especially in the first quadrant, in which both $S_d|_{C=C^*}$ and K are positive and increase together, thereby promoting flame surface generation. In the rear part of the jet ($x/H > 3$), a decrease of the curvature term $\langle\kappa_c\rangle_S$ toward negative values is observed (see Figure 11.4b), promoting surface destruction at the flame tip. Differently from the M10 case (see Figure 11.4a),

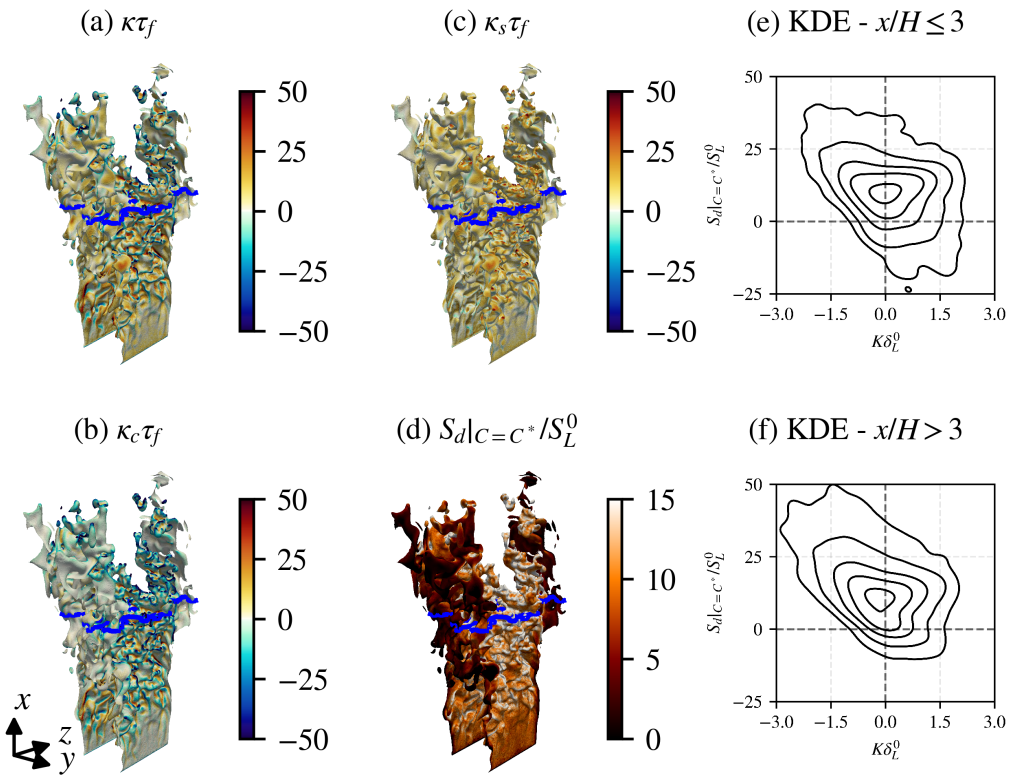

Figure 11.6: H25 case: total stretch κ (a) and its curvature κ_c (b) and strain κ_s (c) components, normalized by τ_f, displacement speed $S_d|_{C=C^*}$ (d) normalized by S_L^0, and Kernel Density Estimates of $S_d|_{C=C^*}$ with respect to the curvature K in the first region $x/H \leq 3$ (e) and second region $x/H > 3$ (f), retrieved on the isosurface of $C = C^*$ at $t = 4\tau$. The blue line in the isosurfaces of $C = C^*$ corresponds to $x/H = 3$.

however, the switch from flame surface generation to destruction, i.e., where $\langle\kappa\rangle_S = 0$, occurs further downstream. In other terms, the contribution of positive curvature remains relevant also in the downstream part of the jet, as highlighted from the KDE in Figure 11.5f. This attenuates the action of flame destruction as a surface variation mechanism at the tip, marking a substantial difference with respect to the CH_4 flame.

Similar features can be observed also in the H10 case (see Figure 11.4c), with the main difference being the reduction of the strain term $\langle\kappa_s\rangle_S$, especially in the first region ($x/H \leq 2$), due to the reduced bulk velocity U_B. The comparison of the behaviors at the flame tip of the M10 (see Figure 11.5f) and H10 (see Figure 11.7f) cases, which share the same value of U_B, allows to further highlight the influence of TD effects. Indeed, a much more limited increase of $S_d|_{C=C^*}$ is observed for $K < 0$ in the H10 flame, a result that has been related by Coulon et al. [79] to the shift of the diffusive contribution of $S_d|_{C=C^*}$ toward positive values. Consequently, the values reached for positive and negative curvatures are comparable in the H10 case, confirming the reduced importance, with respect to the M10 case, of annihilation phenomena on the flame surface variation at the tip.

Finally, Figure 11.8 shows the average of the (density-weighted) displacement speed S_d/S_L^0 conditioned by the normalized flame stretch $\kappa\tau_f$, together with the joint PDF of the two quantities, retrieved from multiple isosurfaces at $C = C^*$ spanning a time window equal to τ. Overall, the H_2 flames (see Figure 11.8b-c) feature a wider stretch distribution with respect to the CH_4 one (see Figure 11.8a), consistent with the higher resistance to stretch of these flames (see Sec-

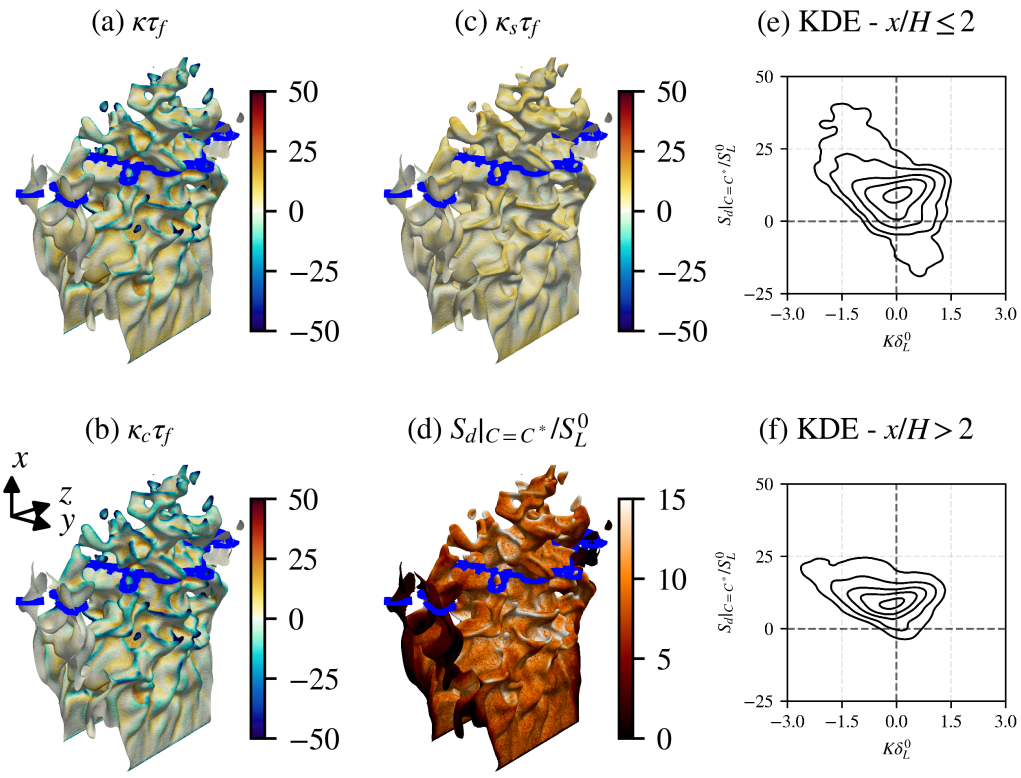

Figure 11.7: H10 case: total stretch κ (a) and its curvature κ_c (b) and strain κ_s (c) components, normalized by τ_f, displacement speed $S_d|_{C=C^*}$ (d) normalized by S_L^0, and Kernel Density Estimates of $S_d|_{C=C^*}$ with respect to the curvature K in the first region $x/H \leq 2$ (e) and second region $x/H > 2$ (f), retrieved on the isosurface of $C = C^*$ at $t = 4\tau$. The blue line in the isosurfaces of $C = C^*$ corresponds to $x/H = 2$.

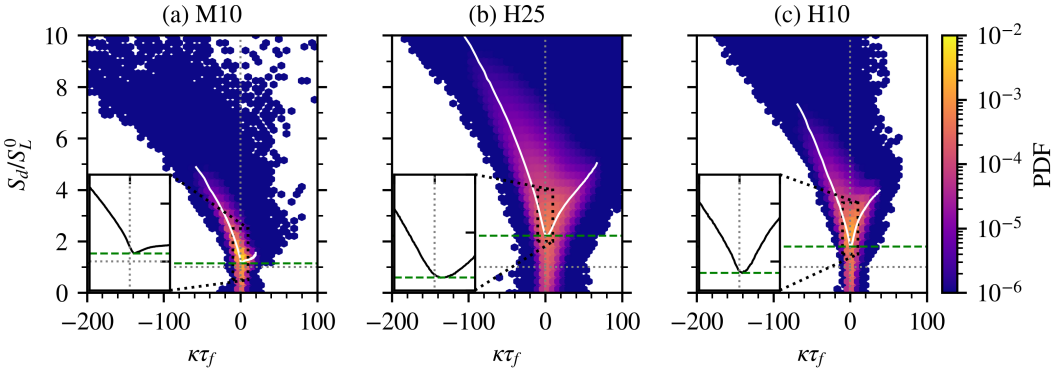

Figure 11.8: Averages of the normalized displacement speed S_d/S_L^0 conditioned by the normalized flame stretch $\kappa\tau_f$ (white and black lines) with the corresponding joint PDF (in logarithmic scale) retrieved from isosurfaces at $C = C^*$ in a time window of duration τ. The insets highlight the low-stretch region $|\kappa\tau_f| \leq 10$.

tion 4.2.2). Focusing on the positive stretch region ($\kappa\tau_f > 0$), a sensible enhancement of S_d is observed for the H_2 flames, coherently with the previous observations. This further confirms the increased importance, for thermodiffusively unstable flames, of the flame surface generation term in the balance of the flame surface density described by Equation (2.66). Finally, it can be observed that the marginal mean values of S_d/S_L^0 at $\kappa \approx 0$ (green dashed lines in Figure 11.8) are close to the values of $\overline{I_0}$ retrieved in Figure 11.2c, consistently with one of the approaches proposed

in the literature to estimate the stretch factor (see Section 2.7.3).

11.2 Acoustic radiation

The differences in the acoustic field among the three cases are described hereafter, with a particular focus on the flame-generated noise. The underlying reasons for these differences will be discussed in Section 11.3, by relating them to the different features in the flame–turbulence interaction observed in Section 11.1.

11.2.1 General features of the flow and acoustic fields

A qualitative assessment of the acoustic field is provided in Figures 11.9 and 11.10, which report instantaneous fields of the normalized fluctuating pressure $p' = p - \bar{p}$ (on the left) and dilatation $\nabla \cdot \mathrm{u}$ (on the right) for the three cases in the xy and xz planes, respectively. The red dashed insets highlight the acoustic radiation from the center of the flame brushes, while the white dotted insets are taken at the flame tip. The isosurfaces of $C = C^*$ colored by the local HRR, previously reported in Figure 11.1, are added for reference.

The dilatation and pressure fields are normalized to account for the differences in terms of thermal power and bulk velocity among the three cases. The dilatation is normalized by the ratio of the slot width H over the speed of sound in the far field medium c_∞, while the pressure is normalized by a reference pressure p_{ref}. Based on Equation (7.22) and on combustion noise scaling laws [48, 318] (see Section 7.1.3), this reference pressure is here defined as:

$$p_{ref} = \frac{\gamma - 1}{4\pi c_\infty^2} \frac{Y_{F,u} \rho_u H U_B^2 H_F}{L_f}. \tag{11.3}$$

Its value is equal to 20.2 Pa, 59.6 Pa, and 17.5 Pa for the M10, H25, and H10 cases, respectively. Further details on the derivation of this quantity are provided in Appendix F.

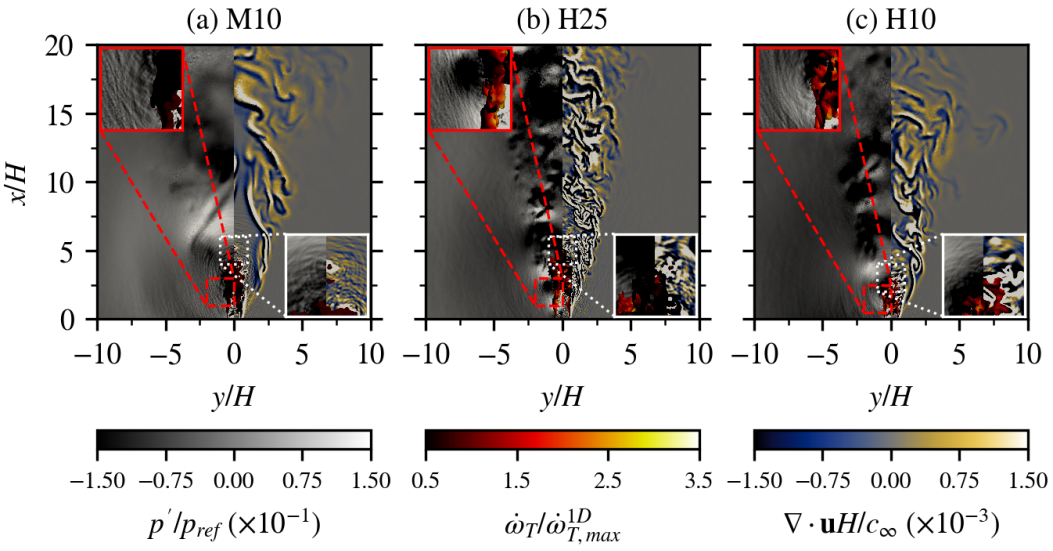

Figure 11.9: Normalized fields of fluctuating pressure p'/p_{ref} (left) and dilatation $\nabla \cdot \mathrm{u}H/c_\infty$ (right), and isosurfaces of $C = C^*$ coloured by the normalized HRR $\dot{\omega}_T/\dot{\omega}^{1D}_{T,max}$ at $t = 4\tau$ in the xy plane for the three cases.

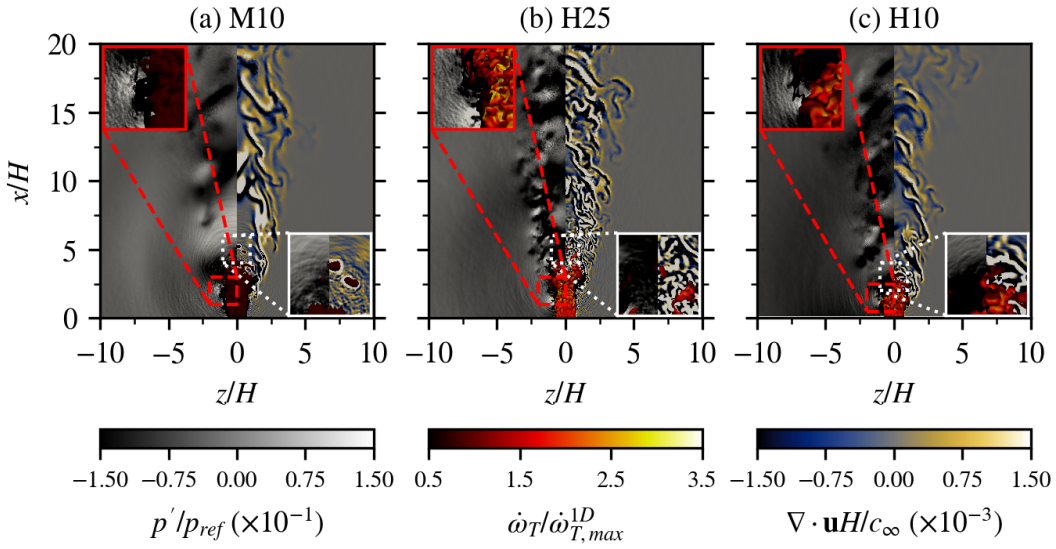

Figure 11.10: Normalized fields of fluctuating pressure p'/p_{ref} (left) and dilatation $\nabla \cdot \mathbf{u}H/c_\infty$ (right), and isosurfaces of $C = C^*$ coloured by the normalized HRR $\dot{\omega}_T/\dot{\omega}^{1D}_{T,max}$ at $t = 4\tau$ in the xz plane for the three cases.

By comparing the CH_4 flame (see Figure 11.9a) with the H_2 ones (see Figure 11.9b-c), some first qualitative differences can be observed in the acoustic radiation. Indeed, the CH_4 flame shows a strong contribution originating at the flame tip, which originates from the rapid consumption of the detached flame pockets, a well-known noise generation mechanism for these flames (see Section 7.2.1). For the H_2 flames, on the other hand, the contribution from the flame tip seems less evident, consistently with the differences in the stretch components observed in this region in Section 11.1.2.

Moreover, relevant differences are present also in the outer shear layer, as highlighted by the dilatation field. Indeed, all flames present Kelvin–Helmholtz shear layer instability structures, which arise from the strong velocity gradient between the high-velocity jet and the low-velocity ambient air, and are a known source of acoustic radiation in turbulent jets [183] (see Section 7.3). Nevertheless, the M10 case shows only large scale phenomena, while the two H_2 flames present more spatially refined structures. While for the H25 case this difference could be imputed to the higher bulk velocity, the presence of similar features in the low-velocity H10 case suggests that the observed discrepancies are related to the different transport properties of CH_4 and H_2. Analogous observations can be made also in the xz plane reported in Figure 11.10, with some differences in proximity of the flame root, which can be related to the absence, in this direction, of the equilibrium combustion products coflow in the adopted numerical configuration (see Section 10.1.1).

To further investigate the differences in the outer shear layer, Figure 11.11 reports the normalized fields of excess density ρ_e (on the left), defined as in Equation (7.14), and reduced temperature $(T - T_u)/(T_{ad} - T_u)$ (on the right) in the xy plane for the three cases. Focusing on the temperature first, a clear difference is observed in the burned gases region. The CH_4 flame presents a uniform distribution, with temperature equal to the adiabatic value, while the H_2 flames show strong fluctuations, even reaching super-adiabatic conditions, a clear indicator of TD effects [23, 134], as highlighted in the dotted white inset in the bottom right corner. The same mechanism, based on the H_2 differential diffusion, impacts also the outer shear layer, resulting in a more pronounced entrainment of the cold ambient air with the hot combustion products. As a result, the mixing of the two fluids is promoted, reducing the radial extension of the burned gases re-

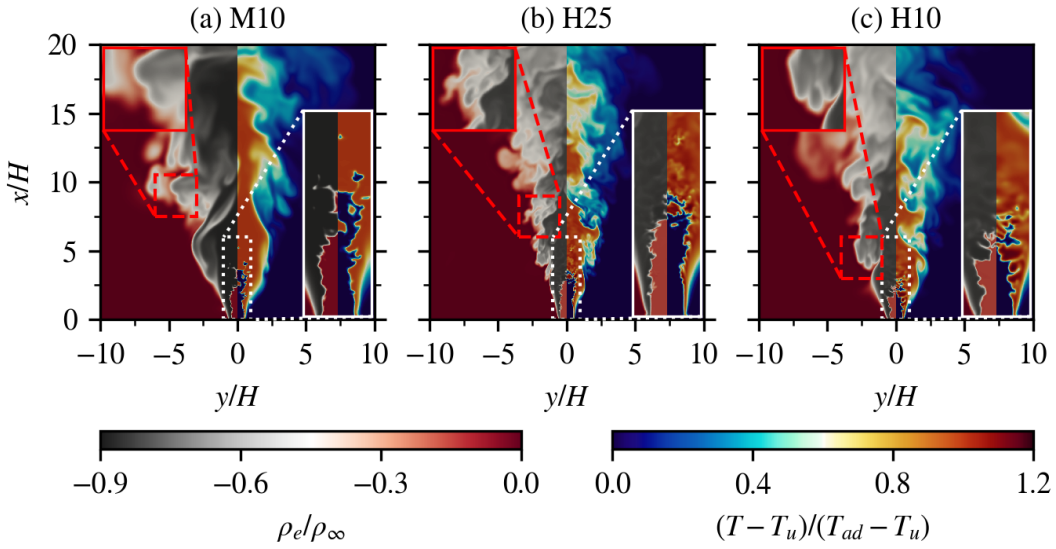

Figure 11.11: Normalized fields of excess density ρ_e/ρ_∞ (left) and temperature $(T-T_u)/(T_{ad}-T_u)$ (right) in the xy plane for the three cases.

gion. Moreover, finer-scale structures, propagating toward the cold ambient, are present in the H_2 flames, while the CH_4 flame presents only large scale structures, as observable from the field of ρ_e in the dashed red inset in the top left corner. In other terms, differential diffusion seems to amplify the K-H shear layer instability at this non-reacting interface, by strengthening the variability of the density field in the burnt gases region and near the outer shear layer. This can be related to the baroclinic vorticity generation mechanism enhancing the K-H instability [54], thereby promoting finer-scale mixing. This will be further discussed in Section 11.4, by analyzing the coherent structures resulting from the SPOD of the pressure field in the different cases.

The impact of these differences on the acoustic spectrum are investigated in Figure 11.12, which reports the Power Spectral Density (PSD) of pressure at fixed streamwise position $x/H = 8$ and variable spanwise position y/H. If not otherwise specified, the PSD is estimated in this Chapter using the periodogram method by Welch [420] with 6 Hanning windows and 50% overlap. Since the intensity of the acoustic radiation is impacted by the distance from the flame (e.g., see Equation (7.22)), the PSD in Figure 11.12 is normalized as [209]:

$$S_\varsigma^+(St) = \frac{S_\varsigma(St)}{\int_0^\infty S_\varsigma(St)dSt}, \tag{11.4}$$

where ς is a generic quantity and St is the Strouhal number, here defined as $St = fH/U_B$.

As discussed in Section 7.1.2, a typical combustion noise spectrum is characterized by a low-frequency ascending part and a high-frequency descending one, in between which the peak of the acoustic spectrum is located at the frequency f_{peak} (or, in non-dimensional terms, at the Strouhal number St_{peak}). Figure 11.12 shows that the shape of the spectra is not significantly impacted by the spanwise position y in the high-frequency range, i.e., for $St > St_{peak}$. Nevertheless, strong differences arise among the different probes in the low-frequency range ($St < St_{peak}$). Notably, a stronger spectral content is observed in this region for $y/H < 7$, and especially for $2 \leq x/H \leq 3$, i.e., in correspondence of the outer shear layer. In the low-frequency range, noise associated with the turbulent flow is relevant [96, 160], and indirect combustion noise has been shown to prevail

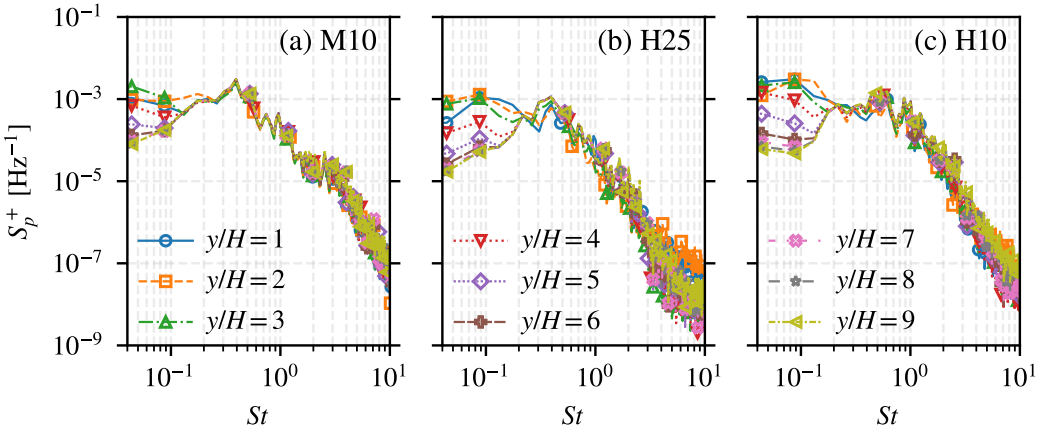

Figure 11.12: Normalized power spectral density of pressure S_p^+ at $x/H = 8, z/H = 0$ and variable distance along the y axis for the three cases.

over the direct one [43, 291, 361]. In this sense, the spectra in Figure 11.12 suggest that, in this near-jet region, the pressure perturbation due to velocity and excess density gradients at the outer shear layer between the combustion products and the ambient air dominates the direct combustion noise generated from the flame.

Despite the qualitative similarities in the shape of the spectra among the three cases, a clear difference arises between the CH_4 and H_2 flames, which is consistent with the observations made for Figure 11.11. Indeed, while, for the M10 case, the PSD in the low-frequency region remains in all cases lower than the peak value associated with flame-generated noise (see Section 11.2.2), for the H_2 flames this becomes, for $y/H \leq 3$, equal or even higher than the peak value. Given that the M10 and H10 cases have the same bulk velocity, hence similar contributions due to the hydrodynamic pressure fluctuations, these differences in the low-frequency region are to be associated to an enhanced contribution of the previously discussed excess density term. Beyond $y/H = 7$, the normalized PSD spectra collapse in the whole frequency range for all cases. This indicates that the pressure fluctuation is dominated, in this region, by flame-generated propagating acoustic waves. Therefore, the region with radial distance from the jet axis $r_{yz}/H \geq 7$, with $r_{yz} = (y^2 + z^2)^{1/2}$, is here considered as the acoustic far field in the sense of spectral convergence. Even though this value is not very large compared to the size of the reacting region and the compactness and strict far field conditions cannot be considered as completely fulfilled [49, 145, 355], this distance is deemed sufficient for the analysis performed in the present study (see Section 11.2.2).

The directivity of the acoustic radiation is now investigated. First, the non-normalized Overall Sound Pressure Level ($OASPL^*$) is considered, defined as:

$$OASPL^* = 20 \log_{10} \left(\frac{p'_{rms}}{p_0} \right), \tag{11.5}$$

where p'_{rms} is the temporal r.m.s. of the local pressure fluctuation, and $p_0 = 2.0 \times 10^{-5}$ Pa is a reference acoustic pressure [48]. Figure 11.13 reports the $OASPL^*$ as a function of the azimuthal angle θ in the yz plane both in the near (a) and far field (b), as a function of the polar angle φ in the xy plane (c), and as a function of the streamwise position in the far field (d). On top of each plot, a scheme is reported to show the position of the probes with respect to the flame. In the xz plane, a directivity is observed at $x/H = 2$ (see Figure 11.13a), which can be associated with

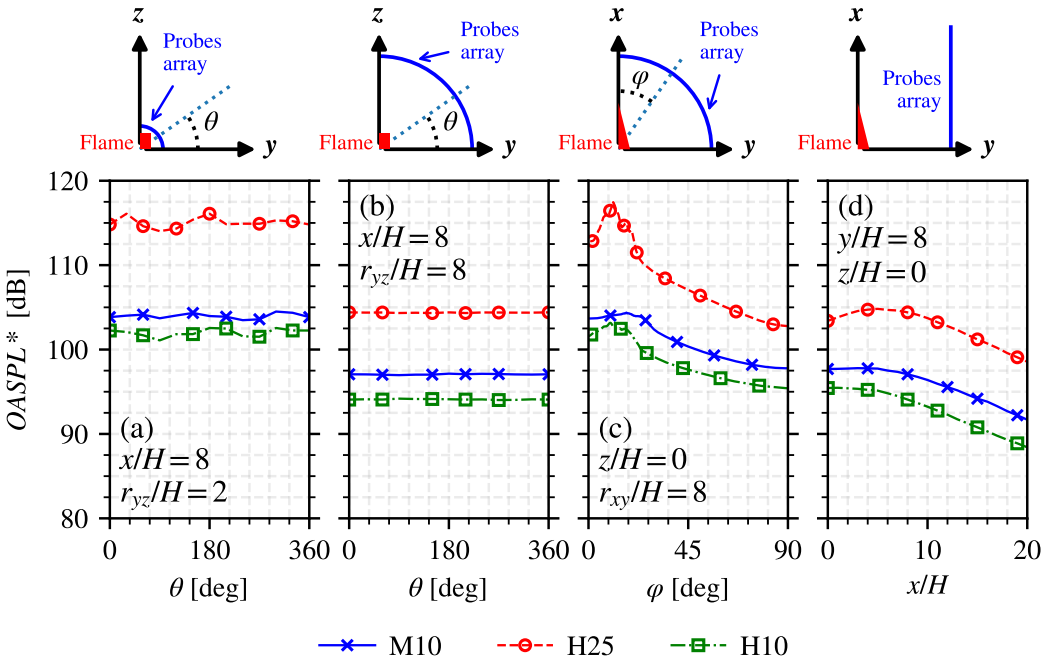

Figure 11.13: Non-normalized $OASPL$ for the three cases as a function of the azimuthal angle $\theta = \tan^{-1}(z/y)$ in the yz plane at a radial distance $r_{yz} = (y^2 + z^2)^{1/2}$ equal to $2H$ (a) and $8H$ (b), as a function of the polar angle $\varphi = \tan^{-1}(y/x)$ in the xy plane at a radial distance $r_{xy} = (x^2 + y^2)^{1/2}$ equal to $8H$ (c), and as a function of the streamwise position x/H for fixed coordinates $y = 8H$ and $z = 0$ (d). The schemes on top of each plot describe the position of the probes with respect to the flame.

the differences in the xy and xz plane previously discussed in Figures 11.9 and 11.10. In this sense, the $OASPL^*$ drops in proximity of the z-axis, corresponding to $\theta = 90°$ and $\theta = 270°$, further sustaining the role of density variations associated with the interface between burned gases and ambient air in the acoustic field near the jet. On the other hand, a nearly-isotropic behavior is observed in the far field at $x/H = 8$ (see Figure 11.13b), coherently with the monopolar nature of direct combustion noise [400]. Moving to the directivity in the xy plane (see Figure 11.13c), the region impacted by the hydrodynamic and indirect noise sources is evident, with a peak in the $OASPL^*$ observable in correspondence of the outer shear layer, i.e., for $\varphi = 15°$ for the H_2 flames and $\varphi = 30°$ for the CH_4 one, coherently with the differences in the radial extension of the burned gases region shown in Figure 11.11. Finally, a directivity is observed far from the jet (see Figure 11.14d) for $x/H < 8$, where the acoustic field may be impacted by the coflow inlet boundary [44]. For $x/H \geq 8$, instead, the $OASPL^*$ varies linearly with the distance, coherently with Equation (7.22), suggesting that in this region the acoustic radiation is related mostly, if not solely, to direct combustion noise radiated from the flame.

In all cases shown in Figure 11.13, it is observed that the intensity of the acoustic radiation is stronger for the H25 flame, followed by the M10 and by the H10 ones. This is consistent with the higher thermal power of the H25 case with respect to the other ones (see Table 10.2). To remove this bias, Figure 11.14 reports the same directivity analysis of Figure 11.13, but considering the normalized Overall Sound Pressure Level:

$$OASPL = 20 \log_{10} \left(\frac{p'_{rms}}{p_{ref}} \right), \tag{11.6}$$

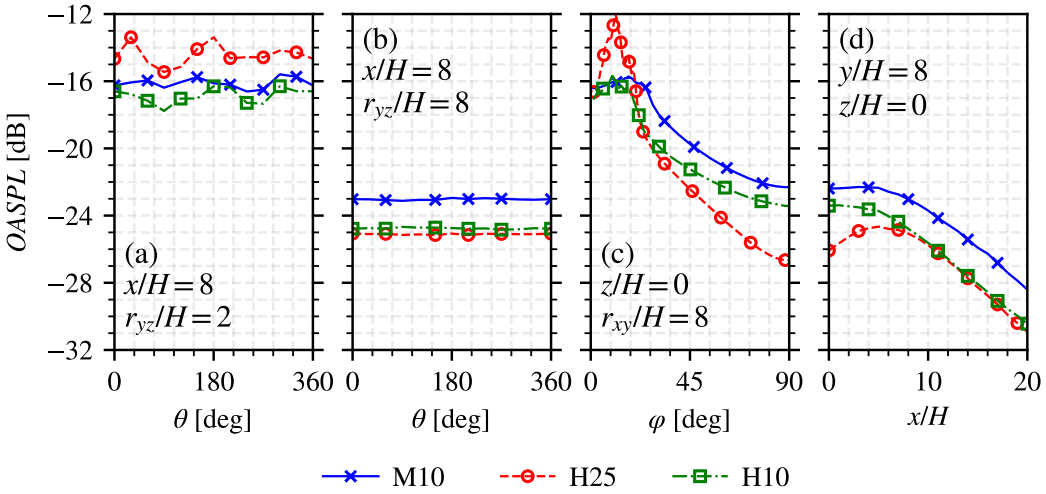

Figure 11.14: Normalized $OASPL$ for the three cases as a function of the azimuthal angle $\theta = \tan^{-1}(z/y)$ in the yz plane at a radial distance $r_{yz} = (y^2 + z^2)^{1/2}$ equal to $2H$ (a) and $8H$ (b), as a function of the polar angle $\varphi = \tan^{-1}(y/x)$ in the xy plane at a radial distance $r_{xy} = (x^2 + y^2)^{1/2}$ equal to $8H$ (c), and as a function of the streamwise position x/H for fixed coordinates $y = 8H$ and $z = 0$ (d).

where p_{ref} is the reference pressure previously defined in Equation (11.3). Evidently, the directivity of each flame is not impacted by the normalization, since this induces, in logarithmic scale, only a vertical shift of the values. Nevertheless, stark differences appear when comparing the different flames at the same spatial location. Focusing on the directivity in the xz plane near the jet (see Figure 11.14a), i.e., the region where the hydrodynamic contribution associated with the shear layer is more relevant, the M10 and H10 cases, with same bulk velocity, show comparable values, while the high-velocity H25 case presents a higher $OASPL$. On the other hand, far from the jet (see Figure 11.14b), where flame-generated noise prevails [147], the two H_2 flames have almost identical $OASPL$ values. Moving to the directivity in the xy plane (see Figure 11.14c), the H25 flame, characterized by a higher velocity, dominates in the near field, while the slower M10 and H10 flames present a stronger $OASPL$ for $\varphi \geq 30$. Finally, a superposition of the $OASPL$ values is observed for the two H_2 flames far from the jet for $x/H \geq 7$ (see Figure 11.14d). Overall, even though a collapse of all cases is not achieved, probably due to the fact that the simplified approach adopted in the definition of p_{ref} (see Appendix F) does not include any correlation volume effect [318], the normalization with p_{ref} still allows for a more adequate comparison of the different cases, sustaining the validity of this choice.

11.2.2 Direct combustion noise

Based on the analysis of directivity in Figure 11.14, the acoustic radiation of the three flames is here compared from the pressure temporal traces at $x/H = 8$ and $r_{yz}/H = 8$. Given the monopolar nature of the acoustic radiation in this region (see Figure 11.14b), the average of the pressure traces of 12 equally distributed probes in the azimuthal direction is considered, thus exploiting ergodicity to improve the quality of the spectral analysis. The corresponding (normalized) Sound Pressure Level (SPL) spectra for the three cases are reported in Figure 11.15, with SPL defined as:

$$SPL = 10 \log_{10} \left(\frac{S_p \Delta f}{p_{ref}^2} \right), \tag{11.7}$$

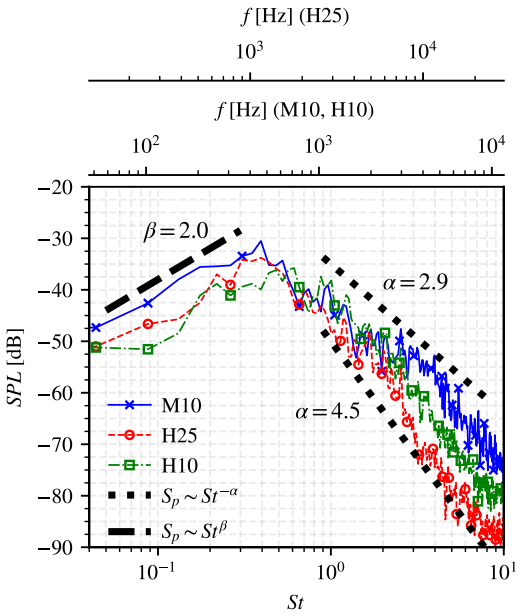

Figure 11.15: SPL spectra at $x/H = 8$ and $r_{yz}/H = 8$, averaged over 12 equally distributed probes in the azimuthal direction, for the three cases. The corresponding ranges of frequency f (in Hz) are reported on top.

where Δf is the frequency resolution (in Hz) and p_{ref} is the reference pressure defined in Equation (11.3). The spectra are reported as a function of the Strouhal number St, while the corresponding values of frequency f (in Hz) are reported on top to ease the analysis.

The resulting spectra are coherent with the literature on combustion noise (see Section 7.1.2), with power law dependencies in the low- (black dashed line) and high-frequency (black dotted lines) regions. The M10 and H25 cases both peak at $St_{peak} \approx 0.4$, while the H10 case peaks at $St_{peak} \approx 0.6$. This shift in St_{peak} is to be expected, given that the peak frequency of the combustion noise spectrum scales as U_B/L_f (see Section 7.1.2). Since the differences in terms of U_B are implicitly accounted for by the definition of St, the M10 and H25 cases, with comparable L_f, have similar St_{peak} values, while the shorter H10 flame has a higher St_{peak}. In terms of frequency f, however, the H_2 flames are both shifted to higher values with respect to the CH_4 one. Indeed, $f_{peak} \approx 460$ Hz for the M10 flame, while it rises to $f_{peak} \approx 1150$ Hz and to $f_{peak} \approx 720$ Hz for the H25 and H10 cases, respectively. This shift toward higher frequencies is coherent with previous experimental investigations of thermoacoustic instabilities of H_2 flames [286].

Similar features are observed in the low-frequency range ($St < St_{peak}$), with the same slope (in logarithmic scale) $\beta \approx 2.0$ for all cases, a value in agreement with previous works in the literature [209, 241, 319]. On the other hand, more enhanced discrepancies are observed in the high-frequency range, above the peak St value. Indeed, the M10 case shows a slope (in logarithmic scale) $\alpha \approx 2.9$, coherent with the ranges $2.2 \leq \alpha \leq 3.4$ found by Beillard [22] and $2.1 \leq \alpha \leq 3.2$ obtained by Rajaram and Lieuwen [319] for premixed hydrocarbon unconfined turbulent flames, while a steeper decay is observed for both H_2 flames, with $\beta = 4.5$. Still, for $St < 1$, the (normalized) spectra of the three flames are almost superimposed, while the steeper decay of the H_2 flames is more accentuated for $St > 1$, where, conversely, an enhancement of the SPL values is observed for the M10 case. This is significant, since the region at $St > 1$ was identified by Brouzet et al. [41] as the one where flame annihilation events are the dominant noise sources for premixed hydrocarbon flames (see Section 7.2.1), being these sudden, hence high-frequency phenomena.

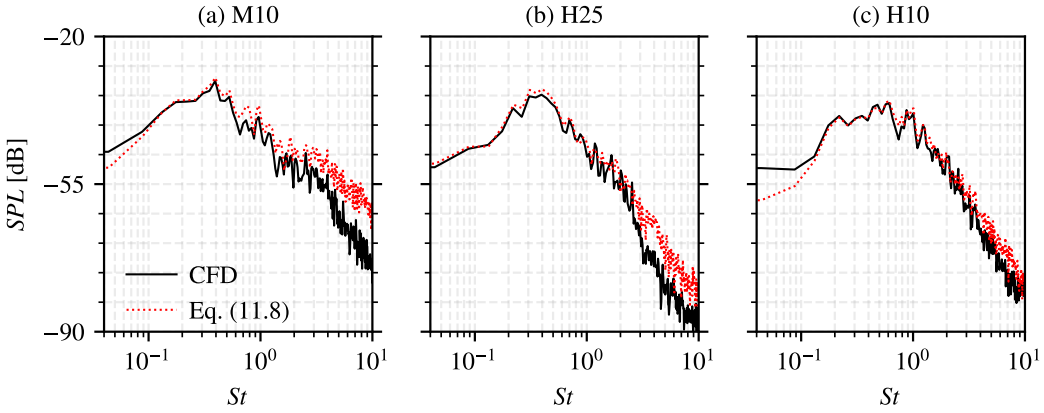

Figure 11.16: Normalized *SPL* spectra at $x/H = 8$ and $r_{yz}/H = 8$ directly extracted from the CFD results and averaged over 12 equally distributed probes in the azimuthal direction (solid black lines) and computed from dq/dt via Equation (11.8) (dotted red lines) for the three cases.

Therefore, the reduced acoustic radiation in this high-*St* band for the H_2 flames is coherent with a reduced importance of flame annihilation as source of noise, due to its slower dynamics (see Section 7.4). This is consistent with the analysis of the flame–turbulence interaction in Section 11.1, and with the spectral analysis of combustion noise performed for the harmonically forced laminar M-shaped flame in Section 9.2.4.

To further explain the differences observed between the two fuels, Figure 11.16 compares the *SPL* spectra directly recorded during the simulation (black solid lines) and reconstructed from the time derivative of the volume integrated HRR dq/dt (dotted red lines) by applying Equation (7.22), reported hereafter for convenience:

$$p'(\mathrm{x},t) = \frac{\gamma-1}{4\pi|\mathrm{x}|c_\infty^2}\left.\frac{dq}{dt}\right|_{t-|\mathrm{x}|/c_\infty}. \tag{11.8}$$

The distance $|\mathrm{x}|$ in Equation (11.8) is taken from the mean center of the flame, i.e., from the point located on the x-axis at $x = L_f/2$.

An almost perfect match is found between the recorded and reconstructed *SPL* for $St \leq 3$, confirming that the unsteady temporal fluctuation of HRR is the dominant noise source in this region far from the reacting jet. Some minor discrepancies are found at higher *St*, especially for the M10 case (see Figure 11.16a), which may be imputed to the temporal interpolation of the acoustic source term [44].

As a final remark, it has been verified that the HRR spectrum is well related to the one of OH* intensity. This is highlighted in Figure 11.17, which reports the PSD spectra $PSD_{I/\bar{I}}$ of the intensities of volume-integrated HRR and OH* concentration, normalized by their respective time-averaged values, for the H25 case. The PSD is here computed by applying the periodogram method by Welch [420] without tapering to temporal signals of duration τ. Further details on the OH* distribution are given in Appendix G.

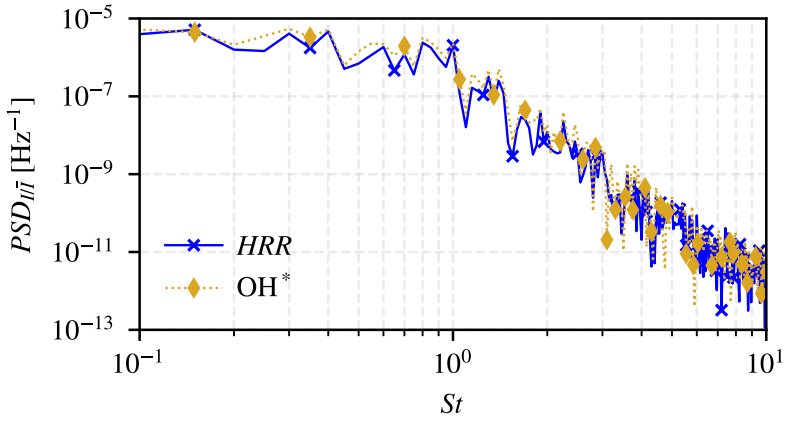

Figure 11.17: PSD of normalized HRR and OH* retrieved over one flow through time for the H25 case.

Some minor differences at high St are observed, but overall the OH* spectrum well retrieves the HRR one. Therefore, this strong correspondence suggests that, from a combustion diagnostic point of view, OH* chemiluminescence can be used to investigate combustion noise also in turbulent lean premixed H_2–air flames, corroborating the observations made for the laminar case in Section 9.3.

11.3 Impact of thermodiffusive effects on combustion noise

The preceding Section has shown the dominant role of the unsteady flame dynamics, via its action on the HRR fluctuations, in the far field acoustic radiation. Here, we intend to relate the differences in the flame–turbulence interaction observed in Section 11.1, most notably the impact of TD effects on the flame surface generation and destruction process and on the local HRR variations, to the differences in the acoustic spectra observed in Section 11.2.2, in order to gain a further understanding of the underlying mechanisms responsible for combustion noise generation in lean premixed H_2 flames.

11.3.1 Flame surface area variations and stretch effects

Figure 11.18 shows the spatial field in the xy plane of the local temporal r.m.s. of the magnitude of the gradient of progress variable $|\nabla C|_{rms}$, which is related to the flame surface density (see Equation (2.62)), normalized by its maximum value in the corresponding 1D laminar flame. The isocontour at $\widetilde{C} = C^*$ is reported in white to denote the mean flame position. Overall, the distributions are comparable among the different flames in terms of intensity of the fluctuations. This is consistent with the similarities in the temporal traces of $\mathcal{A}_T/\mathcal{A}_0$ reported in Figure 11.2b, and related to the analogies in the turbulence fields. Nevertheless, two qualitative differences can be observed. First, the CH_4 flames presents more widespread fluctuations in the downstream region (i.e., for $\widetilde{C} > C^*$), coherently with the analysis of stretch components in Section 11.1 and, in particular, with the detachment and subsequent rapid consumption of flame pockets at the tip. Secondly, the H_2 flames show more intense fluctuations of $|\nabla C|$ on the fresh gases side, i.e., for $\widetilde{C} < C^*$, which well relate to the generation of flame surface area due to inwardly-propagating finger-like structures, associated with TD instabilities [27, 79, 325].

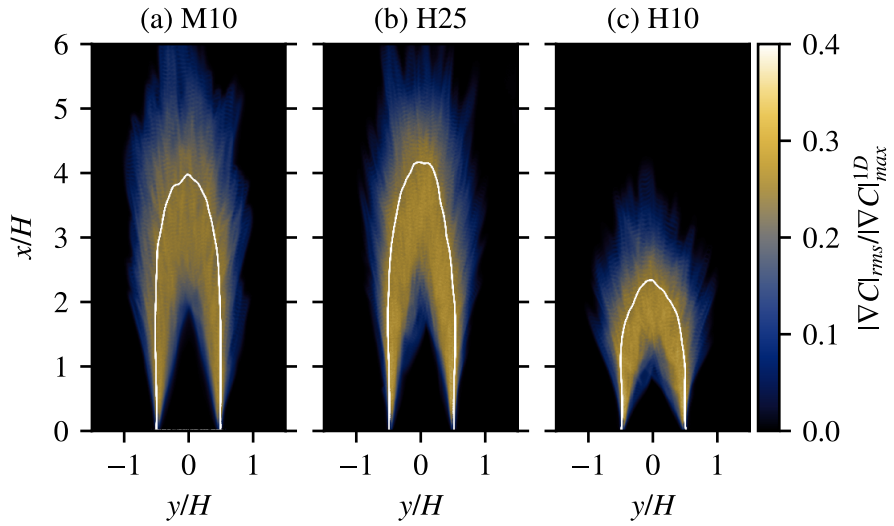

Figure 11.18: Normalized temporal r.m.s. fields of the magnitude of the gradient of progress variable $|\nabla C|_{rms} \,/\, |\nabla C|^{1D}_{max}$ in the xy plane for the three cases. The white lines denote contours of mean progress variable $\widetilde{C} = C^*$.

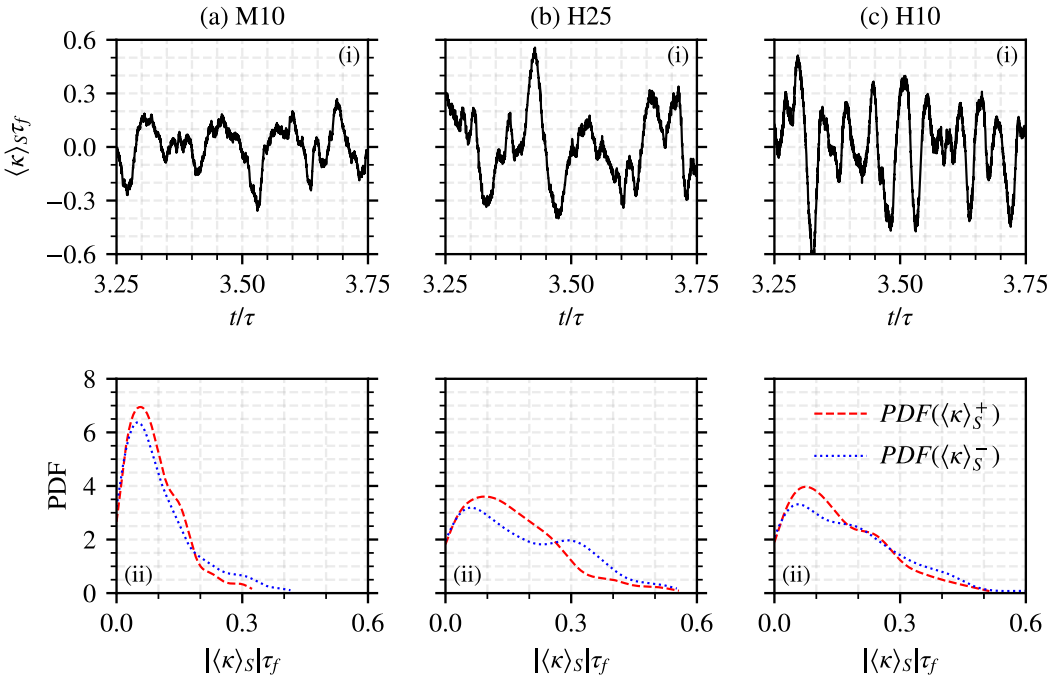

Figure 11.19: Normalized global flame stretch traces $\langle\kappa\rangle_S\tau_f$ (i) and conditional PFDs of its positive $\langle\kappa\rangle_S^+$ and negative $\langle\kappa\rangle_S^-$ contributions (ii) for the three cases.

In spite of the apparent similarities, the impact of stretch effects on the temporal variation of the flame surface area in the thermodiffusively unstable H_2 flames is non-negligible. In this sense, Figure 11.19 shows the temporal evolution of the total surface-averaged flame stretch $\langle\kappa\rangle_S$ (top), previously defined in Equation (11.1) and related to the temporal derivative of A_T, together with the corresponding PDFs of its positive ($\langle\kappa\rangle_S^+$) and negative ($\langle\kappa\rangle_S^-$) contributions (bottom), i.e., the PDFs of $\langle\kappa\rangle_S$ conditioned by its sign. From the temporal traces (see Figure 11.19i), it can

be observed that the H_2 flames are prone to larger values of stretch, hence of flame surface deformation, coherently with the results reported in Figure 11.8 for the local stretch. This is further highlighted by the PDF distributions (see Figure 11.19ii), showing that the H_2 flames reach higher values of mean flame stretch, in both the positive and negative directions.

Moreover, the strength of the positive and negative contributions differs when passing from CH_4 to H_2. Indeed, while all flames are statistically stationary, meaning that the positive and negative contributions balance out on average to achieve the condition $\overline{dA_T/dt} = 0$ [44], an increased importance of the positive contribution (i.e., of the flame surface generation component) in the statistical distribution is observed when passing from the thermodiffusively stable CH_4 flame to the unstable H_2 ones. This can be quantified by the skewness of the PDF distribution, which passes from -0.37 for the M10 case to -0.16 and -0.25 for the H25 and H10 cases, respectively. The stronger negative skewness for the M10 flame is observable in Figure 11.19a-ii from the longer tail of the PDF of $\langle\kappa\rangle_S^-$ (blue dotted curve) with respect to $\langle\kappa\rangle_S^+$ (red dashed curve). Indeed, this indicates that extreme negative stretch events, albeit rare, are not balanced by comparable positive stretch ones. Physically, this means that the CH_4 flame is more prone to strong destructive flame annihilation events, which, as discussed in Section 7.2.1, play a major role in the generation of combustion noise at high frequencies. On the other hand, the more positive skewness for the H_2 flames, indicating a reduced asymmetry toward the negative side, sustains the increased importance of flame generation previously discussed in Section 11.1. As a result, the importance of flame annihilation on the overall flame dynamics and, consequently, on the high-frequency combustion noise, is reduced.

To further relate the radiated sound to the flame surface area dynamics, a generalization of the classical combustion noise flamelet theory [2, 69] is proposed hereafter. Recalling the discussion in Section 7.1.1, Equation (7.5), which is reported hereafter for convenience, holds for $Le = 1$ flames:

$$p'(\mathrm{x},t) = \frac{\rho_\infty}{4\pi|\mathrm{x}|}\left(\frac{\rho_u}{\rho_b}-1\right) S_L^0 \left.\frac{dA_T}{dt}\right|_{t-|\mathrm{x}|/c_\infty}. \tag{11.9}$$

However, as discussed in Section 9.2, the effect of stretch on the flame speed needs to be taken into account to make this theory applicable to lean premixed H_2 flames. While this was done in an approximate form, by considering the time-averaged consumption speed for the lowly-stretched laminar flames in Section 9.2, a more rigorous approach is now applied for the present turbulent cases. In this sense, a suitable starting point is Equation (7.6), recalled hereafter:

$$p'(\mathrm{x},t) = \frac{\rho_\infty}{4\pi\,|\mathrm{x}|}\left(\frac{\rho_u}{\rho_b}-1\right) \frac{d}{dt}\int_{A_T} S_d dA\Big|_{t-|\mathrm{x}|/c_\infty}. \tag{11.10}$$

This is valid for arbitrary Lewis numbers and incorporates the effects of stretch on the flame dynamics through S_d. As discussed in Section 2.5.1, within a finite thickness flame, the value of S_d is highly sensitive to the definition of the flame surface [83], i.e., to the selected isosurface $C = C^*$. To remove this ambiguity, here S_d refers to the density-weighted displacement speed (see Equation (2.38)). Recalling Equations (2.68) and (2.69), one obtains:

$$\int_{A_T} S_d dA = \underbrace{\frac{1}{A_0}\int_{A_T} S_d dA}_{S_T} A_0 = S_T A_0 = S_L^0 I_0 A_T, \tag{11.11}$$

which shows the influence of stretch on the combustion noise source term through I_0. Substi-

tuting Equation (11.11) into Equation (11.10) yields:

$$p'(\mathrm{x},t) = \frac{\rho_\infty}{4\pi\,|\mathrm{x}|}\left(\frac{\rho_u}{\rho_b}-1\right) S_L^0\,\frac{d(I_0\mathcal{A}_T)}{dt}\bigg|_{t-|\mathrm{x}|/c_\infty}. \tag{11.12}$$

Equation (11.12) generalizes the classical expression of Equation (11.9) by introducing the stretch factor I_0. This provides a unified description of the acoustic radiation of both equidiffusive and non-equidiffusive turbulent premixed flames. In particular, Equation (11.12) shows that the combustion noise source term is governed by the temporal variation of the turbulent flame surface area, modulated by the influence of stretch.

Moreover, for a fixed operating condition, the global value of I_0 is often observed to vary weakly in time for a statistically steady state [17, 27, 79, 244] (see Figure 11.2c). Under this assumption, Equation (11.12) reduces to:

$$p'(\mathrm{x},t) = \frac{\rho_\infty}{4\pi\,|\mathrm{x}|}\left(\frac{\rho_u}{\rho_b}-1\right) S_L^0\overline{I_0}\,\frac{d\mathcal{A}_T}{dt}\bigg|_{t-|\mathrm{x}|/c_\infty}, \tag{11.13}$$

where $\overline{I_0}$ is the time-averaged value of I_0. Equation (11.13) highlights that differential diffusion effects amplify the acoustic emission by a factor $\overline{I_0}$, all else being equal.

The validity of this theoretical framework is verified by applying it to the present DNS dataset. Figure 11.20 compares the temporal traces of normalized fluctuating pressure p'/p_{ref}, directly extracted from the calculations at the same location of the spectra of Figure 11.15, with those reconstructed a posteriori from $d\mathcal{A}_T/dt$ using the classical flamelet theory [2, 69] in Equation (11.9) (see Figure 11.20i) or the modified version developed in the present work to include stretch effects, either in the temporal derivative (see Figure 11.20ii) by applying Equation (11.12) or in the mean (see Figure 11.20iii) by using Equation (11.13). In all cases, a Pearson correlation coefficient (see Equation (6.5)) not lower than 0.85 is obtained between the recorded pressure signals and those reconstructed through Equation (11.9), confirming that the radiated pressure is linearly associated with the temporal fluctuations of $\mathcal{A}_T$. Nevertheless, while the amplitude of p'/p_{ref} is well predicted by Equation (11.9) for the M10 case, an underestimation is consistently found for the H_2 flames, confirming the failure of the classical combustion noise theory for these flames, in agreement with the laminar cases in Section 9.2. This is quantified by the concordance correlation coefficient r_c [238] (see Equation (9.3)), which takes into account also the local distance between the values of the two distributions. Its value is equal to 0.83 for the M10 case, while it drops to 0.55 and 0.68 for the H25 and H10 cases, respectively. By introducing the stretch factor I_0 in the temporal derivative using Equation (11.12) (see Figure 11.20ii), no relevant differences, as expected, are observed for the CH_4 flame, since this is not affected by stretch effects, i.e., $I_0 \approx 1$ (see Figure 11.2c). However, a much better agreement is observed for the H_2 flames, with the recorded and reconstructed p' signals almost superimposed, and the values of r_c being not lower than 0.9. The validity of the proposed extension of the flamelet theory for thermodiffusively unstable flames is thus confirmed. Most notably, considering the time-averaged stretch factor $\overline{I_0}$ (see Figure 11.20iii) has only a limited negative influence on the amplitude of the predicted noise radiation. Therefore, Equation (11.13) is a valid solution to assess the radiated sound from the flame surface area of thermodiffusively unstable lean premixed H_2 flames, especially when direct measurements of pressure or HRR are not feasible.

It should be noted that in the laminar cases of Section 9.2, for which flame surface deformations were limited, $\overline{S_c} \approx S_L^0\overline{I_0}$, thus explaining why Equation (9.6) adequately described the HRR fluctuations for the lean premixed H_2 flame. In this turbulent case, however, $\overline{S_T} > S_L^0\overline{I_0}$

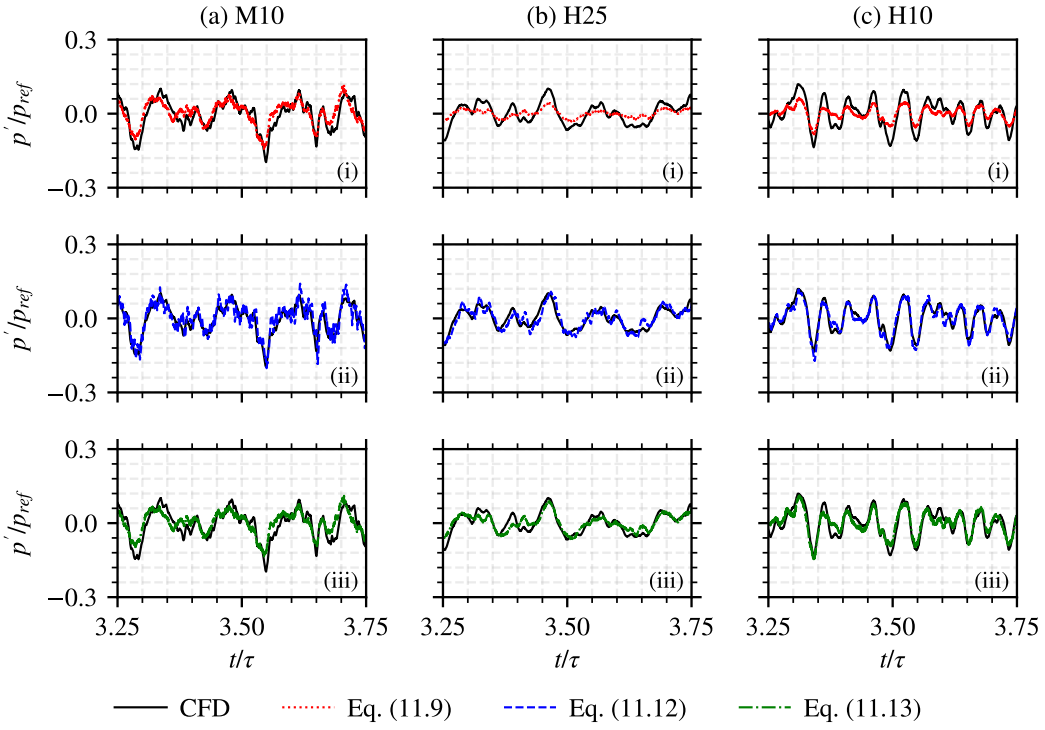

Figure 11.20: Normalized pressure fluctuation traces p'/p_{ref} directly extracted from the CFD results and averaged over 12 equally distributed probes in the azimuthal direction (solid black lines) and computed (i) from dA/dt with Equation (11.9) (dotted red lines), (ii) from $d(I_0 A)/dt$ with Equation (11.12) (dashed blue lines) and (iii) from $\overline{I_0}\,dA/dt$ with Equation (11.13) (dash-dotted green lines) for the three cases.

(see Figure 11.2b-c), meaning that the simplification made in Section 9.2 is not valid anymore. This may also explain the overprediction observed for acoustically forced laminar flames by Talei et al. [390] when comparing the recorded noise levels with those reconstructed from the surface area fluctuations following Equation (9.6) (see Section 7.4).

From a physical point of view, the validity of Equations (11.12) and (11.13) means that stretch effects, by promoting the wrinkling of the surface of thermodiffusively unstable flames, effectively enhance the generation of sound. Nevertheless, Equation (11.13) highlights that the amplitude of the radiated sound is modulated not only by $\overline{I_0}$, but also by the laminar flame speed S_L^0 and by the expansion ratio across the flame front ρ_u/ρ_b. In the present study, while the surface fluctuations are comparable among the CH_4 and H_2 flames, given that they are subjected to analogous turbulence fields, and S_L^0 is the same by choice (see Table 10.1), the lean H_2 flames feature a lower value of the expansion ratio ρ_u/ρ_b with respect to the stoichiometric CH_4 flame, given the lower adiabatic flame temperature T_{ad} (see Table 10.1). This counterbalances the enhancement of combustion noise generated by TD effects through the stretch factor.

11.3.2 Local heat release rate dynamics

The differences between CH_4 and H_2 flames in the burning rate and HRR, which have been characterized globally in Section 11.1, are here analyzed locally to further understand the impact of TD effects on the combustion noise source term. To this scope, Figure 11.21 compares the normalized temporal r.m.s. of the local HRR $\dot{\omega}_{T,rms}/\dot{\omega}^{1D}_{T,max}$ in the xy plane for the three flames,

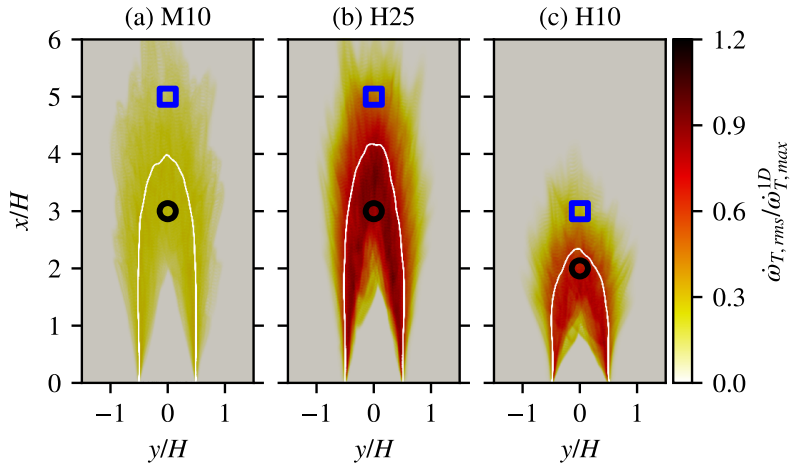

Figure 11.21: Normalized temporal r.m.s. fields of the HRR $\dot{\omega}_{T,rms}/\dot{\omega}^{1D}_{T,max}$ in the xy plane for the three cases. The white lines denote contours of mean progress variable $\widetilde{C} = C^*$. The markers correspond to the positions of the probes in Fig. 11.22.

together with isocontours at $\widetilde{C} = C^*$ (in white) to highlight the mean flame position. As expected, the CH_4 flame (see Figure 11.22a) shows an almost uniform value of $\dot{\omega}_{T,rms}$ across the entire flame brush, whose normalized intensity is close to the one of $|\nabla C|_{rms} \,/\, |\nabla C|^{1D}_{max}$ shown in Figure 11.4a. This further confirms that, for this thermodiffusively stable flame, the variability in the local reactivity is caused by the sole action of turbulence on the flame surface, which, as discussed in Sections 11.1 and 11.3.1, is dominated by annihilation events, especially at the flame tip. On the other hand, the H_2 flames show much stronger fluctuations of the local HRR in the inner region of the flame, i.e., for $\widetilde{C} < C^*$, which well relate to the enhancement of the flame surface generation mechanism associated with TD instabilities [25] (see Sections 11.1 and 11.3.1).

Further insights can be obtained from Figure 11.22, which reports, for each flame, the temporal traces of the normalized local HRR fluctuations $\dot{\omega}'_T = \dot{\omega}_T - \overline{\dot{\omega}_T}$ (top) and the corresponding PSD (bottom) for two probes, identified by the markers in Figure 11.21. These are located in the unburned gases region upstream of the mean flame surface ($\widetilde{C} < C^*$, black circle in Figure 11.21) and in the downstream burned gases region ($\widetilde{C} > C^*$, blue square in Figure 11.21). It should be noted that $\dot{\omega}'_T$, being a small scale phenomenon, is highly intermittent. Therefore, its value can be significantly higher than the time average $\overline{\dot{\omega}_T}$ [209, 241, 385]. Furthermore, $\dot{\omega}_T = 0$ whenever the local equivalence ratio falls below the lean flammability limit, and $\dot{\omega}'_T$ is consequently limited, on the negative side, by the condition $\dot{\omega}'_T \geq -\overline{\dot{\omega}_T}$ [209].

When comparing the temporal traces for the CH_4 and H_2 flames, significant differences arise. Indeed, for the M10 case (see Figure 11.22a-i), the two probes show comparable signals, in terms of shape of the distributions and amplitude of the oscillations, with the maximum positive value close to $\dot{\omega}^{1D}_{T,max}$. The sole relevant difference is the larger number of bursts, denoting the presence of the flame at the given location within the considered time window, for the probe at $\widetilde{C} < C^*$, which is to be expected given the higher availability of reactants in this zone. Therefore, the CH_4 flame locally displays a sort of intermittency: the HRR fluctuates with repeatable amplitude, and the main source of variability is represented by the occurrence of the bursts in time. On the other hand, both the H25 (see Figure 11.22b-i) and H10 (see Figure 11.22c-i) flames consistently show an enhancement of HRR fluctuations, due to the action of TD effects, as previously discussed in Section 11.1. This is more accentuated in the probe located in the unburned gas region, co-

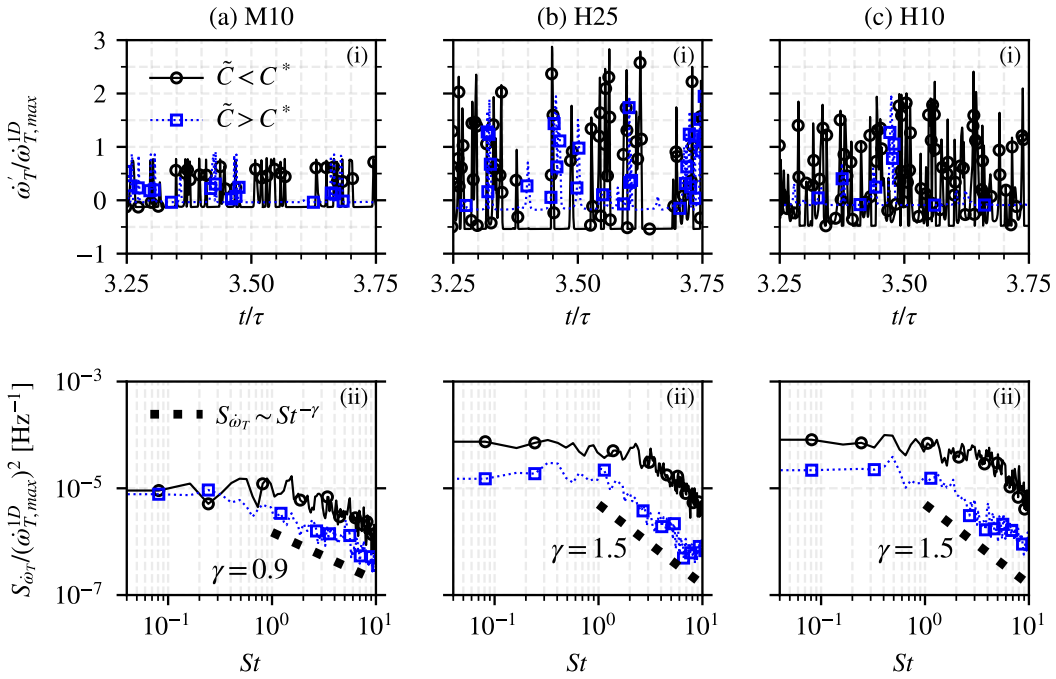

Figure 11.22: Normalized temporal traces of local HRR fluctuations $\dot{\omega}'_T$ (i) and corresponding power spectral densities (ii) in the unburnt ($\widetilde{C} < C^*$) and burnt ($\widetilde{C} > C^*$) gas regions for the three cases.

herently with the results in Figure 11.21, while at $\widetilde{C} > C^*$ this enhancement is less accentuated. Furthermore, while the amplitude of the HRR bursts in the CH_4 flame is almost constant, for the H_2 a more accentuated variability is observed. This indicates that, for the H_2 flames, the local HRR is modulated not only by the sole effect of turbulence on the flame surface, which leads to the intermittent behavior observed for the CH_4 flame in Figure 11.22a-i, but also by the stretch-induced enhancement associated with TD effects.

These differences reflect in the corresponding spectra (see Figure 11.22ii). Coherently with the literature [209], all HRR spectra can be divided in two regions: a low-frequency ($St < St_c$) regime and a high-frequency ($St > St_c$) one, where St_c is a cut-off Strouhal number denoting the change in the HRR spectral behavior: for $St < St_c$, the PSD is almost constant, while, for $St > St_c$, the PSD starts to decay following a power law (linear in logarithmic scale). For the CH_4 flames (see Figure 11.22a-ii), the spectra at the two locations nearly collapse, especially in the low-frequency region, while slight differences are observable in the high-frequency one, due to a shift of St_c toward lower values when moving downstream, from $St \approx 1$ at $\widetilde{C} < C^*$ to $St \approx 0.5$ at $\widetilde{C} > C^*$. This is consistent with the reduced occurrence of burst events observed in the temporal traces (see Figure 11.22a-i). On the other hand, for the H_2 flames (see Figure 11.22b-ii and c-ii), a clear reduction in the value of the PSD is observable when moving downstream, consistently with the weaker amplitudes of the HRR bursts observed in the temporal signals at $\widetilde{C} > C^*$ (see Figure 11.22b-i and c-i). The value of St_c increases with respect to the CH_4 flame, being it equal to $St_c \approx 2$ for the probe at $\widetilde{C} < C^*$ and to $St_c \approx 1$ for the probe at $\widetilde{C} > C^*$, which means that the energetic low-frequency region is broader. Lapenna et al. [220], in their curvature-based analysis of turbulent flames, reported an increase in the cut-off wavenumber k_c and a broader range of unstable wavenumbers when passing from thermodiffusively stable to unstable flames, thereby indicating that turbulence can interact synergistically with TD instabilities over a wider range of

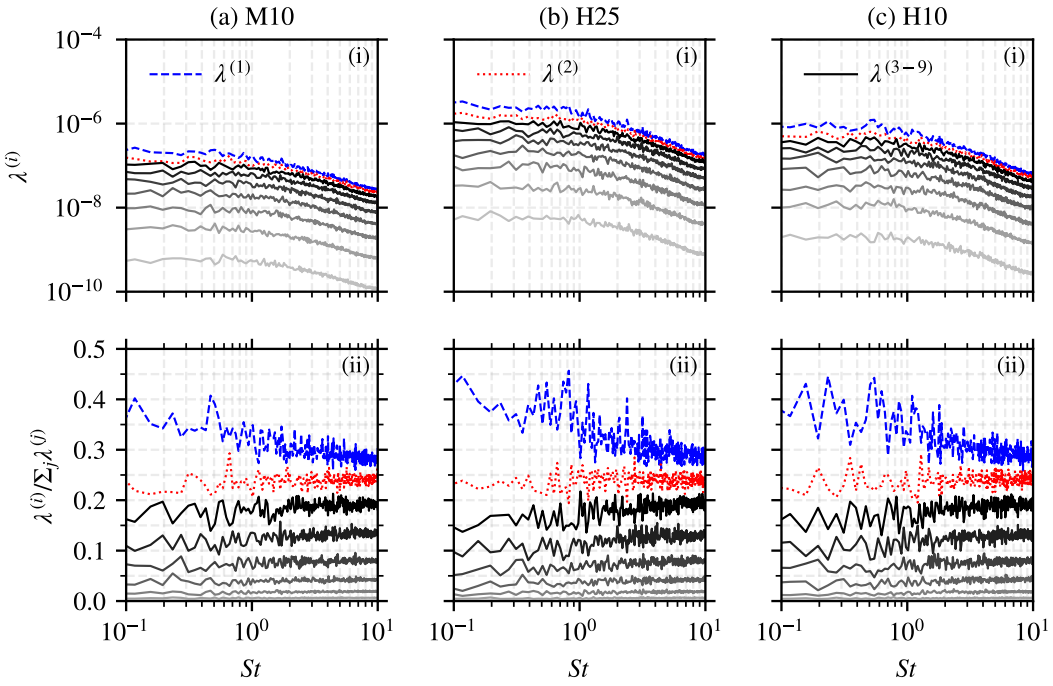

Figure 11.23: HRR SPOD eigenvalues $\lambda^{(i)}$ (i) and corresponding energy share $\lambda^{(i)}/\Sigma_j\lambda^{(j)}$ (ii) for the three cases.

scales. By relating spatial and temporal scales [313], the larger cut-off wavenumber k_c observed in [220] is coherent with the larger value of St_c observed in the present work. For $St > St_c$, on the other hand, the H_2 flames show a steeper decay in the local HRR spectra, with the exponent of the roll-off power law passing from -0.9 for CH_4 to -1.5 for H_2, thus indicating a suppression of strong HRR fluctuations at high frequencies. This well relates to the observations made for laminar H_2 flames by Berger et al. [25], who showed, by means of linear stability analysis, that TD instabilities are favored at large scales, while stabilization occurs at small ones (see Section 4.2.3). This stabilization mechanism is consistent with the reduction in the flame speed upon annihilation observed in [388, 390, 421] (see Section 7.4), and to the consequent reduced impact of flame annihilation phenomena on the high-frequency content discussed in Section 11.3.1. Finally, this spectral behavior directly relates to the different roll-off in the acoustic spectra observed for CH_4 and H_2 flames in Figure 11.15. Therefore, this transfer of HRR spectral energy from the small scales (at high-frequency) to the large scales (at low-frequency) represents the underlying mechanism for the differences in the acoustic spectra observed between the CH_4 and H_2 flames.

To corroborate the analysis performed on the local temporal signals, the spectra retrieved from the SPOD of the normalized HRR $\dot{\omega}_T/\dot{\omega}^{1D}_{T,max}$, performed on the *xy* plane following the methodology presented in Section 3.4.1, is now considered. This allows to exploit the spatial information from a wider dataset to retrieve the spectral behavior of HRR.

Figure 11.23 shows the spectra of the eigenvalues $\lambda^{(i)}$ obtained for the three flames, together with the corresponding energy share $\lambda^{(i)}/\Sigma_j\lambda^{(j)}$ of each mode. The overall behavior is similar across the different modes, with an almost flat curve in the low St region and a subsequent monotonic decrease for higher St, consistently with the results for the local HRR in Figure 11.22. For the M10 case, the decay starts at $St_c \approx 0.5$, while for the H_2 flames it occurs from $St_c \approx 1$, confirming the broader extension of the low-frequency energetic region observed in Figure 11.22. Furthermore, for all cases a non-low-rank behavior is present [346], with the energy at each fre-

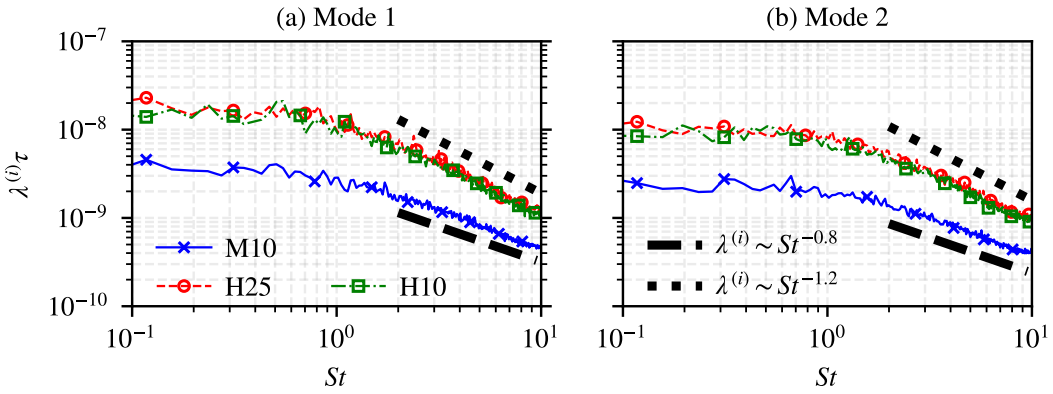

Figure 11.24: Compensated HRR SPOD eigenvalues $\lambda^{(i)}\tau$ for the first (a) and second (b) mode.

quency spread over several comparable flow structures. This indicates that the HRR dynamics is coherent in frequency, but multi-structure spatially. For this reason, the spatial modes are not considered in the present analysis. Nevertheless, the energy share plot (see Figure 11.23ii) shows that the first two modes capture about 60% of the total energy, especially in the low-frequency region, where a stronger dominance of the first mode is observed for all cases. Consequently, the remaining of the analysis focuses on the first two modes.

Figure 11.24 shows the eigenvalue spectra of the first two modes, compensated by the flow-through time τ to remove the dependence on the advection rate. In this way, a collapse of the spectra for the H_2 flames is observed. This confirms that the differences in the spectral behavior observed in Figure 11.22 between CH_4 and H_2 flames are a consequence of the inherent properties of the two fuels, with particular reference to the impact of TD instabilities on the HRR dynamics. In this sense, the SPOD spectra in Figure 11.24 consistently retain the two main features of the local ones in Figure 11.22. First, the enhancement of the amplitude for H_2 flames with respect to the CH_4 one indicates that the amplitude of normalized HRR fluctuations is stronger in the thermodiffusively unstable flames. Secondly, the steeper roll-off observed at $St > 1$ is confirmed, with the decay exponent for the power law passing from 0.8 for the CH_4 flame to 1.2 for the H_2 ones. This confirms that, in lean premixed H_2 flames, TD instabilities, by their multiscale action on the local HRR distribution, combined with their influence on the flame surface area dynamics discussed in Section 11.3.1, shape the combustion noise spectrum, enhancing the low-frequency component and weakening the high-frequency one.

11.4 Modal analysis of noise generation mechanisms

The analysis in Sections 11.2 and 11.3 has highlighted three main differences in the acoustic radiation between the CH_4 and H_2 flames. First, an impact of differential diffusion effects on the outer shear layer between combustion products and ambient air has been found, inducing stronger variations in the density field and an enhancement of the K-H shear layer instability. The latter acts as a stronger low-frequency noise source in the H_2 cases with respect to the CH_4 one. Secondly, an enhancement of the acoustic radiation has been observed for H_2 flames at $St < 1$, related to the stronger HRR fluctuations at low frequencies induced by TD instabilities. Finally, a steeper roll-off of the acoustic spectrum has been identified for H_2 flames with respect to the CH_4 one at $St > 1$. This has been associated to the stabilizing action of TD effects at the small

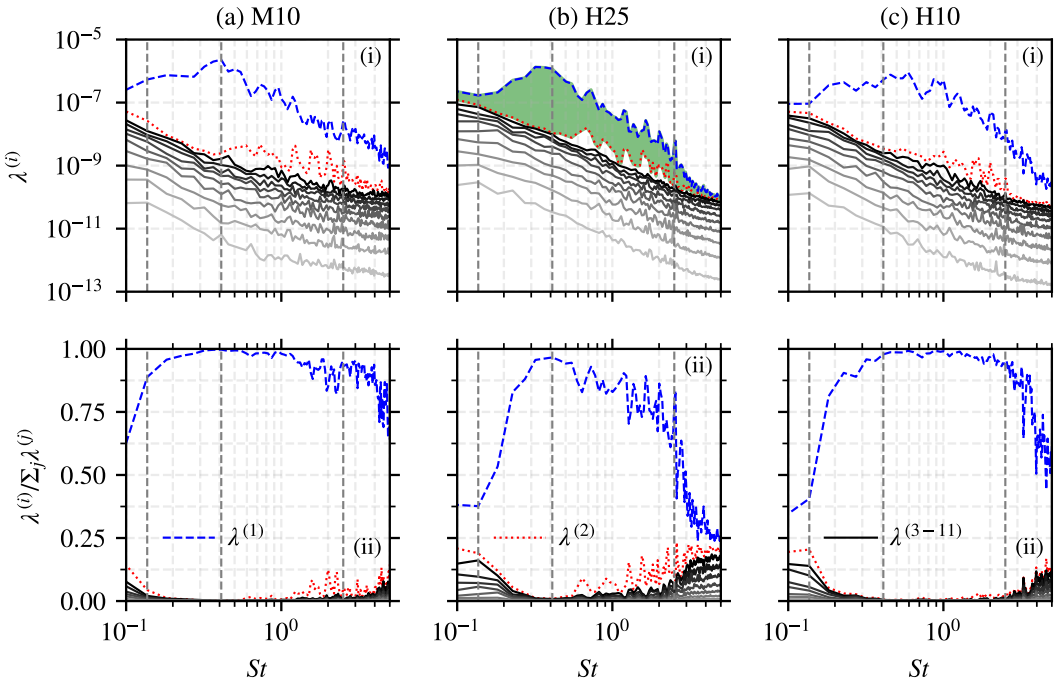

Figure 11.25: Pressure SPOD eigenvalues $\lambda^{(i)}$ (i) and corresponding energy share $\lambda^{(i)}/\Sigma_j\lambda^{(j)}$ (ii) for the three cases. The green shaded area highlights the differences between the first two modes. The vertical dashed gray lines correspond to the modes shown in Figures 11.26, 11.28 and 11.29.

spatial scales, leading to the reduced impact of high-frequency flame annihilation events on the acoustic radiation of the H_2 flames. In the present Section, SPOD of the normalized pressure field (see Section 3.4.1) is adopted to extract the coherent structures that correlate with the radiated sound at different frequencies and to characterize the different noise generation mechanism.

Figure 11.25 shows the eigenvalue $\lambda^{(i)}$ spectra for the three cases, together with the energy share $\lambda^{(i)}/\Sigma_j\lambda^{(j)}$ of each mode. Differently from the HRR (see Figure 11.23), a low-rank behavior is now clearly observable, with the first mode dominating the spectral content, especially for $0.2 \leq St \leq 1$. A higher-rank behavior is observed outside this range, especially for the H_2 flames.

Focusing on the low-frequency acoustic radiation first, Figure 11.26 reports the spatial distributions of the first two modes for the three cases at $St = 0.15$ in the xy plane, together with the mean flame and outer shear layer positions, identified, respectively, by the contours of mean progress variable $\widetilde{C} = C^*$ (black line) and of mean Bilger's mixture fraction [30] $\widetilde{\xi} = 0.5Y_{F,u}$ (white line). A clear difference arises between the CH_4 and H_2 flames in the first mode. Indeed, for the former (see Figure 11.26a-i), no coherent structures are observed, but only a radiating mode originating from the flame. A weak contribution is found in correspondence of the outer shear layer. For the H_2 flames (see Figure 11.26b-i and c-i), on the other hand, strong wavepacket structures are observable, coherent with the K-H instability deforming the outer shear layer [42, 54, 304] (see Section 7.3). These are stronger for the high velocity H25 case (see Figure 11.26a-ii), consistently with the hydrodynamic nature of this instability. In the second mode (see Figure 11.26ii), H_2 flames show analogous structures as in the first one, but in a weaker form, given the lower energy. Moreover, the K-H wavepackets are present also in the CH_4 flame, confirming the presence, albeit limited and only in the sub-leading mode, of these structures for the thermodiffusively stable case. This sustains the analysis in Section 11.2.1, where it has been observed that instabilities

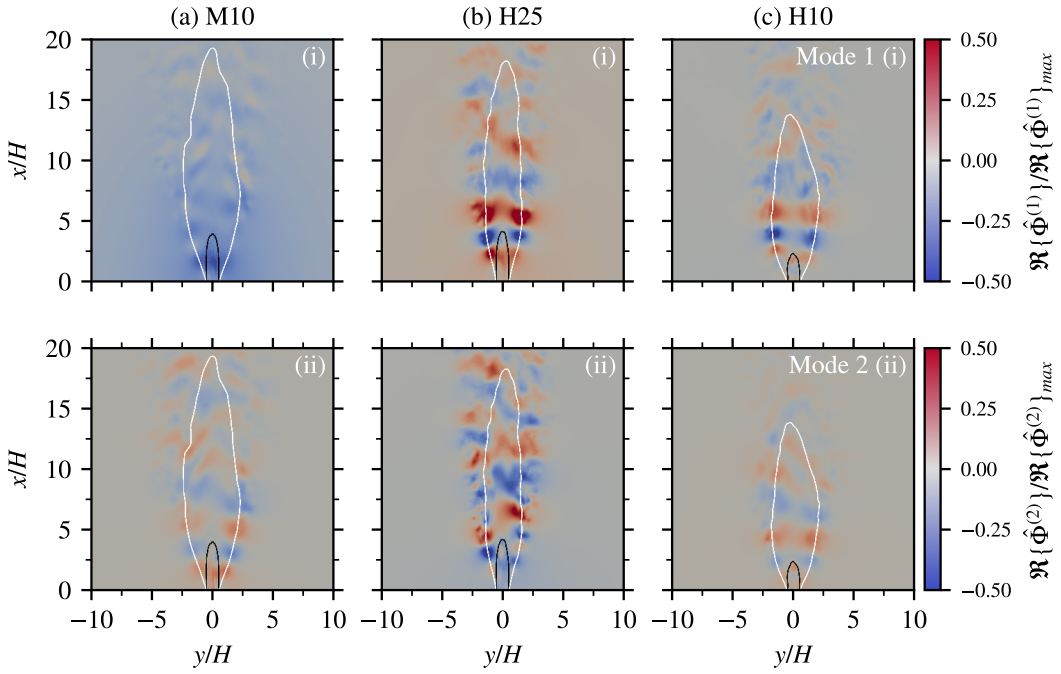

Figure 11.26: Spatial distributions of the first (i) and second (ii) pressure SPOD mode at $St = 0.15$ for the three cases. The black and white lines denote, respectively, contours of mean progress variable $\widetilde{C} = C^*$ and of mean mixture fraction $\widetilde{\xi} = 0.5Y_{F,u}$.

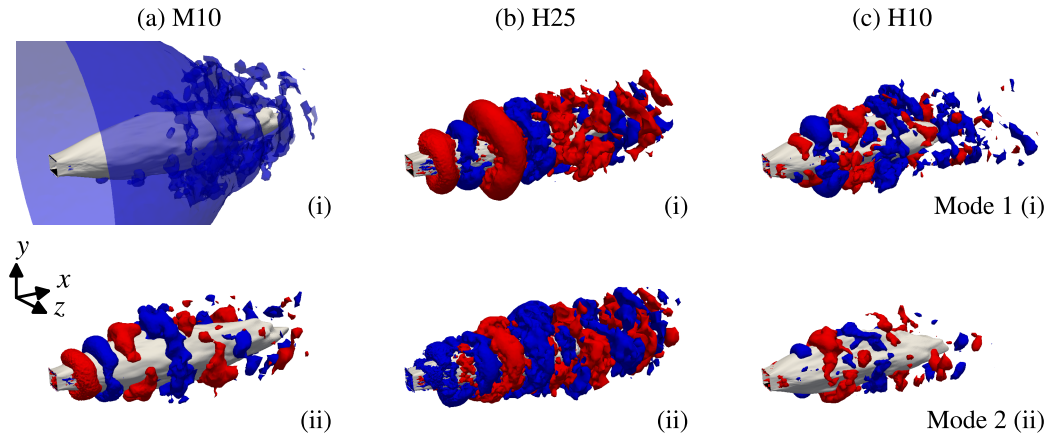

Figure 11.27: Isosurfaces of the first (i) and second (ii) pressure SPOD mode at $St = 0.15$ for the three cases taken at -10% (blue) and $+10\%$ (red) of their respective maximum value. The white isosurface corresponds to the mean mixture fraction $\widetilde{\xi} = 0.5Y_{F,u}$.

at the outer shear layer are a stronger source of pressure fluctuations in the H_2 flames rather than in the CH_4 flame.

The differences between the two fuels are further highlighted in Figure 11.27, which shows contours of the two modes taken at $\pm 10\%$ of the maximum value for the three cases. The radiating nature of the first SPOD mode for the M10 case (see Figure 11.27a-i) is evident, while the H_2 flames show strong, spatially extended low-frequency coherent structures contouring the mean outer shear layer position (denoted by the white isosurface taken at $\widetilde{\xi} = 0.5Y_{F,u}$), which are enhanced for the high-velocity H25 case. Similar structures are present in the second mode for all

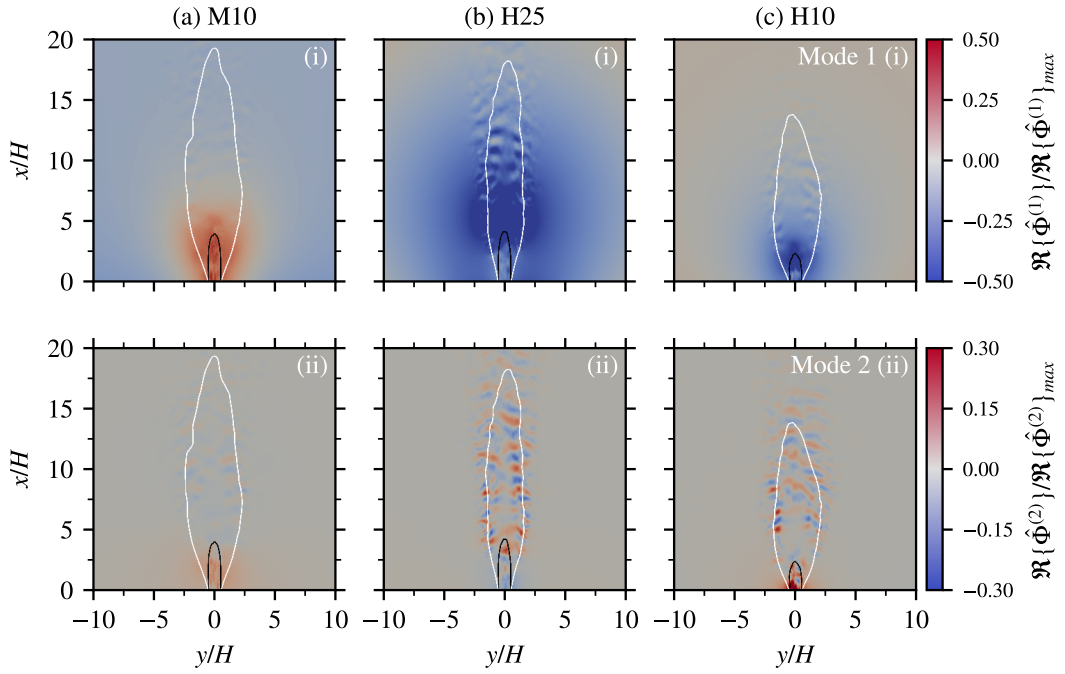

Figure 11.28: Spatial distributions of the first (i) and second (ii) pressure SPOD mode at $St = 0.40$ for the three cases. The black and white lines denote, respectively, contours of mean progress variable $\widetilde{C} = C^*$ and of mean mixture fraction $\widetilde{\xi} = 0.5Y_{F,u}$.

flames (see Figure 11.27ii), with a similar influence of the bulk velocity for H_2 flames as for the first one. This indicates that, for the M10 case, flame-generated acoustic radiation, associated with the first mode, is the dominant noise generation mechanism at low St, while the outer shear layer provides a second-order contribution. This is coherent with the strong difference in the energy share of the two modes observed in Figure 11.25a-ii. For the H_2 flames, on the other hand, the K-H instability at the outer shear layer has a dominant contribution. Energy is therefore transferred from the first to the second mode, consistently with the proximity in the energy share of the two modes observed at this frequency in Figure 11.25b-ii and c-ii. This difference can be related, on one hand, to the differences in the value of T_{ad} and ρ_b between the CH_4 and H_2 flames, since shear layer instabilities are less pronounced as the temperature ratio increases [42, 341, 398] (see Section 7.2.2), and, on the other hand, to the stronger variability in the density field induced by differential diffusion effects, previously observed in Section 11.2.1.

Figure 11.28 reports the spatial modes in the xy plane at $St = 0.40$, i.e., in the mid-frequency range. Here, the first mode (see Figure 11.28i) has a radiating nature, centered in proximity of the mean flame position, for all cases, consistently with the dominance of flame-generated noise in this frequency region (see Section 11.2.2). Still, a non-negligible trace of the wavepacket-like structures originated at the outer shear layer are visible in the H_2 flames. Therefore, for these flames, the low-frequency acoustic disturbance originated at the outer shear layer persists over a broader frequency range than in the CH_4 case. This is even more evident when looking at the second mode, for which no relevant coherent structures are present in the CH_4 case, while clear, albeit weak, wavepackets are visible in correspondence of the outer shear layer for the H_2 flames. This difference can be associated to the finer-scale structures and improved mixing observed in this spatial region (see Figure 11.11), which translate in a persistence of these structures at higher frequencies.

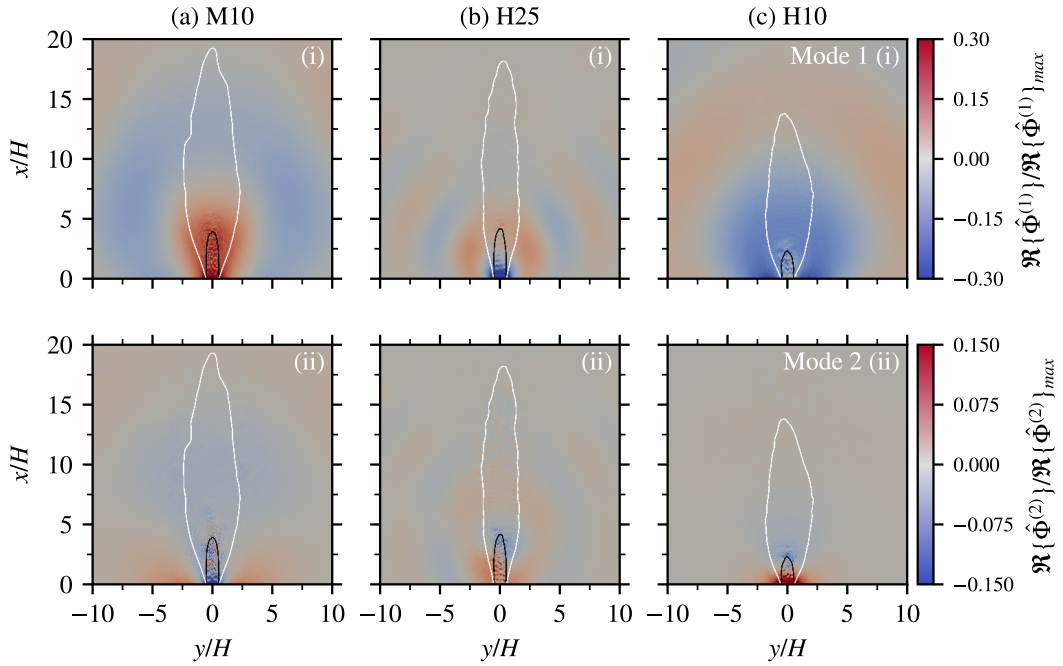

Figure 11.29: Spatial distributions of the first (i) and second (ii) pressure SPOD mode at $St = 2.5$ for the three cases. The black and white lines denote, respectively, contours of mean progress variable $\widetilde{C} = C^*$ and of mean mixture fraction $\widetilde{\xi} = 0.5Y_{F,u}$.

Finally, the high-frequency noise generation is considered by taking into account the spatial modes in the xy plane at $St = 2.5$, provided in Figure 11.29. In this frequency regime, the pressure field is governed by the noise generated by the turbulent flame, while no outer shear layer structures are present either in the first mode (see Figure 11.29i), which is purely radiating, or in the second one (see Figure 11.29ii), for which no relevant structures are present. The weak energy of the second mode indicates that the reduced energy share of the first mode at this St observed in Figure 11.25ii is not associated to stronger higher-rank modes. Rather, it is related to the insurgence of a weakly coherent regime and to the global weakening of the energy due to the high-frequency decay of the acoustic radiation. Based on this modal decomposition, it is confirmed that the differences in the spectral decay observed in this frequency region are to be imputed to the differences in the HRR dynamics at the flame front discussed in Section 11.3.2, since the noise generated in the flame brush remains the dominant acoustic source in this frequency range.

11.5 Influence of the Karlovitz number

The impact of thermodiffusive effects and instabilities on the dynamics of lean premixed H_2–air flames, and, consequently, on their acoustic radiation, has been discussed in the preceding Sections. As detailed in Section 4.3.2, an impact of the Karlovitz number Ka on TD instabilities has been observed in the literature, with the turbulent mixing overcoming the TD response at high values of Ka [23, 236, 332]. Moreover, under these highly turbulent conditions, other noise sources, associated with turbulent structures, can become relevant, in addition to HRR fluctuations [160]. This Section intends to better understand how the coupling between turbulence and TD instabilities at different Ka values affects the noise generation mechanisms in

Table 11.1: Main parameters for the simulations at different *Ka*. For all cases: $S_L^0 = 0.38$ m/s, $\delta_L^0 = 450$ μm, $U_0 = 25$ m/s, $\tau_0 = 6.824$ ms, $P_{th,0} = 4.3$ kW.

Description	Value		
	Low *Ka*	Mid *Ka*	High *Ka*
Karlovitz number *Ka*	8	48	190
Slot width H/H_0	1.0	0.4	0.2
Bulk velocity U_B/U_0	1.0	2.5	5.0
Thermal power $P_{th}/P_{th,0}$	1.0	0.4	0.2
Jet Reynolds number *Re*	10830	10830	10830
Inlet Mach number *M*	0.066	0.17	0.33
Turbulence intensity u'/U_B	0.1	0.1	0.1
Integral length scale of turbulence l_t/H	0.25	0.25	0.25
Kolmogorov length scale η/Δ_x	0.40	0.23	0.11
Average length of the turbulent flame brush L_f/H	4.35	12.0	16.3
Flow through time τ/τ_0	1.0	0.4	0.2
Mesh cells	208×10^6	113×10^6	78×10^6

lean premixed H_2–air flames.

To this scope, the previously investigated H25 flame, hereafter referred to as the low *Ka* case, is compared to other two flames with increased value of *Ka*. The same computational domain and numerical methodology adopted in the previous Sections are retained, with two main differences. First, to focus on the sole direct combustion noise, the flames are placed in an environment of equilibrium combustion products at the adiabatic flame temperature, in analogy with previous combustion noise studies in the literature (e.g., [44]), and not in ambient air. This eliminates the contribution of the density variations in the shear layer to the acoustic field, associated with excess density indirect noise, previously discussed in Section 11.2.1. Secondly, as in [23], the slot width H is reduced to assess the impact of increasing *Ka* at same jet Reynolds number *Re*. As a consequence, the transversal section of the channel, of size $H \times 1.5H$, is variable across the different cases.

On the other hand, the length of the inlet channel remains unchanged and equal to $3H_0$, where $H_0 = 8.5$ mm is the slot width of the low *Ka* case (i.e., the previously discussed H25 flame). Moreover, the size of the region of interest for the acoustic analysis (i.e., a cylinder of radius $10H_0$ and length $L_x = 20H_0$) is fixed, as well as the placement of the outlet boundary at the radius $35H_0$. The grid resolution for the unstructured 3D tetrahedral mesh has been defined according to the criteria described in Section 10.2. As in the previous simulations, the element size in the flame region is not greater than $\Delta_x = 100$ μm, thereby allowing to resolve the flame front without any artificial thickening, and to ensure a reasonable time step Δ_t, based on the global acoustic *CFL* condition ($CFL \leq 0.7$). The influence of the mesh on the numerical results has been assessed for the three cases (see Appendix C), with no significant discrepancies found by further refining the grid size. The main parameters for the simulations and the grid size of the three cases are given in Table 11.1. For all flames, the simulated physical time is equal to $4\tau_0$, after reaching statistical convergence. For the mid and high *Ka* cases, the computational cost of the production runs has been about 80% and 90% of the one of the low *Ka* case (see Section 10.2.3), respectively.

The location of the three cases in the Borghi–Peters turbulent combustion diagram [301] is reported in Figure 11.30. It can be observed that the low *Ka* case is fully in the thin reaction zone regime, while the other two cases are at the transition between this regime and the broken

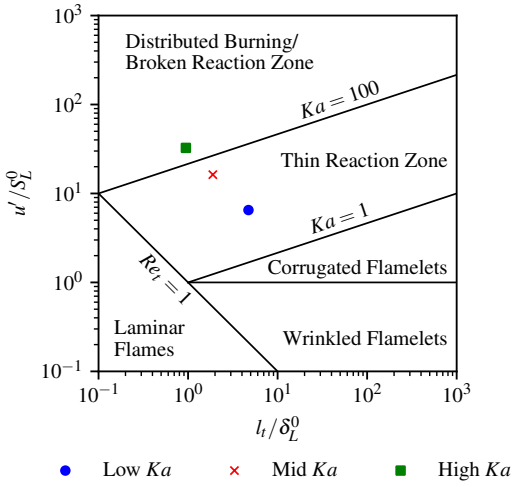

Figure 11.30: Location of the three cases in the Borghi–Peters turbulent combustion diagram [301].

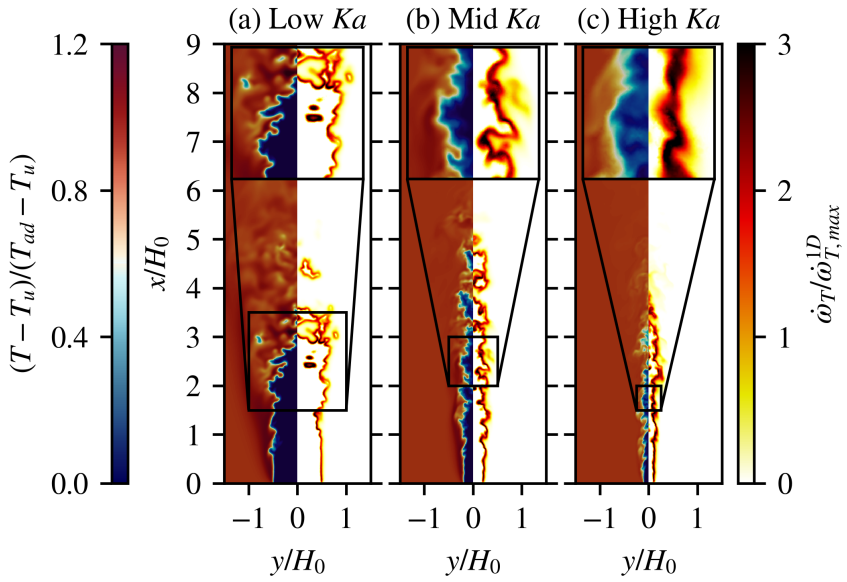

Figure 11.31: Instantaneous distributions of reduced temperature $(T - T_u)/(T_{ad} - T_u)$ (left) and of normalized HRR $\dot{\omega}_T/\dot{\omega}^{1D}_{T,max}$ (right). The insets highlight the differences in the flame front among the three cases.

reaction zone (see Section 2.7.4).

11.5.1 Flame–turbulence interaction

First, the main differences in the structures of the three flames, as well as in their interaction with the turbulence field are discussed. Figure 11.31 shows the instantaneous distributions of reduced temperature $(T - T_u)/(T_{ad} - T_u)$ and of HRR $\dot{\omega}_T$, normalized by its maximum value $\dot{\omega}^{1D}_{T,max}$ (see Table 10.1) in the corresponding 1D laminar unstretched premixed flame, for the three cases. As in [23], distinct regions of super-adiabatic temperature appear in the low *Ka* case, but are reduced as *Ka* increases, indicating weaker TD effects. Moreover, although all flames exhibit a strong HRR variability, its origin differs. At low *Ka*, wrinkling is mostly induced by TD insta-

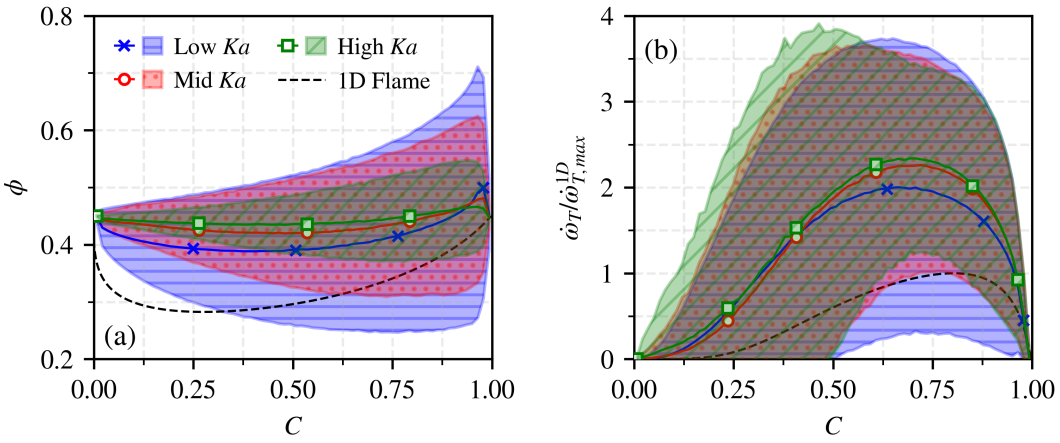

Figure 11.32: Mean (lines) $\pm 3\sigma$ (colored area), where σ is the standard deviation, of the local equivalence ratio ϕ (a) and of the normalized HRR $\dot{\omega}_T/\dot{\omega}^{1D}_{T,max}$ (b), conditioned by C. The results for the corresponding 1D unstretched laminar flame (black dashed line) are added for reference.

bilities, producing cellular structures and enhancing the flame front wrinkling along the entire flame brush. At mid *Ka*, TD effects are stronger in the first region of the jet ($x/H < 3$), yielding a more elongated flame brush, whose local HRR is overall higher than that of the low *Ka* case, but more uniform. This trend is amplified at high *Ka*, as turbulence dominates over TD instabilities [23, 332], and the flame becomes thicker (see inset in Figure 11.31c), consistently with the expected behavior for a combustion process occurring in the broken reaction zone [311].

It is recalled that *Ka* represents the ratio between the flame characteristic timescale, i.e., $\tau_f = \delta^0_L/S^0_L \approx 1.2$ ms, and the timescale $\tau_m = u'(\eta)/\eta$ of the turbulent transport at the Kolmogorov scale [311] (see Section 2.7.4). Therefore, this reduction of TD instabilities for increasing *Ka* is associated to the competition of the two time scales [236]. At low *Ka*, $\tau_m \sim \tau_c$ and the flow unsteadiness resonates with the flame, leading to stronger local flame fluctuations and to an enhancement of TD instabilities [236]. Conversely, when $\tau_m \ll \tau_c$, as it occurs at high *Ka*, the flame is not able to respond to the rapid flow perturbations, weakening TD instabilities [236].

Figure 11.32 reports the mean of the local equivalence ratio ϕ (defined with the mixture fraction ξ) and of the normalized HRR $\dot{\omega}_T/\dot{\omega}^{1D}_{T,max}$, conditioned by C. The range within three times the standard deviation σ (corresponding to 99.7% of the distribution) are added in the colored areas to show the variability of the two quantities in each case. As *Ka* increases, the variability of ϕ is reduced, as highlighted from the values of σ in Figure 11.32a, confirming the reduced extra wrinkling associated with TD instabilities [23]. On the other hand, the mean value of ϕ increases, and the flame becomes richer at higher *Ka*. This is coherent with the results in [23], and is associated to the increased turbulence strain rate, which promotes the TD process in the flame normal direction, without inducing TD instabilities. The trends observed for ϕ directly impact the HRR (see Figure 11.32b). Indeed, while all cases show a sensible scatter and an enhancement with respect to the corresponding 1D unstretched laminar flame (black dashed line) [23, 27], the variability is stronger for the low *Ka* case, where TD instabilities are promoted. For the other cases, instead, the variability of HRR is reduced and mostly associated to the action of turbulence. Still, the peak HRR mean value increases for higher *Ka*, coherently with the previously observed increase in the mean ϕ value. Overall, these results corroborate the qualitative observations made for Figure 11.31.

The differences among the three cases in the interplay between TD instabilities and turbu-

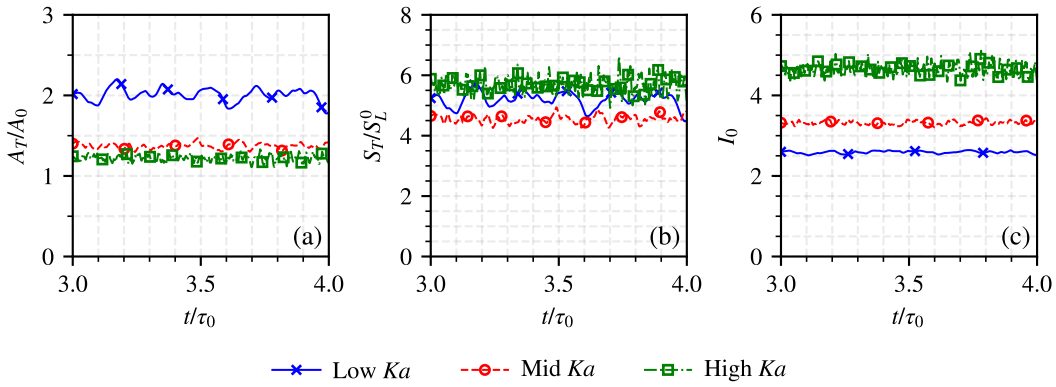

Figure 11.33: Normalized turbulent flame surface A_T/A_0, normalized flame consumption speed S_T/S_L^0, and stretch factor I_0 over a duration τ_0.

lence are further highlighted in Figure 11.33, which reports, for all cases, the temporal evolution over a time duration τ_0 of the turbulent flame surface A_T (see Equation (2.63)), of the turbulent flame consumption speed S_T (see Equation (2.59)), and of the stretch factor I_0 (see Equation (2.71)). As in Section 11.1, the reference flame surface A_0 is taken as the area of the mean progress variable field at $\widetilde{C} = C^* = 0.80$, where C^* corresponds to the maximum HRR in the 1D laminar flame, while S_T is normalized by S_L^0. Consistently with a reduction of the flame surface wrinkling associated with TD instabilities [23], it can be observed that A_T/A_0 is sensibly lowered when passing from the low Ka case to the higher Ka ones. The value of S_T/S_L^0, instead, remains comparable among the different cases. Nevertheless, it is important to highlight that this result may be biased by the reduction of A_0 as Ka increases (see Equation (2.59)), due to the smaller area of the rectangular channel section. Indeed, when compared to the low Ka case, A_0 is reduced by approximately 60% at mid Ka, and by 80% at high Ka. On the other hand, I_0 is independent of A_0 (see Equation (2.71)) and, consequently, provides a more meaningful comparison. In this sense, Figure 11.33c shows that I_0 increases as the value of Ka becomes higher, with the time-averaged value $\overline{I_0}$, passing from 2.6 for the low Ka case to 3.3 and 4.6 for the mid Ka and high Ka cases, respectively. This increase in I_0 is consistent with the results obtained in the previous work by Berger et al. [23], and is associated to the increase of the mean mixture fraction due to the augmented turbulent flame strain rate, which compensates for the attenuated flame surface wrinkling at high Ka due to the reduced importance of TD instabilities.

11.5.2 Acoustic radiation

Figure 11.34 shows, for the three cases, an instantaneous isosurface of progress variable $C = C^*$ colored by the normalized HRR $\dot{\omega}_T/\dot{\omega}_{T,max}^{1D}$, together with the fields of fluctuating pressure $p' = p - \bar{p}$ and of dilatation $\nabla \cdot \mathrm{u}$. As in Section 11.2, the fields are normalized to account for the differences in terms of channel section and bulk velocity. The reference pressure p_{ref} is defined similarly to Equation (11.3), but accounting for the differences in the slot width H across the three cases:

$$p_{ref} = \frac{\gamma - 1}{4\pi c_\infty^2 H_0} \frac{Y_F^u \rho_u H^2 U_B^2 H_F}{L_f}. \tag{11.14}$$

Its value is equal to 8.47 Pa, 7.62 Pa and 11.2 Pa for the low, mid and high Ka cases, respectively.

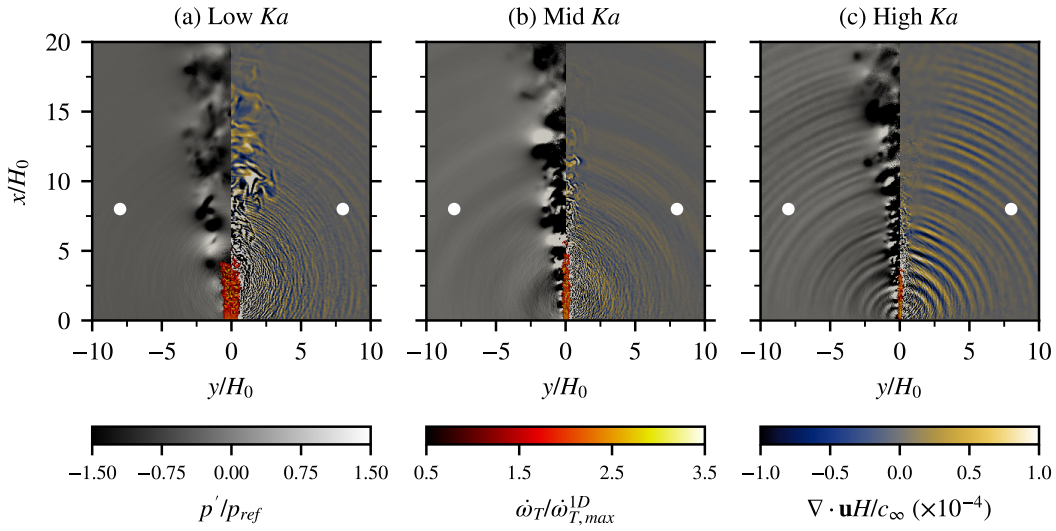

Figure 11.34: Instantaneous normalized fields of fluctuating pressure p'/p_{ref} and dilatation $\nabla \cdot \mathbf{u}H/c_\infty$, and isosurface of $C = C^*$ colored by the normalized HRR $\dot{\omega}_T/\dot{\omega}^{1D}_{T,max}$ in the xy plane. The blue dots mark the probe locations for the spectra of Figure 11.35.

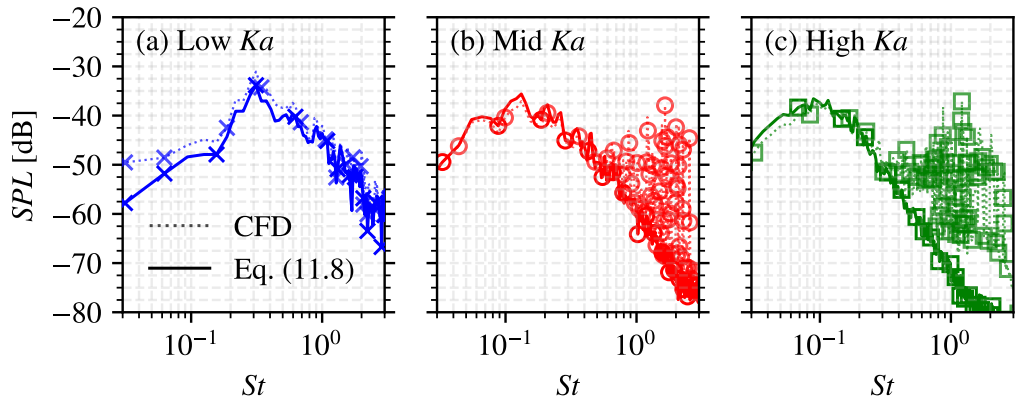

Figure 11.35: Normalized SPL spectra at $x/H = 8$ and radial distance $8H$ from the jet axis extracted from the CFD results and averaged over 12 probes (dotted lines) and computed from dq/dt through Equation (11.8) (solid lines).

Noise radiation from the flame can be observed for all cases in Figure 11.34. As Ka increases, however, additional high-frequency noise arises, with reducing wavelength for increasing Ka. This is superimposed to the direct combustion noise, which is broadband [96]. The distinction between this additional noise and the flame-generated one is even more evident in Figure 11.35. Here, the spectra of normalized SPL (dotted lines), averaged over 12 equally distributed probes in the azimuthal direction at $x/H = 8$ and radial distance $8H$ from the jet centerline (white dots in Fig. 11.34), are compared with the SPL spectra reconstructed from the volume-integrated HRR using Equation (11.8) (solid lines). The normalized SPL is evaluated from the PSD of pressure as in Equation (11.7). The PSD is averaged over 12 equally distributed probes in the azimuthal direction at $x/H_0 = 8$ and radial distance $8H_0$ from the jet centerline, i.e., the same probe location considered in Section 11.2.2. In this Section, the PSD is evaluated using the periodogram method by Welch [420], applying a Hanning window of size τ with 50% overlap.

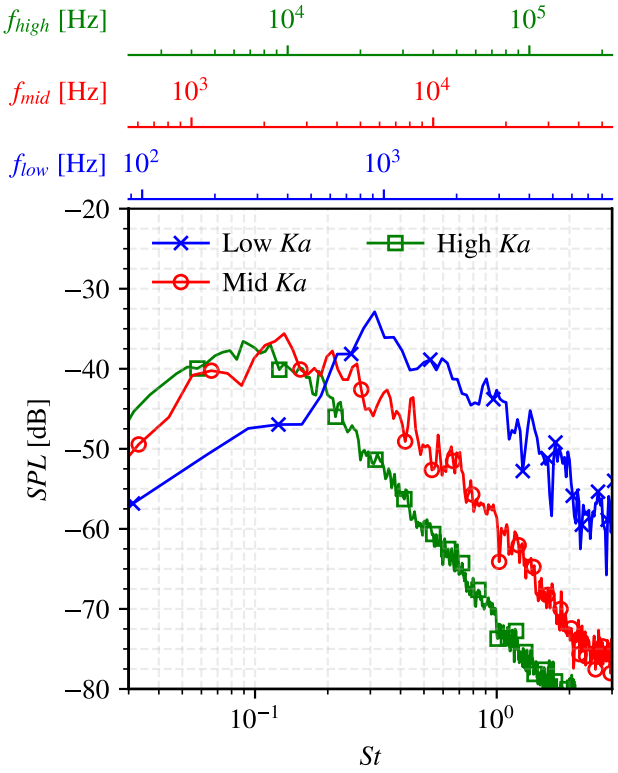

Figure 11.36: Normalized SPL spectra as a function of the Strouhal number St at $x/H_0 = 8$ and radial distance $8H_0$ from the jet axis reconstructed from the HRR through Equation (11.8). The corresponding frequency f ranges (in Hz) for the three cases are reported on top.

As expected for combustion noise (see Section 7.1.2), all spectra in Figure 11.35 show a low-frequency region, where the *SPL* increases, and a high-frequency one, where it decays. In between the two, the peak of the acoustic spectrum is located. For the low *Ka* case, this is located at $St_{peak} = 0.31$, while it moves to $St_{peak} = 0.13$ and $St_{peak} = 0.09$ for the mid *Ka* and high *Ka* cases, respectively. This is due to the combined variation of U_B and L_f (see Table 11.1), to which the peak of the combustion noise spectrum is related (see Section 7.1.2).

A strong agreement is found between the recorded (dotted lines) and reconstructed (solid lines) *SPL* spectra for the low *Ka* case (see Figure 11.35a) at all *St* values, coherently with the results in Section 11.2.2. For the other two cases (see Figure 11.35b-c), a good match is found for $St < 0.3 - 0.5$. At higher *St* values, however, the (multi-)tonal noise observed in Figure 11.34 overcomes the direct combustion noise. Consistently with [160], where it was observed that turbulence-generated noise can become comparable to or dominate over the contribution of HRR fluctuations, the absence of the high-frequency noise component in the HRR-reconstructed *SPL* suggests that this is not flame-driven, but rather originates from the turbulence, whose intensity grows with *Ka* in the present configuration. Nevertheless, direct combustion noise, which is the focus of this work, shapes the acoustic spectrum in the low- and mid-*St* regions, and determines the peak *SPL* value, thereby confirming its major role in the acoustic radiation for all *Ka* values.

The remaining of the analysis focuses on the noise directly related to HRR fluctuations, to

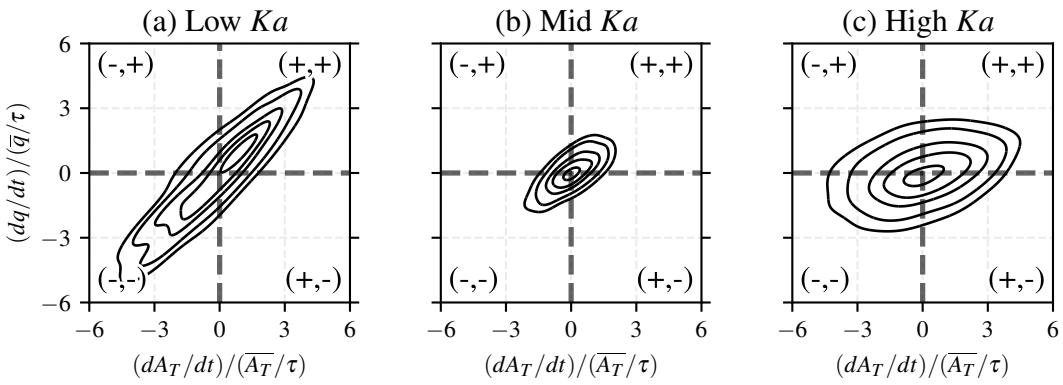

Figure 11.37: Kernel Density Estimates of the normalized volume-integrated HRR time derivative $(dq/dt)/(\bar{q}/\tau)$ with the normalized flame surface time derivative $(dA_T/dt)/(\overline{A_T}/\tau)$ retrieved from a signal of duration τ_0 for the three cases.

elucidate how the differences in the flame–turbulence interactions at varying *Ka* discussed in Section 11.5.1 directly affect the acoustic radiation. Figure 11.36 reports the HRR-reconstructed *SPL* spectra of Figure 11.35, together with the corresponding ranges of frequency f (in Hz) on top. It can be observed that the mid and high *Ka* flames (circle-marked red and square-marked green lines) show quite similar features, in terms of normalized *SPL* peak value ($SPL_{max} \approx -36$ dB) and overall shape of the spectra, while the low *Ka* case (cross-marked blue line) presents a higher normalized *SPL* peak value ($SPL_{max} \approx -34$ dB). This can be attributed to the competition between two time scales, one characteristic of the flame τ_f (see Section 11.5.1), and the other one of the acoustic field τ_a. In terms of frequencies, the former is characterized by $f_{flame} = 1/\tau_f$, while the latter is associated to the peak frequency of the acoustic spectrum $f_{peak} = 1/\tau_a$. In the present case, f_{flame} is around 860 Hz for all flames. On the other hand, f_{peak} increases for varying *Ka*, from 920 Hz in the low *Ka* case ($St_{peak} = 0.31$) to 2420 Hz at mid *Ka* ($St_{peak} = 0.13$), and to 6540 Hz at high *Ka* ($St_{peak} = 0.09$). Therefore, for the low *Ka* case, f_{flame} is close to f_{peak}, and the HRR fluctuations induced by TD instabilities enhance the acoustic radiation. At higher *Ka*, instead, the flame characteristic frequency is shifted to the first part of the spectrum (i.e., $f < f_{peak}$). This misalignment between the acoustic and flame time scales, combined to the overall suppression of TD instabilities at high *Ka* [23, 236, 332] (see Section 11.5.1), attenuates the impact of TD effects on noise.

Finally, Figure 11.37 reports the KDE between the time derivatives of volume-integrated HRR q and flame surface A_T, normalized by their respective time-averaged values and by τ over a signal of duration τ_0 (see Table 11.1). It is recalled that dA_T/dt is associated with the surface-averaged flame stretch (see Equation (11.1)). This analysis allows for assessing if HRR fluctuations, and therefore noise generation, are promoted by flame surface annihilation, as in thermodiffusively stable flames [353, 387], or by flame surface generation. It can be observed that, in the low *Ka* case (see Figure 11.37a), the distribution is shifted toward the first quadrant, where the highest probability is found, indicating that flame surface creation dominates over flame annihilation to generate HRR fluctuations, coherently with the analysis performed in Section 11.3.1. As *Ka* increases, the variability of HRR fluctuations is lowered, consistently with the reduced impact of TD instabilities on the flame dynamics, and the highest probability region shifts toward the third quadrant. This is consistent with the analysis of [23], who observed that the balance of the production and consumption terms changes as *Ka* increases, due to the strong reduction of the production term. Therefore, shifting from the thin reaction zone regime to the broken reaction

Table 11.2: Parameters for the turbulent slot jet flame computed with different schemes.

Description [unit]	Value		
	UCSD	1S_FGS	1S_FGS_LE1
Laminar flame speed S_L^0 [m/s]	0.38	0.34	0.34
Laminar flame thickness δ_L^0 [μm]	450	460	460
Adiabatic flame temperature T_{ad} [K]	1535	1535	1540
Maximum HRR in the 1D laminar flame $\dot{\omega}_{T,max}^{1D}$ [W/m^3]	1.50×10^9	2.40×10^9	2.50×10^9
Average length of the turbulent flame brush L_f/H [-]	4.35	4.36	11.9

zone one, the impact of flame surface generation associated with TD instabilities is reduced, and flame annihilation becomes more important as source of HRR fluctuations and, consequently, of combustion noise. Interestingly, the mid *Ka* (see Figure 11.37b) and high *Ka* (see Figure 11.37c) cases have comparable distributions for the HRR time derivative. Nevertheless, the high *Ka* case shows a broader distribution for the fluctuations of $\mathcal{A}_T$, which is induced by the stronger turbulence intensity, leading to a further destruction of the flame surface. This suggests a saturation of the flame response to surface variations, and is consistent with the similarities in the *SPL* spectra between the mid and high *Ka* cases observed in Figure 11.35.

11.6 Impact of the chemical and transport modeling

The analysis on the impact of the chemical modeling and of the Lewis number, performed in Section 9.4 for the acoustically forced laminar M-shaped flame, is here extended to the turbulent slot jet configuration. To this scope, results obtained with the detailed San Diego mechanism (UCSD) [339] for the low *Ka* case discussed in Section 11.5 are compared with additional simulations, performed with the global reaction mechanism derived in Chapter 5 (1S_FGS). Moreover, the impact of thermodiffusive effects is further assessed by comparing the results with an additional simulation, performed with the one-step scheme by fixing unity Lewis numbers for all species (1S_FGS_LE1), in analogy with the previous analysis in Section 9.4.

The same numerical domain and methods presented in Chapter 10 are adopted, and the environment is composed of equilibrium burnt gases at the adiabatic flame temperature, as in Section 11.5. Therefore, the sole difference among the three cases shown hereafter is represented by the chemical and transport modeling, allowing to isolate their effect on the acoustic radiation. The values of the parameters adopted for the reaction rate and the transport model of the reduced schemes are reported in Appendix A. Some relevant laminar flame properties, evaluated from 1D simulations with Cantera [137], and characteristic quantities of the turbulent H_2–air flame, computed with the three schemes, are reported in Table 11.2. As in the previous Sections, the length of the turbulent flame L_f is estimated from the maximum extension of the mean progress variable field at $\widetilde{C} = C^*$, where C^* is the value of C corresponding to the maximum HRR in the 1D laminar flame, equal to 0.80, 0.92, and 0.85 for the UCSD, 1S_FGS, and 1S_FGS_LE1 schemes, respectively. It can be observed that the reduced scheme with realistic transport properties (i.e., the 1S_FGS mechanism) well captures the value of L_f predicted with the detailed UCSD scheme. When imposing $Le = 1$ in the 1S_FGS_LE1 scheme, on the other hand, the length sensibly increases, due to the reduced burning rate of the turbulent flame in the absence of TD effects [27].

The differences in the shape of the turbulent flame brush are further highlighted by Figure 11.38, which reports the instantaneous isosurfaces of the turbulent slot flame at $C = C^*$ col-

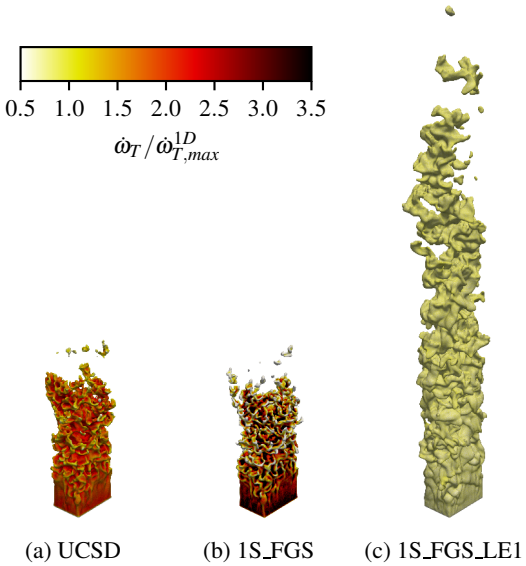

Figure 11.38: Instantaneous isosurfaces of $C = C^*$ colored by the normalized HRR $\dot{\omega}_T/\dot{\omega}^{1D}_{T,max}$ for the UCSD [339] (a), 1S_FGS (b), ans 1S_FGS_LE1 (c) mechanisms.

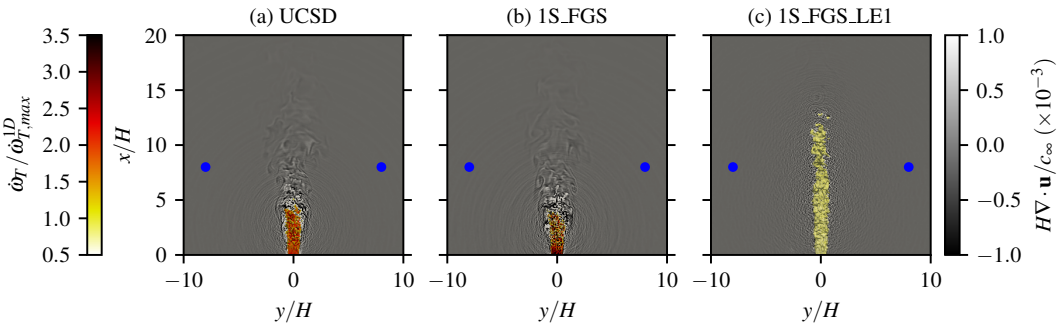

Figure 11.39: Instantaneous normalized HRR $\dot{\omega}_T/\dot{\omega}^{1D}_{T,max}$ and dilatation $D\nabla\cdot\mathbf{u}/c_\infty$ for the UCSD [339] (a), 1S_FGS (b), and 1S_FGS_LE1 (c) mechanisms. The blue dots denote the position of the pressure probes of the spectra in Figure 11.40.

ored by the normalized local HRR $\dot{\omega}_T/\dot{\omega}^{1D}_{T,max}$. By comparing first the UCSD (see Figure 11.38a) and 1S_FGS (see Figure 11.38b) cases, it is observed that the reduced scheme is able to well capture the global flame shape, as well as the length of the turbulent flame brush and the small-scale local flame front wrinkling induced by TD instabilities [79]. Nevertheless, the impact of TD effects on the local HRR is exaggerated, with values of HRR much higher (lower) in the region of positive (negative) curvature. This overestimation of stretch effects is coherent with what observed in the laminar case of Section 9.4 (see Figure 9.20f-g). Moving to the 1S_FGS_LE1 (see Figure 11.38c), as expected, significant differences arise. Notably, no local HRR variations are present, with its value corresponding to the one of the unstretched 1D case. This results in a much longer flame brush, as anticipated in Table 11.2, and to the presence of only a turbulence-induced wrinkling, with no TD instabilities.

The impact on the acoustic radiation is assessed qualitatively in Figure 11.39, which shows the normalized dilatation field in the *xy* plane, together with the isosurfaces of Figure 11.38. An overall good agreement is observed in the dilatation field between the UCSD (see Figure 11.39a) and 1S_FGS (See Figure 11.39b) schemes, with acoustic waves radiating from the flame. Further-

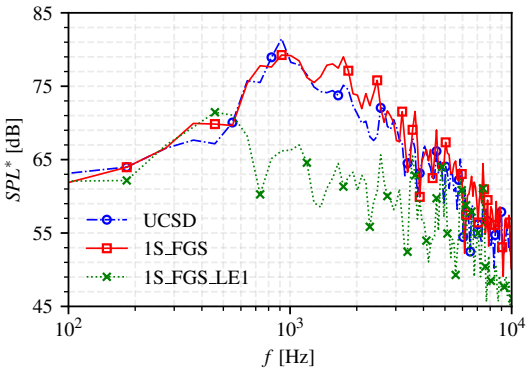

Figure 11.40: Far-field non-normalized SPL^* spectra for the UCSD [339], 1S_FGS and 1S_FGS_LE1 mechanisms.

more, additional local structures are observed in correspondence of the shear layer between the turbulent jet and the ambient (red arrows in Figure 11.39a-b). These are coherent with the structures observed in Section 11.2.1 at the interface between combustion products and ambient air, where they have been related to the effect of differential diffusion on the density and temperature fields. The impact of transport properties on these structures is further confirmed from the 1S_FGS_LE1 case (see Figure 11.39c), for which the dilatation variations at the shear layer are absent. Moreover, for this thermodiffusively stable flame, noise radiation from the detached pocket at the flame tip is observable, coherently with the literature for hydrocarbons (see Section 7.2.1).

Figure 11.40 compares, for the three schemes, the spectra of non-normalized Sound Pressure Level (SPL^*), defined as:

$$SPL^* = 10 \log_{10} \left(\frac{S_p \Delta f}{p_0^2} \right), \tag{11.15}$$

where $p_0 = 2 \times 10^{-5}$ Pa [48]. Since in this Section a single operating point is considered, the spectra are non-normalized to enhance the impact of the chemical and transport modeling on the radiated sound. As in Section 11.5, the PSD of pressure S_p is taken from a pressure signal of duration 4τ (where $\tau = 6.824$ ms is the flow through time), averaged over 12 probes equally distributed in the azimuthal direction. The periodogram method by Welch [420] is applied, with four Hanning windows and a 50% overlap. The position of the probes at $x/H = 8$ and $r_{yz}/H = 8$ is denoted by blue dots in Figure 11.39.

Comparing the UCSD and 1S_FGS cases, an excellent agreement can be found in the low-frequency part, as well as in the position of the peak, located for both schemes at $f_{peak} \approx 920$ Hz. This is consistent with the almost identical values of L_f (see Table 11.2), to which f_{peak} is related (see Section 7.1.2). However, the peak SPL value is about 2 dB lower for the 1S_FGS scheme. Stronger differences arise in the high-frequency range ($f > f_{peak}$). Here, the 1S_FGS scheme predicts a higher noise emission, especially in the range 1000 Hz $< f <$ 3000 Hz, where two peaks at 1730 Hz and 2450 Hz appear. This result is somehow opposite to the one observed for CH_4 flames in [44], where reduced kinetics was shown to produce a stronger peak value and a lower SPL in the high-frequency range. However, this is coherent with the results for the high-frequency laminar case in Section 9.4 (see Figure 9.19) and can be explained by the stronger local HRR variability predicted by the reduced scheme in correspondence of the cellular structures related to TD instabilities (see Figure 11.38). Nevertheless, the global agreement between the UCSD and 1S_FGS mechanisms is significantly good. Indeed, considering the non-normalized Overall Sound Pressure Level $OASPL^*$ (see Equation (11.5)), the difference between the two is

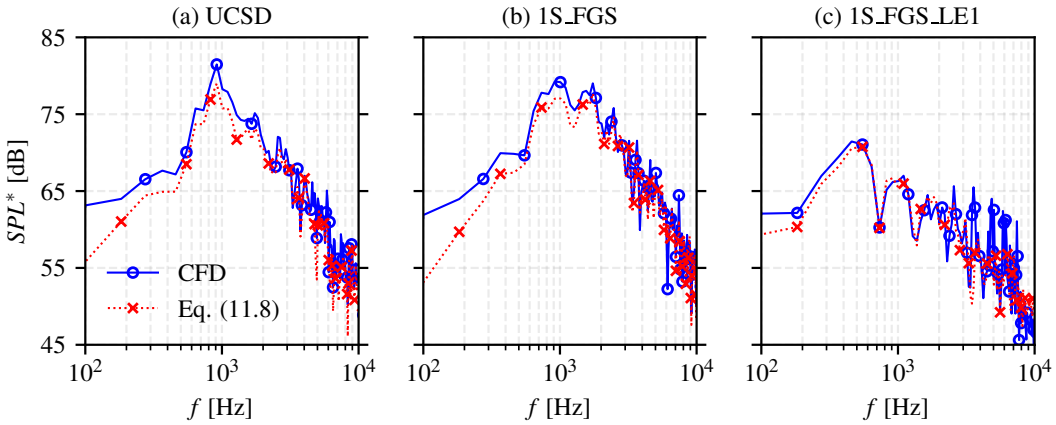

Figure 11.41: Non-normalized far-field SPL^* spectra recorded from CFD (top) and reconstructed from the HRR signal via Equation (11.8) (bottom) for the UCSD [339] (a), 1S_FGS (b) and 1S_FGS_LE1 (c) mechanisms.

lower than 1 dB (90.0 dB and 90.9 dB for the UCSD and 1S_FGS mechanisms, respectively).

As for the 1S_FGS_LE1 case, a shift of f_{peak} to a lower value (460 Hz) is observed, coherently with the longer flame brush (see Section 7.1.2). Furthermore, a sensibly lower SPL value is observed at the peak ($SPL^*_{max} = 81.6$ dB) and in the high-frequency range. Despite the presence of relevant high-frequency peaks, which may be associated to the stronger annihilation events (see Section 7.2.1), the $OASPL^*$ is now equal to 81.6 dB, i.e., 10 dB lower than the 1S_FGS case. This indicates that, even though annihilation events still occur in the $Le = 1$ case, sub-unity Le flames show enhanced HRR fluctuations at multiple spatial scales, induced by the synergy between TD instabilities and turbulence [27] (see Section 4.3.1), which favor the acoustic radiation, in agreement with the comparative analysis of CH_4–air and H_2–air flames performed in Section 11.3. Moreover, differences in the high-frequency roll-off are found between the $Le \neq 1$ and $Le = 1$ cases, with the former having a steeper decay. This result is consistent with the observations reported in Section 11.2.2, providing additional evidence that the differences observed therein between CH_4 and H_2 flames are associated with TD effects and with the different values of Le.

To further confirm the assumption that noise emission is dominated by HRR fluctuations and in analogy with previous Sections, Figure 11.41 compares the SPL^* spectra recorded at the far-field probes with those reconstructed from the HRR through Equation (11.8). Focusing on the UCSD and 1S_FGS mechanisms first, a very good agreement can be observed between the recoreded and reconstructed spectra, especially in the high-frequency region. The peaks previously observed in Figure 11.40 for the 1S_FGS case at 1730 Hz and 2450 Hz are present also in the HRR-reconstructed spectrum (see Figure 11.41e), confirming that their origin lies in the overprediction of HRR fluctuations due to TD instabilities with the reduced scheme. Interestingly, for the reconstructed spectrum, the amplitude of the peak at 1730 Hz is slightly higher than the one of the acoustic peak at 920 Hz. As for the 1S_FGS_LE1 case, an overall good agreement is present also in this case. However, the reconstructed spectrum (see Figure 11.41f) is not able to capture the high-frequency pressure peaks observed in the recorded one. This may be imputed to an inability of the volume-integrated HRR time derivative considered in Equation (11.8) to well capture noise emitted due to local annihilation events, such as those occurring at the flame tip (see Figure 11.39), due to the interference of multiple annihilation events occurring at the same time across the flame.

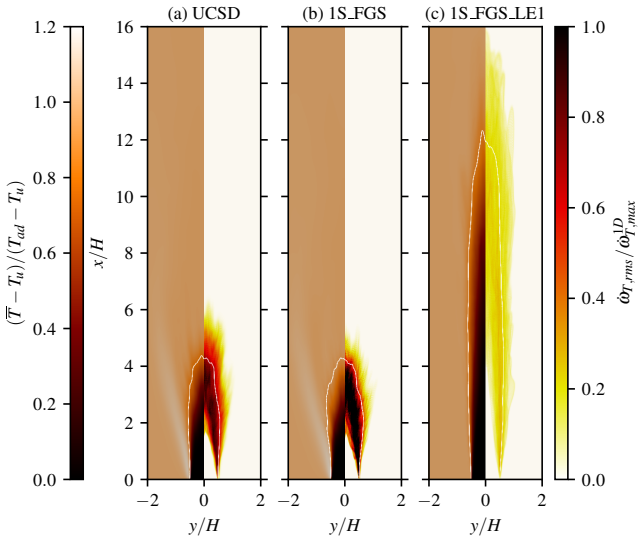

Figure 11.42: Normalized fields of temporal average of temperature $(\overline{T}-T_u)/(T_{ad}-T_u)$ (left) and temporal root-mean-square of HRR $\dot{\omega}_{T,rms}/\dot{\omega}^{1D}_{T,max}$ obtained over a flow through time τ for the UCSD [339] (a), 1S_FGS (b) and 1S_FGS_LE1 (c) mechanisms. The white line denotes the isocontour at $\widetilde{C}=C^*$.

Given the importance of HRR fluctuations on the acoustic radiation, the impact of chemical modeling on it is further analyzed in Figure 11.42, which reports the temporal average of temperature $(\overline{T}-T_u)/(T_{ad}-T_u)$ (left), normalized by the unburned and adiabatic flame temperatures, and the temporal r.m.s. of normalized HRR $\dot{\omega}_{T,rms}/\dot{\omega}^{1D}_{T,max}$ (right). Focusing on the temperature field first, it can be observed that the 1S_FGS scheme well retrieves the behavior of the detailed UCSD mechanism, with the presence of super-adiabatic regions, marker of TD effects [134, 221], which are, as expected, absent for the 1S_FGS_LE1 case. Nevertheless, in the UCSD case, due to the presece of the wider post-flame region, the temperature variation is more gradual with respect to the reduced scheme, affecting also the HRR fluctuations. Indeed, the UCSD scheme still releases a significant amount of heat in the post-flame zone, while this is almost non-existent for the reduced scheme. However, both schemes predict the strongest HRR fluctuations in the first region of the flame front ($\widetilde{C}<C^*$), which is coherent with the formation of finger-like structures characteristic of TD instabilities [79]. The 1S_FGS scheme predicts much stronger fluctuations, coherently with previous observations (see Figure 11.38), thus confirming the origin of the higher predicted acoustic output for this flame. Finally, the 1S_FGS_LE1 scheme shows an almost uniform HRR r.m.s. across the whole flame brush, with its value much lower than the thermodiffusively unstable cases, leading to the observed differences in the acoustic radiation.

11.7 Summary and concluding remarks

The acoustic radiation of turbulent lean premixed hydrogen–air flames was investigated through numerical simulations. The analysis focused on the impact of thermodiffusive effects on combustion noise, as well as on the influence of the Karlovitz number and of the chemical and transport modeling.

First, a thermodiffusively stable stoichiometric methane–air slot jet flame was compared with two lean hydrogen–air flames at different bulk velocity, characterized by comparable laminar

flame properties and subjected to the same turbulence intensity. Thermodiffusive effects were shown to strongly modify the flame–turbulence interaction, with a direct impact on the dynamics of both the turbulent flame surface and of the local heat release rate, thus affecting the acoustic radiation. Coherently with previous studies, the time derivative of the volume-integrated heat release rate was identified as the dominant noise source in the far field for all configurations considered. Furthermore, a theoretical framework extending the classical combustion noise flamelet theory to thermodiffusively unstable flames was proposed and validated, relating the flame-generated noise to the time derivative of the flame surface area. This analysis highlighted the role of flame stretch, showing that, all else being equal, the amplitude of the pressure fluctuations associated with combustion noise is modulated by the stretch factor I_0. This sustains the enhancing effect of thermodiffusive instabilities on acoustic radiation.

An enhancement of the flame surface generation term was consistently observed in the hydrogen flames, reducing the impact of destructive flame annihilation events, which instead are dominant for hydrocarbon flames. These differences in flame surface dynamics were reflected in the spectral behavior of the heat release rate. Analysis of local heat release rate spectra, corroborated by SPOD spectra, showed enhanced low-frequency fluctuations for the thermodiffusively unstable flames. At the same time, a reduced high-frequency spectral content was observed, associated with the stabilizing action of thermodiffusive instabilities at the small scales. From an acoustic perspective, these features translated into two peculiar characteristics of direct combustion noise in the lean premixed hydrogen flames, namely an enhancement of the acoustic radiation around the peak frequency and a steeper high-frequency spectral roll-off.

The influence of fuel properties on the noise generation at the shear layer between combustion products and ambient air was also investigated. In hydrogen flames, differential diffusion was found to induce stronger density gradients at this interface, leading to an enhancement of the associated Kelvin–Helmholtz instability structures compared to the methane flame. A SPOD analysis of the pressure field revealed the presence of coherent low-frequency structures for both hydrogen flames. Due to the insurgence of finer scale structures in the thermodiffusively unstable cases, the wavepackets associated with the shear layer instability were found to persist at higher frequencies than in the methane flame. Overall, these results suggest that thermodiffusive effects impact not only the direct combustion noise, via their action on the flame surface and the heat release rate, but also the indirect noise sources, associated to excess density gradients, given the impact of differential diffusion on the local temperature and composition of the combustion products.

Subsequently, the impact of Karlovitz number Ka variations on the acoustic radiation was investigated. Coherently with the literature [23, 332], thermodiffusive instabilities were found to be hindered for increasing Ka, resulting in a reduced flame front wrinkling and flame surface generation, while an increase in the stretch factor I_0 was found. The different impact of thermodiffusive instabilities on the flame dynamics, both in terms of flame surface variations and heat release rate fluctuations, were shown to impact the acoustic radiation. Indeed, it was observed that, as the value of Ka increases, the frequency range where thermodiffusive instabilities and turbulence are synergistic is shifted toward values below the peak frequency of the acoustic spectrum. As a result, thermodiffusive instabilities and their influence on direct combustion noise are attenuated. Moreover, flame-generated noise was observed to remain the dominant acoustic source at low and intermediate frequencies, while additional turbulence-induced high-frequency noise was found at mid and high Ka. Discrepancies were observed also in the peak value and in the shape of the acoustic spectra between the low Ka case and the other two. This was associated to the differences in the underlying mechanisms describing the flame dynamics. Indeed, for the low Ka cases,

heat release rate fluctuations, main driver of direct combustion noise, were promoted by flame surface generation, while at higher *Ka* flame annihilation became more important, coherently with the behavior of thermodiffusively stable flames. This confirmed the reduced importance of thermodiffusive instabilities for the flame dynamics and the combustion noise at high *Ka*.

Finally, the impact of chemical and transport modeling was considered, by comparing the results obtained with the detailed San Diego mechanisms [339] with those deriving from the reduced scheme developed in Chapter 5, either with realistic Lewis numbers or all unity values. Overall, a strong agreement was found between the detailed and reduced schemes in the prediction of the global features of the flame and of its acoustic radiation. Still, coherently with the analysis performed for the laminar case in Section 9.4, an overestimation of the local heat release rate in highly curved region, resulting from an exaggerated stretch response, was found. This induced an overprediction of the high-frequency noise component with respect to the detailed mechanism. The imposition of unity Lewis numbers for all species led to a strong reduction of the acoustic radiation, thereby confirming the noise-enhancing role of thermodiffusive effects in turbulent lean premixed hydrogen flames.

Conclusion and Perspectives

In this dissertation, some of the key challenges of hydrogen combustion were addressed: the chemical modeling, the suitability of the excited hydroxyl radical OH* as marker of heat release rate, and combustion noise. The work was based on high-fidelity numerical simulations, eventually coupled with experimental measurements, to provide a detailed understanding of the physical and chemical mechanisms of hydrogen combustion. In this framework, two datasets were produced using the AVBP code [350]: one, presented in Chapter 8, for a harmonically forced laminar M-shaped flame under varying forcing levels, and the other, introduced in Chapter 10, for a turbulent slot jet flame with different flow conditions.

Summary of the main findings

The main findings of this dissertation are recalled in the following.

1. *Development of a one-step scheme for hydrogen combustion*

   In Chapter 5, a reduced reaction mechanism for hydrogen combustion based on a single global reaction was derived and validated for multiple canonical laminar premixed flame configurations. The scheme was designed to be applicable over a wide range of operating conditions, in terms of varying pressure, unburned gas temperature, and flame stretch. To this end, the Pre-Exponential Adjustment method [120] was extended to couple equivalence ratio effects with a scaling law dependent on pressure. In addition, a correction for the thermal flame thickness was introduced. Despite some limitations in predicting the stretch response, the reduced mechanism showed good agreement with detailed kinetics, while significantly reducing the computational cost.

2. *Relation between OH* chemiluminescence and heat release rate*

   The suitability of the chemiluminescence of the excited hydroxyl radical OH* as a marker of heat release rate was investigated in Chapter 6 for both premixed and diffusion hydrogen–air flames. First, its behavior was compared with the one observed in conventional hydrocarbon flames. A marked shift between the peaks of OH* and heat release rate distributions was identified when transitioning from methane or methane–hydrogen fuel mixtures to pure hydrogen. This discrepancy was traced back to differences in the OH* formation pathways and to the key role of the H radical in hydrogen kinetics.

   The influence of the combustion regime was then examined. While OH* proved to be a limited marker of heat release rate in premixed hydrogen–air flames, its reliability significantly improved in diffusion flames, at least away from the extinction stretch limit. This behavior was linked to the distinct reactions governing the heat release rate in the two regimes. After being established in laminar one-dimensional configurations, these findings

were corroborated by the analysis of experimental and numerical results of turbulent diffusion and partially premixed flames stabilized over the HYLON injector [6]. This comparison also highlighted the necessity of including OH* kinetics in simulations to enable meaningful validation against experiments.

Finally, the impact of operating conditions was assessed. Variations in equivalence ratio and, consequently, in flame temperature, were shown to alter the post-flame OH* concentration, further degrading its spatial correlation with heat release rate near stoichiometric conditions. Moreover, two-dimensional simulations of lean premixed expanding flames demonstrated that thermodiffusive instabilities further weaken this correlation. Nevertheless, despite these spatial limitations, a good agreement was found between the volume-integrated temporal signals of OH* and heat release rate in Chapter 9. This confirms that OH* chemiluminescence remains a valuable experimental diagnostic tool for investigating combustion noise and thermoacoustic instabilities.

3. *Response of laminar premixed flames to harmonic inflow perturbations*

   In Chapter 9, the acoustic radiation of harmonically forced laminar premixed M-shaped flames was investigated. The role of thermodiffusive effects was first assessed by comparing stoichiometric methane–hydrogen flames with lean hydrogen flames. In the former case, tip closing led, under moderate acoustic forcing, to mutual flame interactions and intense noise radiation. In contrast, the lean hydrogen flame exhibited an open tip, preventing strong annihilation events and thereby attenuating acoustic emission.

   It was shown that the combustion noise flamelet theory [2, 69] relating flame surface and heat release rate fluctuations remains valid for hydrogen flames, provided that the effect of stretch on the flame speed is accounted for. Increasing the forcing frequency in hydrogen flames triggered the detachment of flame pockets at the tip. Owing to cellular structures induced by thermodiffusive effects, these pockets were continuously deformed, with a shape significantly different from the toroidal one typically observed in hydrocarbon flames. However, because of the strong differential diffusion of hydrogen relative to heat, these events had little impact on global heat release rate fluctuations and, consequently, on radiated noise. This resulted in a steeper high-frequency roll-off in the acoustic spectrum compared to the methane–hydrogen flame.

   The influence of chemical and transport modeling was also examined through simulations employing the reduced scheme developed in Chapter 5, combined either with realistic transport properties or with artificially modified species Lewis numbers to suppress differential and/or preferential diffusion. Good agreement between reduced and detailed kinetics was obtained for realistic transport properties, at least at moderate forcing frequencies. A separate analysis of differential and preferential diffusion revealed that they yield opposite effects on flame annihilation dynamics, with preferential diffusion partially mitigating differential diffusion effects, an observation that may be relevant in the broader context of hydrogen combustion modeling.

4. *Acoustic radiation of turbulent premixed flames*

   Chapter 11 addressed the acoustic radiation of turbulent lean premixed hydrogen–air slot jet flames. Comparison with a reference methane–air flame showed that thermodiffusive effects and instabilities strongly modify the spectral characteristics of direct combustion noise, enhancing the low-frequency component, while attenuating the high-frequency

one. This behavior was associated with differences in flame annihilation dynamics, in the balance between flame surface generation and destruction, and in local heat release rate fluctuations, which are modulated not only by turbulence, but also by stretch-induced variations in the burning rate.

An extension of the classical combustion noise theory [2, 69] was proposed and validated, relating the acoustic radiation to the time derivative of the flame surface area, modulated by the stretch factor I_0. Spectral Proper Orthogonal Decomposition revealed that hydrogen differential diffusion affects also the shear layer between hot products and ambient air, generating strong density gradients and promoting low-frequency pressure fluctuations associated with the Kelvin–Helmholtz instability. These findings suggest that thermodiffusive effects influence both direct and indirect noise generation mechanisms.

The role of the Karlovitz number was also investigated. As its value increased, the frequency range in which turbulence and thermodiffusive instabilities acted synergistically shifted below the peak of the acoustic spectrum, thereby weakening the low- and mid-frequency acoustic radiation. Moreover, the flame dynamics approached those of purely thermodiffusively unstable flames.

The reduced scheme introduced in Chapter 5 proved capable of accurately predicting global flame dynamics and acoustic radiation in turbulent conditions. However, it overestimated the local heat release rate in highly curved regions, due to an exaggerated stretch response. This led to discrepancies in high-frequency acoustic radiation. Finally, enforcing unity Lewis numbers for all species produced a marked reduction in acoustic emission, confirming the key role of thermodiffusive effects and instabilities in enhancing combustion noise in turbulent lean premixed hydrogen flames.

Future work and outlooks

This dissertation provided a comprehensive study of hydrogen combustion dynamics across laminar and turbulent configurations, with particular emphasis on thermodiffusive effects and their influence on the acoustic radiation. By combining reduced chemical modeling, detailed kinetic analyses, optical diagnostics assessment, and high-fidelity numerical simulations, it clarified how hydrogen distinctive transport and chemical properties fundamentally alter flame structure, stretch response, and combustion noise generation. At the same time, it established the conditions under which reduced chemistry and chemiluminescence diagnostics can be reliably employed, thereby offering practical insights for the interpretation of simulations and experiments.

Nevertheless, this work also highlighted the need for further research, both from a fundamental and an applied perspective. In this sense, the following research paths are indicated.

1. *Chemical modeling*

   The reduced one-step mechanism developed in this thesis could be further refined to improve the prediction of stretch sensitivity, particularly in highly curved or strongly strained regions, where stronger deviations from detailed kinetics were observed. In this context, the integration of the variable Lewis number approach developed in the framework of the Stretched Thickened Flame model [89] with the here proposed correction for the flame thickness could provide a practical solution to further extend the validity of the global reaction mechanism.

2. *Combustion diagnostics*

   The present work clarified the limitations of OH chemiluminescence as a spatial marker of heat release rate in hydrogen flames. In continuity with the literature [254], future work could explore alternative optical markers, providing a more reliable correlation with heat release rate. This will require joint experimental and numerical work to identify suitable candidates, which should be relatively easy to access both in measurements and simulations at the same time, especially in turbulent or unstable regimes.

3. *Impact on combustion instabilities*

   The results presented in this work indicate a direct link between thermodiffusive instabilities and direct combustion noise. In confined systems, acoustic radiation affects the flame dynamics, potentially leading to combustion instabilities [96, 172, 310]. Therefore, further research is needed to assess how thermodiffusive effects influence combustion instabilities through their impact on noise generation. In this context, the dataset developed in this work could be exploited to derive flame transfer functions relating harmonic inflow perturbations to heat release rate fluctuations. This is directly feasible for the laminar dataset, whereas additional forced simulations would be required for the turbulent one.

4. *Development of turbulent combustion models for noise prediction*

   The study of combustion noise of turbulent hydrogen–air flames in the present work relied on Direct Numerical Simulations, with the application of no combustion model. Nevertheless, the investigation of more demanding configuration will inevitably require the adoption of Large Eddy Simulations. Then, the modeling of stretch effects, small-scale wrinkling associated with thermodiffusive instabilities, and of both differential and preferential diffusions of hydrogen, which were shown to shape the acoustic radiation, requires further improvements. This research path, inserted in the current research effort for hydrogen turbulent combustion modeling [7, 163, 351], is the fundamental step necessary to extend the current results to a broader range of operating conditions.

5. *Extension to engineering-relevant configurations*

   The development of reliable reduced chemical schemes and turbulent combustion modeling will allow for the numerical simulation of engineering-relevant configurations. In particular, the effect of increased pressure will need to be assessed. Indeed, the sensitivity to stretch effects and thermodiffusive instabilities is expected to be amplified in high-pressure turbulent flames [326], as well as the impact of non-equidiffusion on defining the heat release rate fluctuations and the acoustic radiation. Therefore, further work is required to assess the noise generation mechanisms of turbulent lean premixed hydrogen–air flames under operating conditions relevant to gas turbines. To this scope, reliable reference data will be needed for validation, highlighting the necessity for coordinated modeling and validation efforts to achieve sufficiently accurate numerical simulations at a reasonable computational cost in this regime.

References

[1] R. G. Abdel-Gayed, D. Bradley, M. N. Hamid, and M. Lawes. "Lewis number effects on turbulent burning velocity". In: *Symposium (International) on Combustion* 20 (1985), pp. 505–512.

[2] D. I. Abugov and O. I. Obrezkov. "Acoustic noise in turbulent flames". In: *Combustion, Explosion, and Shock Waves* 14.5 (1978), pp. 606–612.

[3] P. W. Agostinelli, D. Laera, I. Boxx, L. Gicquel, and T. Poinsot. "Impact of wall heat transfer in Large Eddy Simulation of flame dynamics in a swirled combustion chamber". In: *Combustion and Flame* 234 (2021), p. 111728.

[4] C. Altantzis, C. E. Frouzakis, A. G. Tomboulides, M. Matalon, and K. Boulouchos. "Hydrodynamic and thermodiffusive instability effects on the evolution of laminar planar lean premixed hydrogen flames". In: *Journal of Fluid Mechanics* 700 (2012), pp. 329–361.

[5] A. Aniello, D. Laera, L. Berger, A. Attili, and T. Poinsot. "Introducing thermodiffusive effects in large-eddy simulation of turbulent combustion for lean hydrogen-air flames". In: *Center for Turbulence Research, Proceedings of the Summer Program*. 2022, pp. 267–277.

[6] A. Aniello, D. Laera, S. Marragou, H. Magnes, L. Selle, T. Schuller, and T. Poinsot. "Experimental and numerical investigation of two flame stabilization regimes observed in a dual swirl H2-air coaxial injector". In: *Combustion and Flame* 249 (2023), p. 112595.

[7] A. Aniello, T. Poinsot, L. Selle, and T. Schuller. "Hydrogen substitution of natural-gas in premixed burners and implications for blow-off and flashback limits". In: *International Journal of Hydrogen Energy* 47.77 (2022), pp. 33067–33081.

[8] Ansaldo Energia. *GT36 sequential combustion technology achieves 100% hydrogen*. https://www.ansaldoenergia.com/about-us/media-center/power-generation-news-insights/detail-news/gt36-sequential-combustion-technology-achieves-100-hydrogen. 2024.

[9] antares Development Team. *Antares Documentation Release 2. 0. 0*. https://cerfacs.fr/antares/. 2023.

[10] S. Arrhenius. "Über die Dissociationswärme und den Einfluss der Temperatur auf den Dissociationsgrad der Elektrolyte". In: *Zeitschrift für Physikalische Chemie* 4.1 (1889), pp. 96–116.

[11] A. J. Aspden, M. S. Day, and J. B. Bell. "Characterization of low Lewis number flames". In: *Proceedings of the Combustion Institute* 33.1 (2011), pp. 1463–1471.

[12] A. J. Aspden. "A numerical study of diffusive effects in turbulent lean premixed hydrogen flames". In: *Proceedings of the Combustion Institute* 36 (2017), pp. 1997–2004.

[13] A. J. Aspden, M. S. Day, and J. B. Bell. "Three-dimensional direct numerical simulation of turbulent lean premixed methane combustion with detailed kinetics". In: *Combustion and Flame* 166 (2016), pp. 266–283.

[14] A. J. Aspden, M. S. Day, and J. B. Bell. "Towards the distributed burning regime in turbulent premixed flames". In: *Journal of Fluid Mechanics* 871 (2019), pp. 1–21.

[15] A. J. Aspden, M. S. Day, and J. B. Bell. "Turbulence–flame interactions in lean premixed hydrogen: transition to the distributed burning regime". In: *Journal of Fluid Mechanics* 680 (2011), pp. 287–320.

[16] A. J. Aspden, M. S. Day, and J. B. Bell. "Turbulence-chemistry interaction in lean premixed hydrogen combustion". In: *Proceedings of the Combustion Institute* 35 (2015), pp. 1321–1329.

[17] A. Attili, S. Luca, D. Denker, F. Bisetti, and H. Pitsch. "Turbulent flame speed and reaction layer thickening in premixed jet flames at constant Karlovitz and increasing Reynolds numbers". In: *Proceedings of the Combustion Institute* 38 (2021), pp. 2939–2947.

[18] B. O. Ayoola, R. Balachandran, J. H. Frank, E. Mastorakos, and C. F. Kaminski. "Spatially resolved heat release rate measurements in turbulent premixed flames". In: *Combustion and Flame* 144 (2006), pp. 1–16.

[19] G. I. Barenblatt, Y. B. Zel'dovich, and A. G. Istratov. "On diffusional–thermal stability of a laminar flame". In: *Prikladnaya Mekhanika i Tekhnicheskaya Fizika* 3.4 (1962), pp. 21–26.

[20] J. K. Bechtold and M. Matalon. "Hydrodynamic and diffusion effects on the stability of spherically expanding flames". In: *Combustion and Flame* 67.1 (1987), pp. 77–90.

[21] M. J. Bedard, T. L. Fuller, S. Sardeshmukh, and W. E. Anderson. "Chemiluminescence as a diagnostic in studying combustion instability in a practical combustor". In: *Combustion and Flame* 213 (2020), pp. 211–225.

[22] A. Belliard. "Etude expérimentale de l'émission sonore des flammes turbulentes". PhD thesis. Université de Provence (Aix-Marseille I), France, 1997.

[23] L. Berger, A. Attili, M. Gauding, and H. Pitsch. "Effects of Karlovitz number variations on thermodiffusive instabilities in lean turbulent hydrogen jet flames". In: *Proceedings of the Combustion Institute* 40 (2024), p. 105219.

[24] L. Berger, A. Attili, M. Gauding, and H. Pitsch. "LES combustion model for premixed turbulent hydrogen flames with thermodiffusive instabilities: a priori and a posteriori analysis". In: *Journal of Fluid Mechanics* 1003 (2025), A33.

[25] L. Berger, A. Attili, and H. Pitsch. "Intrinsic instabilities in premixed hydrogen flames: Parametric variation of pressure, equivalence ratio, and temperature. Part 1 - Dispersion relations in the linear regime". In: *Combustion and Flame* 240 (2022), p. 111935.

[26] L. Berger, A. Attili, and H. Pitsch. "Intrinsic instabilities in premixed hydrogen flames: parametric variation of pressure, equivalence ratio, and temperature. Part 2–Non-linear regime and flame speed enhancement". In: *Combustion and Flame* 240 (2022), p. 111936.

[27] L. Berger, A. Attili, and H. Pitsch. "Synergistic interactions of thermodiffusive instabilities and turbulence in lean hydrogen flames". In: *Combustion and Flame* 244 (2022), p. 112254.

[28] L. Berger, K. Kleinheinz, A. Attili, and H. Pitsch. "Characteristic patterns of thermodiffusively unstable premixed lean hydrogen flames". In: *Proceedings of the Combustion Institute* 37 (2019), pp. 1879–1886.

[29] J. M. Bergthorson. "Recyclable metal fuels for clean and compact zero-carbon power". In: *Progress in Energy and Combustion Science* 68 (2018), pp. 169–196.

[30] R. W. Bilger. "The structure of turbulent nonpremixed flames". In: *Symposium (International) on Combustion* 22 (1989), pp. 475–488.

[31] D. J. Bodony. "Generation of sound by the scattering of entropy disturbances". In: *Center for Turbulence Research, Proceedings of the Summer Program*. 2008, p. 355.

[32] M. Boger, D. Veynante, H. Boughanem, and A. Trouvé. "Direct numerical simulation analysis of flame surface density concept for large eddy simulation of turbulent premixed combustion". In: *Symposium (International) on Combustion* 27 (1998), pp. 917–925.

[33] P. Boivin, C. Jiménez, A. L. Sánchez, and F. A. Williams. "An explicit reduced mechanism for H2–air combustion". In: *Proceedings of the Combustion Institute* 33.1 (2011), pp. 517–523.

[34] R. Borghi. "On the structure and morphology of turbulent premixed flames". In: *Recent Advances in the Aerospace Sciences*. Springer, 1985, pp. 117–138.

[35] R. Borghi. "Mise au point sur la structure des flammes turbulentes". In: *Journal de Chimie Physique* 81.6 (1984), pp. 361–370.

[36] H. Böttler, A. Scholtissek, X. Chen, Z. Chen, and C. Hasse. "Premixed flames for arbitrary combinations of strain and curvature". In: *Proceedings of the Combustion Institute* 38 (2021), pp. 2031–2039.

[37] S. L. Bragg. "Combustion noise". In: *Journal of the Institute of Fuel* 36.1 (1963), pp. 12–16.

[38] K. N. C. Bray. "Turbulent flows with premixed reactants". In: *Turbulent Reacting Flows*. Ed. by P. A. Libby and F. A. Williams. Berlin, Heidelberg: Springer Berlin Heidelberg, 1980, pp. 115–183.

[39] K. N. C. Bray. "Studies of the turbulent burning velocity". In: *Proceedings of the Royal Society of London. Series A: Mathematical and Physical Sciences* 431.1882 (1990), pp. 315–335.

[40] D. Brouzet. "Investigation of direct combustion noise in turbulent premixed jet flames using direct numerical simulations". PhD thesis. University of Melbourne, Australia, 2020.

[41] D. Brouzet, A. Haghiri, M. Talei, and M. J. Brear. "Annihilation events topology and their generated sound in turbulent premixed flames". In: *Combustion and Flame* 204 (2019), pp. 268–277.

[42] D. Brouzet, A. Haghiri, M. Talei, M. J. Brear, O. T. Schmidt, G. Rigas, and T. Colonius. "Role of coherent structures in turbulent premixed flame acoustics". In: *AIAA Journal* 58.6 (2020), pp. 2635–2642.

[43] D. Brouzet, B. Krisna, and M. Ihme. "Multi-modal effects on indirect noise induced by turbulent entropy fields". In: *Journal of Fluid Mechanics* 1010 (2025), R3.

[44] D. Brouzet, M. Talei, M. J. Brear, and B. Cuenot. "The impact of chemical modelling on turbulent premixed flame acoustics". In: *Journal of Fluid Mechanics* 915 (2021), A3.

[45] D. Brouzet, B. Krisna, D. McCormick, C. A. Reimann, J. Mendoza, and M. Ihme. "Analysis of direct and indirect noise in a next-generation aviation gas turbine combustor". In: *Combustion and Flame* 260 (2024), p. 113249.

[46] M. P. Burke, Z. Chen, Y. Ju, and F. L. Dryer. "Effect of cylindrical confinement on the determination of laminar flame speeds using outwardly propagating flames". In: *Combustion and Flame* 156.4 (2009), pp. 771–779.

[47] T. D. Butler and P. J. O'Rourke. "A numerical method for two dimensional unsteady reacting flows". In: *Symposium (International) on Combustion* 16 (1977), pp. 1503–1515.

[48] S. Candel, D. Durox, S. Ducruix, A.-L. Birbaud, N. Noiray, and T. Schuller. "Flame dynamics and combustion noise: progress and challenges". In: *International Journal of Aeroacoustics* 8 (2009), pp. 1–56.

[49] S. Candel, D. Durox, and T. Schuller. "Flame interactions as a source of noise and combustion instabilities". In: *10th AIAA/CEAS Aeroacoustics Conference* (Manchester, UK). 2004, p. 2928.

[50] S. M. Candel and T. J. Poinsot. "Flame stretch and the balance equation for the flame area". In: *Combustion Science and Technology* 70.1-3 (1990), pp. 1–15.

[51] T. Capurso, D. Laera, E. Riber, and B. Cuenot. "NOx pathways in lean partially premixed swirling H2-air turbulent flame". In: *Combustion and Flame* 248 (2023), p. 112581.

[52] T. Capurso, M. Stefanizzi, M. Torresi, and S. M. Camporeale. "Perspective of the role of hydrogen in the 21st century energy transition". In: *Energy Conversion and Management* 251 (2022), p. 114898.

[53] J. Carpio, B. Li, D. Fernández-Galisteo, A. L. Sánchez, and F. A. Williams. "Systematically derived one-step kinetics for hydrogen-air gas-turbine combustion". In: *Combustion and Flame* 250 (2023), p. 112633.

[54] M. Casel, K. Oberleithner, F. Zhang, T. Zirwes, H. Bockhorn, D. Trimis, and T. L. Kaiser. "Resolvent-based modelling of coherent structures in a turbulent jet flame using a passive flame approach". In: *Combustion and Flame* 236 (2022), p. 111695.

[55] P. G. Cath, C. A. Crommelin, and H. Kamerlingh Onnes. "Isothermals of di-atomic substances and their binary mixtures. XIX. A preliminary determination of the critical point of hydrogen". In: *Koninklijke Nederlandse Akademie van Wetenschappen Proceedings* 20 (1918), pp. 178–184.

[56] A. V. Cavalieri, P. Jordan, and L. Lesshafft. "Wave-packet models for jet dynamics and sound radiation". In: *Applied Mechanics Reviews* 71.2 (2019), p. 020802.

[57] A. V. Cavalieri, D. Rodríguez, P. Jordan, T. Colonius, and Y. Gervais. "Wavepackets in the velocity field of turbulent jets". In: *Journal of Fluid Mechanics* 730 (2013), pp. 559–592.

[58] Q. Cazères, P. Pepiot, E. Riber, and B. Cuenot. "A fully automatic procedure for the analytical reduction of chemical kinetics mechanisms for computational fluid dynamics applications". In: *Fuel* 303 (2021), p. 121247.

[59] V. Ceglie, M. Stefanizzi, T. Capurso, F. Fornarelli, and S. M. Camporeale. "Thermoacoustic combustion stability analysis of a bluff body-stabilized burner fueled by methane–air and hydrogen–air mixtures". In: *Energies* 16.7 (2023), p. 3272.

[60] N. Chakraborty, D. Alwazzan, M. Klein, and R. S. Cant. "On the validity of Damköhler's first hypothesis in turbulent Bunsen burner flames: A computational analysis". In: *Proceedings of the Combustion Institute* 37 (2019), pp. 2231–2239.

[61] N. Chakraborty and R. S. Cant. "Effects of Lewis number on flame surface density transport in turbulent premixed combustion". In: *Combustion and Flame* 158.9 (2011), pp. 1768–1787.

[62] F. Charlette, C. Meneveau, and D. Veynante. "A power-law flame wrinkling model for LES of premixed turbulent combustion Part I: non-dynamic formulation and initial tests". In: *Combustion and Flame* 131.1-2 (2002), pp. 159–180.

[63] S. Chaudhuri, V. Akkerman, and C. K. Law. "Spectral formulation of turbulent flame speed with consideration of hydrodynamic instability". In: *Physical Review E—Statistical, Nonlinear, and Soft Matter Physics* 84.2 (2011), p. 026322.

[64] X. Chen, H. Böttler, A. Scholtissek, C. Hasse, and Z. Chen. "Effects of stretch-chemistry interaction on chemical pathways for strained and curved hydrogen/air premixed flames". In: *Combustion and Flame* 232 (2021), p. 111532.

[65] H. Chu, L. Berger, T. Grenga, Z. Wu, and H. Pitsch. "Effects of differential diffusion on hydrogen flame kernel development under engine conditions". In: *Proceedings of the Combustion Institute* 39.2 (2023), pp. 2129–2138.

[66] S. H. Chung and C. K. Law. "An invariant derivation of flame stretch". In: *Combustion and Flame* 55 (1984).

[67] P. Clavin and G. Joulin. "Premixed flames in large scale and high intensity turbulent flow". In: *Journal de Physique Lettres* 44.1 (1983), pp. 1–12.

[68] P. Clavin and G. Searby. *Combustion waves and fronts in flows: flames, shocks, detonations, ablation fronts and explosion of stars*. Cambridge University Press, 2016.

[69] P. Clavin and E. D. Siggia. "Turbulent Premixed Flames and Sound Generation". In: *Combustion Science and Technology* 78.1-3 (1991), pp. 147–155.

[70] P. Clavin and F. A. Williams. "Effects of molecular diffusion and of thermal expansion on the structure and dynamics of premixed flames in turbulent flows of large scale and low intensity". In: *Journal of Fluid Mechanics* 116 (1982), pp. 251–282.

[71] P. Clavin. "Dynamic behavior of premixed flame fronts in laminar and turbulent flows". In: *Progress in Energy and Combustion Science*. 11.1 (1985), pp. 1–59.

[72] P. Clavin and P. Garcia. "The influence of the temperature dependence of diffusivities on the dynamics". In: *Journal de Mécanique Théorique et Appliquée* 2.2 (1983), pp. 245–263.

[73] C. Clemen, M. Ravikanti, N. La Bianca, R. Eggels, B. Wurm, and K. Young. "Considerations for hydrogen fueled aerospace gas turbine combustion sub-system design". In: *Turbo Expo: Power for Land, Sea, and Air*. Vol. 87943. American Society of Mechanical Engineers. 2024, V03AT04A016.

[74] T. P. Coffee, A. J. Kotlar, and M. S. Miller. "The overall reaction concept in premixed, laminar, steady-state flames. I. Stoichiometries". In: *Combustion and Flame* 54.1-3 (1983), pp. 155–169.

[75] T. P. Coffee, A. J. Kotlar, and M. S. Miller. "The overall reaction concept in premixed, laminar, steady-state flames. II. Initial temperatures and pressures". In: *Combustion and Flame* 58.1 (1984), pp. 59–67.

[76] O. Colin, F. Ducros, D. Veynante, and T. Poinsot. "A thickened flame model for large eddy simulations of turbulent premixed combustion". In: *Physics of Fluids* 12.7 (2000), pp. 1843–1863.

[77] O. Colin and M. Rudgyard. "Development of High-Order Taylor-Galerkin Schemes for LES". In: *Journal of Computational Physics* 162.2 (2000), pp. 338–371.

[78] O. Colin. "Simulations aux grandes échelles de la combustion turbulente prémélangée dans les statoréacteurs". PhD thesis. Institut National Polytechnique de Toulouse, France, 2000.

[79] V. Coulon, J. Gaucherand, V. Xing, D. Laera, C. Lapeyre, and T. Poinsot. "Direct numerical simulations of methane, ammonia-hydrogen and hydrogen turbulent premixed flames". In: *Combustion and Flame* 256 (2023), p. 112933.

[80] A. E. Dahoe. "Laminar burning velocities of hydrogen–air mixtures from closed vessel gas explosions". In: *Journal of Loss Prevention in the Process Industries* 18.3 (2005), pp. 152–166.

[81] G. Damköhler. "Der einfluss der turbulenz auf die flammengeschwindigkeit in gasgemischen". In: *Zeitschrift für Elektrochemie und angewandte physikalische Chemie* 46.11 (1940), pp. 601–626.

[82] G. Darrieus. "Propagation d'un front de flamme". In: *La Technique Moderne* 30.18 (1938).

[83] H. L. Dave and S. Chaudhuri. "Evolution of local flame displacement speeds in turbulence". In: *Journal of Fluid Mechanics* 884 (2020), A46.

[84] G. Daviller, G. Oztarlik, and T. Poinsot. "A generalized non-reflecting inlet boundary condition for steady and forced compressible flows with injection of vortical and acoustic waves". In: *Computers & Fluids* 190 (2019), pp. 503–513.

[85] G. Daviller, J. Dombard, G. Staffelbach, J. Herpe, and D. Saucereau. "Prediction of Flow Separation and Side-loads in Rocket Nozzle Using Large-eddy Simulation". In: *International Journal of Computational Fluid Dynamics* 34.7-8 (2020), pp. 622–632.

[86] M. Day, J. Bell, P.-T. Bremer, V. Pascucci, V. Beckner, and M. Lijewski. "Turbulence effects on cellular burning structures in lean premixed hydrogen flames". In: *Combustion and Flame* 156.5 (2009), pp. 1035–1045.

[87] M. Day, S. Tachibana, J. Bell, M. Lijewski, V. Beckner, and R. K. Cheng. "A combined computational and experimental characterization of lean premixed turbulent low swirl laboratory flames II. Hydrogen flames". In: *Combustion and Flame* 162.5 (2015), pp. 2148–2165.

[88] L. De Nardi, H. J. Vargas Ruiz, Q. Douasbin, O. Dounia, and T. Poinsot. "LES modeling of high-pressure nitrogen cross-flow jet impact on hydrogen-air deflagration". In: *Proceedings of the Combustion Institute* 40 (2024), p. 105263.

[89] N. Detomaso, J.-J. Hok, O. Dounia, D. Laera, and T. Poinsot. "A generalization of the Thickened Flame model for stretched flames". In: *Combustion and Flame* 258 (2023), p. 113080.

[90] Y. Ding, D. Durox, N. Darabiha, and T. Schuller. "Chemiluminescence of burner-stabilized premixed laminar flames". In: *Combustion Science and Technology* 191.1 (2019), pp. 18–42.

[91] G. Dixon-Lewis. "Flame structure and flame reaction kinetics II. Transport phenomena in multicomponent systems". In: *Proceedings of the Royal Society of London. Series A: Mathematical and Physical Sciences* 307.1488 (1968), pp. 111–135.

[92] N. A. K. Doan and N. Swaminathan. "Analysis of markers for combustion mode and heat release in MILD combustion using DNS data". In: *Combustion Science and Technology* 191.5-6 (2019), pp. 1059–1078.

[93] P. Domingo and L. Vervisch. "Recent developments in DNS of turbulent combustion". In: *Proceedings of the Combustion Institute* 39.2 (2023), pp. 2055–2076.

[94] D. R. Dowdy, D. B. Smith, S. C. Taylor, and A. Williams. "The use of expanding spherical flames to determine burning velocities and stretch effects in hydrogen/air mixtures". In: *Symposium (International) on Combustion* 23.1 (1991), pp. 325–332.

[95] A. P. Dowling. "Thermoacoustic Sources and Instabilities". In: *Modern Methods in Analytical Acoustics: Lecture Notes*. Ed. by D. G. Crighton, A. P. Dowling, J. E. Ffowcs Williams, M. Heckl, and F. G. Leppington. London, UK: Springer, 1992, pp. 378–405.

[96] A. P. Dowling and Y. Mahmoudi. "Combustion noise". In: *Proceedings of the Combustion Institute* 35.1 (2015), pp. 65–100.

[97] J. F. Driscoll, J. H. Chen, A. W. Skiba, C. D. Carter, E. R. Hawkes, and H. Wang. "Premixed flames subjected to extreme turbulence: Some questions and recent answers". In: *Progress in Energy and Combustion Science* 76 (2020), p. 100802.

[98] J. Duclos, D. Veynante, and T. Poinsot. "A comparison of flamelet models for premixed turbulent combustion". In: *Combustion and Flame* 95.1-2 (1993), pp. 101–117.

[99] S. Ducruix, T. Schuller, D. Durox, and S. Candel. "Combustion dynamics and instabilities: Elementary coupling and driving mechanisms". In: *Journal of Propulsion and Power* 19.5 (2003), pp. 722–734.

[100] M. Durand. "Characterization of lean premixed hydrogen-enriched methane-air flames in steady and acoustically forced laminar flows". PhD thesis. Institut National Polytechnique de Toulouse, France, 2026.

[101] D. Durox, T. Schuller, and S. Candel. "Combustion dynamics of inverted conical flames". In: *Proceedings of the Combustion Institute* 30.2 (2005), pp. 1717–1724.

[102] T. Echekki and J. H. Chen. "Analysis of the contribution of curvature to premixed flame propagation". In: *Combustion and Flame* 118.1-2 (1999), pp. 308–311.

[103] F. N. Egolfopoulos and C. K. Law. "Chain mechanisms in the overall reaction orders in laminar flame propagation". In: *Combustion and Flame* 80.1 (1990), pp. 7–16.

[104] F. N. Egolfopoulos and C. K. Law. "An experimental and computational study of the burning rates of ultra-lean to moderately-rich H2/O2/N2 laminar flames with pressure variations". In: *Symposium (International) on Combustion* 23 (1991), pp. 333–340.

[105] C. El Hachem, M. Durand, N. Barléon, Q. Douasbin, T. Schuller, and E. Riber. "Joint numerical and experimental study of OH* chemiluminescence in a premixed hydrogen–air laminar M-flame". In: *Combustion and Flame* 288 (2026), p. 114939.

[106] T. Ellingsen and E. Palm. "Stability of linear flow". In: *Physics of Fluids* 18.4 (1975), pp. 487–488.

[107] A. Ern and V. Giovangigli. *Multicomponent transport algorithms*. Springer, 1994.

[108] T. Falkenstein, A. Rezchikova, R. Langer, M. Bode, S. Kang, and H. Pitsch. "The role of differential diffusion during early flame kernel development under engine conditions-Part I: Analysis of the heat-release-rate response". In: *Combustion and Flame* 221 (2020), pp. 502–515.

[109] A. Favre et al. "Statistical equations of turbulent gases". In: *Problems of hydrodynamics and continuum mechanics* (1969), pp. 231–266.

[110] D. Fernández-Galisteo, V. N. Kurdyumov, and P. D. Ronney. "Analysis of premixed flame propagation between two closely-spaced parallel plates". In: *Combustion and Flame* 190 (2018), pp. 133–145.

[111] D. Fernández-Galisteo, A. L. Sánchez, A. Liñán, and F. A. Williams. "One-step reduced kinetics for lean hydrogen–air deflagration". In: *Combustion and Flame* 156.5 (2009), pp. 985–996.

[112] D. Fernández-Galisteo, A. Weiss, A. L. Sánchez, and F. A. Williams. "A one-step reduced mechanism for near-limit hydrogen combustion with general stoichiometry". In: *Combustion and Flame* 208 (2019), pp. 1–4.

[113] J. E. Ffowcs Williams and M. S. Howe. "The generation of sound by density inhomogeneities in low Mach number nozzle flows". In: *Journal of Fluid Mechanics* 70.3 (1975), pp. 605–622.

[114] T. Fiala and T. Sattelmayer. "Nonpremixed counterflow flames: scaling rules for batch simulations". In: *Journal of Combustion* 2014 (2014), p. 484372.

[115] T. Fiala and T. Sattelmayer. "On the use of OH* radiation as a marker for the heat release rate in high-pressure hydrogen liquid rocket combustion". In: *49th AIAA/ASME/SAE/ASEE Joint Propulsion Conference*. 2013, p. 3780.

[116] F. Flemming, A. Sadiki, and J. Janicka. "Investigation of combustion noise using a LES/-CAA hybrid approach". In: *Proceedings of the Combustion Institute* 31.2 (2007), pp. 3189–3196.

[117] E. Flores-Montoya, A. Aniello, T. Schuller, and L. Selle. "Predicting flashback limits in H2 enriched CH4/air and C3H8/air laminar flames". In: *Combustion and Flame* 258 (2023), p. 113055.

[118] M. L. Frankel and G. I. Sivashinsky. "The effect of viscosity on hydrodynamic stability of a plane flame front". In: *Combustion Science and Technology* 29.3-6 (1982), pp. 207–224.

[119] B. Franzelli, E. Riber, and B. Cuenot. "Impact of the chemical description on a Large Eddy Simulation of a lean partially premixed swirled flame". In: *Comptes Rendus Mécanique* 341.1-2 (2013), pp. 247–256.

[120] B. Franzelli, E. Riber, L. Y. Gicquel, and T. Poinsot. "Large eddy simulation of combustion instabilities in a lean partially premixed swirled flame". In: *Combustion and Flame* 159.2 (2012), pp. 621–637.

[121] C. E. Frouzakis, N. Fogla, A. G. Tomboulides, C. Altantzis, and M. Matalon. "Numerical study of unstable hydrogen/air flames: Shape and propagation speed". In: *Proceedings of the Combustion Institute* 35 (2015), pp. 1087–1095.

[122] C. Fureby, T. Nilsson, D. M. Peterson, T. M. Ombrello, and D. R. Eklund. "Large-eddy simulation of supersonic combustion in a Mach 2 cavity model scramjet combustor". In: *AIAA Journal* 63.1 (2025), pp. 219–232.

[123] H. Gambassi, N. Sekularac, P. Ziade, M. Mohamad, and X. Fang. "Detecting and characterizing thermoacoustic oscillations in an industrial combustor with the spectral proper orthogonal decomposition". In: *Applications in Energy and Combustion Science* 23 (2025), p. 100344.

[124] F. Garnier. "Étude de la structure et de la stabilisation de flammes jets d'hydrogène par simulation aux grandes échelles". PhD thesis. Université de Toulouse, France, 2025.

[125] J. Gaucherand, D. Laera, C. Schulze-Netzer, and T. Poinsot. "DNS of Turbulent Premixed Ammonia/Hydrogen Flames: The Impact of Thermo-Diffusive Effects". In: *Flow, Turbulence and Combustion* 112.2 (2024), pp. 587–614.

[126] J. Gaucherand, C. Schulze-Netzer, D. Laera, and T. Poinsot. "A subgrid-scale model to account for thermo-diffusive effects in artificially thickened LES models for lean turbulent premixed ammonia/hydrogen flames". In: *Proceedings of the Combustion Institute* 40 (2024), p. 105198.

[127] A. Gazi, G. Vourliotakis, G. Skevis, and M. A. Founti. "Assessment of chemical markers for heat-release rate correlations in laminar premixed flames". In: *Combustion Science and Technology* 185.10 (2013), pp. 1482–1508.

[128] GE Vernova. *Hydrogen fueled gas turbines*. https://www.gevernova.com/gas-power/future-of-energy/hydrogen-fueled-gas-turbines. Accessed on February 25, 2026.

[129] Y. Gentil, G. Daviller, and S. Moreau. "Combustion noise modelling of thermally perfect and multi-species gas flow in nozzles". In: *Journal of Fluid Mechanics* 1014 (2025), A39.

[130] Y. Gentil, G. Daviller, S. Moreau, N. C. Treleaven, and T. Poinsot. "Theoretical analysis and numerical validation of the mechanisms controlling composition noise". In: *Journal of Sound and Vibration* 585 (2024), p. 118463.

[131] Y. Gentil, N. Sekularac, S. Moreau, and G. Daviller. "Analysis of Direct and Indirect Combustion Noise in a Real Helicopter Engine: Core, Turbine, and Far-Field". In: *Flow, Turbulence and Combustion* (2025), pp. 1–34.

[132] A. Ghani and T. Poinsot. "Flame quenching at walls: A source of sound generation". In: *Flow, Turbulence and Combustion* 99 (2017), pp. 173–184.

[133] G. K. Giannakopoulos, C. E. Frouzakis, S. Mohan, A. G. Tomboulides, and M. Matalon. "Consumption and displacement speeds of stretched premixed flames-theory and simulations". In: *Combustion and Flame* 208 (2019), pp. 164–181.

[134] G. K. Giannakopoulos, A. Gatzoulis, C. E. Frouzakis, M. Matalon, and A. G. Tomboulides. "Consistent definitions of "Flame Displacement Speed" and "Markstein Length" for premixed flame propagation". In: *Combustion and Flame* 162.4 (2015), pp. 1249–1264.

[135] R. G. Gilbert, K. Luther, and J. Troe. "Theory of thermal unimolecular reactions in the fall-off range. II. Weak collision rate constants". In: *Berichte der Bunsengesellschaft für physikalische Chemie* 87.2 (1983), pp. 169–177.

[136] I. Glassman, R. A. Yetter, and N. G. Glumac. *Combustion*. Academic Press, 2014.

[137] D. G. Goodwin, H. K. Moffat, I. Schoegl, R. L. Speth, and B. W. Weber. *Cantera: An Object-oriented Software Toolkit for Chemical Kinetics, Thermodynamics, and Transport Processes*. https://www.cantera.org. Version 3.0.0. 2023.

[138] X. Gou, J. A. Miller, W. Sun, and Y. Ju. *Implementation of PLOG function in Chemkin II and III*. 2011.

[139] J. Goulier, A. Comandini, F. Halter, and N. Chaumeix. "Experimental study on turbulent expanding flames of lean hydrogen/air mixtures". In: *Proceedings of the Combustion Institute* 36 (2017), pp. 2823–2832.

[140] J. Graña-Otero and S. Mahmoudi. "Excited OH kinetics and distribution in H2 premixed flames". In: *Fuel* 255 (2019), p. 115750.

[141] V. Granet, O. Vermorel, T. Léonard, L. Gicquel, and T. Poinsot. "Comparison of Nonreflecting Outlet Boundary Conditions for Compressible Solvers on Unstructured Grids". In: *AIAA Journal* 48.10 (2010), pp. 2348–2364.

[142] R. S. Graves, T. G. Kollie, D. L. McElroy, and K. E. Gilchrist. "The thermal conductivity of AISI 304L stainless steel". In: *International Journal of Thermophysics* 12.2 (1991), pp. 409–415.

[143] J. F. Grcar, J. B. Bell, and M. S. Day. "The Soret effect in naturally propagating, premixed, lean, hydrogen–air flames". In: *Proceedings of the Combustion Institute* 32 (2009), pp. 1173–1180.

[144] E. G. Groff. "The cellular nature of confined spherical propane-air flames". In: *Combustion and Flame* 48 (1982), pp. 51–62.

[145] A. Guitton. "Etude expérimentale des relations entre les champs hydrodynamiques et acoustiques des jets libres". PhD thesis. Université de Poitiers, France, 2009.

[146] Ö. L. Gülder. "Turbulent premixed flame propagation models for different combustion regimes". In: *Symposium (International) on Combustion* 23 (1991), pp. 743–750.

[147] S. Ha and T. Lieuwen. "Direct combustion noise: Pressure–heat release coherence of an open turbulent flame". In: *Combustion and Flame* 284 (2026), p. 114653.

[148] L. C. Haber, U. Vandsburger, W. R. Saunders, and V. K. Khanna. "An examination of the relationship between chemiluminescent light emissions and heat release rate under non-adiabatic conditions". In: *Turbo Expo: Power for Land, Sea, and Air*. Vol. 78552. American Society of Mechanical Engineers. 2000, V002T02A041.

[149] A. Haghiri, M. Talei, M. J. Brear, and E. R. Hawkes. "Sound generation by turbulent premixed flames". In: *Journal of Fluid Mechanics* 843 (2018), pp. 29–52.

[150] J. M. Hall and E. L. Petersen. "An optimized kinetics model for OH chemiluminescence at high temperatures and atmospheric pressures". In: *International Journal of Chemical Kinetics* 38 (2006), pp. 714–724.

[151] M. G. Hall. *Cell-Vertex Multigrid Solution of the Euler Equations for Transonic Flow Past Aerofoils*. Tech. rep. United Kingdom: PAS Aerofoils, 1987.

[152] I. Han and K. Y. Huh. "Roles of displacement speed on evolution of flame surface density for different turbulent intensities and Lewis numbers in turbulent premixed combustion". In: *Combustion and Flame* 152.1-2 (2008), pp. 194–205.

[153] Y. Hardalupas and M. Orain. "Local measurements of the time-dependent heat release rate and equivalence ratio using chemiluminescent emission from a flame". In: *Combustion and Flame* 139 (2004), pp. 188–207.

[154] A. P. Hardaya, W. D. Kulatilaka, B. S. Soriano, and J. H. Chen. "Heat release surrogates for NH3/H2/N2–air premixed flames". In: *Proceedings of the Combustion Institute* 40 (2024), p. 105432.

[155] H. A. Hassan. "Scaling of combustion-generated noise". In: *Journal of Fluid Mechanics* 66.3 (1974), pp. 445–453.

[156] C. I. Heghes. "C1-C4 Hydrocarbon Oxidation Mechanism". Ph. D. Thesis. Ruprecht Karl University of Heidelberg, Germany, 2007.

[157] Y. Hidaka, S. Takahashi, H. Kawano, M. Suga, and W. C. Gardiner Jr. "Shock-tube measurement of the rate constant for excited hydroxyl(A2. SIGMA. +) formation in the hydrogen-oxygen reaction". In: *The Journal of Physical Chemistry* 86.8 (1982), pp. 1429–1433.

[158] B. Higgins, M. McQuay, F. Lacas, J.-C. Rolon, N. Darabiha, and S. Candel. "Systematic measurements of OH chemiluminescence for fuel-lean, high-pressure, premixed, laminar flames". In: *Fuel* 80 (2001), pp. 67–74.

[159] J. O. Hirschfelder, C. F. Curtiss, and R. B. Bird. *The molecular theory of gases and liquids*. John Wiley & Sons, 1964.

[160] J. Z. Ho and M. Talei. "Sound sources in turbulent hydrogen/methane premixed jet flames". In: *Journal of Sound and Vibration* 620 (2026), p. 119407.

[161] J. Z. Ho, M. Talei, and R. L. Gordon. "Direct numerical simulation of stoichiometric hydrogen/methane premixed jet flames". In: *International Journal of Hydrogen Energy* 81 (2024), pp. 831–841.

[162] V. Hoferichter, C. Hirsch, T. Sattelmayer, A. Kalantari, E. Sullivan-Lewis, and V. McDonell. "Comparison of two methods to predict boundary layer flashback limits of turbulent hydrogen-air jet flames". In: *Flow, Turbulence and Combustion* 100.3 (2018), pp. 849–873.

[163] J.-J. Hok, O. Dounia, N. Detomaso, T. Jaravel, Q. Douasbin, and O. Vermorel. "A modeling strategy for the Thickened Flame simulation of propagating lean hydrogen–air flames". In: *International Journal of Hydrogen Energy* 78 (2024), pp. 1133–1141.

[164] J.-J. Hok, O. Dounia, and O. Vermorel. "A Thickened flame model extension for the simulation of lean hydrogen-air explosions in confined environments". In: *Combustion and Flame* 275 (2025), p. 114070.

[165] T. Howarth and A. Aspden. "An empirical characteristic scaling model for freely-propagating lean premixed hydrogen flames". In: *Combustion and Flame* 237 (2022), p. 111805.

[166] T. Howarth, E. Hunt, and A. Aspden. "Thermodiffusively-unstable lean premixed hydrogen flames: Phenomenology, empirical modelling, and thermal leading points". In: *Combustion and Flame* 253 (2023), p. 112811.

[167] M. S. Howe. "Indirect combustion noise". In: *Journal of Fluid Mechanics* 659 (2010), pp. 267–288.

[168] E. Hu, Z. Huang, J. He, C. Jin, and J. Zheng. "Experimental and numerical study on laminar burning characteristics of premixed methane–hydrogen–air flames". In: *International Journal of Hydrogen Energy* 34.11 (2009), pp. 4876–4888.

[169] Y. Hu, J. Tan, L. Lv, and X. Li. "Investigations on quantitative measurement of heat release rate using chemiluminescence in premixed methane-air flames". In: *Acta Astronautica* 164 (2019), pp. 277–286.

[170] I. R. Hurle, R. B. Price, T. M. Sugden, and A. Thomas. "Sound emission from open turbulent premixed flames". In: *Proceedings of the Royal Society of London. Series A: Mathematical and Physical Sciences* 303.1475 (1968), pp. 409–427.

[171] F. Iannone et al. "CRESCO ENEA HPC clusters: a working example of a multifabric GPFS Spectrum Scale layout". In: *2019 International Conference on High Performance Computing & Simulation (HPCS)*. IEEE. 2019, pp. 1051–1052.

[172] M. Ihme and H. Pitsch. "On the generation of direct combustion noise in turbulent non-premixed flames". In: *International Journal of Aeroacoustics* 11 (2012), pp. 25–78.

[173] M. Ihme. "Combustion and engine-core noise". In: *Annual Review of Fluid Mechanics* 49 (2017), pp. 277–310.

[174] M. Ihme, H. Pitsch, and D. Bodony. "Radiation of noise in turbulent non-premixed flames". In: *Proceedings of the Combustion Institute* 32 (2009), pp. 1545–1553.

[175] F. P. Incropera, D. P. DeWitt, T. L. Bergman, and A. S. Lavine. *Fundamentals of Heat and Mass Transfer*. 6th ed. Hoboken, NJ: John Wiley & Sons, 2007.

[176] International Civil Aviation Organization (ICAO). *States adopt net-zero 2050 global aspirational goal for international flight operations*. https://www.icao.int/Newsroom/Pages/States-adopts-netzero-2050-aspirational-goal-for-international-flight-operations.aspx. 2022.

[177] International Energy Agency (IEA). *Global Hydrogen Review 2025*. https://www.iea.org/reports/global-hydrogen-review-2025. 2025.

[178] International Energy Agency (IEA). *World Energy Outlook 2025*. https://www.iea.org/reports/world-energy-outlook-2025. 2025.

[179] J. Jarosinski. "Thickness of laminar flames". In: *Combustion and Flame* 56 (1984), pp. 337–342.

[180] C. Jiménez, A. Haghiri, M. J. Brear, M. Talei, and E. R. Hawkes. "Sound generation by premixed flame annihilation with full and simple chemistry". In: *Proceedings of the Combustion Institute* 35 (2015), pp. 3317–3325.

[181] J. Jiménez. "Coherent structures in wall-bounded turbulence". In: *Journal of Fluid Mechanics* 842 (2018), P1.

[182] G. Jomaas, C. K. Law, and J. Bechtold. "On transition to cellularity in expanding spherical flames". In: *Journal of Fluid Mechanics* 583 (2007), pp. 1–26.

[183] P. Jordan and T. Colonius. "Wave packets and turbulent jet noise". In: *Annual Review of Fluid Mechanics* 45.1 (2013), pp. 173–195.

[184] G. Joulin and P. Clavin. "Linear stability analysis of nonadiabatic flames: diffusional-thermal model". In: *Combustion and Flame* 35 (1979), pp. 139–153.

[185] G. Joulin and T. Mitani. "Linear stability analysis of two-reactant flames". In: *Combustion and Flame* 40 (1981), pp. 235–246.

[186] B. Karlovitz, D. W. Denniston Jr, D. H. Knapschaefer, and F. E. Wells. "Studies on Turbulent flames: A. Flame Propagation Across velocity gradients B. turbulence Measurement in flames". In: *Symposium (International) on Combustion* 4 (1953), pp. 613–620.

[187] A. Karmarkar, S. Gupta, I. Boxx, S. Hemchandra, and J. O'Connor. "Impact of precessing vortex core dynamics on the thermoacoustic instabilities in a swirl-stabilized combustor". In: *Journal of Fluid Mechanics* 946 (2022), A36.

[188] V. P. Karpov, A. N. Lipatnikov, and P. Wolanski. "Finding the Markstein number using the measurements of expanding spherical laminar flames". In: *Combustion and Flame* 109.3 (1997), pp. 436–448.

[189] W. E. Kaskan. "Abnormal excitation of OH in H2/O2/N2 flames". In: *The Journal of Chemical Physics* 31.4 (1959), pp. 944–956.

[190] T. Kathrotia, M. Fikri, M. Bozkurt, M. Hartmann, U. Riedel, and C. Schulz. "Study of the H + O + M reaction forming OH*: Kinetics of OH* chemiluminescence in hydrogen combustion systems". In: *Combustion and Flame* 157.7 (2010), pp. 1261–1273.

[191] T. Kathrotia, U. Riedel, A. Seipel, K. Moshammer, and A. Brockhinke. "Experimental and numerical study of chemiluminescent species in low-pressure flames". In: *Applied Physics B* 107.3 (2012), pp. 571–584.

[192] T. Kathrotia, U. Riedel, and J. Warnatz. "A numerical study on the relation of OH*, CH*, and C2* chemiluminescence and heat release in premixed methane flames". In: *Proceedings of the European Combustion Meeting*. 2009.

[193] M. Katsuki, Y. Mizutani, M. Chikami, and T. Kittaka. "Sound emission from a turbulent flame". In: *Symposium (International) on Combustion* 21 (1988), pp. 1543–1550.

[194] A. Kaufmann, F. Nicoud, and T. Poinsot. "Flow forcing techniques for numerical simulation of combustion instabilities". In: *Combustion and Flame* 131.4 (2002), pp. 371–385.

[195] R. J. Kee, M. E. Coltrin, P. Glarborg, and H. Zhu. *Chemically reacting flow: theory, modeling, and simulation*. John Wiley & Sons, 2017.

[196] A. P. Kelley and C. K. Law. "Nonlinear effects in the extraction of laminar flame speeds from expanding spherical flames". In: *Combustion and Flame* 156.9 (2009), pp. 1844–1851.

[197] A. Kéromnès, W. K. Metcalfe, K. A. Heufer, N. Donohoe, A. K. Das, C.-J. Sung, J. Herzler, C. Naumann, P. Griebel, O. Mathieu, et al. "An experimental and detailed chemical kinetic modeling study of hydrogen and syngas mixture oxidation at elevated pressures". In: *Combustion and Flame* 160 (2013), pp. 995–1011.

[198] S. Kheirkhah and Ö. L. Gülder. "A revisit to the validity of flamelet assumptions in turbulent premixed combustion and implications for future research". In: *Combustion and Flame* 239 (2022), p. 111635.

[199] N. Kidin, V. Librovich, J. Roberts, and M. Vuillermoz. "On sound sources in turbulent combustion". In: *Dynamics of flames and reactive systems*. Ed. by R. I. Soloukhin, A. K. Oppenheim, J. R. Bowen, and N. Manson. New York: AIAA, 1984, pp. 343–355.

[200] H. Y. Kim and N. I. Kim. "Optimized global reaction mechanisms for H2, CO, CH4, and their mixtures". In: *International Journal of Hydrogen Energy* 48.62 (2023), pp. 24101–24112.

[201] A. N. Kolmogorov. "The local structure of turbulence in incompressible viscous fluid for very large Reynolds numbers". In: *Doklady Akademii Nauk SSSR* 30 (1941), pp. 301–305.

[202] A. A. Konnov. "Yet another kinetic mechanism for hydrogen combustion". In: *Combustion and Flame* 203 (2019), pp. 14–22.

[203] A. A. Konnov, A. Mohammad, V. R. Kishore, N. I. Kim, C. Prathap, and S. Kumar. "A comprehensive review of measurements and data analysis of laminar burning velocities for various fuel+air mixtures". In: *Progress in Energy and Combustion Science* 68 (2018), pp. 197–267.

[204] S. Kotake and K. Takamoto. "Combustion noise: effects of the shape and size of burner nozzle". In: *Journal of Sound and Vibration* 112.2 (1987), pp. 345–354.

[205] R. H. Kraichnan. "Diffusion by a random velocity field". In: *Physics of Fluids* 13.1 (1970), pp. 22–31.

[206] M. C. Krejci, O. Mathieu, A. J. Vissotski, S. Ravi, T. G. Sikes, E. L. Petersen, A. Kérmonès, W. Metcalfe, and H. J. Curran. "Laminar flame speed and ignition delay time data for the kinetic modeling of hydrogen and syngas fuel blends". In: *Journal of Engineering for Gas Turbines and Power* 135.2 (2013).

[207] A. I. Krikunova. "M-shaped flame dynamics". In: *Physics of Fluids* 31.12 (2019).

[208] B. Kruljevic, N. Darabiha, D. Durox, N. Vaysse, A. Renaud, R. Vicquelin, and B. Fiorina. "Experimentation and simulation of a swirled burner featuring cross-flow hydrogen injection with a focus on the OH* chemiluminescence". In: *Combustion and Flame* 273 (2025), p. 113945.

[209] A. D. Kumar, J. C. Massey, A. B. Murugavel, Z. X. Chen, and N. Swaminathan. "Spectral characteristics of the heat release rate in confined turbulent flames". In: *Journal of Fluid Mechanics* 1007 (2025), A29.

[210] A. D. Kumar, J. C. Massey, P. R. Soundararajan, I. Boxx, and N. Swaminathan. "Intrinsic thermoacoustic instability in hydrogen enriched partially premixed flames". In: *Physics of Fluids* 37.3 (2025).

[211] A. D. Kumar, P. R. Soundararajan, C. J. Li, J. C. Massey, and N. Swaminathan. "Characteristics of heat release rate spectra in turbulent flames with different fuels". In: *Fuel* 415 (2026), p. 138409.

[212] K. Kuo. *Principles of Combustion*. John Wiley, 1986.

[213] M. Kuznetsov, S. Kobelt, J. Grune, and T. Jordan. "Flammability limits and laminar flame speed of hydrogen–air mixtures at sub-atmospheric pressures". In: *International Journal of Hydrogen Energy* 37.22 (2012), pp. 17580–17588.

[214] O. C. Kwon and G. M. Faeth. "Flame/stretch interactions of premixed hydrogen-fueled flames: measurements and predictions". In: *Combustion and Flame* 124.4 (2001), pp. 590–610.

[215] G. Lacaze, E. Richardson, and T. Poinsot. "Large eddy simulation of spark ignition in a turbulent methane jet". In: *Combustion and Flame* 156.10 (2009), pp. 1993–2009.

[216] D. Laera and S. M. Camporeale. "A weakly nonlinear approach based on a distributed flame describing function to study the combustion dynamics of a full-scale lean-premixed swirled burner". In: *Journal of Engineering for Gas Turbines and Power* 139.9 (2017), p. 091501.

[217] P. Laffitte. *La propagation des flammes dans les mélanges gazeux*. Hermann et Cie., 1939.

[218] N. Lamoureux, N. Djebaıli-Chaumeix, and C.-E. Paillard. "Laminar flame velocity determination for H2–air–He–CO2 mixtures using the spherical bomb method". In: *Experimental Thermal and Fluid Science* 27.4 (2003), pp. 385–393.

[219] L. Landau. "On the theory of slow combustion". In: *Acta Physicochimica URSS* (1944), pp. 77–85.

[220] P. E. Lapenna, G. Troiani, F. D'Alessio, and F. Creta. "Synergistic interplay of thermodiffusive instability and turbulence in premixed flames". In: *Proceedings of the Combustion Institute* 40 (2024), p. 105499.

[221] P. E. Lapenna, L. Berger, F. Creta, and H. Pitsch. In: *Hydrogen for Future Thermal Engines*. Ed. by E.-A. Tingas. Cham, Switzerland: Springer, 2023, pp. 93–139.

[222] C. J. Lapeyre, A. Misdariis, N. Cazard, D. Veynante, and T. Poinsot. "Training convolutional neural networks to estimate turbulent sub-grid scale reaction rates". In: *Combustion and Flame* 203 (2019), pp. 255–264.

[223] V. Latour, D. Durox, A. Renaud, and S. Candel. "Experiments on symmetry breaking of azimuthal combustion instabilities and their analysis combining acoustic energy balance and flame describing functions". In: *Journal of Fluid Mechanics* 985 (2024), A31.

[224] M. Lauer and T. Sattelmayer. "On the adequacy of chemiluminescence as a measure for heat release in turbulent flames with mixture gradients". In: *Journal of Engineering for Gas Turbines and Power* 132.6 (2010), p. 061502.

[225] M. R. W. Lauer. "Determination of the heat release distribution in turbulent flames by chemiluminescence imaging". PhD thesis. Technische Universität München, Germany, 2011.

[226] B. E. Launder and D. B. Spalding. "The numerical computation of turbulent flows". In: *Computer Methods in Applied Mechanics and Engineering* 3.2 (1974), pp. 269–289.

[227] C. K. Law. "Propagation, structure, and limit phenomena of laminar flames at elevated pressures". In: *Combustion Science and Technology* 178.1-3 (2006), pp. 335–360.

[228] C. K. Law and C. J. Sung. "Structure, aerodynamics, and geometry of premixed flamelets". In: *Progress in Energy and Combustion Science* 26.4-6 (2000), pp. 459–505.

[229] C. K. Law. *Combustion Physics*. Cambridge, UK: Cambridge University Press, 2006.

[230] C. Law. "Dynamics of stretched flames". In: *Symposium (International) on Combustion* 22 (1989), pp. 1381–1402.

[231] P. Lax and B. Wendroff. "Systems of conservation laws". In: *Communications on Pure and Applied Mathematics* 13 (1960), p. 217.

[232] J.-P. Legier, T. Poinsot, and D. Veynante. "Dynamically thickened flame LES model for premixed and non-premixed turbulent combustion". In: *Center for Turbulence Research, Proceedings of the Summer Program*. Vol. 12. Stanford, CA, 2000, pp. 157–168.

[233] H. Levinsky. "Why can't we just burn hydrogen? Challenges when changing fuels in an existing infrastructure". In: *Progress in Energy and Combustion Science* 84 (2021), p. 100907.

[234] B. Lewis and G. Von Elbe. *Combustion, flames and explosions of gases*. Academic Press, 1961.

[235] M. Leyko, F. Nicoud, and T. Poinsot. "Comparison of Direct and Indirect Combustion Noise Mechanisms in a Model Combustor". In: *AIAA Journal* 47 (2009), pp. 2709–2716.

[236] T. Li, B. Böhm, and A. Dreizler. "Experimental Insights into Thermodiffusive Instabilities in Lean Hydrogen Combustion". In: *Engineering* (2025).

[237] M. J. Lighthill. "On sound generated aerodynamically I. General theory". In: *Proceedings of the Royal Society of London. Series A: Mathematical and Physical Sciences* 211.1107 (1952), pp. 564–587.

[238] L. I.-K. Lin. "A concordance correlation coefficient to evaluate reproducibility". In: *Biometrics* 45 (1 1989), pp. 255–268.

[239] C. Lind and J. Whitson. *Explosion hazards associated with spills of large quantities of hazardous materials. Phase II. Final report*. Tech. rep. Naval Weapons Center, China Lake, Calif. (USA), 1977.

[240] F. A. Lindemann, S. Arrhenius, I. Langmuir, N. R. Dhar, J. Perrin, and W. C. M. Lewis. "Discussion on "the radiation theory of chemical action"". In: *Transactions of the Faraday Society* 17 (1922), pp. 598–606.

[241] Y. Liu and T. Echekki. "Modelling of combustion noise spectrum using temporal correlations of heat release rate from turbulent premixed flames". In: *21st AIAA/CEAS Aeroacoustics Conference*. 2015, p. 2970.

[242] A. J. Lock, A. M. Briones, X. Qin, S. K. Aggarwal, I. K. Puri, and U. Hegde. "Liftoff characteristics of partially premixed flames under normal and microgravity conditions". In: *Combustion and Flame* 143 (2005), pp. 159–173.

[243] Z. Lu and Y. Yang. "Modeling pressure effects on the turbulent burning velocity for lean hydrogen/air premixed combustion". In: *Proceedings of the Combustion Institute* 38 (2021), pp. 2901–2908.

[244] S. Luca, A. Attili, E. Lo Schiavo, F. Creta, and F. Bisetti. "On the statistics of flame stretch in turbulent premixed jet flames in the thin reaction zone regime at varying Reynolds number". In: *Proceedings of the Combustion Institute* 37 (2019), pp. 2451–2459.

[245] J. L. Lumley. "The structure of inhomogeneous turbulent flows". In: *Atmospheric Turbulence and Radio Wave Propagation* (1967), pp. 166–178.

[246] J. Luque and D. R. Crosley. "Transition Probabilities in the $A^2\Sigma^+$–$X^2\Pi_i$ Electronic System of OH". In: *The Journal of Chemical Physics* 109.2 (1998), pp. 439–448.

[247] L. Magri, J. O'Brien, and M. Ihme. "Compositional inhomogeneities as a source of indirect combustion noise". In: *Journal of Fluid Mechanics* 799 (2016), R4.

[248] Q. Malé, C. J. Lapeyre, and N. Noiray. "Hydrogen reaction rate modeling based on convolutional neural network for large eddy simulation". In: *Data-Centric Engineering* 6 (2025), e11.

[249] F. E. Marble and S. M. Candel. "Acoustic disturbance from gas non-uniformities convected through a nozzle". In: *Journal of Sound and Vibration* 55.2 (1977), pp. 225–243.

[250] R. Mari. "Influence des transferts thermiques sur la structure et la stabilisation de flamme à haute pression dans les moteurs fusées cryothechniques". PhD thesis. Institut National Polytechnique de Toulouse, France, 2015.

[251] N. M. Marinov, C. K. Westbrook, and W. J. Pitz. "Detailed and global chemical kinetics model for hydrogen". In: *Transport Phenomena in Combustion*. Ed. by S. H. Chan. Vol. 1. Washington D. C.: Taylor & Francis, 1996, pp. 118–129.

[252] G. H. Markstein. "Experimental and theoretical studies of flame-front stability". In: *Journal of the Aeronautical Sciences* 18.3 (1951), pp. 199–209.

[253] G. Markstein. "Experimental studies of flame-front instability". In: *Nonsteady Flame Propagation*. Vol. 75. Elsevier, 1964, pp. 75–105.

[254] G. J. Marshall and R. W. Pitz. "Evaluation of heat release indicators in lean premixed H2/Air cellular tubular flames". In: *Proceedings of the Combustion Institute* 37 (2019), pp. 2029–2036.

[255] P.-A. Masset, F. Duchaine, A. Pestre, and L. Selle. "Modelling challenges of volume-averaged combustion in inert porous media". In: *Combustion and Flame* 251 (2023), p. 112678.

[256] M. Matalon, C. Cui, and J. Bechtold. "Hydrodynamic theory of premixed flames: effects of stoichiometry, variable transport coefficients and arbitrary reaction orders". In: *Journal of Fluid Mechanics* 487 (2003), pp. 179–210.

[257] M. Matalon and B. Matkowsky. "Flames in fluids: their interaction and stability". In: *Combustion Science and Technology* 34.1-6 (1983), pp. 295–316.

[258] M. Matalon and B. J. Matkowsky. "Flames as gasdynamic discontinuities". In: *Journal of Fluid Mechanics* 124 (1982), pp. 239–259.

[259] M. Matalon. "The Darrieus–Landau instability of premixed flames". In: *Fluid Dynamics Research* 50.5 (2018), p. 051412.

[260] S. Mathur and S. Saxena. "Methods of calculating thermal conductivity of binary mixtures involving polyatomic gases". In: *Applied Scientific Research* 17.2 (1967), pp. 155–168.

[261] F. Mauss, N. Peters, B. Rogg, and F. A. Williams. "Reduced Kinetic Mechanisms for Premixed Hydrogen Flames". In: *Reduced Kinetic Mechanisms for Applications in Combustion Systems*. Ed. by N. Peters and B. Rogg. Berlin, Heidelberg: Springer, 1993, pp. 29–43.

[262] A. C. McIntosh. "Deflagration fronts and compressibility". In: *Philosophical Transactions of the Royal Society of London. Series A* 357.1764 (1999), pp. 3523–3538.

[263] A. C. McIntosh. "The linearised response of the mass burning rate of a premixed flame to rapid pressure changes". In: *Combustion Science and Technology* 91.4-6 (1993), pp. 329–346.

[264] M. Merk, W. Polifke, R. Gaudron, M. Gatti, C. Mirat, and T. Schuller. "Measurement and simulation of combustion noise and dynamics of a confined swirl flame". In: *AIAA Journal* 56.5 (2018), pp. 1930–1942.

[265] J. V. Michael, J. W. Sutherland, L. B. Harding, and A. F. Wagner. "Initiation in H2/O2: rate constants for H2+ O2→ H+ HO2 at high temperature". In: *Proceedings of the Combustion Institute* 28 (2000), pp. 1471–1478.

[266] A. Millán-Merino and P. Boivin. "A new single-step mechanism for hydrogen combustion". In: *Combustion and Flame* 268 (2024), p. 113641.

[267] Y. Mizobuchi, T. Nambu, and T. Takeno. "Numerical study of tip opening of hydrogen/air Bunsen flame". In: *Proceedings of the Combustion Institute* 37 (2019), pp. 1775–1781.

[268] M. Mizomoto, Y. Asaka, S. Ikai, and C. Law. "Effects of preferential diffusion on the burning intensity of curved flames". In: *Symposium (International) on Combustion* 20 (1985), pp. 1933–1939.

[269] E. Mollo-Christensen. *Measurements of near field pressure of subsonic jets*. Tech. rep. Advisory Group for Aeronautical Research and Development, 1963.

[270] E. Mollo-Christensen. "Jet Noise and Shear Flow Instability Seen From an Experimenter's Viewpoint". In: *Journal of Applied Mechanics* 34.1 (Mar. 1967), pp. 1–7.

[271] C. L. Morfey. "Amplification of aerodynamic noise by convected flow inhomogeneities". In: *Journal of Sound and Vibration* 31.4 (1973), pp. 391–397.

[272] T. Morinière, D. Laera, and T. Schuller. "Experimental and Numerical Investigation of the Acoustic Response of a Hollow-cone Fuel Spray in a Swirling Air Flow". In: *Flow, Turbulence and Combustion* 116.1 (2026), p. 11.

[273] I. A. Mulla, A. Dowlut, T. Hussain, Z. M. Nikolaou, S. R. Chakravarthy, N. Swaminathan, and R. Balachandran. "Heat release rate estimation in laminar premixed flames using laser-induced fluorescence of CH2O and H-atom". In: *Combustion and Flame* 165 (2016), pp. 373–383.

[274] Y. Nada, N. Shiwaku, S. Kikuta, M. Tannahashi, and T. Miyauchi. "Fractal characteristics of hydrogen–air turbulent premixed flames". In: *5th Asia-Pacific Conference on Combustion*. 2005.

[275] H. N. Najm, P. H. Paul, C. J. Mueller, and P. S. Wyckoff. "On the adequacy of certain experimental observables as measurements of flame burning rate". In: *Combustion and Flame* 113.3 (1998), pp. 312–332.

[276] P. zur Nedden, M. E. G. Eck, F. Lückoff, C. O. Paschereit, and A. Orchini. "Burner and Flame Transfer Matrices of Jet-Stabilized Flames: Influence of Jet Velocity and Fuel Properties". In: *Journal of Engineering for Gas Turbines and Power* 147.3 (2025), p. 031024.

[277] R.-H. Ni. "A multiple-grid scheme for solving the Euler equations". In: *AIAA Journal* 20.11 (1982), pp. 1565–1571.

[278] Z. M. Nikolaou and N. Swaminathan. "Heat release rate markers for premixed combustion". In: *Combustion and Flame* 161.12 (2014), pp. 3073–3084.

[279] P. A. Nogueira, A. V. Cavalieri, P. Jordan, and V. Jaunet. "Large-scale streaky structures in turbulent jets". In: *Journal of Fluid Mechanics* 873 (2019), pp. 211–237.

[280] N. Noiray, D. Durox, T. Schuller, and S. Candel. "A unified framework for nonlinear combustion instability analysis based on the flame describing function". In: *Journal of Fluid Mechanics* 615 (2008), pp. 139–167.

[281] V. Nori and J. Seitzman. "Evaluation of chemiluminescence as a combustion diagnostic under varying operating conditions". In: *46th AIAA Aerospace Sciences Meeting and Exhibit*. 2008, p. 953.

[282] V. N. Nori and J. M. Seitzman. "CH* chemiluminescence modeling for combustion diagnostics". In: *Proceedings of the Combustion Institute* 32 (2009), pp. 895–903.

[283] A. G. Olabi, C. Onumaegbu, T. Wilberforce, M. Ramadan, M. A. Abdelkareem, and A. H. Al–Alami. "Critical review of energy storage systems". In: *Energy* 214 (2021), p. 118987.

[284] S. A. Orszag. "Analytical theories of turbulence". In: *Journal of Fluid Mechanics* 41.2 (1970), pp. 363–386.

[285] P. Palies, D. Durox, T. Schuller, and S. Candel. "Nonlinear combustion instability analysis based on the flame describing function applied to turbulent premixed swirling flames". In: *Combustion and Flame* 158.10 (2011), pp. 1980–1991.

[286] H. Paniez, S. Marragou, H. Magnes, and T. Schuller. "High-frequency thermo-acoustic instability in a dual swirl H2 burner". In: *Proceedings of the Combustion Institute* 40 (2024), p. 105679.

[287] C. Panoutsos, Y. Hardalupas, and A. Taylor. "Numerical evaluation of equivalence ratio measurement using OH* and CH* chemiluminescence in premixed and non-premixed methane–air flames". In: *Combustion and Flame* 156.2 (2009), pp. 273–291.

[288] C. Pantano, S. Sarkar, and F. A. Williams. "Mixing of a conserved scalar in a turbulent reacting shear layer". In: *Journal of Fluid Mechanics* 481 (2003), pp. 291–328.

[289] T. Passot and A. Pouquet. "Numerical simulation of compressible homogeneous flows in the turbulent regime". In: *Journal of Fluid Mechanics* 181 (1987), pp. 441–466.

[290] R. Paul and K. Bray. "Study of premixed turbulent combustion including Landau-Darrieus instability effects". In: *Symposium (International) on Combustion* 26.1 (1996), pp. 259–266.

[291] K. Pausch, S. Herff, F. Zhang, H. Bockhorn, and W. Schröder. "Noise sources of lean premixed flames". In: *Flow, Turbulence and Combustion* 103.3 (2019), pp. 773–796.

[292] B. Pedro-Beltran, Z. Shahin, M. Meinke, S. Herff, D. Krug, and W. Schröder. "Impact of thermal and differential-preferential diffusion on the dynamics and acoustics of hydrogen–air slit flames". In: *Combustion and Flame* 286 (2026), p. 114810.

[293] P. Pelce and P. Clavin. "Influence of hydrodynamics and diffusion upon the stability limits of laminar premixed flames". In: *Journal of Fluid Mechanics* 124 (1982), pp. 219–237.

[294] D. A. Pennell, M. R. Bothien, A. Ciani, V. Granet, G. Singla, S. Thorpe, A. Wickstroem, K. Oumejjoud, and M. Yaquinto. "An introduction to the Ansaldo GT36 constant pressure sequential combustor". In: *Turbo Expo: Power for Land, Sea, and Air*. Vol. 50855. American Society of Mechanical Engineers. 2017, V04BT04A043.

[295] C. Pérez Arroyo, J. Dombard, F. Duchaine, L. Gicquel, B. Martin, N. Odier, and G. Staffelbach. "Towards the Large-Eddy Simulation of a full engine: Integration of a 360 azimuthal degrees fan, compressor and combustion chamber. Part I: Methodology and initialisation". In: *Journal of the Global Power and Propulsion Society* May (2021), pp. 1–16.

[296] C. Pérez Arroyo, J. Dombard, F. Duchaine, L. Gicquel, B. Martin, N. Odier, and G. Staffelbach. "Towards the Large-Eddy Simulation of a full engine: Integration of a 360 azimuthal degrees fan, compressor and combustion chamber. Part II: Comparison against stand-alone simulations". In: *Journal of the Global Power and Propulsion Society* May (2021), pp. 1–16.

[297] H. Pers, A. Aniello, and T. Schuller. "Transition from hydrodynamic flashback to wall-ignition in hydrogen-enriched laminar premixed burners". In: *Combustion and Flame* 266 (2024), p. 113514.

[298] A. Pestre. "Numerical simulations of aeronautical engine ignitions under realistic high altitude conditions". PhD thesis. Institut National Polytechnique de Toulouse, France, 2023.

[299] N. Peters. *Turbulent combustion*. Cambridge, UK: Cambridge University Press, 2000.

[300] N. Peters and F. Williams. "The asymptotic structure of stoichiometric methane–air flames". In: *Combustion and Flame* 68.2 (1987), pp. 185–207.

[301] N. Peters. "The turbulent burning velocity for large-scale and small-scale turbulence". In: *Journal of Fluid Mechanics* 384 (1999), pp. 107–132.

[302] N. Peters. "Laminar flamelet concepts in turbulent combustion". In: *Symposium (International) on Combustion* 21 (1988), pp. 1231–1250.

[303] R. H. Petrucci, F. G. Herring, J. D. Madura, and C. Bissonnette. *General Chemistry: Principles and Modern Applications*. 10th ed. Pearson Education, 2011.

[304] E. Pickering, G. Rigas, P. A. S. Nogueira, A. V. G. Cavalieri, O. T. Schmidt, and T. Colonius. "Lift-up, Kelvin–Helmholtz and Orr mechanisms in turbulent jets". In: *Journal of Fluid Mechanics* 896 (2020), A2.

[305] A. L. Pillai, S. Inoue, T. Shoji, S. Tachibana, T. Yokomori, and R. Kurose. "Investigation of combustion noise generated by an open lean-premixed H2/air low-swirl flame using the hybrid LES/APE-RF framework". In: *Combustion and Flame* 245 (2022), p. 112360.

[306] A. L. Pillai. "Numerical Investigation of Combustion Noise of Turbulent Flames". PhD thesis. Kyoto University, Japan, 2018.

[307] H. Pitsch. "The transition to sustainable combustion: Hydrogen-and carbon-based future fuels and methods for dealing with their challenges". In: *Proceedings of the Combustion Institute* 40 (2024), p. 105638.

[308] T. Poinsot, D. Veynante, and S. Candel. "Diagrams of premixed turbulent combustion based on direct simulation". In: *Symposium (International) on Combustion* 23.1 (1991), pp. 613–619.

[309] T. J. Poinsot and S. K. Lele. "Boundary Conditions for Direct Simulations of Compressible Viscous Flows". In: *Journal of Computational Physics* 101.1 (1992), pp. 104–129.

[310] T. Poinsot. "Prediction and control of combustion instabilities in real engines". In: *Proceedings of the Combustion Institute* 36 (2017), pp. 1–28.

[311] T. Poinsot and D. Veynante. *Theoretical and Numerical Combustion*. RT Edwards, Inc., 2005.

[312] S. B. Pope. "The evolution of surfaces in turbulence". In: *International Journal of Engineering Science* 26.5 (1988), pp. 445–469.

[313] S. B. Pope. *Turbulent Flows*. Cambridge University Press, 2000.

[314] S. Popp, G. Kuenne, J. Janicka, and C. Hasse. "An extended artificial thickening approach for strained premixed flames". In: *Combustion and Flame* 206 (2019), pp. 252–265.

[315] R. B. Price, I. R. Hurle, and T. M. Sugden. "Optical studies of the generation of noise in turbulent flames". In: *Symposium (International) on Combustion* 12 (1969), pp. 1093–1102.

[316] F. Proch and A. M. Kempf. "Numerical analysis of the Cambridge stratified flame series using artificial thickened flame LES with tabulated premixed flame chemistry". In: *Combustion and Flame* 161.10 (2014), pp. 2627–2646.

[317] J. Quinard, G. Searby, B. Denet, and J. Graña-Otero. "Self-turbulent flame speeds". In: *Flow, Turbulence and Combustion* 89.2 (2012), pp. 231–247.

[318] R. Rajaram, J. Gray, and T. Lieuwen. "Premixed combustion noise scaling: total power and spectra". In: *12th AIAA/CEAS Aeroacoustics Conference (27th AIAA Aeroacoustics Conference)*. 2006, p. 2612.

[319] R. Rajaram and T. Lieuwen. "Acoustic radiation from turbulent premixed flames". In: *Journal of Fluid Mechanics* 637 (2009), pp. 357–385.

[320] W. J. M. Rankine. "On the thermodynamic theory of waves of finite longitudinal disturbance". In: *Philosophical Transactions of the Royal Society of London* 160 (1870), pp. 277–288.

[321] E. Ranzi, A. Frassoldati, A. Stagni, M. Pelucchi, A. Cuoci, and T. Faravelli. "Reduced kinetic schemes of complex reaction systems: fossil and biomass-derived transportation fuels". In: *International Journal of Chemical Kinetics* 46.9 (2014), pp. 512–542.

[322] L. Rayleigh. "The explanation of certain acoustical phenomena". In: *Nature* 18 (1878), pp. 319–321.

[323] M. Reyes, F. Tinaut, B. Giménez, and J. V. Pastor. "Effect of hydrogen addition on the OH* and CH* chemiluminescence emissions of premixed combustion of methane-air mixtures". In: *International Journal of Hydrogen Energy* 43.42 (2018), pp. 19778–19791.

[324] O. Reynolds. "On the dynamical theory of incompressible viscous fluids and the determination of the criterion". In: *Philosophical Transactions of the Royal Society of London, Series A* 186 (1895), pp. 123–164.

[325] M. Rieth, A. Gruber, F. A. Williams, and J. H. Chen. "Enhanced burning rates in hydrogen-enriched turbulent premixed flames by diffusion of molecular and atomic hydrogen". In: *Combustion and Flame* 239 (2022), p. 111740.

[326] M. Rieth, A. Gruber, and J. H. Chen. "The effect of pressure on lean premixed hydrogen-air flames". In: *Combustion and Flame* 250 (2023), p. 112514.

[327] M. Rieth, A. Gruber, E. R. Hawkes, and J. H. Chen. "Direct numerical simulation of low-emission ammonia rich-quench-lean combustion". In: *Proceedings of the Combustion Institute* 40 (2024), p. 105558.

[328] H. Ritchie, P. Rosado, and M. Roser. "CO2 and Greenhouse Gas Emissions". In: *Our World in Data* (2023). https://ourworldindata.org/co2-and-greenhouse-gas-emissions.

[329] S. Robinson et al. "Coherent motions in the turbulent boundary layer". In: *Annual Review of Fluid Mechanics* 23.1 (1991), pp. 601–639.

[330] R. S. Rogallo and P. Moin. "Numerical Simulation of Turbulent Flows". In: *Annual Review of Fluid Mechanics* 16 (1984), pp. 99–137.

[331] N. Rouland, T. Naess, E. Riber, and B. Cuenot. "Impact of detailed transport on the prediction of NOx formation in hydrogen–air flames". In: *Fuel* 392 (2025), p. 134830.

[332] G. Russell, T. Howarth, A. Skiba, C. Carter, and A. Aspden. "Turbulence-flame interactions in high-Karlovitz-number lean premixed hydrogen piloted jet flames". In: *Proceedings of the Combustion Institute* 41 (2025), p. 105868.

[333] Safran. *Full throttle on the hydrogen turbine for the BeautHyFuel project!* https://www.safran-group.com/news/full-throttle-hydrogen-turbine-beauthyfuel-project-2024-04-02. 2024.

[334] P. Sagaut. *Large eddy simulation for incompressible flows: an introduction*. Springer, 2006.

[335] J. G. R. von Saldern, J. P. Beuth, J. M. Reumschüssel, A. Jaeschke, C. O. Paschereit, and K. Oberleithner. "Low-frequency streaky structures in turbulent hydrogen jet flames". In: *Combustion and Flame* 278 (2025), p. 114231.

[336] A. L. Sánchez and F. A. Williams. "Corrigendum to "Recent advances in understanding of flammability characteristics of hydrogen"". In: *Progress in Energy and Combustion Science* 54 (2016), pp. 93–94.

[337] A. L. Sánchez and F. A. Williams. "Recent advances in understanding of flammability characteristics of hydrogen". In: *Progress in Energy and Combustion Science* 41 (2014), pp. 1–55.

[338] H. I. H. Saravanamuttoo, G. F. C. Rogers, and H. Cohen. *Gas turbine theory*. Pearson Education, 2001.

[339] P. Saxena and F. A. Williams. "Testing a small detailed chemical-kinetic mechanism for the combustion of hydrogen and carbon monoxide". In: *Combustion and Flame* 145.1-2 (2006), pp. 316–323.

[340] R. W. Schefer, W. D. Kulatilaka, B. D. Patterson, and T. B. Settersten. "Visible emission of hydrogen flames". In: *Combustion and Flame* 156.6 (2009), pp. 1234–1241.

[341] S. Schlimpert, A. Feldhusen, J. H. Grimmen, B. Roidl, M. Meinke, and W. Schröder. "Hydrodynamic instability and shear layer effects in turbulent premixed combustion". In: *Physics of Fluids* 28.1 (2016).

[342] S. Schlimpert, S. R. Koh, K. Pausch, M. Meinke, and W. Schröder. "Analysis of combustion noise of a turbulent premixed slot jet flame". In: *Combustion and Flame* 175 (2017), pp. 292–306.

[343] S. Schlimpert, S. Hemchandra, M. Meinke, and W. Schröder. "Hydrodynamic instability and shear layer effect on the response of an acoustically excited laminar premixed flame". In: *Combustion and Flame* 162.2 (2015), pp. 345–367.

[344] J. Schlup and G. Blanquart. "Validation of a mixture-averaged thermal diffusion model for premixed lean hydrogen flames". In: *Combustion Theory and Modelling* 22.2 (2018), pp. 264–290.

[345] P. J. Schmid. "Dynamic mode decomposition of numerical and experimental data". In: *Journal of Fluid Mechanics* 656 (2010), pp. 5–28.

[346] O. T. Schmidt and T. Colonius. "Guide to Spectral Proper Orthogonal Decomposition". In: *AIAA Journal* 58.3 (2020), pp. 1023–1033.

[347] O. T. Schmidt, A. Towne, G. Rigas, T. Colonius, and G. A. Bres. "Spectral analysis of jet turbulence". In: *Journal of Fluid Mechanics* 855 (2018), pp. 953–982.

[348] M. Schneider, H. Nicolai, V. Schuh, M. Steinhausen, and C. Hasse. "Flame-wall interaction of thermodiffusively unstable hydrogen/air flames, Part I: Characterization of governing physical phenomena". In: *Combustion and Flame* 279 (2025), p. 114320.

[349] M. Schneider, F. Rong, M. Steinhausen, C. Hasse, and H. Nicolai. "Flame–wall interaction of lean premixed hydrogen/air flames: Impact of transport models". In: *Proceedings of the Combustion Institute* 41 (2025), p. 105955.

[350] T. Schonfeld and M. Rudgyard. "Steady and unsteady flow simulations using the hybrid flow solver AVBP". In: *AIAA Journal* 37.11 (1999), pp. 1378–1385.

[351] V. Schuh, C. Hasse, and H. Nicolai. "An extension of the artificially thickened flame approach for premixed hydrogen flames with intrinsic instabilities". In: *Proceedings of the Combustion Institute* 40 (2024), p. 105673.

[352] V. Schuh, D. Kaddar, A. Bähr, M. Bode, C. Hasse, and H. Nicolai. "An Extended Artificially Thickened Flame Model for Turbulent Hydrogen and Hydrogen-Enriched Flames With Intrinsic Instabilities Under Gas Turbine Relevant Conditions". In: *Journal of Engineering for Gas Turbines and Power* 148.2 (2026), p. 021007.

[353] T. Schuller, D. Durox, and S. Candel. "Self-induced combustion oscillations of laminar premixed flames stabilized on annular burners". In: *Combustion and Flame* 135 (2003), pp. 525–537.

[354] T. Schuller, T. Poinsot, and S. Candel. "Dynamics and control of premixed combustion systems based on flame transfer and describing functions". In: *Journal of Fluid Mechanics* 894 (2020), P1.

[355] T. Schuller, D. Durox, and S. Candel. "Dynamics of and noise radiated by a perturbed impinging premixed jet flame". In: *Combustion and Flame* 128 (2002), pp. 88–110.

[356] C. D. Schumann, Q. Cazères, J. C. Massey, C. J. Li, Y. Tanaka, and N. Swaminathan. "SkeleCHy: A skeletal mechanism for low hydrocarbon content blends with hydrogen". In: *Combustion and Flame* 275 (2025), p. 114036.

[357] L. Selle, G. Lartigue, T. Poinsot, R. Koch, K.-U. Schildmacher, W. Krebs, B. Prade, P. Kaufmann, and D. Veynante. "Compressible large eddy simulation of turbulent combustion in complex geometry on unstructured meshes". In: *Combustion and Flame* 137.4 (2004), pp. 489–505.

[358] L. Selle, F. Nicoud, and T. Poinsot. "Actual impedance of nonreflecting boundary conditions: Implications for computation of resonators". In: *AIAA Journal* 42 (2004), pp. 958–964.

[359] K. Seshadri. "Multistep asymptotic analyses of flame structures". In: *Proceedings of the Combustion Institute* 26 (1996), pp. 831–846.

[360] K. Seshadri, N. Peters, and F. Williams. "Asymptotic analyses of stoichiometric and lean hydrogen-air flames". In: *Combustion and Flame* 96.4 (1994), pp. 407–427.

[361] C. Shao, K. Maeda, and M. Ihme. "Analysis of core-noise contributions in a realistic gas-turbine combustor operated near lean blow-out". In: *Proceedings of the Combustion Institute* 38 (2021), pp. 6203–6211.

[362] A. S. Sharipov, B. I. Loukhovitski, A. V. Pelevkin, and M. R. Korshunova. "A detailed kinetic submechanism for OH* chemiluminescence in hydrogen combustion revisited. Part 1". In: *Combustion and Flame* 263 (2024), p. 113407.

[363] A. S. Sharipov, B. I. Loukhovitski, A. V. Pelevkin, and M. R. Korshunova. "A detailed kinetic submechanism for OH* chemiluminescence in hydrogen combustion revisited. Part 2". In: *Combustion and Flame* 263 (2024), p. 113417.

[364] T. Shoji, Y. Iwasaki, K. Kodai, S. Yoshida, S. Tachibana, and T. Yokomori. "Effects of flame behaviors on combustion noise from lean-premixed hydrogen low-swirl flames". In: *AIAA Journal* 58.10 (2020), pp. 4505–4521.

[365] M. Sieber, C. O. Paschereit, and K. Oberleithner. "Spectral proper orthogonal decomposition". In: *Journal of Fluid Mechanics* 792 (2016), pp. 798–828.

[366] Siemens Energy. *Zero Emission Hydrogen Turbine Center*. https://www.siemens-energy.com/global/en/home/products-services/solutions-usecase/hydrogen/zehtc.html. Accessed on February 25, 2026.

[367] Y. L. Sinai. "The generation of combustion noise by chemical inhomogeneities in steady, low-Mach-number duct flows". In: *Journal of Fluid Mechanics* 99.2 (1980), pp. 383–397.

[368] G. Sivashinsky. "Diffusional-thermal theory of cellular flames". In: *Combustion Science and Technology* 15.3-4 (1977), pp. 137–145.

[369] A. W. Skiba, T. M. Wabel, C. D. Carter, S. D. Hammack, J. E. Temme, and J. F. Driscoll. "Premixed flames subjected to extreme levels of turbulence part I: Flame structure and a new measured regime diagram". In: *Combustion and Flame* 189 (2018), pp. 407–432.

[370] J. Smagorinsky. "General circulation experiments with the primitive equations: I. The basic experiment". In: *Monthly Weather Review* 91.3 (1963), pp. 99–164.

[371] A. Smirnov, S. Shi, and I. Celik. "Random flow generation technique for large eddy simulations and particle-dynamics modeling". In: *Journal of Fluids Engineering* 123.2 (2001), pp. 359–371.

[372] G. P. Smith, J. Luque, C. Park, J. B. Jeffries, and D. R. Crosley. "Low pressure flame determinations of rate constants for OH (A) and CH (A) chemiluminescence". In: *Combustion and Flame* 131 (2002), pp. 59–69.

[373] G. P. Smith, C. Park, and J. Luque. "A note on chemiluminescence in low-pressure hydrogen and methane–nitrous oxide flames". In: *Combustion and Flame* 140.4 (2005), pp. 385–389.

[374] T. J. B. Smith and J. K. Kilham. "Noise generation by open turbulent flames". In: *The Journal of the Acoustical Society of America* 35.5 (1963), pp. 715–724.

[375] W. R. Smith and R. W. Missen. *Chemical Reaction Equilibrium Analysis: Theory and Algorithms*. Wiley, 1982.

[376] Y. Song, L. Marrodán, N. Vin, O. Herbinet, E. Assaf, C. Fittschen, A. Stagni, T. Faravelli, M. U. Alzueta, and F. Battin-Leclerc. "The sensitizing effects of NO2 and NO on methane low temperature oxidation in a jet stirred reactor". In: *Proceedings of the Combustion Institute* 37 (2019), pp. 667–675.

[377] B. S. Soriano, L. D. Owen, and J. H. Chen. "Edge flame speed analysis of a swirl-stabilized spray flame using sustainable aviation fuels: A direct numerical simulation study". In: *Combustion and Flame* 277 (2025), p. 114213.

[378] D. B. Spalding. *Some Fundamentals of Combustion*. Butterworths Scientific Publications, 1955.

[379] R. C. Steele, A. C. Jarrett, P. C. Malte, J. H. Tonouchi, and D. G. Nicol. "Variables affecting NOx formation in lean-premixed combustion". In: *Journal of Engineering for Gas Turbines and Power* 119.1 (1997), pp. 102–107.

[380] W. C. Strahle. "A More Modern Theory of Combustion Noise". In: *Recent Advances in the Aerospace Sciences*. Ed. by C. Casci and C. Bruno. Springer, 1985, pp. 103–114.

[381] W. C. Strahle. "Combustion noise". In: *Progress in Energy and Combustion Science* 4.3 (1978), pp. 157–176.

[382] E. Suillaud, K. Truffin, O. Colin, and D. Veynante. "Direct Numerical Simulations of high Karlovitz number premixed flames for the analysis and modeling of the displacement speed". In: *Combustion and Flame* 236 (2022), p. 111770.

[383] C. J. Sun, C. J. Sung, L. He, and C. K. Law. "Dynamics of weakly stretched flames: quantitative description and extraction of global flame parameters". In: *Combustion and Flame* 118.1-2 (1999), pp. 108–128.

[384] T. Suzuki and T. Colonius. "Instability waves in a subsonic round jet detected using a near-field phased microphone array". In: *Journal of Fluid Mechanics* 565 (2006), pp. 197–226.

[385] N. Swaminathan, G. Xu, A. Dowling, and R. Balachandran. "Heat release rate correlation and combustion noise in premixed flames". In: *Journal of Fluid Mechanics* 681 (2011), pp. 80–115.

[386] K. Taira, S. L. Brunton, S. T. Dawson, C. W. Rowley, T. Colonius, B. J. McKeon, O. T. Schmidt, S. Gordeyev, V. Theofilis, and L. S. Ukeiley. "Modal analysis of fluid flows: An overview". In: *AIAA Journal* 55.12 (2017), pp. 4013–4041.

[387] M. Talei, M. J. Brear, and E. R. Hawkes. "A comparative study of sound generation by laminar, combusting and non-combusting jet flows". In: *Theoretical and Computational Fluid Dynamics* 28 (2014), pp. 385–408.

[388] M. Talei, M. J. Brear, and E. R. Hawkes. "A parametric study of sound generation by premixed laminar flame annihilation". In: *Combustion and Flame* 159 (2012), pp. 757–769.

[389] M. Talei, M. J. Brear, and E. R. Hawkes. "Sound generation by laminar premixed flame annihilation". In: *Journal of Fluid Mechanics* 679 (2011), pp. 194–218.

[390] M. Talei, E. R. Hawkes, and M. J. Brear. "A direct numerical simulation study of frequency and Lewis number effects on sound generation by two-dimensional forced laminar premixed flames". In: *Proceedings of the Combustion Institute* 34 (2013), pp. 1093–1100.

[391] C. K. W. Tam. "The spectral shape of combustion noise". In: *International Journal of Aeroacoustics* 14.3-4 (2015), pp. 431–456.

[392] C. K. W. Tam, F. Bake, L. S. Hultgren, and T. Poinsot. "Combustion noise: modeling and prediction". In: *CEAS Aeronautical Journal* 10 (2019), pp. 101–122.

[393] A. Thomas and G. T. Williams. "Flame noise: sound emission from spark-ignited bubbles of combustible gas". In: *Proceedings of the Royal Society of London. Series A: Mathematical and Physical Sciences* 294.1439 (1966), pp. 449–466.

[394] S. K. Thumuluru and T. Lieuwen. "Characterization of acoustically forced swirl flame dynamics". In: *Proceedings of the Combustion Institute* 32 (2009), pp. 2893–2900.

[395] G. Tissot, F. C. Lajús Jr, A. V. Cavalieri, and P. Jordan. "Wave packets and Orr mechanism in turbulent jets". In: *Physical Review Fluids* 2.9 (2017), p. 093901.

[396] G. Tissot, M. Zhang, F. C. Lajús Jr, A. V. Cavalieri, and P. Jordan. "Sensitivity of wavepackets in jets to nonlinear effects: the role of the critical layer". In: *Journal of Fluid Mechanics* 811 (2017), pp. 95–137.

[397] A. Towne, O. T. Schmidt, and T. Colonius. "Spectral proper orthogonal decomposition and its relationship to dynamic mode decomposition and resolvent analysis". In: *Journal of Fluid Mechanics* 847 (2018), pp. 821–867.

[398] A. Trouve, S. Candel, and J. Daily. "Linear stability of the inlet jet in a ramjet dump combustor". In: *26th Aerospace Sciences Meeting*. 1988, p. 149.

[399] A. Trouvé and T. Poinsot. "The evolution equation for the flame surface density in turbulent premixed combustion". In: *Journal of Fluid Mechanics* 278 (1994), pp. 1–31.

[400] J.-M. Truffaut. "Étude expérimentale de l'origine du bruit émis par les flammes de chalumeaux". PhD thesis. Université de Provence (Aix-Marseille I), France, 1998.

[401] S. D. Tse, D. L. Zhu, and C. K. Law. "Morphology and burning rates of expanding spherical flames in H2/O2/inert mixtures up to 60 atmospheres". In: *Proceedings of the Combustion Institute* 28 (2000), pp. 1793–1800.

[402] T. Turányi. "Reaction Kinetics of Hydrogen Combustion". In: *Hydrogen for Future Thermal Engines*. Ed. by E.-A. Tingas. Cham: Springer International Publishing, 2023, pp. 65–92.

[403] K. Turgut, A. Chinnayya, P. Boivin, and O. Dounia. "A simplified thermodynamically-consistent single-step mechanism for hydrogen combustion". In: *International Journal of Hydrogen Energy* 177 (2025), p. 151527.

[404] United Nations Framework Convention on Climate Change (UNFCC). *The Paris Agreement - Publication*. https://unfccc.int/documents/184656. 2018.

[405] H. A. Uranakara, S. Chaudhuri, H. L. Dave, P. G. Arias, and H. G. Im. "A flame particle tracking analysis of turbulence–chemistry interaction in hydrogen–air premixed flames". In: *Combustion and Flame* 163 (2016), pp. 220–240.

[406] C. M. Vagelopoulos, F. N. Egolfopoulos, and C. K. Law. "Further considerations on the determination of laminar flame speeds with the counterflow twin-flame technique". In: *Symposium (International) on Combustion* 25 (1994), pp. 1341–1347.

[407] A. Valera-Medina, H. Xiao, M. Owen-Jones, W. I. F. David, and P. J. Bowen. "Ammonia for power". In: *Progress in Energy and Combustion Science* 69 (2018), pp. 63–102.

[408] F. H. Vance, P. de Goey, and J. A. van Oijen. "The effect of thermal diffusion on stabilization of premixed flames". In: *Combustion and Flame* 216 (2020), pp. 45–57.

[409] F. H. Vance, Y. Shoshin, L. P. H. De Goey, and J. A. van Oijen. "A physical relationship between consumption and displacement speed for premixed flames with finite thickness". In: *Proceedings of the Combustion Institute* 38 (2021), pp. 2215–2223.

[410] T. Varga, T. Nagy, C. Olm, I. G. Zsély, R. Pálvölgyi, É. Valkó, G. Vincze, M. Cserháti, H. J. Curran, and T. Turányi. "Optimization of a hydrogen combustion mechanism using both direct and indirect measurements". In: *Proceedings of the Combustion Institute* 35 (2015), pp. 589–596.

[411] H. Vargas Ruiz, D. Laera, G. Lartigue, S. Mashruk, A. Valera-Medina, and L. Gicquel. "Extension of the dynamic Thickened Flame model for partially-premixed multi-fuel multi-injection combustion and application to an ammonia–hydrogen swirled flame". In: *Combustion and Flame* 274 (2025), p. 113992.

[412] S. Verhelst and T. Wallner. "Hydrogen-fueled internal combustion engines". In: *Progress in Energy and Combustion Science* 35.6 (2009), pp. 490–527.

[413] S. Verhelst, R. Woolley, M. Lawes, and R. Sierens. "Laminar and unstable burning velocities and Markstein lengths of hydrogen–air mixtures at engine-like conditions". In: *Proceedings of the Combustion Institute* 30 (2005), pp. 209–216.

[414] L. Vervisch, E. Bidaux, K. N. C. Bray, and W. Kollmann. "Surface density function in premixed turbulent combustion modeling, similarities between probability density function and flame surface approaches". In: *Physics of Fluids* 7.10 (1995), pp. 2496–2503.

[415] D. Veynante and L. Vervisch. "Turbulent combustion modeling". In: *Progress in Energy and Combustion Science* 28.3 (2002), pp. 193–266.

[416] D. Wacks, I. Konstantinou, and N. Chakraborty. "Effects of Lewis number on the statistics of the invariants of the velocity gradient tensor and local flow topologies in turbulent premixed flames". In: *Proceedings of the Royal Society of London. Series A: Mathematical and Physical Sciences* 474.2212 (2018), p. 20170706.

[417] K. Walsh, M. Long, M. Tanoff, and M. Smooke. "Experimental and computational study of CH, CH*, and OH* in an axisymmetric laminar diffusion flame". In: *Symposium (International) on Combustion* 27 (1998), pp. 615–623.

[418] B. Wang, W. Wei, S. Ma, and G. Wei. "Construction of one-step H2/O2 reaction mechanism for predicting ignition and its application in simulation of supersonic combustion". In: *International Journal of Hydrogen Energy* 41.42 (2016), pp. 19191–19206.

[419] X. Wang, H. Huo, and V. Yang. "Supercritical combustion of general fluids in laminar counterflows". In: *51st AIAA Aerospace Sciences Meeting including the New Horizons Forum and Aerospace Exposition*. 2013, p. 1165.

[420] P. Welch. "The use of fast Fourier transform for the estimation of power spectra: A method based on time averaging over short, modified periodograms". In: *IEEE Transactions on Audio and Electroacoustics* 15.2 (1967), pp. 70–73.

[421] I. S. Wichman and R. Vance. "A study of one-dimensional laminar premixed flame annihilation". In: *Combustion and Flame* 110.4 (1997), pp. 508–523.

[422] C. R. Wilke. "A Viscosity Equation for Gas Mixtures". In: *Journal of Chemical Physics* 18 (1950), pp. 517–519.

[423] F. A. Williams. "Progress in knowledge of flamelet structure and extinction". In: *Progress in Energy and Combustion Science* 26.4-6 (2000), pp. 657–682.

[424] Y. X. Xin, C. S. Yoo, J. H. Chen, and C. K. Law. "A DNS study of self-accelerating cylindrical hydrogen–air flames with detailed chemistry". In: *Proceedings of the Combustion Institute* 35 (2015), pp. 753–760.

[425] J. Xing, A. L. Pillai, and R. Kurose. "Heat release rate surrogate for ammonia–hydrogen premixed flames under various conditions". In: *Applications in Energy and Combustion Science* 15 (2023), p. 100193.

[426] H. Yamashita, M. Shimada, and T. Takeno. "A numerical study on flame stability at the transition point of jet diffusion flames". In: *Symposium (International) on Combustion* 26 (1996), pp. 27–34.

[427] S. Yan, Y. Gong, Z. Duan, Q. Guo, and G. Yu. "Investigation of the correlation between OH*, CH* chemiluminescence and heat release rate in methane inverse diffusion flame". In: *Energy* 283 (2023), p. 129162.

[428] H. M. Yang and N. I. Kim. "Global reaction mechanisms for H2 + NH3 + CO + CH4 at conditions up to 600 K and 5 atm". In: *International Journal of Hydrogen Energy* 101 (2025), pp. 998–1013.

[429] L. Yang, Y. Wang, T. Zirwes, F. Zhang, H. Bockhorn, and Z. Chen. "Effects of Intrinsic Instabilities on the Response of Premixed Hydrogen/Air Conical Flames to Inlet Flow Perturbations". In: *Flow, Turbulence and Combustion* 112.4 (2024), pp. 1275–1297.

[430] S. Yang, A. Saha, F. Wu, and C. K. Law. "Morphology and self-acceleration of expanding laminar flames with flame-front cellular instabilities". In: *Combustion and Flame* 171 (2016), pp. 112–118.

[431] S. Yoo, C. K. Law, and S. Tse. "Chemiluminescent OH* and CH* flame structure and aerodynamic scaling of weakly buoyant, nearly spherical diffusion flames". In: *Proceedings of the Combustion Institute* 29 (2002), pp. 1663–1670.

[432] F. Young and U. Ahmed. "Lean hydrogen-air premixed flames subjected to high-frequency acoustic oscillations". In: *Proceedings of the Combustion Institute* 41 (2025), p. 105950.

[433] T. Yusaf, A. S. F. Mahamude, K. Kadirgama, D. Ramasamy, K. Farhana, H. A. Dhahad, and A. R. A. Talib. "Sustainable hydrogen energy in aviation – A narrative review". In: *International Journal of Hydrogen Energy* 52.C (2023), pp. 1026–1045.

[434] J. Zeldowitsch and D. Frank-Kamenetzki. "A theory of thermal propagation of flame". In: *Dynamics of Curved Fronts*. Elsevier, 1988, pp. 131–140.

[435] F. Zhang, T. Zirwes, Y. Wang, Z. Chen, H. Bockhorn, D. Trimis, and D. Stapf. "Dynamics of premixed hydrogen/air flames in unsteady flow". In: *Physics of Fluids* 34.8 (2022).

[436] M. Zhao, D. Buttsworth, and R. Choudhury. "Experimental and numerical study of OH* chemiluminescence in hydrogen diffusion flames". In: *Combustion and Flame* 197 (2018), pp. 369–377.

[437] H. Zhou, J. Xue, H. Gao, and N. Ma. "Hydrogen-fueled gas turbines in future energy system". In: *International Journal of Hydrogen Energy* 64 (2024), pp. 569–582.

[438] Z. Zhu, H. Wang, E. R. Hawkes, K. Luo, and J. Fan. "Direct numerical simulations of head-on quenching of statistically planar turbulent premixed flames on rough walls". In: *Combustion and Flame* 278 (2025), p. 114245.

Appendix

Parva sæpe scintilla contempta magnum excitavit incendium.

A spark neglected has often raised a conflagration.

— Quintus Curtius Rufus
Histories of Alexander the Great, 1st century

A

Parameters for the simplified transport model

In the following, the parameters for the simplified transport model described in Section 3.3.4 and adopted in the numerical simulations performed in this dissertation are reported.

Table A.1 lists the values used for the follwing three reaction mechanisms:

- The San Diego scheme [339] (UCSD) for hydrogen–air flames.
- The scheme derived by Pestre [255, 298] (CH4_15_138_9_AP) for methane–hydrogen–air flames.
- The two-step scheme [357] (CH4-2S) for methane–air flames.

Table A.1: Parameters adopted for the simplified transport model to compute the molecular and the diffusivities for the UCSD, CH4_15_256_9_AP and CH4-2S mechanisms.

Parameter [unit]		UCSD	CH4_15_138_9_AP	CH4-2S
μ_{ref} [kg/(m s)]		8.06×10^{-5}	7.01×10^{-5}	1.81×10^{-5}
T_{ref} [K]		2645	2206	300
α		0.65	0.64	0.68
Pr		0.66	0.70	0.68
Sc_k	H_2	0.23	0.21	-
	H_2O	0.58	0.55	0.54
	H	0.14	0.12	-
	OH	0.53	0.49	-
	HO_2	0.80	-	-
	H_2O_2	0.81	-	-
	O_2	0.80	0.75	0.74
	O	0.52	0.49	-
	N_2	0.91	0.74	0.73
	CH_4	-	0.68	0.68
	CO_2	-	0.96	0.95
	CO	-	0.76	0.75
	CH_3	-	0.68	-
	CH_2O	-	0.87	-
	C_2H_6	-	1.00	-
	C_2H_2	-	0.82	-
	$CH_2(L_1)$	-	0.67	-

Table A.2 reports the parameters defining the reaction rate and the transport properties for the reduced schemes adopted in the simulations of laminar M-shaped flames shown in Section 9.4.

Table A.2: Parameters adopted for the reaction rate and the transport model for the global reaction mechanisms in the laminar case. Reaction rate constant: $k = AT^{\beta} \exp[-E_a/(RT)]$, units are cm^3 mol s cal K.

Parameter		1S_FGS	1S_FGS_LE1	1S_FGS_NOPREF	1S_FGS_NODIFF
A		5.00×10^{15}	2.03×10^{15}	5.68×10^{15}	1.75×10^{15}
β		-0.045	-0.045	-0.045	-0.045
E_a		32971	32971	32971	32971
n_{H_2}		1.272	1.272	1.272	1.272
n_{O_2}		0.636	0.636	0.636	0.636
Pr		0.434	0.458	0.453	0.437
Sc_k	H_2	0.173	0.458	0.180	0.437
	O_2	0.533	0.458	0.180	1.347
	H_2O	0.806	0.458	0.180	2.035
	N_2	0.625	0.458	0.180	1.578

Table A.3 gives the parameters defining the reaction rate and the transport properties for the reduced schemes adopted in the simulations of turbulent slot jet flames shown in Section 11.6.

Table A.3: Parameters adopted for the reaction rate and the transport model for the global reaction mechanisms in the turbulent case. Reaction rate constant: $k = AT^{\beta} \exp[-E_a/(RT)]$, units are cm^3 mol s cal K.

Parameter		1S_FGS	1S_FGS_LE1
A		5.92×10^{15}	2.35×10^{15}
β		-0.045	-0.045
E_a		32971	32971
n_{H_2}		1.272	1.272
n_{O_2}		0.636	0.636
Pr		0.495	0.520
Sc_k	H_2	0.197	0.520
	O_2	0.608	0.520
	H_2O	0.918	0.520
	N_2	0.712	0.520

B

Simplifications in the OH* chemical description

The simplifications made for the computation of OH* in the numerical simulations reported in Chapter 6 are elucidated in the following.

Impact of minor N-containing species

Figure B.1 compares the normalized distributions of OH* molar concentration for lean ($\phi = 0.35$, top) and stoichiometric ($\phi = 1.0$, bottom) unstrained premixed laminar hydrogen–air flames at $T_u = 300$ K and $p = 1$ atm (a), $T_u = 600$ K and $p = 1$ atm (b), and $T_u = 600$ K and $p = 10$ atm (c) obtained with and without the NO_x reaction subset. All calculations are performed with the San Diego scheme [339] for hydrogen combustion and the OH* sub-scheme by Sharipov et al. [362, 363]. The NO_x kinetics is described by the reaction subset included in the CRECK chemistry model [376]. It can be observed that, for the operating conditions of interest, the impact of the minor N-containing species on the OH* distribution remains negligible. Consequently, these species are not considered for the numerical simulations in this work, thereby improving the computational efficiency.

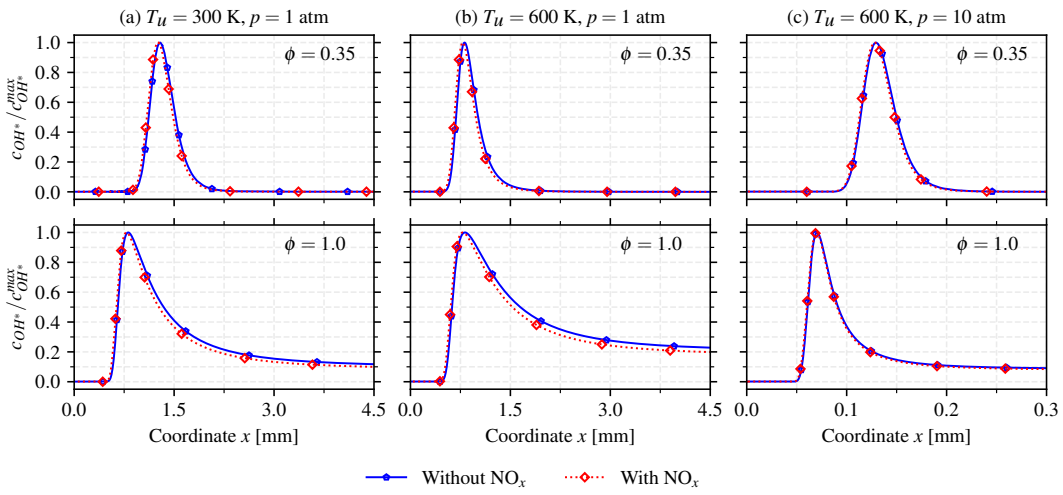

Figure B.1: Normalized distributions of OH^* molar concentration for unstrained lean ($\phi = 0.35$, top) and stoichiometric ($\phi = 1.0$, bottom) premixed flames at $T_u = 300$ K and $p = 1$ atm (a), $T_u = 600$ K and $p = 1$ atm (b), and $T_u = 600$ K and $p = 10$ atm (c). Comparison of results obtained with and without the NO_x kinetics.

Quasi-Steady State approximation for OH*

In the framework of the Quasi-Steady State approximation, the OH* concentration is evaluated as:

$$c_{\mathrm{OH}^*} = \frac{\dot{\omega}_{prod,\mathrm{OH}^*}}{\omega_{cons}}, \tag{B.1}$$

where $\dot{\omega}_{prod,\mathrm{OH}^*}$ is the production rate of OH* and ω_{cons} is the inverse of the reaction time of OH* consumption, accounting for all the OH*-consuming reactions [140].

Figure B.2 compares the normalized distributions of OH* concentration for lean ($\phi = 0.35$, top) and stoichiometric ($\phi = 1.0$, bottom) unstrained premixed laminar hydrogen–air flames at $T_u = 300$ K and $p = 1$ atm (a), $T_u = 600$ K and $p = 1$ atm (b), and $T_u = 600$ K and $p = 10$ atm (c) obtained with and without considering the QSS approximation for the OH* radical. It can be clearly observed that, for the operating conditions of interest, no significant modification in the OH* distribution is introduced by the QSS approximation. Indeed, the error due to this approximation, defined as:

$$|\Delta_{QSS}| = \frac{\left|c_{\mathrm{OH}^*}^{exact} - c_{\mathrm{OH}^*}^{QSS}\right|}{c_{\mathrm{OH}^*}^{exact}} = \frac{\left|\dot{\omega}_{prod,\mathrm{OH}^*} - \dot{\omega}_{cons,\mathrm{OH}^*}\right|}{\dot{\omega}_{cons,\mathrm{OH}^*}}, \tag{B.2}$$

is of an order of magnitude not greater than 10^{-3} for all the operating conditions considered. Therefore, the adoption of the QSS approximation to evaluate the OH* concentration in CFD numerical simulations is well justified.

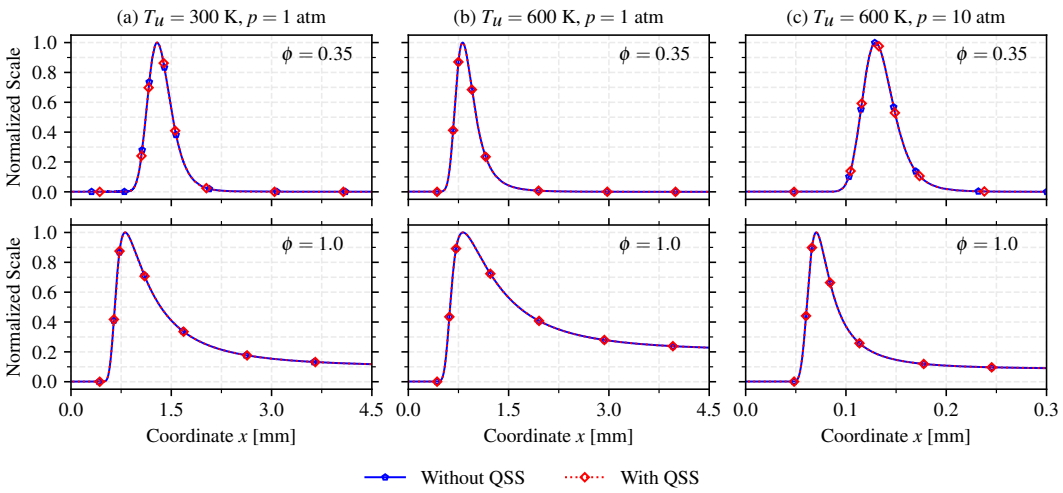

Figure B.2: Normalized distribution of OH^* concentration for unstrained lean ($\phi = 0.35$, top) and stoichiometric ($\phi = 1.0$, bottom) premixed flames at $T_u = 300$ K and $p = 1$ atm (a), $T_u = 600$ K and $p = 1$ atm (b), and $T_u = 600$ K and $p = 10$ atm (c). Comparison of results obtained with and without considering the QSS approximation. All calculations are performed with the San Diego scheme [339] for hydrogen combustion and the OH^* sub-scheme by Sharipov et al. [362, 363], as described in Table 6.2.

Post-processing routine

To illustrate, from a practical point of view, the procedure followed to implement the QSS approximation in the post-processing routine, a flowchart is provided in Figure B.3. For clarity, here the more simple OH* sub-scheme by Kathrotia et al. [190, 191], reported in Table 6.1, is considered, but an analogous procedure can be applied to any OH* sub-mechanism. The inputs are:

- The mass fraction of the species involved in the OH* sub-scheme Y_{spec}, of size $N_s \times N$.
- The density field ρ, of size N.
- The temperature field T, of size N.
- The number of grid elements in the CFD solution N.
- The number of species involved in the OH* sub-scheme N_s.
- The list of species involved in the OH* sub-scheme N_s.
- The dictionary i_{spec} mapping each species to an index in the array Y_{spec}.
- The molar weights of the species involved in the OH* sub-scheme MW_{spec}.

It should be noted that the number of reactions in the flow chart is equal to 22, since the forward and backward steps of the reversible reactions in Table 6.1 are treated separately.

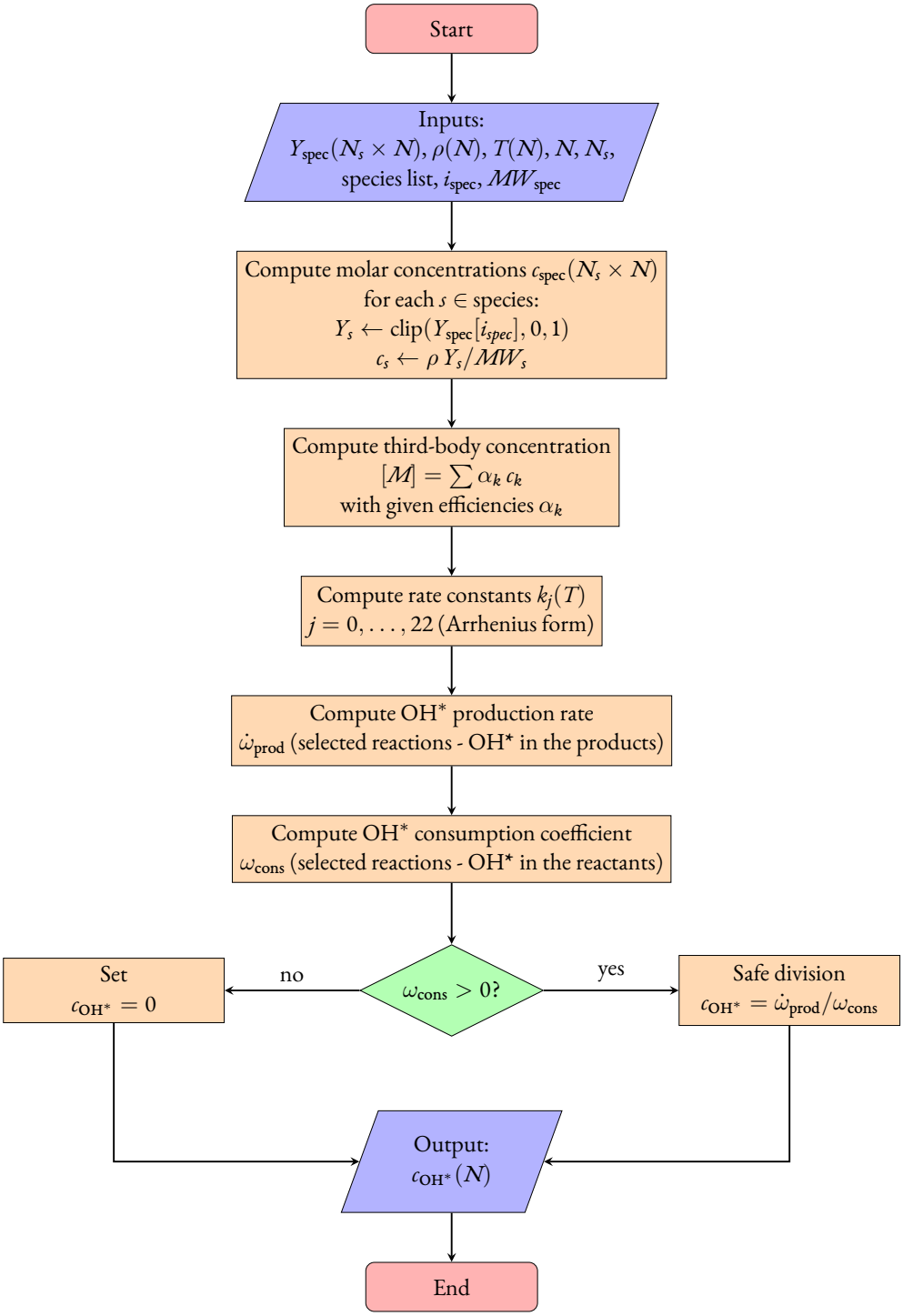

Figure B.3: Flowchart of the QSS-based post-processing routine to compute OH* molar concentration from CFD fields using OH* sub-scheme by Kathrotia et al. [190, 191].

C

Influence of the mesh size

The influence of mesh size on the datasets developed in Chapters 8 and 10 is assessed in this Appendix.

Laminar M-shaped jet flame

For the laminar case described in Chapter 8, no relevant variations of the flame structure were observed by further refining the grid size in the reacting region. Figure C.1 compares the HRR and OH molar concentration fields obtained for two grid resolutions (i.e., $\Delta_x = 80$ μm and $\Delta_x = 60$ μm), while Figure C.2 compares the radial profiles of the two quantities at three different heights from the burner outlet. Figures C.3 and C.4 propose the same analysis for the hydrogen flame considering three grid resolutions: $\Delta_x = 80$ μm, $\Delta_x = 60$ μm, and $\Delta_x = 40$ μm.

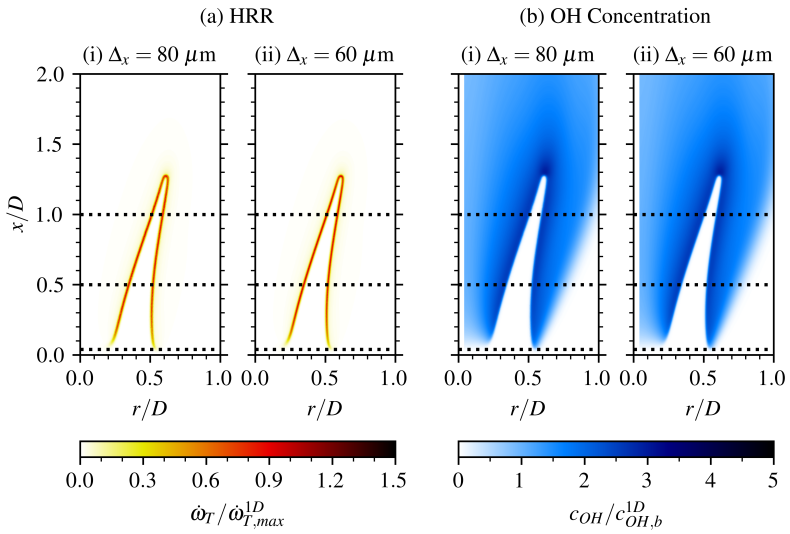

Figure C.1: Distributions of normalized heat release rate $\dot{\omega}_T/\dot{\omega}^{1D}_{T,max}$ (a) and normalized OH molar concentration $c_{OH}/c^{1D}_{OH,b}$ (b) for the CH_4-H_2 flame computed with grid resolutions Δ_x equal to 80 μm (i) and 60 μm (ii). The dotted horizontal lines correspond to the plots in Figure C.2.

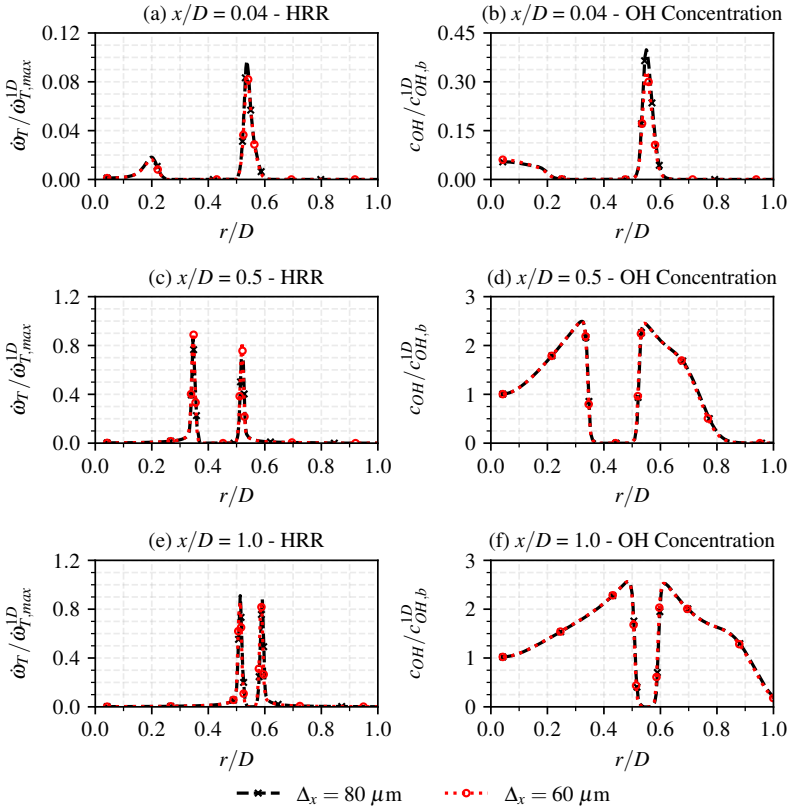

Figure C.2: Radial profiles of normalized heat release rate $\dot{\omega}_T/\dot{\omega}^{1D}_{T,max}$ (a) and normalized OH molar concentration $c_{OH}/c^{1D}_{OH,b}$ (b) for the CH_4-H_2 flame computed with grid resolutions Δ_x equal to 0.08 mm (i) and 0.06 mm (ii).

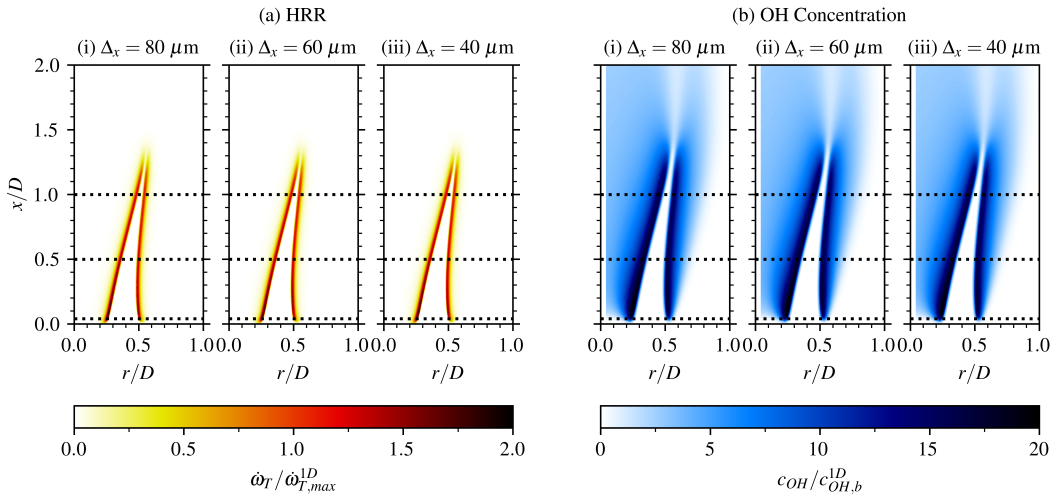

Figure C.3: Distributions of normalized heat release rate $\dot{\omega}_T/\dot{\omega}^{1D}_{T,max}$ (a) and normalized OH molar concentration $c_{OH}/c^{1D}_{OH,b}$ (b) for the H_2 flame computed with grid resolutions Δ_x equal to 0.08 mm (i), 0.06 mm (ii) and 0.04 mm (iii). The dotted horizontal lines correspond to the plots in Figure C.4.

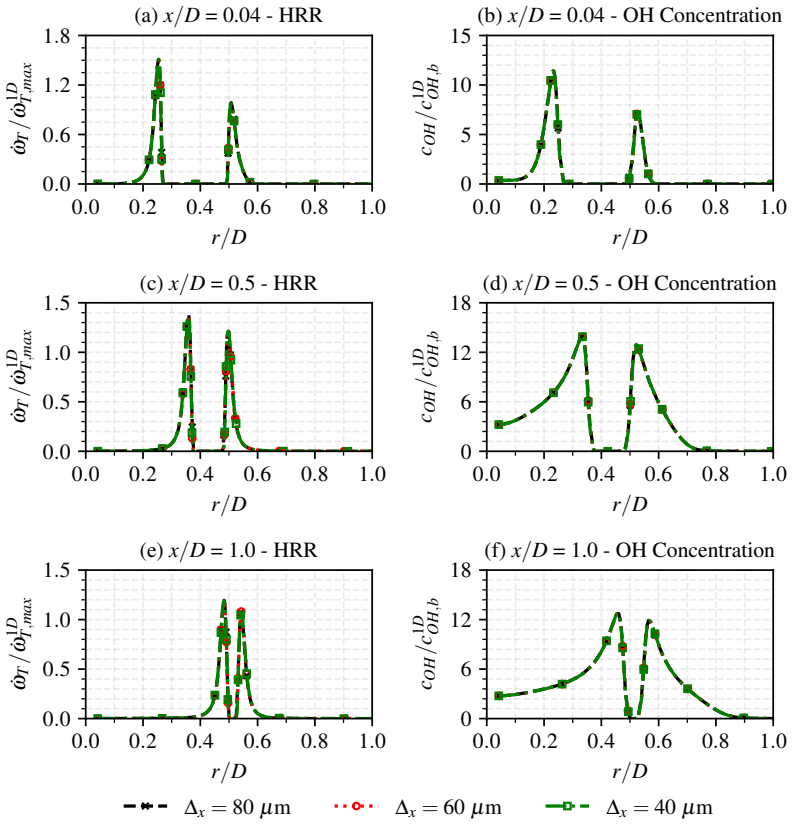

Figure C.4: Radial profiles of normalized heat release rate $\dot{\omega}_T/\dot{\omega}^{1D}_{T,max}$ (a) and normalized OH molar concentration $c_{OH}/c^{1D}_{OH,b}$ (b) for the H_2 flame computed with grid resolutions Δ_x equal to 80 μm (i), 60 μm (ii) and 40 μm (iii).

Turbulent slot jet flame

Among the cases reported in Sections 11.1 to 11.4, a study of influence of the mesh size was performed for the H25 case, since it is prone to thermodiffusive instabilities and features the smallest Kolmogorov length scale (see Table 10.2). To this scope, two additional simulations were performed by considering a maximum grid resolution in the reacting region Δ_x equal to 80 μm and 60 μm. Figure C.5 reports the conditional mean of the hydrogen reaction rate $\dot{\omega}_{H_2}$, normalized by the maximum value in the corresponding 1D laminar unstretched flame $\dot{\omega}^{1D}_{H_2,max}$, related to the progress variable C, defined as in Equation (10.1). The results are not affected by successive refinements, demonstrating that $\Delta_x = 100$ μm is sufficient, coherently with the previous work by Malé et al. [248] for turbulent premixed hydrogen–air flames under analogous conditions.

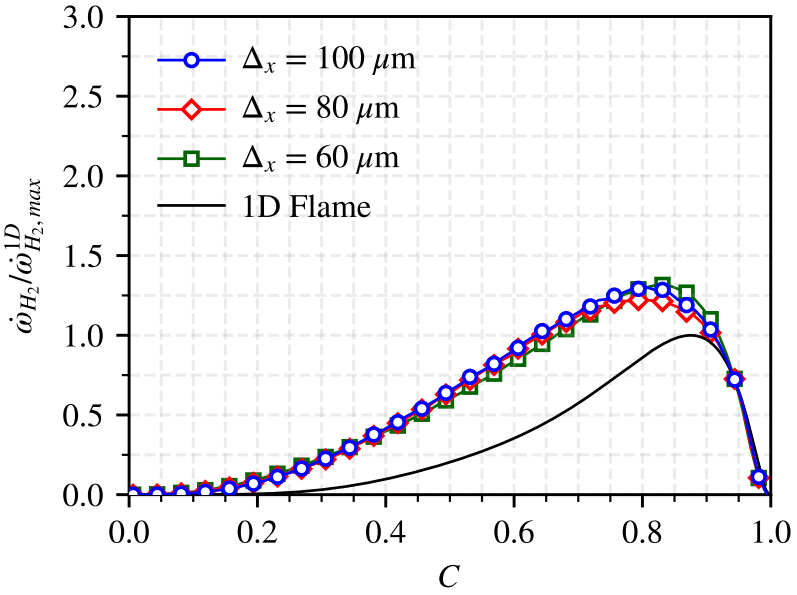

Figure C.5: Conditional mean of the normalized hydrogen reaction rate $\dot{\omega}_{H_2}/\dot{\omega}^{1D}_{H_2,max}$ with respect to the progress variable C for different mesh resolutions. The hydrogen reaction rate for the corresponding 1D laminar unstretched flame (black line) is added for reference.

Furthermore, the impact of the grid size was assessed for the higher *Ka* hydrogen flames investigated in Section 11.5. To this scope, additional simulations were performed for the mid *Ka* case with maximum grid size in the reacting region Δ_x equal to 72.5 μm and 45 μm, and for the high *Ka* case with $\Delta_x = 45$ μm. The results of this analysis are shown in Figure C.6, highlighting the absence of any significant impact of reduced grid size. This justifies the choice of $\Delta_x = 100$ μm for all the cases considered in Section 11.5.

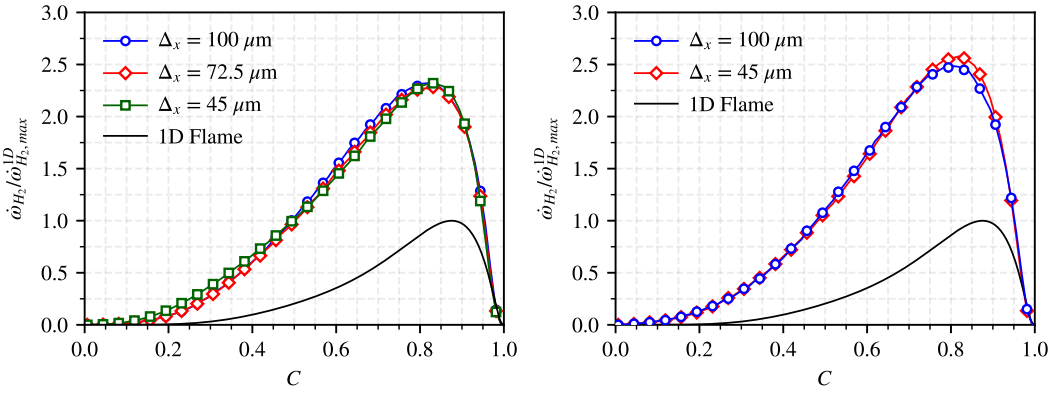

(a) Mid Ka. **(b)** High Ka.

Figure C.6: Conditional mean of the normalized hydrogen reaction rate $\dot{\omega}_{H_2}/\dot{\omega}^{1D}_{H_2,max}$ with respect to the progress variable C for different mesh resolutions in the mid Ka (a) and high Ka (b) cases. The hydrogen reaction rate for the corresponding 1D laminar unstretched flame (black line) is added for reference.

D

Spectral analysis of turbulence

For the turbulent configurations considered in Chapter 11, the turbulence injected in the unburned mixture is the dominant source of velocity fluctuations affecting the flames [79, 125].

First, the turbulence for the low *Ka* cases in Sections 11.1 to 11.4 is considered. For these configurations, additional perturbations in the velocity field originate from the turbulence developed in the wall-bounded channel flow upstream of the flame, leading to a deviation of the turbulent field from the injected one. To quantify the evolution of turbulence in the inlet channel, Figure D.1 reports, for the three cases, the power spectral densities of the turbulent kinetic energy S_{TKE} at different positions, with $S_{TKE} = (S_u + S_v + S_w)/2$, where S_u, S_v and S_w are the power spectral densities of the velocity components in the x, y and z directions, respectively. The turbulence decays quite slowly, and a similarity can be observed among the three cases in the shape and magnitude of the power spectral densities, especially for the probes in proximity of the flame. Due to the high viscous dissipation, lower power spectral density is observed for the probes near the outer shear layer, as well as for the farthest probe in the axial direction of the H10 case, being this latter fully in the combustion products (see Figure D.2).

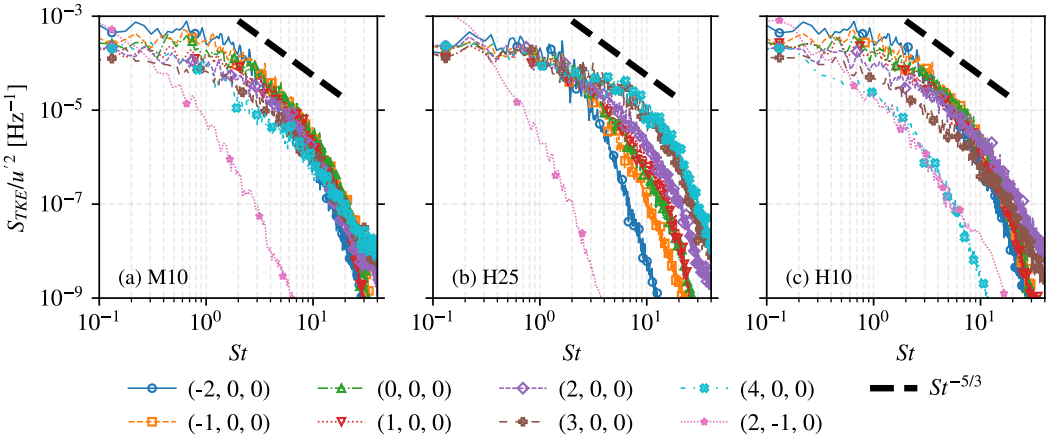

Figure D.1: Power spectral density of the turbulent kinetic energy S_{TKE}, normalized by $u' = 2.5\,\mathrm{m\,s^{-1}}$, retrieved from different probes for the M10 (a), H25 (b) and H10 (c) turbulent flames. The coordinates of the probes are given as $(x/H, y/H, z/H)$. The line at $St^{-5/3}$ is added for reference.

Moreover, shear-induced turbulence is developed in the inner shear layers surrounding the fresh gases and outer shear layers surrounding the burnt gases. The former induces an increase in viscosity due to the high temperature increase generated across the flame front, while the latter is a non-reacting interface, with no-relevant influence on the flame dynamics. Both add significant dissipation to the turbulent structures, as it can be observed from Figure D.2, which reports the turbulence dissipation rate $\tilde{\varepsilon}$ for the different cases, with $\tilde{\cdot}$ denoting the Favre average performed in time over a window of duration τ and in the span-wise direction z for the whole extension of the slot, *i.e.* between $z/H = -0.75$ and $z/H = 0.75$. The contours of progress variable $\tilde{C} = C^*$ (in white) and of $\tilde{\xi} = 0.5 Y_{F,u}$ (in red) are reported too, to highlight the position of the inner and outer shear layers. The markers correspond to the positions of the probes of the spectra of Figure D.1.

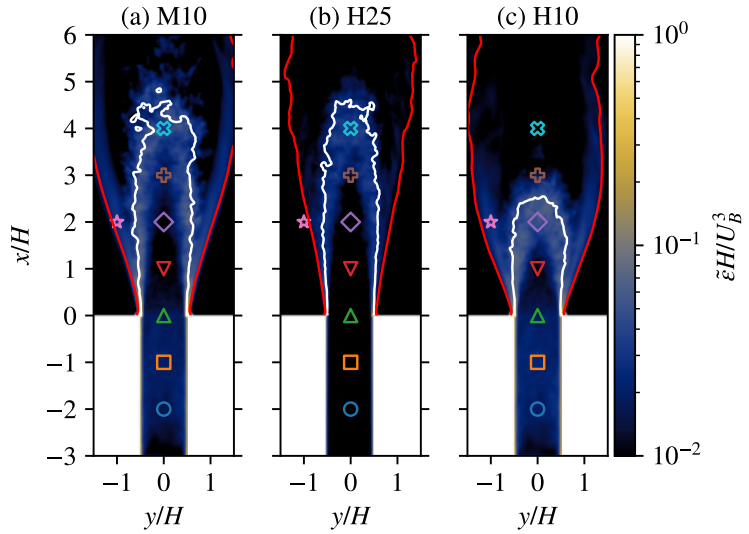

Figure D.2: Normalized turbulence dissipation rate $\tilde{\varepsilon}H/U_B^3$ and contours of progress variable $\tilde{C} = C^*$ (in white) and mixture fraction $\tilde{\xi} = 0.5 Y_{F,u}$ (in red) for the M10 (a), H25 (b) and H10 (c) turbulent flames. The markers denote the position of the probes of Figure D.1.

The analysis of turbulence spectra is replicated for the higher *Ka* cases in Section 11.5, and is reported in Figure D.3. Analogous considerations as for Figure D.1 can be made. It is noted that the contribution of the wall-bounded channel flow upstream of the flame is more pronounced for the low *Ka* case, while at higher *Ka* the turbulent fluctuations imposed at the inlet are more strongly preserved up to the flame region.

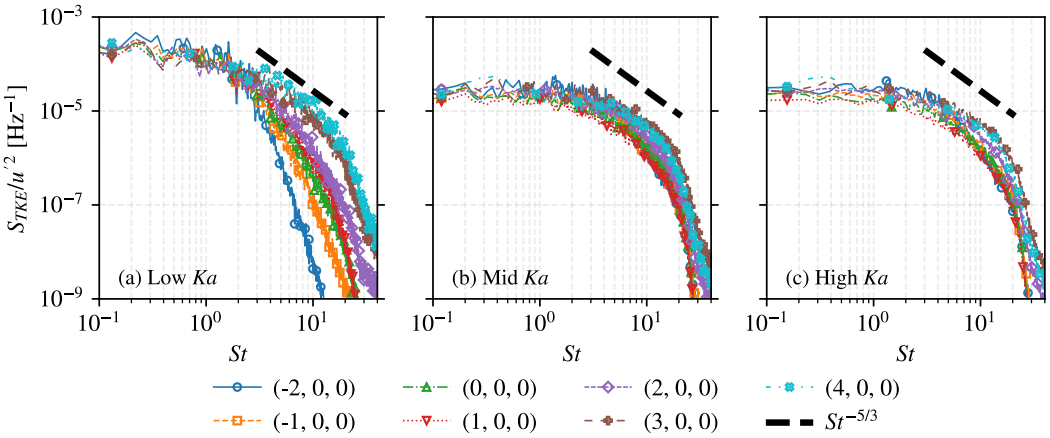

Figure D.3: Power spectral density of the turbulent kinetic energy S_{TKE}, normalized by $u' = 2.5$ m s^{-1}, retrieved from different probes for the low *Ka* (a), mid *Ka* (b) and high *Ka* (c) turbulent flames. The coordinates of the probes are given as $(x/H, y/H, z/H)$. The line at $St^{-5/3}$ is added for reference.

E

Additional results for the forced laminar M-shaped flames

In this Appendix, additional results for the laminar M-shaped methane–hydrogen–air flame discussed in Sections 9.1 and 9.2.1 are provided, by considering higher amplitude or frequency of the harmonic inflow forcing.

Results for the flame at $u_{rms}/\bar{u} = 0.24$ and $f_a = 228$ Hz

Figure E.1 reports the normalized HRR, together with the normalized field of dilatation $\nabla \cdot \mathrm{u}$, at six different instants. A similar dynamics as for the low amplitude case can be observed (see Figure 9.2a), and analogous considerations on the dynamics of the flame tip and of the pinch-off can be made. The main difference is represented, in this case, by the presence of a second annihilation event at the flame tip (see Figure E.1c), with the formation of two separated pockets.

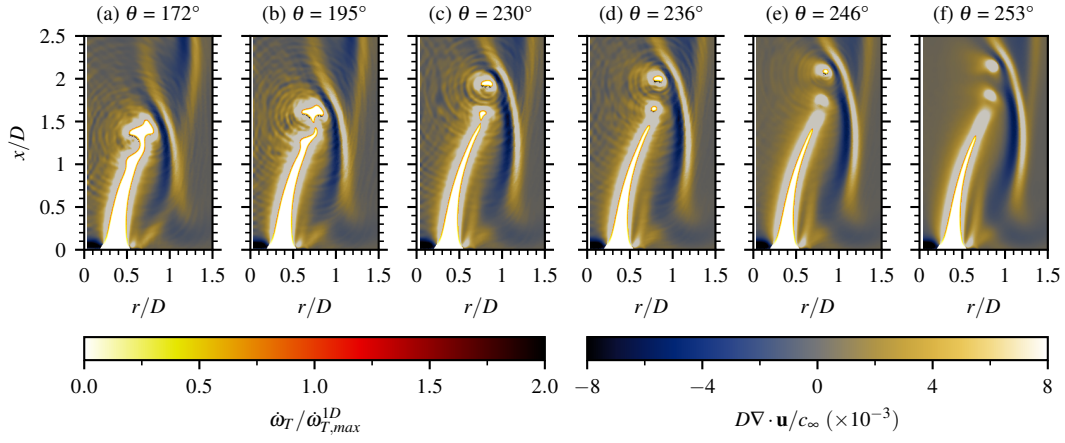

Figure E.1: Snapshots of normalized HRR $\dot{\omega}_T/\dot{\omega}^{1D}_{T,max}$ in the unburnt and flame front region, identified by $c \leq 0.95$, and normalized dilatation $D\nabla \cdot \mathbf{u}/c_\infty$ at six different instants for the CH_4-H_2 flame at $u_{rms}/\bar{u} = 0.24$ and $f_a = 228$ Hz.

This is evident also in Figure E.2a, which shows the temporal signals of pressure fluctuation p', both recorded and reconstructed from the heat release rate (HRR). Indeed, a third negative peak appears, associated with the further separation of the main detached pocket, i.e., to the second annihilation event. It should be noted that the two pockets are consumed almost at the same time (see Figure E.1e-f), which explains why a sole negative peak associated with the consumption of the pockets is observed. As shown in Figure E.2b, the flamelet theory linking HRR and flame surface fluctuations holds also in this case. Finally, Figure E.2c highlights that the consumption of the detached flame pocket lasts longer when compared to the low amplitude case (see Figure 9.3a), due to its larger size. Still, the phenomenon remains sufficiently rapid, thereby generating sound.

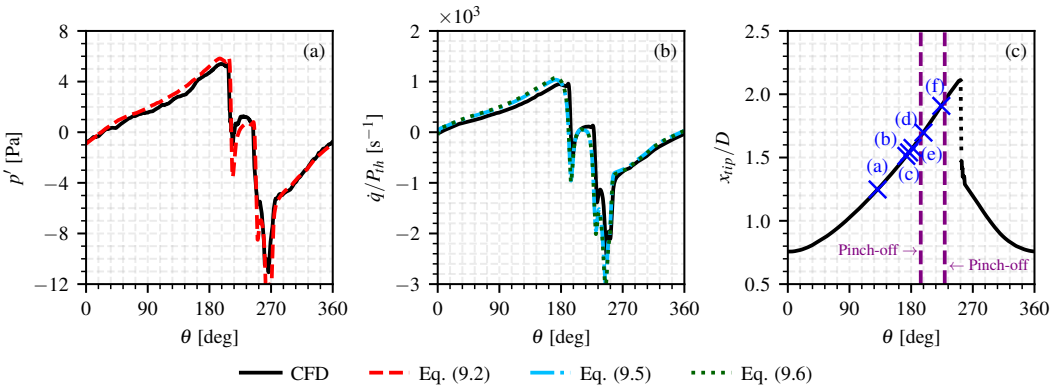

Figure E.2: Phase-averaged temporal history for the CH_4-H_2 flame at $f_a = 228$ Hz and $u_{rms}/\bar{u} = 0.24$: pressure fluctuation p' from simulations and reconstructed from Equation (9.2) (a), normalized time derivative of the volume-integrated HRR $\dot{q}/P_{th}$ from simulations and reconstructed from the flame surface via Equations (9.5) and (9.6) (b), and normalized flame tip position x_{tip}/D from numerical simulations (c). The purple dashed lines identify the flame pinch-off events. The blue crosses correspond to flame patterns in Figure E.1.

Results for the flame at $u_{rms}/\bar{u} = 0.17$ and $f_a = 456$ Hz

Figure E.3 reports the normalized HRR, together with the normalized field of dilatation $\nabla \cdot \mathrm{u}$, at six different instants. It can be observed that the pinch-off at the flame tip is enhanced by the increased frequency, with the detachment of a pocket of larger size. Also in this case a second annihilation event occurs, which is however generated in the large detached pocket rather than in the jet flame (see Figure E.3c).

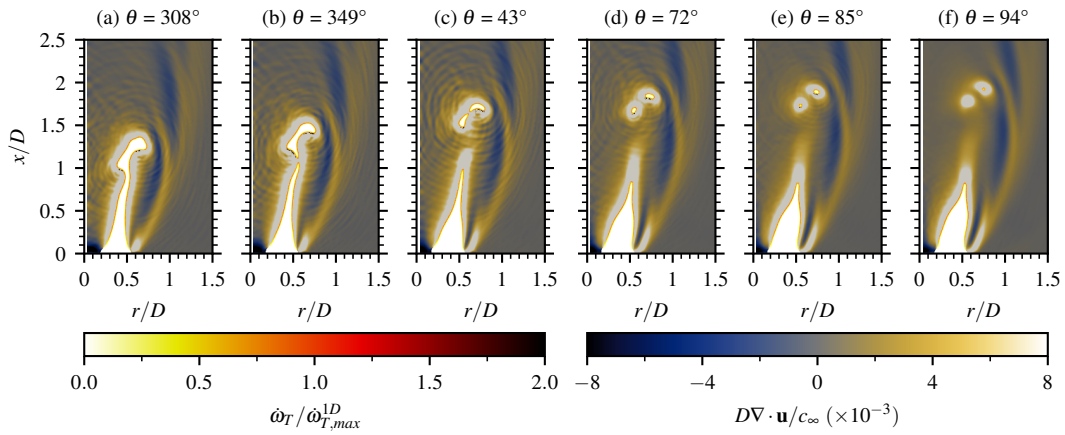

Figure E.3: Snapshots of normalized HRR $\dot{\omega}_T/\dot{\omega}^{1D}_{T,max}$ in the unburnt and flame front region, identified by $c \leq 0.95$, and normalized dilatation $D\nabla \cdot \mathbf{u}/c_\infty$ at six different instants for the CH_4-H_2 flame at $u_{rms}/\bar{u} = 0.17$ and $f_a = 456$ Hz.

For the temporal signals in Figure E.4, similar considerations as for the previous case forced at $u_{rms}/\bar{u} = 0.24$ and $f_a = 228$ Hz can be made, with the presence also here of a third negative peak in the acoustic radiation, associated to the second annihilation event. The comparison of Figure E.4c with the corresponding one for the H_2 flame (see Figure 9.10c) highlights the much longer consumption of the detached pocket, due to the peculiar H_2 flammability characteristics discussed in Chapter 9.

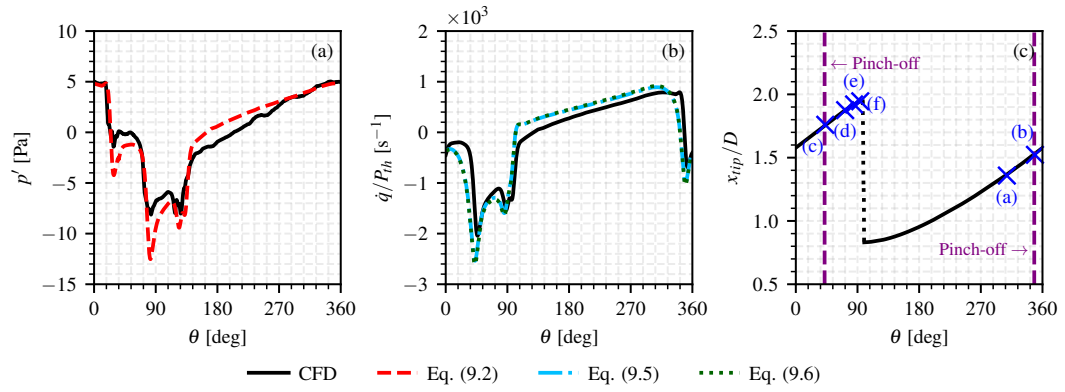

Figure E.4: Phase-averaged temporal history for the CH_4-H_2 flame at $f_a = 456$ Hz and $u_{rms}/\bar{u} = 0.17$: pressure fluctuation p' from simulations and reconstructed from Equation (9.2) (a), normalized time derivative of the volume-integrated HRR $\dot{q}/P_{th}$ from simulations and reconstructed from the flame surface via Equations (9.5) and (9.6) (b), and normalized flame tip position x_{tip}/D from numerical simulations (c). The purple dashed lines identify the flame pinch-off events. The blue crosses correspond to flame patterns in Figure E.3.

F

Definition of the reference acoustic pressure

Details on the derivation of the reference acoustic pressure adopted in Sections 11.2 and 11.5 are provided in this Appendix.

The acoustic power $\mathcal{P}$ radiated from an open turbulent premixed flame scales with the product of the squares of the flame thermal power P_{th} and of a characteristic frequency $f_{char} = U_B/L_f$ (see Section 7.1.3). The following relation may be established:

$$\begin{aligned}\mathcal{P} \approx \frac{(\gamma-1)^2}{4\pi\rho_\infty c_\infty^5} f_{char}^2 P_{th}^2 &= \frac{(\gamma-1)^2}{4\pi\rho_\infty c_\infty^5}\left(\frac{U_B}{L_f}\right)^2 \left(Y_{F,u}\rho_u \mathcal{A}_{channel} U_B H_F\right)^2 \\ &= \frac{(\gamma-1)^2}{4\pi\rho_\infty c_\infty^5}\left(\frac{Y_{F,u}\rho_u 1.5 H^2 U_B^2 H_F}{L_f}\right)^2 .\end{aligned} \tag{F.1}$$

Recalling Equation (7.22) and the definition of the acoustic power:

$$\mathcal{P} = \frac{\overline{p'^2}}{\rho_\infty c_\infty} 4\pi |\mathrm{x}|^2 , \tag{F.2}$$

an expression for $\overline{p'}$ can then be derived:

$$\overline{p'} = \sqrt{\mathcal{P}\frac{\rho_\infty c_\infty}{4\pi |\mathrm{x}|^2}} \approx \sqrt{\frac{(\gamma-1)^2}{4\pi\cancel{\rho_\infty} c_\infty^{\cancel{4}}}\left(\frac{Y_{F,u}\rho_u 1.5 H^2 U_B^2 H_F}{L_f}\right)^2 \frac{\cancel{\rho_\infty c_\infty}}{4\pi |\mathrm{x}|^2}}. \tag{F.3}$$

For the cases in Section 11.2, the constant term 1.5^2 is neglected and a reference distance $|\mathrm{x}| = H$ is assumed. Then:

$$\overline{p'} \approx \sqrt{\frac{(\gamma-1)^2}{4\pi c_\infty^4}\left(\frac{Y_{F,u}\rho_u H^2 U_B^2 H_F}{L_f}\right)^2 \frac{1}{4\pi H^2}} = \frac{(\gamma-1) Y_{F,u}\rho_u H^{\cancel{2}} U_B^2 H_F}{4\pi c_\infty^2 L_f \cancel{H}}, \tag{F.4}$$

which corresponds to the expression of p_{ref} given in Equation (11.3).

For the cases in Section 11.5, instead, a reference distance $|\mathrm{x}| = H_0$ is taken, leading to:

$$\overline{p'} \approx \sqrt{\frac{(\gamma-1)^2}{4\pi c_\infty^4}\left(\frac{Y_{F,u}\rho_u H_0^2 U_B^2 H_F}{L_f}\right)^2 \frac{1}{4\pi H^2}} = \frac{(\gamma-1)Y_{F,u}\rho_u H^2 U_B^2 H_F}{4\pi c_\infty^2 L_f H_0}, \tag{F.5}$$

which corresponds to the expression of p_{ref} given in Equation (11.14).

G

OH* distribution in the turbulent premixed slot jet flame

The relation between OH* and HRR is here investigated in the turbulent H25 slot jet flame presented in Chapter 10. This flame is at atmospheric conditions and is characterized by an equivalence ratio $\phi = 0.45$ and a bulk velocity of the jet $U_B = 25$ m/s.

Figure G.1 shows the time-averaged (over one flow-through time $\tau = 6.824$ ms) normalized HRR field, together with isolines of the normalized OH* concentration at 20%, 50%, and 90%. The x and y coordinates are scaled by the slot width $H = 8.5$ mm. The OH* distribution is retrieved with the QSS post-processing routine described in Appendix B, based on the sub-scheme by Kathrotia et al. [190, 191] (see Table 6.1).

As in the turbulent partially premixed flame shown in Figure 6.9, the OH* distribution captures the global shape of the flame, but with an axial shift between the locations of the maxima of the two distributions, denoted by the green dashed (for HRR) and dotted (for OH*) lines. This further confirms that the peak shift is characteristic of premixed H_2–air flames, independently of the flame configuration under investigation.

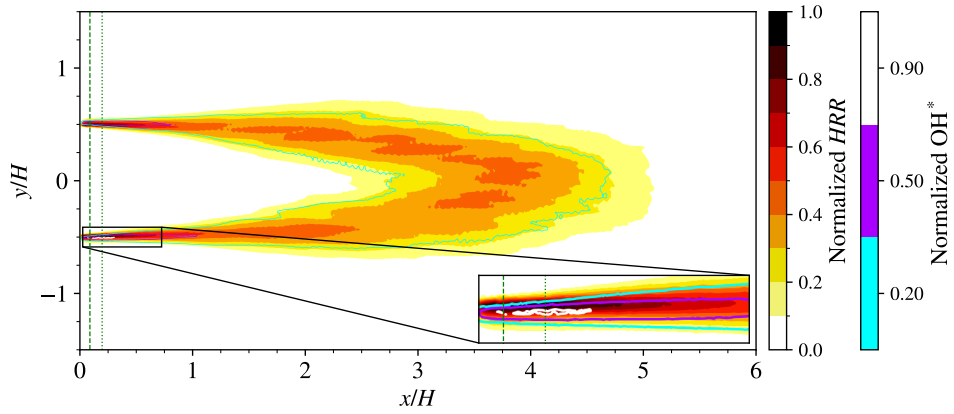

Figure G.1: Normalized distribution of HRR in the H25 slot hydrogen–air jet premixed flame at atmospheric conditions, together with isolines at 20%, 50% and 90% of normalized OH* concentration. The quantities are time-averaged over one flow-through time. The inset highlights the region of maximum HRR and OH*. The horizontal green lines highlight denote the axial peak positions of the HRR (dashed line) and OH* (dotted line) distributions.

The temporal correlation between the two quantities is investigated in Figure G.2. First, the intensities I of the volume-integrated HRR and OH*, normalized by their respective temporal means $\bar{I}$, are considered in Figure G.2a. Overall, coherently with the laminar case in Figure 9.16, the two signals show a good temporal correlation. This is further confirmed by the time derivatives of the two signals, reported in Figure G.2b. Nevertheless, as in the laminar case of Figure 9.16, some minor discrepancies arise in the instantaneous values.

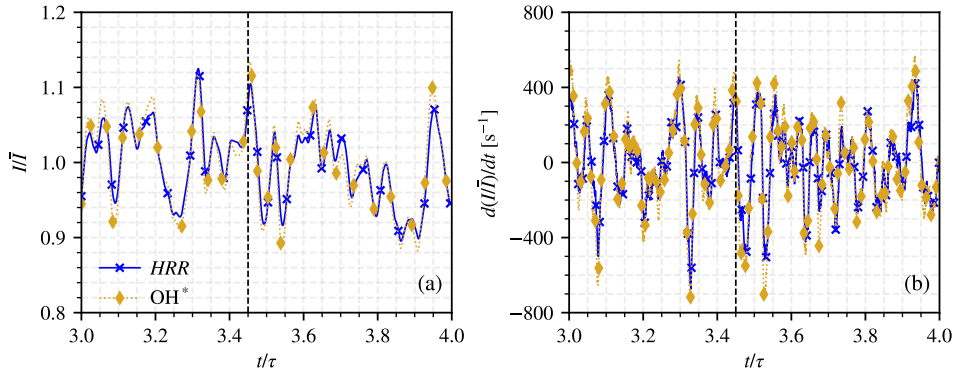

Figure G.2: Temporal signals of normalized HRR and OH* over one flow-through time τ (a), and corresponding time derivatives (b). The dashed vertical lines correspond to the snapshot in Figure G.3.

To clarify this aspect, Figure G.3 shows a representative instantanoeus normalized field of HRR, together with isolines of OH* at 20%, 50% and 90% of the maximum value, taken at $t/\tau = 3.45$, corresponding to the black dashed vertical lines in Figure G.1. Coherently with the laminar expanding flame in Figure 6.15 and with the acoustically forced M-shaped flame in Figure 9.17, also in this turbulent configuration the OH* is not able to accurately follow the strong local variation of HRR induced by TD effects and instabilities, leading to some discrepancies in the instantanoues signals.

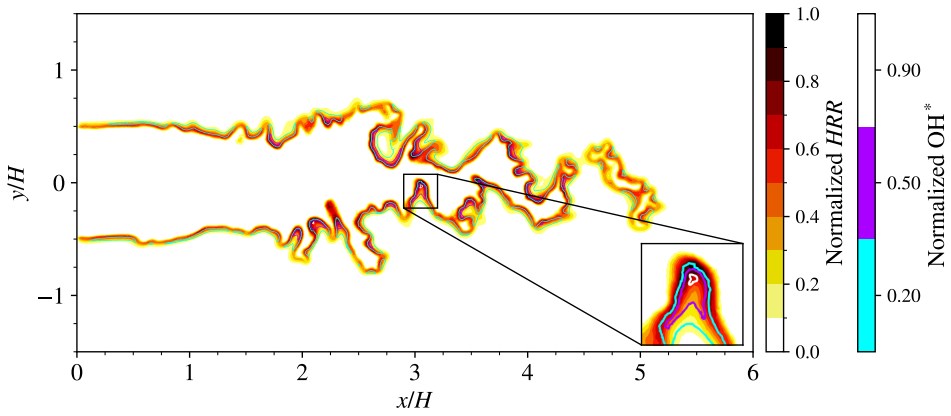

Figure G.3: Instantaneous normalized distributions of HRR in the H25 slot hydrogen–air jet premixed flame at atmospheric conditions, together with isolines at 20%, 50% and 90% of normalized OH^* concentration. The inset highlights the region of maximum HRR and OH^*.

This dissertation was typeset using LaTeX, originally developed by Leslie Lamport and based on Donald Knuth's TeX. The body text is set in 11-point Egenolff-Berner Garamond, a revival of Claude Garamont's humanist typeface. A template that can be used to format a PhD thesis with this look and feel has been released under the permissive MIT (X11) license and can be found online at github.com/suchow/Dissertate or from its author, Jordan Suchow, at suchow@post.harvard.edu. Said template has been rearranged and adapted in this dissertation for the Polytechnic University of Bari. The logo of the university is used under the Logo Usage Policy of the Polytechnic University of Bari.